Molecular Layer Deposition – Chemistry and Morphology of Thin Polyurethane Layers on native Metals

Dissertation

zur Erlangung des Grades des

Doktors der Ingenieurwissenschaften (Dr.-Ing.)

der Naturwissenschaftlich-Technischen Fakultät

der Universität des Saarlandes

von

Dipl.-Chem. Dipl.-Ing. Frank Fug

Saarbrücken 2022

Tag des Kolloquiums:	17. Februar 2023
Dekan:	Prof. Dr. Ludger Santen
Berichterstatter:	Prof. Dr. Wulff Possart
	Prof. Dr. Guido Kickelbick
Akademischer Mitarbeiter:	Dr.-Ing. Frank Aubertin
Vorsitz:	Prof. Karen Lienkamp

Acknowledgments

I would like to express my sincere thanks to Prof. Dr. Wulff Possart for his qualified support, his willingness to discuss and his experience on my way to becoming a scientist. Many thanks for all our discussions and support during difficult phases of this project.

I would like to thank my colleagues, Ludovic Krogh, Maren Weidner, Christophe Nies, Léo Depollier and Ernesto Sanchez for the intensive scientific exchange, the friendly cooperation and the pleasant and enjoyable time in the laboratory and at Polymeria.

Many thanks to the students Hendrik Jost, Christian Otto, Benjamin Gilbert, Adrien Petry, Morgane Andres, Aisha Ahmed and Claudius Pirro I supervised during my research. Thank you for the time, perseverance and commitment to bring forward the MLD research.

I thank our technicians, Peter Kohl, Werner Rauber and Jürgen Klesen, for their ingenious inventions, technical solutions and customised tools but also for the implementation of the MLD system.

For the support and unbureaucratic access to the scanning force microscope of the Chair of Prof. Dr. Motz I would like to thank Dr. Mohammad Zamanzade as well as the Chair of Prof. Dr. Mücklich for the visible light microscopy measurements.

I owe many thanks for the kind support by the German DFG (PO 577/23-1) and by the National Research Fund (FNR), Luxembourg within the project (3907394).

Finally, thank you to my partner, family and friends, who supported me throughout this long project.

Abstract

Polymers play an increasing role in thin films and coatings. The properties of such polymer layers can differ substantially from their bulk behaviour. Molecular Layer Deposition (MLD) is an emerging thin film deposition technique. In this work polyurethane (PU) layers are prepared by MLD onto native surfaces of Al and Cu oxides and their chemistry, morphology and stability are assessed.

Alcohol and isocyanate deposits show a significant different behaviour. Alcohols do only undergo weak physical interactions with the metal oxides as they rapidly desorb. Isocyanates form stable layers. Part of it undergoes a strong attachment to the substrate that involves the formation of urethane-like functionalities between the isocyanate groups and hydroxide/oxide from the metal surface.

Sequential deposition of isocyanate and alcohol reveal further singular properties. The topography of the layers is metal specific and dependant on the deposited alcohol and the deposition sequence. In each case rough deposits are achieved. Stability of all prepared layers against THF is poor. No crosslinked polymer network is formed but rather short-chained oligomers.

Significant improvement is achieved through increased storage temperature. Beside faster urethane formation, topography is much more homogeneous and stability is significantly better.

Kurzzusammenfassung

Polymere spielen in dünnen Beschichtungen eine immer größere Rolle. Die Eigenschaften solcher Polymerschichten können sich erheblich vom Bulk unterscheiden. Molecular Layer Deposition (MLD) ist eine neue Technik zur Abscheidung dünner Schichten. Polyurethanschichten (PU) werden mittels MLD auf nativen Oberflächen von Al- und Cu-Oxiden hergestellt und ihre Chemie, Morphologie und Stabilität bewertet.

Alkohol- und Isocyanatschichten zeigen ein deutlich unterschiedliches Verhalten. Alkohole gehen nur schwache physikalische Wechselwirkungen mit den Metalloxiden ein. Isocyanate bilden stabile Schichten. Ein Teil davon geht eine starke Bindung mit dem Substrat ein, bei der sich zwischen den Isocyanatgruppen und den Hydroxiden/Oxiden der Metalloberfläche urethanähnliche Funktionalitäten bilden.

Durch die sequentielle Abscheidung von Isocyanat und Alkohol werden weitere Eigenschaften sichtbar. Die Topographie der Schichten ist metallspezifisch und abhängig vom abgeschiedenen Alkohol und der Abscheidungsreihenfolge. In jedem Fall werden raue Schichten erzielt. Die Stabilität gegenüber THF ist schlecht. Es bildet sich kein Polymernetzwerk, sondern eher kurzkettige Oligomere.

Eine signifikante Verbesserung wird durch eine Erhöhung der Lagertemperatur erreicht. Neben der schnelleren Urethanbildung ist die Topographie wesentlich flacher und die Stabilität ist deutlich besser.

List of abbreviations

Al	Aluminium
ALD	Atomic Layer Deposition
AOM	Axis of the molecule
APTES	3-amino-propyl trietoxysilane
ATR	Attenuated Total Reflection
Au	Gold
BDO	2-butyne-1,4-diol
Cu	Copper
CVD	Chemical Vapour Deposition
DETA	Diethylene triamine
DF	Darkfield microscopy
DFT	Density Functional Theory
DIC	Differential interference microscopy
DICD	1,4-diisocyantato butane
DPG	Dipropylene glycol
DRIFT	Diffuse reflectance Fourier transform IR spectroscopy
ED	Ethylenediamine
EPDM	ethylene propylene diene rubber
ERAS	External Reflection Adsorption Spectroscopy
FFKM	Perfluoro elastomer
FTIR	Fourier transform infrared
Ge	Germanium
IR	Infrared
KBr	Potassium bromide
LAIP	Chair for Adhesion and Interphases in Polymers
LN_2	Liquid nitrogen
MCT	Mercury cadmium tellurite
MDI	methylene phenyl diisocyanate
MIR	Mid infrared region (4000 – 400 cm^{-1})
MLD	Molecular Layer Deposition

PD	1,4-phenylene diisocyanate
PID	Proportional-integral-derivative controller
POM	Plane of the molecule
p-polarised	Parallel polarisation respective to the plane of incidence
PTFE	Polytetrafluorethylene
PVC	Polyvinylchloride
PVD	Physical Vapour Deposition
QCM	Quartz Crystal Microbalance
QM	Quantum mechanical modelling
RT	Room temperature
SFM	Scanning Force Microscopy
Si	Silicon
s-polarised	Perpendicular polarisation respective to the plane of incidence
TAEA	tris-(2-aminoethyl)amine
TEM	Transmission electron microscopy
TETA	Triethylene tetramine
THF	Tetrahydrofuran
UHV	Ultra-high vacuum
VDP	Vapour Deposition Polymerisation
XPS	X-Ray photoelectron spectroscopy
ZnSe	Zinc selenide

Table of contents

1 Introduction 1

2 Problem statement and experimental approach 3
2.1 Problem statement 3
2.2 Experimental approach 5

3 Characterisation methods 7
3.1 Quartz Crystal Microbalance (QCM) 7
3.2 Infrared spectroscopy 12
3.2.1 Attenuated Total Reflection (ATR) 12
3.2.1.1 Experimental procedures 13
3.2.2 External Reflection Absorption Spectroscopy (ERAS) 15
3.2.2.1 Experimental procedures 19
3.2.3 Transmission 25
3.2.4 Processing of IR spectra 25
3.2.5 Comparison of IR spectra 28
3.2.6 Band assignment 29
3.3 Thermogravimetric analysis (TGA) 32
3.3.1 Experimental procedures 32
3.4 Optical microscopy 35
3.4.1 Differential interference contrast microscopy (DIC) 35
3.4.2 Dark-field microscopy (DF) 35
3.5 Scanning force microscopy (SFM) 36
3.5.1 Experimental procedures 38

4 Molecular Layer Deposition Setup 41
4.1 MLD principle in literature 41
4.2 MLD apparatus - requirements and features 44
4.2.1 Gas stage 46
4.2.2 Evaporation stage 48
4.2.3 Reactor chamber 54
4.2.4 Vacuum stage 56
4.3 Parameter definition for the MLD process 57
4.3.1 Influence of gas flow and pressure 57
4.3.2 Temperature influence 61
4.4 Experimental procedures 66

5 Components of the polyurethane system 73
5.1 Metal substrates 73
5.1.1 Aluminium 75
5.1.2 Copper 77
5.2 4,4-methylene diphenyl diisocyanate 79
5.2.1 Isocyanate chemistry 79
5.2.2 IR band assignment in the bulk 83
5.2.3 Thermal stability 93
5.3 The polyetherpolyols 96
5.3.1 IR band assignment in the bulk 97
5.3.2 Thermal stability 99
5.3.2.1 Dipropylene glycol 99
5.3.2.2 Polyethertriol K55 102
5.4 Tetrahydrofuran THF 104

6 Thin monomer deposits on metals 107
6.1 Literature review of interactions of monomer and polymer deposits with substrates 107
6.1.1 Layers prepared by MLD 107
6.1.2 Polyurethane layers prepared by other techniques 111
6.2 Properties and behaviour of the substrates 114
6.2.1 Impact of THF on the substrate 114
6.2.2 Effect of storage time in air 118
6.2.3 Influence of an MLD deposition cycle on the substrate state 121
6.2.4 Behaviour of the substrates - Conclusion 124
6.3 Reproducibility and stability of deposits 125
6.4 Thin layers of alcohols 130
6.4.1 Deposition behaviour 130
6.4.2 DPG layers on native metals 135
6.4.3 Triol layers on native metals 142
6.4.4 Intermediate conclusion 146
6.5 Thin layers of 4,4'-methylene diphenyl diisocyanate 149
6.5.1 Adsorption behaviour 149
6.5.2 Effect of the metal substrate 151
6.5.3 Impact of substrate temperature 165
6.5.3.1 Effect of temperature during storage after deposition 165
6.5.3.2 Influence of the substrate temperature during deposition 172
6.5.4 Intermediate conclusion 178
6.6 Conclusions 182

7 Thin polymer deposits 184
7.1 Implications from the monomer behaviour 184
7.2 Polyol deposit on top of a stable MDI deposit 186
7.2.1 Stable MDI deposits as prepared from solution 186
7.2.2 Deposition of few triol molecules on the stable MDI deposit 189
7.2.3 Higher amounts of triol onto the MDI deposit 193
7.2.4 Intermediate conclusion 201
7.3 Impact of polyol and deposition sequence 202
7.3.1 DPG deposited on top of 4,4'-MDI 204
7.3.1.1 Layer chemistry 204
7.3.1.2 Layer Topography 213
7.3.1.3 Urethane layer stability against THF 219
7.3.1.4 Intermediate conclusion 226
7.3.2 Deposition of triol instead of diol 231
7.3.2.1 Differences during storage time 231
7.3.2.2 Comparison of the deposits after 24 h of storage 234
7.3.2.3 Layer topography after storage 238
7.3.2.4 Layer stability towards THF 245
7.3.3 Intermediate conclusion 249
7.4 Temperature influence 251
7.4.1 Increased deposition temperature 252
7.4.2 Effect of increased storage temperature 255
7.4.3 Comparison of layer behaviour 258
7.4.4 Impact on topography 260
7.4.5 Conclusion on temperature influence 263
7.5 Outcomes for thin urethane layers prepared by MLD 264

8 Conclusion 267

9 Outlook 271

10 References 273

11 Appendix 291
11.1 Technical data on characterisation methods 291
11.1.1 Quartz crystal microbalance 291
11.1.2 Infrared spectroscopy 292
11.1.3 Thermogravimetric Analysis (TGA) 293
11.1.4 Scanning force microscopy (SFM) 294
11.2 Technical data on substrate preparation 295
11.3 Physical properties of the monomers 296
11.3.1 4,4'-methylene diphenyl diisocyanate (4,4'-MDI) 296
11.3.2 Dipropylene glycol (DPG) 296
11.3.3 Baygal®K55 296
11.3.4 Tetrahydrofuran (THF) 297
11.4 Technical Data of the MLD apparatus 298
11.4.1 Pipes and tubing 298
11.4.2 Evaporation unit 298
11.4.3 Reactor chamber 300
11.5 Thin monomer deposits 301
11.5.1 DPG layers on native Cu 301
11.5.2 Triol layers on native Cu 303
11.5.3 4,4'-MDI layers on native Cu 306
11.5.4 Temperature influence on 4,4'-MDI layers 308
11.6 Thin polymer deposits 313
11.6.1 DPG deposited on top of 4,4'-MDI on Cu 313
11.6.2 Triol deposited on top of 4,4'-MDI on Al 314
11.6.3 Triol deposited on top of 4,4'-MDI on Cu 316
11.6.4 4,4'-MDI deposited on top of triol on Al 319
11.6.5 4,4'-MDI deposited on top of triol on Cu 322

1 Introduction

The development of new products and technologies with particular properties requires new materials. Beside bulk materials, combinations of materials are used more and more. In sandwich and composite materials properties of each single material can often be combined allowing an increased range of applications. The combination of materials considerably extends the performance range beyond that of each single component. This is not only true for bulk materials but also applies for thin layers and coatings. Even more such thin films can exhibit particular features that differ from the bulk material. Improved functionality of existing products, creation of nanostructured coatings and nanocomposites as well as ecological aspects like reduced consumption of rare materials and of power are a few advantages of such coatings [1].

Over the 20th century many techniques were developed and made significant technologic developments possible such as magnetic recording media, integrated circuits, LEDs, optical coatings, hard coatings on cutting tools, thin film solar cells and batteries to name a few. Not only does the material itself but also its preparation techniques greatly influence its properties [2-4]. Many thin film deposition techniques were first focussed on classic metallic and inorganic coatings. Over the last decades the development progressively extended to organometallic hybrid layers and organic deposits.

The preparation of new materials using thin films requires adequate deposition techniques. Thus new methods needs to be developed or existing methods can be extended to other materials.

Polymers are another class of materials that play an increasing role in thin films and coatings. The properties of thin and ultra-thin polymer layers can differ substantially from their bulk behaviour. This is due, in part, to the increasing influence of confinement as well as the influence of the interactions between the polymer constituents and substrate or atmosphere. Physical depositions of polymers as Langmuir-Blodgett, Dip and Spin coating but also chemical deposition techniques as Chemical Vapour Deposition (CVD) or Plasma enhanced polymerisation are current thin polymer film preparation techniques. Molecular Layer Deposition (MLD) is an emerging polymer deposition technique and adapts the principle of atomic layer deposition (ALD). In this case two bifunctional monomers are separately evaporated and sequentially deposited onto the surface to be coated. The polymerisation reaction only then takes place and the polymer chains progressively form. In contrast to the aforementioned techniques where polymers are arbitrarily formed, MLD promises a much better control on the polymerisation process. So far report on this technique is scarce in literature and no technical application is available yet.

In a first part of this work, the MLD apparatus is set up and the influence of the major parameters is analysed. This knowledge on the deposition system enables to understand and control the processes during layer preparation.

Second, beside the control of the deposition itself it is crucial to understand what happens during layer formation and that requires adequate layer characterisation. Assessment of the layer chemistry, morphology and stability provide a link between deposition parameters and properties of the layer. Thus, from these results the MLD regime can be optimised further. Successful layer preparation is only possible with the combination of both parts.

In this work both aspects are investigated in order to prepare thin polyurethane layers on native metal surfaces. Polyurethane (PU) represents a technically versatile polymer. By varying its components a wide range of properties and thus applications are feasible as for example as structural adhesives, foams, lacquers, coatings and paints to name a few [5].

Polyurethanes are prepared by polyaddition of an alcohol with an isocyanate. If both monomers possess only two functional groups (i.e. alcohol or isocyanate) linear chains are obtained. Higher functionalities will lead to PU networks. The choice for each monomer (number of functionalities and chain length) greatly influences the morphology of the obtained polymer and thus its properties. Besides this versatility the study of thin PU layers offers further potential outcomes.

MLD of polyurethanes has only scarcely been reported in literature and profound characterisation of the obtained polymer is missing. Preparation of polymer networks with this technique has not been reported at all. The results from this work provide new knowledge on the influence of the monomers towards network formation (e. g. different conformal flexibility) and thus on controlling the structure of the formed layer.

Moreover, the substrate plays an important role. It is shown that monomers as well as the formed PU undergo chemical interactions with the substrate. This is crucial for the stability of the prepared layers. From an application point of view good practical adhesion of the coating is required in order to be viable. Although quite different polymers prepared by MLD are being reported, this question has only been answered insufficiently. Especially for polyurethanes where the fundamental adhesion mechanisms on metals have not been fully understood yet, preparation of thin and ultra-thin layers gives access to these interactions. As the stability of our obtained layers is also characterised, the outcomes of this work can contribute to other polyurethane applications like adhesion science.

Finally, the obtained results are compared to thin PU layers prepared by spin coating or adsorption from solution in order to correlate research outcomes and find complementary results.

2 Problem statement and experimental approach

The main objective of this work consists in providing a proof of principle for the preparation of thin polyurethane layers on native aluminium and copper by means of gas phase deposition. Section 2.1 frames the objectives and the aims of this work. Section 2.2 provides a more detailed view of the chosen experimental approach and the classification of the different chapters.

2.1 Problem statement

The first aim of this work consists to set up a Molecular Layer Deposition apparatus. As a viable technical application is not available yet requirements of such a complex system has first to be defined. As gases of monomers are led through pipes contamination of the MLD system is possible through condensation of the monomers on cold walls for example. Hence, avoidance of contamination has also to be considered during this phase. Based on the requirements and features of the MLD system a multitude of parameters is obtained, which can influence the layer deposition. Hence, the interdependency and the precision of these parameters must be determined as well as their importance on the later layer deposition.

Once the parameters identified a suitable experimental procedure for layer deposition has to be developed. This procedure should allow controlled and reproducible deposits.

As second step polyurethane layers are prepared and characterised. Polyurethane has been chosen for several reasons. First, this polymer exhibits versatile properties that can be adjusted by the choice of the polyisocyanate and alcohol but also by the preparation process [5]. PU is also utilised in a large variety of applications ranging from thin polymer coatings to foams, sealants and adhesives. Previous work aimed on the characterisation of the intermolecular interactions and morphology of thin PU films (e. g. [6, 7]) provides valuable information on the chemistry of thin PU layers in contact with native metals but also profound research on the characterisation methods of thin films. Other work was aimed at the characterisation of ultra-thin monomer adsorbates from solution (e. g. [8-11]) and revealed specific monomer-metal adhesive interactions. Furthermore stable PU networks were achieved that withstand tetrahydrofuran (THF) rinses. Thus, these studies confirmed that in principle thin PU layers can be achieved. This complementary work will allow to draw parallels between solvent based and gas phase deposition and validate previous findings by using other methods.

In order to be able to prepare PU layers with MLD several steps are however necessary.

First, the behaviour of each monomer has to be studied. Especially their evaporation ability and thermal stability have to be verified as monomers are now evaporated in the MLD. Thermal decomposition or undesired chemical side reactions should be avoided. Commercially available monomers contain besides the base component also a variety of additives and fillers in order to adapt the polymer properties for a given application. During the evaporation step these additives can interfere with the monomer evaporation.

The measurement of the deposited amount of molecules in the reactor chamber of the MLD can however not distinguish between monomers or other molecules. Hence, in order to facilitate the characterisation, monomers with a minimum of additives are used. They are chosen in order to provide a high technical relevance. The lack of additives also ensures a general validity of the results as they are not distorted by the additives. For comparability with previous work 4,4'-methylene diphenyl diisocyanate (MDI) and Baygal® K55 polyol (referred as triol) is used. Furthermore, dipropylene glycol (DPG) is also used in order to prepare a non-crosslinked PU.

The substrates are prepared with high purity aluminium and copper deposited by physical vapour deposition (PVD) on silicon wafers. This allows for a reproducible preparation of flat and smooth surfaces, which is required for the chosen characterisation methods. As the prepared substrates are stored under air atmosphere native layers of oxide and hydroxide but also adsorbates of water and ambient contaminations are formed.

Thin monomer layers are prepared and characterised in terms of chemistry using infrared spectroscopy (FTIR-ERAS) and morphology using differential interference contrast microscopy (DIC) and scanning force microscopy (SFM). Stability of the layers is probed by sequential solvent rinses using THF. Removal of weakly attached molecules allows accessing the strong adhesive interactions with the metal substrate. Good stability is the key for a strongly attached PU layer and hence good performance of the prepared layer.

As the substrates are in contact with ambient air and nitrogen in the MLD for prolonged times, adsorption of contaminants from the ambient has not to be neglected and could possibly modify the adsorption behaviour of the monomers compared to layers prepared from solution adsorption. Indeed, during solvent deposition the solvent can remove the contaminants, which is not the case in the MLD. Strictly speaking, the nitrogen gas is the solvent in the MLD. Hence, MLD blank tests should provide some insights on the adsorption of contaminants throughout the complete experimental procedure.

Once the monomer deposits are characterised and the deposition regime optimised PU layers can be prepared by sequential deposition of isocyanate and alcohol. The deposition sequence and quantity will be dependent from the previously obtained results. Characterisation of the layers is performed similarly as for the monomer layers. The achieved stability towards THF rinses and hence the formation of strong metal polymer interactions is crucial at this stage in order to obtain polymer layers with good performance. If required, improvements of the deposition regime are performed in order to achieve better layers. It is reminded that this study aims to provide a proof of principle for PU-MLD layers and thus screening of all possible properties (as for example mechanical tests, glass transition, refractive index, etc.) of the prepared layers is not considered here and left open for further advanced studies.

2.2 Experimental approach

The characterisation of thin polymer layers deposited on metal substrates requires several adequate methods. Chapter 3 highlights the necessary principles of the used characterisation methods as well as the general experimental procedures.

During layer preparation in the MLD a quartz crystal microbalance is used as a tool to control the amount of deposited material. Its principle but also its limitations are detailed in section 3.1.

The characterisation of the adsorbed molecules, their interactions with the substrate and between each other as well as chemical reactions is realised with IR spectroscopy (Section 3.2). Using FTIR with the external reflection adsorption setup (ERAS) the thin layer is integrally measured over its thickness.

In order to probe the stability of the achieved layers and hence their performance they are rinsed several times with tetrahydrofuran (THF). These rinses remove weakly attached molecules and allow characterising the remaining material and hence the interactions between the deposited molecules and the metal substrates.

The bulk monomers are characterised using attenuated total reflection (IR-ATR). Spectra obtained by ATR and ERAS possess different optical situations and cannot be directly compared. Hence, spectra calculation based on the optical laws is necessary and outlined in this section. Furthermore, general spectra processing used in this thesis is also detailed.

Finally, spectra interpretation requires a precise band assignment. As band catalogues are not precise enough, results from quantum mechanical modelling is also used.

The thermal stability and the evaporability of the chosen monomers are verified by thermogravimetric analysis (TGA) coupled with IR transmission (section 3.3). The analysis of the gases allows to verify that no significant thermal degradation takes place.

Section 3.4 and 3.5 details the methods used for the characterisation of the topography of the layers either by optical means (differential interference contrast optical microscopy – DIC and dark field microscopy - DF) or by scanning force microscopy (SFM).

In chapter 4 the MLD apparatus, its requirements and features are detailed. Literature review regarding molecular layer deposition and its related deposition techniques provides a technical background for the requirements of the MLD. A layer growth model is presented and critically discussed. Furthermore major process parameters are identified and their interdependency studied. Finally an adequate experimental procedure is developed for this customised setup.

The chosen isocyanate and alcohols as well as the metal substrates are outlined in Chapter 5. Bulk properties and thermal stability of the monomers are analysed and possible reactions outlined.

In chapter 6 the behaviour of each monomer as thin deposit is analysed. Literature review of preparation of monomer layers on metals and characterisation of their interactions provides a solid background for the interpretation of the measured IR spectra. Blank tests realised for the different steps in the preparation procedure (THF rinses, MLD deposition and IR chamber storage) are necessary to identify the role and behaviour of adsorbed contaminants from the ambient. Each monomer is analysed regarding its deposition behaviour, stability and possible desorption, nature and strength of the chemical interactions with the substrate, influence of the metal as well as the morphology of the layer. The influence of the variation of relevant layer preparation parameters on these features is if necessary also studied. The aim of this chapter is however not to study the influence of each MLD parameter on the layer. The achieved results allow an optimisation of the deposition and the development of a deposition procedure for the polymer layer. Furthermore, a layer model that takes the observed behaviour into account can be proposed.

From the behaviour of each monomer layer an adequate strategy has to be developed in chapter 7 before preparing PU layers. A first step is to verify that sequentially deposited isocyanates and alcohols are capable to attach to the substrate and hence form a stable layer. From here various PU layers can be prepared by varying the deposited alcohol and the deposition sequence. Variation of deposition parameters should be only done under consideration of their impact on the behaviour of each monomer. Similarly to the previous chapter the chemistry and stability of the prepared layers are characterised using IR spectroscopy. Topography is analysed by SFM, DIC and DF. The previously introduced layer model can then be updated. The obtained results should provide a proof of principle that PU layers can successfully be prepared by MLD.

Chapter 8 summarises the main results of this work while open questions and further research are outlined in chapter 9.

3 Characterisation methods

The essential characterisation methods used in this work are detailed. They start with infrared spectroscopy and thermal analysis for the characterisation of the bulk monomers. Deposition of the evaporated monomers onto a substrate in the MLD apparatus is monitored by a quartz crystal microbalance. Chemistry and morphology of the obtained monomer and resulting polymer layers are characterised with IR spectroscopy, optical and scanning force microscopy.

3.1 Quartz Crystal Microbalance (QCM)

In the late 1950s the quartz crystal microbalance was developed. A thin disk of α-quartz with electrodes on both sides (Fig. 3-1c) is commonly used in QCMs. Due to the piezoelectric properties and the specific crystalline orientation of the quartz (Fig. 3-1a, b), application of a voltage between both electrodes causes a deformation of the crystal plate [12, 13]. Depending on the orientation of the cut through the crystal various transversal, longitudinal or torsional deformations are obtained. The most commonly used AT-cut[1] yields a shear deformation (Fig. 3-2). The crystal plate is electrically excited at its resonance frequency, f_0, generating a standing wave across the thickness of the plate [15].

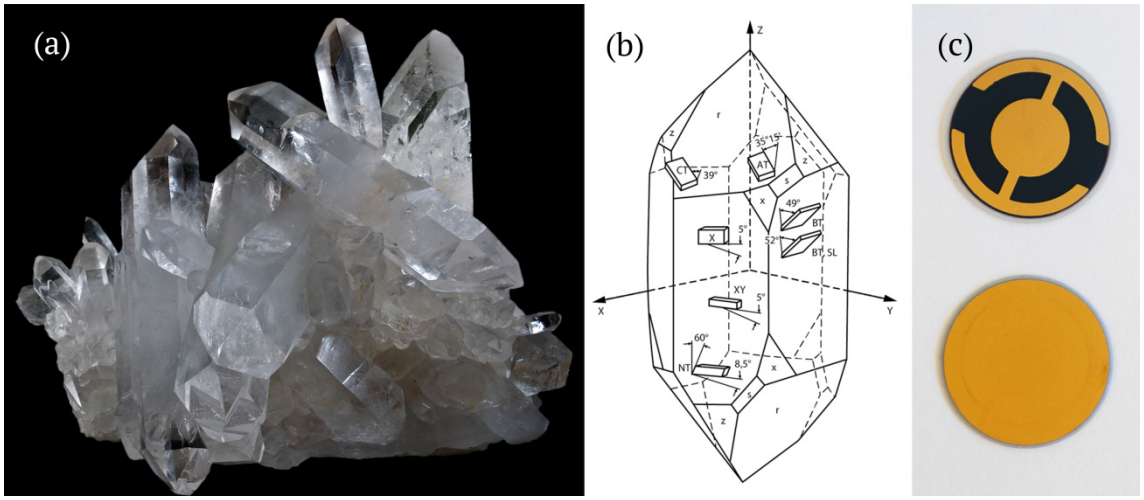

Fig. 3-1 (a) Rock type natural α-quartz crystals [16], (b) Cut orientations [14] and (c) top and bottom view of QCM quartz plates with gold electrodes.

[1] **AT**-cut: The **A**mbient **T**emperature crystal cut has a low temperature coefficient at room temperature [14]. In this work RC-cut crystals are used. They possess similar properties to AT-cut crystals.

Sauerbrey showed that changes in resonance frequency are related to mass change on the crystal. He introduced a relationship between mass difference, Δm, and frequency change, Δf - c.f. eq. (3.1), thus allowing to obtain a measure of the added or removed mass [17, 18]. Monitoring the mass growth with QCM during deposition regimes of PVD, ALD, CVD etc. is nowadays routine.

$$\Delta m = -\Delta f \cdot A_Q \cdot \frac{\sqrt{\mu_Q \cdot \rho_Q}}{2 \cdot f_0} \tag{3.1}$$

with

$$\Delta f = f - f_0 \tag{3.2}$$

and the mass difference, Δm [g], the quartz surface area, A_Q [cm^2], density, ρ_Q $\left[\frac{g}{cm^3}\right]$ and shear modulus, μ_Q $\left[\frac{g}{cm \cdot s^2}\right]$, of the quartz.

However, some assumptions need to be verified for this relation to be valid [19] and in order to obtain a reliable mass. First, a deposited layer on the quartz has to be rigid. This applies well for metal layers but not necessarily for molecular layers and polymers. As the shear deformation occurs (c. f Fig. 3-2) non rigid layers may respond by a retarded deformation and will also have a shear modulus that is different from the quartz.

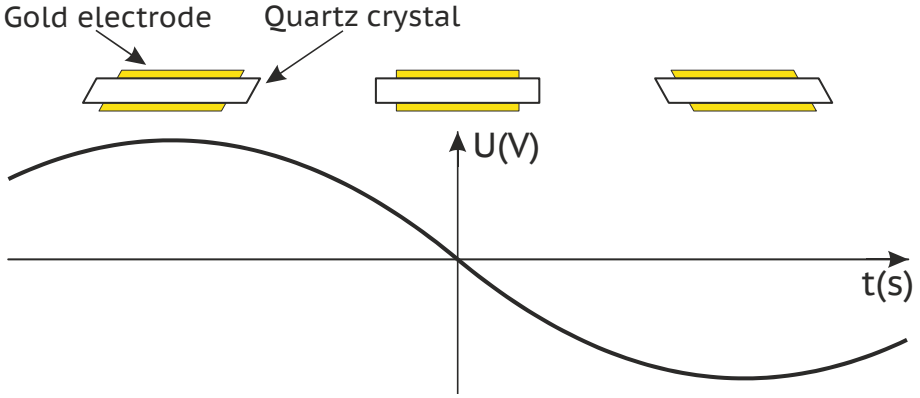

Fig. 3-2 Shear deformation of an AT- (or RC-) cut quartz crystal when a sinusoidal voltage is applied between both gold electrodes.

Second, the ratio of mass change, Δm, due to the deposited layer and mass of the crystal, m_Q, must be small:

$$\frac{\Delta m}{m_Q} \leq 0.02 \tag{3.3}$$

This condition is fulfilled as only thin layers in the nanometre range are to be deposited. Third, related to the previous condition, the frequency change, Δf, has to be small, which is also true in our case:

$$\frac{\Delta f}{f_0} < 0.05 \tag{3.4}$$

Using Sauerbrey's equation (3.1) the mass of the deposited material is obtained. Thickness, Δd, of the layer is calculated in a next step:

$$\Delta d = \frac{\Delta m}{A_{layer} \cdot \rho_{layer}} \tag{3.5}$$

with surface area, A_{layer}, and density, ρ_{layer}, of the deposited layer.

In order to obtain accurate values the real surface area of the layer and its density are needed. The real surface area could be obtained by using the roughness of the quartz crystal and assuming that the deposited layer is homogeneous and exactly reproduces that roughness. This has to be proven by scanning force microscopy for example. Second, the density of the prepared layer is unknown. Due to defects in the molecular packaging of the layer, one has to assume that the density of the layer is smaller than in the condensed phase.

To make things more complicated, the resonance frequency, f_0, of the quartz plate not only depends on the deposited mass, Δf_m, but from many other factors. For example, [20-22] state that f_0 is also influenced by environmental pressure causing a Δf_p, viscosity and density of the deposited material resulting in Δf_v, roughness with Δf_r and temperature producing Δf_T:

$$\Delta f = \Delta f_m + \Delta f_p + \Delta f_v + \Delta f_r + \Delta f_T \tag{3.6}$$

For the developed MLD apparatus, effects of pressure and temperature are to be pointed out:

Frequency increases linearly with pressure:

$$\Delta f_p = C_p \cdot P \tag{3.7}$$

with C_p a crystal-specific constant that is gas independent.

The temperature dependency is given as:

$$\Delta f_T = -C_T \cdot f_0 \cdot \Delta T \tag{3.8}$$

where C_T depends on the design and preparation of the quartz plates. For AT-cut crystals with typical dimensions[2] the frequency shift is about -2.4 Hz/K [21]. Depending on the cutting angle the C_T value is limited to a defined temperature range. Although AT-cut crystals are claimed to have low temperature sensitivity, their Δf_T shift is not negligible when preparing layers in the nanometre range.

[2] Typical dimensions are 5 mm radius, 0.2 mm thickness and f_0 = 6 MHz.

Beyond the linear range the frequency shift increases and becomes nonlinear. The temperature and pressure effects on our QCM setup within the MLD will be discussed in more detail in chapter 4.3.

It has also to be noted that adsorption may differ between the gold-plated QCM quartz on one hand and the very smooth metal coated silicon wafer that is used as substrate for layer preparation.

In conclusion, a quantitative mass measurement is difficult and would require a very precise mass calibration. As the exact relationship between the deposited molecules and the resulting total frequency shift is affected by unknown variables as the density, coupling with quartz plate, surface and morphology of the obtained layer, the indicated thicknesses by the QCM has to be taken with caution. However, if the preparation parameters of the layer remain identical, Δm and hence Δd can nevertheless be used as a control parameter to reproduce the deposition process and monitor the layer growth. In this work A_{layer} and A_Q are defined as being the geometrical surface, A_{geo}, of the quartz. The density of the obtained layers, ρ_{layer}, is set to the density of the deposited monomer, ρ_{Mono}. Thus equation (3.5) is approximated by

$$\Delta d = \frac{\Delta m}{A_{geo} \cdot \rho_{Mono}} \tag{3.9}$$

The installed QCM (*Inficon SQC 310*) inside the MLD reactor chamber is composed of three components that are linked together using coaxial cables:

◊ *Quartz crystal and quartz crystal holder assembly*

The AT-cut type quartz is coated on both sides with gold electrodes (Fig. 3-1c, parameters given in the Appendix 11.1.1). It is placed in the quartz crystal holder (Fig. 3-3) and fixed by gold plated springs. They are also utilised as electrical contact with the upper side electrode. The hole in the crystal holder has a diameter of 8.1 mm and is smaller than the diameter of the quartz (14 mm). Thus the geometric surface, A_{geo} = 0.52 cm^2, where molecules can adsorb corresponds to the region of the quartz that is exposed to the reactor chamber through that hole.

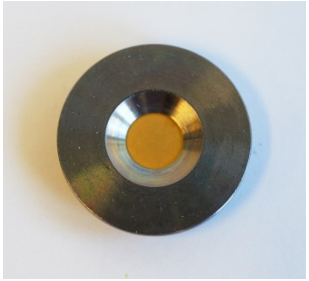

Fig. 3-3 Top view of the quartz crystal holder with attached QCM quartz.

The quartz holder is easily placed and removed from the reactor chamber. The holder with the quartz is placed inside the crystal holder assembly where further springs make electrical contact with the lower face of the crystal. The assembly accommodates electrical tubing as well as two pipes for cooling or heating. These tubes pass through a vacuum flange in order to be connected outside of the reactor chamber and enabling vacuum inside the MLD apparatus.

◊ *Oscillator and controller*

The oscillator is connected on one side with the crystal holder assembly and on the other side with the controller. The controller determines the resonance frequency of the quartz and is connected to the computer.

The oscillator and the controller are placed in a thermally insulating box. The temperature inside that box is kept constant using a PID controlled heater in order to avoid any frequency drift due to temperature changes in the electronics. Temperature effects on the QCM electronics are discussed in more detail in chapter 4.3.2.

Further information on the topic of the Quartz Crystal Microbalance can be found in [23-27].

3.2 Infrared spectroscopy

Mid Infrared spectroscopy (MIR) utilises absorption of electromagnetic radiation in matter in the wavenumber range of 4000 – 400 cm^{-1}. Absorption of infrared light enhances the amplitude of vibrational and rotational modes of intramolecular motion and is seen as bands in the IR spectra. That absorption only takes place if it goes with a change in the dipole moment of the given mode. The features of the IR absorption bands (position, intensity, width and shape) give indirect information on the chemical structure of the sample, inter- and intramolecular interactions, molecular orientation (for example in thin films using polarised light). Infrared spectroscopy also allows for monitoring of chemical reactions and their kinetics.

In the next paragraphs the different IR techniques used throughout this work are briefly outlined as well as band assignment and processing of obtained spectra.

3.2.1 Attenuated Total Reflection (ATR)

The bulk properties of the studied monomers and related components are characterised by IR-ATR spectroscopy. It is based on the internal reflection of IR light (e. g. [28-30]). The path of the IR light is shown in Fig. 3-4.

The light passing through an optically denser material, $\hat{n}_{crystal}(\tilde{\nu})$, is totally reflected at the plane interface to an optically thinner material, $\hat{n}_{sample}(\tilde{\nu})$, provided the angle of incidence, φ_1, is equal or larger than the critical angle of total reflection, φ_c. For non-adsorbing materials this angle is defined as:

$$\varphi_c = \arcsin\left(\frac{n_{sample}}{n_{crystal}}\right) \tag{3.10}$$

When $\varphi_1 > \varphi_c$, an evanescent wave with exponential decay of the electric field strength is formed at the interface between both materials (e. g. [29]).

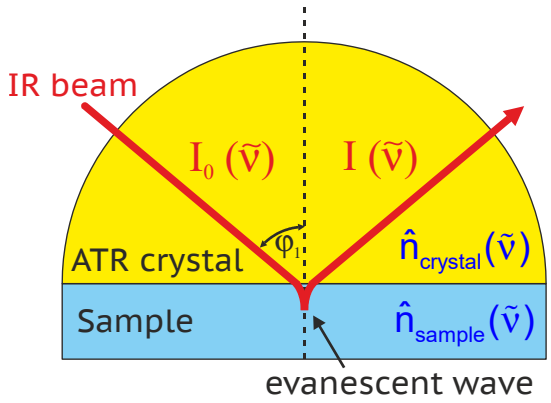

Fig. 3-4 Optical configuration of the attenuated total reflection (ATR) using a hemi-spherical internal reflection element (yellow); based on [7].

Typical materials for the IR internal reflection unit are ZnSe and Ge. Both exhibit high refractive indices (n = 2.4 for ZnSe and n = 4 for Ge) compared to organic materials (typically n ≈ 1.5). In this work a ZnSe hemisphere is used as ATR crystal[3].

The penetration depth, d_p, of the evanescent wave can be approximated as (for $\varphi_1 > \varphi_c$ and n_{sample} is non-adsorbing IR light [31]):

$$d_p = \frac{1}{2 \cdot \pi \cdot \tilde{\nu} \cdot \sqrt{n_{crystal}^2 \sin^2 \varphi_1 - n_{sample}^2}} \tag{3.11}$$

with the wavenumber, $\tilde{\nu}$, of the light. In the MID IR, d_p is between approx. 2.5 and 25 µm. Calculation of the penetration depth for adsorbing materials is more complicated and needs the definition of an effective thickness as described in detail in [29]. This leads to smaller d_p values. Although ATR is described in literature [32] as surface sensitive method, d_p is by far larger than thin films of a few nanometers. From equation (3.11) it is obvious that d_p is dependent of the wavenumber, thus smaller wavenumbers give deeper penetration and thus more intense bands.

3.2.1.1 Experimental procedures

Prior to any measurement, the ZnSe crystal, its holder and the sample cell (cf. Fig. 3-5) are carefully cleaned with acetone and dried in a dry air stream. If necessary the sample cell is in addition cleaned in an ultrasonic bath. After the crystal is reattached to its holder an IR single beam reference spectrum (REF) is recorded.

An angle of incidence of 60 ° with p-polarised light is chosen for all experiments. Further parameters of the ATR measurements are given in Appendix 11.1.2.

Two experimental setups are used for the IR-ATR measurement depending on the state of bulk monomer at room temperature.

[3] The used ZnSe crystal has a cubic symmetry and thus isotropic optical properties.

◊ *Liquid monomers*

For liquid monomers the sample cell with attached pipes (Fig. 3-5a, cf. [33]) is utilised. The cell is pressed against the crystal by a screw and sealed with an EPDM[4] O-ring (Fig. 3-5b+c). Now, the monomer is injected via one of the pipes into the cell with a glass syringe (Fig. 3-5d). The second pipe is also fitted to a syringe without piston and serves as overflow. For full optical contact between the monomer and the ZnSe, air bubbles must not remain inside the cell. This is achieved by pumping the liquid back and forth while tilting the assembly. Once the cell is filled with liquid the syringes are removed and both pipes are closed with PTFE plugs.

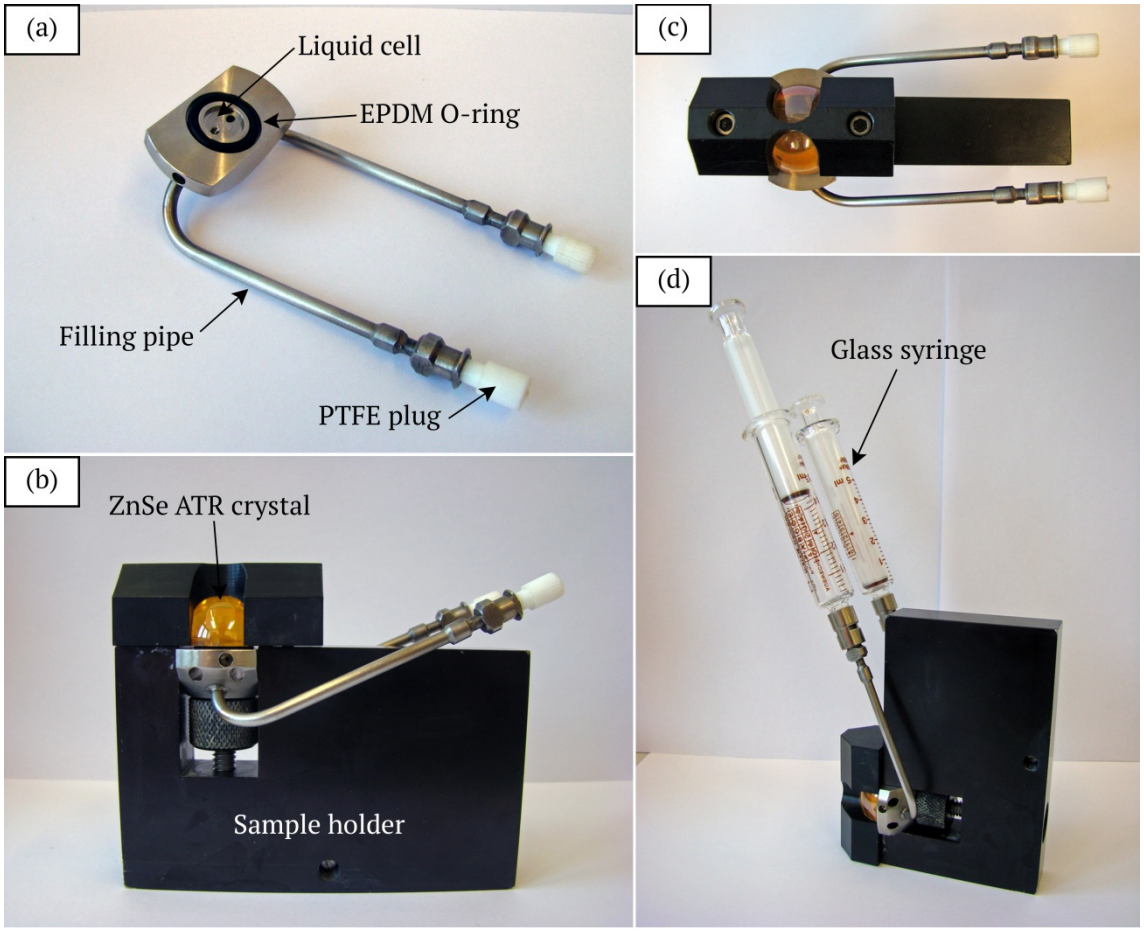

Fig. 3-5 (a) Liquid sample cell with PTFE plugs, sample cell pressed against ZnSe ATR crystal – (b) side and (c) top view, (d) sample assembly with vertically attached glass syringes for optimal filling.

[4] EPDM - Ethylene propylene diene rubber.

◊ *Solid monomers*

Solid monomers are characterised in the molten state. A sample cell without tubes is used (Fig. 3-6a) in order to avoid clogging of the pipes by solidification. Therefore, after measurement of the reference spectrum for the assembled crystal holder with crystal, sample cell and a glass vial with the monomer are heated in an oven at 80 °C[5].

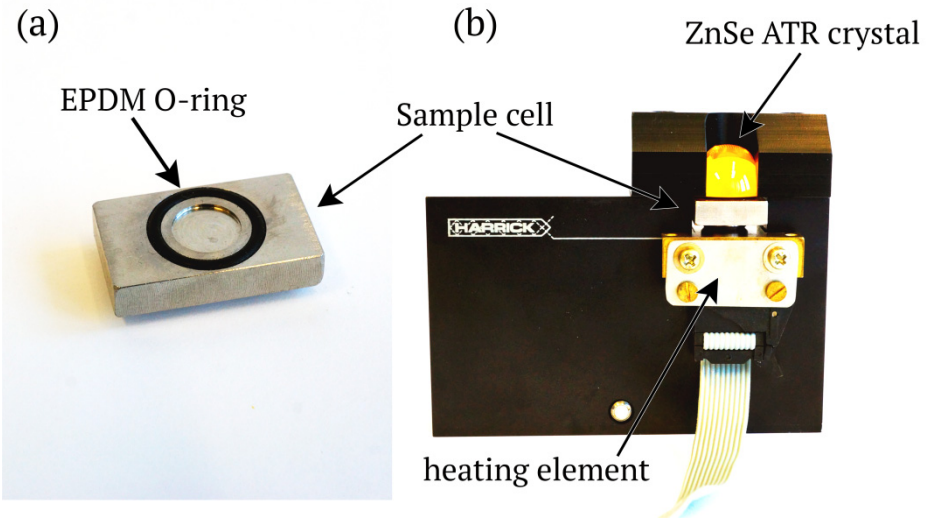

Fig. 3-6 (a) Solid sample cell, (b) Sample cell and heating element pressed against ZnSe ATR crystal.

The molten substance is then filled into the tempered sample cell and rapidly pressed against the ZnSe crystal. Again the absence of trapped air bubbles is checked. A preheated electric heater (60 °C) is then put in place underneath the sample cell and fixed with a metal spacer (Fig. 3-6b). This avoids solidification during the IR measurement.

Once the assembly is completed it is transferred into the measurement chamber of the spectrometer. An IR sample single beam spectrum (SAM) is then recorded.

3.2.2 External Reflection Absorption Spectroscopy (ERAS)

Thin organic layers on a metal substrate are characterised by IR-ERAS. This technique is sensitive for adsorbed molecules in the mono- and sub-monolayer range as well (e.g. [6, 8-10, 33-48]). The optical path and typical setup for ERAS is shown in Fig. 3-7. Prerequisite is a smooth, plane and reflective substrate.

[5] This temperature is higher than the melting temperature of the monomer to avoid solidification during filling and installation of the sample cell into the crystal holder.

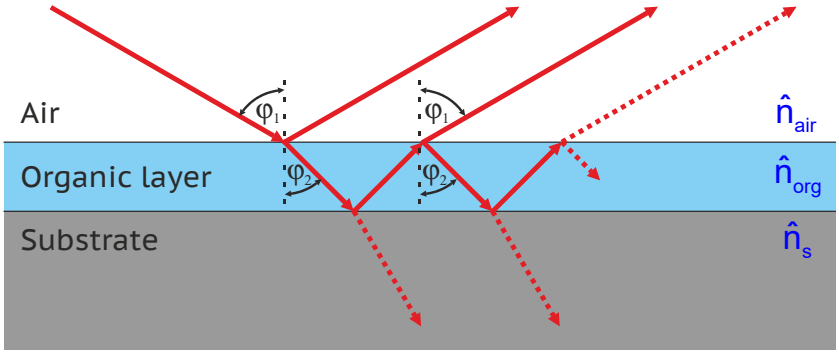

Fig. 3-7 Optical configuration of the external reflection absorption spectroscopy (ERAS); based on [7].

As the optical path of the IR light is complex in this setup each step is detailed hereafter. Fig. 3-8 details the different electric field vectors on the optical path. At first, polarisation of the IR beam is not considered.

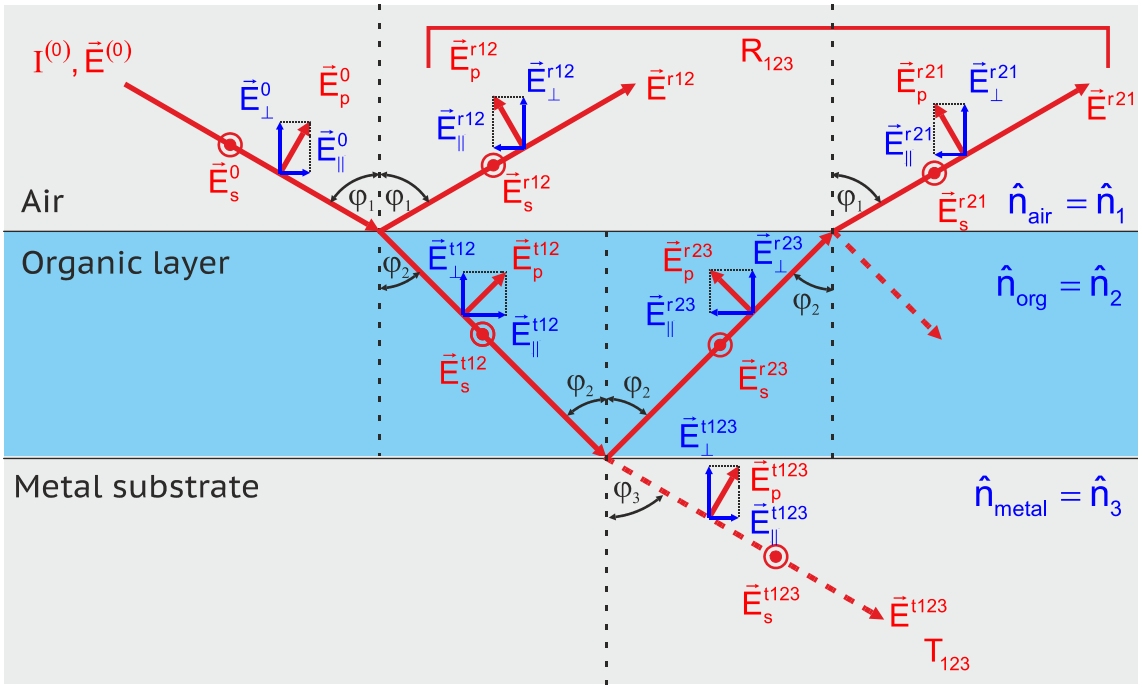

Fig. 3-8 Reflection and transmission of an electromagnetic wave on a three layer model; incident (0), reflected (r) and transmitted (t) electric field vectors $\vec{E}$ with s- and p-polarised parts; based on [7].

The incident IR beam $\vec{E}^0$ passes through the air in the spectrometer and arrives at the interface with the organic layer at an angle of incidence of φ_1. Here one part is reflected as $\vec{E}^{r12}$ and the other part, $\vec{E}^{t12}$, is transmitted into the organic layer with an angle φ_2.The angle φ_2 of the transmitted light is correlated with φ_1, $\hat{n}_{air}$ and $\hat{n}_{org}$ through Snellius' law (3.12)

$$\frac{\sin\varphi_1}{\sin\varphi_2} = \frac{\hat{n}_{org}}{\hat{n}_{air}} \tag{3.12}$$

As the refractive index $\hat{n}_{org}$ of the organic layer is larger than $\hat{n}_{air}$, it results that $\varphi_2 < \varphi_1$.

The transmitted part of the light, $\vec{E}^{t12}$, continues its path through the organic layer until it arrives at the interface with the metal substrate. Here again one part, $\vec{E}^{r23}$, is reflected back into to organic layer while the other part, $\vec{E}^{t123}$, is transmitted into the substrate. As only reflected light is measured with the ERAS setup, latter part of the light is lost. Similarly as for the interface air/organic layer the angle φ_3 is correlated with φ_2, $\hat{n}_{org}$ and $\hat{n}_{metal}$ through Snellius' law (3.13)

$$\frac{\sin\varphi_2}{\sin\varphi_3} = \frac{\hat{n}_{metal}}{\hat{n}_{org}} \tag{3.13}$$

The reflected part of the IR beam, $\vec{E}^{r23}$, passes again through the organic layer and reaches the interface with the air[6]. Here too, one part is reflected back into the organic layer while the other part is transmitted into the air as $\vec{E}^{r21}$. With high IR intensities and high quality organic layers further multiple reflections occur. As the IR beams reflected towards the detector ($\vec{E}^{r12}$ and $\vec{E}^{r21}$) possess different optical path length a phase difference appears an hence interference occur. The resultant reflection coefficient, $\hat{r}_{123}$, is obtained from equation (3.14) [7, 49]

$$\hat{r}_{123} = \frac{\hat{r}_{12} + \hat{r}_{23} \cdot e^{2 \cdot i \cdot \beta}}{1 - \hat{r}_{21} \cdot \hat{r}_{23} \cdot e^{2 \cdot i \cdot \beta}} \tag{3.14}$$

with the reflection coefficient, $\hat{r}_{i,j}$, at the interface between medium i and j[7] and

the optical phase thickness, β,

$$\beta = 2\pi \cdot \nu \cdot d \cdot \sqrt{\hat{n}_{org}^2 - \hat{n}_{air}^2 \cdot \sin^2(\varphi_1)} \tag{3.15}$$

with the organic layer thickness, *d*.

The overall reflectivity, R_{123}, is related with the reflection coefficient, $\hat{r}_{123}$, through equation (3.16) as only IR intensities are measured.

$$R_{123} = \left|\hat{r}_{123}\right| \tag{3.16}$$

Instead of using non polarised light the incident IR beam can be either polarised perpendicular (s-polarisation) or parallel (p-polarised) to the plane of incidence.

[6] As this part passes through the organic layer ist could also be named as $\vec{E}^{t23}$.

[7] The reflection coefficient is calculated using the Fresnel equations, which correspond to the ratio of the reflected eletric field vector, $\vec{E}^{rij}$, to the incident electric field vector, $\vec{E}^{0ij}$.

In this case polarisation specific electric field vectors of either s-polarised ($\vec{E}_s^0$, $\vec{E}_s^{r12}$, $\vec{E}_s^{t12}$, etc.) or p-polarised ($\vec{E}_p^0$, $\vec{E}_p^{r12}$, $\vec{E}_r^{t12}$, etc.) light has to be taken into account. The resulting reflection coefficients, $\hat{r}_{123}^s$ and $\hat{r}_{123}^p$ are obtained from equation (3.14) by using the appropriate $\hat{r}_{i,j}^s$ and $\hat{r}_{i,j}^p$.

One limitation exists however. On metal substrates an incident electric field will generate an image electric field - Fig. 3-9. Electric field components that exhibit a vector parallel to the metal surface will generate an induced antiparallel electric field vector in the metal. Hence, this deletes the resulting electric field and there is no light to provide any spectral information from the organic layer. This is the case for s-polarised light. In the case of vectors perpendicular to the metal surface parallel electric field vectors are generated, which doubles the resulting amplitude.

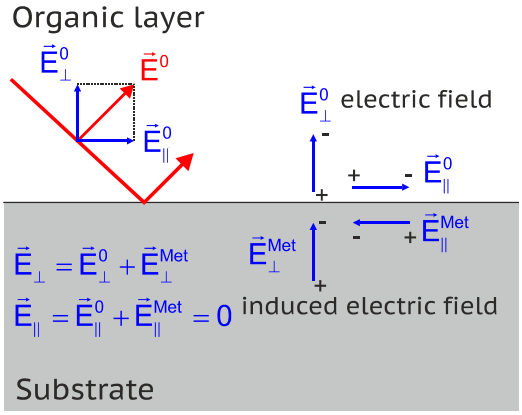

Fig. 3-9 Formation of image electric field vectors in a metal substrate.

Furthermore all p-polarised electric field vectors can be split into a perpendicular ($\vec{E}_\perp^0$, $\vec{E}_\perp^{rij}$ and $\vec{E}_\perp^{tij}$) and parallel ($\vec{E}_\parallel^0$, $\vec{E}_\parallel^{rij}$ and $\vec{E}_\parallel^{tij}$) vector with respect to the substrate plane (Fig. 3-8 – blue vectors). Only the perpendicular part, $\vec{E}_\perp^x$ gains information about the layer as the parallel part, $\vec{E}_\parallel^x$, is also cancelled out. Hence, the resulting $\hat{r}_{123}^p$ needs to take this into account.

In order to maximise IR band adsorption $\vec{E}_\perp^x$ should be increased. This means, that the angle of incidence, φ_1, of the IR beam is increased to a grazing angle. As $\vec{E}_\perp^x$ increases, $\vec{E}_\parallel^x$ is reduced.

Transition dipole moments induced by the vibrational modes of molecules also interact with the metal. Indeed, different orientations of molecules on a metal surface and thus different orientations of the transition dipole moments will lead to the formation of image dipoles in the metal substrate as represented in Fig. 3-10. The resulting overall dipole moment is in both extreme cases either doubled (Fig. 3-10a) or completely cancelled out (Fig. 3-10b). Intermediate positions are not shown but present of course.

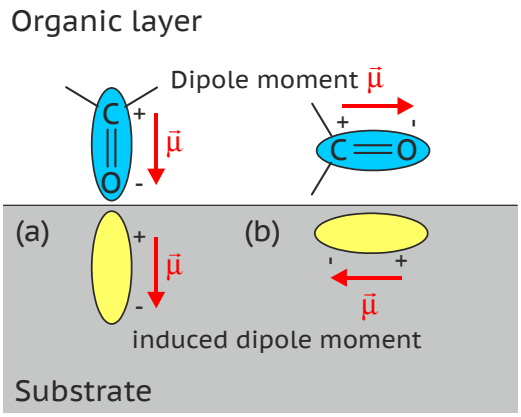

Fig. 3-10 Formation of counter dipoles in a metal substrate as polarisable functional groups take particular orientations. Extreme cases when the dipole is (a) perpendicular or (b) parallel to the metal surface; based on [36].

As consequence the IR adsorption intensity, which is related to the magnitudes of the transition dipole moment, the electric field and the concentration - equation (3.17) is changed for that particular vibration.

$$I \propto \left|\vec{E}\right| \cdot \left|\vec{E} \cdot \Delta\vec{\mu}\right| \cdot c \tag{3.17}$$

As IR light is only adsorbed for the cases where $\Delta\vec{\mu}$ not $\perp$ to $\vec{E}$ and $\Delta\vec{\mu} > 0$ polarised light helps to further discriminate orientations. As example if relative band intensities are different between a thin layer and a bulk spectrum of the same material preferential orientation of the molecules on the substrate is possible.

Finally, one aspect has been omitted so far. As technical relevant substrates are to be used, the metal is covered by a thin oxide layer. Hence, the previous layer models should be extended to a four-layer model. Calculations in [50] showed that these thin oxide layers do not significantly modify the electric field vectors arriving at the detector. Hence, the three layer model shown previously is sufficient at this point.

3.2.2.1 Experimental procedures

The customised sample holder is represented in Fig. 3-11. It is based on a similar sample holder used in [33, 36]. It is composed of a L-shaped support that snugly fits into the measuring chamber of the spectrometer. On that support a height adjustable sample plate holder is attached[8].

[8] The height of the sample plate holder is adjusted in order to maximize the reflected light intensity. Once set, the position is fixed with the screws and is not modified anymore.

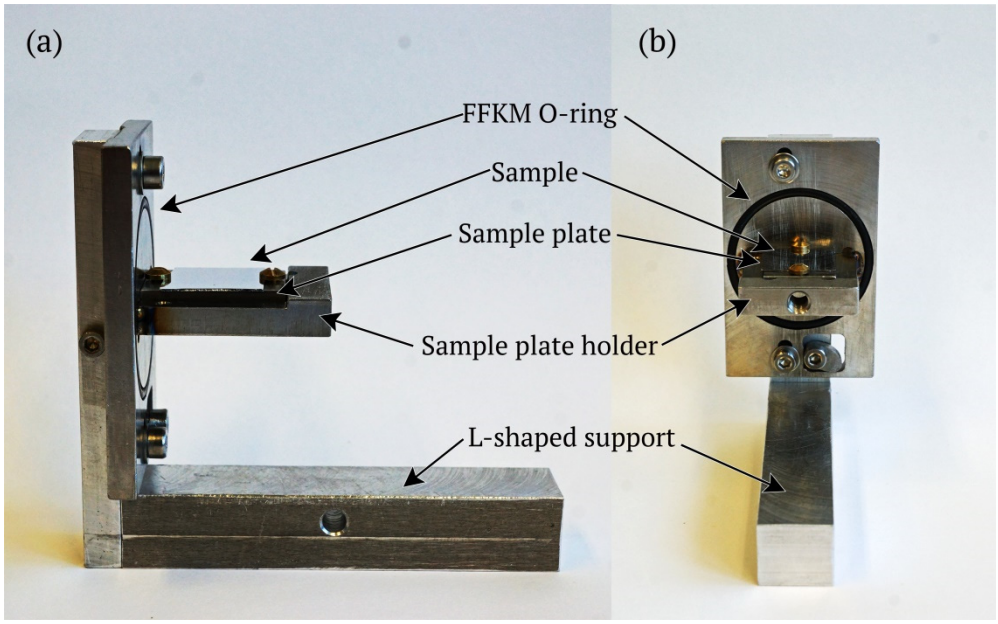

Fig. 3-11 Customised ERAS sample holder. (a) Side view and (b) front view.

The sample is mounted on a sample plate (Fig. 3-12) and attached with two screws. This sample plate also fits into the MLD reactor chamber. The sample plate is placed on the sample plate holder. This assembly ensures that the sample has nearly the same position in the IR spectrometer before and after layer preparation in the MLD. Inexact positioning of the sample leads to undesired wavy artefacts in the IR spectrum which can corrupt the adsorption bands.

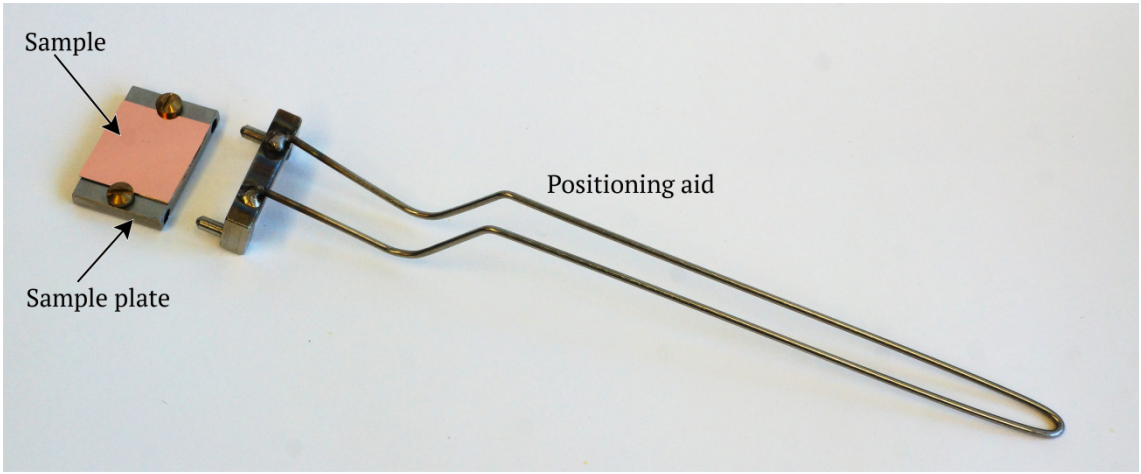

Fig. 3-12 Sample plate with fixed substrate. The positioning aid helps to place the sample plate into the MLD reactor and into the sample plate holder

For rinsing the sample with solvent, a rinsing cylinder can be mounted onto the sample holder – Fig. 3-13. This cylinder is sealed at the backplate with a FFKM[9] O-ring. At the front side two flexible tubes can be fitted at the tube clips in order to inject solvent by a syringe.

[9] FFKM - perfluorated elastomer.

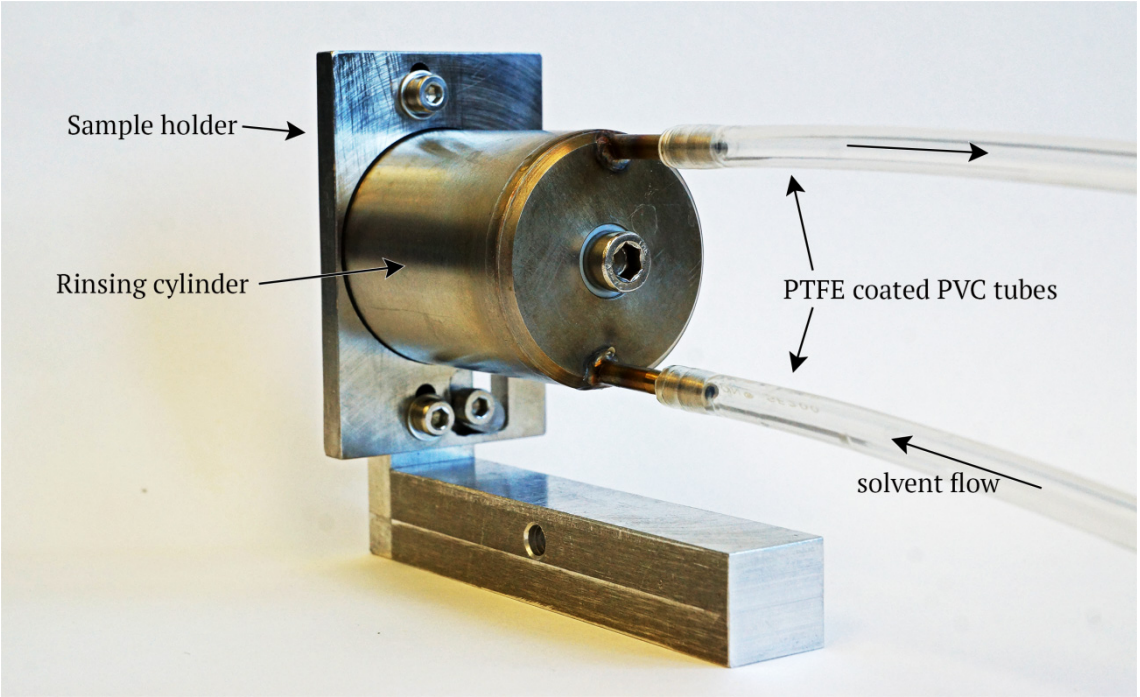

Fig. 3-13 Sample holder with attached rinsing cylinder with two PTFE coated PVC tubes. The cylinder is filled with solvent via the lower tube.

The following steps are performed for each experiment:

◊ *Step 1: Cleaning*

Prior to any measurement the complete assembly is cleaned with solvents. The support with sample plate holder and unscrewed cylinder are rinsed with acetone. The sample plate and its two screws are cleaned with THF in an ultrasonic bath for 5 to 10 min. and then rinsed with fresh THF. The PTFE coated PVC pipes are carefully cleaned with acetone.

All parts are dried with pressurised clean air in order to remove any remains of solvent. Two 100 ml glass syringes and other necessary glassware are cleaned with soapy water, followed by acetone rinse.

◊ *Step 2: 1st reference spectrum*

Once all parts are cleaned and dry, the metal coated Si-wafer square is placed on the sample plate and fixed with the screws. To avoid breaking the Si-wafer they are only lightly tied down[10]. The sample plate with sample is then placed on the sample plate holder using the positioning aid shown in Fig. 3-12. As a small clearance is present between sample plate and holder it is crucial to push the plate against one of the long sides as well as the back side. This defines the reference position for the further measurements. The whole assembly is then placed into the measuring chamber of the IR spectrometer.

[10] Nevertheless, the sample should not move during further handling.

The position of the sample plate is rechecked and adjusted if necessary. A 1st reference single beam spectrum (REF-1) is then recorded for the bare substrate. The measurement parameters are given in Appendix 11.1.2.

◊ *Step 3: THF rinse and 2nd reference spectrum*

Although all substrates are prepared following a fixed regime it is important to prepare the organic layers on a reproducible starting state of the metal surface. Thus the metal surface is rinsed with THF prior deposition. After the 1st reference the sample assembly is removed from the measurement chamber[11] and attached to the table using a metal clamp. The rinsing cylinder is then screwed onto the sample holder. The tube links are placed vertically. A flexible PVC tube with inner PTFE lining is attached to each tube clip. At the other end of the tubes a glass syringe is joined. The glass syringes are clamped to a metal stand and kept vertical and above the cylinder as shown in Fig. 3-14.

The syringe at the lower tube clip is filled with 60 ml of THF. The solvent is then pumped inside the cylinder until it arrives in the second syringe. The THF remains in the cell for 1 min. then it is pumped back into the first syringe. This pumping procedure is repeated two more times. Thus the substrate is rinsed 3 times for 1 min. with THF. This rinsing step removes those molecules from the substrate surface that prefer to dissolve into THF. Once all THF is pumped back into the lower syringe, the syringes are removed. Dried air is then blown through the cylinder for 20 min. (10 min. through each tube clip) allowing complete removal of remaining THF. The cylinder is then removed and the sample holder transferred into the spectrometer. The sample plate position is adjusted if necessary. A 2nd reference single beam spectrum (REF-2) is then recorded for the rinsed bare substrate. This substrate spectrum serves as reference for all following IR spectra. In order to minimise sample positioning errors, the maximum intensity value at the top of the bell-shaped single beam spectrum is controlled (at about 1815 cm^{-1}).

[11] Ideally the THF rinse should be performed inside the spectrometer in order to reduce the risk of sample misplacement. But in our case the sample chamber is narrow and deep which makes the correct attachment of the rinsing cylinder awkward. Furthermore, as the sample has to be removed and placed in the MLD reactor for the layer preparation, repositioning for the spectrometer is inevitable.

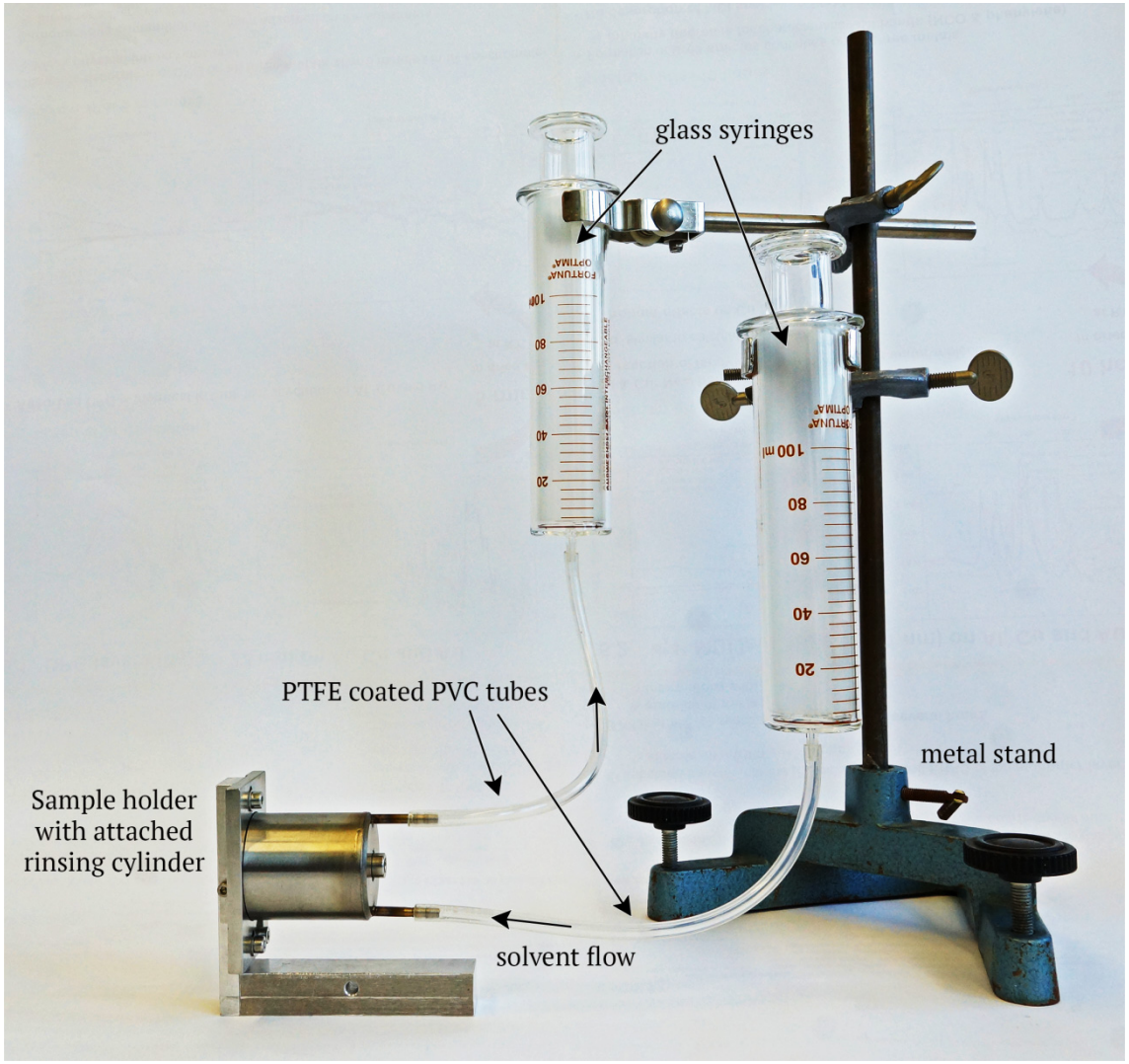

Fig. 3-14 Sample holder with rinsing cylinder attached to the two glass syringes. The right syringe is filled with solvent which is then pumped into the cylinder. The exceeding solvent flows through the upper pipe into the left syringe.

◊ *Step 4: Organic layer deposition and characterisation*

The sample plate with attached substrate is removed from the sample holder and transferred into the MLD reactor for deposition. After layer preparation (detailed procedure is outlined in chapter 4.4) the sample plate is mounted on the sample holder and put into the spectrometer again. The position of the sample is carefully adjusted until the maximum intensity of the single beam spectrum is as close as possible to the value for the REF-2 spectrum. Only then sample spectra (SAM) are recorded. Measurements from a few minutes up to several days are possible. This is detailed later in each specific chapter.

If the organic layer is prepared by adsorption from a diluted monomer solution, similar steps as for the 2nd reference rinse are applied. The sample cell with the substrate is removed from the spectrometer, the cylinder and the syringes are attached. The lower syringe is filled with 60 ml monomer solution which is then injected inside the cylinder.

This solution remains in contact with the substrate for 3 min. and then removed. During this period molecules adsorb on the metal surface. A new syringe, filled with 60 ml of fresh THF is then attached to the lower tube and injected and maintained in the cylinder for 1 min. This removes the dissolvable part of adsorbed monomer molecules. After THF removal the cylinder is purged with dried air for 20 min. The sample assembly is transferred back into the spectrometer, the position of the sample is adjusted as described above and sample spectra are recorded.

Sample temperature can be varied inside the spectrometer by a heating plate which is attached underneath the sample plate holder (Fig. 3-15). Contact with the sample plate is achieved without altering its vertical position. The heater is preheated at the chosen temperature before contact with the sample plate. The heater must be removed when performing THF rinses.

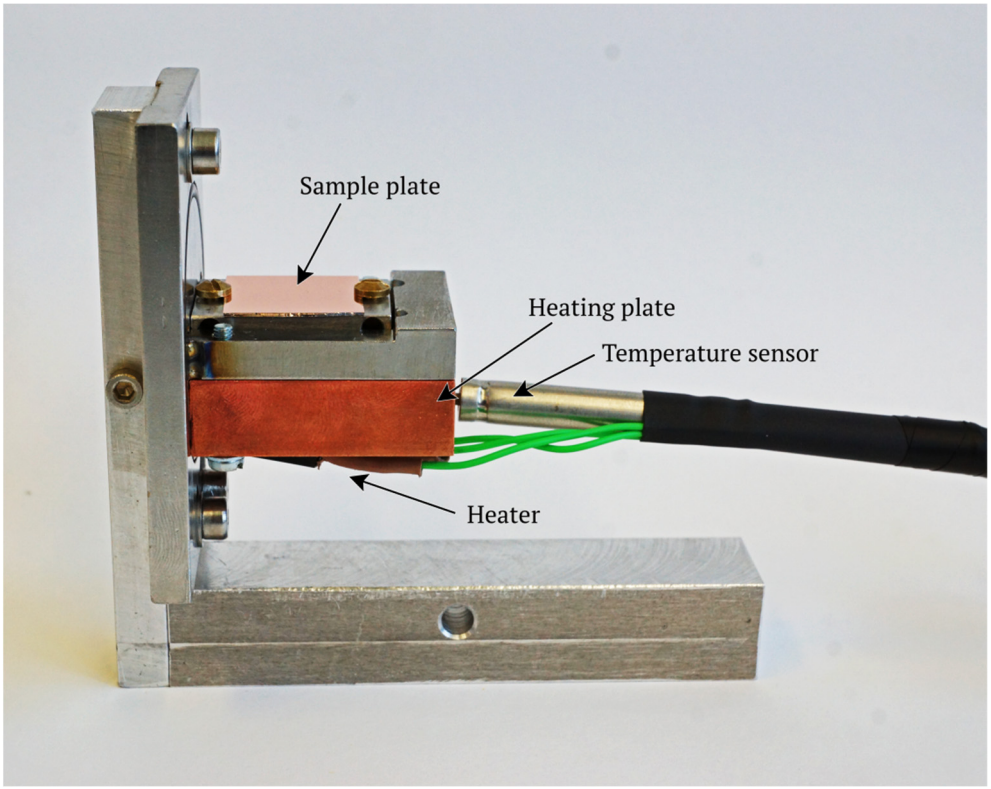

Fig. 3-15 Sample holder with attached heater.

◊ *Step 5: Stability testing towards a solvent*

In order to assess the adsorption strength of the deposited molecules further THF rinses are applied. The setup is the same as described in the previous paragraphs. The sample is exposed to the THF for 1 min. and then removed. The cylinder is purged with dried air for 20 min. and the sample is measured by ERAS again (1st THF rinse). More of these rinsing steps follow (2nd, 3rd THF rinse and so forth). Step by step, they wash weakly bonded molecules (i.e. physisorbed) away from the substrate while strongly bonded (e.g. chemisorbed) molecules remain and are characterised by the corresponding reflectance spectra. The rinses are continued until the IR spectra of two subsequent rinses do not significantly change. At that point a stable layer is achieved.

3.2.3 Transmission

A TGA[12] - IR transmission spectroscopy hyphenation is utilised to characterise the thermal stability of the monomers. In this apparatus the gases evolving from the crucible in the TGA are transferred into a transmission gas cell as shown in Fig. 3-16. The cell and the transfer tube from the TGA are heated to 200 °C to avoid condensation.

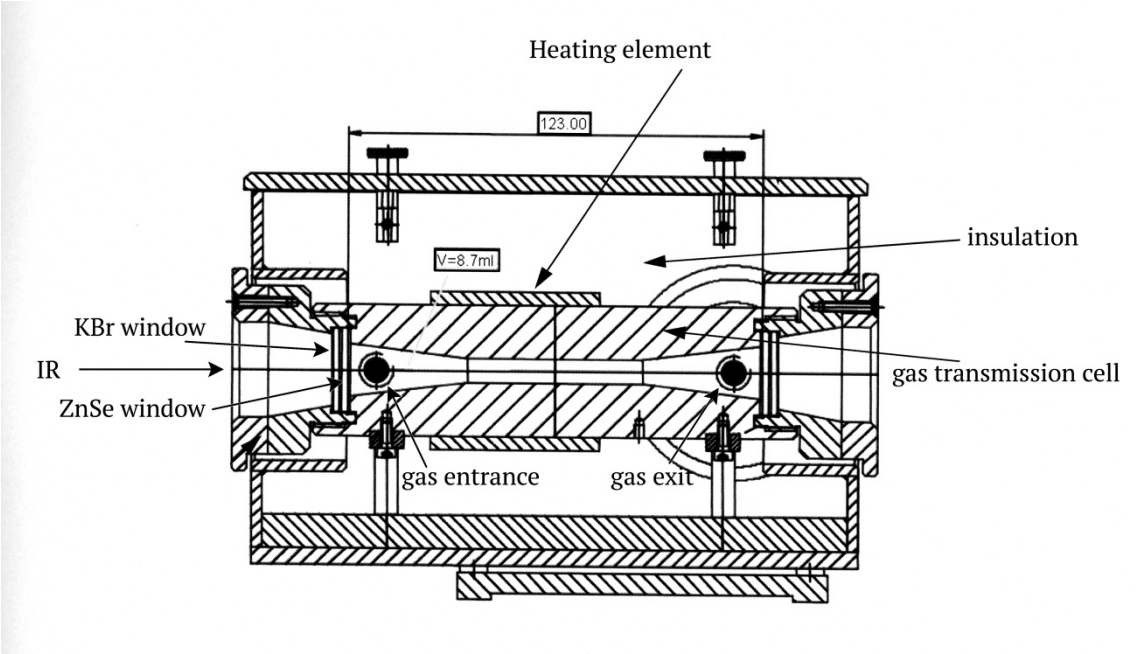

Fig. 3-16 Cross section of the IR Transmission gas cell; based on [51].

As the IR transmission measurements are part of the TGA analysis of the monomers, the experimental procedure for the IR survey is described in chapter 3.3.1 and the measurement parameters are given in Appendix 11.1.3.

3.2.4 Processing of IR spectra

The single beam IR spectra obtained in the transmission, ATR and ERA spectroscopy modes, include characteristic IR light adsorption peaks from the interaction of the sample with the IR light. However, water and CO_2 present in the air but also any contaminants in the IR light path (e.g. mirrors or windows) also lead to characteristic peaks. In order to remove all influences from the spectrometer itself (IR source, mirrors and absorbing substances in the light path) the sample single beam spectra (SAM) are divided by a related reference single beam spectrum (REF) in order to obtain a reflectance or transmittance spectrum.

[12] TGA - thermogravimetric analysis

◊ *Atmospheric correction of IR spectra*

Gaseous contaminants in the air (mainly H_2O and CO_2) are reduced by using dried CO_2 purified air. As the concentration of gaseous CO_2 and H_2O can vary over time, slight differences between REF and SAM spectra lead to adsorption peaks of these species. Especially for the weak spectra from thin layers characterised with ERAS this can hamper band identification.

Two spectral regions are particularly affected. In the region at 2350 – 2200 cm^{-1} the modes ν_a-CO_2 and the ν_a-NCO of isocyanates are very close. Gaseous water exhibits a multitude of sharp peaks between 4000 and 3200 cm^{-1} as well as between 2000 and 1300 cm^{-1}. Latter region is particularly crucial as many bands of the monomers and the urethane groups also appear here.

In order to reduce the parasitic bands, modified[13] spectra of gaseous water and carbon dioxide (e.g. R_{H_2O}; Fig. 3-17b) are subtracted from the reflectance/transmittance spectra $R_{original}$. The intensity of the contamination spectra is scaled by a factor, x, in order to cancel band intensities out:

$$R_{corr} = R_{original} - x \cdot R_{H_2O} \tag{3.18}$$

Correction spectra are recorded for each IR technique using the same spectrometer configuration as used for the sample measurements.

We note in passing that such spectra corrections are never perfect and thus slight residual CO_2 and H_2O bands can remain. This can distort band shape of weak bands and thus needs to be kept in mind for later discussion.

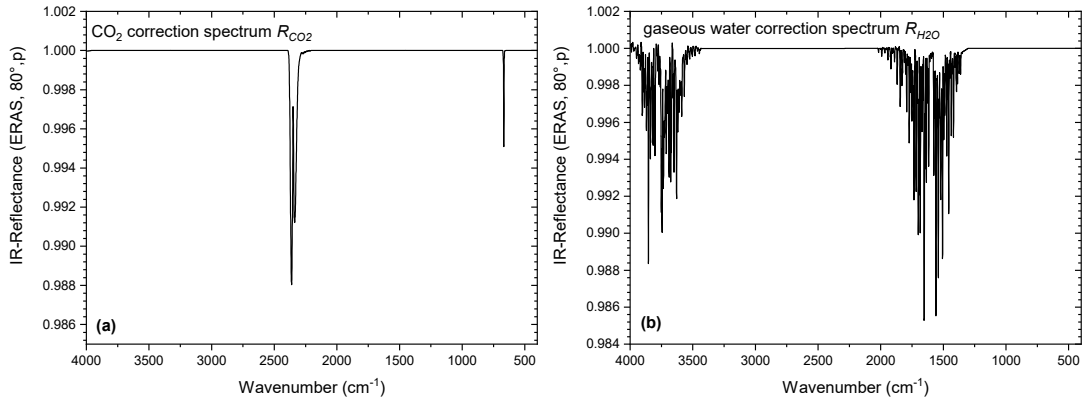

Fig. 3-17 Modified ERA correction spectra of (a) CO_2 and (b) gaseous water.

[13] A spectrum of H_2O and CO_2 is modified in such a way that only the bands of the contaminants are present. The baseline in between is set as straight line.

◊ *Baseline adjustment*

Due to reflectivity changes of the samples or fluctuations in IR source intensity and detector stability slight intensity differences occur in the associated REF and SAM single beam spectra. Hence division of SAM by REF results in a baseline shift. For better comparison between different spectra, their baselines are therefore shifted[14] vertically to 1.0 at a given wavenumber. The position for this setting is chosen in a region where no bands are present and baselines are horizontal.

In most cases, spectra had to be shifted differently for each spectral region. Atmospheric correction and baseline adjustment are performed on nearly all spectra shown in this work without further notice.

Sometimes, bands or spectral regions are stretched individually to similar band intensity for better comparison of band shapes. This particular processing is mentioned for the respective spectra.

◊ *Particular features*

Three more features in the presented IR spectra have to be mentioned here. First, many spectra contain a sharp spike as an artefact at 1340 cm^{-1} – Fig. 3-18a. This artefact is electronic by origin and does not affect the rest of the spectrum.

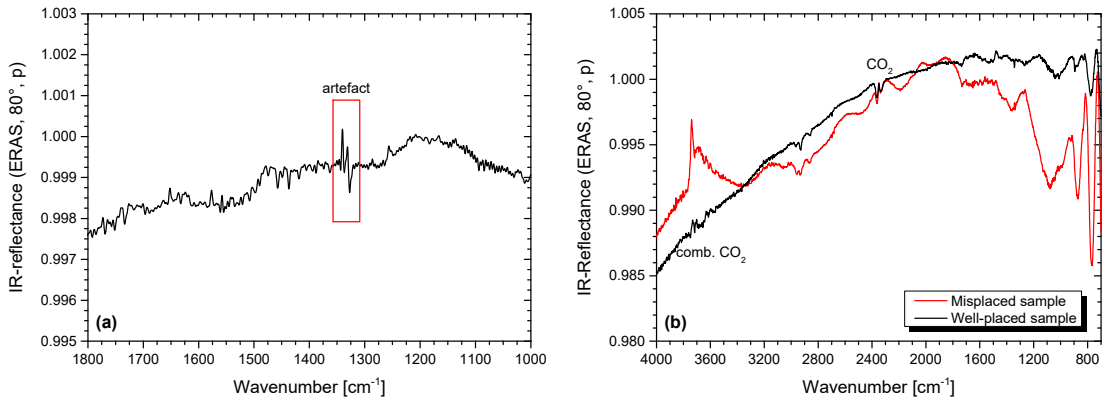

Fig. 3-18 (a) Artefact appearing in IR spectra at ca. 1340 cm^{-1}. (b) Baselines in the IR spectra of a well-placed (black) and a misplaced ERAS sample after one THF rinse.

Second, removing a sample from and remounting it in the spectrometer (e.g. during layer preparation or solvent rinses) may go with a slight positioning error that affects the SAM and REF spectra. As an undesired consequence, the whole baseline shows a wavelike distortion in the resulting reflection spectrum, cf. e.g Fig. 3-18b. Such distortions can even modify shape and position of real adsorption bands as seen around 3600 cm^{-1} in Fig. 3-18b. They have to be considered particularly when

[14] This vertical shift does not modify the intensity or shape of the bands in the spectra.

discussing weak broad bands. Furthermore bending of the complete baseline is also observed frequently.

Third, tilting of the baseline can occur for long measuring time. This can be due to a change of the deposited organic layer itself e.g. during desorption or rearrangement of molecules on the surface but also due to inhomogeneous deposits. However, baseline tilt can also be triggered by refilling the MCT detector with liquid N_2. In this case the baseline progressively changes during the 8 h interval between each cooling. In most cases both effects are present. Thus baseline tilt should be attributed to sample changes with caution.

3.2.5 Comparison of IR spectra

Measured IR spectra are also embossed by the optical situation of the utilised IR technique. Thus, direct comparison of IR spectra obtained by different techniques is forbidden. The genuine material properties are described by their respective optical function, $\hat{n}(\tilde{\nu})$,

$$\hat{n}(\tilde{\nu}) = n(\tilde{\nu}) + i \cdot K(\tilde{\nu}) \tag{3.19}$$

with real part, $n(\tilde{\nu})$, the refractive index and imaginary part, $K(\tilde{\nu})$, the absorption index. The optical situation includes effects of the angle of incidence, polarisation of light, optical function of the ATR crystal, or film thickness. Moreover the penetration depth of the IR light into the sample and hence the information depth to be attributed to the spectrum, does also change for each method. With ERAS, IR light passes through the complete organic layer and is reflected at the lower interface while in ATR the penetration depth into the quasi-semi-infinite sample depends on the wavelength. Comparison of ATR and ERAS spectra of the same sample reveals significant differences in absolute and relative peak intensities as well as slight shifts in peak position – cf. e.g. [9].

Correct characterisation of the interactions of adsorbed molecules with the metal surfaces requires however a suitable comparison of spectra obtained by these two reflection techniques. This issue is solved by using spectra calculation based on the optical function for the bulk state of the given material. All details and the physics of this method are described elsewhere [6, 7, 49, 52, 53]. Briefly, in a first step the optical function of the bulk organic material $\hat{n}_{bulk}(\tilde{\nu})$ is calculated from the corresponding ATR spectrum[15]. With $\hat{n}_{bulk}(\tilde{\nu})$ and the optical functions for the metal substrate and its corresponding oxide, the IR-ERA spectrum is then calculated for a compact organic film of chosen thickness following the optical model from Fig. 3-19.

[15] As an alternative the optical function of the ERAS thin layer could be determined and compared to the optical function of the bulk monomers. However, as the signal-to-noise ratio is quite low in ERAS, the obtained optical function $\hat{n}_{thinlayer}(\tilde{\nu})$ would be very likely incorrect [49].

During this step, the given experimental parameters of the optical situation (polarisation and angle of incidence) are also required for the calculation. Based on previous work the oxide layer thickness is set to 3 nm [7].

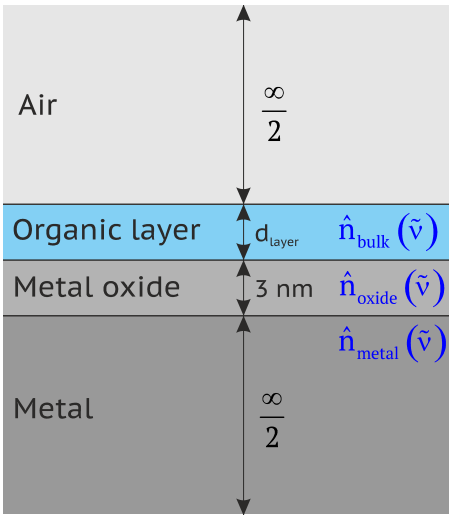

Fig. 3-19 Optical model used for IR-ERA spectra calculation; based on [9].

The obtained ERA spectrum corresponds to a thin adsorbed compact organic layer that would possess the same morphology and chemical properties as the bulk. Now, this calculated bulk-like ERA spectrum is suited for comparison with the spectrum measured for the corresponding real adsorbed layer. Any spectral difference comes from specific changes of molecular orientation, physical and chemical interactions in the real organic layer under the influence of the substrate surface. This method was successfully used in the case of thin PU and epoxy films as well as on PU monomer adsorbates on native metal surfaces [6, 8-10, 53].

3.2.6 Band assignment

Detailed interpretation of IR spectra requires a precise assignment of the observed adsorption bands. Commonly bands are assignment with the help of band catalogues (e.g. [54-57]) or electronic databases (e.g. [58]). They are based on infrared spectra measured for very many well-defined model samples. The catalogues for organic molecules are based on the phenomenological observation that the so-called characteristic IR bands can be assigned to specific functional groups, i.e. to a limited number of specified atoms of the molecule. This concept is referred to as a '*group frequency approach*'. Sometimes it is extended to the idea that a given characteristic mid IR absorption band results from the vibration of just this specific atom group, and some authors attribute the characteristic group frequency to a '*local mode*' (cf. e.g. [59]). Eigenvibrations of molecules, however, are localized only in very exceptional cases (e.g. for MIR vibrations of light hydrogen atoms bonded to much heavier atoms like carbon or in the near infrared region for special overtone vibrations in some molecules which then are rightly called '*local modes*'). Instead, large parts of the molecule or even all atoms contribute to most vibrational modes.

Owing to varying intra- and intermolecular environment in the model samples, the catalogues propose a *frequency range* for a given functional group instead of the sharp frequency it must have in any given situation.

Hence, in many cases it is essentially impossible to determine exactly which groups or parts of the molecule contribute to a given IR band. Band intensities are also often only roughly classified as being strong, medium or weak. Last not least rare molecules are missing in the catalogues. Thus in many cases such band catalogues do not provide a precise band assignment. Sophisticated QM modelling gives a way out of these limitations as it can provide the eigenfrequency spectrum of molecules. Band assignment presented throughout this work is based on two studies.

In the first one [7, 53] eigenfrequencies of polyurethane and epoxy monomers as well as corresponding reaction products were calculated using QM density functional theory (DFT). Such modelling requires several consecutive steps. Here for the isolated molecule, the conformer with minimal energy was simulated first. Then DFT was applied to obtain all vibrational modes, their frequency and vector of the transition dipole moment. Finally the atoms involved in each eigenvibration were identified and vibrations were named. The polyurethane monomers considered in [7, 53] are very close to those used in this work and thus the obtained band assignment is very suitable.

With ongoing work on the preparation and characterisation of thin polyurethane layers on metals (e.g. [8-10]) it became evident that QM simulations of isolated monomers provide limited band assignment possibilities only. In order to understand complex interactions of monomer (isocyanate and alcohol in this case) and polymer (urethane but also side reaction products) functional groups with metal surfaces, the simulation needs to be extended to molecules placed on a metal cluster. Thus in a second study the author of this thesis conducted the corresponding experimental work while the Chair for Theoretical Chemistry (Prof. Dr. M. Springborg) at Saarland University took responsibility for the QM simulations.

The aims of this study were twofold. First, *all* conformational states of the isolated monomers were to be simulated by DFT and the conformational transitions accessible at room temperature were identified. Then, the IR spectra were to be calculated for each conformer and superimposed to a common spectrum. Second, the monomer conformational states and their IR spectra were to be simulated on a metal oxide surface using the same parameters. It was planned to calculate spectra for the isocyanate and alcohol components and for urethane linkages on an amorphous aluminium oxide surface. Due to circumstances at the Chair of Theoretical Chemistry, only spectra of 4,4'-methylene diphenyl diisocyanate were obtained [60]. Some outcomes of this study are discussed in chapter 5.2.2.

Although state-of-art quantum mechanical modelling is a valuable tool for band assignment, some restrictions have to be taken into account with respect to both studies. Only isolated molecules were simulated. Thus, intermolecular interactions are not considered. They may lead to significant frequency shifts for some bands. Moreover, vibrational frequencies are obtained as sharp values thus not accounting natural band broadening due to temperature and other factors. Finally, approximations necessary for any DFT functional and basis set, result in numerical inaccuracies for band position and intensity. As a consequence QM calculations are used with caution for refining band assignment.

3.3 Thermogravimetric analysis (TGA)

Molecular layer deposition requires a source of gaseous monomers. Thus, prior to deposition it is important to verify the thermal stability of the chosen monomers and determine the temperature for an adequate evaporation rate. Thermogravimetric analysis (TGA) under inert atmosphere is the method of choice to get this information. The mass change, Δm, of a sample is obtained for a selected temperature-time profile. Typically a linear temperature sweep is defined and one obtains:

$$\Delta m = m(T) - m_0 \tag{3.20}$$

with $m(T)$ the mass at a given temperature and m_0 the initial mass of the sample. Mass losses occur during evaporation, thermal decomposition or chemical reaction with evaporation of small molecules [61]. The sample is placed in a small furnace.

During the whole measurement nitrogen gas, which is the carrier in MLD, flows at given rate through the furnace. The evolving gases are to be analysed in order to verify that only monomer molecules are evaporated. Therefore these gases pass through a gas transmission cell of an infrared spectrometer (c.f. chapter 3.2.3) for analysis.

3.3.1 Experimental procedures

The parameters used of for TGA and IR transmission spectroscopy are given in appendix 11.1.3.

◊ *Preparation*

Prior to any measurement the IR MCT detector is cooled properly with liquid nitrogen to a stable state. IR spectra are recorded not before 30 min. after cooling. First, the transfer pipe (Fig. 3-20) and the transmission cell are heated to 200 °C in order to avoid condensation of the gases. The gas selector (Fig. 3-20) is set to transfer the evolved gases towards the IR and is also heated to ca. 120 °C.

The gas flow is set to 240 ml/min of N_2 trough the furnace[16] and 10 ml/min through the balance. The total gas flow transferred into the transmission cell is hence 250 ml/min.

Gold plated aluminium pans are used for the experiments. The gold (99.99 %) is deposited via physical vapour deposition (PVD) in the same way as for the MLD samples (cf. Chapter 0). The gold layer avoids chemical reactions or interactions of the monomers with the aluminium and its oxide/hydroxide respectively.

[16] Typical TGA gas flow is about 25 ml/min. However in order to enable fast transfer towards the IR and to reduce condensation in the pipes a much higher gas flow was chosen.

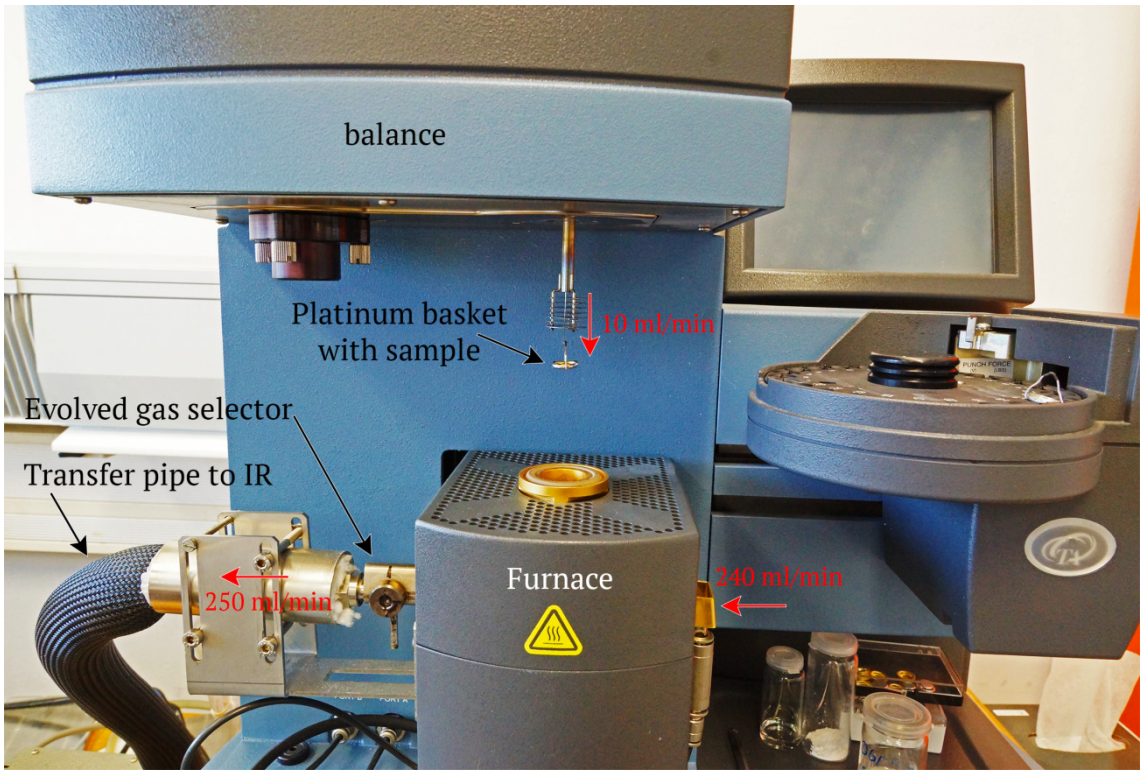

Fig. 3-20 Overview of the TGA apparatus with open furnace and the attached transfer pipe towards the IR spectrometer. The red arrows show the gas flows.

◊ *Sample measurement*

Once stable conditions are achieved the pan is placed into a platinum basked (Fig. 3-21) and loaded into the TGA furnace from the auto sampler. The balance is then tared with the empty pan and after 5 min. later a reference single beam IR spectrum is recorded (REF). Then the basket is unloaded and the pan filled with a small amount of sample (19 - 21 mg). The filled pan is transferred back into the furnace and the measurement is started. First, the sample is kept at 40 °C for 5 min. in order to remove all air entered into the furnace (and subsequently the IR transmission cell). Then the sample is heated up to 400 °C at a rate of 10 K/min.

IR sample spectra (SAM) are continuously recorded until the TGA arrives at the final temperature. Knowing the duration for recording a single spectrum, the temperature in the furnace[17] is retrieved. The sample is unloaded after cooldown of the furnace. The transfer pipe, gas cell and evolved gas selector are kept hot and purged with 250 ml/min of dried air for several hours in order to keep them clean.

[17] Of course the gases take a little time to flow from the furnace into the IR cell. The time necessary to record one sample spectrum is ca. 7 s. During this time 29 ml of gas has flown through the system. Considering the small section of the transfer pipe only 1-2 ml are needed. Moreover the gas cell contains 8.7 ml of gas (Fig. 3-16), so it has been purged 3 times with the evolved gases. Furthermore during the 7 s the temperature has increased of only 1.2 K in the furnace. Thus the time lag between furnace and IR chamber is negligible in our case.

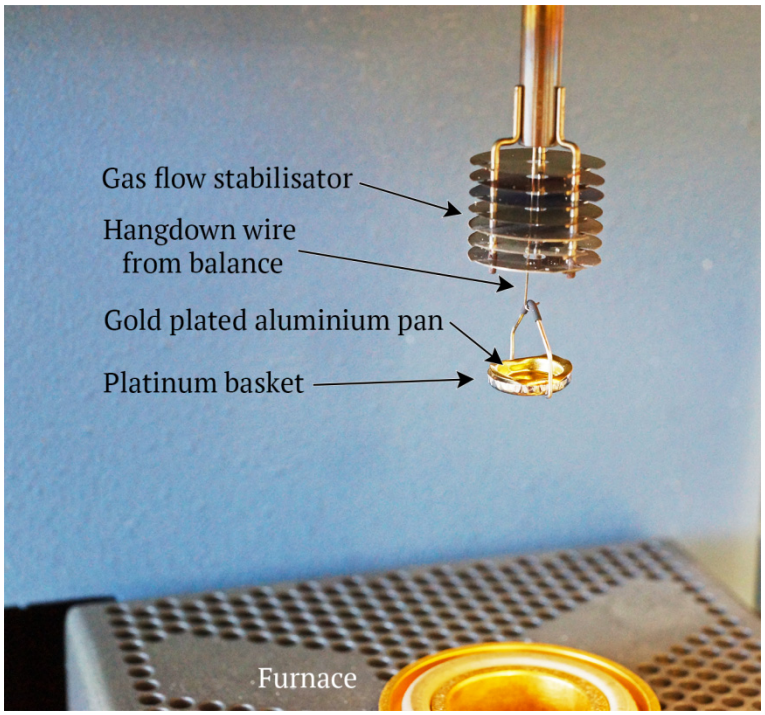

Fig. 3-21 Detail of the gold plated aluminium pan placed inside of the platinum basket. A few mg of sample are placed into the pan.

3.4 Optical microscopy

Optical microscopy is fast and convenient for a qualitative evaluation of layer homogeneity and topography. Differential interference microscopy (DIC) and dark field microscopy (DF) with a Leica DM6000 were used on certain samples at the start of this work before switching to scanning force microscopy. These commonly used optical methods are described in detail elsewhere [62-64].

3.4.1 Differential interference contrast microscopy (DIC)

Differential interference contrast transforms height differences and changes in refractive index in samples into a relief-like image. This makes them appear as three-dimensional. However DIC is not capable to distinguish if this relief is either caused by a hill or by a hole.

3.4.2 Dark-field microscopy (DF)

Dark-field microscopy is another way to depict topography changes. Now, only diffracted light passes through the objective while reflected light is removed. In the case of our non-transparent samples reflection dark-field microscopy is used. The sample is illuminated obliquely from one side.

As reflected light is not seen the sample images are generally black or dark except at those regions where light scattering occurs. Thus the method is quite sensitive to small topographic differences as they show up as bright objects.

3.5 Scanning force microscopy (SFM)

Scanning force microscopy (SFM) is based on the measurement of localised interactions taking place between a sharp probe and a sample. A typical setup is shown in Fig. 3-22. The probe consists of a cantilever with a sharp tip. The tip is brought into interaction range with the sample which induces a bending of the cantilever trough attractive or repulsive forces.

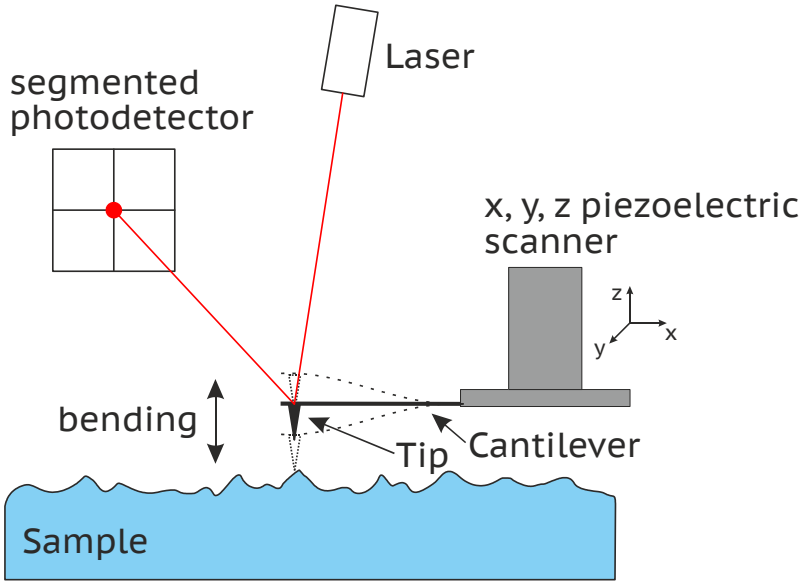

Fig. 3-22 Setup scheme of the scanning force microscope (SFM).

A laser beam is reflected from the backside of the cantilever towards a four-segment positional photodetector and enables to precisely monitor this bending. The tip is scanned across the sample surface using a piezoelectric x-y-actuator. During imaging the tip-sample interactions are kept constant using a piezoelectric z-actuator. Thus the change of z position provides the topographic image of the sample. Detailed information about this technique can be found in [65-68].

Depending on the tip-to-sample distance as well as specific tips SFM can be operated at various measuring modes and provides not only topographic imaging but other properties as for example local mechanical, electric, magnetic and thermal properties on the nanometre scale [68]. Contact mode, non-contact mode and tapping mode are the three basic modes. For contact mode the tip is continuously in contact with the sample and the deflection is induced by repulsive forces. In non-contact mode the tip does not touch the sample and attractive forces dominate. In tapping mode the tip vibrates at the cantilever resonance frequency and periodically penetrates into the sample. Thus repulsive and attractive forces alternate. As the tip only briefly contacts the sample possible damage during imaging is minor. This is particularly relevant for soft samples like organic layers. Contact mode would be too much aggressive and could alter the layer. Therefore in this work all SFM measurements are done in tapping mode on the Bruker Dimension Icon®.

This mode can further be subdivided for specific parameter measurements. Two modes were mainly used and are briefly outlined hereafter.

◊ *Standard tapping mode*

The cantilever is vibrating at its resonance frequency (Black curve in Fig. 3-23). A change in distance between tip and sample modifies the forces on the tip and thus resonance frequency is changed. The piezoelectric z-controller will adjust the tip distance in order to keep the resonance frequency constant. Thus the topographic image is obtained. Simultaneously, dynamic stiffness variations are recorded that relate to the phase difference between cantilever modulation and tip vibration ('phase contrast' image). When the tip scans over sample regions with different stiffness the set amplitude of the tip is reached at different positions of the z piezo. This leads to a phase shift (blue and magenta curves in Fig. 3-23) that is imaged for the whole scan area. Interpretation must be done carefully as it is prone to experimental artefacts.

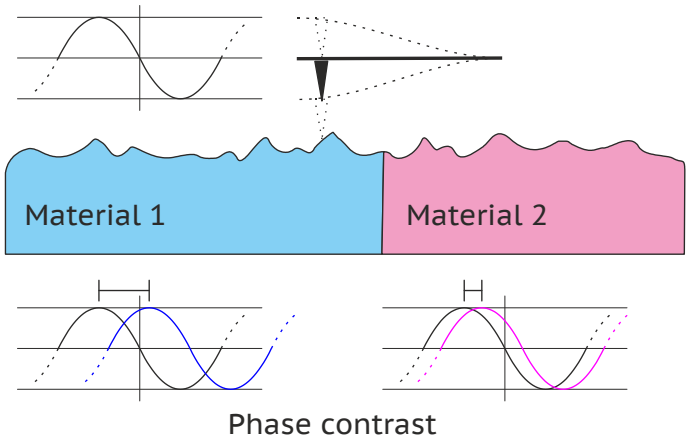

Fig. 3-23 Schematic principle of the phase contrast imaging using SFM.

◊ *Scanasyst*

This mode can be seen as fully automated imaging mode. Necessary parameters in order to properly track the sample surface as well as the resonance frequency of the cantilever are automatically tuned. The mode is perfect for topographic images without artefacts. This enables also to obtain good values for parameters to set for other measuring modes. Although the software also provides mapping for mechanical modulus and adhesion forces they are highly prone to artefacts as their respective set points are constantly changing. Thus this mode is only used to check sample and tip quality prior other measuring modes.

3.5.1 Experimental procedures

All SFM measurements are carried out after at least 24 h of IR survey as described in chapter 3.2.2.1. First, the sample assembly is removed from the IR spectrometer and the sample unscrewed from the sample holder[18].

The SFM is then prepared for sample characterization. The probe (cantilever with tip) is mounted onto the piezoelectric scanner and adequate positioning is checked with the built-in camera. Only then the sample is placed on the x-y-table and held in place with light vacuum suction.

For the characterisation software to work properly the sample and the cantilever are separately focused on the camera objective and these settings saved. This requires that the tip is near the sample surface but still disengaged.

As the next step the laser beam is positioned on the cantilever approximatively above the tip and its position marked in the program. The diode array is also aligned in such a way that the laser spot is exactly positioned in the middle of the four segments.

Once the laser beam is correctly set up, the position where the sample is characterised is selected in the camera view. If necessary the focus is adjusted. The initial setup of the scanning force microscope is accomplished and the characterisation method is loaded into the software.

◊ *Standard tapping mode*

For a new sample, topography is measured first using the Scanasyst mode. Amongst many parameters that are automatically adjusted the proportional and integral gains are the two important parameters here. They are used for the piezoelectric x- and y-actuators to be able to follow the surface topography. Hence the Scanasyst mode will provide satisfactory values for both parameters as well as a good topographic image.

The tip is then disengaged from the surface and the tapping mode method is loaded. No automatisms are present here. So first of all the resonance frequency is tuned and saved before engaging the tip on the surface. Now the values of the proportional and integral gain obtained previously are entered and the quality of the topographic image is checked. If necessary both parameters are slightly adapted until the topography image has a satisfactory quality. Two further parameters are also important for this mode: the amplitude set point as well as the drive amplitude. The first will change the distance between the tip and the sample and thus changes the maximal force which pushes the tip into the sample. The drive amplitude changes the amplitude of the vibration of the tip and thus the penetration depth of the tip. Typical values of these parameters as well as the specifications of the utilised probes are given in Appendix 11.1.4.

[18] Removal of the sample from the holder is necessary as the cantilever assembly of the SFM can hit the protruding screws. Hence after SFM characterisation, further IR spectra cannot be recorded as huge sample misalignment is inevitable.

Both parameters affect the phase contrast image significantly. Thus in order to obtain reproducible measurements and allow comparison between samples it is crucial that following conditions are obeyed:

First, after one set of parameters has been determined the scanned area is scanned at least two times. If topography and phase image do not change between both scans, the tip has not damaged the sample.

Second, different areas of the sample are measured. The obtained results must be comparable.

Third, in order to allow comparability between samples the chosen parameters should be varied only slightly. This may be difficult if the morphology of the layers is different. Furthermore wear of the tip requires an adaptation of the relevant parameters and hence leads to a significant change of phase contrast value. Thus great caution is necessary when comparing phase images. In this work it is mostly used to identify the presence and coverage of an inorganic substrate with organic molecules.

.

4 Molecular Layer Deposition Setup

In this chapter the customised Molecular Layer Deposition apparatus is described in detail. Literature review of gas phase deposition techniques and the principle of MLD are discussed in section 4.1. The requirements for such an MLD setup are outlined in section 4.2 followed by a precise description of the apparatus itself and its components needed to meet these requirements. Many parameters can affect the MLD process and its stability. Thus, the interdependency of these parameters and more important the precision of these parameters must be determined before successful layer preparation can be achieved (cf. section 4.3). From these results an experimental procedure is developed in 4.4 that allows for the reproducible deposition of defined layers. Experimental work [69-75] under my supervision significantly contributed to this chapter.

4.1 MLD principle in literature

During the last decades very many and different thin film deposition techniques have been introduced. In comparison to wet techniques, deposition from the gas phase offers elegant technical solutions in terms of versatility, effectiveness, independence of substrate shape, and environmental benignity. Gas phase deposition can be classified into Physical Vapour Deposition (PVD), Chemical Vapour Deposition (CVD), Atomic Layer Deposition (ALD) or Molecular Layer Deposition (MLD).

PVD includes methods which evaporate solid material and condense it on the surface of the substrate without chemical changes [1, 3, 76]. The process works in vacuum because it avoids collisions of vaporized material with atoms from the atmosphere. PVD is very well suited for the formation of pure metal films, alloys, oxides, organics, etc.. Macromolecules, however, cannot evaporate without decomposition as soon as chain entanglement becomes effective.

CVD covers a large variety of processes where solid material layers are deposited from a vapour of chemical precursors in combination with a chemical reaction in the vapour or at the substrate surface [1, 3, 77]. The reaction is activated by heat or other routes of energy supply. CVD produces inorganic layers like Si, oxides, nitrides, carbides or refractory metals. Polymer films can be made but in general it is most difficult to control the resulting structures and properties - see below.

ALD is based on sequential, self-limiting chemical reactions on a substrate [1, 78]. The vapours of two or more metal-organic precursors, each containing one or more elements of the finally deposited material, are sequentially brought into contact with the substrate. Each precursor shall form only a monolayer on the substrate and hence excess molecules can be removed by inert gas flushing after each deposition step. The reaction inside a single or between several precursor monolayers removes the organic parts and forms a monolayer of the desired coating on the substrate (e.g. elements, semiconductors, oxides and other inorganic compounds).

Film structure and thickness are controlled on the nanoscale by the number of deposition cycles and by variation of the deposited precursors. That results in nano-structured thin inorganic layers with new features.

The production of thin polymer films is becoming increasingly important. Control on formation process and resulting properties are key issues and this work aims to provide fundamental knowledge to both of them. However, none of the deposition techniques mentioned above can meet that goal. Both deposition and film properties are hard to control and structural gradients appear. This holds for the so-called PVD of polymers and the monomer vapour deposition polymerisation (VDP) as well. PVD works only with those polymers that decompose into defined fragments which, secondly, reform to polymer molecules after condensation on the substrate. Not much detail is reported on the properties but the molecular weight is known to be significantly smaller in the layer than before evaporation. VDP [2, 79] is a special CVD process with monomers that polymerize on the substrate by various types of activation and reaction. Plasma polymerisation is a special CVD version as the monomer molecules undergo fragmentation and ionisation in the gas phase [80, 81].

MLD was developed as a modification of the ALD concept and enables the deposition of thin polymer films [82, 83]. The monomers must have at least two functional groups and undergo chemical reactions with the surface of the substrate. As in ALD, the evaporated monomers undergo self-limiting reactions both with the surface and with the second monomer. Thus, only monomer monolayers form and react with each other by addition or condensation. A film growth model illustrating the principle of MLD is proposed in [82, 84] - Fig. 4-1.

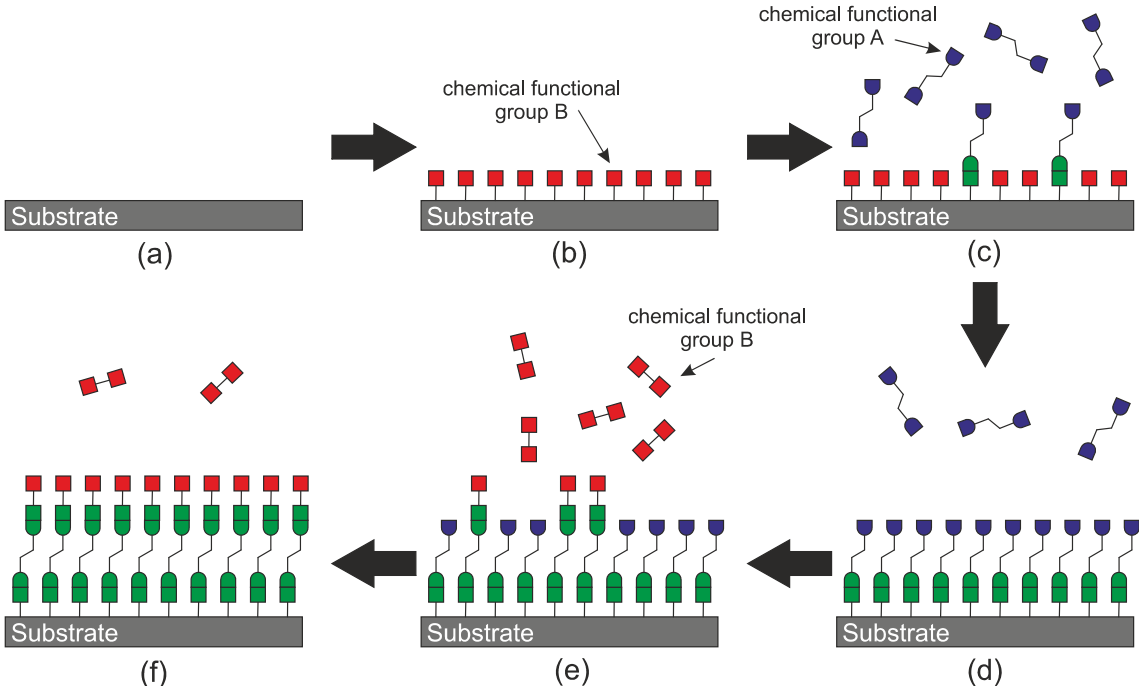

Fig. 4-1 Schematic layer growth model of the MLD principle based on sequential, self-limiting reactions, based on [84].

Three steps are proposed:

◊ *Sample preparation – Step (a – b)*

Most sample surfaces are treated in order to provide specific functional groups by grafting for example amine groups to enable self-limiting reactions [82]. Many publications assume that the monomers only bind covalently to the substrate (or to grafted functional groups) [83]. Other forms of interactions are not considered. See also section 6.1 for detailed discussion on these interactions.

◊ *Deposition of the first monomer – Step (c – d)*

The first monomer is then deposited by pulse-like injection of evaporated monomer A. Ideally the substrate surface is fully covered by the monomer. During this pulse the monomer reacts with the substrate surface and/or with the grafted functionalities.

The monomer pulse is followed by an inert gas purge in order to remove any excess molecules that have not reacted. In case of condensation reactions the by-products are removed too. An attached monolayer of monomer A remains. One functionality of each bifunctional monomer has reacted with the surface functionalities.

◊ *Deposition of the second monomer – Step (e – f)*

Next monomer B is applied in a similar way followed by a purge. It can now react with the free functionalities of the previously deposited monomer A. Layer growth is achieved by repeating the monomer depositions sequentially.

Although thin polymer films prepared by MLD have a high potential for technical applications, the actual state-of-art of this technique does not provide many information regarding experimental setups. In many cases modified ALD reactors providing non-stationary gas flow conditions (i.e. constant pressure and gas flow) are used (e.g. [83, 85, 86]). Details on the monomer evaporators, layout of pipes, and precision of the deposition parameters are often lacking.

Furthermore the proposed simple layer growth model has a few limitations. First, from the self-limiting character of deposition intermolecular interactions between molecules are either not considered or assumed to be very weak. In reality most reactive functional groups tend to undergo some kind of interactions and hence more than one monolayer of each monomer could be deposited. If these interaction forces are strong enough purges with inert gas could not remove them. This would completely change the layer growth.

Second, it is expected that all polymer chains will grow linearly and form a comb-like morphology. This is energetically highly unfavourable as polymer chains naturally form entanglements and coils. Hence, with ongoing layer growth morphology would continuously change and hence also modify the amount and accessibility of the functional groups. Monomers could also be able to react with two surface sites or two chains, respectively.

Third, layer growth is often defined as growth per cycle. This ratio between thickness growth of the layer during each deposition cycle and theoretical layer growth based on the length of the deposited molecule is frequently used to discuss the deposition performance. In most cases the growth per cycle rate is smaller than the theoretical growth [83]. Hence, this is a first indication that the forming polymer chains do not grow linearly and present defects. Due to their conformational flexibility, chain polymers can rather easily change the film structure (e. g. loss of chain alignment, recombination of chains, etc.) upon external influences (e. g. mechanical or friction strain), the initial properties of the film can irreversibly be modified.

Hence, this proposed model is already questionable. From the obtained results of this work a model update can be iteratively proposed.

Finally, the type and extent of adsorption of molecules onto a substrate depend on numerous influencing factors of the adsorbate, e.g. chemical composition, gas pressure and the substrate e.g. chemical composition or surface topography. Not to be forgotten is also the presence of other adsorbates (e.g. carbonaceous contaminants), which may have to be displaced. Last but not least, temperature is of very great importance [87].

The reverse of adsorption is desorption. For desorption to take place, some activation energy must be applied, as the adsorbate must be raised from its potential minimum. A dynamic equilibrium develops between adsorption and desorption [88], which is of decisive importance for the layer formation in the MLD process. Factors influencing the adsorption-desorption equilibrium during MLD are evaporation temperature, gas flow rate and substrate temperature. In addition, the storage temperature of the sample after deposition also affects this equilibrium.

As fundamental technical information on the MLD is lacking, detailed understanding of the processes taking place during deposition is necessary. In the next section the requirements and features of the customised MLD setup are presented.

4.2 MLD apparatus - requirements and features

The apparatus should comprise four parts: the carrier gas stage, monomer evaporation stage, reactor chamber and vacuum stage (Fig. 4-2).

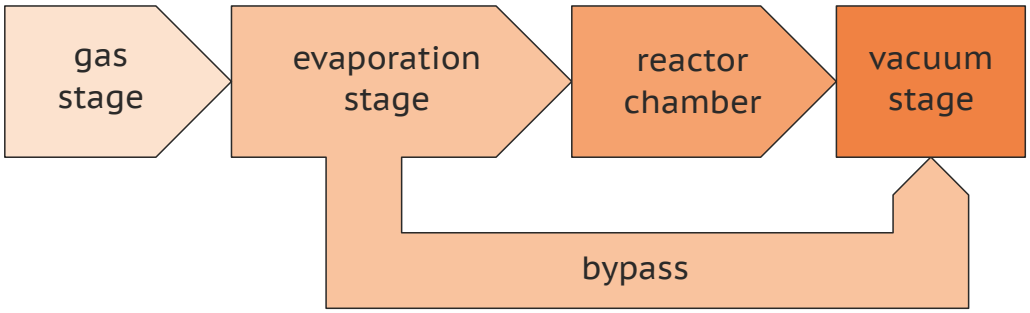

Fig. 4-2 Schematic view of the four MLD stages. The arrows symbolise the carrier gas flow from the gas stage to the vacuum stage. The evaporation stage is equipped with a bypass leading directly to the vacuum stage. See also Fig. 4-3 for the implemented setup.

A customised MLD apparatus was designed and built at LAIP taking into account the previously described features. By extensive testing it was iteratively fine-tuned to allow adequate deposition conditions. Fig. 4-3 shows the experimental setup of the MLD with its different stages. In this section the different parts and features of the final apparatus are described in detail while the different development stages are described elsewhere [70, 72, 73].

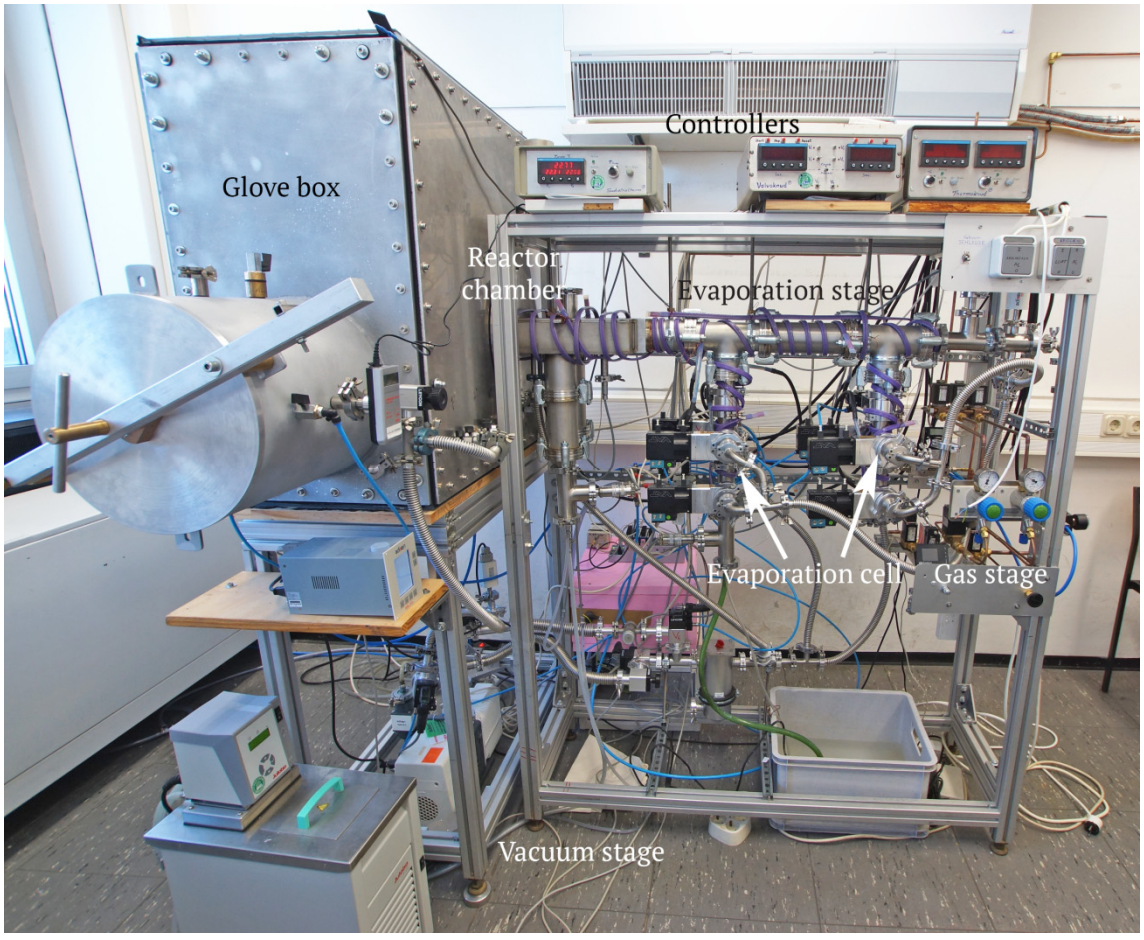

Fig. 4-3 View of the customised MLD apparatus without wall pipe insulation.

4.2.1 Gas stage

In the gas stage the carrier gases are conditioned for the MLD. It provides means of measurement and regulation of the gas flow as well as the ability to switch between gases. The gas stage must allow a precise and stable carrier gas supply in order to meet stationary gas flow conditions in the evaporation stage and reactor chamber (see also 4.2.3). Nitrogen or dried air can be chosen as carrier gases. This stage is shown in Fig. 4-4 and schematically in Fig. 4-5.

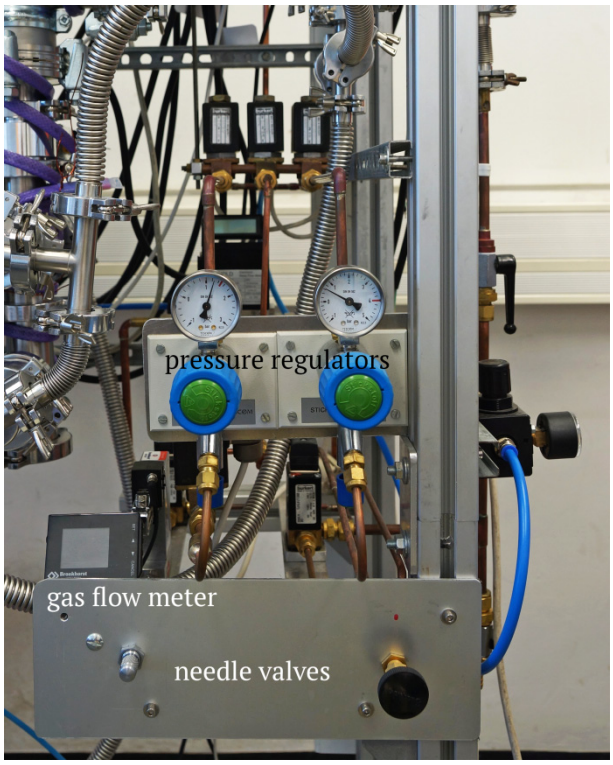

Fig. 4-4 Detailed view of the gas stage of the MLD apparatus.

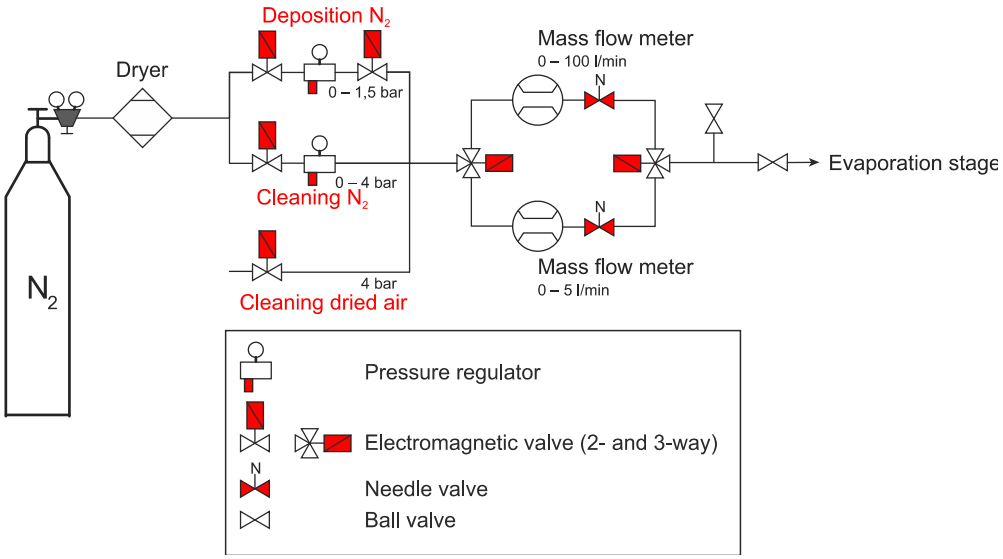

Fig. 4-5 Schematic view of the gas stage.

Nitrogen[19] is obtained from a pressurised gas cylinder at ca. 200 bar. The pressure regulating valve at the cylinder reduces this pressure to 5 bar. The nitrogen passes through a phosphor pentoxide P_4O_{10} dryer in order to remove any water that is introduced during the replacement of a cylinder.

Two circuits enable to choose if nitrogen is either used during the deposition cycle or during the cleaning cycle. Each circuit is fitted with a second pressure regulator that further reduces the pressure (max. 1.5 bar for deposition and 4 bar for cleaning) depending on the necessary gas flow required. A third circuit enables dried air from the lab supply as carrier gas. Each circuit is opened or closed using electromagnetic valves. The deposition line is protected with a second valve after the pressure regulator in order to avoid damaging the pressure regulator if pressures higher than 1.5 bar are applied. During deposition and cleaning of the MLD only one of three lines is opened.

The three lines merge at a three-way valve. Then each line leads into a mass flow meter followed by a needle valve. The mass flow meter for gases is based on the measurement of relative temperature differences due to the heat transport of the carrier gas [89]. Both mass flow meters distinguish by their flow range. The upper one measures flows of up to 100.0 ± 0.1 l/min and is used during the cleaning cycle. The lower one is much more precise and measures a flow of up to 5.000 ± 0.001 l/min. It is only used during the deposition cycle.

As the mass flow meter indicates the gas flow at normal atmospheric pressure, calculation of the gas flow at a given pressure is thus possible. A reduction in pressure leads to a higher gas flow. The gas flow indicated in this work always refers to the evaporation stage. The gas flow itself is regulated by a needle valve (Fig. 4-5). This needle valve determines the difference between gas stage pressure on one side and evaporation stage pressure on the other side.

From each needle valve the two lines join together at another three-way valve. The single outlet passes through a ball valve and flows into the evaporation stage. All electromagnetic valves in this stage are interconnected in such a way that choosing either deposition or cleaning cycle as well as the appropriate carrier gas will open and close the required valves. The flow diagram of both cycles is represented in Fig. 4-6.

[19] 99.999 % clean nitrogen is used here. Thus, a maximum of 5 ppm of water and 0.2 ppm of hydrocarbon contaminations are present.

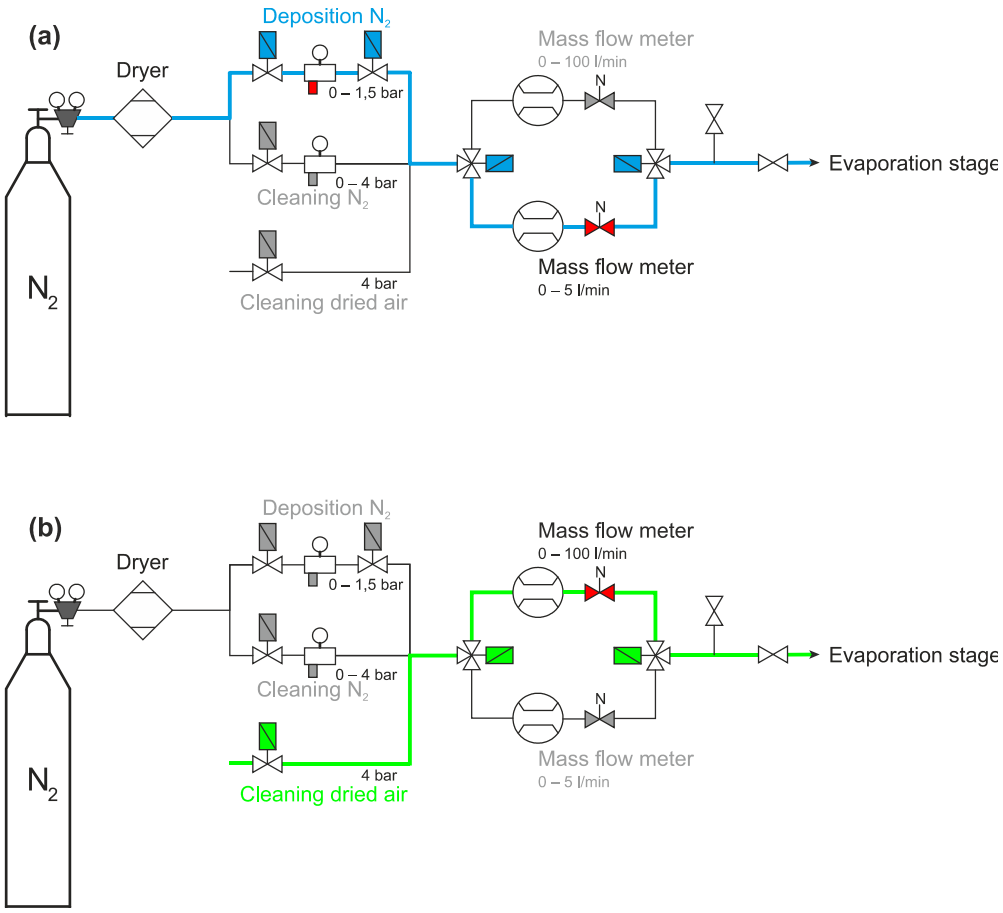

Fig. 4-6 Flow of the carrier gas for the deposition cycle (a) and the cleaning cycle (b). The coloured lines represent the gas flow.

During deposition (Fig. 4-6a) only a small gas flow of nitrogen is necessary and the precise mass flow meter is used. During cleaning (Fig. 4-6b) a strong flow of dried air and thus the mass flow meter with higher gas flow is used.

4.2.2 Evaporation stage

As two monomers are necessary for the polyaddition of polyurethane two evaporation cells provide the vapours of two monomers and the carrier gas feeds them into the reactor chamber for deposition on a solid substrate. The schematic of the evaporation stage, the reactor chamber and the vacuum stage is represented in Fig. 4-7. A view of the evaporation stage and reactor chamber is shown in Fig. 4-8.

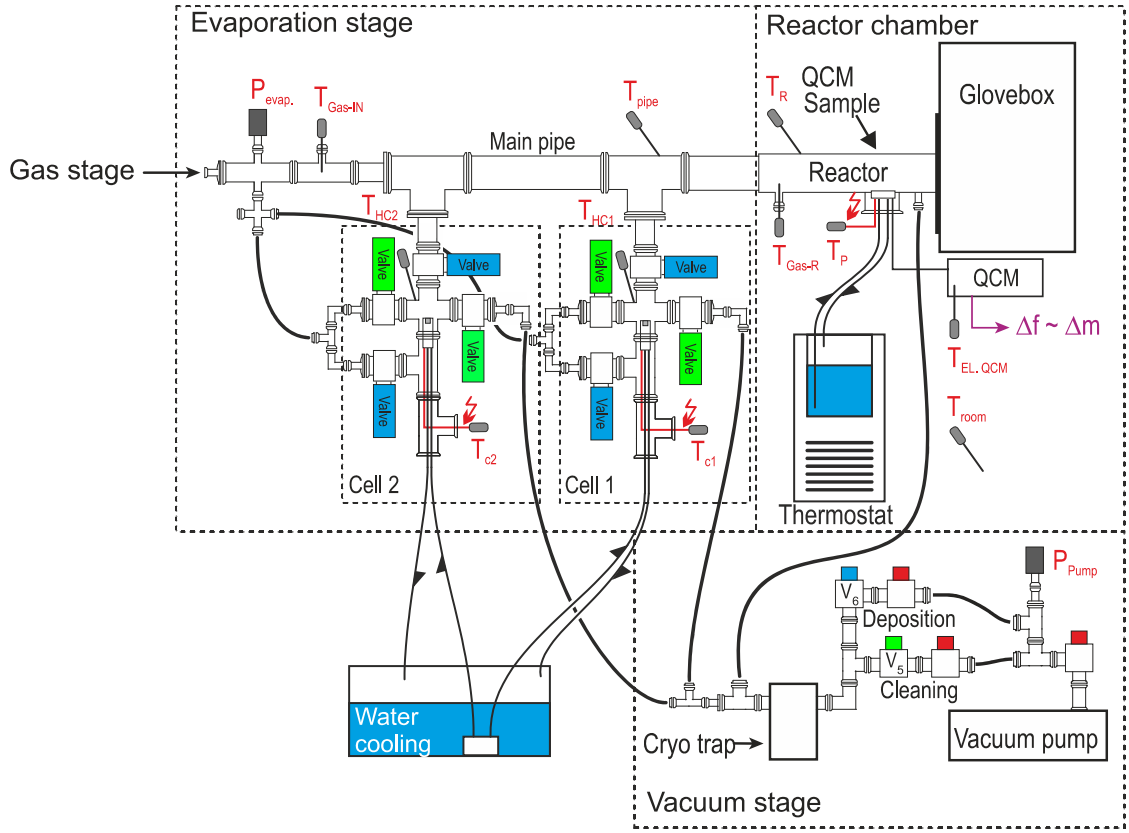

Fig. 4-7 Overview of the evaporation stage, reactor chamber and vacuum stage of the MLD.

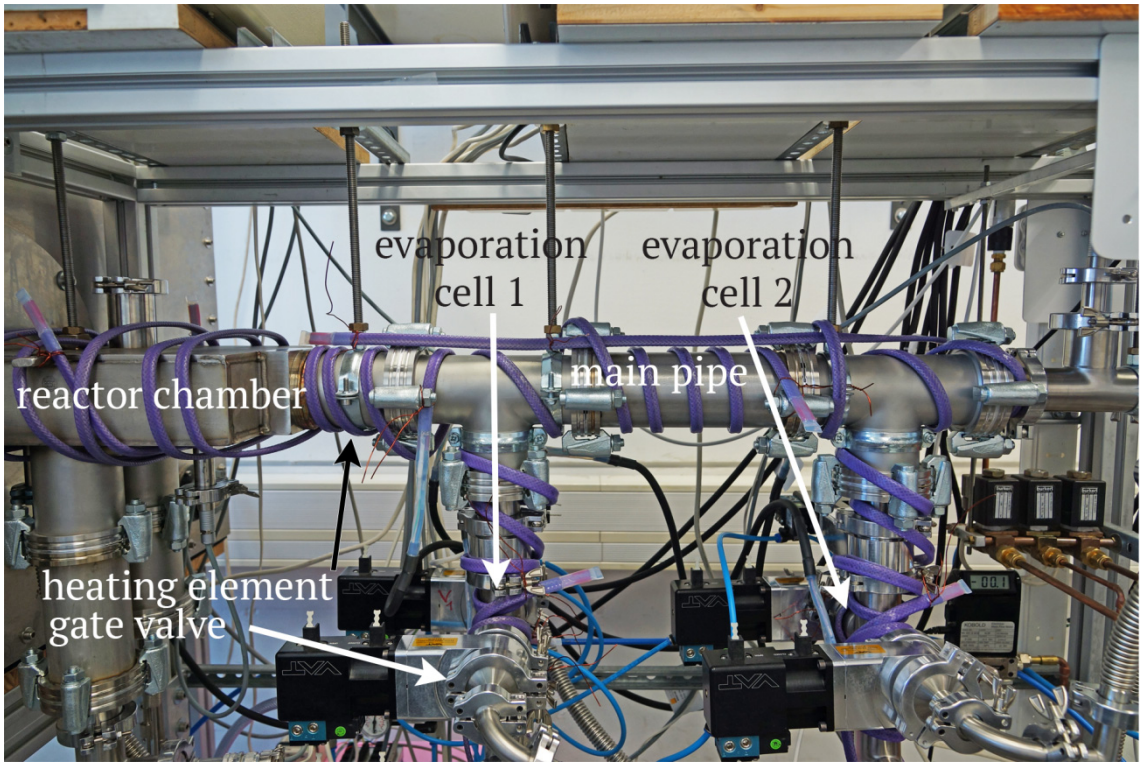

Fig. 4-8 View of the main pipe with the two evaporation cells of the evaporation stage. The carrier gas arrives from the left side. The reactor chamber is located on the right side. Insulation removed.

In this stage all pipes, tubes and valves are made of stainless steel. Their diameters are given in Table 11-13 in Appendix 11.4. The gas temperature, $T_{Gas\text{-}IN}$ is also measured in the main pipe. The gas flow from the gas stage arrives at the main pipe and is distributed to the reactor chamber and also to the two evaporation cells using flexible metal tubes. The pressure inside the evaporation stage, $P_{evap.}$, is measured at the main pipe. Right after the needle valves in the gas stage, $P_{evap.}$ is constant throughout the evaporation stage with its two evaporation cells, the reactor chamber and up to the cryo trap and regulation valves in the vacuum stage.

◊ *Evaporation cell*

Both self-made evaporation cells are identical. The metal tube with the carrier gas from the main pipe splits up in two pipes connected to gate valves (Fig. 4-9 and Fig. 4-10). Both entrance gate valves lead to different parts of the evaporation cell. This is necessary in order to control if monomers are transferred into the reactor chamber or not. Thus a second pipe is necessary to bypass the reactor chamber if one or both monomers are not to be deposited. In case monomers are not to be deposited, the evaporation cells need also to be tightly separated by gate valves from the piping to the reactor chamber. This ensures that no further monomers leak into the reactor.

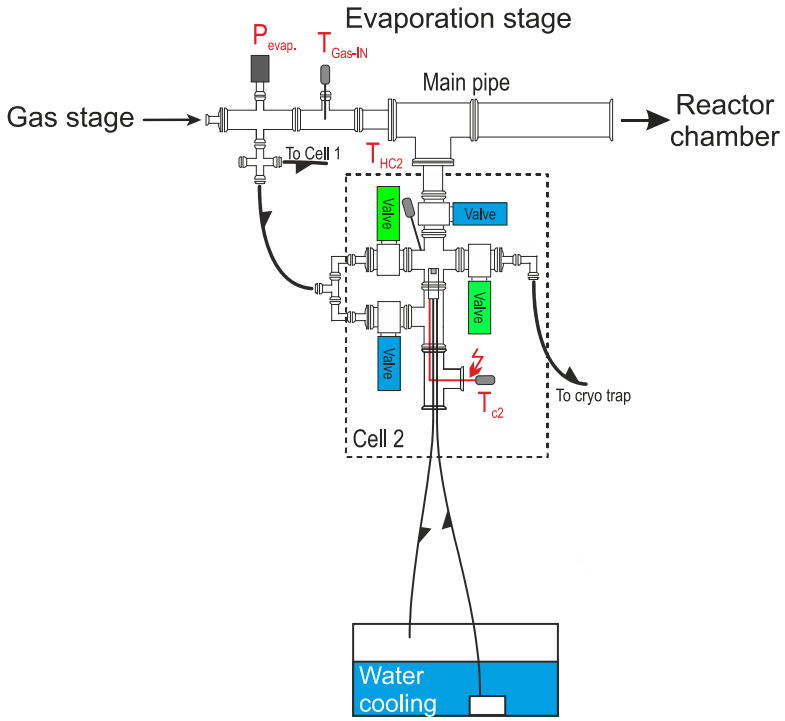

Fig. 4-9 Detail of evaporation cell with attached main pipe, carrier gas tubes and water cooling. The green valves are used for cleaning/non deposition mode and the blue valves during deposition.

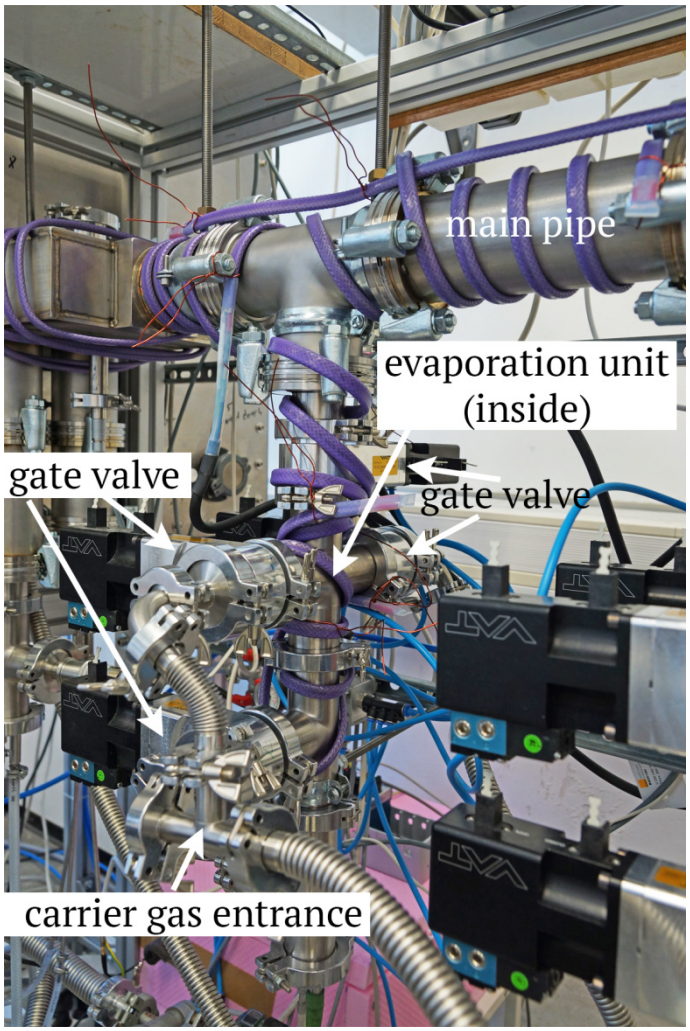

Fig. 4-10 View of evaporation cell 1. Insulation removed.

The evaporation unit is the central part of the evaporation cells (Fig. 4-11). Monomers for evaporation are placed in a small stainless steel crucible which fits into the electrically heated temperature cartridge. The temperature of each evaporation cell has to be regulated individually in order to ensure a constant evaporation rate of the monomer. Rate fluctuations will impinge reproducibility of the deposition regime.

A temperature probe measures T_{c2} at the base of the crucible. T_{c2} is the actuating variable for the *Thermoknud* controller (Appendix 11.4.2 - Fig. 11-2) to adjust and control the evaporation temperature (cf. Appendix 11.4.2). The water cooling lines are used to cool down the crucible in order to avoid excessive contamination of the pipes when monomers are not deposited.

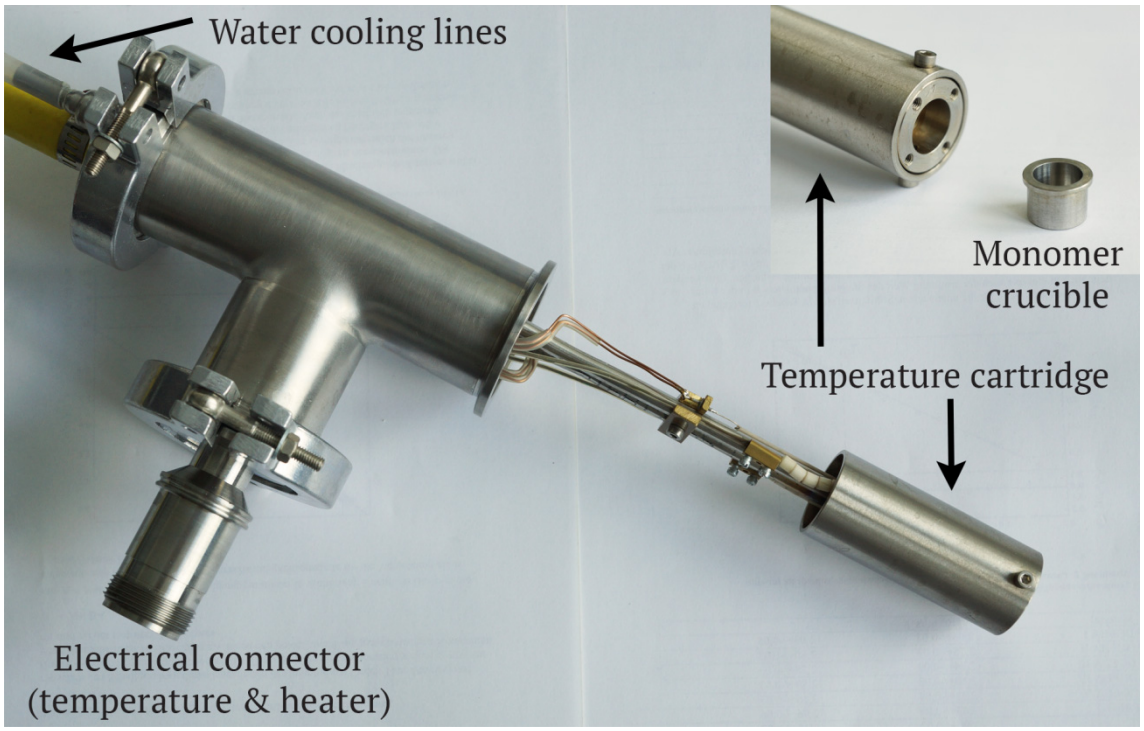

Fig. 4-11 View of one evaporation unit and its monomer crucible.

After passing one of the entrance gate valves the carrier gas takes up the evaporating monomers and exits the evaporation cell via two other gate valves (Fig. 4-9). Depending on the chosen entrance and exit gate valves the carrier gas can flow into two different paths.

First, when both green gate valves are opened (Fig. 4-12a), the carrier gas flows horizontally over the crucible and exits the evaporation cell at the tube to the cryo-trap. Thus, evaporating monomers are not carried to the reactor chamber and no deposition occurs. This corresponds to the bypass mode shown in Fig. 4-2. This mode is used during cleaning and non-deposition cycles of the deposition regime.

Second, when both blue gate valves are opened (Fig. 4-12b) the carrier gas enters the evaporation cell beneath the temperature cartridge and flows vertically along the crucible. The carrier gas loaded with monomer gas now returns to the main pipe and joins the gas flow from the entrance into the reactor chamber. This mode is used when monomers are deposited. The vertical flow of the carrier gas along the crucible reduces monomer condensation at the pipe intersection.

All gate valves are controlled by *Valvoknud* (Appendix 11.4.2 - Fig. 11-3). They are connected in such a way that the gate valves of same colour are opened or closed together. Time-controlled switching between deposition and non-deposition mode is also possible.

Finally, monomer condensation has to be reduced inside the MLD. Therefore the main pipe, the pipes leading from the evaporation unit to the main pipe and the reactor chamber itself are heated by electric wires coiled around the pipes and connected in four groups (main pipe, evaporation cells 1 and 2, and reactor chamber – violet heating elements in Fig. 4-10). On top silicone foam insulation reduces thermal losses to the lab. The temperatures of the pipes and the reactor wall are measured (T_{pipe}, T_{HC1}, T_{HC2} and T_R in Fig. 4-7) and controlled by a customised Labview program (Appendix 11.4.2 - Fig. 11-4). The maximum temperature is about 110 °C and is used during cleaning of the MLD.

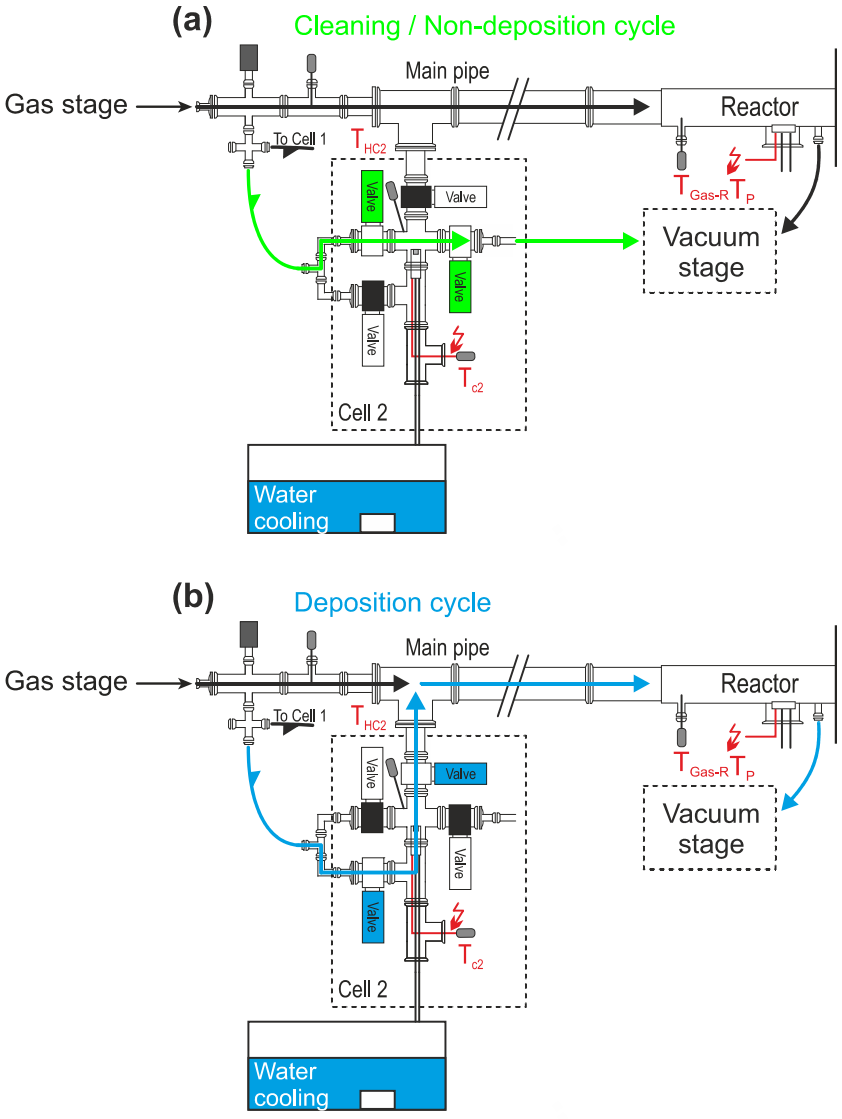

Fig. 4-12 Carrier gas flow through the evaporation cell during (a) cleaning/non-deposition mode and (b) deposition mode. The coloured gate valves are open.

4.2.3 Reactor chamber

Here the monomer molecules can adsorb from the carrier gas onto the substrate. Placement and removal of the substrate should be easy by appropriate tools or aids that can serve for the layer characterisation as well. In addition, the reactor chamber must contain an option to monitor and control the vapour deposition regime.

Moreover the substrate and the monitoring unit should be held at constant temperature because temperature fluctuations induce changes in adsorption/desorption equilibrium, polymerisation rate or side reactions.

◊ *Deposition monitoring*

Deposits during layer preparation are controlled by a quartz crystal microbalance (QCM) placed right aside the substrate position inside the reactor chamber of the MLD - Fig. 4-13. Both holders are placed at the same vertical level to ensure same deposition conditions. QCM sensitivity allows to measure deposits in the nanometre thickness range provided the QCM is operated under properly controlled conditions in terms of temperature, pressure (cf. chapter 3.1), carrier gas current density and stabilised electronics, (cf. section 4.3). The QCM quartz holder is set to constant $T_{QCM} = T_{sample}$ by a water cooler. In order to avoid frequency fluctuations of QCM due to temperature changes in the electronics of the QCM, the electronics are placed in an insulated box with an integrated regulated heater. Its temperature, $T_{EL.-QCM}$, is also controlled via the Labview program.

◊ *Requirements for the carrier gas*

Many research groups use non-stationary deposition regimes (c.f. 4.1). As the QCM requires constant pressure inside the MLD apparatus throughout the deposition process and as the pressure is related to the gas flow, stationary and laminar gas flow conditions are required in our case. Hence, the gas and vacuum stages must allow a precise and stable carrier gas and vacuum control. Stationary gas flow conditions (and hence constant pressure) have further benefits. Adsorption and desorption of molecules on the substrate surface are sensitive to pressure and gas flow changes as well making the deposition control less precise.

Furthermore, non-stationary conditions let monomer pulses flush into the reaction chamber leading to fluctuating concentration. Under stationary conditions concentration of monomers in the carrier gas is constant and low during the deposition phase. Thus, cluster formation of molecules in the gas is reduced and more homogenous depositions should be obtained. With lower monomer concentration layer growth is slower and control is easier.

Only laminar gas flow avoids heterogeneous and fluctuating distribution of monomers in the gas phase and, hence, non-homogeneous layer growth. As the gas flow is split up to supply the different evaporation cells and recombined for the reactor chamber, the diameter of the pipes has to be chosen appropriately. Calculating the Reynolds number (R_e) for the reactor chamber gives a measure of turbulence of the gas. For pipes the critical Reynolds number lies around 2300. The lower the Reynolds number the less turbulent the flow. In [70, 71] R_e of ca. 5.4 was calculated for a maximum gas flow of 21 l/min of nitrogen, which corresponds to a gas current velocity of 2.5 cm/s through the designed reactor chamber. Thus the gas flow in the reactor chamber is laminar.

Adapted pipe diameters ensure that the R_e numbers are significantly lower than the critical value of 2300. Of course at pipe intersections and junctions local turbulences occur but vanish well before reaching the reactor chamber.

From the main pipe the carrier gas flows into the reactor chamber (Fig. 4-13) where the monomers adsorb on a substrate. The reactor is a cuboid of 30 x 20 cm^2 with a height of 7 cm. The entrance is specifically shaped in order to quickly fade any turbulence in the carrier gas. Inside the reactor a substrate on its sample plate (c.f. Fig. 3-12) sits on the sample holder. Similar to the evaporation units it can be electrically heated to constant T_{sample} using the *SubstratTherm* controller (Appendix 11.4.3 - Fig. 11-5) and the water cooler. T_{sample} is measured at the base of the sample plate. The carrier gas temperature, $T_{Gas\text{-}R}$ at the entrance of the reactor chamber and the temperature of the reactor walls, T_R are also measured.

After passing over sample and QCM, the carrier gas is pumped towards the vacuum stage.

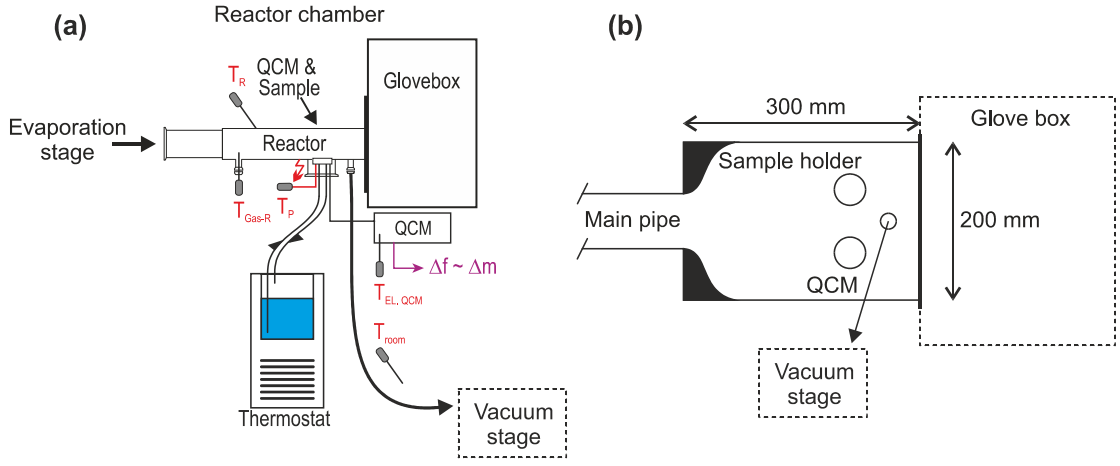

Fig. 4-13 (a) Side and (b) top view of the reactor chamber with attached Glove box, thermostatic water cooler and QCM electronics.

◊ *Sample transfer*

In order to handle the prepared samples while reducing side reactions with gaseous water from the atmosphere and thus avoiding chemical reactions, a glove box is attached to the reactor door. This box is continuously flushed with dried air. An air lock permits the transfer of samples to and from the glove box.

4.2.4 Vacuum stage

During non-deposition mode the carrier gas from the evaporation cells directly flows into the vacuum stage. The carrier gas that has passed through the reactor chamber during both modes also flows into the vacuum stage (Fig. 4-14). First, the reunited gas flow passes through a LN_2-cooled cryo-trap. Here gaseous monomers condensate from the carrier gas in order to avoid contamination of vacuum pump and environment.

After the cryo-trap the gas can flow through two different valves, depending on the chosen mode. During cleaning the high gas flow passes through a large regulation valve (V_6 – green valve in Fig. 4-14). During deposition and non-deposition mode the small flow of carrier gas passes through a small needle valve (V_5 – blue valve in Fig. 4-14).

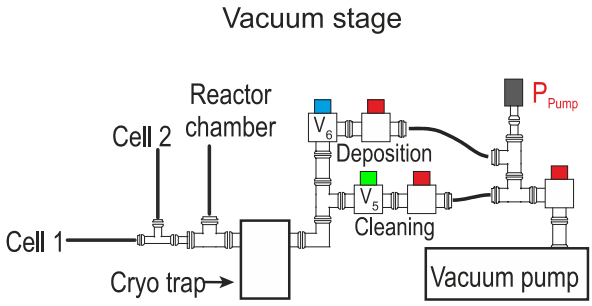

Fig. 4-14 Detail of the vacuum stage with electro pneumatic open/close valves (red) and regulation valves (blue and green).

These valves set a second limit for the pressure inside the evaporation cell and the reactor chamber. For stationary gas flow conditions (constant gas flow and pressure) the needle valves in the gas stage and vacuum stage have to be adjusted in such a way that the same flow of gas molecules passes through both of them. A difference here induces a pressure change inside the evaporation stage and the reactor chamber. After each valve an electro pneumatic valve enables to choose the needle valve the gas flows through. They are also controlled by the *Valvoknud* controller. Finally, a rotary vane pump maintains pressure in the MLD. A pressure gauge measures p_{Pump} at the suction inlet of the pump. This pump also provides vacuum for the operation of the air lock of the glove box.

4.3 Parameter definition for the MLD process

The aim of this section is to illustrate how some parameters as gas flow, pressure and temperature do influence the MLD but also the layer deposition and hence the layer properties itself. This knowledge is necessary to establish a process regime that reduces at most all negative influences on the layer preparation step.

4.3.1 Influence of gas flow and pressure

The volume of a gas changes with varying pressure as both parameters are linked positively in the ideal gas law as long as the amount of molecules does not change. As a consequence if the volume flow is modified in the evaporation stage, the pressure changes and vice versa. For stationary gas flow conditions with constant pressure inside the MLD, the same flow of carrier gas molecules must enter the evaporation stage through the gas stage and exit at the vacuum stage. Thus, the respective needle valves have to be adjusted accordingly.

All in all, stationary flow conditions are only achieved if gas flow and pressure inside the evaporation stage is kept constant. Once the needle valves set correctly, pressure and gas flow should not change. Preliminary tests [73] revealed however that this is not the case. Several factors were identified that cause a variation of the gas flow and thus of the pressure

◊ *Thermal sensitivity of the mass flow meter*

The gas flow is deduced from the temperature difference of the gas between two heating elements in the flow sensor [89]. A change in temperature of the carrier gas induces a change of the indicated gas flow which leads to an incorrect gas flow indication despite the gas flow is unaffected as it is regulated by the manually operated needle valves (see above). Nevertheless a change in gas flow indication could trigger an unskilled operator to change the needle valve and thus generate an unwanted gas flow change.

◊ *Heating of electromagnetic valves in the gas stage*

The path of the carrier gas through the gas stage is switched using electromagnetic valves. When such an electromagnetic valve is switched on, the corresponding electric current generates heat which heats up the valve itself and the attached copper piping. Inherently the carrier gas is also heated and thus generates a change in the gas flow indication. Once a valve is switched a certain time is necessary to reach a stable thermal equilibrium. The switching of valves only takes place when passing from one mode to another (e.g. when passing from cleaning mode to deposition mode). Thus, before obtaining a stable and accurate gas flow, the thermal equilibrium of the valves must recover.

◊ *Thermal sensitivity of the needle valves*

A change in the carrier gas temperature not only affects the gas flow meter but also the needle valves. As temperature changes the needle valve extends or shrinks slightly and hence change the gas flow. The same effect is observed if room temperature is changed as shown in Fig. 4-15. In this example, stationary flow conditions (500 mbar and 4 l/min in the evaporation stage[20]) are initially set and not modified. The thermal equilibrium of the electromagnetic valves is also reached. Then the room temperature is changed by opening or closing windows. As temperature (blue line) slowly rises over the first 90 min the gas flow (red line) progressively drops from 4.00 l/min to 3.83 l/min leading to a drop of pressure (black line) of ca. 20 mbar. After 90 min the windows are opened and the temperature drops again. In parallel the gas flow and the pressure raise again. As temperature raise the needle valve extends and the gas flow is reduced. This experiment shows that changes of the temperature of the carrier gas and all of components it flows through have a significant influence on gas flow and pressure.

Even by using an air conditioning unit, slight variation of gas flow and pressure is still measured. Therefore, manual adjustment is necessary at the needle valves at the gas and vacuum stage from time to time when variations are greater than ± 1 mbar for the pressure or ± 0.01 l/min for the gas flow.

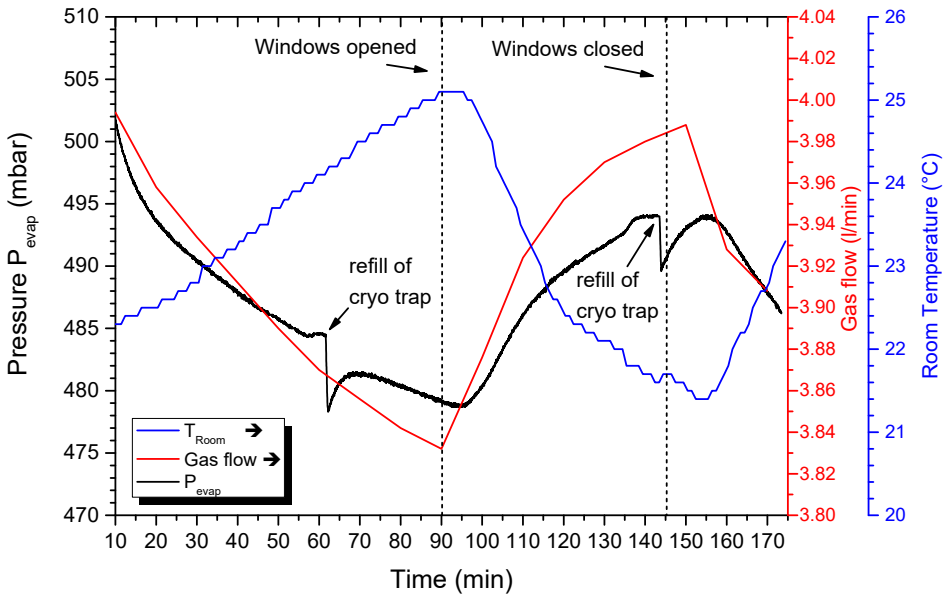

Fig. 4-15 Influence of room temperature change (blue line) on the gas flow (red line) and pressure P_{evap} (black line) inside the MLD. Stationary gas flow conditions (500 mbar and 4 l/min) are set before temperature is changed.

[20] All further indicated gas flows are referenced to the evaporation stage and not to the indicated gas flows of the gas stage.

◊ *Refill of the cryo-trap with liquid nitrogen*

During the MLD process the cryo-trap in the vacuum stage has to be regularly refilled with liquid nitrogen. This goes with a sharp drop of pressure of about 5 mbar - Fig. 4-15. With the addition of liquid nitrogen, the gas inside the cryo-trap is cooled down instantly and thus induces a drop of pressure. Until thermal equilibrium is re-established in the cryo-trap the pressure progressively increases and stabilises again. Usually the initial pressure is not recovered and thus manual adjustment of the pressure is necessary after each refill with liquid nitrogen.

◊ *Impact of pressure or gas flow variation on the deposition process*

The boiling point of a liquid is reached when the vapour pressure of the liquid becomes equal to the surrounding pressure. Thus a pressure variation in the MLD affects the boiling temperature of the monomers. As evaporating monomers are continuously removed by the carrier gas no equilibrium of the saturation vapour pressure is reached. Hence by changing the pressure inside the MLD, the monomer evaporation rate changes. A lower pressure leads to higher evaporation and thus higher monomer concentration in the carrier gas.

Similarly, if the gas flow changes, the evaporated monomers are more or less diluted in the carrier gas. Here a higher gas flow yields a higher monomer dilution and higher gas velocities in the pipes and reactor chamber.

Hence, the adsorption and desorption of monomers on the substrate changes. In order to obtain a reproducible deposition regime it is necessary to keep both parameters constant.

◊ *Influence of pressure and gas flow variations on the QCM*

As shown in section 3.1, the resonance frequency of the QCM quartz is influenced by the pressure. In order to quantify this impact on the frequency and thus on the deposited thickness the pressure is varied step-wise at steady gas flow - Fig. 4-16. For this experiment, gas flow of 4 l/min N_2 is set, the QCM quartz is tempered at 10 °C and the reactor chamber and gas pipes are heated to 80 °C.

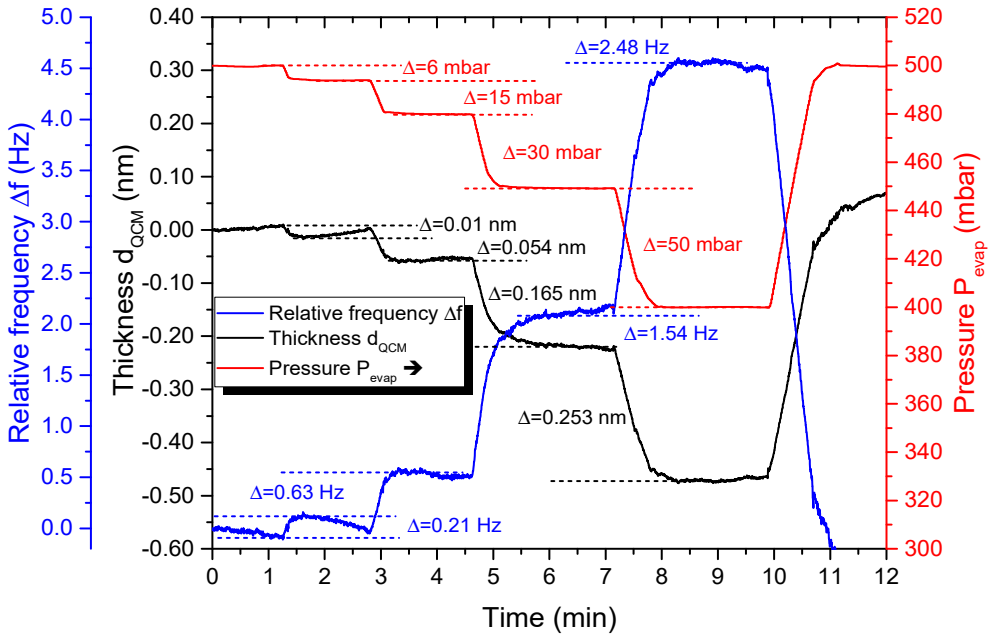

Fig. 4-16 Influence of pressure p_{evap} change (red line) on the frequency (blue line) and calculated thickness (black line) during stationary gas flow conditions (4 l/min). The QCM quartz is maintained at 10 °C and the reactor chamber and gas pipes are heated to 80 °C. At the curves, the indicated Δ-values refer to the change of corresponding parameter during one step.

A pressure drop of 6 mbar, similar to a drop observed during a cryo-trap refill, yields a frequency increase of 0.21 Hz (and a drop of 0.01 nm in thickness). After the pressure drop, frequency slightly decreases although the pressure is kept constant. This is due to small temperature fluctuations which are discussed below. As stated above, pressure has to be adjusted manually by ± 1 mbar during the plateaus. Hence, such a small fluctuation leads to a thickness change of < 0.01 nm.

For all measured pressure steps an average frequency increase of 0.05 Hz/mbar is obtained. As these changes are very small, small pressure fluctuations do not impinge the thickness measurement of the QCM. However, rapid pressure changes as observed during the refill operation of the cryo-trap should be avoided during layer deposition. This experiment also confirms that stationary gas flow conditions are mandatory for monitoring layer growth during deposition. If non-stationary conditions were used, pressure drop during monomer gas injection would inevitably alter the thickness monitoring and would lead to false values.

Similar experiments with step-wise changed gas flow at constant pressure showed that the resonance frequency of the quartz is not influenced.

4.3.2 Temperature influence

Besides pressure and gas flow different temperatures can be set in the MLD apparatus. Thus their impact on the process and related components has also to be checked.

◊ *Temperature sensitivity of the QCM electronics*

During the parameter interdependency survey it was found that the electronic unit of the QCM induces frequency shifts upon temperature change. In order to reduce the effect of temperature variations (e.g. room temperature fluctuations), the electronics is placed in an insulated box with a regulated heating element. The experiment in Fig. 4-17 documents this behavior. In order to avoid the influence of the quartz temperature itself, the crystal temperature is regulated with the thermostatic bath at 9.20 °C in the reactor chamber without carrier gas flow or vacuum.

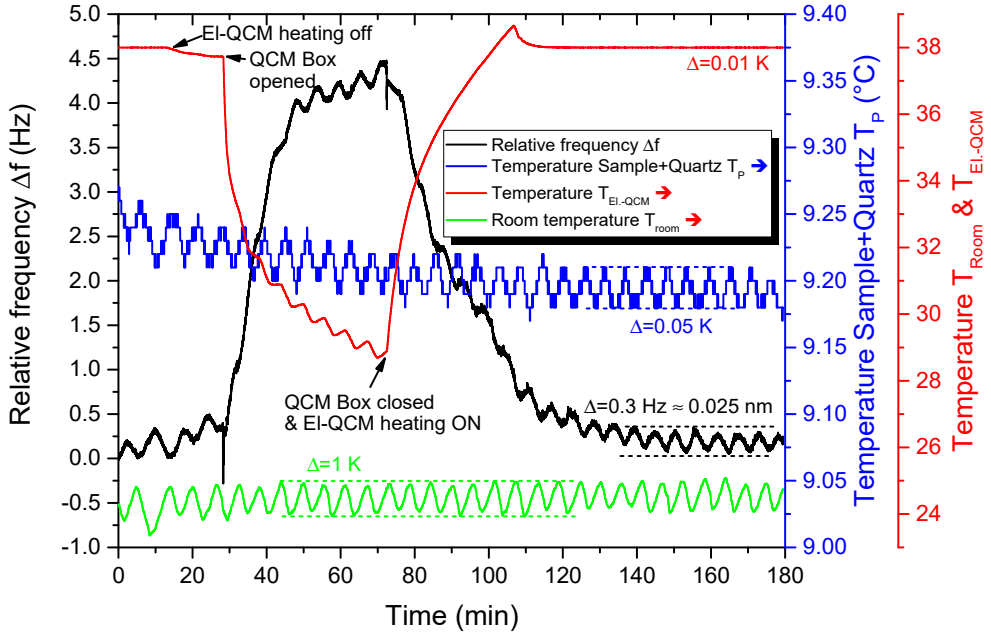

Fig. 4-17 Impact of a temperature change in the QCM electronics on the apparent quartz resonance frequency displayed by the QCM. The quartz is annealed at 9.20 °C (blue line), the room temperature (green line) is controlled with an air conditioner. The temperature inside the insulated box of the QCM electronics (red line) is modified by switching the box heating on and off and by opening the box.

At the start of the experiment the temperature $T_{El.\text{-}QCM}$ is 38.00 °C ± 0.005 K. Then the heating is switched off and 10 min. later a slight opening of the box leads to a rapid temperature drop of ca. 9 K.

Once the temperature in the box drops the frequency increases. Over the 9 K temperature drop the frequency increases of 4.5 Hz (0.45 nm) which corresponds to about 0.05 Hz/K. This is even more significant than the pressure-induced frequency change. Therefore, the precise temperature control inside the insulated box is mandatory.

◊ *Thermal sensitivity of the QCM quartz*

The experiment from Fig. 4-17 shows another effect. Besides the frequency jump due to the change of the electronics temperature a sinusoidal fluctuation of the frequency is observed throughout the whole experiment. The frequency difference is of ca. 0.30 Hz (0.025 nm). The quartz temperature (blue line) and the room temperature (green line) are also shown in Fig. 4-17 for comparison. Both temperatures fluctuate in a similar way but with different amplitudes. The temperature amplitude at the quartz is much smaller (ΔT_P = 0.05 K) than for room temperature (ΔT_{Room} = 1 K). In order to identify which temperature change is responsible for the frequency fluctuation the experiment is extended - Fig. 4-18. While the temperature of the electronics and the quartz crystal are regulated the air conditioning unit is switched off after 45 min and switched back on 25 min later.

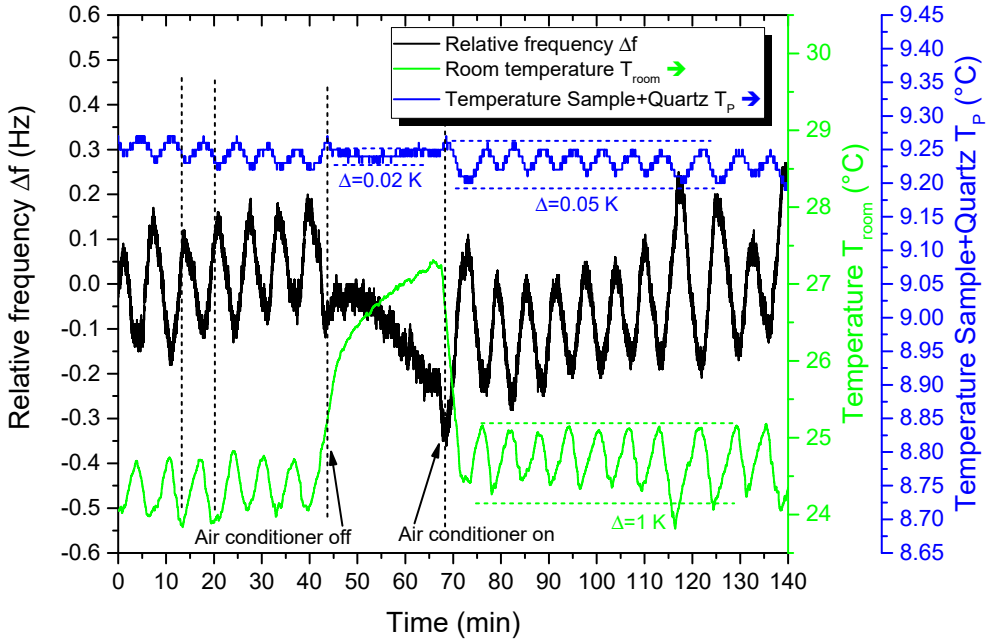

Fig. 4-18 Impact of the room temperature on the resonance frequency (black line) of the quartz. The quartz is tempered at 9.20 °C (blue line), the room temperature (green line) is modified by switching the air conditioning unit on and off.

During room temperature regulation the air conditioner switches on and off every 3-4 min. in this experiment[21]. Thus, the room temperature has a fluctuation of about 1 K. At the same time, the quartz and sample temperature (blue line) also exhibit a fluctuation of 0.05 K. As soon as the air conditioner is switched off the room temperature increases. At the same time T_P, the temperature of sample and quartz reduces fluctuation to 0.02 K and the frequency fluctuation stops. Furthermore, the average frequency starts to decrease as room temperature increases. T_P is maintained at 9.24 °C.

[21] As more heat is dissipated during the experiment when pipe and reactor heating is switched on, the switching interval becomes shorter.

Thus, it is concluded that the frequency fluctuations of ± 0.15 Hz are caused by the air conditioning unit. This also induces the higher temperature fluctuations of T_P. If the frequency shift was due to the quartz temperature fluctuation only, the frequency should stay constant or have a smaller fluctuation when the air conditioner is off. However, the frequency shift follows the room temperature change. As quartz and QCM electronics are temperature regulated a possible cause are the electrical connections leading from the electronics to the quartz crystal. Hence, the observed frequency fluctuation is a combination of electronic effects from the wiring and from the fluctuation of the quartz temperature. In [73] it was also found out that for room temperatures above 28 °C the regulated heating inside the insulated box for the QCM electronics fails and uncontrolled frequency drifts are observed. From these experiments we conclude that the room temperature change has an important impact on the frequency of the QCM through the electronics and the electrical connections. Indirectly room temperature also modifies the needle valve and thus the gas flow. The induced pressure change also reflects in a change of frequency.

An experimental proof for the temperature dependence of the quartz crystal is shown in Fig. 4-19 and Fig. 4-20. Here, the room temperature is regulated by the air conditioning unit, the QCM electronics is kept at 38 °C and T_P, the quartz and sample temperature, is increased stepwise from 10 °C to 80 °C while stationary gas flow conditions (500 mbar and 4 l/min) are maintained. With each temperature step the resonance frequency drops and thus a deduced layer thickness would increase apparently - Fig. 4-19. For a 10 K temperature increase a frequency drop of 121 – 145 Hz is found yielding an apparent thickness change of ca. 12.6 – 14.9 nm. This artefact is by far more important than the temperature and pressure effects discussed above. Thus a precise temperature control of the quartz is mandatory. It is also noted that with each temperature step the frequency and apparent thickness change becomes higher (from 129.96 Hz; 12.63 nm @ 30 °C up to 145.35 Hz; 14.87 nm @ 80 °C) confirming the nonlinear temperature dependence of the quartz.

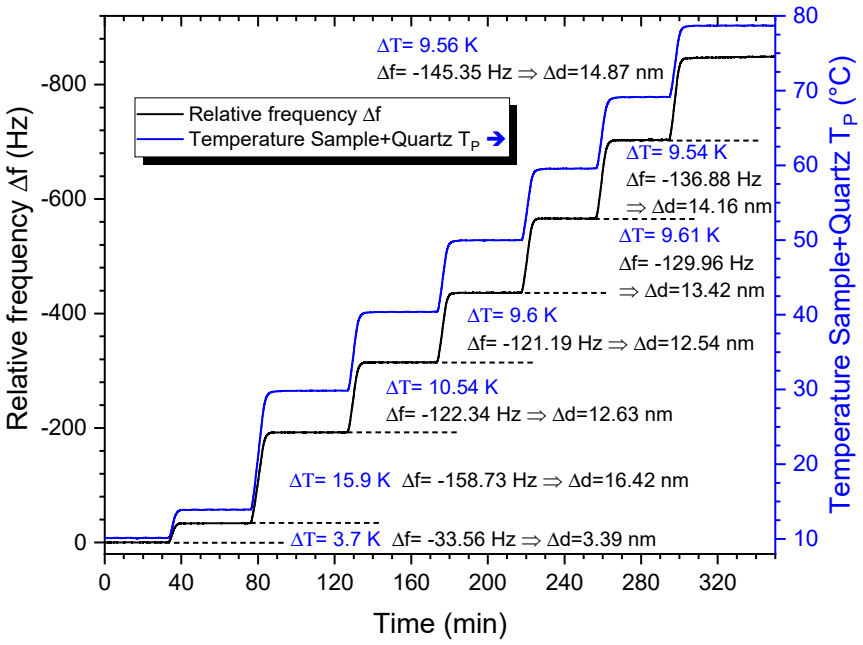

Fig. 4-19 Impact of step-wise increase of the quartz temperature (blue line) on the quartz frequency (black line) with stationary gas flow conditions. The apparent thickness change is also indicated.

As room temperature fluctuation induces a temperature fluctuation of the thermostatic bath for the quartz and sample as well as a frequency fluctuation, it is interesting to observe how this fluctuation changes at different quartz temperatures - Fig. 4-20.

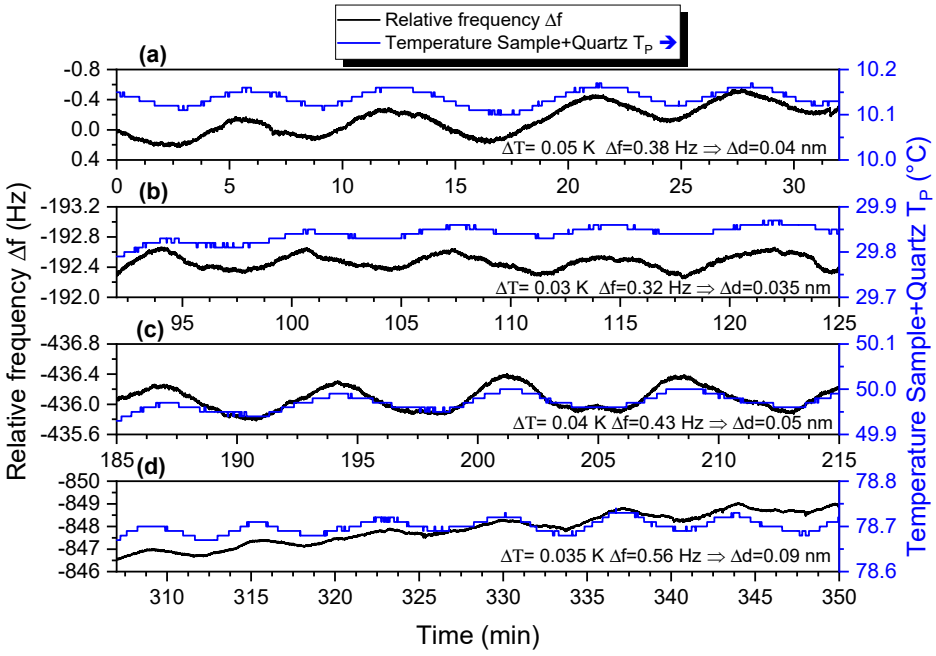

Fig. 4-20 Detail of the temperature and frequency fluctuations at four T_P-plateaus as induced by the given room temperature fluctuations. (a) T_P = 10 °C, (b) 30 °C, (c) 50 °C and (d) 80 °C.

At each quartz temperature plateau, the fluctuation of T_P varies very slightly from 0.03 to 0.05 K. The frequency fluctuation however, becomes stronger when T_P is higher (from 0.32 Hz to 0.56 Hz). Hence, as the crystal becomes more temperature sensitive, the room temperature induced frequency fluctuation is more pronounced. It is also noted that at 80 °C the frequency continues to drop about 1.85 Hz (0.2 nm) over 30 min. while the temperature is constant. It is very likely that the 30 min. at that temperature are not enough to obtain a stable state at the quartz.

◊ *Sample temperature*

The thermostatic bath as well anneals substrate and sample in the reactor chamber. Thus besides impinging the thickness readout of the QCM, temperature also affects the deposition process on the sample via the adsorption/desorption equilibrium of molecules [76, 90, 91]. Indeed, at higher temperatures released adsorption energy can more easily be retrieved and induces desorption. Hence the overall deposition rate decreases with increasing temperature. Temperature also changes the chemical reaction rate of the deposited monomers either with the substrate or with other adsorbed monomers. Finally, higher temperatures increase the mobility of the adsorbed monomers on the substrate surface and the morphology of the prepared layer can change. Hence, the sample temperature has a significant impact on the layer properties.

◊ *Evaporation cell temperature*

The evaporation cell temperature affects the evaporation rate of the monomer. Higher cell temperatures lead to faster evaporation and hence to higher monomer concentration in the carrier gas which finally influences the deposition regime on the substrate as shown in [75]. Higher monomer concentration also leads to increased contamination of the pipes. It is therefore necessary to control the evaporation cell temperature during deposition.

◊ *Influence of the temperatures of the pipes and reactor walls*

As the pipes in the evaporation stage and the reactor chamber are heated to reduce condensation of monomers on their walls, the carrier gas passing through them also gets heated up. This has several implications on the MLD process. First, higher pipe wall temperature reduces the ability of the monomer molecules to condensate on their way to the substrate. Second, an increased carrier gas temperature leads to a higher mobility of the monomers in the gas phase. This increases the self-diffusion of the monomers throughout the gas pipe and helps to obtain a more homogeneous deposition.

Higher temperature can however on the other hand facilitate chemical reactions of the functional groups with for example residual water molecules in the gas.

This section has revealed that many parameters do influence the deposition regime. Moreover an unexpectedly high sensitivity of the QCM apparatus upon temperature changes was validated. In order to reduce this effect to a minimum and achieve fluctuations below 1 Hz (apparent thickness fluctuation of ca. 0.1 nm), temperature control of ΔT_P = 0.05 K, $\Delta T_{El.-QCM}$ = 0.01 K and ΔT_{Room} = 1 K is mandatory. Furthermore, pressure fluctuation should not exceed 2 mbar and 0.02 l/min for the gas flow.

Thermal stability of all components must be reached before deposition can start. Thus for preparation of polyurethane layers using MLD, an experimental procedure was developed that takes all the observed effects into account. Aiming at the feasibility of MLD to prepare polyurethane layers and their characterisation, this work leaves the analysis of the effects of systematic variation of each processing parameter on the obtained layer to future studies.

4.4 Experimental procedures

This section details the general experimental procedure for thin polymer layer preparation by MLD. The two monomers for polyurethane formation are deposited one by one. It consists of nine steps. If a different experimental procedure is used for certain experiments, the differences are outlined accordingly.

◊ *Step 1: Substrate preparation*

24 h prior to MLD monomer deposition the substrates are prepared by physical vapour deposition (PVD) of the high purity metal onto a silicon wafer (details cf. section 5.1). Right after PVD, the substrates are transferred with short contact to laboratory atmosphere into the air lock of the MLD glove box and stored under dried air until the deposition experiment is started. The preparation of the substrates is carried out the day before MLD in order to allow the reproducible formation of the native oxide layer as well as ubiquitous carbonaceous and water contamination layers.

◊ *Step 2: MLD preparation and cleaning*

This step is carried out at the day of monomer deposition. First the metal pipes of the evaporation stage and the reactor chamber are heated to 110 °C. During that heating period of 90-120 min, the thermostat temperature, T_P, for the sample and QCM is set to 50 °C. The gas flow meters are switched on and allowed to achieve their thermal equilibrium. The water cooler of both evaporation cells is also switched on.

All glassware necessary for the initial THF rinse of the substrate (cf. section 3.2.2.1) is cleaned with soapy water followed by acetone. The QCM quartz, the quartz crystal holder, the monomer crucibles, the sample plate and its two screws are cleaned with THF in an ultrasonic bath.

The L-shaped support and the rinsing cylinder of the ERAS sample holder as well as the PTFE-coated PVC pipes are rinsed with acetone and dried with pressurised clean air.

◊ *Step 3: MLD cleaning cycle and IR reference spectra*

Once the metal pipes have reached 110 °C the cleaning cycle of the MLD is performed with empty evaporation cells and without QCM quartz and substrate. First, the vacuum pump and the *Valvoknud* controller are switched on and the cryo-trap is filled with liquid nitrogen. Then the vacuum valve V_5 of the cleaning branch in the vacuum stage (Section 4.2.4 - Fig. 4-14 green valve) is opened for a few seconds until the pressure $p_{evap} = 500 \pm 50$ mbar is reached inside the MLD. At this pressure, the cleaning gas flow of dried air (Section 4.2.1 - Fig. 4-6b green flow) is set to 60 l/min at the gas stage and the vacuum valve is opened again. In order to maintain p_{evap} the adjacent regulation valve is adjusted. When pressure and gas flow are set the gate valves of both evaporation cells are initially set to the non-deposition mode using the *Valvoknud* controller (Section 4.2.2 - Fig. 4-12a green flow) for 15 min then changed into deposition mode (Fig. 4-12b blue flow) for another 15 min. After the 30 min cleaning cycle, the gate valves go back into non-deposition mode. The switching between both deposition modes allows the high gas flow of air to remove residual monomers from all pipes of the evaporation unit and from the reactor chamber.

During the cleaning of the MLD preparatory work on the substrate is performed in parallel. The prepared metal substrate from step 1 is mounted on the ERAS sample holder and a 1st IR-ERA reference spectrum (REF-1) is recorded. Then the sample is rinsed with pure THF and a 2nd IR-ERA reference spectrum (REF-2) is recorded (cf. section 3.2.2.1, Step 2 and 3 for details). If the initial substrate cleaning and IR reference measurements take more than 30 min. then the MLD cleaning cycle is extended until REF-2 is obtained.

The MLD cleaning cycle is terminated by closing the vacuum valve V_5. The dried air gas flow is maintained until atmospheric pressure is reached and is then also switched off.

Now the sample attached to its sample plate and the quartz crystal holder with QCM quartz are transferred into the glove box[22]. During the evacuation of the air lock the monomer crucibles are filled with their respective monomers. Each evaporation cell is opened and the crucible placed inside the temperature cartridge. The water cooling of the cells is switched off during this operation. Once the air lock purged with dried air and the evaporation cells filled, the substrate and the QCM quartz are placed into the reactor chamber. The MLD is now ready for the stabilisation phase.

[22] The air lock is evacuated for 10 min. and then purged with dried air before being opened from the inside the glove box.

◊ *Step 4: MLD stabilisation phase*

As outlined above stationary and stable conditions in the MLD are crucial before starting the layer deposition. Once the sample, quartz and monomers are placed in the reactor chamber and evaporation cells, respectively, the cryo-trap is refilled with liquid nitrogen. Depending on the length of the stabilisation phase it must be refilled several times. It is noted that for each refill a drop of pressure is induced and thus a change in resonance frequency of the quartz. Thus a refill should always be followed by a few minutes of further stabilisation. Refilling the cryo-trap during the layer deposition must be avoided.

The temperature of substrate and quartz is set to the chosen deposition temperature (in most cases 10 °C). The temperatures of pipes and reactor chamber are set to 80 °C. The minimum stabilisation time corresponds to the time to achieve these new temperatures. The pressure is then set to 500 mbar. Therefore the cleaning valve V_6 is opened shortly in order to suck the reactor lid tight and to reach a pressure close to 500 mbar. Then the vacuum deposition valve, V_5 (Section 4.2.4 - Fig. 4-14 blue valve) is opened as well as the nitrogen gas flow in the gas stage (Section 4.2.1 - Fig. 4-6a blue flow). The target pressure of 500 mbar is adjusted with the adjustment needle valve in the vacuum stage and the gas flow is set at the gas stage with the appropriate needle valve. The gate valves of the evaporation cells are set to non-deposition mode. From this point on, all parameters (temperatures, pressure, quartz resonance frequency) are recorded in the Labview program until the end of the deposition experiment.

The evolution of the apparent thickness and a few selected parameters over the stabilisation phase is shown in Fig. 4-21a. At zero time quartz and sample are placed into the reactor chamber (end of step 3). As the quartz and sample holder are heated at 50 °C an initial drop of resonance frequency leading to an increase of the apparent thickness over the first 5 min. is recorded as the quartz is heated. As the carrier gas flow is switched off during the transfer the temperature inside the reactor chamber increases (Fig. 4-21b – red line). Once quartz and sample are placed in the reactor chamber, pressure and gas flow are set. Due to the rapid pressure drop, the resonance frequency of the quartz and thus the apparent thickness change. During the first two minutes the gas flow and pressure reach their equilibrium. After 5 min. the sample and QCM temperature are set to the desired deposition temperature (here 10 °C). The thermostatic bath requires 20 min. to reach this temperature - Fig. 4-21a. As the temperature of sample and quartz changes, the resonance frequency changes too. As the temperatures of the metal pipes and reactor chamber change, the carrier gas temperature also changes, leading to small modification of the resonance frequency (0.08 nm shift over 70 min. - Fig. 4-21c).

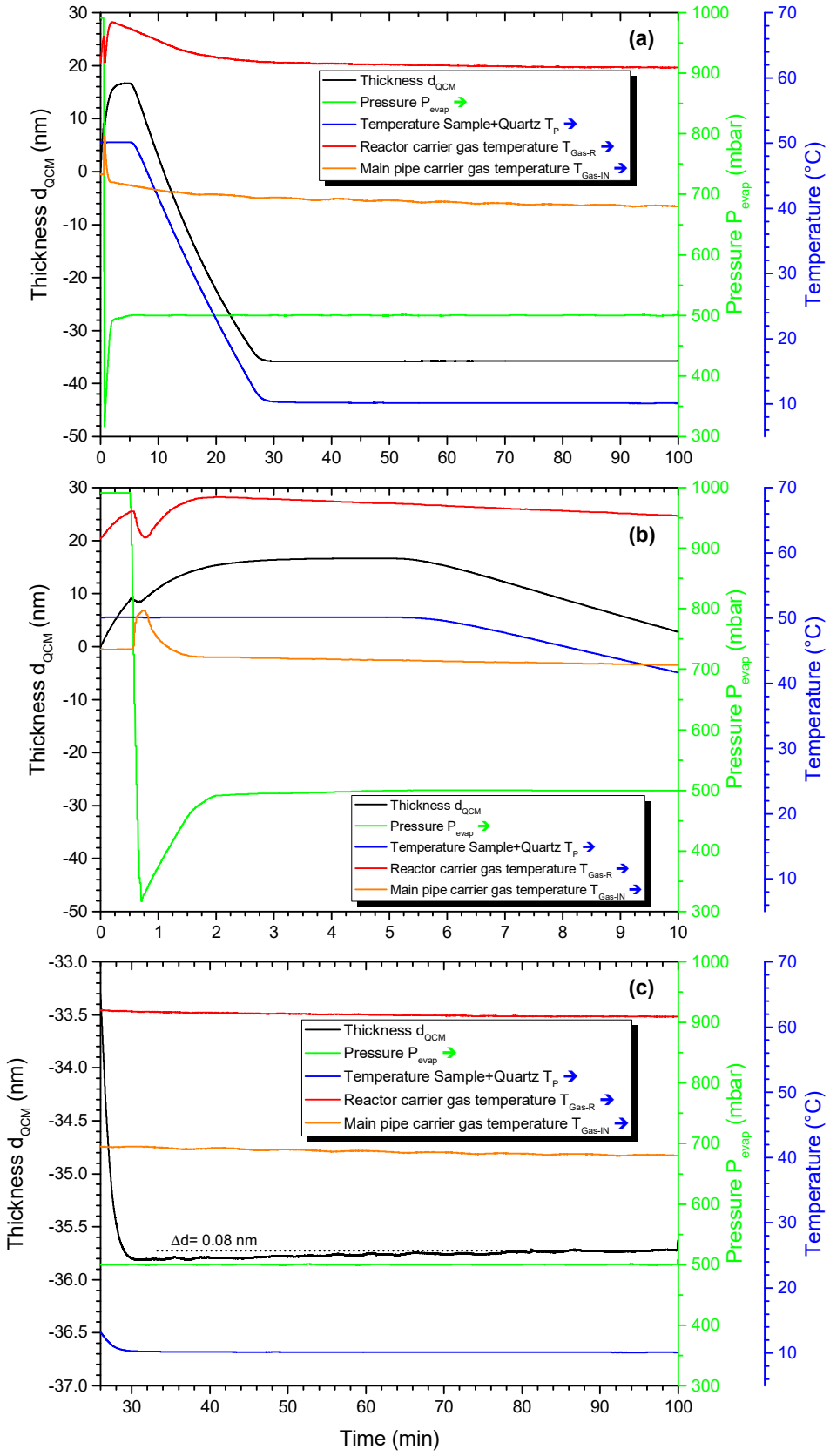

Fig. 4-21 Evolution of QCM thickness, pressure, sample and quartz temperature and carrier gas temperature in the evaporation stage and reactor chamber during the stabilisation phase. (a) Overview. Zooms for the first 10 min (b) and after 30 min (c). This experiment is carried out at 5 l/min N_2, 500 mbar and 10 °C sample temperature.

The electromagnetic valves in the gas stage and the adjacent needle valve also reach a thermal equilibrium. The gas flow fluctuations diminish. A stable state is obtained when all these parameters become stable and the frequency of the QCM then fluctuates with the room temperature only. The corresponding apparent thickness fluctuation below 0.1 nm can be considered as result of parameter fluctuations and thus insignificant. The stabilisation phase can take up to two hours.

◊ *Step 5: Heating of the evaporation cells*

When a stable state is reached the evaporation cells with the monomers can be heated. The heating time allows for some extra stabilisation time. Both cells can be heated at the same time or the second monomer can be heated during/after deposition of the first one depending on the experiment and chosen monomer[23]. During heat-up the gate valves are in the non-deposition mode.

First, the water cooler of the chosen evaporation cell is switched off and the *Thermoknud* controller switched on. Heating of the monomer consists of two phases. During the preheating phase the cell is continuously heated up to a certain temperature. Then the temperature setting is set to the target value and intermittent heating regulates the selected temperature. The necessary set points for each monomer are given in Appendix 11.4.2 - Table 11-14. The same procedure is repeated for the second cell. Upon reaching the desired temperature and before starting the deposition the cryo-trap is refilled with liquid nitrogen.

◊ *Step 6: Monomer deposition*

The monomer deposition can now be started. Fig. 4-22 shows the evolution of the layer thickness as measured by the QCM during the deposition step. The gate valves of the evaporation cell containing the first monomer are switched to deposition mode (at 0 min.) while the second cell remains in its non-deposition setting. As soon as the gate valves are switched the thickness evolution on the QCM is monitored. The gaseous monomers take a certain time to be carried from the cell to substrate and quartz by the nitrogen flow. The deposition is either continued for a certain time (e.g. deposition during 1 hour) or up to a certain thickness of the achieved layer (in this example it is 10 nm). Then the gate valves are switched back to non-deposition mode. Similar as for the initial time lag, monomers in the carrier gas between the gate valves and the reactor chamber as well as those desorbing from the pipe walls will still arrive at the substrate and can adsorb. Thus, in order to obtain a defined layer thickness the gate valves must be switched before reaching the target thickness. Monomer adsorption progressively slows down and reaches a plateau.

[23] The moment chosen for heating the second monomer mainly depend on the evaporation temperature of the substance (and the time to reach it) as well as the moment when the 2nd monomer is deposited.

If monomers tend to desorb from the substrate, after the plateau the thickness decreases as shown in this example. If only one monomer is deposited the experiment is stopped at this point and continued at step 8.

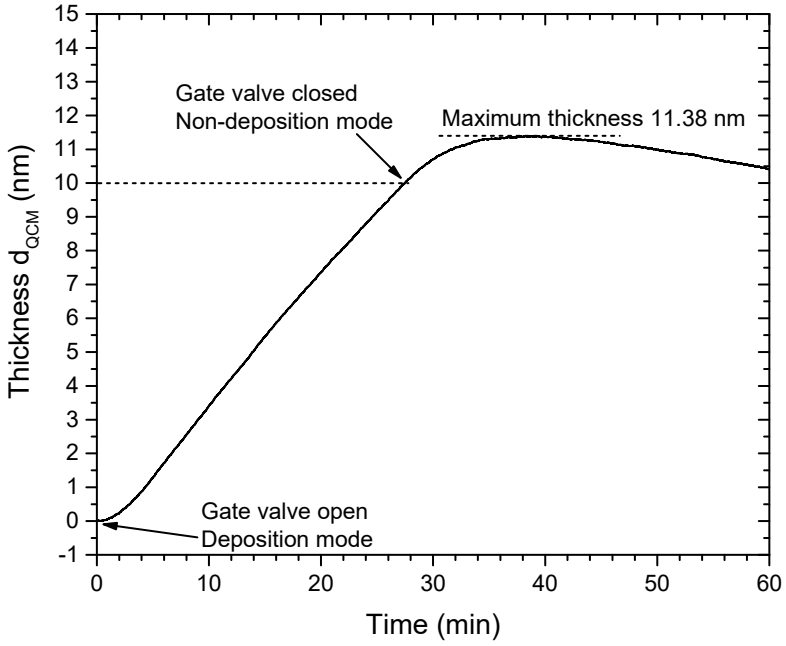

Fig. 4-22 Evolution of QCM thickness during the layer deposition of triol. Gate valve of the evaporation cell is opened at 0 min. and closed after reaching 10 nm. This experiment is carried out at 2 l/min N_2, 500 mbar and 10 °C sample temperature.

◊ *Step 7: Deposition of the second monomer*

Once the thickness of the first monomer layer has reached its plateau (or before desorption begins) the second monomer is provided as described in step 6. The gate valves of the second evaporation cell are now switched over while the first cell is cooled using the water cooler. After deposition, the gate valves are set to non-deposition mode and the cell is also cooled down.

◊ *Step 8: Sample transfer and characterisation*

Once the deposition plateau is reached the vacuum valve at the vacuum stage is closed. The carrier gas continues to flow into the MLD until atmospheric pressure is reached. Gas flow valves are then closed too. The coated substrate is removed from the reactor chamber and rapidly transferred through the air lock into the IR spectrometer. IR-ERA sample spectra are then recorded and the layer characterised (cf. section 3.2.2.1 – Step 4 and 5). MLD parameter recording in Labview is also switched off.

◊ *Step 9: Final MLD cleaning cycle*

The last step of this procedure consists in the cleaning of the MLD. The cleaning cycle is similar to step 1. The sample temperature is increased to 50 °C, the monomer crucibles are removed from the evaporation units and the cryo-trap is re-filled again with liquid nitrogen. Then a carrier gas flow of 60 ml/min of dried air at ca. 500 mbar is set. During the 30 min. cleaning the gate valves of both evaporation cells are switched back and forth between both modes. Once cleaning is finished atmospheric pressure is restored, the vacuum pump, the gas flow meters, the thermostatic bath, the water cooling and all controllers are switched off. The monomer crucibles and the quartz crystal are cleaned with THF.

The MLD apparatus, its features and requirements, the parameter influence and the developed experimental procedure have been discussed. In the next chapter the substrate and the monomer properties are described before moving to the discussion of the obtained results.

5 Components of the polyurethane system

In this chapter the native metal substrates as well as the studied monomers are introduced. The characterisation of their bulk properties is also discussed here after. This mainly consists in their IR band assignment, thermal stability and to some extend their topographic features.

5.1 Metal substrates

In this part the utilised non-coated substrates and their properties as obtained after the preparation regime are summarised. In this work native surfaces of aluminium and copper are used. Both are relevant metals for many technologic applications. Aluminium and its alloys are for example used in lightweight constructions, airplanes and automotive. In these examples adhesive joints and polymer coatings are two main technical applications of polymers. Copper is commonly used as electrically and thermally conductive material. It is also used as alloying element for various metal alloys. In the field of microelectronics copper is very often in contact with epoxies used as support boards. Thus both metals are very suitable for the study of the development of metal-polymer interphases. Beside the oxide and hydroxide layer on Al and Cu adsorbed water and carbonaceous contaminations from the ambient atmosphere are omnipresent [92-96].

The chosen characterisation methods, in particular IR-ERAS and SFM, but also the preparation of thin layers in the nanometre range requires particularly flat surfaces with low roughness. Thus, surface roughness should not exceed the thickness of the polymer deposit to not impinge layer morphology. Moreover, the chemical state of the surface must be well defined and reproducible. From these requirements it is not possible to use technical surfaces of these metals. Their roughness generally lies in the order of a few microns and higher and their chemical composition is often inhomogeneous with big differences.

To circumvent this, the metal substrates are prepared by physical vapour deposition (PVD) of the high purity metals onto silicon wafers. The polished monocrystalline wafers possess a very flat surface with low roughness in the sub nanometre range which is transferred over to the surface of the deposited metal. Nevertheless the substrates prepared this way possess technically relevant chemical surface states. During PVD the metal is electrically heated in a tungsten basket until it starts to evaporate under high vacuum conditions. The evaporating atoms spread linearly and deposit as a layer on the Si wafer [76]. It is to note in passing that the morphology and topography of the prepared metal coatings are determined by the preparation technique and its parameters [3].

The prepared metal coating must be thick enough so that the underlying Si wafer is not visible anymore by the infrared beam and the metal can be considered as semi-infinite medium. This is achieved with at least 100 nm thick metal coatings.

◊ *Experimental procedure*

The Si wafer is broken into squares of ca. 2 x 2 cm^2 and any scrapings and debris are removed with pressurised air.

24 h prior of the MLD deposition two[24] Si squares are transferred into the PVD chamber and placed on a mobile tray (Fig. 5-1a). The necessary amount of high purity metal wire (Al & Cu 99.999 %; Au[25] 99.99 %) is coiled and placed in a small tungsten wire basket (Fig. 5-1b). The masking shutter is placed below the basket. This avoids deposition of contaminations during initial heat-up of the wire.

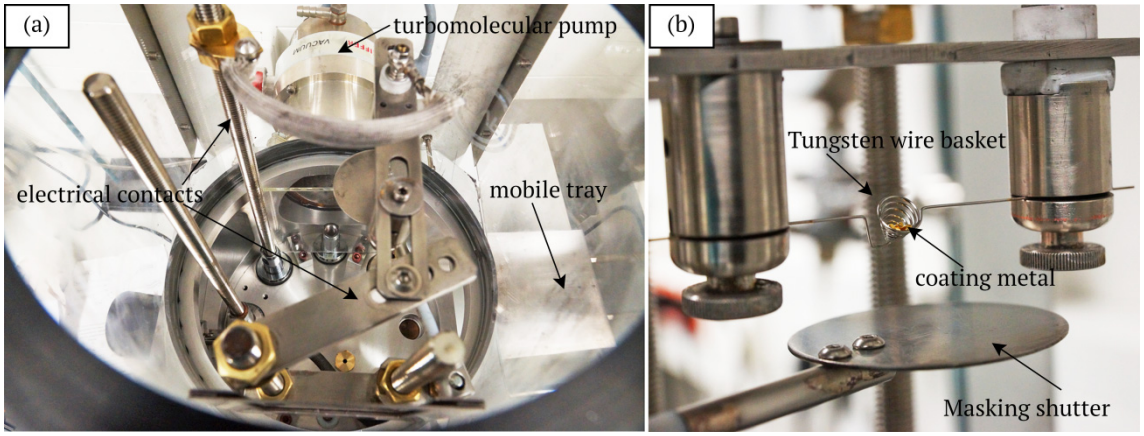

Fig. 5-1 Physical Vapour Deposition (PVD) setup. (a) View inside vacuum chamber with sample tray placed outside for sample loading. (b) Zoom onto the tungsten wire basket filled with coiled coating metal.

Next, the PVD chamber is evacuated to high vacuum. This vacuum is maintained for at least 45 min. prior deposition. The wire basket is then electrically heated with an initial current of 10 A leading to light glowing and desorption of volatile contaminants. Then the current is increased to the given value for each metal (c.f. Appendix 11.2). Only then the masking shutter is removed and evaporating metal atoms can reach the Si wafer. Once complete evaporation of the metal in the basket is reached the shutter is placed back and the heating current switched off. The PVD chamber is finally purged with argon.

The metal coated substrates are removed and stored under dried air until the MLD experiment is carried out next day. After contact with ambient air, the metal coatings instantaneously form their native oxide/hydroxide layer as well as the top contamination layer of adsorbed water and carbonaceous compounds.

The obtained substrate surface can be represented as a model shown in Fig. 5-2.

[24] Only one sample is required for the MLD coating. The spare substrate can either be used as backup or for further characterisation with SFM for example.
[25] The aluminium pans for thermogravimetric analysis (TGA) are coated with gold.

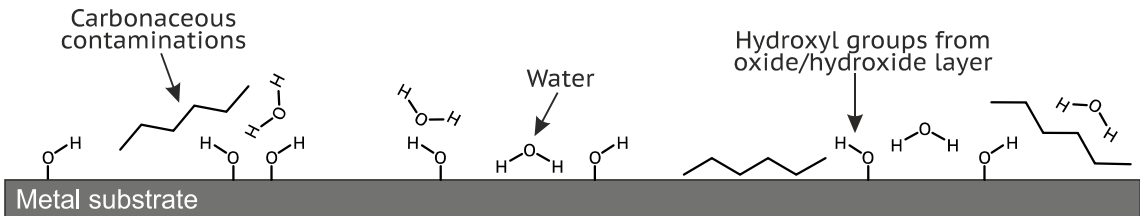

Fig. 5-2 Model of the prepared native metal substrate surface with adsorbed water and carbonaceous contaminations from the atmosphere. The OH groups linked to the surface represent the natively formed oxide/hydroxide layer.

5.1.1 Aluminium

The Al-PVD layers exhibit grey mirror-like flat surfaces upon visual inspection. Fig. 5-3 shows the topography and the phase contrast of such a layer as measured by tapping mode SFM. The 2D height image (Fig. 5-3a) reveals that with the chosen parameters homogeneous fine-grained polycrystalline deposits are obtained. The average roughness R_{RMS} is about 1.7 nm. Most crystallite height variation is of about 7 nm (Fig. 5-4a). A few crystallites protrude from the surface. The maximum height difference between the lowest and highest point (peak-to-valley) is at most 20 nm. The phase contrast (Fig. 5-3b and Fig. 5-4a) is uniform and gives phase differences of ca. 13 degrees when moving from one crystallite to the other.

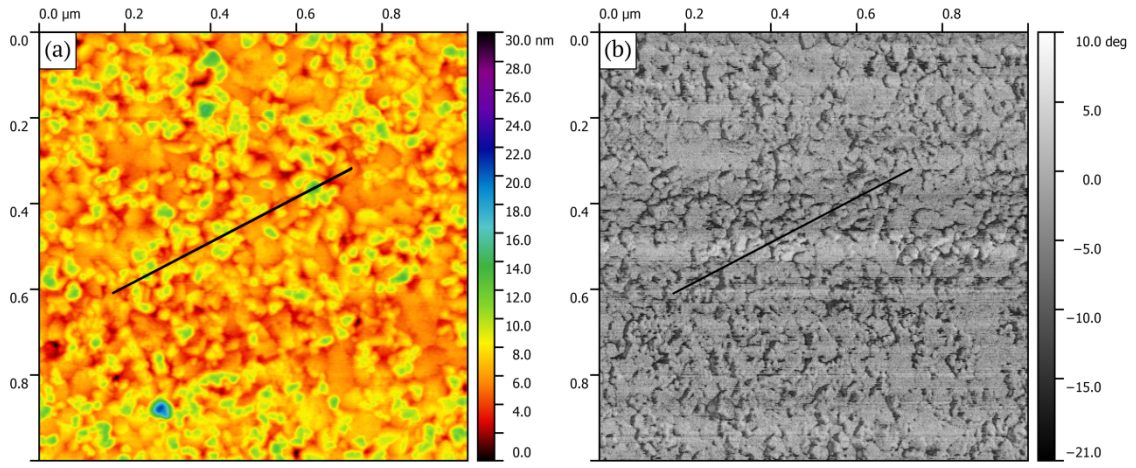

Fig. 5-3 Tapping mode SFM (a) topography and (b) phase contrast image of a virgin Al-PVD coating on Si wafer. 1 x 1 µm² scan. The black lines indicate the location of height and phase contrast profiles given in Fig. 5-4a.

The height distribution shows that most crystallites are 3 to 10 nm high with a maximum at around 6.5 nm. These values are much smaller than the wavelength in IR spectroscopy and hence they are too small to impinge our thin layer IR spectroscopic analysis which presumes flat and uniform layers. Thus, the prepared Al substrates are very suitable for the preparation and characterisation of thin layers in the nanometre range.

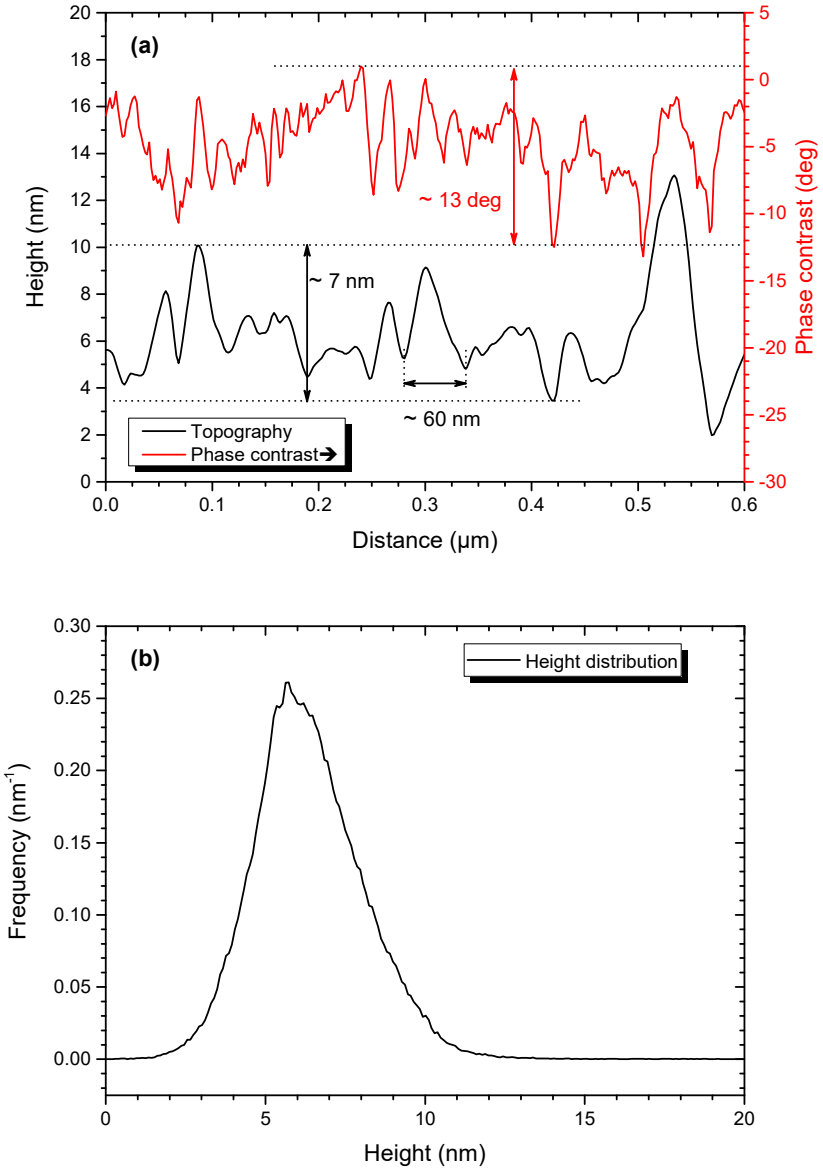

Fig. 5-4 (a) Topography (black) and phase contrast (red) profiles along the black lines in Fig. 5-3. (b) Height distribution of the 1 x 1 µm² scan of the native Al (cf. Fig. 5-3a).

Results from X-Ray photoelectron spectrometry (XPS) [94, 97] shows that the formed oxides and hydroxides are present as a 3 – 4 nm plain layer. Water adsorbs on and inside this amorphous layer. As it cannot be detected in the XPS, water is only weakly attached and hence removed by the UHV.

Carbonaceous contaminations from the ambient are also present on top of the amorphous Al_2O_3 layer. They mainly consist of aliphatic hydrocarbons with C-O, C=O, O-C=O and O-C-O functionalities. They do not form a closed layer as Al is predominant in the spectra. All in all the thickness of the oxide layer and the adsorbed carbonaceous contaminations on top does not exceed 5 – 8 nm.

5.1.2 Copper

The pink-reddish Cu-PVD layers are also very flat and smooth. They exhibit a polycrystalline morphology (Fig. 5-5a) with an average roughness R_{RMS} of ca. 1.4 nm. The average height difference of the crystallites is of about 5 nm (Fig. 5-6a). The peak-to-valley height difference is at most 14 nm and thus more homogeneous than on Al. The phase contrast (Fig. 5-5b) is similar for each crystallite. The boundaries of each crystallite give rise to phase differences of maximum 30 degrees.

The height distribution (Fig. 5-6b) shows that most crystallites are 2 to 8 nm high with a maximum at around 5.4 nm. Similar to Al the as prepared Cu substrates meet all requirements for the chosen characterisation methods.

XPS of prepared copper substrates show similar results as for the Al [94]. A 3-4 nm thin native oxide layer of Cu oxide and hydroxide is present on top of the metallic Cu. Cu^{2+} species and hydroxides dominate at the interface with the air. Carbonaceous contaminations, similar to Al, are also present here.

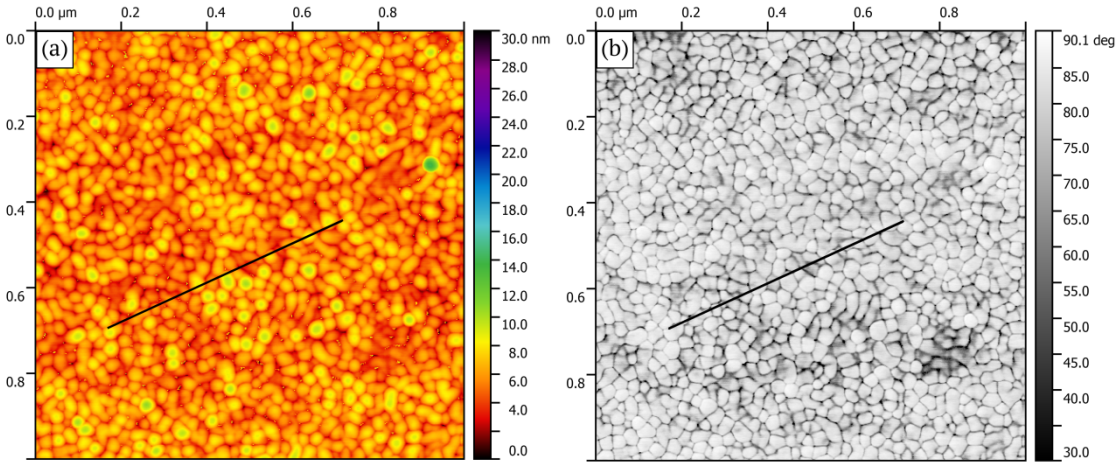

Fig. 5-5 Tapping mode SFM (a) topography and (b) phase contrast image of a virgin Cu-PVD coating on Si wafer. 1 x 1 µm² scan. The black lines indicate the location of height and phase contrast profiles given in Fig. 5-6a.

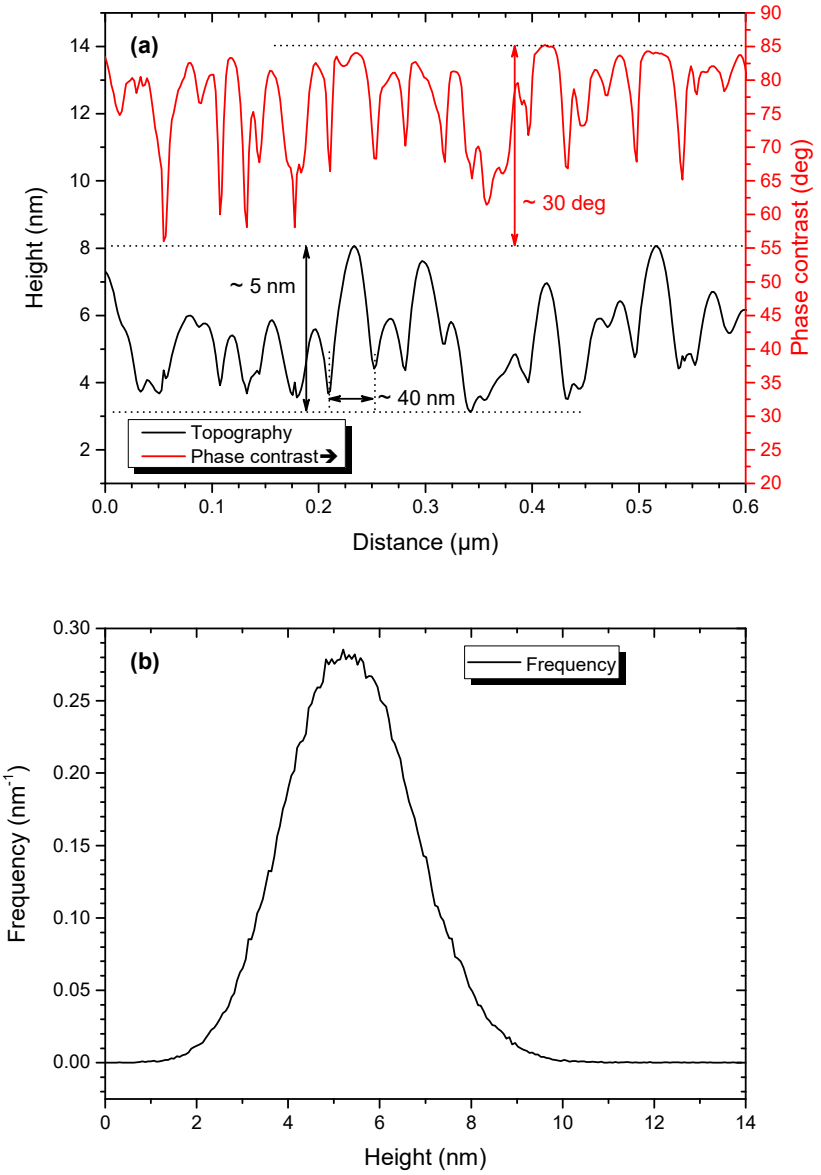

Fig. 5-6 (a) Topography (black) and phase contrast (red) profiles along the black lines in Fig. 5-5. (b) Height distribution of the 1 x 1 µm^2 scan of the native Cu (cf. Fig. 5-5 a).

5.2 4,4-methylene diphenyl diisocyanate

4,4'-methylene diphenyl diisocyanate (4,4'-MDI), its related isomers (2,4'-MDI and 2,2'-MDI) as well as toluene diisocyanate (TDI) are the most used aromatic isocyanates for polyurethanes [5, 98-101]. In this work the bifunctional 4,4'-MDI is utilised as hardener for the polyurethane system (Fig. 5-7). Pure 4,4'-MDI is a white crystalline solid at room temperature (physical properties are given in Appendix 11.3.1).

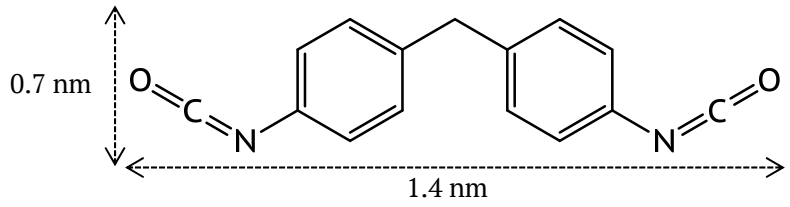

Fig. 5-7 Chemical structure of the 4,4'-methylene diphenyl diisocyanate (4,4'-MDI).

5.2.1 Isocyanate chemistry

The isocyanate group is one of the most reactive functionalities in the organic chemistry. An exhaustive description of the reactions involving NCO groups is provided in literature [102-105]. In this section the most important reactions are only briefly outlined.

The high reactivity of the NCO group is due to the electrophilic character of the carbon atom. It is surrounded by electronegative oxygen and nitrogen and hence depleted in electron density. Furthermore, the electrophilic character is stabilised through various inductive (-I) and mesomeric (-M) electron density delocalisation [36, 106]. Most reactions involving the NCO group are hence related to an addition reaction with nucleophilic partners.

◊ *Reaction of isocyanate with other species*

Technically speaking, nucleophilic addition reactions are the most utilised for isocyanate chemistry. The nucleophilic partner requires hydrogen atoms attached to an electronegative atom. They include primary, secondary and tertiary alcohols as well as primary and secondary amines. The reaction rate depends on the electrophilic character of the NCO carbon and the nucleophilic character of the reaction partner [102, 103]. Reaction of an isocyanate with a hydroxyl group leads to the formation of urethane - Fig. 5-8.

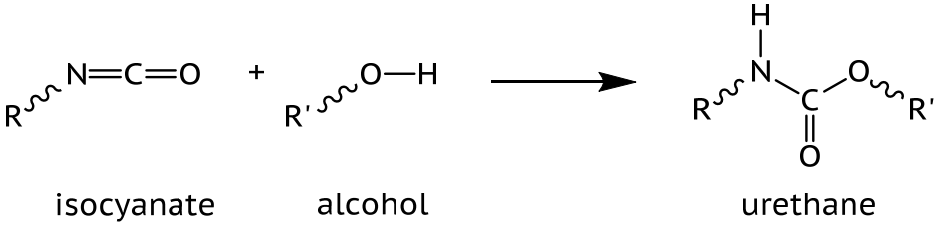

Fig. 5-8 Urethane formation by nucleophilic addition of an alcohol on an isocyanate.

In passing it is to mention that three possible reaction mechanisms are discussed in literature [107, 108]. They involve cyclic or ionic transition states. A third mechanism based on the ionic transition state requires the complexation of a second hydroxyl group.

Using the aforementioned addition reaction polyurethane can be prepared. Polyaddition requires at least di- or multifunctional alcohols and di- or multifunctional isocyanates [5, 104]. Bifunctional monomers will lead to linear polymer chains while more functionalities will form crosslinks. The choice of the alcohol (e.g. chain lengths, polyether or polyester type) and the polyisocyanate (e.g. aliphatic or aromatic) allows preparing a large variety of polyurethanes [5]. This also greatly influences the material properties and hence their application as for example foams, elastomers, adhesives and coatings to name a few.

The urethane formation can be catalysed using either basic substances (e.g. tertiary amines) or metal salts (e.g. Sn, Zn, Fe, Cu) [103, 107]. Furthermore, as the urethane group possess a carbonyl group and an acidic proton on the nitrogen hydrogen bonding is possible. The carbonyl group can form hydrogen bonds with hydroxyl groups from unreacted alcohols. The hydrogen at the nitrogen can form hydrogen bonds with an isocyanate. In both cases the reactivity of the monomers is increased and the urethane conversion can be auto-catalysed.

At high temperatures (120-140 °C) or using catalysts urethane groups can react with free isocyanates and form allophanates - Fig. 5-9.

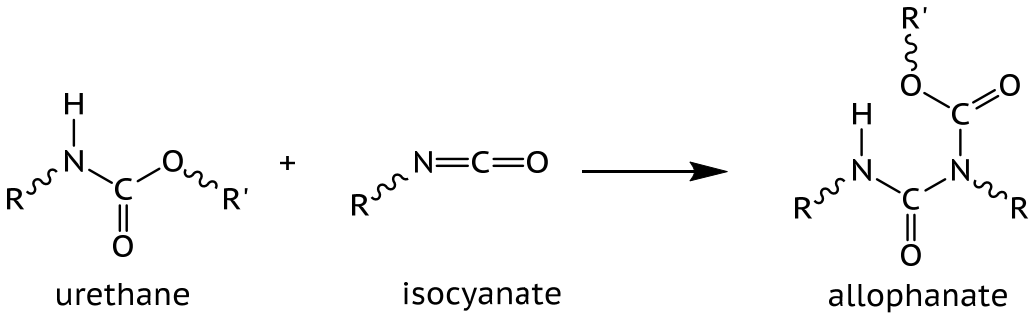

Fig. 5-9 Allophanate formation by reaction of urethane with isocyanate at elevated temperatures.

Besides the reaction with alcohol isocyanate can react similarly with amines. Now urea groups are formed instead of urethane groups - Fig. 5-10. As amines are much more nucleophilic the urea formation is much faster than urethane formation. The formed urea groups can also undergo hydrogen bonding and thus auto-catalyse their formation [109].

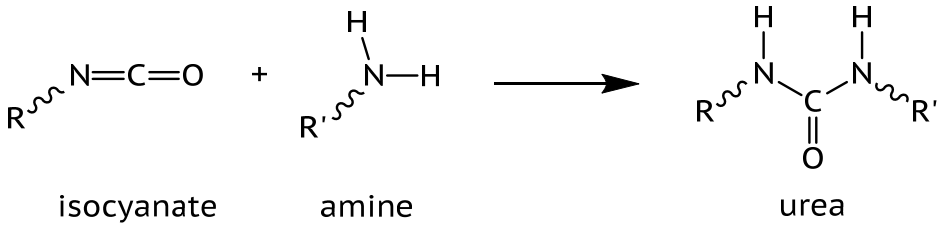

Fig. 5-10 Formation of urea by reaction of isocyanate with amine.

Reaction of polisocyanates with di- or multifunctional amines will lead to the formation of polyureas, which have similar applications as polyurethanes. In many cases both polymers are even copolymerised.

Urea groups are also formed when isocyanates are in contact with water. As H_2O is also a nucleophilic molecule it reacts with isocyanate leading to the formation of an amine and CO_2. This amine then reacts with a second isocyanate and an urea is formed Fig. 5-11.

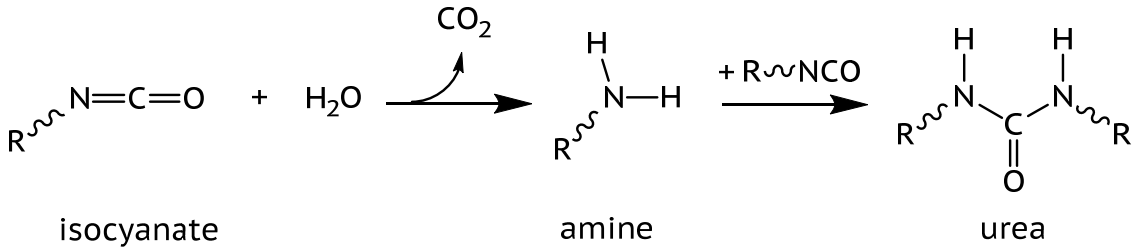

Fig. 5-11 Formation of urea by reaction of isocyanate with water.

This reaction has a high technical relevance as the evolved CO_2 can be used as blowing gas in order to fabricate foams. Furthermore, this reaction has not to be neglected as the utilised substrates present adsorbed water from the atmosphere – cf. section 5.1. Hence, part of the deposited isocyanates can react and form urea groups. See also section 6.1.2 for detailed discussion.

Urea groups are capable to react with isocyanates at elevated temperature. A biuret structure is obtained - Fig. 5-12. Formation of the biuret structure is highly reduced if aromatic isocyanates are utilised [102].

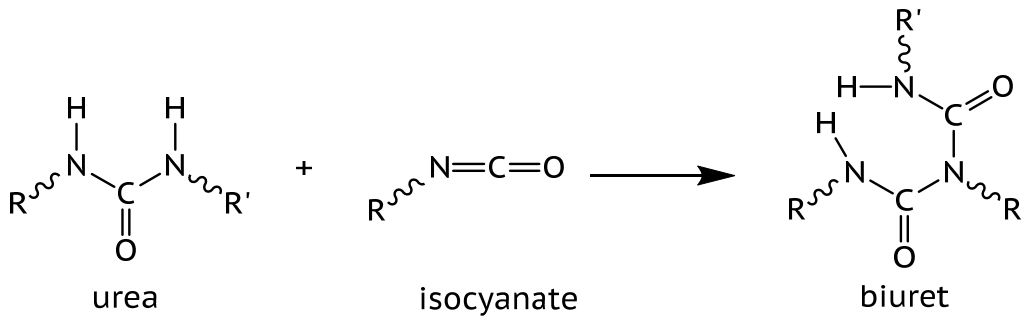

Fig. 5-12 Biuret formation by reaction of urea with isocyanate at elevated temperatures.

◊ *Reactions between isocyanates*

Beside the addition reaction with nucleophilic molecules isocyanate is also capable to react with another isocyanate group [101, 102]. In this case isocyanate can di- and trimerize.

Dimerization leads to the formation of an uretdione group – Fig. 5-13. Aliphatic isocyanates require the addition of a catalyst in order to enable dimerization. Aromatic isocyanates however, can already dimerize at RT if two isocyanate groups can arrange in a favourable orientation [110]. For example in solid 4,4'-MDI the isocyanates arrange in a particular way to form a crystal lattice, which facilitates the formation of uretdione groups.

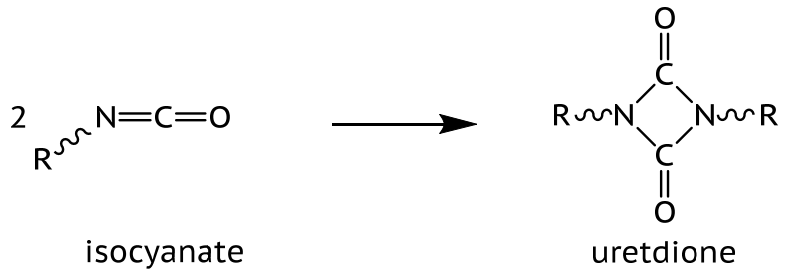

Fig. 5-13 Dimerization of two isocyanates into a uretdione group.

Hence, in order to reduce dimerization, but also reaction with moisture from the air 4,4'-MDI must be stored at -20 °C. At this temperature side reactions (mainly dimerization to urethdione) are significantly slowed down. Furthermore, uretdione formation is reversible at elevated temperatures (>160 °C).

Unfortunately elevated temperatures facilitate other side reactions as for example trimerization and hence formation of isocyanurates – Fig. 5-14. Thermal stability of these species is much higher than for the uretdione.

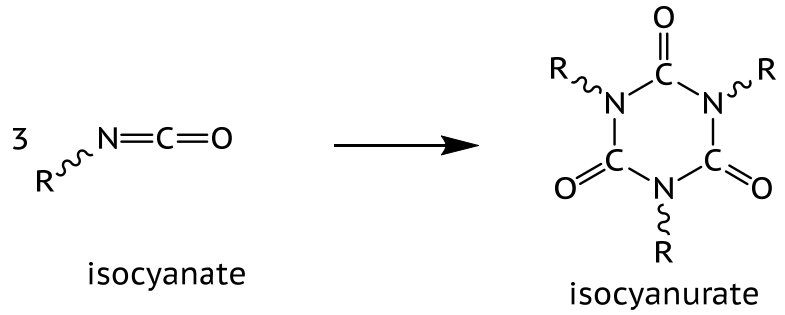

Fig. 5-14 Formation of isocyanurate by trimerization of three isocyanate groups.

Isocyanates can also condensate into carbodiimide groups, which in turn can further react with an isocyanate to form uretonimine groups - Fig. 5-15. These reactions require either high temperatures or the use of a catalyst [111].

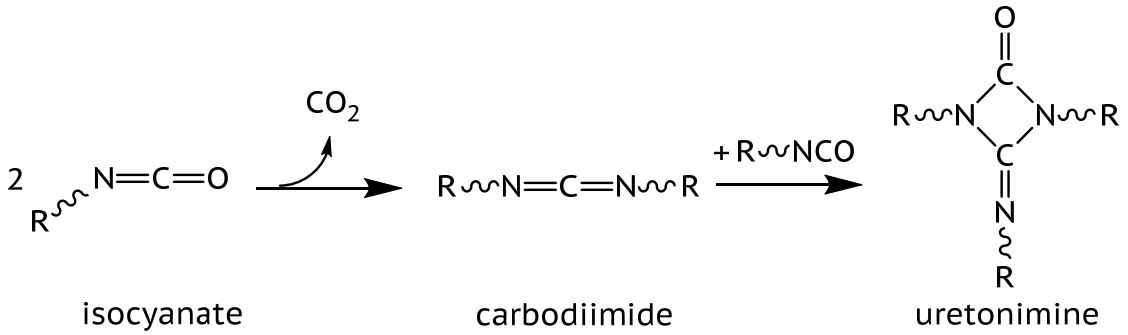

Fig. 5-15 Condensation of isocyanates into carbodiimide and formation of uretonimine by cycloaddition.

All these side reactions cannot be avoided during the evaporation of the monomer melt inside the MLD. However, even if these species with higher molecular weight are formed either over storage or due to increased temperature during the evaporation they evaporate at much higher temperatures as 4,4'-MDI and hence should remain in the crucible.

5.2.2 IR band assignment in the bulk

Due to the high reactivity of the isocyanate groups many new functional groups can be formed. Thus, a precise IR band assignment of the MDI is required as a starting point. As outlined in chapter 3.2.6 band assignment using band catalogues is not precise and many functional groups based on the isocyanate are not detailed. Thus, analysis of vibrational modes using quantum mechanical modelling is necessary. The band assignment shown hereafter is based on two complementary studies [7, 60].

◊ *Conformational analysis of the 4,4'-MDI*

As described in [60] the first step of quantum mechanical modelling consists in determining the energetically most favourable conformer. Fig. 5-16 shows the fully optimised molecule and introduces the notation used for describing the geometry.

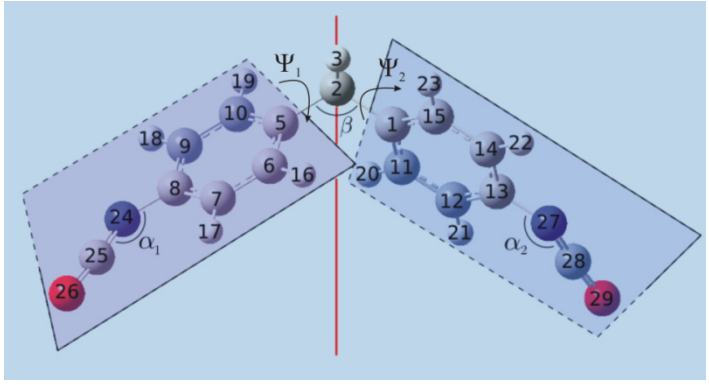

Fig. 5-16 Optimised spatial structure of the isolated 4,4'-MDI molecule. Oxygen: red, nitrogen: blue, carbon: grey and big, hydrogen: grey and small [60].

The carbon atoms 1, 2 and 5 define the Plane Of the Molecule (POM) and span the angle $\beta = 114.6°$, i.e. a value close to the ideal value for sp^3-hybridised carbon atoms. The Axis Of the Molecule passing through carbon atom 2 (AOM – red line), the carbons 8, 13, and the nitrogen atoms 24 and 27 all lie roughly in the POM. Due to the sp^2 hybridisation of the nitrogen atoms, the angle $\angle CNC \equiv \alpha$ is 139.8 ° and the isocyanate atoms are in-plane with the adjacent phenylene ring (sketched in bluish grey in Fig. 5-16). Both phenylene rings are twisted by equal angles, $\psi_1 = \psi_2 = 55$ ° with respect to the POM but in opposite directions. To be precise, ψ_1 and ψ_2 are the dihedral angles formed by the atoms 1, 2, 5, 6 and 5, 2, 1, 11, respectively (Fig. 5-16).

In order to evaluate the structural flexibility and to search for other conformers, the energy landscape is scanned by rotating the phenylene rings together with their attached isocyanate group. ψ_1 and ψ_2 were varied in steps of 10 ° in the range (-90 ° … 270 °) and (0 ° … 360 °) respectively, with 0 ° corresponding to the phenylene ring in the POM. The rotation is done clockwise when looking from the methylene group (between the phenylene rings) towards the isocyanate. Initially the NCO groups are positioned in the plane of their corresponding phenylene ring (cf. Fig. 5-17).

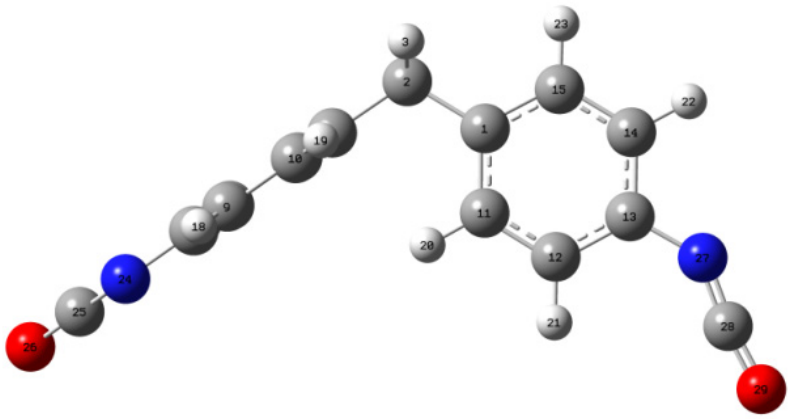

Fig. 5-17 Starting geometry for the energy landscape evaluation. $\Psi_1 = -90$ ° and $\Psi_2 = 0$ °. The left isocyanate group points behind the paper plane [60].

The energy map as function of (ψ_1, ψ_2) was calculated as follows. At first, a total of eight local energy minima (i.e. conformations) were identified. The corresponding molecule structures are the so-called conformers. Subsequently, for scanning the (ψ_1, ψ_2) beyond those energy minima, we fixed all other structural values at those for the structurally closest total-energy minimum.

That provides an idea of the shape of the energy map offside the conformations. Fig. 5-18 presents the result as a function of dihedral angles ψ_1 and ψ_2.

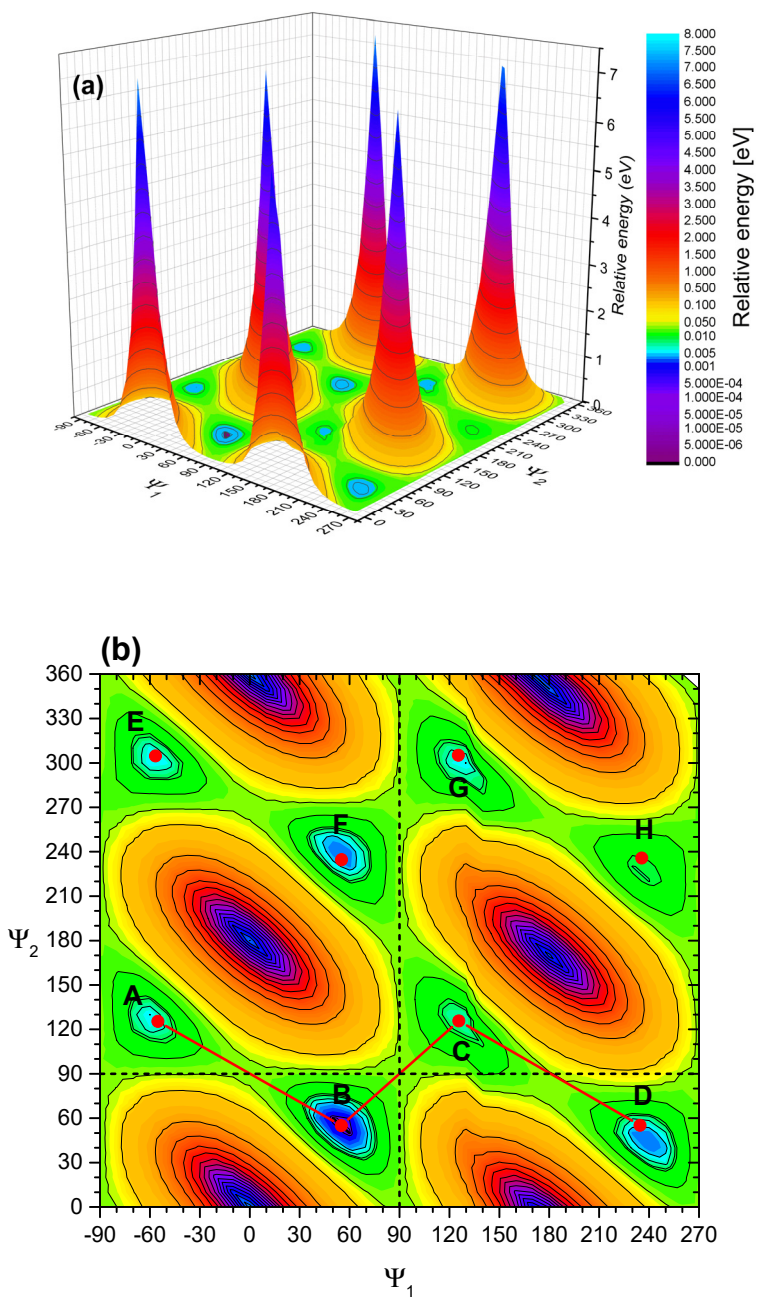

Fig. 5-18 (a) Cavalier perspective and (b) top view of the energy surface generated by the rotation of the phenylene rings keeping their bonded isocyanates in the plane of the ring. The eight energy-optimised conformers are indicated by the capitals **A** – **H** and the red dots in (b) for the shallow energy minima, as well as the optimal path (red) connecting **A**, **B**, **C** and **D**.

A closer look into the valleys reveals the eight shallow energy minima (shaded in light blue in Fig. 5-18a) – the conformers **A** to **H** of the 4,4'-MDI. Their optimised positions are shown in Fig. 5-18b (red dots).

Table 5-1 gives the angles (α, β, ψ_1 and ψ_2), dipole moment, μ, and energy difference, $E - E_E$, of all relaxed conformer structures. Fig. 5-19 depicts the molecular geometry of conformers **A** - **D** for illustration.

Table 5-1 Parameters of the eight optimised 4,4'-MDI conformers. The conformation E is chosen as reference for the energy difference.

	∠CNC angle $\alpha \approx \alpha_1 \approx \alpha_2$	Methylene angle β	Dihedral angle ψ_1	Dihedral angle ψ_2	Dipole moment μ	Relative energy $E - E_E$
Conformer	(degree)				(Debye)	(meV)
A	138.8	114.5	-55.2	125.4	2.827	+1.88
B	139.8	114.5	55.0	55.0	3.072	+0.20
C	139.9	114.6	125.7	125.7	2.464	+3.49
D	138.8	114.5	234.6	55.2	2.827	+1.88
E	139.9	114.2	-56.7	304.7	3.086	0
F	139.8	114.5	55.2	234.6	2.827	+1.82
G	139.9	114.5	125.4	305.2	2.827	+1.82
H	139.9	114.6	235.7	235.8	2.464	+3.53

Accordingly, the conformers **A**, **D**, **F** and **G** possess the same dipole moment but a slight energy difference of 0.06 meV. In addition, conformers **B**, **E** and **C**, **H**, respectively, form pairs with similar dipole moments and energies. If it is possible to pass from one conformer to another one by only rigid body rotation of the whole molecule (i.e. without any change of internal atom co-ordinates) then these conformers are identical and must have the same energy and dipole moment.

Now, conformer **A** can be rotated to conformer **G**. Similarly **F** is obtained by rotation of **D**. Thus **A** is identical to **G** and **D** is identical to **F**. In other words, conformer pairs **A/G** and **D/F** are related through a C_2 operation. A look at their geometries shows that conformers **E** to **H** can be transformed into conformers **A** to **D** by a mirror operation in a plane parallel to the POM, so that for the energy and the dipole moment, **A** = **F**, **B** = **E**, **C** = **H** and **D** = **G**. We add that the two structures **B** and **C** possess a C_2 symmetry. That is only approximately the case for conformer **A**, for which the different positions of the isocyanate groups disturb this symmetry.

The fact that the data in Table 5-1 do not completely match these conclusions is due to the shallowness of the total-energy landscape as shown in Fig. 5-18. The variations in the values can hence be taken as a measure for the accuracy of the data. Ultimately, the initial eight conformational states group in three classes **I**, **II** and **III** (Table 5-2).

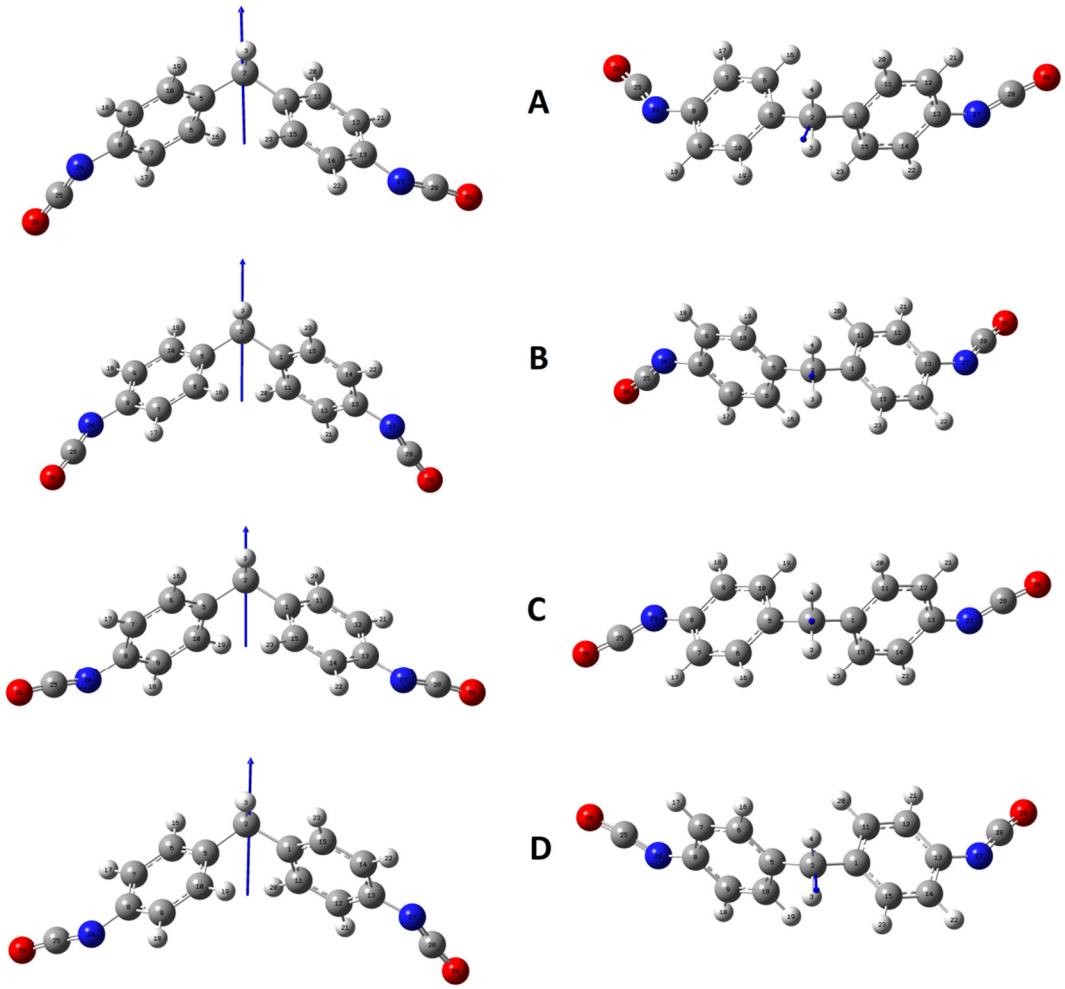

Fig. 5-19 The three conformers **A** - **C** of 4,4'-MDI with different physico-chemical properties and conformer **D** for comparison (left column: side view; right column: top view). **A** at ψ_1 = -55.2° & ψ_2 = 125.4°, **B** at ψ_1 = 55.0° & ψ_2 = 55.0°, **C** at ψ_1 = 125.7° & ψ_2 = 125.7°, and **D** at ψ_1 = 234.6° & ψ_2 = 55.2°. The blue arrows represent the corresponding dipole moments [60].

Table 5-2 Dipole moment and energy level of the three classes of 4,4'-MDI conformers. Conformer E is chosen as reference for the energy scale.

	Dipole moment	Relative energy
	μ	$E - E_E$
Conformer class	(Debye)	(meV)
I: (A = D) = (F = G)	2.827	+1.88
II: B = E	3.086	0
III: C = H	2.464	+3.53

It is also noted that in any conformation, the phenylene rings are neither perpendicular (ψ_i = 90°) nor parallel (ψ_i = 0°) to the POM but tilted. For all eight conformations, the isocyanate group remains *in the plane* of the adjacent phenylene ring. However, the conformations differ in orientation of the rings / isocyanates with respect to the POM. A closer look reveals that both phenylene rings are always tilted on opposite sides of the POM. From the top view the isocyanates are either located at the same side of the POM (conformer class **I**, with conformer **A** as a representative) or on opposite sides (classes **II** and **III** with conformers **B** and **C**, respectively). Second, relaxation of the 4,4'-MDI molecule at any combination of the two ψ's always results in a conformer of one of the three classes.

For conformers **B** and **C** the total dipole moments are almost along with the AOM. The dipole moment vector of conformer **A** is slightly tilted with respect to the AOM as illustrated in Fig. 5-19.

The energy differences between the conformers are quite small but their dipole moments vary significantly. That originates from the different orientations of the NCO groups that provide a significant contribution to the total dipole moment. Accordingly, varying the angle between the NCO groups will considerably affect the resulting dipole moment of the whole molecule. For instance for conformer **C**, the large angles between the isocyanate groups and the AOM minimize the dipole moment of the 4,4'-MDI, which is accompanied by a rise in total energy.

A possible low-energy path from one conformation to the next is sketched as red line in Fig. 5-18b. A more detailed energy profile along this path was determined by rotating both phenylene rings (with NCO constantly aligned in the ring plane!) simultaneously by the same angle increment in 8 steps from the stable to the transition geometry (located at ψ_2 = 90°) where the red line crosses the black dashed ones in Fig. 5-18b. The result is shown as black curve in Fig. 5-20. The energy barrier between the conformer **B** and each of the other three is roughly 35 meV which is only slightly above the average thermal energy at room temperature (~26 meV).

Another process that may lead from one conformer to another consists in the rotation of just one of the two isocyanate groups, without rotating the phenylene rings. To study this, we changed the dihedral angle γ (defined by the atoms 12, 13, 27 and 28, cf. Fig. 5-16) from 0° (corresponding to the stable structure) to 90° (the transition structure) in steps of 10° starting from the relaxed structures. Fig. 5-20 compares the result (red and blue curves) with the energy profile obtained by varying the ψ angles of the phenylene groups with fixed NCO. The energy maximum corresponds to the perpendicular orientation of the isocyanate group with respect to the phenylene ring (γ = 90°). Rotation of the isocyanate group requires roughly twice the energy (~77 meV) needed for the rotation of the phenylene groups (~35 meV). Thus, cooperative rotation of both phenylene rings is favoured for conformer transitions while each NCO group prefers to remain in the plane of 'its' pendant phenylene ring.

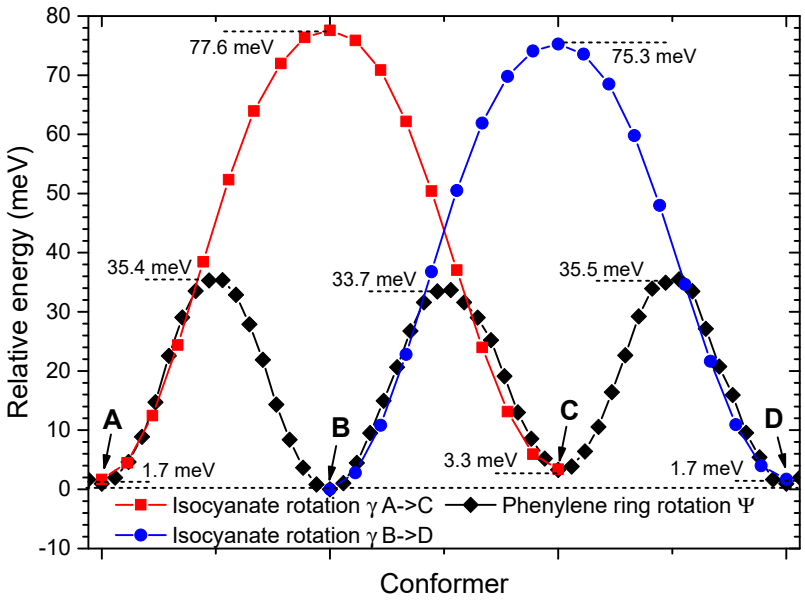

Fig. 5-20 Total energy of the 4,4'-MDI with respect to the conformer B when passing from one conformer to the other by rotating both phenylenes simultaneously (◆, along the red path shown in Fig. 5-18b) or by rotating only one isocyanate group (■ and ●, respectively).

Since the conformational transition energy is in the range of thermal energy at room temperature, all conformers are present in a real sample. Their probability distribution can be obtained using the Boltzmann distribution function. Conformers that can be transformed into others using rigid body motions and mirror planes have the same spatial arrangement of atoms around the centre of the molecule and thus identical energy level and dipole moment. However, such conformers cannot be distinguished with IR spectroscopy. Hence for each conformer class (cf. Table 5-2) the probabilities of each conformer can be added. The Boltzmann distribution also allows to calculate the average dipole moment. With this distribution, we get 2.8 Debye for the average dipole moment which is in excellent agreement with the only experimental value of 2.75 Debye found in literature [112].

◊ *Infrared spectrum calculation and band analysis of the 4,4'-MDI*

For each of the conformers, the IR spectrum can be calculated giving access to any eigenvibration of the isolated 4,4'-MDI molecule. Almost all modes involve motions of nearly all atoms. That proves that the traditional group frequency concept has to be used with great care if at all. Moreover, many modes group together as they have only very little differences in the vibration frequency. Real IR bands possess a natural line width described by a Lorentz line shape, and another line broadening effect due to molecular interactions which usually is summarised as impact broadening. For the 4,4'-MDI conformers, any IR band contains more than one of these broadened normal vibration modes. As the conformational study revealed a facile transition between each conformer IR spectra are calculated for each conformer class.

The calculated IR spectra of the 4,4'-MDI conformers reveal only minor differences. Hence, the IR spectra are not sensitive to the different conformations of the 4,4'-MDI. In order to compare with measured 4,4'-MDI IR spectra, the conformer IR spectra were weighted with the corresponding Boltzmann probabilities and superimposed – see [60] for more details. Such a comparison helps to assess the quality of this quantum-mechanical study. As the interaction of infrared light with molecules is not quantitatively described using DFT, the absolute as well as the normalised intensity of the individual IR bands is not reliable. A comparison of normalised intensity *ratios* is though reasonable to some extent. Slight discrepancies were found which can be related either to molecular interactions in the real sample or numerical errors from the DFT calculation. Despite these differences between experimental and calculated spectra, an accurate band assignment, indicating how the atoms of the molecule are involved in each IR band, is now available for the 4,4'-MDI molecule. The following figures show an IR-ERA spectrum of molten bulk 4,4'-MDI. The spectrum is initially measured with IR-ATR (procedure described in chapter 3.2.1.1 using the molten solid cell). The bulk-like ERA spectrum is then obtained using spectra calculation as outlined in chapter 3.2.5. The obtained ERA spectrum corresponds to a thin adsorbed organic layer that would possess the same morphology and chemical properties as the bulk.

The spectral region above 2600 cm^{-1} (Fig. 5-21a) only exhibits weak CH stretches (3100 – 2800 cm^{-1}) and combination or overtone vibrations.

The very strong asymmetric stretch of the isocyanate groups is located between 2325 and 2200 cm^{-1} (Fig. 5-21b). As several vibrations involving this functional group are located here [60], the shape of the band is asymmetric with a shoulder at lower wavenumbers. Due to the large dipole moment of the NCO group and thus the high intensity, this band is very sensitive to any changes around that chemical group. The shoulder above 2300 cm^{-1} must be discussed with caution as the asymmetric stretch (2300 cm^{-1}) of residual CO_2 could be involved.

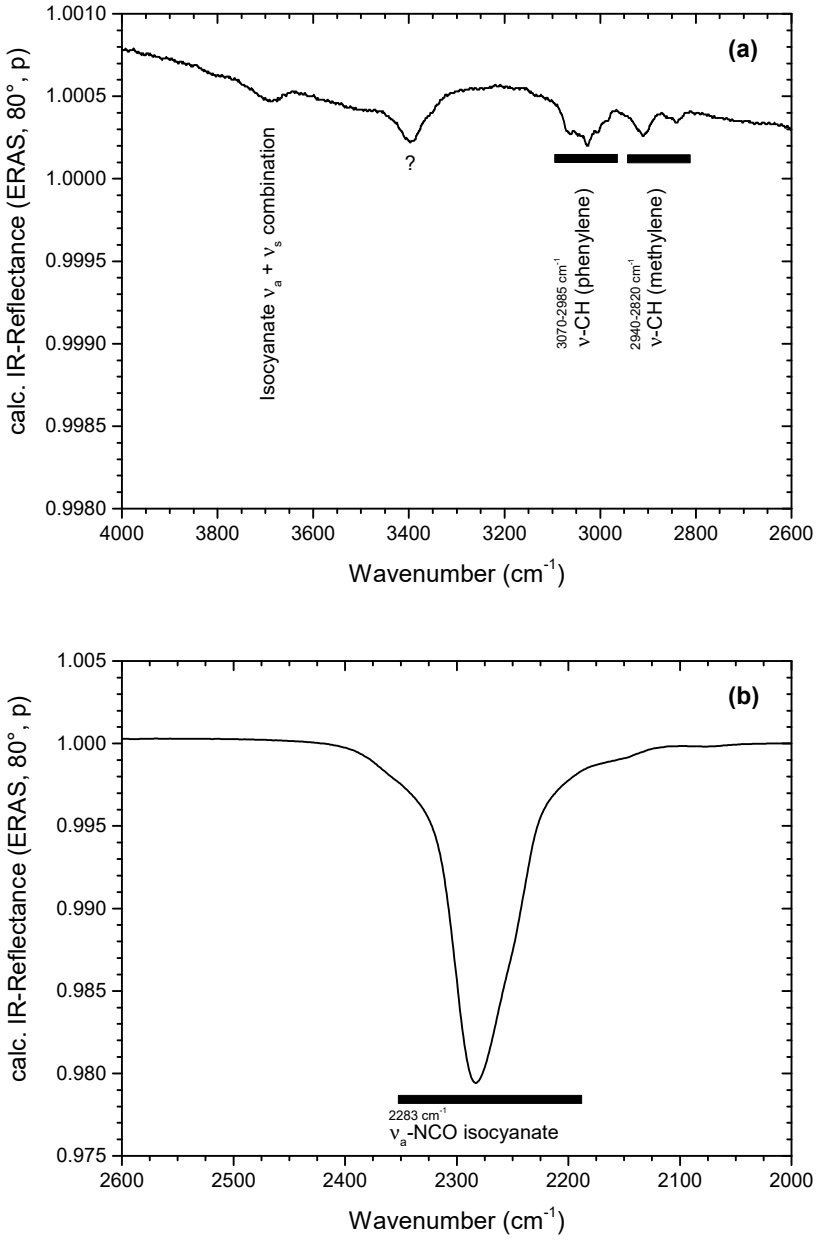

Fig. 5-21 IR-ERA spectrum as calculated from an IR-ATR spectrum of molten 4,4'-MDI. (a) 4000 – 2600 cm^{-1}, (b) 2600 – 2000 cm^{-1}.

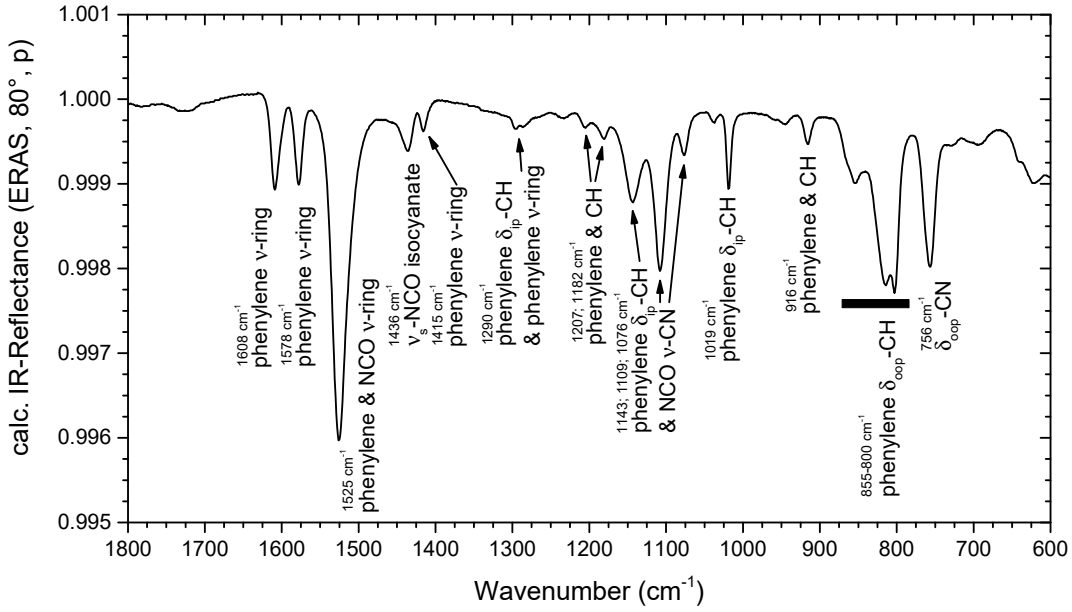

Fig. 5-22 IR-ERA spectrum as calculated from an IR-ATR spectrum of molten 4,4'-MDI, 1800 – 600 cm^{-1}.

Below 1800 cm^{-1} MDI exhibits many bands (Fig. 5-22). They can be roughly grouped into combined stretches of phenyl and isocyanates (1700 – 1400 cm^{-1}) and combined stretches and deformations of phenyl and methyl (1300 – 700 cm^{-1}). It is noted that the combined stretches should not be confound with combination bands. Combined stretches involve simultaneous vibration of several parts of the molecule for one eigenfrequency. Combination bands arise if two distinct eigenfrequencies are excited by one photon.

All vibrations involving isocyanate groups, i.e. mainly the region 1700 – 1400 cm^{-1} are also sensitive for changes in the NCO group similarly as for the isocyanate band itself. These changes include physical and chemical interactions with other molecules as well as with the substrates.

The QM modelling also showed that most bands involve vibrations of more than one functional group or part of the molecule. For example, the phenylene ν-ring stretches (1608 and 1578 cm^{-1}) involves phenylene ring stretches predominantly but the adjacent NCO group also provides a weak contribution. As a consequence, even if the phenylene rings are not prone to chemical reactions in our case, the band can however change shape and intensity due to a modification of the isocyanate group.

Thus, except a few localised vibrations of the CH stretches, most bands and their relative intensities will respond to chemical reactions at the MDI or to changes in the molecule's environment. This comes at a cost however. There is hardly any band in the spectrum that is not influenced during the adsorption on our metal surfaces and no band is available as internal reference as this requires a band that remains unaffected by interaction.

5.2.3 Thermal stability

The most important condition for monomers to be suitable for MLD deposition is that they can be evaporated without being thermally degraded. This can be easily verified using thermogravimetry (TGA). Evaporating molecules or decomposition fragments are removed by the carrier gas and can then be analysed with a coupled IR spectrometer. Thus, observed mass loss can be attributed either to evaporation or chemical degradation. The utilised experimental setup and procedure is outlined in chapter 3.3.1. In order to reproduce the MLD conditions, nitrogen is also used here as carrier gas in order to avoid any reaction with oxygen.

The mass change of a 4,4'-MDI sample over temperature is presented in Fig. 5-23. Mass loss slowly begins at ca. 150 °C and the rate of mass loss (1st derivative – red line) progressively increases with rising temperature. The maximum rate of mass loss is achieved at 270 °C while the complete sample mass is gone at 280 °C.

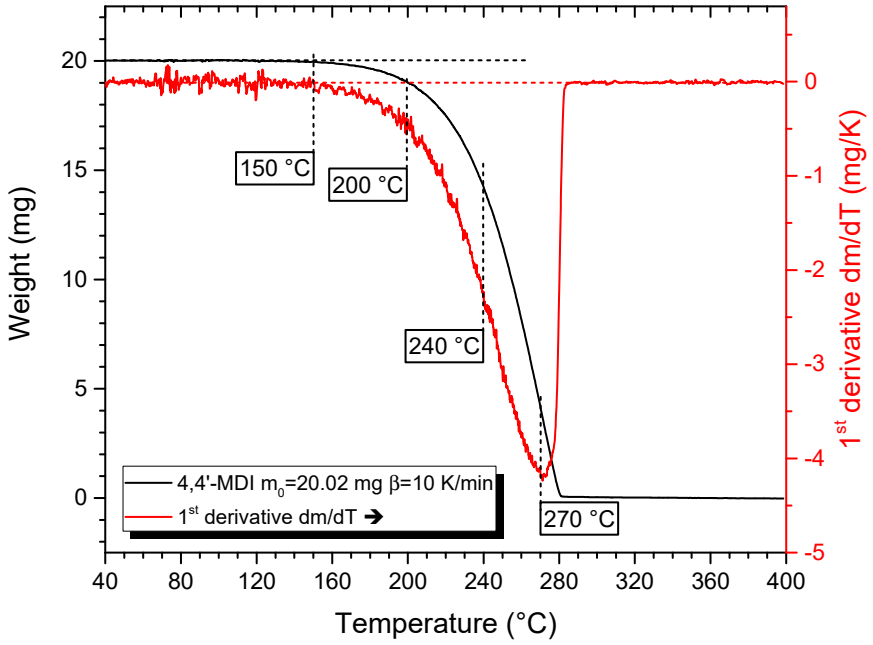

Fig. 5-23 Mass change (black) and corresponding mass loss rate (red) of 4,4'-MDI as function of the sample temperature measured by TGA. The sample is measured in a nitrogen gas flow of 250 ml/min.

No residues remain in the gold plated aluminium pan. The evolved gases from the sample are analysed by IR-transmission spectroscopy over the complete temperature range. First weak bands become visible at 150 °C and increase over time. An intensity maximum is reached at 270 °C followed by a slow decrease of intensity. At the end of the temperature sweep, weak bands are still present in the IR spectra. Three transmission spectra (200, 240 and 270 °C – Fig. 5-24) are chosen as representative for the observed mass loss step. They are compared to a calculated bulk-like ERA spectrum of 4,4'-MDI.

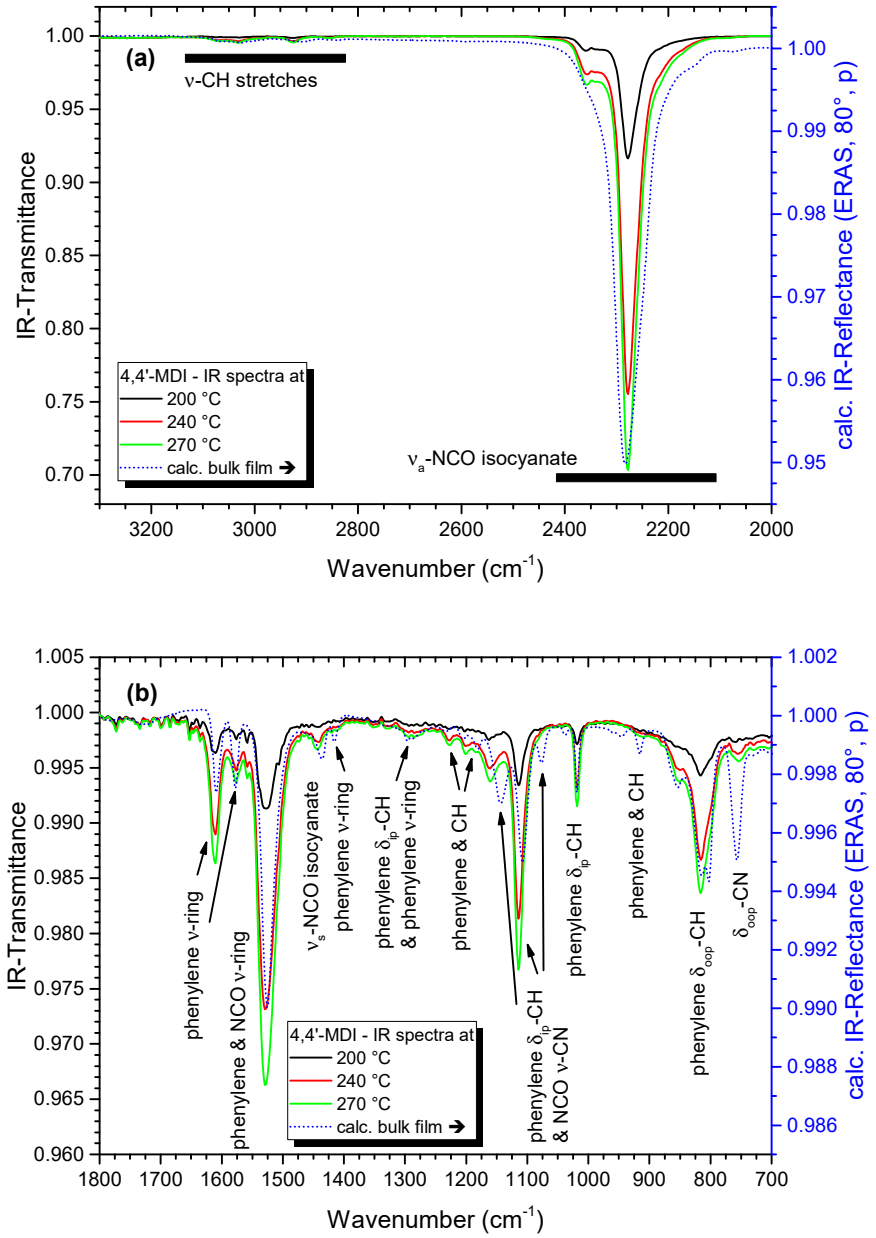

Fig. 5-24 IR transmission spectra of the evolved gases from the TGA experiment shown in Fig. 5-23 at different temperatures. (a) 3300 – 2000 cm^{-1}, (b) 1800 – 700 cm^{-1}. The dotted blue spectrum presents a calculated bulk-like ERA spectrum for qualitative comparison.

The three spectra exhibit the same bands but with different intensities as the carrier gas is loaded with different amounts of molecules. Thus, the same molecules are evolved from the sample throughout the whole step. Compared to the 4,4'-MDI bulk spectrum IR bands are in general very similar. A few notable differences are present, however.

The ν_a-NCO stretch (Fig. 5-24a) has a completely different shape in the gas phase. In the bulk the sharp peak (2283 cm^{-1}) is enclosed by two broad flanks. The band thus extends from 2415 to 2110 cm^{-1}.

In the gas phase, only the flank at lower wavenumbers is present. The sharp peak (2277 cm^{-1}) is slightly shifted to lower wavenumbers. The flank at higher wavenumbers is replaced by a band at 2360 cm^{-1}. Due to the evaporation of the MDI and its dilution into the N_2 intermolecular interactions are different from the melt. The peak at higher wavenumbers could be issued from isocyanate groups that do not interact with each other. As the main peak is still present in the gas phase it is very likely that MDI molecules form small clusters in the gas phase.

The fingerprint region (Fig. 5-24b) also shows slight differences. Although band shape is similar to the bulk relative intensity ratios between bands is different. As an example the two phenylene ring stretches (1610 and 1577 cm^{-1}) have the same intensity in the bulk while the first is much stronger in the gas phase. Similar features are observed below 850 cm^{-1}. Interestingly bands in the region 1250 – 1050 cm^{-1} not only have different intensity ratios but their positions are also shifted to higher wavenumbers in the gas phase. As the vibration of the NCO group also contributes to this band, this behaviour is in accordance with the behaviour of the previously discussed ν_a-NCO stretch.

Nevertheless, the gas phase spectra reflect the same spectral features as the bulk isocyanate and thus it is concluded that it evaporates without noticeable thermal degradation.

The thermogravimetric analysis also shows that at least temperatures of 180 to 200 °C in the evaporation cell of the MLD is necessary for the MDI to be evaporated at a useful rate. Moreover, the IR spectra above 280 °C show that MDI molecules are still present in the gas phase until the end of the temperature sweep at 400°C. Thus, the MDI tends to attach to the heated transfer tube and only detaches at higher temperatures. Therefore MDI is also prone to behave similarly in the MLD.

5.3 The polyetherpolyols

Polyetherpolyols are the most commonly used resins for the preparation of polyurethanes [5, 113]. They are available in different chain lengths and with two or more hydroxyl functionalities. Thus a broad range of polyurethane varieties from linear thermoplastics to highly crosslinked thermosets is possible. Two alcohols were chosen in this work.

Dipropylene glycol (DPG – Fig. 5-25) is a short chained diol. It is a colourless liquid with low viscosity at room temperature. Reaction with 4,4'-MDI leads to the formation of linear PU chains. It is a mixture of its three isomers. They are distinguished by the position of both CH_3 groups either on the α or β carbon with respect to the hydroxyl group.

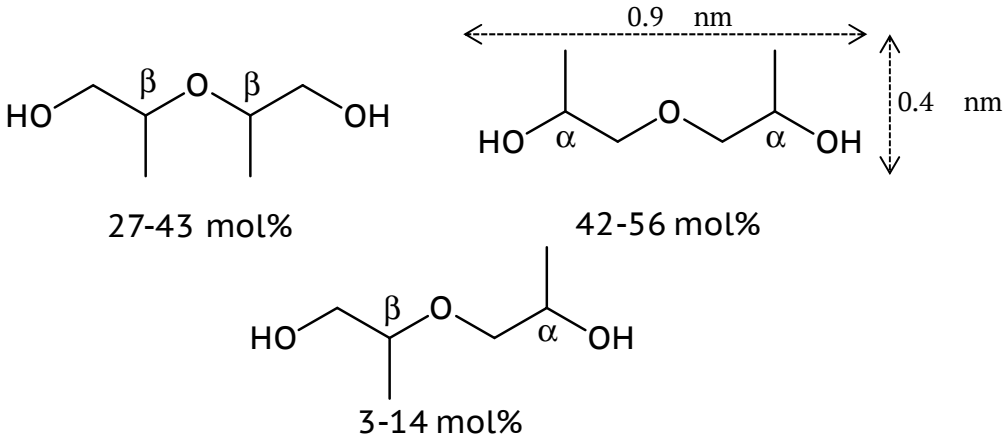

Fig. 5-25 Chemical structure of the dipropylene glycol (DPG) isomers.

Baygal®K55 (Fig. 5-26) is a short-chained triol. As for the DPG it is a colourless liquid that is slightly more viscous at RT. Reaction with isocyanate will form branching points that will lead to a tri-dimensional crosslinked PU network. The physical properties of both monomers are given in Appendix 11.3.2 and 11.3.3.

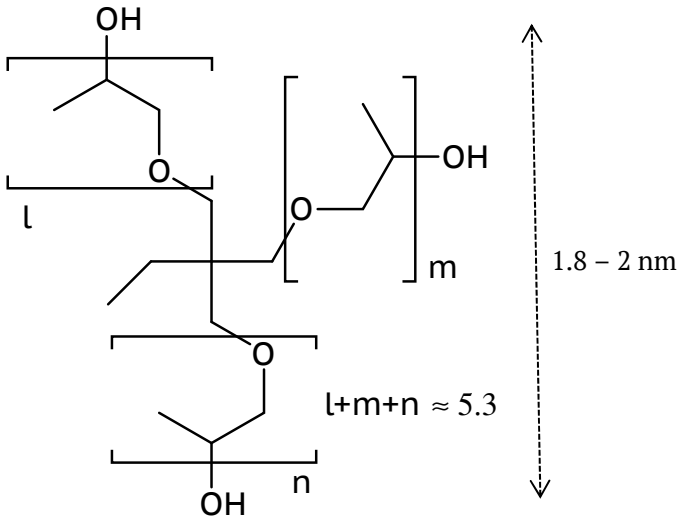

Fig. 5-26 Chemical structure of the Baygal®K55 polyethertriol.

Polyetherpolyols are prone to water uptake from the ambient atmosphere [5, 114, 115] and thus contain a small amount of water at delivery. This does however not strongly impinge our measurements as the monomers are evaporated inside the MLD and the weak amount of water molecules will add to those present in the nitrogen flow.

5.3.1 IR band assignment in the bulk

As diol and triol possess the same functional groups their IR spectra are similar and can be discussed together. Band assignment is based on band catalogues and quantum mechanics [7].

The bulk ATR spectra are recorded using the liquid cell (procedure described in chapter 3.2.1.1). As for the isocyanate the following figures show IR-ERA spectra of bulk DPG and triol.

The OH stretches of the alcohols form a broad asymmetric band between ca. 1630 - 3080 cm^{-1} (Fig. 5-27a). Hydroxyl groups undergo a wide range of hydrogen bonds that lead to wavenumber shifts and intensity changes. Even due to the different chemical structure of both alcohols the peak maximum is different (3436 cm^{-1} for DPG and 3384 cm^{-1} for the triol). A modification of the chemical structure around the OH group as during the formation of urethane linkages for example is prone to induce a change in this band due to the presence of new functional groups as N-H or C=O that are suitable for hydrogen bonds.

The methyl (CH_3) and methylene (CH_2) exhibit various asymmetric and symmetric stretches between 3000 and 2800 cm^{-1}. They exhibit identical wavenumbers for both alcohols but with slight intensity differences. The CH_x groups also present several deformation vibrations between 1550 and 1200 cm^{-1}. They often overlap and are difficult to separate. One band however, the CH_3 symmetric deformation 'umbrella mode', is of particular interest. It is stronger and sharper than the other bands. It represents a signature for the presence of alcohols[26] as it is lacking in the MDI.

Finally, the ether group gives rise to a strong band between 1200 and 1000 cm^{-1}. The band is composed of several vibrations (ν-CO, ν_a-COC and the ν_s-COC) that confer a particular band shape to each alcohol as position and intensity of each vibration is specific. Below 1000 cm^{-1} the spectrum contains several combined vibrations of large parts of the molecule as well as a broad deformation vibration of the hydroxyl groups.

[26] The OH band would be a much better indicator but due to its broadness it is difficult to identify at very low quantities.

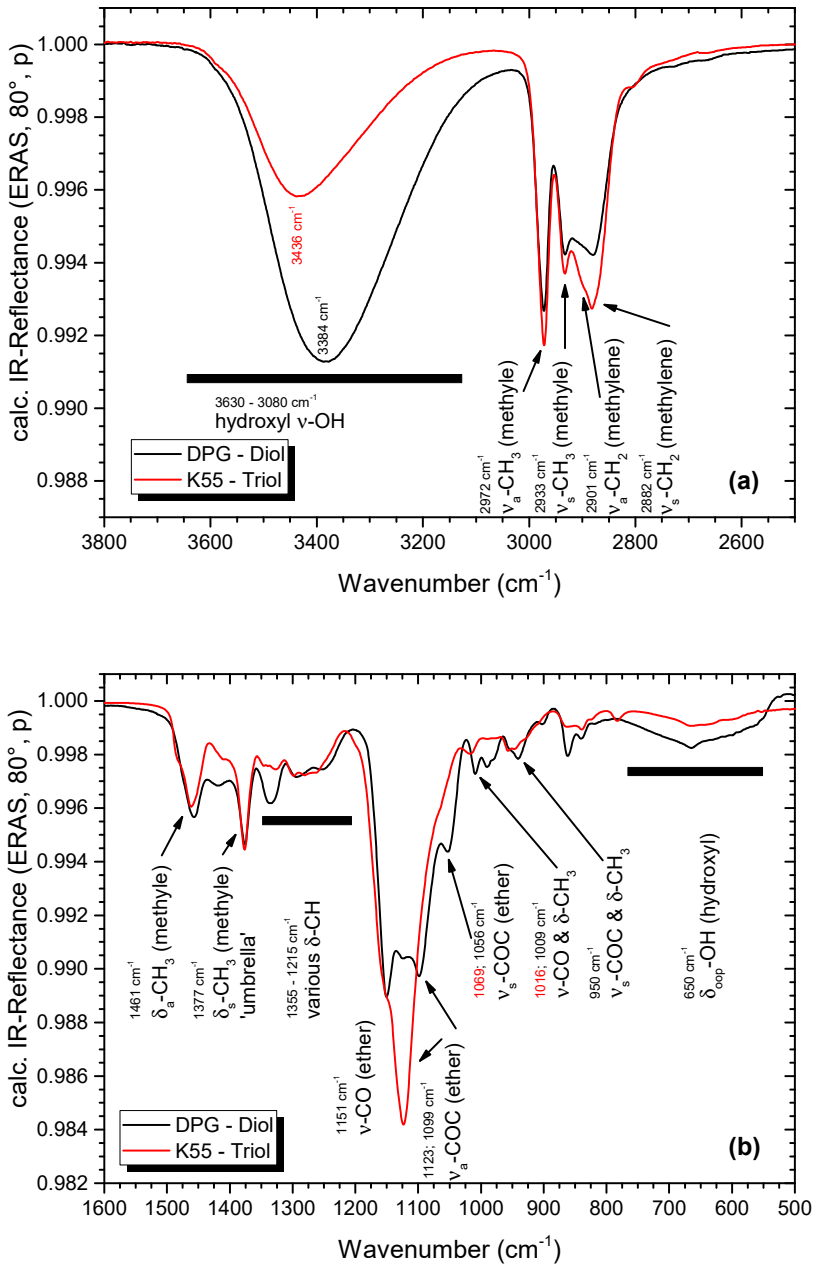

Fig. 5-27 IR-ERA spectra as calculated from IR-ATR spectra of the diol dipropylene glycol (DPG) – black and the triol Baygal®K55 – red. The wavenumbers in red are attributed to the K55 spectrum. (a) 3800 – 2500 cm^{-1}, (b) 1600 – 500 cm^{-1}.

5.3.2 Thermal stability

Similar to the isocyanate, the thermal stability of both alcohols is verified by TGA coupled with IR spectroscopy.

5.3.2.1 Dipropylene glycol

The mass change of the DPG sample as function of the temperature is shown in Fig. 5-28. Molecules slowly start to evaporate at ca. 60 °C. With rising temperature mass loss increases rapidly as the 1st derivative deflection of the mass (red line) grows. The maximum rate of mass loss is obtained at 180 °C (minimum of the 1st derivative). Between 100 °C and 190 °C the whole sample evaporates in one step. Finally, no residues remain as the mass has fallen to 0 mg. DPG undergoes a fast evaporation over a temperature range of 80 K in nitrogen atmosphere.

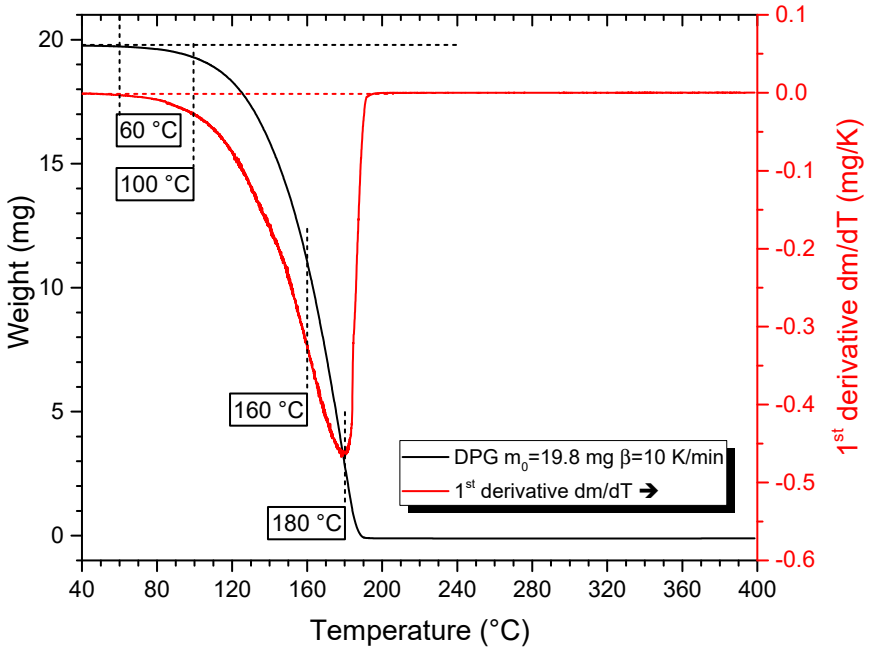

Fig. 5-28 Mass change (black) and corresponding mass loss rate (red) of DPG as function of the sample temperature measured by TGA. The sample is measured in a nitrogen gas flow of 250 ml/min.

In order to verify if DPG does not undergo thermal decomposition IR spectra are recorded during the whole experiment. From 60 °C onwards band intensity progressively rises until reaching a maximum between 170 and 180 °C followed by a rapid intensity drop. This is in accordance with the evolution of the rate of mass loss. When more molecules are carried by the nitrogen flow, band intensity is higher.

Three spectra are chosen to represent the begin (100 °C), the middle (160 °C) and the end (180 °C) of the observed mass loss step. They are shown in Fig. 5-29[27].

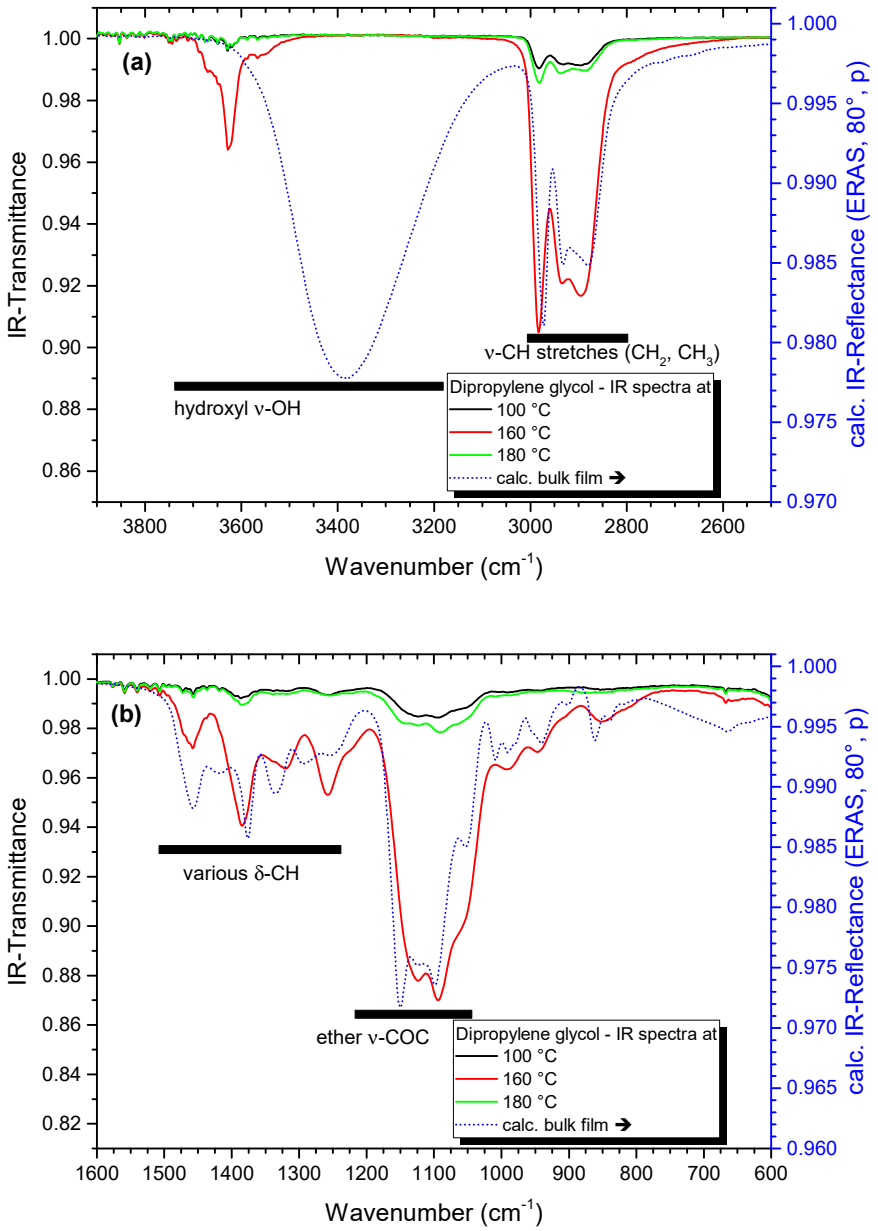

Fig. 5-29 IR transmission spectra of the evolved gases from the TGA experiment shown in Fig. 5-28 at different temperatures. (a) 3900 – 2500 cm^{-1}, (b) 1600 – 600 cm^{-1}. The dotted blue spectrum presents a calculated bulk-like ERA spectrum for qualitative comparison.

The spectra at 100 °C and 180 °C are similar in band shape, position and intensities. The bands are attributed to CH stretches (3000 – 2800 cm^{-1}) and deformations (1500 – 1200 cm^{-1}) and ether stretches (1200 – 1000 cm^{-1}).

[27] It is reminded here that a slight delay between TGA and the coupled IR is present as the evolved gases require some time to flow to the IR and purge the transmission cell. Thus the indicated temperatures are to be taken with a shift of ca. 5 K (c. f. chapter 3.3).

A small sharp peak is identified at 3623 cm^{-1}. As the spectra show similar features at the start and the end of the mass loss step, the same material is evolved from the sample. It is noted that at 180 °C band intensities are already low although mass loss is still not finished in the TGA. This is probably caused by the slight time lag between TGA and IR measurements. The spectrum at 160 °C exhibit the same bands but with a much bigger intensity as more molecules are present in the nitrogen flow.

Comparing this spectrum with a bulk spectrum of DPG many similarities and differences are identified.

The most flagrant discrepancy is seen for the hydroxyl band. The broad band at 3384 cm^{-1} in the bulk is missing completely in the gas phase. Instead a sharp band is located at 3623 cm^{-1}. As DPG molecules are more isolated in the gas phase the intermolecular interactions (mainly from OH and COC groups) are reduced or even completely lost, band position of the vibrations involving these groups will also shift in the IR. Due to the loss of hydrogen bonding of the OH groups the initially broad band with many different interacting states shifts to higher wavenumbers and becomes narrow. This is also observed for the deformation vibration of that group at 650 cm^{-1}.

The CH stretches do not undergo such changes and remain similar to the bulk. The CH deformations give rise to slight variations of relative intensity ratios and slight band shifts. The CH_3 symmetric deformation (‘umbrella mode’) at 1380 cm^{-1} remains the strongest band of these deformations.

The intensity ratios of the vibrations present in the ether band are different in the liquid and the gas phase leading to different band shapes. In particular the ν-CO (1151 cm^{-1}) and ν_s-COC (1056 cm^{-1}) are weaker in the gas phase.

The various bands at 1000 -800 cm^{-1} are also broader in the gas phase.

Nevertheless, the gas phase spectra reflect the same spectral features as the bulk DPG and thus it evaporates without thermal degradation. TGA also shows that DPG evaporates quite fast, hence a low temperature in the evaporation cell of the MLD in the range 80 – 120 °C should be sufficient to allow a slow to moderate deposition rate.

5.3.2.2 Polyethertriol K55

The evolution of the mass of the polyethertriol sample as function of temperature is presented in Fig. 5-30. A slow decrease in mass starts at around 80 °C. From 180 °C onwards, mass loss becomes faster; more molecules leave the sample as the rate of mass loss (1st derivative - red line) increases. Between 180 °C and 360 °C the whole sample evaporates in one single step. Compared to DPG, the triol evaporates at higher temperatures and much slower.

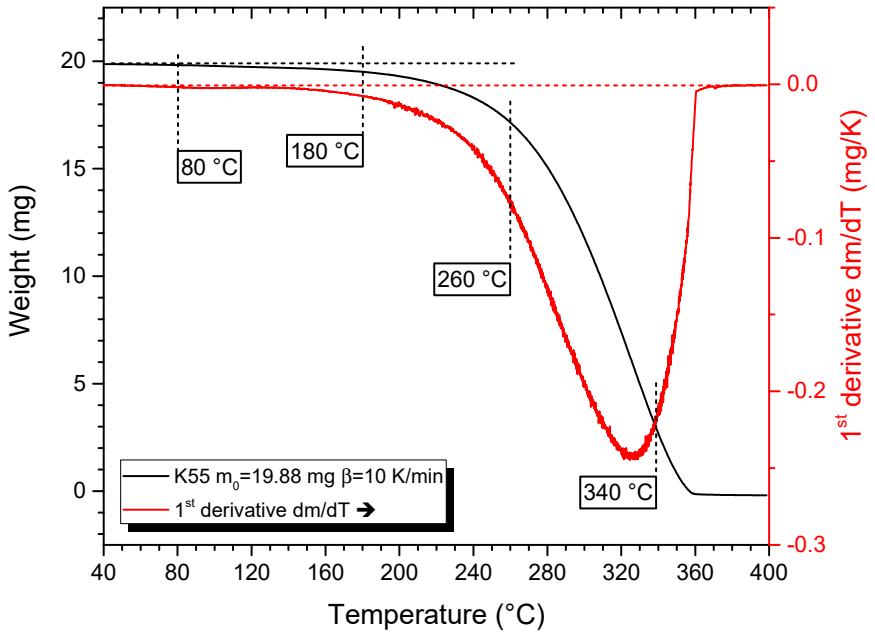

Fig. 5-30 Mass change (black) and corresponding mass loss rate (red) of the triol K55 as function of sample temperature as measured by TGA at a nitrogen gas flow of 250 ml/min.

The evaporated molecules are analysed with IR in order to check if the triol does not undergo thermal decomposition. Band intensity slowly increases at 80 °C and reaches a maximum at 320 – 340 °C followed by a rapid decrease in intensity. Transmission spectra at 180, 260 and 340 °C are shown in Fig. 5-31 and are representative for the observed mass loss step.

The spectrum at 180 °C does only show weak bands of CH stretches (3000 – 2800 cm^{-1}), CH deformations (1500 – 1200 cm^{-1}) and a broad ether stretch (1200 – 1025 cm^{-1}). The OH band is not visible. However, a small peak at 3618 cm^{-1} is present and is attributed to OH stretches without hydrogen bonding, as for the DPG. As the adjacent gaseous water vibrations are in the same order of magnitude, this peak cannot be attributed with certainty. As more molecules evaporate, the spectrum at 260 °C is more intensive and bands can better be distinguished. The bands also become sharper. The peak at 3618 cm^{-1} also grows which confirms that it corresponds to the OH stretch. The CH stretches have similar band shapes as in the bulk but a different intensity ratio as the band at 2974 cm^{-1} - ν_a-CH_3 is weaker.

The deformation vibrations are similar to the bulk. The ether band is shifted to lower frequencies and its shape differs slightly from the bulk (ν-CO is less predominant).

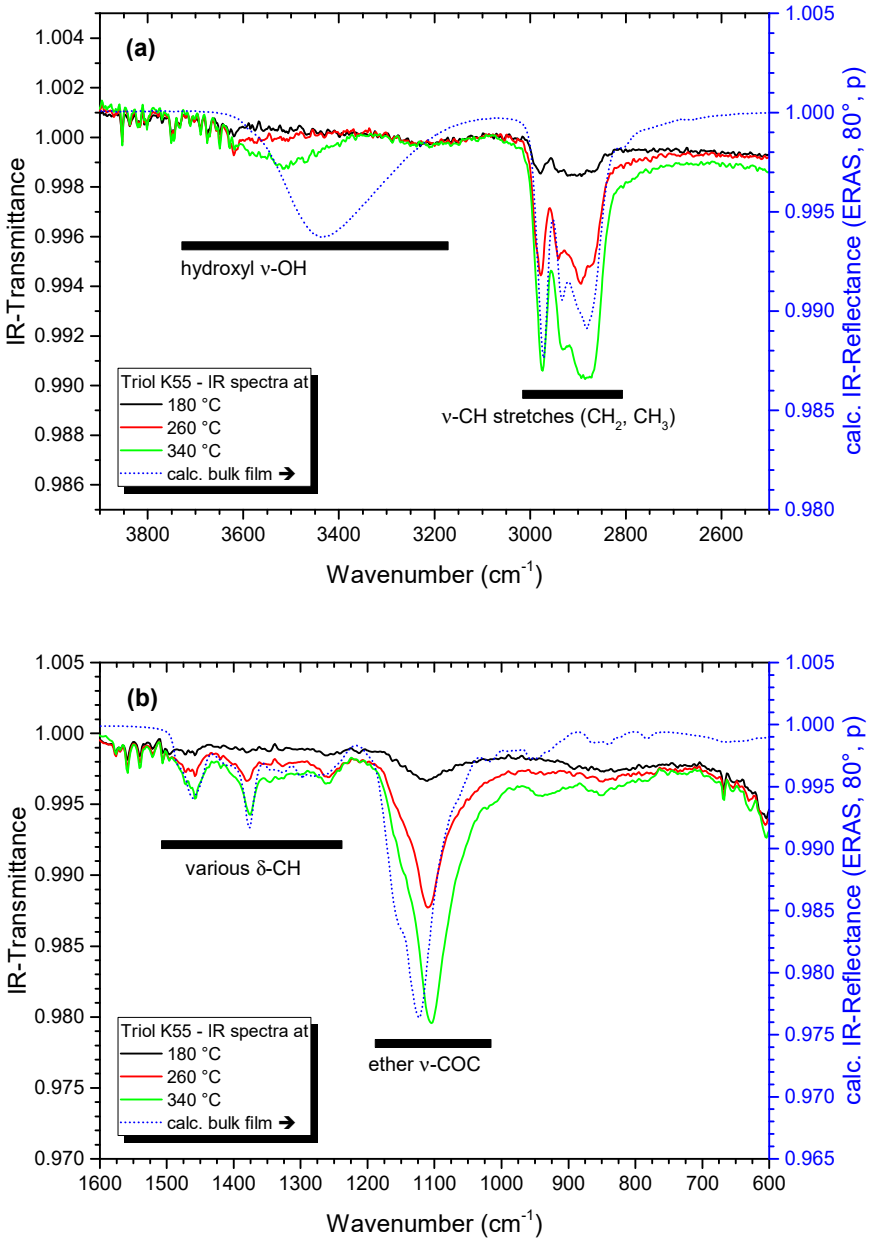

Fig. 5-31 IR transmission spectra of the evolved gases from the TGA experiment shown in Fig. 5-30 at different temperatures. (a) 3900 – 2500 cm^{-1}, (b) 1600 – 600 cm^{-1}. The dotted blue spectrum presents a calculated bulk-like ERA spectrum for qualitative comparison.

At 340 °C the previously observed bands are all present but again gained in intensity. Now the ν-OH is also visible as a broad band at 3516 cm^{-1}, which is still shifted to higher wavenumbers compared to the bulk (3436 cm^{-1}). As the mass loss rate is maximum at this temperature it is very likely that clusters of molecules evaporate and thus a few hydroxyl groups are capable of hydrogen bonding.

As the gas phase spectra possess the same spectral features as the bulk monomer throughout the complete mass loss step it is concluded that this monomer also evaporates under nitrogen atmosphere without thermal degradation. Contrary to the DPG, the triol evaporates at higher temperatures and much slower. Thus, a temperature of at least 180 °C in the evaporation cell of the MLD should be necessary for the K55 to be evaporated.

5.4 Tetrahydrofuran THF

Tetrahydrofuran (Fig. 5-32) is a very well suited solvent for organic monomers. In previous work it was successfully used for the preparation of thin PU spin-coating layers as well as adsorption layers from solution onto metal surfaces (e.g. [7-10, 37]). Isocyanates and polyetherpolyols dissolve rapidly and completely in THF. THF also evaporates very fast at room temperature enabling fast removal of THF traces from layers or after rinses. It also presents the advantage to not chemically modify native surfaces of aluminium and copper. Some physical properties of this cyclic ether are given in Appendix 11.3.4.

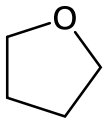

Fig. 5-32 Chemical structure of tetrahydrofuran (THF).

Fig. 5-33 shows the ATR spectrum of liquid THF (c.f. procedure outlined in chapter 3.2.1.1). The two most predominant bands are the asymmetric (1067 cm^{-1}) and symmetric (906 cm^{-1}) COC ether stretches. Besides the ether, CH_2 stretches (3040 – 2770 cm^{-1}) and deformations (1500 – 1140 cm^{-1}) are present. THF can undergo hydrogen bonding with hydroxyl groups from the polyols for example. Interactions with the polar NCO groups are also possible. All these interactions are however reversible.

In this work THF is used for three purposes. First, it is utilised to clean the metal substrates prior deposition of monomers. Second, it serves as solvent for the monomers when they are deposited from solution onto the metals. Finally, THF also serves to study the stability or adhesion strength of the prepared layer as weakly attached molecules are removed by the solvent. Experimental procedures for each case were outlined in chapter 3.2.2.1.

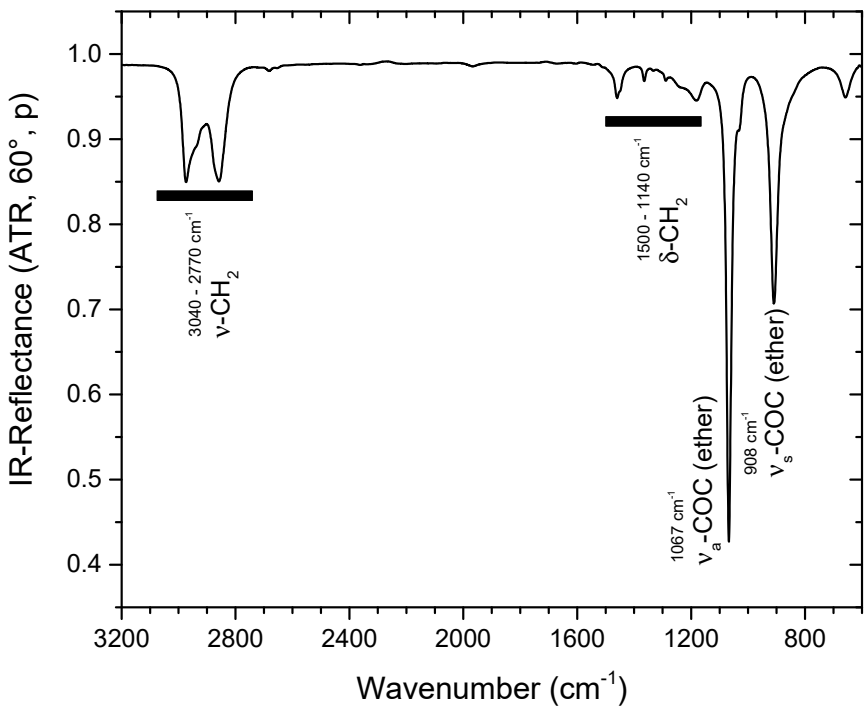

Fig. 5-33 IR-ATR spectrum of liquid tetrahydrofuran (THF).

6 Thin monomer deposits on metals

Before starting to prepare thin polyurethane layers with MLD it is crucial to first study the behaviour of each monomer during and after deposition. Knowledge on the adsorption behaviour as well as the physical and chemical interactions with the metal substrates can be revealed. Moreover, the deposition of monomers allows achieving adequate deposition parameters that can later be used for the sequential deposition of both monomers.

A literature review of relevant results concerning alcohol and isocyanate deposits either by MLD or other techniques is provided in section 6.1.

In 6.2 the properties and state of the metal substrates in regard of MLD deposition cycle, storage time and solvent exposure is characterised first.

Before discussing the prepared monomer deposits it is necessary to verify the reproducibility of MLD deposits and define an adequate degree of comparability of IR spectra. In section 6.3 multiple samples are compared during layer deposition and later at different stages of IR characterisation.

Then each monomer is deposited. The interactions and stability of the deposited layers are characterised using IR spectroscopy. Experimental work [69, 73-75, 116-120] realised under my supervision mainly contributes to this chapter.

6.1 Literature review of interactions of monomer and polymer deposits with substrates

The literature review of the MLD technique was provided in section 4.1 whereas this section focusses on the molecular interactions of monomers and polymers with substrates.

6.1.1 Layers prepared by MLD

MLD research is mainly aimed at the preparation of organic-inorganic hybrid layers (e.g. [121] and the extensive review [83]). Consideration of polymer layers is still limited. So far, polyamide [84, 122-126], -imide [127-131], -urea [132-137], -urethane [138], -thiourea [139], -ester [140] and –imine [141-143] layers have been reported.

In most cases only linear macromolecules are represented while crosslinked polymers have only been marginally reported so far. The preparation of such network films via the gas phase still poses a challenge as they present less conformational flexibility due to the crosslinks of polymer chains and hence more control over the structure as compared to linear macromolecules.

Since the literature on polyurethanes is very sparse, it makes sense to take a closer look at the preparation of polymer layers of similar systems as for example polyurea.

In [132], the production of several polyurea layers by vapour deposition on a germanium surface is presented and discussed. Ethylenediamine (ED) and 1,4-phenylene diisocyanate (PD) serve as monomers. The films are characterised by in situ IR spectroscopy. The authors have investigated two different approaches. First, ED is deposited on the germanium. The corresponding IR spectra contain bands of the free NH_2 groups as well as several new bands that can be assigned to a dative Ge-N bond according to [144]. When PD is deposited over this layer, urea groups with their characteristic amide I (ν-C=O) and amide II (δ-N-H) vibrations are formed. Unreacted isocyanate groups also remain. Thus, the authors conclude that an isocyanate group of PD has reacted with the free NH_2 group. Unfortunately, since the authors use the IR spectrum before this deposition as a reference spectrum after each new layer deposition, it is not clear whether all NH_2 groups have reacted. Further monomer depositions (up to four layers) show a decrease of NH_2 and isocyanate bands, respectively, as well as an increase of urea-specific bands. Since the spectra are not compared against a bare reference surface, it is therefore not evident whether molecules desorb or the same amount of isocyanate or amines is present. The authors assume here that each amine group reacts with one isocyanate and consequently the same number of free isocyanate groups remains. The reaction of the two isocyanate groups of a PD molecule is excluded because of the rigidity of the molecule.

Interestingly, an attempt is made to deposit PD on the uncoated Ge first. Several bands are identified in the IR spectrum, which differ from the isocyanate. Using a quantum mechanical calculation that is not described in detail, the authors assume that the isocyanate undergoes a cycloaddition with the Ge surface - Fig. 6-1.

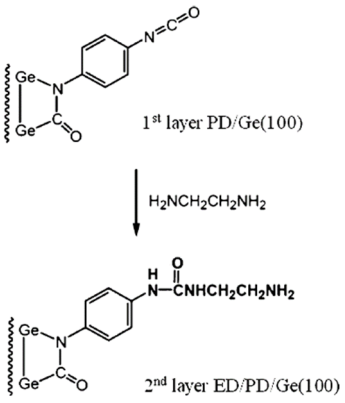

Fig. 6-1 Schematic illustration showing the dative Ge-N bond followed by the reaction of the free isocyanate group with the amine [132].

The addition of ED also leads to the formation of urea, but up to half of the isocyanates attached to the Ge surface seem to give up their attachment. Whether these now react with ED and which molecules are thus formed is not discussed here. The authors conclude that the hypothetical cycloaddition of the isocyanate to Ge is weaker and the amines preferentially adsorb to the surface. Co-adsorption of both monomers or mixing of the molecules is not discussed here.

In [133] the same monomers are deposited at RT on silica surfaces. The SiO_2 substrate is functionalized using 3-amino-propyltriethoxysilane (APTES). After APTES treatment the substrate surface present NH_2 groups. Using DFT, the authors calculate the geometry and length of a molecule that is formed on the NH_2 terminated surface after a deposition cycle of PD and ED. The authors conclude that the layer should grow by 0.65 nm per deposition cycle. The film thickness of samples exposed to different numbers of deposition cycles (up to 75) is then measured by ellipsometry. It turns out that the layer growth is only constant at 0.41 nm per cycle. The authors explain this by phenomena that are already known for ALD and CVD and assume that the layer is first formed by islands that later coalesce into a closed film. Unfortunately, no evidence is provided for this. It is also not clear whether this island formation and coalescence occurs after each deposition cycle or only after several cycles, as the samples are only examined after at least 10 successive depositions of ED and PD.

The weaker growth could also be explained by the so-called capping. In this process, some or all of the functional groups of a monomer can either react with the substrate surface and thus block reactive centres for the formation of new chains. Or, they can also react with at least two different polymer chains and terminate them by means of a bridge. In both cases, fewer functional groups are then available for further reaction. However, the authors exclude this from the outset.

The formed layers are also investigated with FTIR, XPS and TEM. The IR spectra show urea-specific amide bands which are broadened by hydrogen bonding between urea groups of neighbouring chains. One can distinguish between free carbonyl, once hydrogen bonded and twice hydrogen bonded species [145].

Furthermore, all layers were terminated with an ED deposition and consequently no isocyanate bands can be observed in the IR spectra. Presence of free NH_2 groups is not detailed. It is also not discussed whether the resulting urea form small oligomers or long linear chains. The XPS investigations only show the ratio O:N:C which is similar to the theoretically calculated ratio in urea. A detailed analysis of the peaks is not performed.

The temperature during deposition is later varied and it is found that the layer growth decreases with increasing temperature. The authors explain this by the fact that adsorbed molecules potentially dock to the sample surface by means of hydrogen bonds. Hydrogen from the amines could interact with N or O of the isocyanate and migrate from one site to another until it finds the right geometry to react. As the temperature rises, the lifetime of these hydrogen bonds is much shorter. What the molecules do then, however, is not explained. Desorption is not mentioned either.

In [134, 135] the same author present different potential applications for the same urea system prepared by MLD. The papers mainly focus on the applicability of MLD layers for lithographic patterning without revealing further details on the polyurea formation.

In [136] the same research group now presents the production of a cross-linked polyurea. As before, SiO_2 surfaces functionalised with APTES serve as substrates. The isocyanate is now 1,4-diisocyanatobutane (DICB) and the amines are ethylenediamine (ED), diethylenetriamine (DETA), triethylenetetramine (TETA) and tris(2-aminoethyl)amine (TAEA). According to the authors, the deposition works well with all systems. The amines are also changed during deposition and thus a transition from linear to cross-linked polyureas takes place in the layer. The authors also found that the bulkier or larger the monomers, the longer it takes for the surface to saturate and the layer growth to decrease significantly per deposition cycle. It is also assumed that so-called capping takes place. In the XPS investigations, only the ratio N:C:O is evaluated with the astonishing result that despite the slowed layer formation and the possible capping, a stoichiometric ratio is achieved in the end.

In [137] multiwall carbon nanotubes (MWCNT) are coated with polyurea using the MLD method. The monomers 1,4-phenylene diisocyanate (PD) and ethylene diamine (ED) react to form polyurea, which is detected by IR and Raman spectroscopy as well as XPS. Unfortunately, a detailed spectra analysis is missing. Due to the inert surface of the MWCNT, it is assumed that the adsorption is of a strong physical nature and that no covalent linkages exist. However, experimental confirmation of this assumption is not provided. The polyurea coating improves the solubility of the MWCNT in polar solvents. In composites of the coated MWCNT in a polyurethane matrix, the polar coating leads to improved mechanical properties, but no mention is made of how the polyurethane matrix is prepared and thus whether there is a possibility of reaction between the polyureas and the PU or its monomers.

In [138] polyurethane layers on silicon and glass are prepared with MLD to produce ordered zeolite structures. 1,4-Phenylene diisocyanate (PD) and 2-butyne-1,4-diol (BDO) are used as monomers, which are alternately deposited on the substrates after heating to 120 °C and spectroscopically characterised by diffuse-reflectance Fourier transform infrared spectroscopy (DRIFT). The sequential deposition of PD and BDO is repeated 100, 500 and 1000 times, with the intensity of the characteristic urethane bands increasing with the number of cycles. According to measurements with the scanning electron microscope, the thicknesses of the films produced are 95 nm, 360 nm and 610 nm, depending on the number of cycles. Since the aim of this publication is to produce ordered zeolite structures, hardly any details are given on the MLD process. In addition, it is mentioned that the polyurethane layers are no longer detectable on the glass surfaces two hours after deposition. Consequently, chemisorption is ruled out as a form of adsorption of the molecules, which remains completely unmentioned in the paper.

A review of the MLD-specific literature shows that only a few research groups are investigating this topic. Thus, although there is a manageable amount of literature, it is mostly repetitive. In general, there is very little information on the layer formation process. In most cases, there is no measurement of the layer growth during deposition.

In addition, it is not clear whether the pulsed application of monomers leads to self-limitation or saturation of the surface. Desorption of monomers also seems to be an exception. Interestingly, the stoichiometry of the layers is often determined by XPS and the N:O:C ratio. However, it has to be mentioned that XPS requires the layer to be measured in high vacuum for the first time and is also exposed to possible radiation damage. Furthermore, the simplified peak analysis does not indicate whether long polymerised chains are present on the layers or rather smaller oligomers.

Very little is reported about the durability of the layers. In most cases, thermal treatment is taken as the basis for stability testing. The molecules released by the thermal decomposition or which are still on the surface are rarely examined in detail.

Last but not least, successful MLD needs a substrate offering surface sites for chemical bonding to the monomer. In the literature, only few substrates (mainly Si, Ge and soda lime glass) have been considered so far. Their surfaces are often chemically modified by grafting for example amine groups to enable self-limiting reactions. Many publications simply presume that the monomers only bind covalently to the substrate (or to grafted functional groups). However, such bonds or other adhesive interactions of deposited molecules with the substrate surface are not yet identified explicitly. The adsorption of physically interacting molecules is not considered either. Hence, the MLD literature does not take explicit notice of adhesion mechanisms although they are the origin of a polymer interphase which is the major reason for the finding that thin films can behave much different from the bulk polymer. Hence, it is therefore essential to make use of the results of other layer formation processes which are specifically dedicated to polyurethanes.

6.1.2 Polyurethane layers prepared by other techniques

Despite the wide use of PU adhesives in industry, only a handful of publications describe the preparation and characterisation on thin layers on metal substrates using either spin coating or solvent based deposition. They reveal that the fundamental adhesion mechanisms are not well understood yet. In [6, 7, 48, 53] the adhesion between PUs and metal surfaces is decribed and the formation of interphases similarly as in epoxies is revealed. In a few other publications adsorption states of selected PU monomers or polymers have been characterised on the basis of vibrational spectroscopy and XPS results (e.g. [146-153]). But the corresponding binding states of the molecules on metal surfaces have not been revealed sufficiently. Adsorption states of PU-related molecules were also studied by quantummechanical modelling [154-156]. However, very simple molecular structures were modelled and therefore a correlation with more complex multifunctional molecules deserves verification.

FTIR spectroscopy and IR spectra calculation studies [8-10, 33, 36] of technically relevant aromatic diisocyanates (4,4'-methylene diphenyl diisocyanate as well as an isomer mixture – MDI) deposited using highly diluted monomer solutions on native metal surfaces of Al, Cu and Au reveal that adsorbed 4,4'-MDI molecules undergo notable changes of their vibrational state on the native metal surfaces. Once the 4,4'-MDI is in contact with the metal surface after the initial monomer solution rinse, the initially adsorbed amount based on the intensity of the fingerprint region depends on the metal: MDI(Al) ⩾ MDI(Cu) > MDI(Au). Ordered nano-domains form immediately and are characterised by a new sharp ν_a-NCO peak. The spectra also reveal the formation of urea-like species on all metal surfaces via the reaction between the MDI and adsorbed water molecules. The concentration of urea groups is specific to the metal substrate with a greater amount forming on Al and Cu than on Au. Hence, significantly more H_2O molecules are adsorbed on the Al and Cu surfaces. The stability of the prepared layers is assessed by subsequent solvent rinses. Rinsing with THF as a solvent removes a considerable part of the MDI, including the nano-domains. Hence, that part is only physically interacting. It is deposited on top of some more strongly adsorbed MDI layer. Rinsing also removes the generated urea-like species from all metal substrates. Hence, these species do not contribute significantly to the fundamental adhesion of MDI-based PU's on native metal substrates. In addition, THF is able to remove adsorbed MDI molecules almost completely from Au.

The remaining 4,4'-MDI on Al and Cu is distinguished by rich and specific spectral features (mainly new bands around 1700 cm^{-1} and 1400–1150 cm^{-1}) and the modification of existing bands) that differ from the bulk state while unreacted isocyanate groups still exist in the strongly adsorbed layer.

So both the resistance against solvent attack and the new IR bands support the conclusion that the residual 4,4'-MDI molecules adhere in a stable state to the native oxide layers on Al and Cu. Those spectral features do not give a straight answer on what partner the isocyanate group prefers for interaction, however. This structure is not equal to urethane because of the chemical link to the inorganic substrate and hence there is no reason to expect the corresponding IR bands at the same wavenumbers common for organic urethane. Moreover, there is no proof that it must be the addition reaction as several other options are possible: With the inorganic partner, it could be a donor-acceptor interaction as well. The IR spectroscopic findings also do not exclude strong interactions with oxygen or metal sites in the oxide surface on the substrates. The studies also showed that the adhesion of MDI molecules induces some changes on the substrates itself and that at least some part of the initial carbonaceous contamination is displaced on the three metals.

Starting from this work, it is therefore of great interest to check to what extent layers prepared by MLD show similar or different behaviour. Since no solvent is used during MLD, the behaviour of the carbonaceous contaminations is also of great importance.

More recent studies [11, 157] analysed the polymerisation behaviour of PU. Thin to ultra-thin polyurethane adsorbate layers are produced on aluminium and mild steel substrates by co-adsorption of PU components (4,4'-MDI [157] or an MDI isomer mixture [11] and Baygal® K55) from a diluted stoechiometric solution. For this purpose, three different concentrations (A, B and C) of the monomers are used in THF, whereby the concentration is halved in each case. IR-ERA spectroscopy is used to detect PU formation. Based on the intensity ratios, the layer thickness can be correlated with the monomer concentration, which decreases from A to C. A preferential adsorption of the isocyanate is shown for all concentrations on aluminium and for the smallest concentration on mild steel. The reaction runs for several days at RT and is continuously recorded by IR-ERA spectroscopy. After it comes to a standstill, stability tests are also carried out with THF on the layers produced. At all concentrations there is a chemisorbed layer, above which there are oligomers that interact only weakly physically with the lower layer and are removed by the solvent. As the concentration decreases, less material is washed off. Concentration A has a high number of initially only weakly physically bound molecules/oligomers that have a sufficiently high mobility to cross-link. In B and C, on the other hand, this number is lower because a large proportion of the oligomers are immobilised by the substrate. As a result, cross-linking is less pronounced and less material can form stronger interactions with the substrate surface. The substrate thus plays a crucial role in the process of cross-linking, because the closer the oligomers are to the substrate, the more difficult their cross-linking becomes. SFM and DIK images confirm these results. On aluminium, after adsorption of concentration A, the topography consists of a flat, homogeneous layer that covers the nodular surface structure of the aluminium and has a thickness of about 10 nm. Concentrations B and C replicate the topography of the aluminium substrate on aluminium. This condition is only achieved on mild steel at the smallest concentration.

The investigation of thin PU layers reveals a multi-layered problem. On the one hand, it is necessary to identify and understand the monomer-specific interactions with a substrate surface. In addition, these are superimposed by the interphase formation. Progressive washing of the adsorbates by means of solvent rinses is an elegant way to unravel and understand the different interactions and their strength and effect. This problem must undoubtedly also be applied to MLD layers in order to gain a comprehensive knowledge of these layers and their formation.

6.2 Properties and behaviour of the substrates

As mentioned in chapter 5.1 omnipresent carbonaceous contaminations from the ambient atmosphere spontaneously adsorb on prepared surfaces of PVD-deposited metals. Thus, avoiding the adsorption of these species requires very specific conditions as for example ultra-high vacuum and no contact of the substrates with ambient atmosphere. This is on one hand extremely expensive and on the other hand does hardly reflect industrial scale applications. Even in clean rooms adsorbed contaminants are identified [158-160]. During layer preparation by adsorption from a solution or by spin-coating the solvent is in contact with the substrate surface while monomers adsorb. Hence, the contaminations can easily be solvated and ease the adsorption of monomers. However, during the MLD process no solvent is present[28] and thus monomers must displace the carbonaceous contamination in order to adsorb on the very substrate. Nevertheless the contamination will not desorb and hence it will affect the interactions of the deposited monomers with each other and with the native metal surfaces. Furthermore, the solvation effect of THF on these contaminations can also provide valuable information as the substrate and later the thin deposits are rinsed with THF.

6.2.1 Impact of THF on the substrate

Prior to any monomer deposition the substrates are rinsed once with tetrahydrofuran in order to obtain a reproducible initial state (cf. 3.2.2.1 Step 2 and 3). It is thus interesting to characterise what happens during this initial THF rinse. In the experiments shown in Fig. 6-2 and Fig. 6-3 four THF rinses are successively applied to native Al and Cu substrates after 24 h of storage in dried air. In this case, REF-1 spectrum of the unrinsed substrate serves as reference for all spectra following each THF rinse. Hence the obtained spectra only reflect the changes that occur after each rinse. They do not provide a picture of the initially adsorbed species before the 1st rinse as this would require a reference spectrum of an uncontaminated substrate.

Starting with aluminium the spectrum after the 1st THF rinse (Fig. 6-2 – black line) shows extremely weak bands in the CH stretch region (3000 – 2800 cm^{-1}), the carbonyl region (1800 – 1700 cm^{-1}), the CH deformation region (1600 – 1400 cm^{-1}) as well as a few wide weak buckles in the baseline below 1200 cm^{-1}. The intensity of all bands is at most 0.5 ‰. As the bands show ‘downwards’, they indicate few new carbonaceous contaminations that have adsorbed onto the surface with the 1st THF rinse. The baseline buckles are caused by slight sample misplacement that occurs at each THF rinse.

[28] As the monomers are diluted in the N_2 carrier gas, it can be assimilated as gaseous solvent.

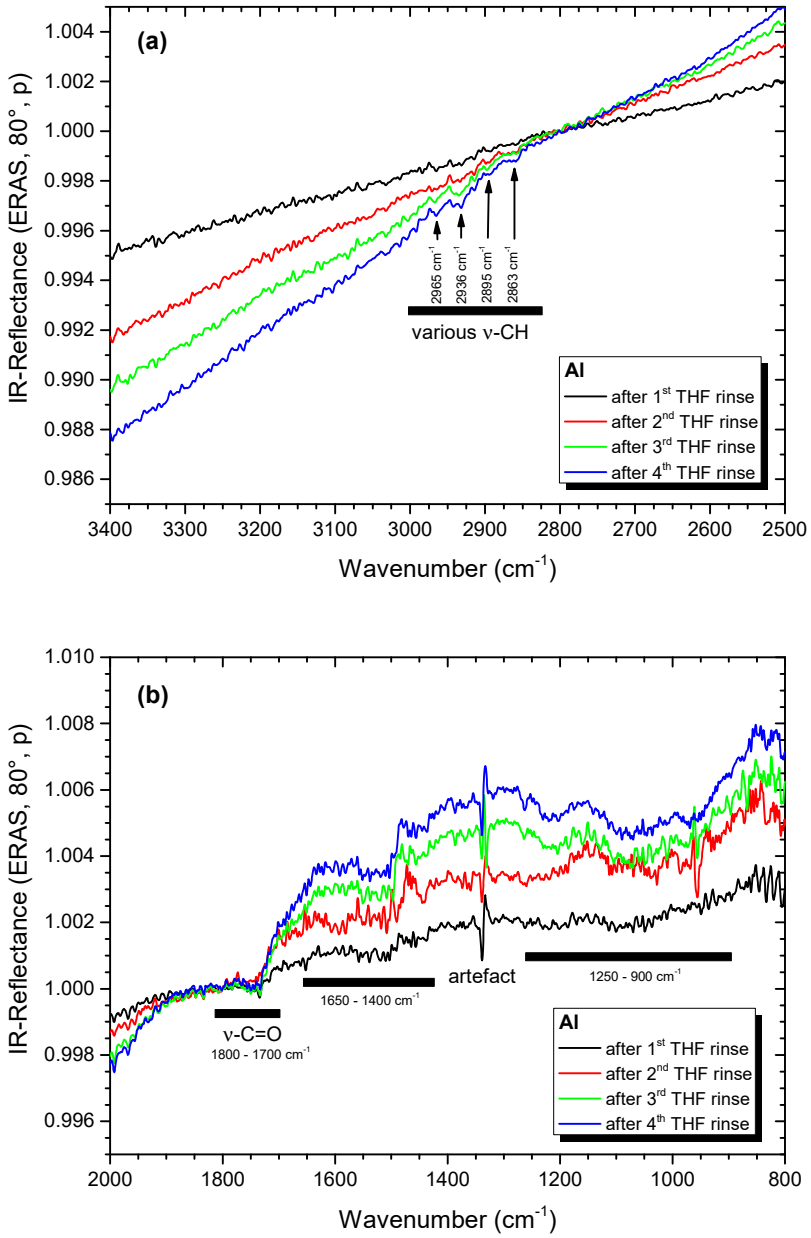

Fig. 6-2 IR-ERA spectra of carbonaceous contaminations present on native Al substrate after four successive THF rinses. (a) 3400 – 2500 cm^{-1}, (b) 2000 – 800 cm^{-1}.

All bands continue to grow with each THF rinse. The CH stretches remain weak but bands below 1800 cm^{-1} become more pronounced. The strongest bands are now in the 1300 – 900 cm^{-1} region and have an intensity of at most 2 ‰ after the 4th rinse. The bands are also more pronounced due to the increasing baseline tilt. In conclusion, these newly deposited contaminations originate from solvation or leaching of materials from components contacting the THF during the rinses. Such components could be the outer tubing of the PTFE lined pipes, the O-ring and the adhesive tape utilised during such a rinsing cycle. In [117] each of these components was put into THF and a few drops of this THF solution were deposited on an Al (or Cu) substrate.

The obtained ERA spectra as well as a pure THF spectrum were compared with the ERA spectra after the different THF rinses of the substrates. While they present bands in the same spectral regions and some bands (e.g. the CH stretches or the carbonyl band) matched, other bands below 1600 cm^{-1} were significantly different. Hence it is concluded that the bands obtained with the substrate rinsing steps do result from organic molecules that adsorbed from the ambient atmosphere during substrate purging after the rinse but not from the components of the setup.

On Cu (Fig. 6-3) a similar behaviour is observed. After the 1st THF rinse, CH stretching bands are at noise level and the region shows a baseline buckle. Below 1800 cm^{-1} a weak band at 1368 cm^{-1} is visible and some wavy background below 1200 cm^{-1} also probably caused by the sample misplacement. Thus the first THF rinse has not caused much change in the adsorbed contaminations. However from the 2nd THF rinse onwards, bands continue to grow. The CH stretches slightly raise above noise, a carbonyl band (1740 cm^{-1}) grows with each rinse and reaches an intensity of 1 ‰. Three bands (1523, 1368 and 1225 cm^{-1}) appear between 1600 and 1200 cm^{-1} which are different from the Al. Thus, contaminations continue to adsorb on Cu with each THF rinse. Each metal has its own affinity for similar but specific contaminations.

Hence on both metals, each THF rinse modifies the contamination state. Contaminations adsorb while the substrate spectrum is taken in dried and filtered air after each rinse[29]. It is noted that the adsorbed contaminations can change over time as they are mainly influenced by the quality of the provided dried air[30].

As a general conclusion, the THF rinses do some cleaning but metal substrates for MLD will always come with some carbonaceous adsorbates unless they are not fully prepared and handled in ultra-high vacuum. Hence any MLD layer will contain such contamination.

The next section answers the question whether the contamination grows simply with contact time to air or if the THF treatment stimulates the adsorption of contamination.

[29] Each THF rinse including the recording of IR spectra takes approximatively 40 min. The four rinses take ca. 3 hours.

[30] For example, the observed carbonyl band appeared during a defect of the air compressor where some oil mist was generated which could not be completely removed by the filters.

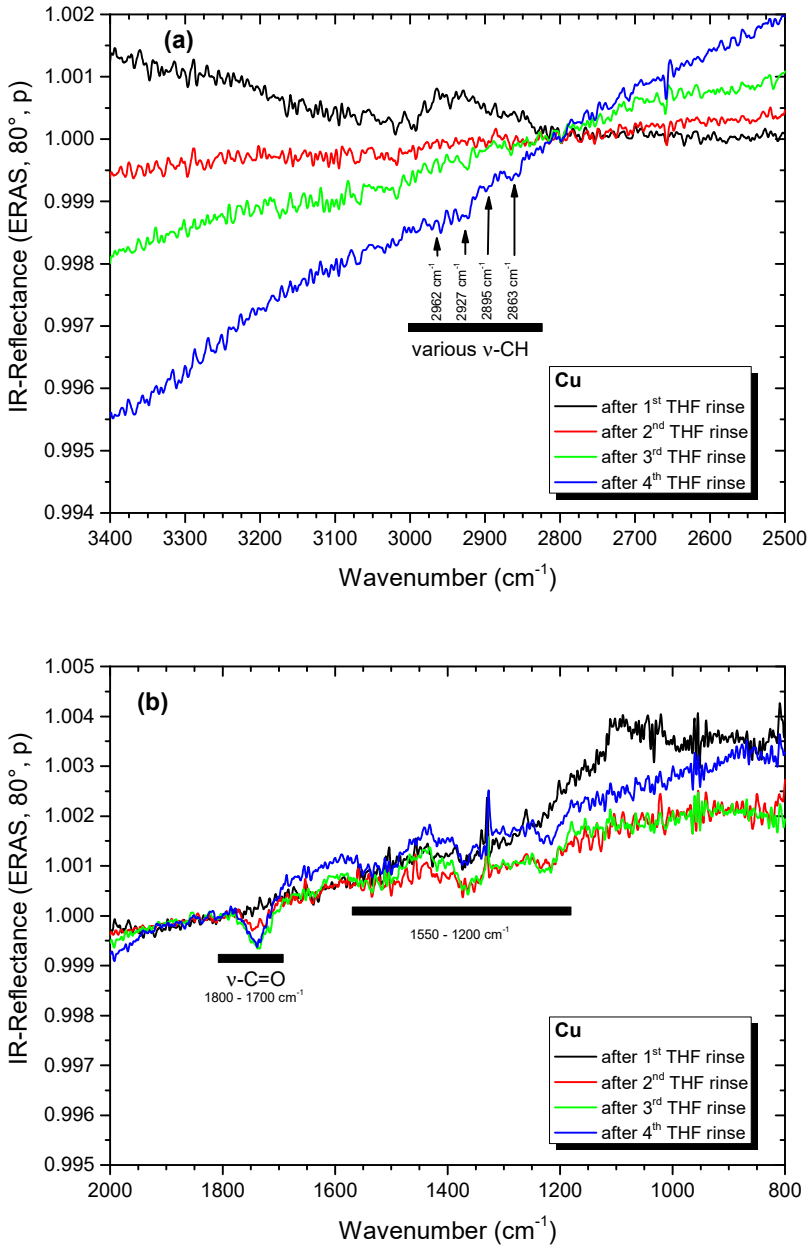

Fig. 6-3 IR-ERA spectra of carbonaceous contaminations present on native Cu substrate after four successive THF rinses. (a) 3400 – 2500 cm^{-1}, (b) 2000 – 800 cm^{-1}.

6.2.2 Effect of storage time in air

In order to answer the previous question another set of experiments is performed on both metals. Again, a 1st THF rinse is applied on the metals and IR spectra are recorded before and after this rinse. Then, a sequence of sample spectra is recorded over 24 h while the rinsed substrate remains in the dried air purging the IR measuring chamber.

Starting with Al, the evolution of the contaminations on the substrate is shown in Fig. 6-4. The spectrum taken after the THF rinse (black line) is comparable to the spectrum after the 1st THF rinse shown in Fig. 6-2.

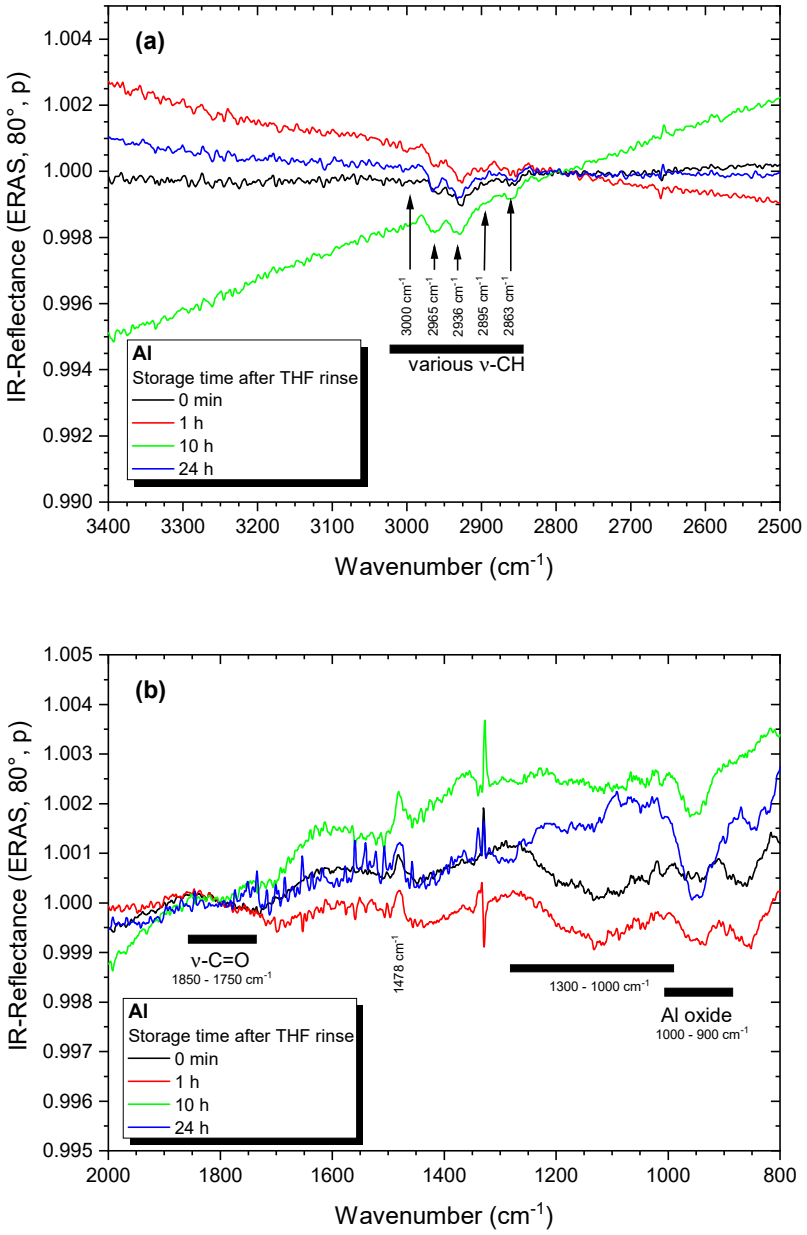

Fig. 6-4 IR-ERA spectra of carbonaceous contaminations present on native Al substrate up to 12 h after a THF rinse. The sample is stored under dried purified air in the measurement chamber of the IR. (a) 3400 – 2500 cm^{-1}, (b) 2000 – 800 cm^{-1}.

During the first hour of storage, shape and intensity of nearly all bands do not change except a growth of the Al oxide lattice vibration band below 1000 cm^{-1} and a slight baseline tilt. A carbonyl band does not appear. The spectra at 0 min. and 1 h (black and red line respectively) also show large buckles that regularly repeat from 1800 cm^{-1} downwards to lower wavenumbers. Due to the regularity of the buckles they are caused by slight sample misplacement and are not to be considered as bands. A negative band at 1500 cm^{-1} is present after the 1st rinse. This could indicate the removal of some species during the 1st rinse. A similar band appeared while performing several rinses (cf. Fig. 6-2b). With ongoing storage time all previously present bands slightly increase in intensity, thus further contaminations adsorb over time. The most notable change is a significant growth of the band of Al oxide lattice vibrations below 1000 cm^{-1}. Hence, over storage time the aluminium oxide is further modified.

Compared with the results obtained for multiple THF rinses these spectra reveal several differences. Hence, different species are adsorbed. Each THF rinse tends to facilitate the adsorption of new contaminants, mainly containing carbonyl groups. During storage however, the amorphous Al oxide is slowly modified which can trigger the adsorption of further contaminations from the atmosphere.

On Cu, a similar behaviour is observed (Fig. 6-5). After the 1st THF rinse the spectrum (black line) shows weak bands of CH stretches, carbonyl and a small band at 1465 cm^{-1}. During the first hour of storage in dried air (red line) these bands slightly diminish in intensity. Furthermore a few new bands emerge below 1300 cm^{-1}. Over the course of the next 9 h of storage a few notable changes occur. The CH stretches do not change, the carbonyl band vanishes and the bands between 1300 and 1000 cm^{-1} have also lost intensity. A new buckle appears below 950 cm^{-1}. Up to 24 h no further changes take place. The disappearance of the carbonyl group indicates that the dried air quality fluctuates over storage time. Hence it is not certain if the carbonyl species are only located in the air or if they initially adsorbed after the THF rinse and then desorbed from the surface as the air quality is getting better. The band below 900 cm^{-1} could be caused by a modification of the Cu oxide lattice. However as this buckle is observed in some spectra of the Al substrate too (for example in Fig. 6-4b - 0 and 1h of storage) and then disappears at later stages precise band attribution is difficult. Moreover below 900 cm^{-1}, the spectra tend to show wavelike distortions that lead to such buckles.

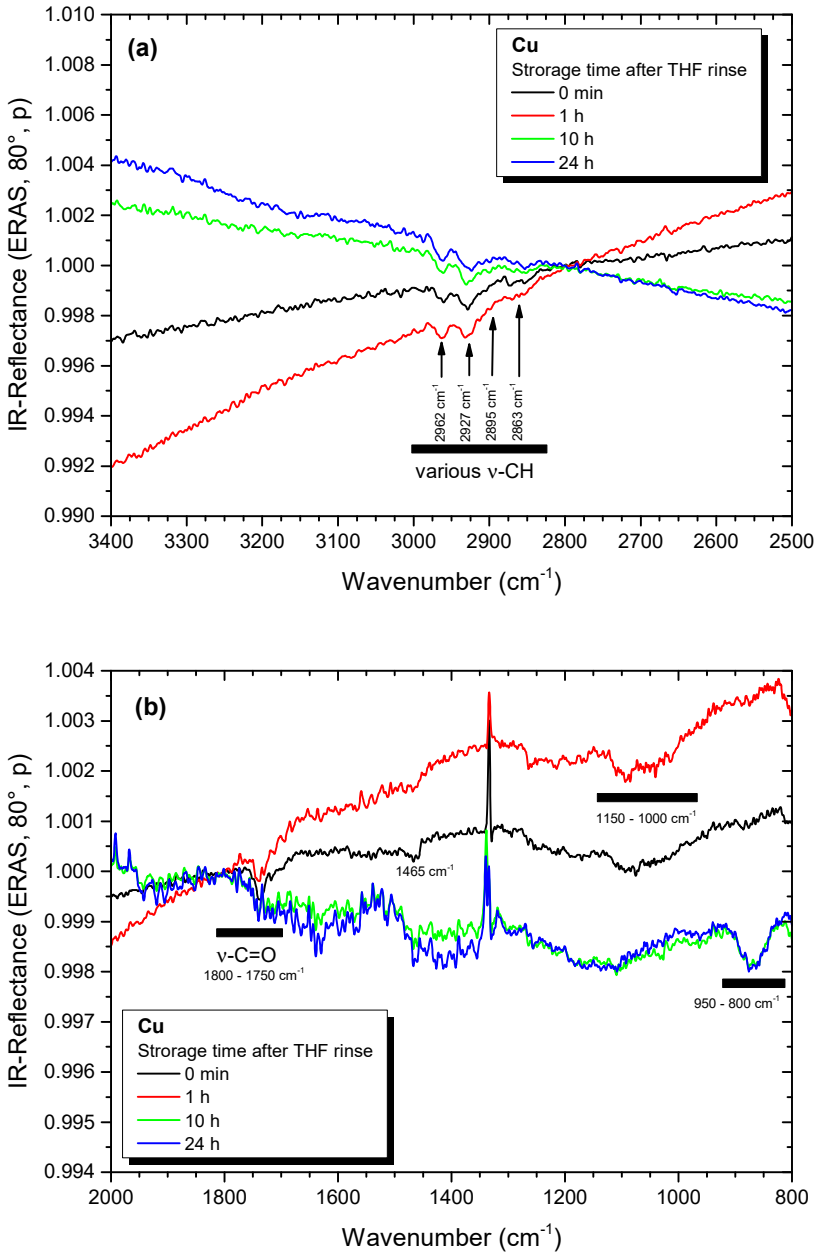

Fig. 6-5 IR-ERA spectra of carbonaceous contaminations present on native Cu substrate up to 24 h after a THF rinse. The sample is stored under dried air in the measurement chamber of the IR. (a) 3400 – 2500 cm^{-1}, (b) 2000 – 800 cm^{-1}.

6.2.3 Influence of an MLD deposition cycle on the substrate state

As last step the behaviour of contaminations during an MLD deposition cycle is analysed. This provides valuable information on how contaminations deal with a carrier gas flow at reduced pressure and if the oxide structures are also somehow modified. In these experiments the MLD process is done exactly as described in section 4.4 but without placing the monomer crucibles inside the MLD. Thus, the substrate also experiences the stabilisation phase with its various temperature steps and the same exposure time with nitrogen flow.

The gate valves of the evaporation cells are also opened and closed at typical deposition times to mimic a sequence of monomer depositions. The substrate is then transferred back into the IR spectrometer and sample spectra are recorded over 24 hours. Then one THF rinse is performed in order to verify the adsorption strength of the ‘deposited’ contaminants.

Starting with Al (Fig. 6-6) the spectrum after the MLD blank test (black line) does show identical features as the substrate stored in dried air (cf. Fig. 6-4). The Al oxide band (1000 – 900 cm^{-1}) is also present. Thus, during the MLD cycle, which takes a few hours (including the stabilisation phase) the Al oxide is also slightly modified and its IR intensity compares to the spectra during storage.

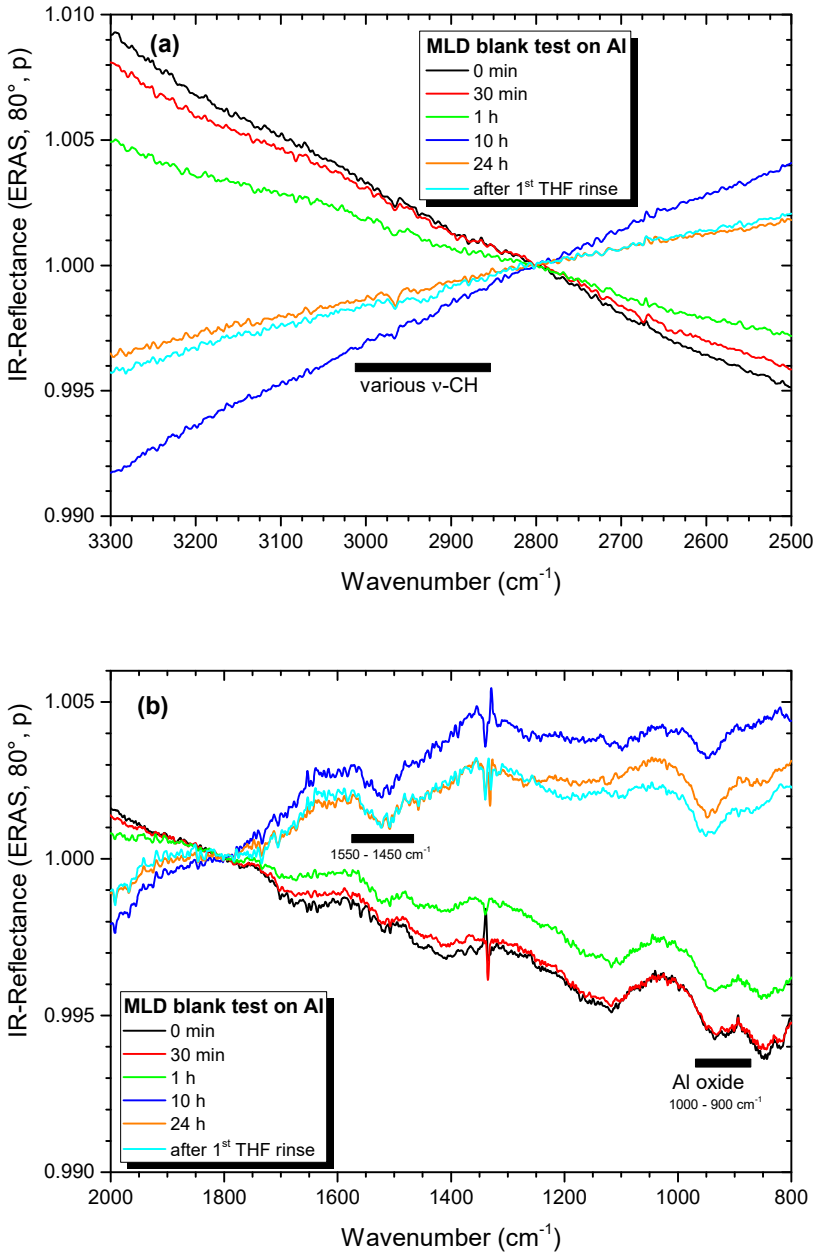

Fig. 6-6 IR-ERA spectra of carbonaceous contaminations on native Al substrate during 24 h after a MLD blank test. The sample is stored under dried air in the measurement chamber of the IR. (a) 3300 – 2500 cm^{-1}, (b) 2000 – 800 cm^{-1}.

Over storage time the Al oxide band grows similarly as discussed previously. A new band between 1550 and 1450 cm^{-1} grows with time. It was also visible in the spectrum after 24 h of storage (cf. Fig. 6-4) as well as after the 4th THF rinse (cf. Fig. 6-2). The THF rinse does not change this picture at all.

On Cu no oxide band is formed and two bands (1600 – 1450 cm^{-1} and 1413 cm^{-1}) grow over time. The baseline underground changes quite significantly below 1300 cm^{-1} with time. This is due to the simultaneous baseline tilt as the cooling state of the detector changes with time.

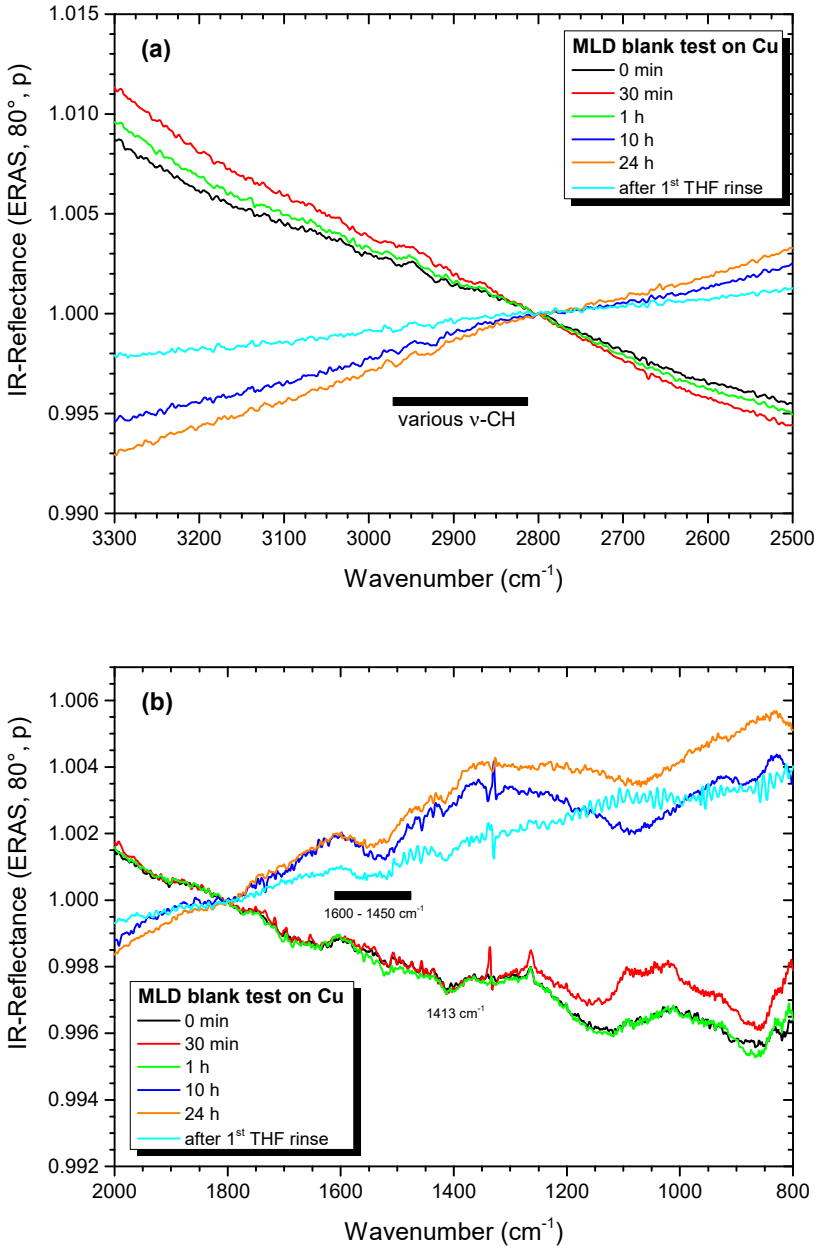

Fig. 6-7 IR-ERA spectra of carbonaceous contaminations present on native Cu substrate up to 24 h after a MLD blank test. The sample is stored under dried air in the measurement chamber of the IR. (a) 3300 – 2500 cm^{-1}, (b) 2000 – 800 cm^{-1}.

Below 900 cm^{-1} a buckle grows over the first hour after the MLD blank test. This is in accordance with the previously measured spectra (cf. Fig. 6-5). However, this buckle disappears during further storage. If this band is attributed to a Cu oxide vibration it is

doubtful that a modification of the oxide lattice is reversed during storage. Hence, this band should be considered as interference.

6.2.4 Behaviour of the substrates - Conclusion

The IR spectroscopic study of the native metal surfaces and their modification throughout an MLD process showed a few points that are necessary to take into account when later discussing the deposited monomer and polymer layers.

First, it was shown that carbonaceous contaminations are omnipresent. The various process steps (blank deposition, storage in the IR and THF rinses) slightly modify the adsorbed organic contaminations and their quantity. The quality of the dried air also contributes to a variation of contaminants that adsorb. In general it is observed that regions of CH stretches (3000 – 2800 cm^{-1}) and deformations (1650 – 1300 cm^{-1}) are impacted by the carbonaceous contaminations. A modification of the carbonyl region (1800 – 1700 cm^{-1}) is also observed on some samples. Similar behaviour was identified on Au as well [74, 117]. Hence contaminations also adsorb on the QCM quartz.

The adsorption of monomers has to cope with the already adsorbed contaminations. For example before adsorbing onto the native oxide on the metal substrate, monomers will have to displace these contaminations. Where will they go? Will they desorb or only mix within the monomer deposit? Ultimately, could the contaminations remain on the substrate surface sites and block strong adsorption of the monomers?

Second, the amorphous oxide layer on Al slightly grows over time and identified by a large band below 1000 cm^{-1}. Adsorption of reactive monomers may also have an impact on the evolution of the oxide layer.

6.3 Reproducibility and stability of deposits

Before we can discuss IR spectra of adsorbed monomer and polymer thin layers it is necessary to verify first to what extend the deposition procedure yields reproducible and stable layers in terms of MLD parameters and layer thickness provided by the QCM. Second the question can be elucidated if the corresponding IR spectra match with the results obtained from the MLD. The reproducibility is discussed on a few representative experiments only.

The layers are prepared by deposition of 4,4'-MDI onto an Al substrate. Deposition is stopped at 0.9 nm and the non-deposition mode is maintained for about 1 hour. The QCM thickness evolution is shown in Fig. 6-8 for three identically prepared layers.

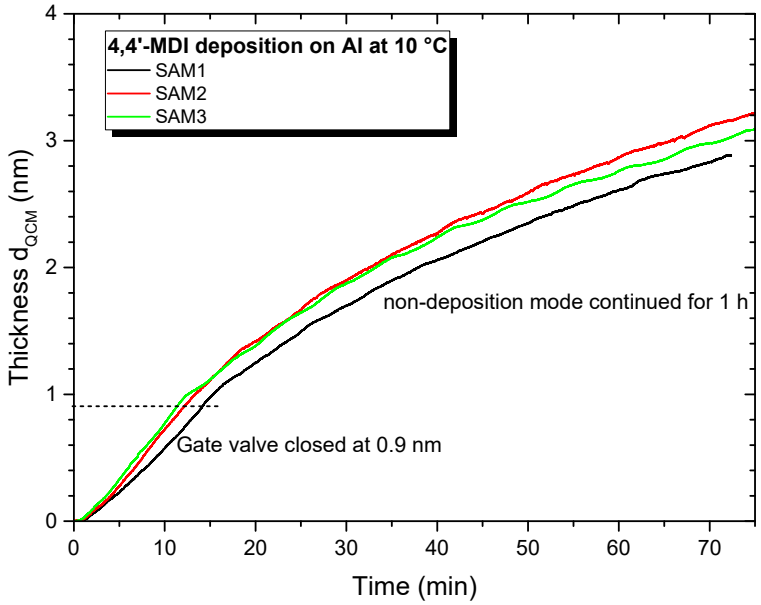

Fig. 6-8 Evolution of the QCM thickness during the deposition of 4,4'-MDI for three samples. Gate valve of the evaporation cell is opened at 0 min. and closed after reaching 0.9 nm. Non-deposition mode is continued for 60 min. This experiment is carried out at 5 l/min N_2, 500 mbar and 10 °C sample temperature. MDI evaporation cell is heated at 180 °C.

During the first 5 minutes of deposition the layer growth is identical for the 3 samples then it starts to go apart. SAM 1 thickness grows slower than for both other samples. This offset continues during the non-deposition mode. As seen in section 4.4 – Fig. 4-22, monomer molecules continue to flow through the pipes from the gate valve of the evaporation cell into the reactor and adsorb onto the substrate. The growth rate difference certainly originates from slight differences in the deposition parameters as evaporation temperature, substrate temperature, pressure, and gas flow. After approx. 60 min. of non-deposition, the thickness reaches between 2.9 nm (SAM 1) and 3.2 nm (SAM 2). Strictly speaking, we have a ranking of the 3 samples (SAM 1 < SAM 2 < SAM 3). Hence, considering small thickness variations the deposition process seems to be reproducible at first glance.

From this point of view the IR spectra of these three samples should be similar and small differences of IR band intensities are expected to follow the previous thickness ranking. The first spectra obtained for these layers are shown in Fig. 6-9.

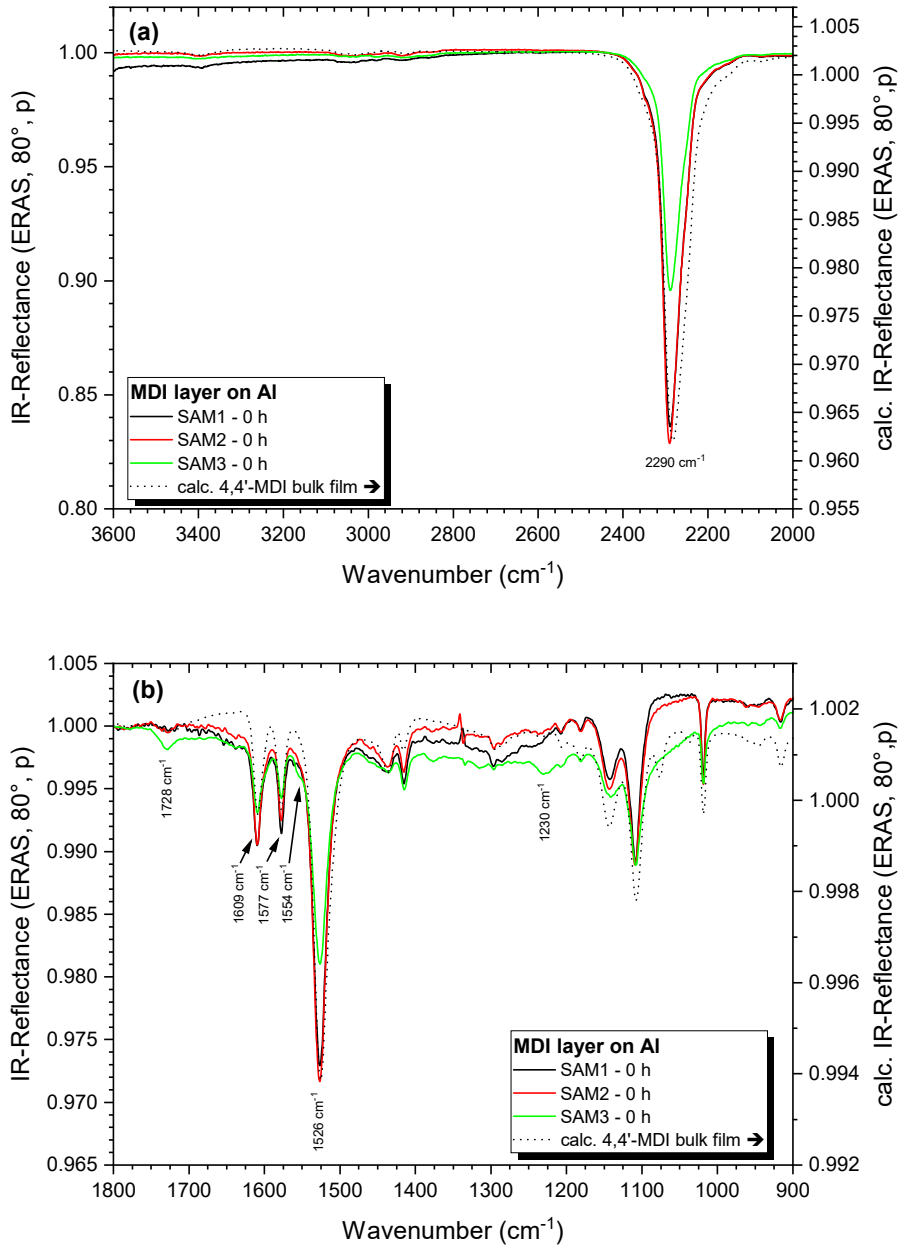

Fig. 6-9 IR-ERA spectra of the 4,4'-MDI layers on three Al samples after transfer and alignment in the IR spectrometer; (a) 3600 – 2000 cm^{-1}, (b) 1800 – 900 cm^{-1}. The dashed line represents a calculated bulk-like ERA spectrum for qualitative comparison.

Since this section only discusses the band intensities of the individual samples and the changes in the spectra compared to the bulk state, a detailed band assignment is not provided here. The detailed discussion on the development of the layers will be presented later in this chapter (see section 6.4 and 6.5).

Band intensity at 2290 cm^{-1} is identical for SAM 1 & 2 but significantly weaker for SAM 3. Similarly, in the fingerprint region bands at 1609, 1577 and 1526 cm^{-1} are weaker on SAM 3 while identical for SAM 1 & 2. Bands between 1200 cm^{-1} and 1000 cm^{-1} are also weaker on SAM 3 compared to the other samples. Hence, the intensity ranking is significantly different from the thickness provided by the QCM during layer preparation. This difference can be partly explained by different transfer and sample position alignment times of the individual samples. This implies that the deposited isocyanate either undergoes some chemical reaction leading to a decrease of intensity of the IR bands or that the isocyanate partially desorbs from the surface.

Comparison of the spectra with bulk MDI reveals new bands at 1728, 1554 and 1230 cm^{-1}. They are more intense for SAM 3. Hence, on one hand this observation reinforces the hypothesis of a reaction. Consequently, the deposited isocyanate could form larger amounts of the reaction species due to the longer transfer and alignment time and achieve different stages. On the other hand the study of the carbonaceous contaminants in the previous section revealed the presence of bands in the same region. Thus, a second hypothesis could be that on SAM 3 more contaminants adsorbed while less isocyanate is deposited. This could explain the observation that for the same QCM thickness less MDI is present on the substrate. In order to refine this situation the samples are stored inside the IR for 24 h and the evolution of the bands monitored.

The spectra obtained after this storage time are shown in Fig. 6-10. Now, the band intensity in Fig. 6-10a is nearly equal on all samples. A new band at 3310 cm^{-1} is also present on all three samples. The CH stretch region is slightly different for each experiment. As intensity is as weak as for the contamination spectra, differences are mainly due to the superposition of contamination bands and bands from the adsorbed/reacted monomers. SAM 1 & 2 also exhibit a slight baseline tilt that is not present in SAM 3. The fingerprint region (Fig. 6-10b), however, shows a few slight differences between the spectra. First, most bands on SAM 3 are stronger than on both other samples. This is mainly visible for the bands at 1750 – 1680, 1555 – 1514, 1414, 1308, 1233 and 1110 cm^{-1}. The growth of these new bands over time as well as the decrease of the original MDI bands is a proof that a chemical reaction of the isocyanate proceeds after deposition on the substrate. Furthermore the intensity of the new bands outgrows those of adsorbed carbonaceous contaminants. Second, for SAM 3 the baseline is different from the other spectra thus inducing a variable shift of whole bands to higher or lower intensities. This can be observed very well between 1800 and 1400 cm^{-1}. The spectra also show that for SAM 3 the bands between 1555 and 1514 cm^{-1} possess a slightly different intensity ratio.

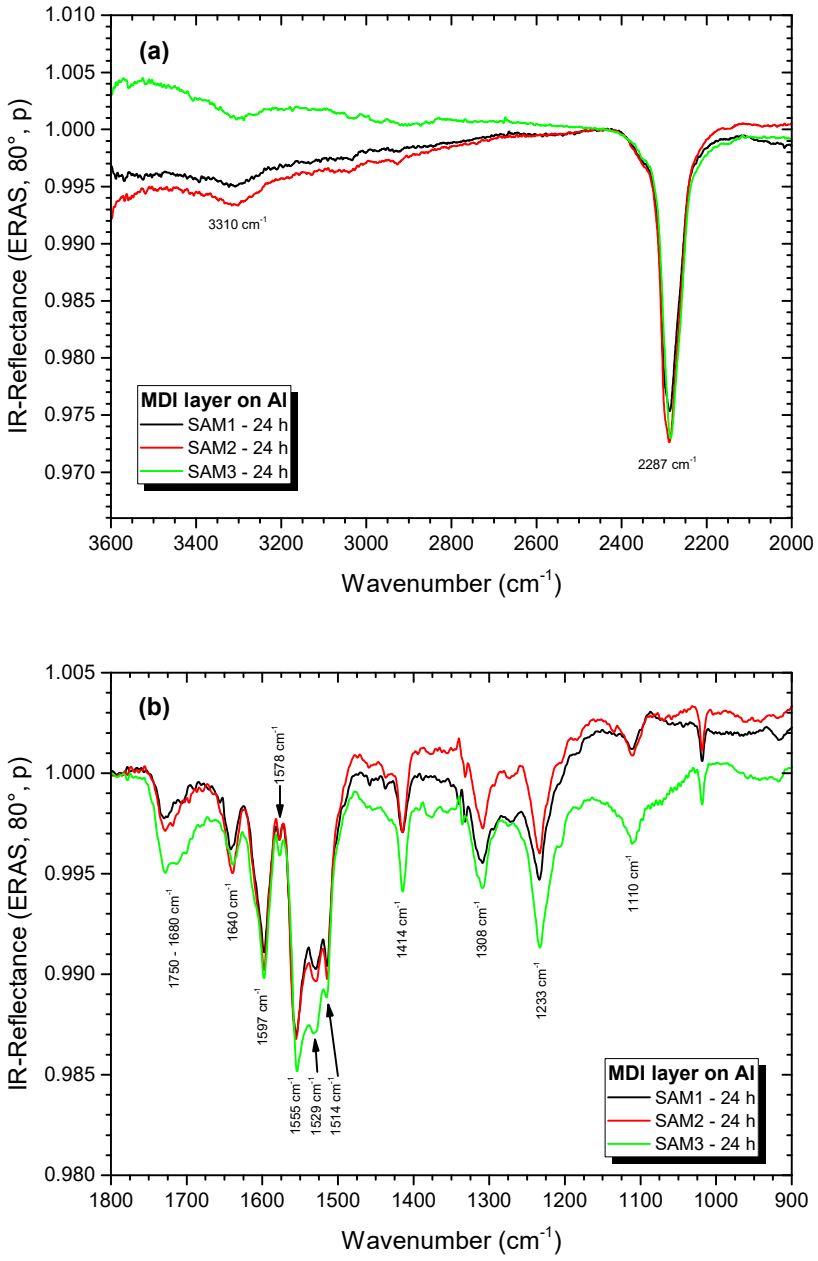

Fig. 6-10 IR-ERA spectra of the three 4,4'-MDI layers on Al after 24 h of storage in dried air at RT in the IR spectrometer. (a) 3600 – 2000 cm^{-1}, (b) 1800 – 900 cm^{-1}.

For SAM 1 & 2 the bands at 1529 and 1514 cm^{-1} have the same intensity while in SAM 3 it is not the case. Similarly many other bands (1750 – 1680, 1414, 1308 and 1233 cm^{-1}) are still stronger. At this stage another hypothesis can be formulated. Relative intensity variation of bands is generally induced by a change of preferential orientation of molecules on a sample. As polarised IR light is used this orientation change induces a variation of the band intensity of some bands in the spectra. Hence, where does this orientation change originate? One possibility could be that the topography of the layers is different.

At this point no proof exists that the prepared layers are homogeneous and perfectly covers the whole surface of the sample and obviously the quartz. Hence, if non homogeneous deposits are achieved the monitored QCM thickness is compromised and hence intensity variations on the spectra are inevitable.

Comparison of more samples prepared by the same procedure leads to an average intensity discrepancy of around 2-3 ‰ and should be considered as lowest limit of reproducibility. This also corresponds to the maximum intensity of adsorbed carbonaceous contaminants that may modify shape and intensity of weak adsorption bands in the concerned regions.

6.4 Thin layers of alcohols

We start with the discussion of the behaviour of thin alcohol layers on native metals followed by isocyanate layers in section 6.5. As both chosen alcohols are non-toxic and easily cleanable they are optimal for initial MLD testing and process parameter tuning.

6.4.1 Deposition behaviour

As the bulk monomers showed a quite different thermal behaviour in terms of evaporation temperature (cf. section 5.3.2) one can expect some impact during the MLD deposition. Thus, before studying the chemical properties of the layers it is interesting to look at the behaviour during deposition in order to determine the optimal parameters. The pressure inside the MLD was set to 500 mbar for all experiments. Thus, the evaporation cell temperature, sample temperature and carrier gas flow rate are the only parameters that are to be adjusted for adequate deposition. Higher evaporation cell temperatures increase monomer concentration in the carrier gas and deposition rate. Higher carrier gas flow rates dilute monomer concentration thus reducing deposition rate [75].

For dipropylene glycol (DPG), optimisation provided evaporation cell temperatures between 80 and 100 °C and carrier gas flow rates between 2 and 5 l/min as appropriate for controlled adsorption[31]. Fig. 6-11 shows the typical adsorption behaviour of DPG in the MLD. At t = 0 the gate valves at the evaporation cell are switched to deposition mode. After 1 min. the monomers in the carrier gas reach the reactor chamber and start to adsorb onto substrate and quartz. A constant deposition rate is reached one minute later. Deposition is continued until a layer thickness of 10 nm. Then the gate valves are switched back to non-deposition mode. The monomers still present in the carrier gas between evaporation cell and reactor chamber continue to flow towards the substrate and thickness continues to increase until a maximum thickness of 14.7 nm is reached at 15 min. Then the thickness starts to decrease, i.e. DPG already starts to desorb from the surface. The rate of desorption is slightly slower than for adsorption. Eventually a plateau is reached. From the quartz crystal, nearly the complete deposit desorbs during 30 min. at 10 °C substrate temperature. The remaining 0.6 nm given by the QCM may indicate a few molecules still adsorbed. However, as the QCM is very sensitive for many parameter changes such small thicknesses should be considered with caution.

[31] These values were found optimal for the other chosen MLD parameters as well: Vacuum of 500 mbar, pipes at 80 °C.

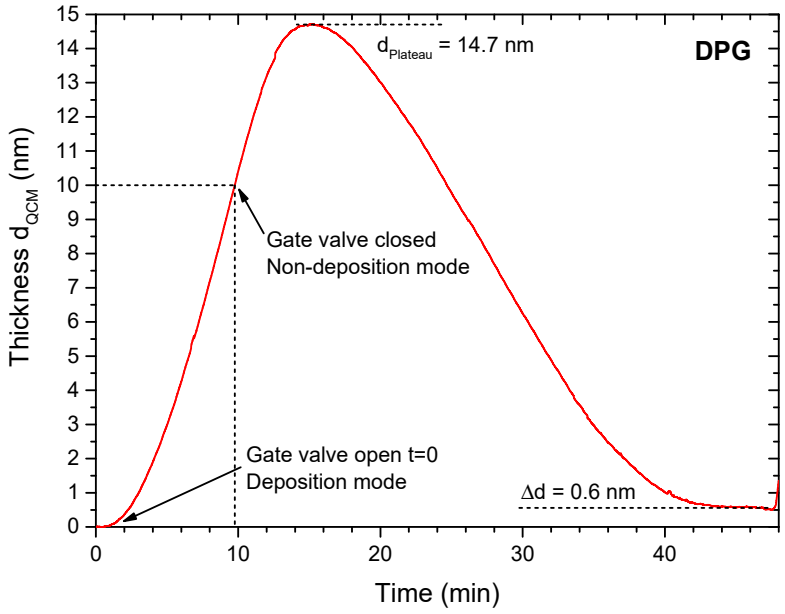

Fig. 6-11 Evolution of the QCM thickness during deposition of DPG. The gate valve of the evaporation cell is opened at 0 min. and closed after 10 nm. This experiment is carried out at 2 l/min N_2, 500 mbar and 10 °C sample temperature. DPG evaporation cell is heated at 90 °C.

This experiment leads to a few conclusions. First, as discussed above (cf. Section 4.1) adsorption and desorption of DPG molecules simultaneously take place during the whole experiment. Growth or decrease of the layer thickness indicates only the predominant effect. During adsorption more molecules are present in the gas phase and strive to cover the substrate while a few of the adsorbed molecules choose to go back into gas phase. As long as enough molecules are present in the gas phase they continue to adsorb[32]. In contrary to claims in literature (cf. section 4.1 and 6.1.1) no self-limited monolayer is obtained for the chosen conditions. At the point of maximum thickness, adsorption and desorption reach an equilibrium as less and less molecules are present in the carrier gas. During the phase of prevailing desorption only few molecules adsorb as compared to the adsorbed DPG molecules that choose to leave the surface and go back into the gas phase.

Second, this behaviour already indicates that the interactions between DPG and a metal surface are weak enough to allow desorption. An increase of the substrate temperature leads to a decrease of the adsorption rate and much smaller thicknesses are achieved. At temperatures above 30 °C layer grows much slower and 10 nm are not reached within a reasonable time[33] anymore. Desorption is also accelerated.

[32] DPG layers of up to 70 nm were deposited that way without reaching a saturation of adsorption. The deposition was stopped at that point to avoid excessive contamination of the MLD.

[33] 1 h deposition duration was chosen as upper limit for the preparation of a layer.

The experiment can be repeated for the triol. Process parameter optimisation revealed an optimal evaporation temperature between 160 and 180 °C which is also in good agreement with the values found by TGA (cf. section 5.3.2.2). Using 180 °C as evaporation cell temperature and the same carrier gas flow of 2 l/min, 500 mbar and 10 °C sample temperature, thickness evolution over time is shown in Fig. 6-12. Adsorption of the triol is slower than for the DPG, 10 nm are reached after about 27 min. This is caused by the interplay of two effects. On one hand the affinity of the triol for the metal surface can be different and on the other hand, and more likely, the monomer concentration in the carrier gas is much weaker than for the DPG as the intermolecular interactions of the triol are more pronounced and hence the evaporation temperature is much higher[34]. After stopping the deposition at 10 nm the layer continues to grow up to 11.4 nm. As for DPG, desorption begins after this maximum is reached. Desorption is much slower now – it takes more than 3 hours. The experiment is stopped at this stage without measurement of further desorption[35]. Preparation of thinner layers of 2 nm at its maximum revealed that desorption stops between 0.6 and 1.2 nm [116]. Hence the slow desorption indicates stronger interactions between triol molecules but also with the substrate and is in agreement with the lower vapour pressure of the triol and its higher molecular weight. Furthermore the rate of desorption also gets slower and slower over time indicating that molecules adsorbed farthest from the metal surface desorb more easily than molecules adsorbed closer to or in contact with the metal oxide surface. This reflects the gradient of different interactions present in the interphase formed between metal – monomer – nitrogen atmosphere.

[34] TGA showed a maximal mass loss rate at 320 °C for the triol compared to 180 °C for DPG.
[35] The cryo trap stays cold for up to 3-4 h only. A refill at this stage would induce a change in the QCM that impinges further thickness indication.

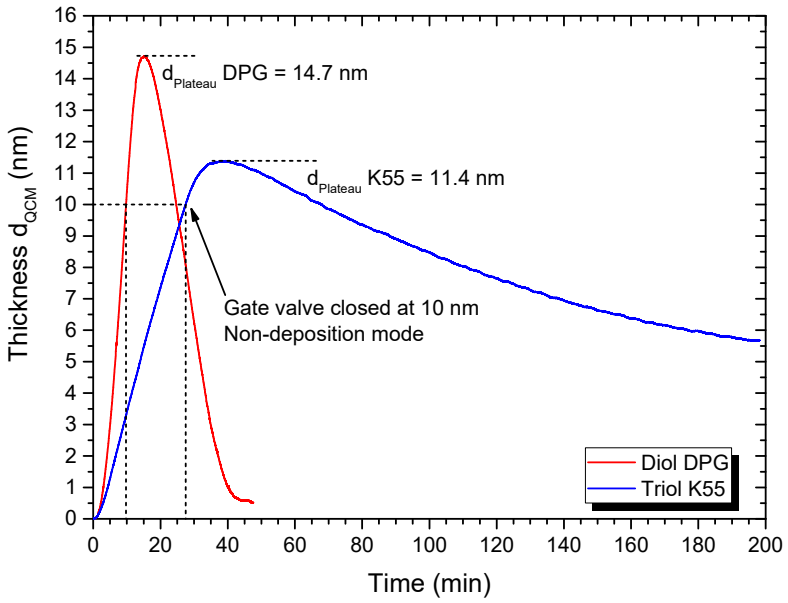

Fig. 6-12 Comparison of layer deposition of DPG (red) and triol (blue) for identical process parameters (2 l/min N_2, 500 mbar and 10 °C sample temperature). Evaporation cell is heated at 90 °C for DPG and 180 °C for the triol.

A change in the deposition parameters induces a modification of the behaviour. For a carrier gas flow rate of 5 l/min, triol adsorption is more non-linear and requires more time (115 min.) to reach 10 nm - Fig. 6-13.

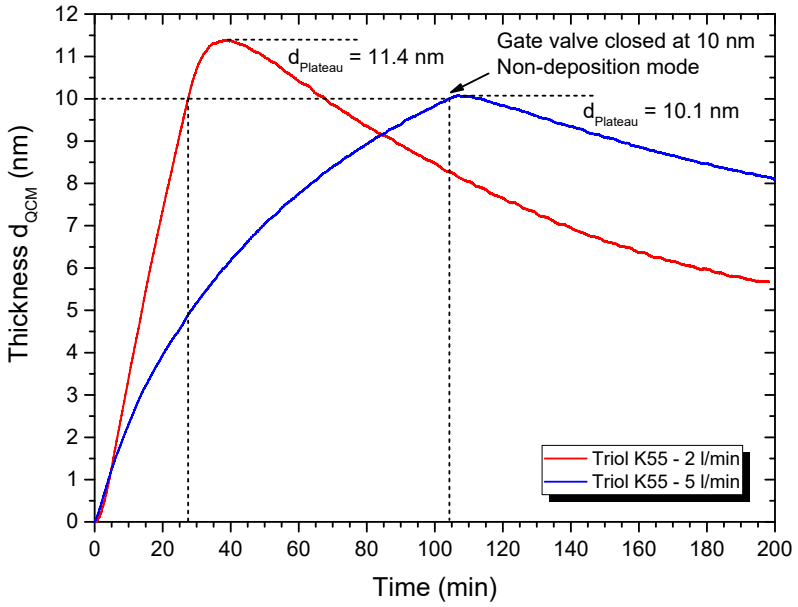

Fig. 6-13 Layer deposition of triol at 2 l/min (red) and 5 l/min (blue) N_2 carrier gas flow rates. Other process parameters are 500 mbar, 10 °C sample temperature and 180 °C evaporation cell temperature.

Interestingly, desorption is slower at a higher flow rate. It is likely, that only those triol molecules adsorb that are capable of undergoing slightly stronger interactions either with the metal oxide or with other triol molecules. Thus, desorption then requires also more time.

The thickness evolution of the multifunctional alcohol layers during and after the deposition process provides several conclusions. Both alcohols do not form stable layers. Most of the deposited molecules desorb quite rapidly from the gold surface of the QCM quartz.[36] For the considered times of adsorption, no plateau was obtained. Assuming the alcohol molecules are all oriented perpendicular to the surface, a monolayer only would be in the order of the length of the molecule, i.e. 0.9 nm for DPG and 1.9 nm for triol (cf. Section 5.3). Correspondingly, on Au after desorption, the residual layers are 0.6 nm (DPG) and 0.6 - 1.2 nm (triol) thick. At this stage it is not possible to state if this corresponds to some molecules that remain adsorbed, to some carbonaceous contaminations and/or a frequency shift over time. Analysis of the layers with IR will allow refining this observation.

Now that the adsorption and desorption behaviour of both alcohols has been studied the chemical properties of the short-living layers can be analysed by infrared spectroscopy. As the monomers desorb once the deposition is stopped, topographic features could not be studied for the alcohols.

[36] Adsorption affinity may be slightly different on aluminium or copper substrates.

6.4.2 DPG layers on native metals

Starting with the diol, the layers on Al and Cu are prepared with the MLD parameters pressure 500 mbar, 2 l/min N_2 carrier gas, 15 °C sample and quartz temperature and 80 °C evaporation cell temperature. Under these conditions switching into non-deposition mode at 8 nm results in layers with a maximum thickness of 22 nm. This higher thickness was chosen as DPG desorbs faster at room temperature during characterisation with IR spectroscopy. Once this maximum is reached the sample is rapidly transferred into the IR spectrometer. Sample spectra are recorded every minute. The results are shown in Fig. 6-14 for Al and in Fig. 6-15 for Cu.

Right after deposition on Al the DPG spectrum (black line) shows strong bands that correspond well to the bulk state at first glance. A few significant differences are present, however. First the strong OH stretch in the layer at 3345 cm^{-1} is broader and skewed to lower wavenumbers as compared to the bulk (3384 cm^{-1}). This indicates stronger association of the DPG hydroxyl groups e.g. in hydrogen bonds. The confinement in the thin layer at the metal surface can enhance this behaviour. The various CH stretches (3000 – 2800 cm^{-1}) and deformations (1500 – 1200 cm^{-1}) are identical to the bulk in shape and intensity ratio as they are not prone to interactions with the substrate. The ether bands (1200 – 1000 cm^{-1}) have the same shape as in the bulk but the intensity ratio of the ν-CO (1151 cm^{-1}) and ν_a-COC (1099 cm^{-1}) is opposite in the layer. As ether groups can also undergo some interactions via their oxygen atom, this changed intensity ratio indicates a modified chemical environment for the ether groups in the layer. The interactions are weak as the position of all ether bands does not change. Shape and intensity of the various bands below 1000 cm^{-1} correspond to the bulk. It is also noted that the baseline is tilted downwards at higher wavenumbers. This indicates an uneven distribution of the deposit. Actually, a sort of fogged substrate surface (mainly visible on darker substrates of Cu or Au) is observed upon sample removal from the MLD reactor. This may be due to some condensation or partial dewetting of the DPG on the surface. Refraction of IR light at these structures results in baseline bending.

During the next few minutes the intensity of all bands as well as the baseline tilt drop dramatically as DPG desorbs rapidly from the Al surface. After 5 min. all bands have vanished and the spectrum does not change anymore over time. Each spectrum still shows the same bands and intensity ratios as in the initial spectrum. Only the OH and ether bands indicate some different interactions compared to the bulk. This also explains the rapid desorption of the alcohol from the surface.

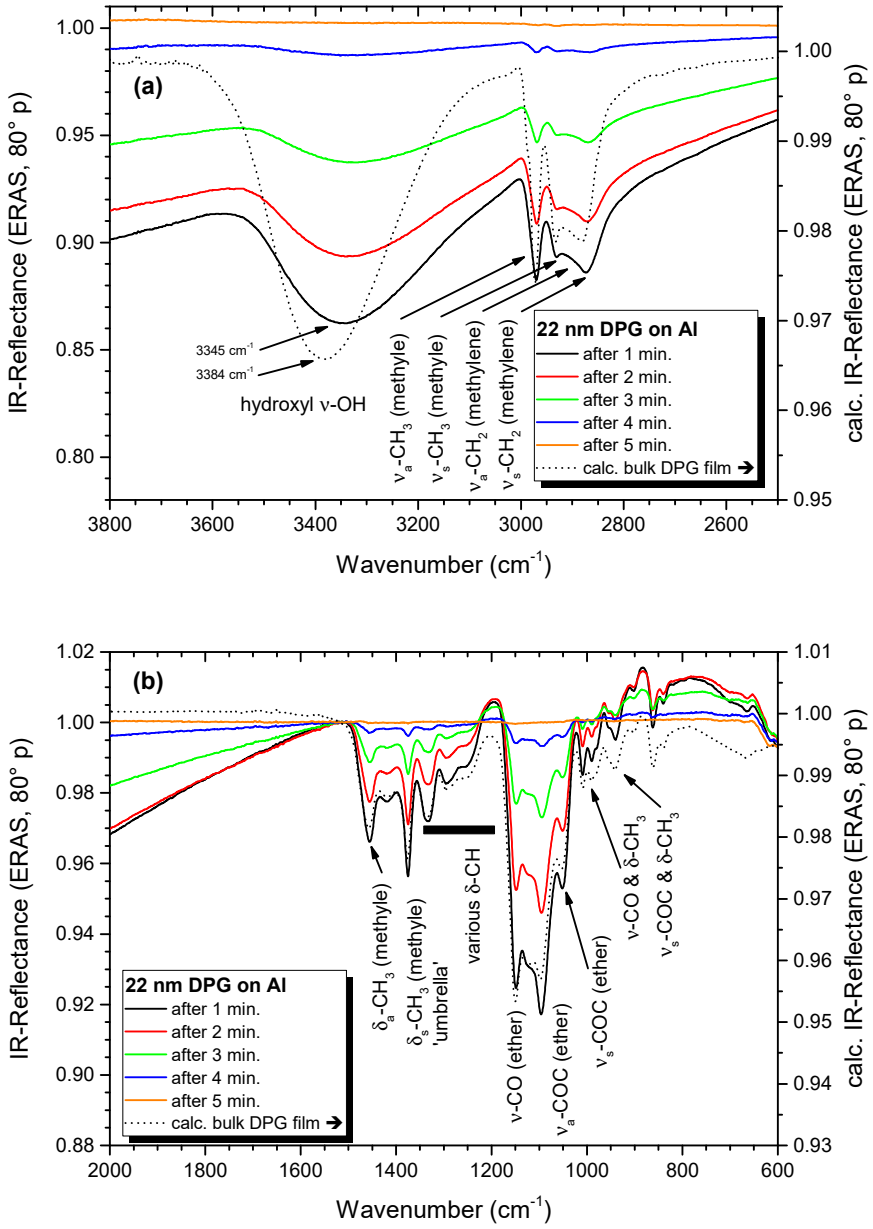

Fig. 6-14 IR-ERA spectra of a 22 nm thin DPG layer on Al during the first 5 minutes of storage in dried air at RT. (a) 3800 – 2500 cm^{-1}, (b) 2000 – 600 cm^{-1}. The dashed spectrum presents a calculated bulk-like ERA spectrum for qualitative comparison. Deposition parameters: 500 mbar, 2 l/min N_2, 15 °C substrate temperature.

On Cu (Fig. 6-15) the same behaviour is observed as on Al. One notable difference is present, however. The OH band is less broadened than on Al. Here the peak is shifted to 3367 cm^{-1} (3345 cm^{-1} on Al) probably due to different interactions. 5 minutes after transfer into the IR spectrometer, all bands also disappeared.

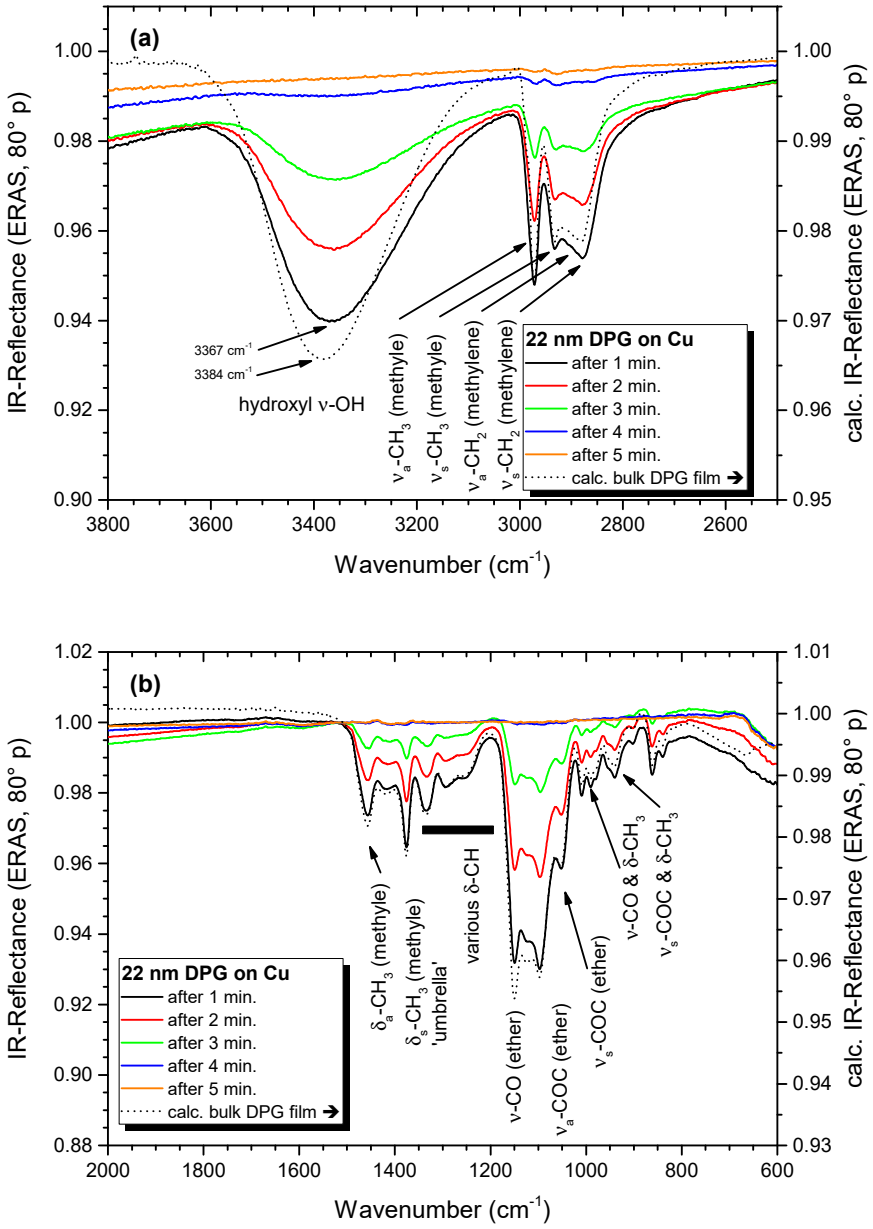

Fig. 6-15 IR-ERA spectra of a 22 nm thin DPG layer on Cu during the first 5 minutes of storage in dried air at RT. (a) 3800 – 2500 cm^{-1}, (b) 2000 – 600 cm^{-1}. The dashed spectrum presents a calculated bulk-like ERA spectrum for qualitative comparison. Deposition parameters: 500 mbar, 2 l/min N_2, 15 °C substrate temperature.

Magnification of the spectra after 5 min. (Fig. 6-16) shows that a few bands are still present on both metals. They include mainly CH stretches (3000 – 2800 cm^{-1}), and bands in the regions 1700 – 1500 cm^{-1}, 1500 – 1350 cm^{-1} as well as 1200 – 1000 cm^{-1}. The CH stretch region is very similar on both metals except a small difference in relative intensity at 2850 cm^{-1}. Below 1800 cm^{-1} bands are specific for the substrate. On Al (black line) a small buckle at 1700 – 1600 cm^{-1} indicates carbonyl groups. The bands at 1500 – 1350 cm^{-1} and 1200 – 1000 cm^{-1} are comparable to DPG bands. Thus, very few DPG molecules seem to remain adsorbed on that metal.

However, the contamination spectrum on the bare substrates (green line) contains a weak carbonyl band and CH stretches as well. Of course, re-adsorption of carbonaceous contaminations from the ambient after DPG deposition is quite natural. Intensity of all bands is below 1 ‰ and ongoing storage does not change the spectra anymore. Hence, most likely contaminants and residual DPG molecules are present on the Al surface after desorption.

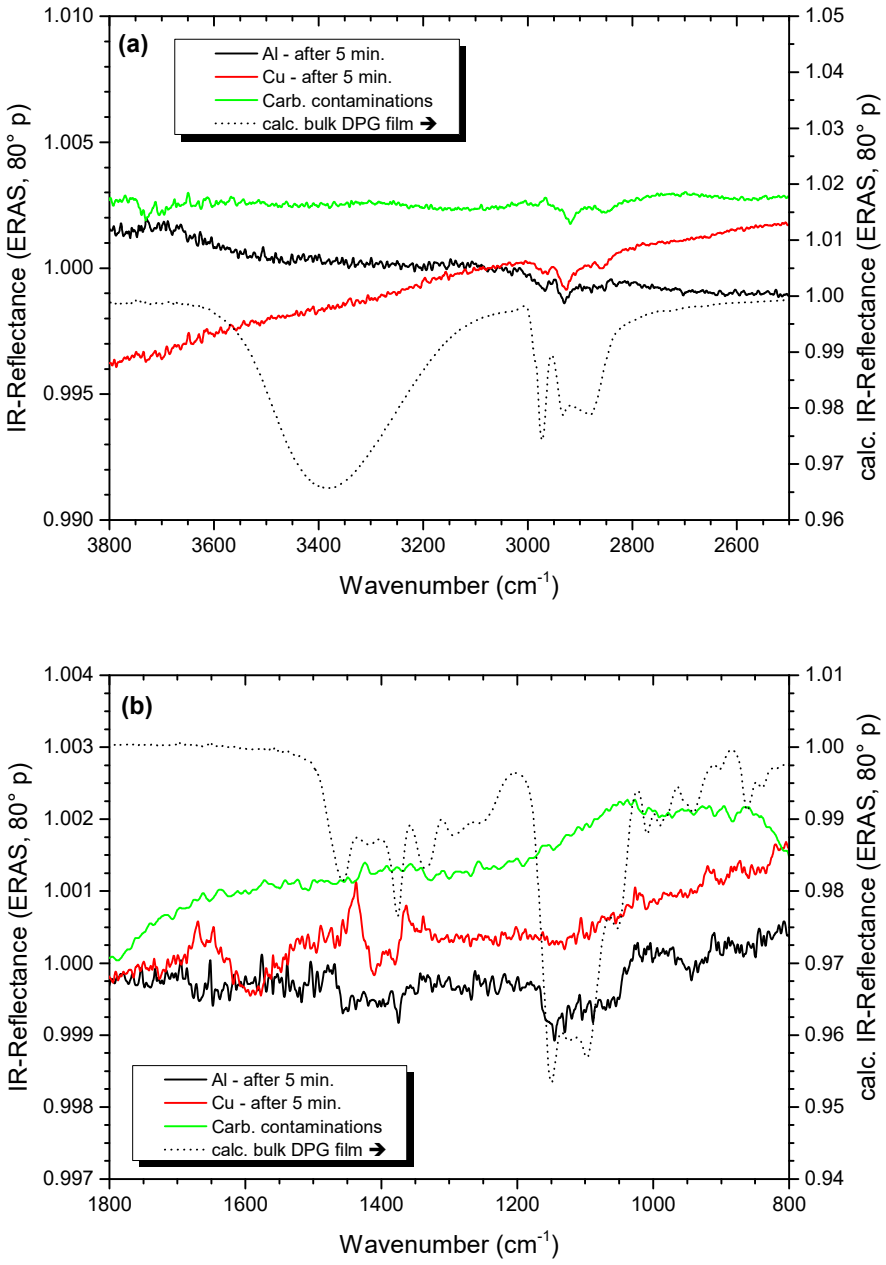

Fig. 6-16 Comparison of IR-ERA spectra of an initially 22 nm thin DPG layer on Al (black line) and Cu (red line) after 5 minutes of storage in dried air at RT. (a) 3800 – 2500 cm^{-1}, (b) 1800 – 800 cm^{-1}. The dashed spectrum presents a calculated bulk-like ERA spectrum and the green line a spectrum of carbonaceous contaminations on Al for qualitative comparison.

On Cu, the bands present in the fingerprint region are much different compared to DPG bands. The bands at 1600 cm^{-1} as well as between 1450 and 1350 cm^{-1} have also been observed in contamination spectra (cf. section 6.2.3). The lack of bands in the ether region indicates that most likely no DPG remains on Cu.

In conclusion, all the interactions of DPG with the native oxide layers of Al and Cu are very weak and most likely of physical nature.

As one aim of the MLD consists in preparing monolayer like deposits, thinner layers of DPG were also prepared. Using the same deposition parameters as for the previous layers, deposition was stopped at 3 nm and layers of 12 nm were obtained. Their IR spectra are compared with those of the 22 nm layers (Fig. 6-17 and Fig. 6-18, note the different scales). As expected, right after deposition all bands are much weaker for the thinner layer but shape and intensity ratios are nearly identical. Only the intensity ratio of the ether bands is slightly different: For the 12 nm layer, ν_a-COC is stronger than ν-CO.

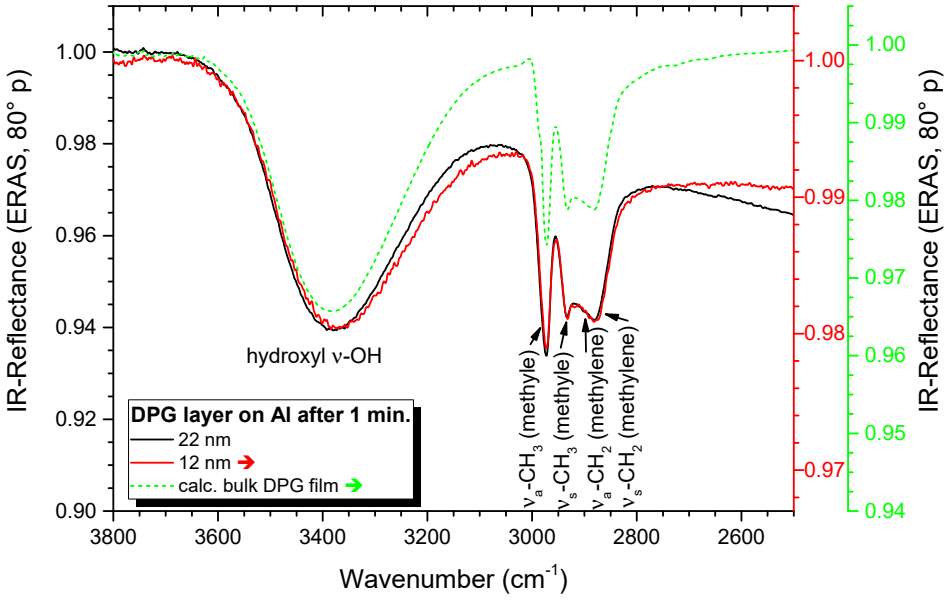

Fig. 6-17 Comparison of IR-ERA spectra of 22 nm (black) and 12 nm (red) DPG layers on Al after deposition. The spectrum of each layer is scaled differently. The dashed spectrum represents a calculated bulk-like ERA spectrum of DPG for comparison.

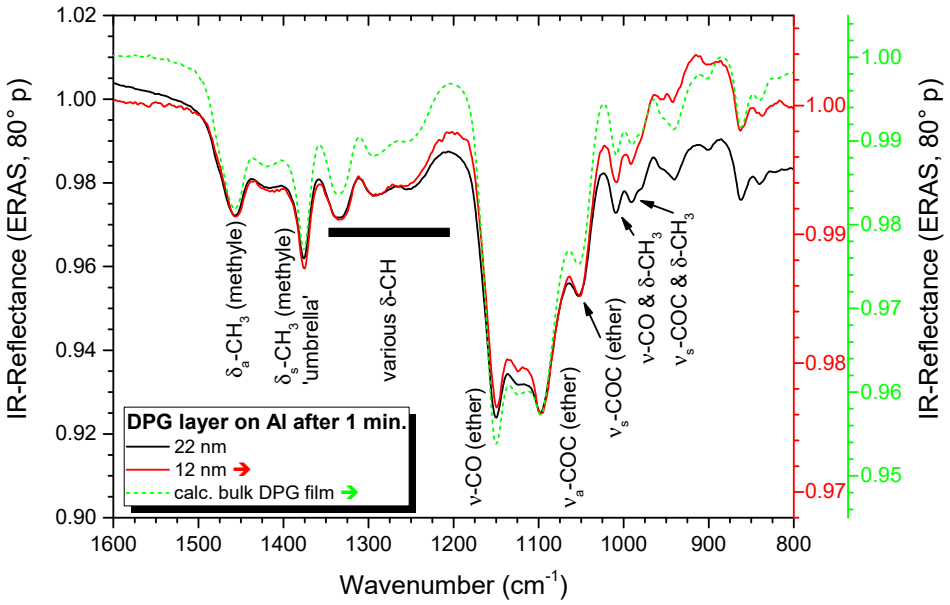

Fig. 6-18 Comparison of IR-ERA spectra of 22 nm (black) and 12 nm (red) DPG layers on Al after deposition. The spectrum of each layer is scaled differently. The dashed spectrum represents a calculated bulk-like ERA spectrum of DPG for comparison.

Desorption from the thin DPG layer proceeds in a similar way as for the 22 nm layer but is completed within 3 min. Comparison of IR spectra after complete desorption exhibit the same features (Fig. 6-19 and Fig. 6-20). Band shape and intensity are identical, different scaling is not necessary. The small differences in the fingerprint region are not significant. Hence both residual layers exhibit exactly the same state.

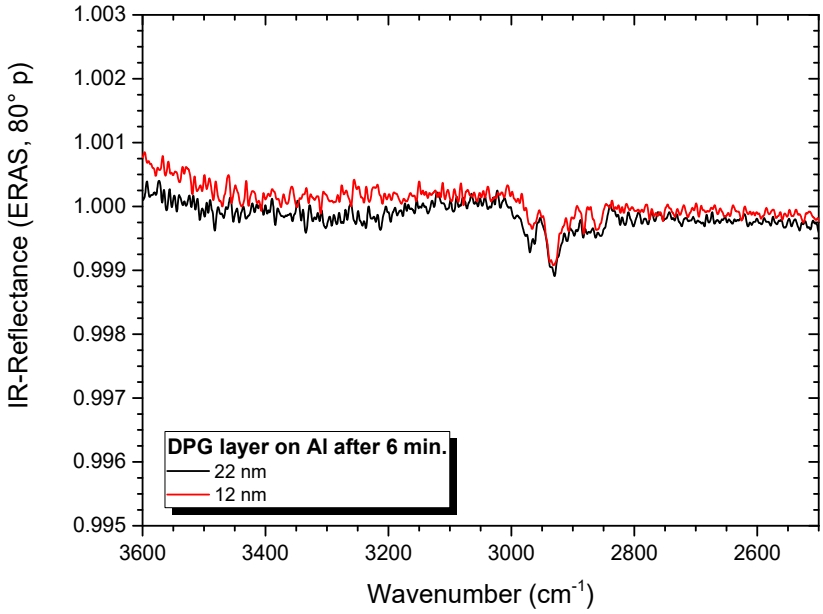

Fig. 6-19 Comparison of IR-ERA spectra of 22 nm (black) and 12 nm (red) DPG layers on Al after complete desorption.

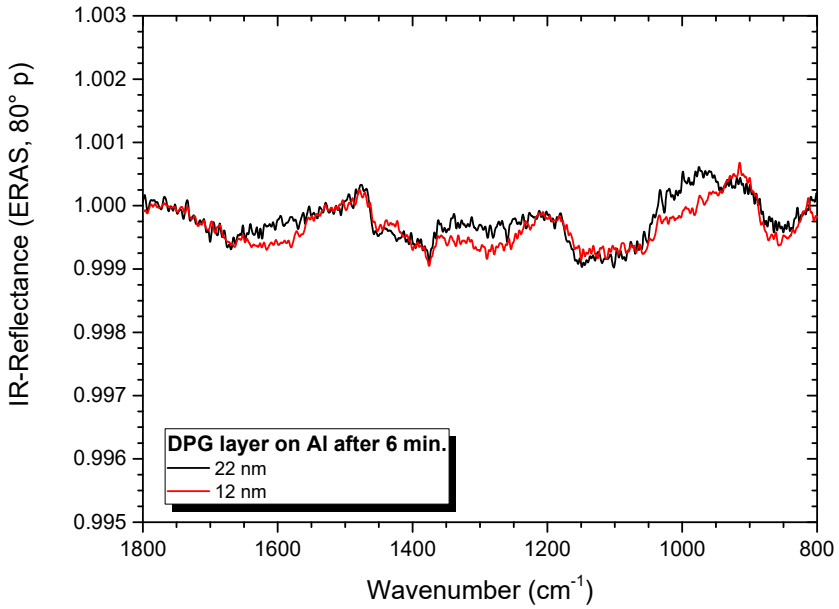

Fig. 6-20 Comparison of IR-ERA spectra of 22 nm (black) and 12 nm (red) DPG layers on Al after complete desorption.

12 nm DPG are also deposited on Cu. The spectral features after deposition (cf. Fig. 11-6) as well as after complete desorption (cf. Fig. 11-7) are identical with the spectra of the corresponding 22 nm layers.

Hence, the thickness of the deposited DPG does not modify the weak interactions with both substrates. Carbonaceous contaminations are identified on both metals after desorption. Thus, contaminations that re-adsorbed after the initial THF rinse and/or during layer deposition are not displaced by the alcohol deposition. All in all, the contaminations present a higher affinity for the substrates than the diol as they remain unhampered by the alcohol deposition. Though the spectra do not provide direct proof one may suspect that the DPG does not penetrate through the contamination layer but adsorbs on top of it. The spectra also do not indicate any chemical modification of the substrates themselves due to the alcohol adsorption.

Facing the very fast desorption SFM measurements of the topography of these deposits are impossible.

6.4.3 Triol layers on native metals

The triol K55 (evaporation cell heated at 180 °C) is deposited from a 2 l/min nitrogen gas flow onto the metal-PVD substrates at 10 °C. As desorption is much slower than for DPG thinner layers are prepared. Deposition is thus stopped at 10 nm and a final thickness of $d_{QCM} \approx 12$ nm is reached under these conditions. The evolution of the triol layers on Al is shown in Fig. 6-21 and following figures.

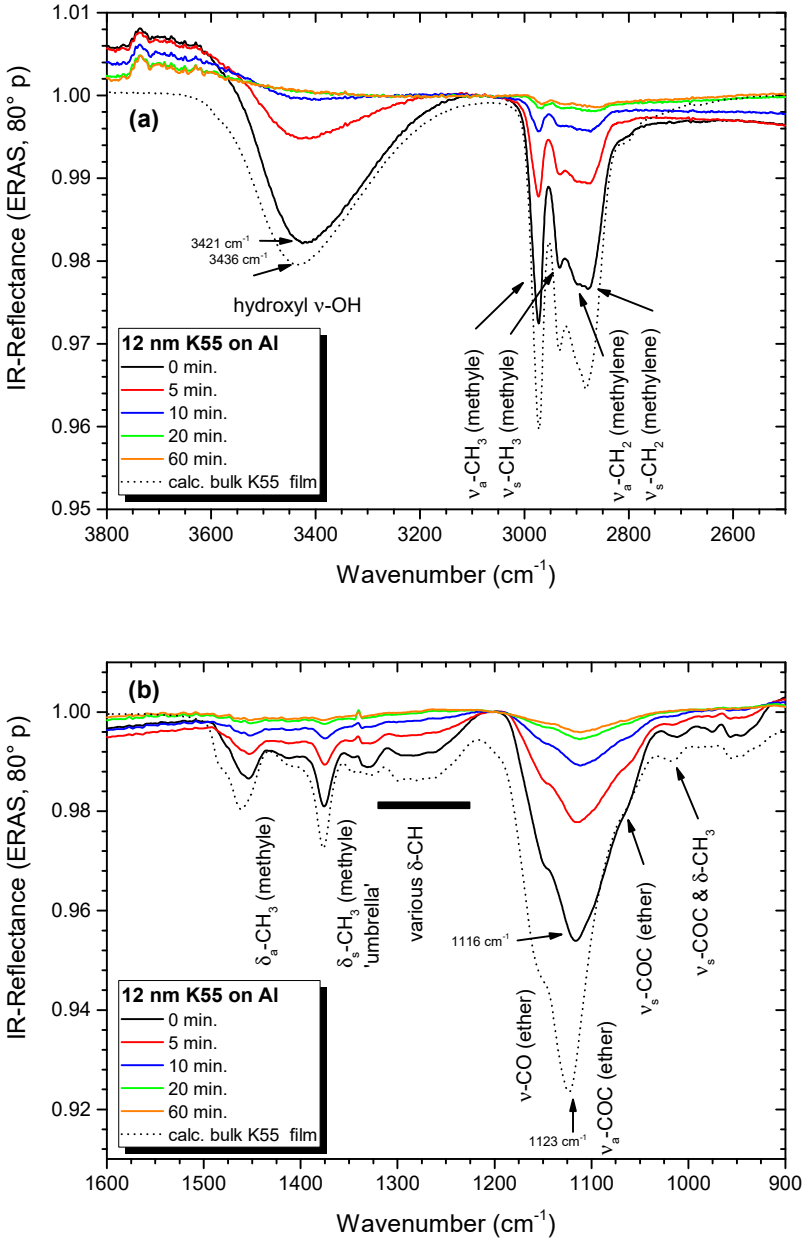

Fig. 6-21 IR-ERA spectra evolution of a 12 nm thin triol layer on Al during the first hour of storage in dried air at RT. (a) 3800 – 2500 cm^{-1}, (b) 1600 – 900 cm^{-1}. The dashed spectrum presents a calculated bulk-like ERA spectrum for qualitative comparison. Deposition parameters: 500 mbar, 2 l/min, 10 °C substrate temperature.

As for DPG, the triol layer on Al shows bulk features after deposition (black line) but with a few differences. The OH stretch (3421 cm^{-1}) is shifted to lower wavenumbers compared to bulk (3436 cm^{-1}). The band shift is however less pronounced than for DPG. The CH_2 stretches present another band shape and intensity ratio as the symmetric stretch at 2875 cm^{-1} is less pronounced in the deposit. Band shape of CH deformations (1325 – 1225 cm^{-1}) is also slightly different from the bulk.

The ether bands (1200 – 1000 cm^{-1}) exhibit the same spectral features as in bulk but the ν_a-COC (1116 cm^{-1}) is shifted to lower wavenumbers (1123 cm^{-1} in bulk). Hence these groups are also prone to undergo some interactions with the aluminium oxide.

Over the first hour of storage intensity of all bands continuously drops as most of the triol desorbed. Desorption is much slower than for DPG. The spectral features do not change over time. Some weak bands remain in the CH (3000 – 2800 cm^{-1}) and ether (1200 – 1000 cm^{-1}) regions as well as the CH_3 'umbrella'-deformation at 1376 cm^{-1}. Slow desorption continues for up to 5 hours (Fig. 6-22 & Fig. 6-23) before constant weak bands remain during further storage. Despite CH stretches and bands between 1600 and 1300 cm^{-1} are also found for re-adsorbed contaminations the large ether band (1110 cm^{-1}) proves that few triol molecules remain on the Al surface. The weak buckle between 1000 and 900 cm^{-1} is assigned to lattice vibrations of the Al oxide that has grown during storage in dried air. But this is not specific to the adsorption of triol.

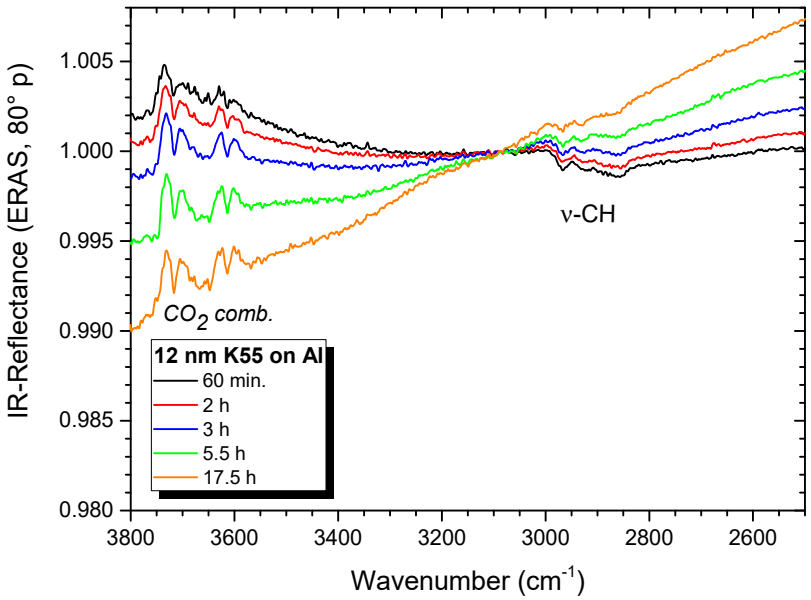

Fig. 6-22 IR-ERA spectra of a triol layer (12 nm initial thickness) on Al during 18 h of storage in dried air at RT. 3800 – 2500 cm^{-1}. Deposition parameters: 500 mbar, 2 l/min, 10 °C substrate temperature.

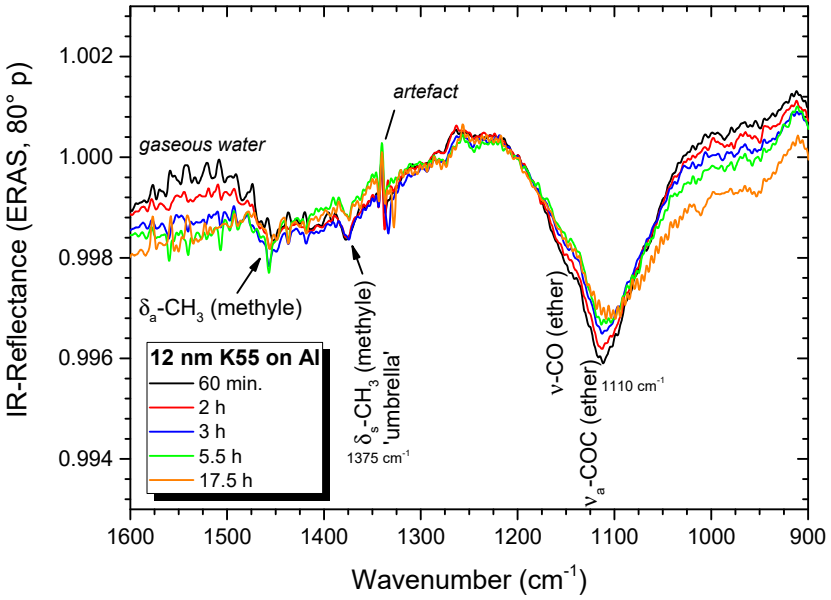

Fig. 6-23 IR-ERA spectra of a triol layer (12 nm initial thickness)on Al during 18 h of storage in dried air at RT. 1600 – 900 cm^{-1}. Deposition parameters: 500 mbar, 2 l/min, 10 °C substrate temperature.

The adsorption strength of the remaining triol molecules is evaluated by two subsequent rinses with THF (c.f. Fig. 6-24). Some weak C-H stretching vibrations remain in the region of 3800 – 2500 cm^{-1} and do not show any change after the 1st rinse. The bands do not originate from the triol but from carbonaceous contaminations adsorbed from the atmosphere during the deposition and right after each THF rinse. The weak CH_3 umbrella mode (1375 cm^{-1}) and the ether vibration (1110 cm^{-1}) from the triol vanished after the 1st rinse as well. Thus, the few remaining triol molecules were washed off the surface as they undergo only weak physical interactions. The 2nd THF rinse does not change the spectrum at all. Removal of the remaining triol molecules during the THF rinses does not affect the Al oxide.

On Cu, the triol layers behave the same way as on Al. Hence, all previously made observations and conclusions are also valid for that metal. The corresponding spectra are shown in Appendix 11.5.2.

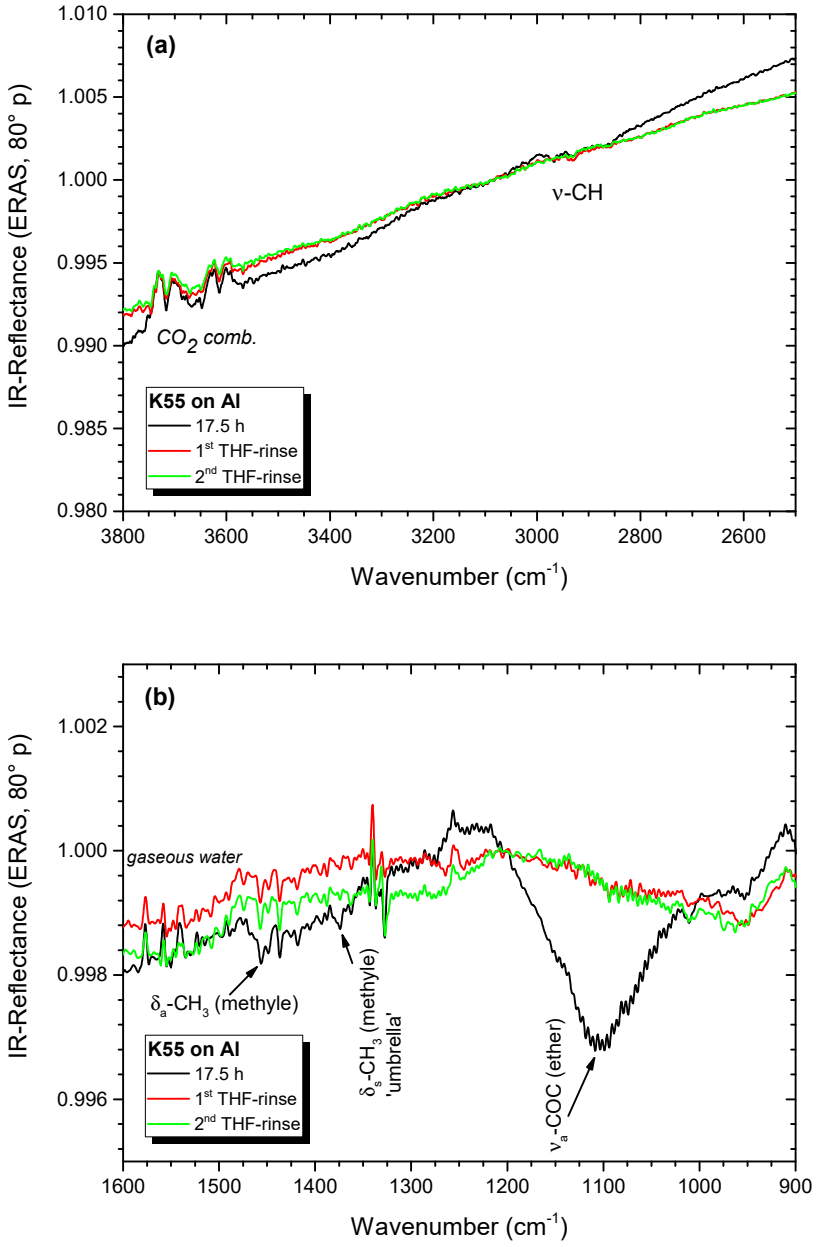

Fig. 6-24 IR-ERA spectra of a 12 nm thin triol layer on Al after 18 h of storage in dried air at RT (black line) and after two subsequent THF rinses (red, green). (a) 3800 – 2500 cm^{-1}, (b) 1600 – 900 cm^{-1}.

6.4.4 Intermediate conclusion

The deposition behaviour of the utilised diol and triol can be schematically summarised in Fig. 6-25 and Fig. 6-26. First, both alcohols adsorb easily onto the native Al and Cu substrates. Layer thickness continues to grow until the deposition is stopped (Fig. 6-25b). Hence, intermolecular forces between the monomers allow for further adsorption on top of the first monolayer – deposition is not self-limited to the first monolayer.

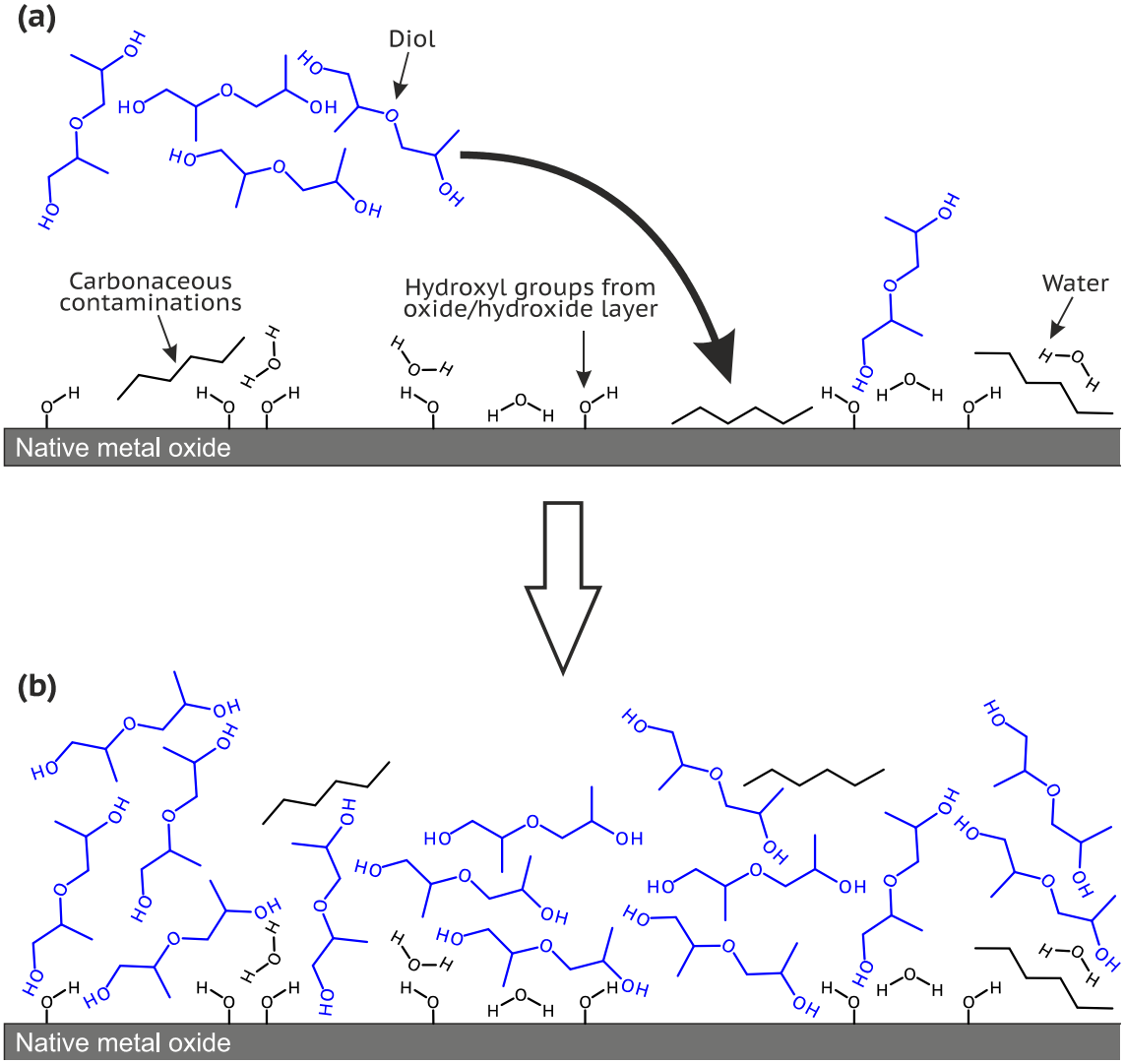

Fig. 6-25 Schematic representation of the formation of alcohol deposits. DPG is shown here but the scheme is also valid for the triol layers. (a) Deposition step inside the MLD onto the virgin native metal substrate. (b) Achieved multiol layer after deposition was stopped.

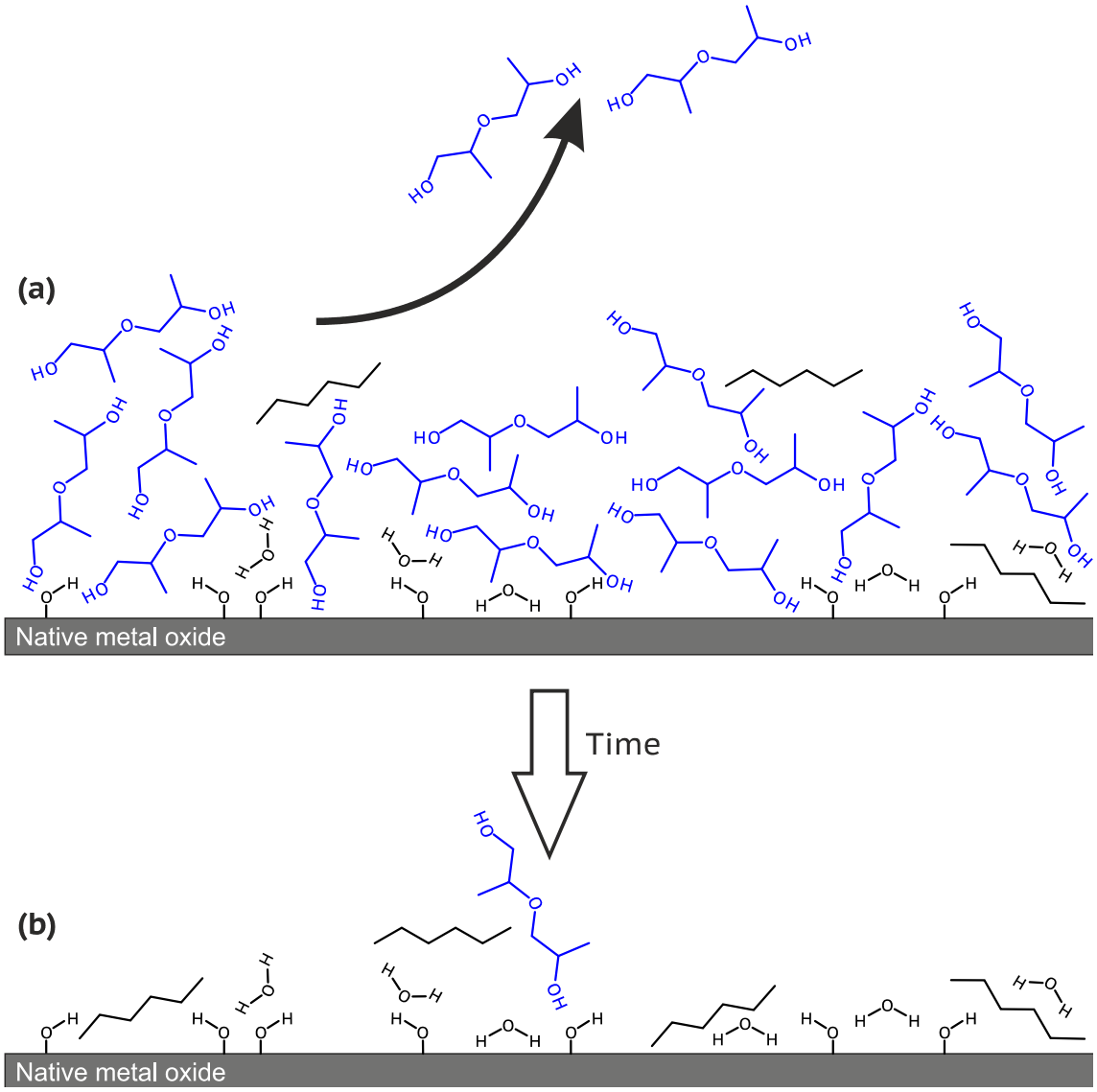

Fig. 6-26 Schematic representation of the behaviour of alcohol deposits after layer deposition. (a) Desorption of the alcohol once deposition is terminated. (b) Almost complete desorption is achieved over time.

Second, once deposition is stopped diol and triol massively desorb from Al and Cu (Fig. 6-26a). Desorption of the diol is fastest. Higher substrate temperature increases desorption rate as intermolecular forces and monomer-substrate interactions are more easily overcome. While DPG completely desorbs at room temperature a few molecules of triol remain. However none of these alcohols is capable to establish strong interactions with the metals (Fig. 6-26b) - remaining molecules are completely removed by a single THF rinse. The alcohols do not link chemically to the oxidised metal substrates but only form *weak physical interactions* which are slightly stronger for the triol. Monomer adsorption itself does not significantly modify the substrates. Hence, this behaviour already shows that some principles of the MLD as described in literature (cf. Chapter 4.1) do not work with our monomers.

Higher substrate temperatures lead to less adsorption as intermolecular physical interactions and physical interactions with the substrate become less effective.

Third, carbonaceous contaminations are still present on the substrates after layer deposition - they are visible upon monomer desorption. Thus, their adsorption is not avoided by the alcohols. Furthermore, the question remains open if the alcohols are even capable to break through the initial contamination layer in order to adsorb onto the amorphous oxides or if they rather adsorb on top of that contamination. The contamination could also mix with the alcohol deposit. IR spectroscopy is not able to distinguish between these cases, however.

In the next section the behaviour of the isocyanate is studied by the same methodology.

6.5 Thin layers of 4,4'-methylene diphenyl diisocyanate

In this section thin isocyanate layers are deposited on native surfaces of Al and Cu. They are then characterised using IR spectroscopy and scanning force microscopy.

6.5.1 Adsorption behaviour

Process parameter optimisation revealed that evaporation cell temperatures of at least 165 °C are required for the deposition of 4,4'-MDI. Adequate deposition rates were found at 180 °C with N_2 carrier gas flow rates of 2 and 5 l/min. The MLD behaviour at two substrate temperatures, T_{sample}, is presented in Fig. 6-27. At t = 0 min the gate valves at the evaporation cell are placed into deposition mode. The MDI requires about 1 min. to pass through the pipes and to reach the reactor chamber and to start to adsorb onto the substrate and QCM quartz. A stationary deposition rate is reached after 5 min.

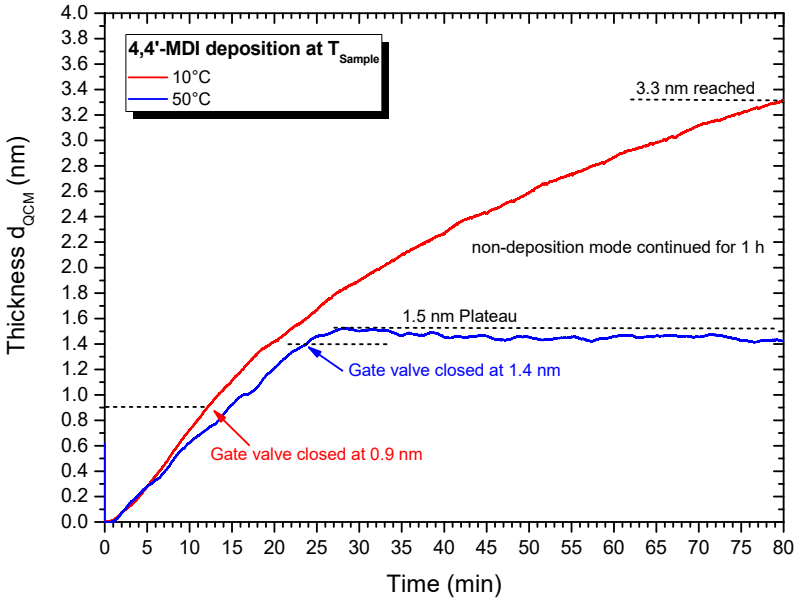

Fig. 6-27 QCM thickness evolution during deposition of 4,4'-MDI for two substrate temperatures. Gate valve of the evaporation cell is opened at 0 min and closed after reaching 0.9 nm (10 °C - red) and 1.4 nm (50 °C - blue), respectively. Deposition is carried out at 5 l/min N_2, 500 mbar and 180 °C evaporation cell temperature.

For T_{sample} = 10 °C (red line) deposition is switched off when 0.9 nm are reached on the QCM. The MDI which is still present in the pipes of the MLD, continues to absorb. 1.4 nm are reached before the deposition rate starts to slow down progressively. During the next hour, further MDI adsorbs and the layer grows to 3.3 nm. As for the alcohols, MDI does not form a monolayer. Layer growth continues as long as monomers are present in the gas stream.

Contrary to the alcohols, no desorption is observed. Thus, intermolecular interactions between MDI molecules must be significantly stronger. Actually, the highly polar NCO group is prone to undergo electron donation from the lone electron pairs of the electronegative oxygen or nitrogen to the electronically depleted carbon - Fig. 6-28.

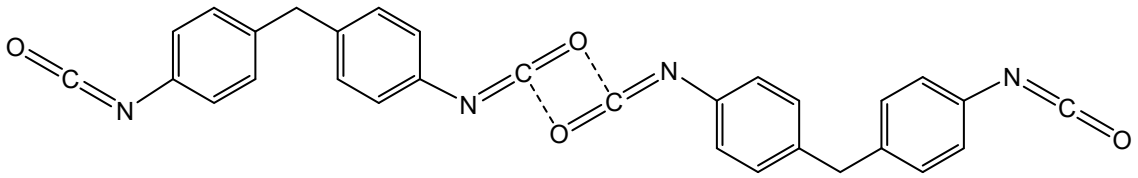

Fig. 6-28 Specific intermolecular interactions between two adjacent isocyanate groups [110].

This particular MDI arrangement is energetically favourable. It is observed in solid MDI crystals[37] but also required for the formation of uretdione by-products [110] (cf. Section 5.2.1).

Increasing T_{sample} to 50 °C during deposition (Fig. 6-27 blue line) affects the adsorption behaviour of this monomer. As long as the gate valve is set on deposition mode adsorption proceeds as for T_{sample} = 10 °C[38].

In the non-deposition mode, adsorption rapidly ceases at 50 °C, however, and a plateau at ca. 1.5 nm is reached. For the next hour in stationary gas flow conditions layer thickness is maintained[39]. Hence, the intermolecular interactions within the MDI layer are strong enough to withstand that increased temperature as again no desorption takes place. Furthermore, MDI monolayers are not achieved even at this temperature. Most likely much higher substrate temperatures are needed to overcome intermolecular interactions. A further temperature increase may induce other undesirable effects, however. First, the native oxide layer may be altered leading to modified substrate – monomer interactions. The effect of temperature on the layer chemistry will be discussed in section 6.5.3. Second, thickness monitoring would also get increasingly less reliable due to much stronger quartz frequency fluctuations (cf. chapter 4.3.2).

Now that the adsorption response on different temperatures has been illustrated the effect of the native metal oxide on the layer chemistry is analysed in the following section.

[37] This is also the reason for the good thermal and moisture stability of solid 4,4'-MDI at low storage temperatures.
[38] The slight difference in deposition rate between both temperatures can be neglected as it is within experimental fluctuation (cf. Fig. 6-8).
[39] The slight decrease in this example originates from a slow change in pressure and the thickness fluctuations due to temperature are now visible as the quartz is more sensitive at higher temperatures.

6.5.2 Effect of the metal substrate

Now 4,4'-MDI is deposited at 30 °C substrate temperature (2 l/min N_2, 500 mbar). Deposition is stopped at 5 nm nominal layer thickness. Then samples are rapidly transferred into the IR spectrometer and layer chemistry is monitored for up to 68 h.

◊ *Behaviour on Aluminium*

The evolution of the IR spectra on the native aluminium oxide is shown in Fig. 6-29. Right after deposition (black line) the characteristic bands (marked in black) of 4,4'-MDI dominate. Position and shape of these bands are close to the calculated bulk spectrum. The asymmetric isocyanate stretch, ν_a-NCO is slightly shifted towards higher wavenumbers (2292 cm^{-1} vs. 2283 cm^{-1} in the bulk). Additionally, a shoulder appears at 2298 cm^{-1} after 10 h of storage. In [9, 10] the spectra of solvent deposited MDI also exhibit a NCO doublet with a sharp peak at higher wavenumbers, the band shift for the MLD layer can be attributed to a few MDI molecules in some well-ordered state (cf. Section 6.1.2).

The isocyanate band drops in intensity over time and the ratio of disordered and well-ordered MDI molecules obviously change, which leads to this shoulder formation as more disordered MDI is consumed. The effect is however much less dominant as in the thicker layers adsorbed from solution [10, 33].

The ν-CH region indicates the characteristic ν-CH bands for MDI as well as carbonaceous contaminations that adsorbed during deposition. The bands in this region slightly grow over storage time as further contaminations adsorb.

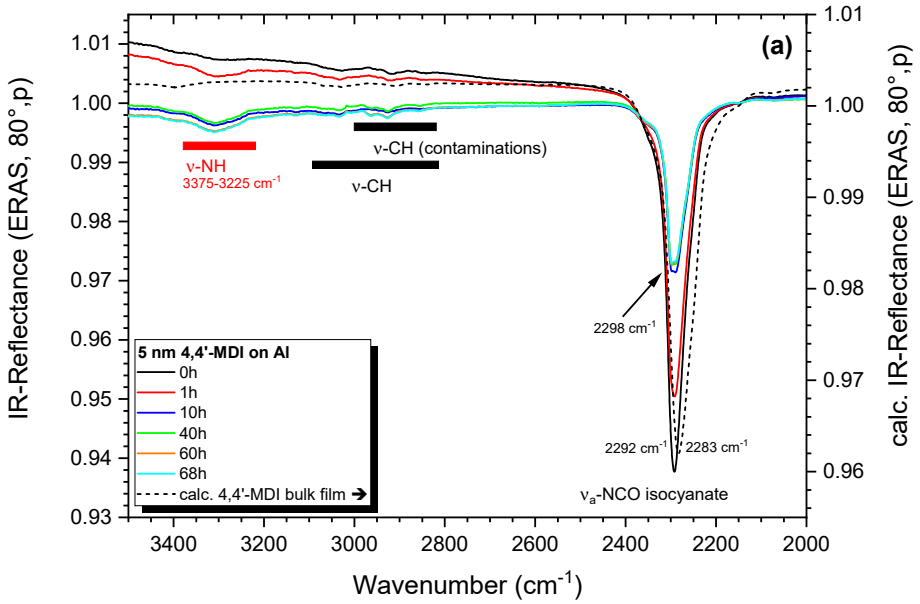

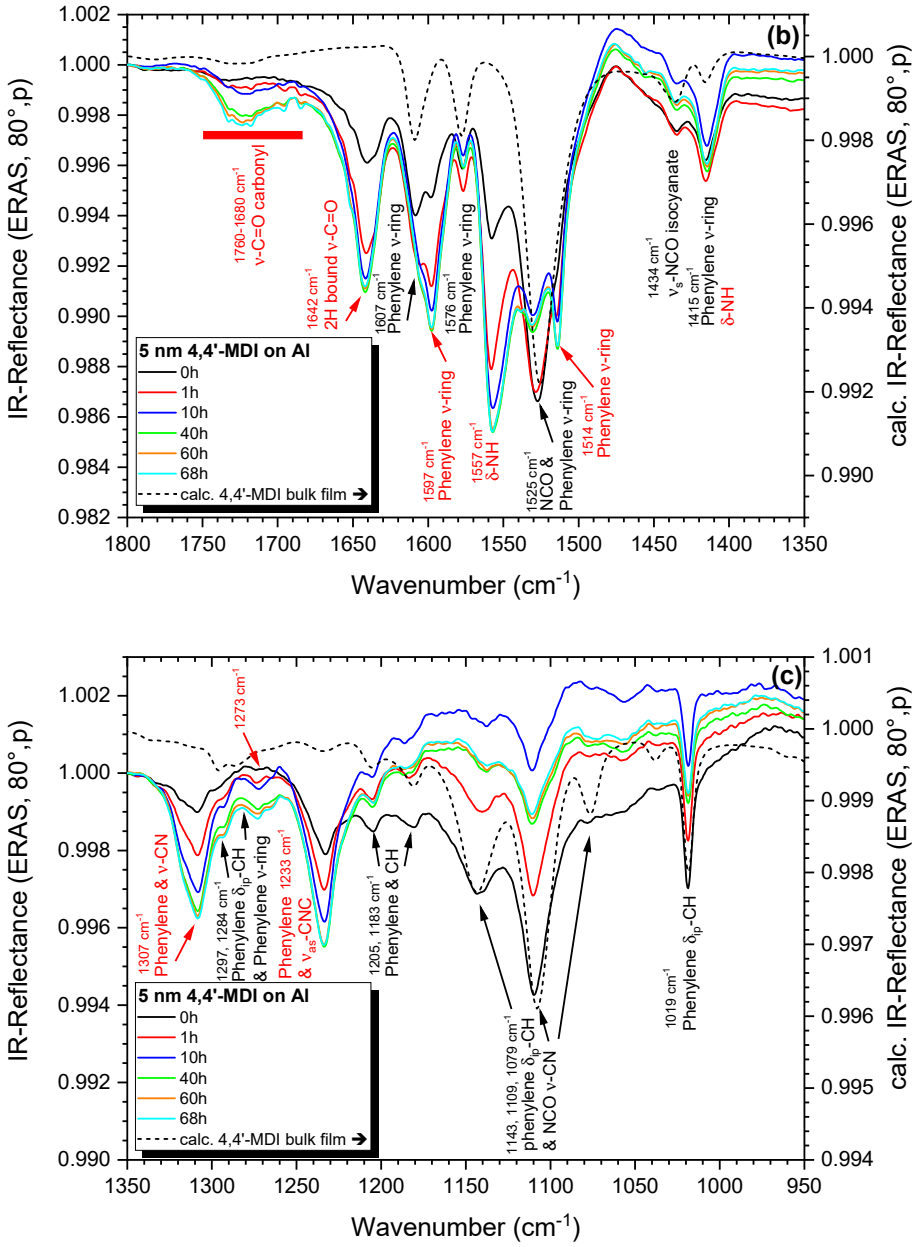

Fig. 6-29 IR-ERA spectra of a 5 nm 4,4'-MDI layer on native Al oxide during 68 h of storage in dried air at RT. Deposition parameters: 500 mbar, 2 l/min, 30 °C substrate temperature. Band assignment for 4,4'-MDI (black) and new species (red). The dashed line represents a calculated bulk-like ERA spectrum for qualitative comparison. (a) 3500 – 2000 cm^{-1}, (b) 1800 – 1350 cm^{-1}, (c) 1350 – 950 cm^{-1}.

Besides the MDI bands, new bands (marked in red in the previous spectra) are present right after deposition. During storage in dried air, characteristic MDI bands drop in intensity while the new bands grow. These new bands form mainly during the first 60 min. after deposition. A slow increase follows until 40 h of storage. Then, no further evolution of the bands is detected up to 68 h.

Hence, new chemical species are formed upon deposition of the isocyanate on native Al oxide. The growing bands (3300, 1725, 1642, 1597, 1557, 1514, 1415, 1307, 1273 and 1233 cm^{-1}) can be attributed to two functional groups. At first glance, they could indicate *urea* functionalities from the reaction of isocyanate with physically adsorbed water. As shown in 5.2.1 - Fig. 5-11 the urea formation requires two reaction steps. This implies that the formed amines and/or the MDI molecules possess enough translational and rotational mobility to react and hence there is no reason to assume that the amine groups react quantitatively with MDI to urea. Actually, this view is supported by the broad ν-NH band (3300 cm^{-1}) that could well accommodate contributions from amine and urea - Fig. 7-30.
On the other hand, MDI can form urethane-like adhesion bonds (cf. Section 6.1.2 and [8, 10]) as the result of a reaction of isocyanate with a hydroxyl group of the amorphous oxide layer. That also goes with the formation of NH-groups and the corresponding IR band at 3300 cm^{-1}.
However, urea species are hard to distinguish from urethane species in the IR spectra as they form similar bands. Therefore, it is not possible to decide at this point whether these bands result from urea groups or from urethane-like adhesion bonds.

◊ *Comparison with layers on Copper*

On copper, 4,4'-MDI layer shows the same behaviour. The corresponding spectra are shown in Appendix 11.5.3, Fig. 11-11 to Fig. 11-13. Comparison of both layers at different storage times reveals some interesting differences.

Starting with the layers right after deposition (Fig. 6-30) isocyanate bands are stronger on the copper substrate. Hence, more MDI adsorbed onto that native metal oxide despite of the same thickness of 5 nm on the gold-plated quartz crystal. Hence the isocyanate possesses a slightly different affinity to the two substrates. Second, intensity of the new bands is also stronger on Cu oxide. Thus more of these species have been formed during deposition, and the reaction rate is specific for the metal oxide. Moreover, a new band (1361 cm^{-1}) arises on Cu but is missing on Al (Fig. 6-30b). This is a first indication for the formation of metal-specific species or interactions.

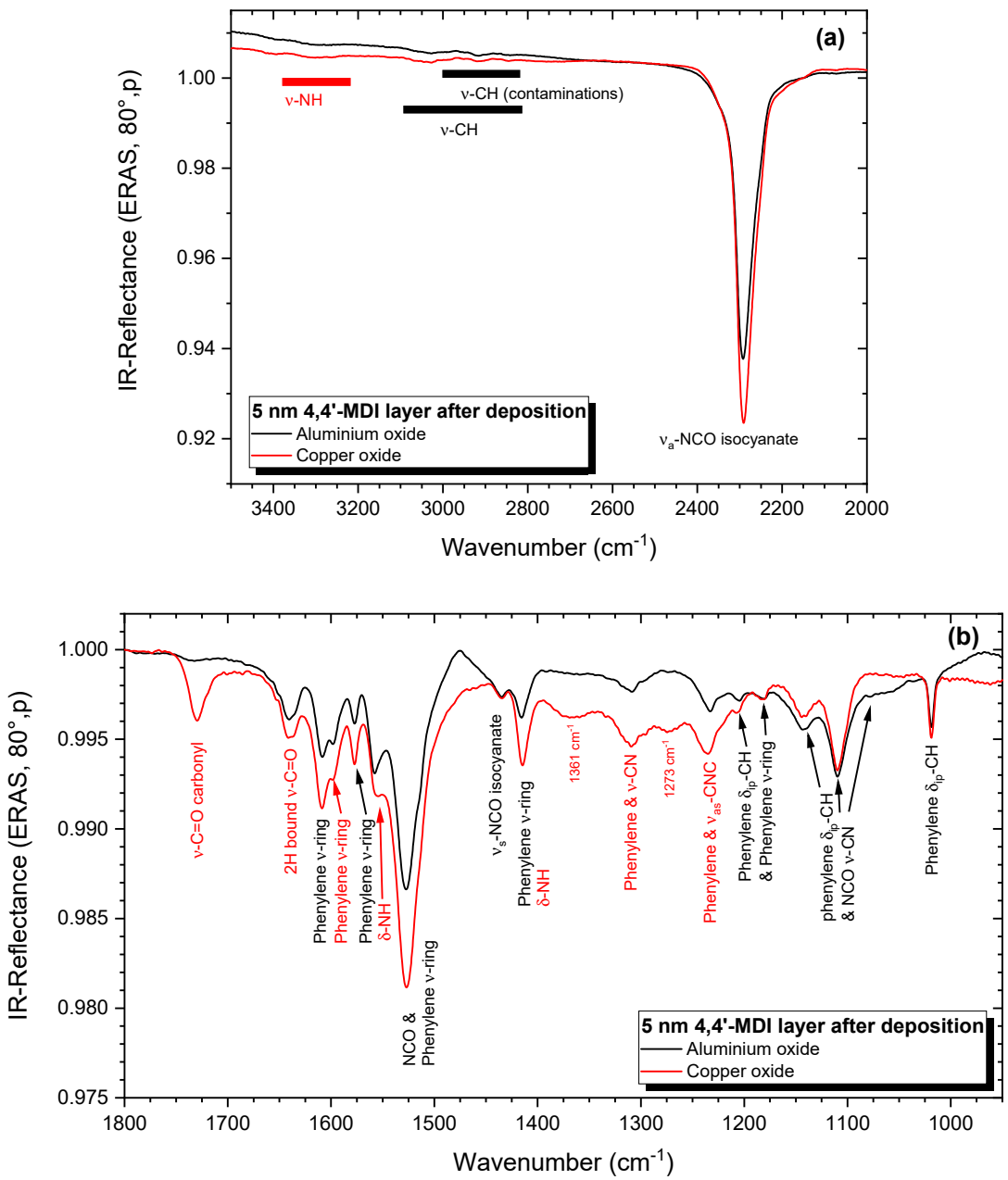

Fig. 6-30 Comparison of thin 4,4'-MDI layers on Al (black) and Cu (red) after deposition. Band assignment for 4,4'-MDI (black) and new species (red). (a) 3500 - 2000 cm^{-1}, (b) 1800 – 950 cm^{-1}.

More interesting however, after 40 h of storage the spectra of residual 4,4'-MDI on Al and Cu oxide (Fig. 6-31) reveal several *metal-specific differences* in the spectral regions of 3300, 1732-1675, 1642, 1597, 1557, 1514, 1415, 1361, 1307, 1273 and 1233 cm^{-1}. For these bands, shape and intensity *ratios* vary with the metal. For example, the bands at 1725, 1514 and 1273 cm^{-1} are much stronger on Cu than on Al while the bands at 3300, 1642, 1597, 1557, 1307 and 1233 cm^{-1} have similar intensities on both metals. On the one hand this is due to the different amount of these species on each metal.

On the other hand, the variation of *relative* band intensities is also a clue that the formed species take different orientations on the metal oxide surfaces[40]. Usually, such orientation is caused by a specific interaction between the organic species and the substrate.

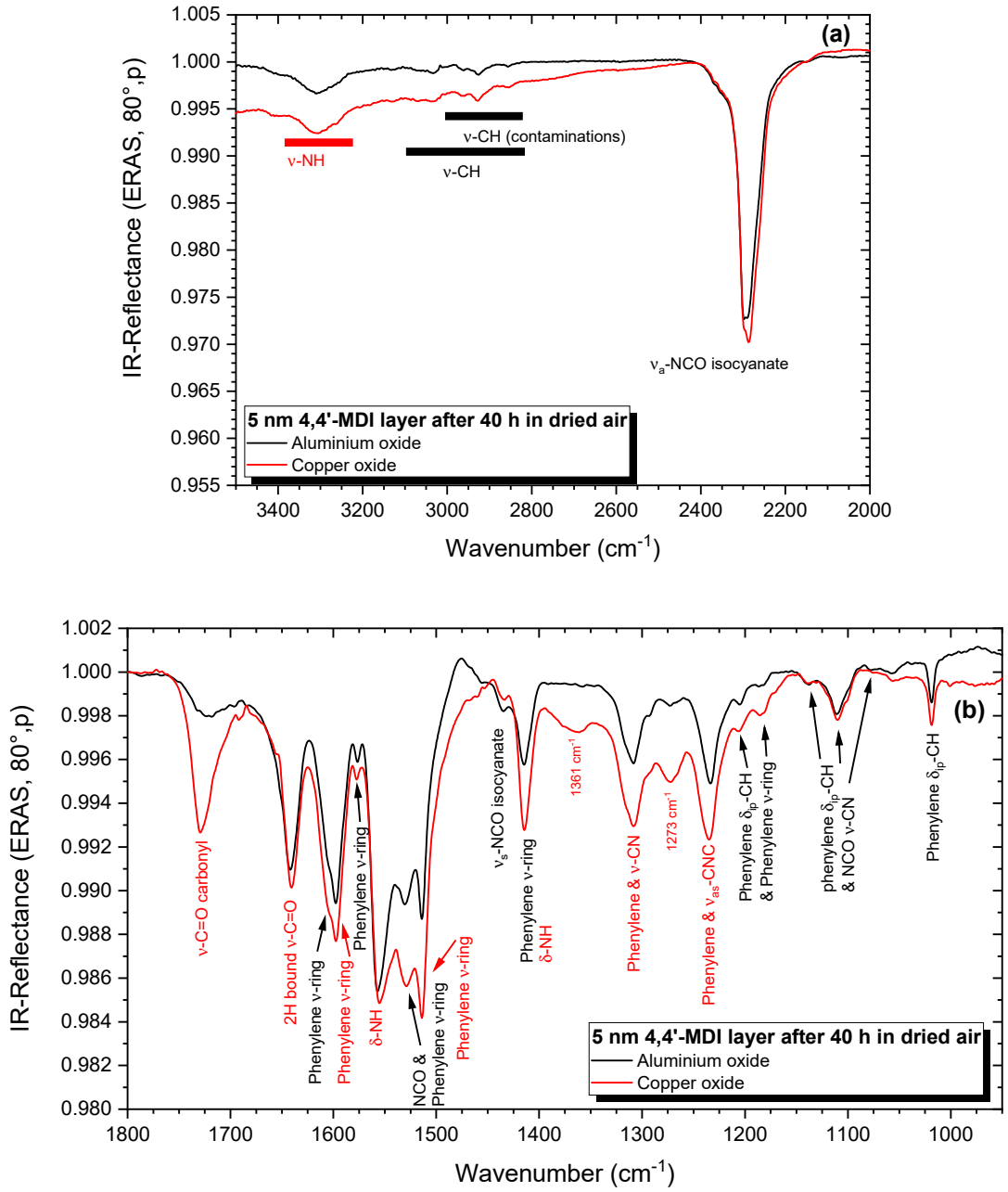

Fig. 6-31 Comparison of thin 4,4'-MDI layers on Al (black) and Cu (red) after 40 h of storage in dried air. Band assignment for 4,4'-MDI (black) and new species (red). (a) 3500 – 2000 cm^{-1}, (b) 1800 – 950 cm^{-1}.

[40] It is recalled that IR-ERA spectra recorded with p-polarised light are sensitive to the orientation of the transition dipole moment of a given vibration.

In conclusion, from the IR spectra of the MDI layers it is not obvious to distinguish between urea species and urethane-like adhesion links with the metal surface but the metal-specific spectral differences provide strong indirect evidence for interactions of the formed species with the different metals.

◊ *Topography of the layers*

Dark field light microscopy of 4,4'-MDI adsorbates on native Al and Cu oxide show first evidence for an inhomogeneity (Fig. 6-32). Both 1.5 nm layers (nominal thickness on the QCM quartz) have been prepared at 5 l/min N_2, 500 mbar and 10 °C substrate temperature. Two structural features are identified. First, the whole surface on both metals is covered by small 'dots'. Their amount and size are metal specific. On Al oxide fewer but bigger dots are present while on Cu oxide much more small dots cover the surface. Second, some bigger 'drops' appear here and there on Al and Cu. Measurement of virgin substrates confirms that both structures are not features of the metal substrate surface but originate from the deposited material (cf. section 5.1). Reduction of the gas flow during deposition to 2 l/min does slightly reduce the area density of 'drops' but the 'dots' remain.

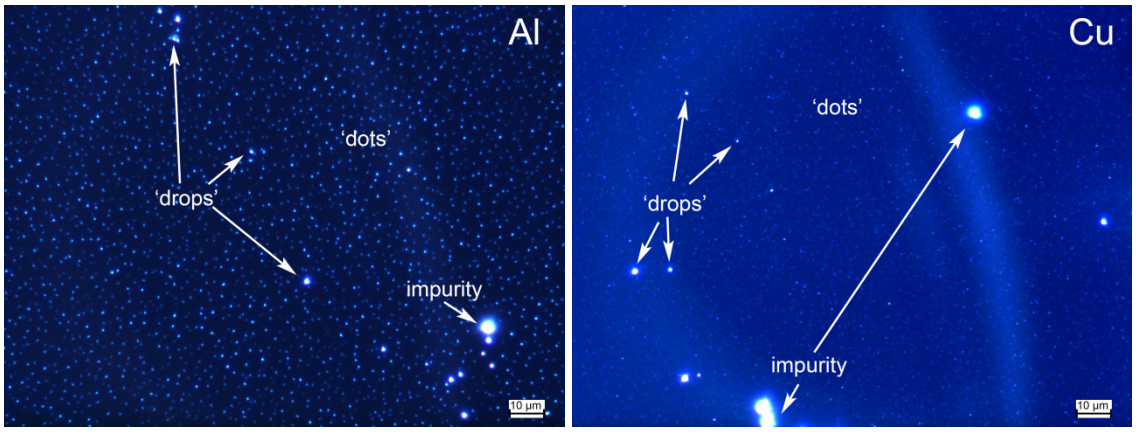

Fig. 6-32 Dark field images (approx. 200 x 150 µm²) of a 1.5 nm 4,4'-MDI layer prepared at 5 l/min N_2, 500 mbar and 10 °C substrate temperature on Al (left) and Cu (right), after ca. 24h of storage in dried air.

However, differential interference contrast and dark field optical microscopy are not capable to indicate if the observed non-homogeneous deposits are caused by protruding topographic structures or if they represent dimples or holes for example. Thus, the same layers are characterised by tapping mode *scanning force microscopy* to give a deeper insight into the morphology. Starting with a 10 x 10 µm² scan on Al and Cu - Fig. 6-33, the results from dark field are verified: The prepared layers are not plain. On Al (Fig. 6-33 left) a relatively flat underground (yellowish) is covered by elongated cones being up to 60 nm high. The lateral size of the cones reaches up to 0.5 µm. The observed cones in the SFM correspond to the dots seen in the dark field image.

On Cu (Fig. 6-33 right) the cones are much smaller and less tall but much more of these elements cover the flat surface. This is in agreement with the smaller but more densely packed dots in the corresponding dark field image.

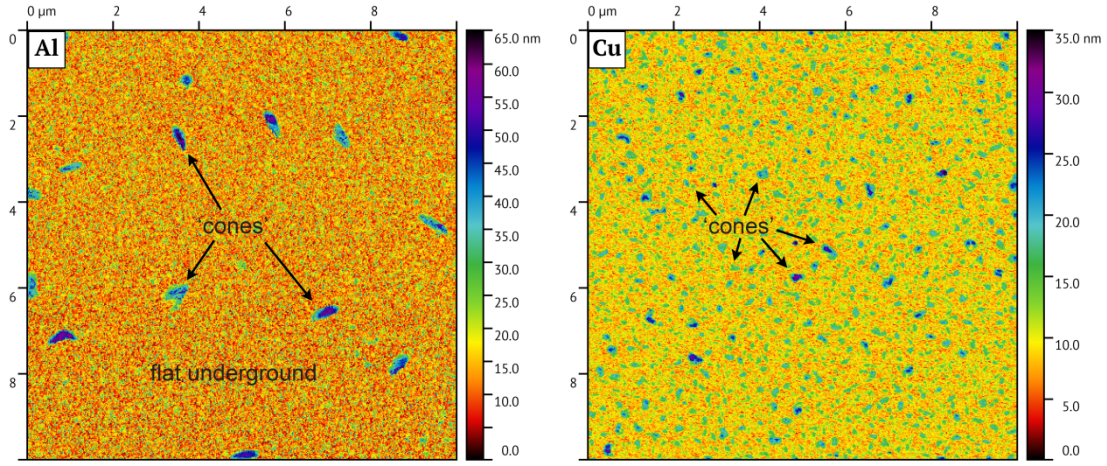

Fig. 6-33 Tapping mode SFM images of 1.5 nm 4,4'-MDI layers on Al (left) and Cu (right). 10 x 10 µm² scan.

According to the height distribution of the 10 x 10 µm² surface area (Fig. 6-34) the predominant structures are found between the 8 and 10 nm height level on both metals. They correspond to the flat regions between the cones. The cones are only minor features on both surfaces. They contribute to the tail above the predominant height level. On Al, the height distributes from 3 nm up to nearly 40 nm and is wider than on Cu where it ranges from 3 to 25 nm. Hence, the topography of the layer on Al is slightly rougher than on Cu.

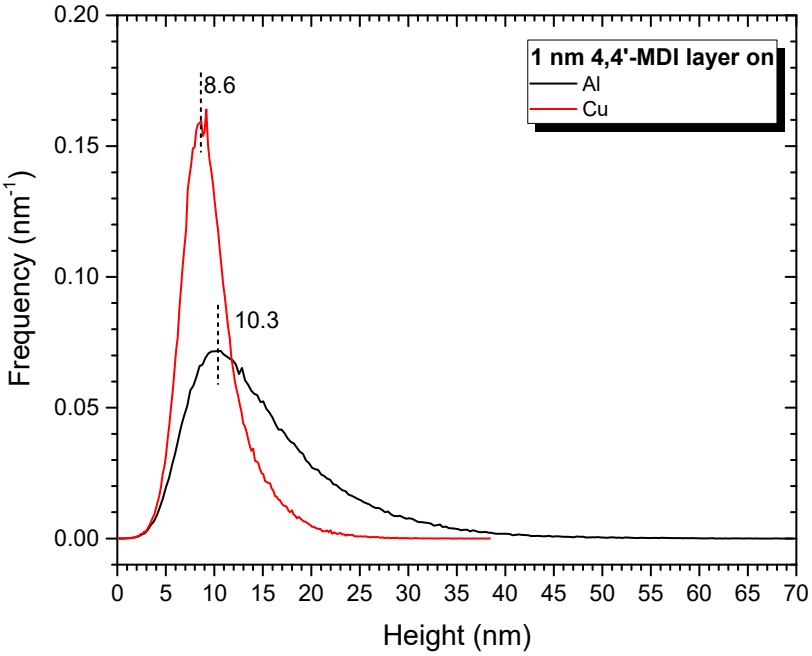

Fig. 6-34 Height distribution of the 10 x 10 µm² scan (cf. Fig. 6-33) of 4,4'-MDI layers on Al (black) and Cu (red).

The following 1 x 1 µm² scans reveal the situation in more detail. On native aluminium oxide (Fig. 6-35a) an extended cone (200 x 500 nm²) is surrounded by a rather flat region that replicates the nodular structure of the polycrystalline aluminium. The flat surface in yellow to light blue reaches from 10 to 20 nm in height with respect to the few deepest regions (dark red).

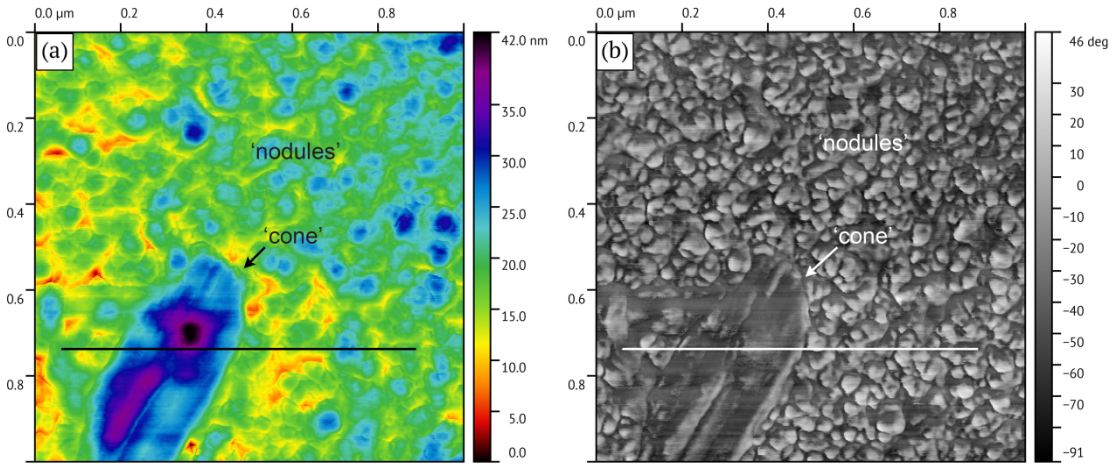

Fig. 6-35 Tapping mode SFM (a) topography and (b) phase contrast image of a 1.5 nm 4,4'-MDI layer deposited on Al. 1 x 1 µm² scan. The lines indicate the location of height and phase contrast profiles given in Fig. 6-36.

Before adsorption, such cones are not present on the Al substrates. Hence it could be assumed that 4,4'-MDI forms these cones and that the surrounding surface remains uncoated. However, a closer look at the phase contrast image (Fig. 6-35b) and at the profile lines for topography and phase contrast (Fig. 6-36) shows that it is not that simple.

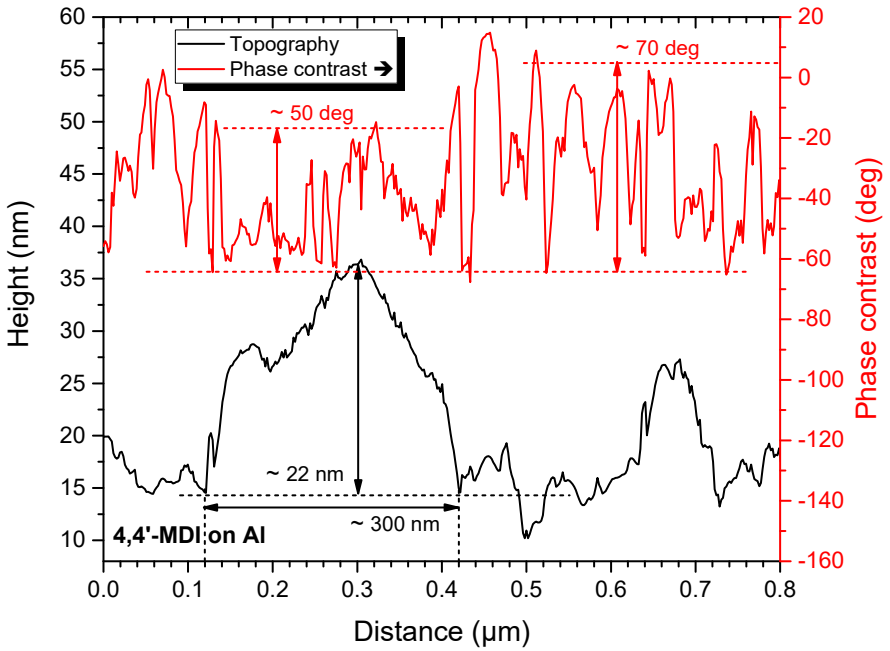

Fig. 6-36 Topography (black) and phase contrast (red) profiles along the line in Fig. 6-35.

At 0.12 – 0.42 µm distance, the topography profile (black curve in Fig. 6-36) clearly intersects a cone (cf. the line in Fig. 6-35a) of ~22 nm height. The corresponding phase contrast varies by some 50°. At approx. 0.64 – 0.72 µm distance, we get another bump of ~12 nm height and the same phase contrast fluctuation of ~50°. Both features are attributed to MDI deposits. In between approx. 0.42 – 0.64 µm, the height level reduces to some 14 ± 3 nm while the corresponding phase contrast fluctuation (Fig. 6-36, red curve) rises to about 70°. This low-height region is attributed to aluminium grains. At the grain boundaries, phase contrast jumps as the interaction of the tip with the sample surface changes abruptly. Intuitively, phase contrast fluctuations should be less on compliant MDI deposits but we have to recall that SFM phase contrast is very sensitive to minor parameter changes.
With this in mind we finally see from Fig. 6-36 that the *average* phase contrast value is very similar for both the MDI deposits and the 'aluminium' region. No harsh phase contrast change is observed when passing a deposited cone. This supports the hypothesis that the whole surface is covered by a very thin MDI layer plus some additional MDI in the cones. Underneath, however, the tip everywhere senses the grain boundaries of the polycrystalline Al surface.

On Cu (Fig. 6-37a) many cones of 100 – 200 nm in diameter and 15 - 30 nm height (greenish to blue) are scattered on the flat surface (red to yellow). Shape, dimensions and occurrence are different from those on Al oxide and hence metal specific. The flat surface regions show some granulation though. But the grain boundaries are much smoother than on uncoated Cu (cf. Fig. 5-5a). This is first evidence that the flat regions are also completely covered with organic material.

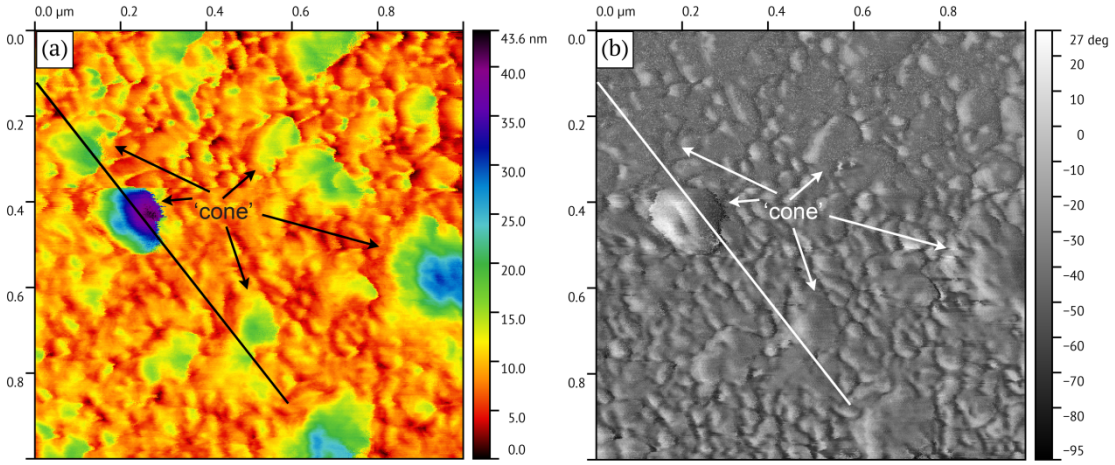

Fig. 6-37 Tapping mode SFM (a) topography and (b) phase contrast image of a 1.5 nm 4,4'-MDI layer deposited on Cu. 1 x 1 µm² scan. The lines indicate the location of height and phase contrast profiles given in Fig. 6-38.

The topography profile line (Fig. 6-38, back line) shows the height difference between the cones and the surroundings. The flat region exhibits small variations of up to 5 nm which are in agreement with fluctuations observed on uncoated metal substrates.

Due to the phase contrast image (Fig. 6-37b) and the corresponding profile line (Fig. 6-38, red line), phase contrast fluctuates by ~40° along the profile line and is close to virgin Cu-PVD fluctuations (30°). On the cones, variations are smaller (~20°) now. On the surrounding flat regions, phase fluctuation follows the topography change. Hence, as on Al, no significant phase difference between cones and flat surface is observed, and it is concluded that the whole Cu surface is covered with MDI molecules as well.

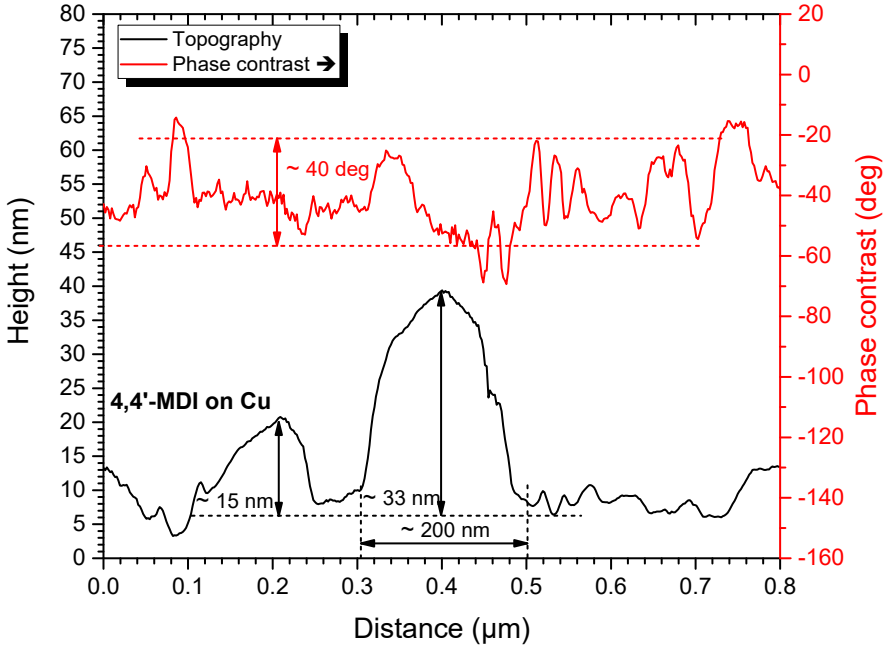

Fig. 6-38 Topography (black) and phase contrast (red) profiles along the lines in Fig. 6-37.

Topography of 4,4'-MDI layers reveals some metal specificities with regard of dimension and coverage of the topographic features. Moreover it is evident now, that QCM measurements provide some average thickness for these irregular MDI deposits. Furthermore the morphology of the deposits on the Au plated quartz is also unknown. Hence, if the deposit is also irregular, the requirements for the thickness calculation (cf. section 3.1) are not met. Thus, all thickness data taken from the QCM during layer deposition can be only taken as relative values for experiment reproducibility for example. The non-uniform deposit can also have consequences for the stability of the deposits. Obviously, MDI molecules in the cones possess fewer interactions with the substrate surface than those in the flat regions.

◊ *Stability against liquid THF*

In order to assess the adhesive interactions of the MDI with the native metal oxides and to discriminate between urea species and chemical adhesion with the metal surface, three subsequent THF rinsing steps are applied to the layer after 68 h of storage. Fig. 6-39 and Fig. 6-40 show the IR-ERA spectra taken after the THF rinses of a MDI layer on Al and Cu, respectively.

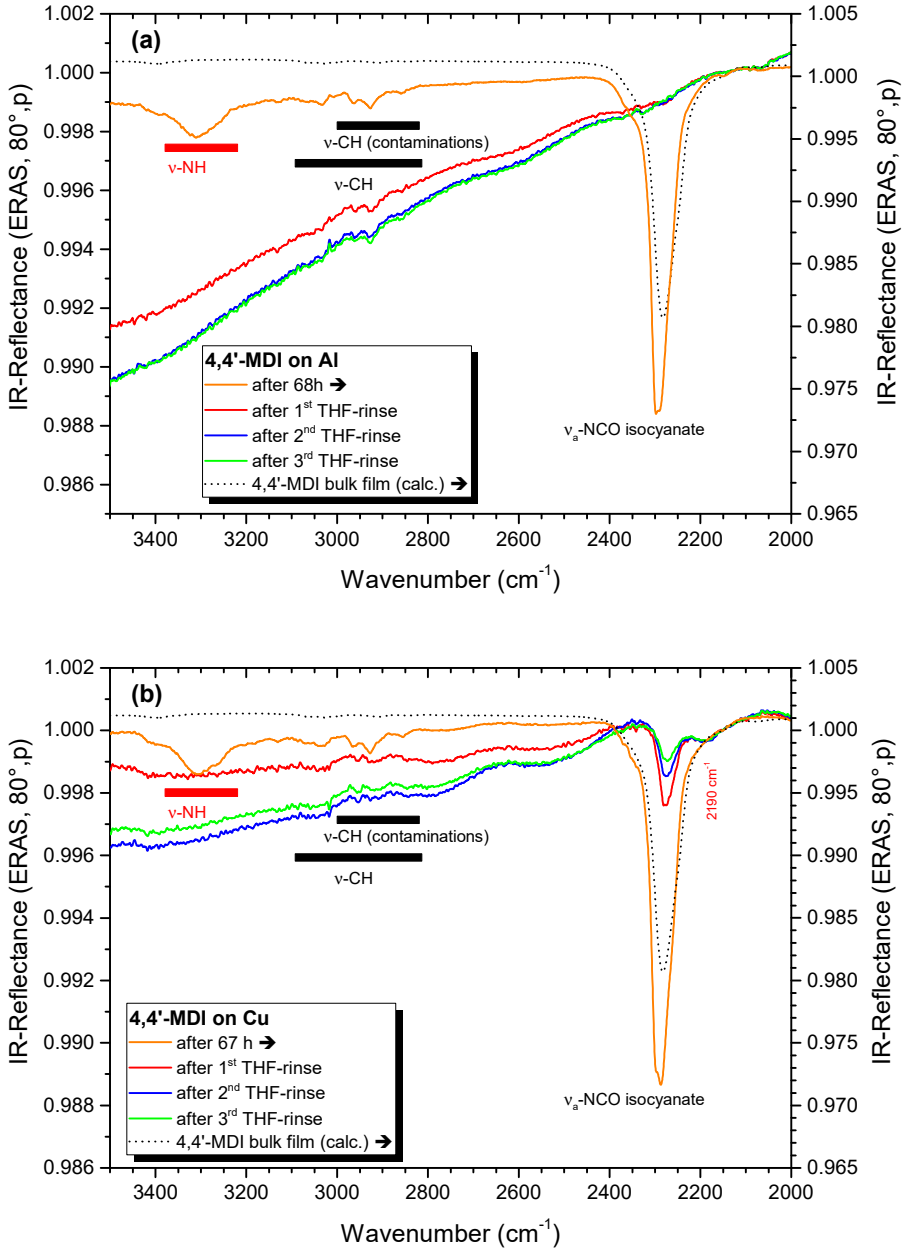

Fig. 6-39 Effect of THF rinsing on the 4,4'-MDI layer. (a) On Al after 68 h in dried air, (b) on Cu after 67 h in dried air. Dashed line represents a bulk-like spectrum for qualitative comparison. Band assignment for 4,4'-MDI (black) and new species (red) refers to the layer prior THF rinses.

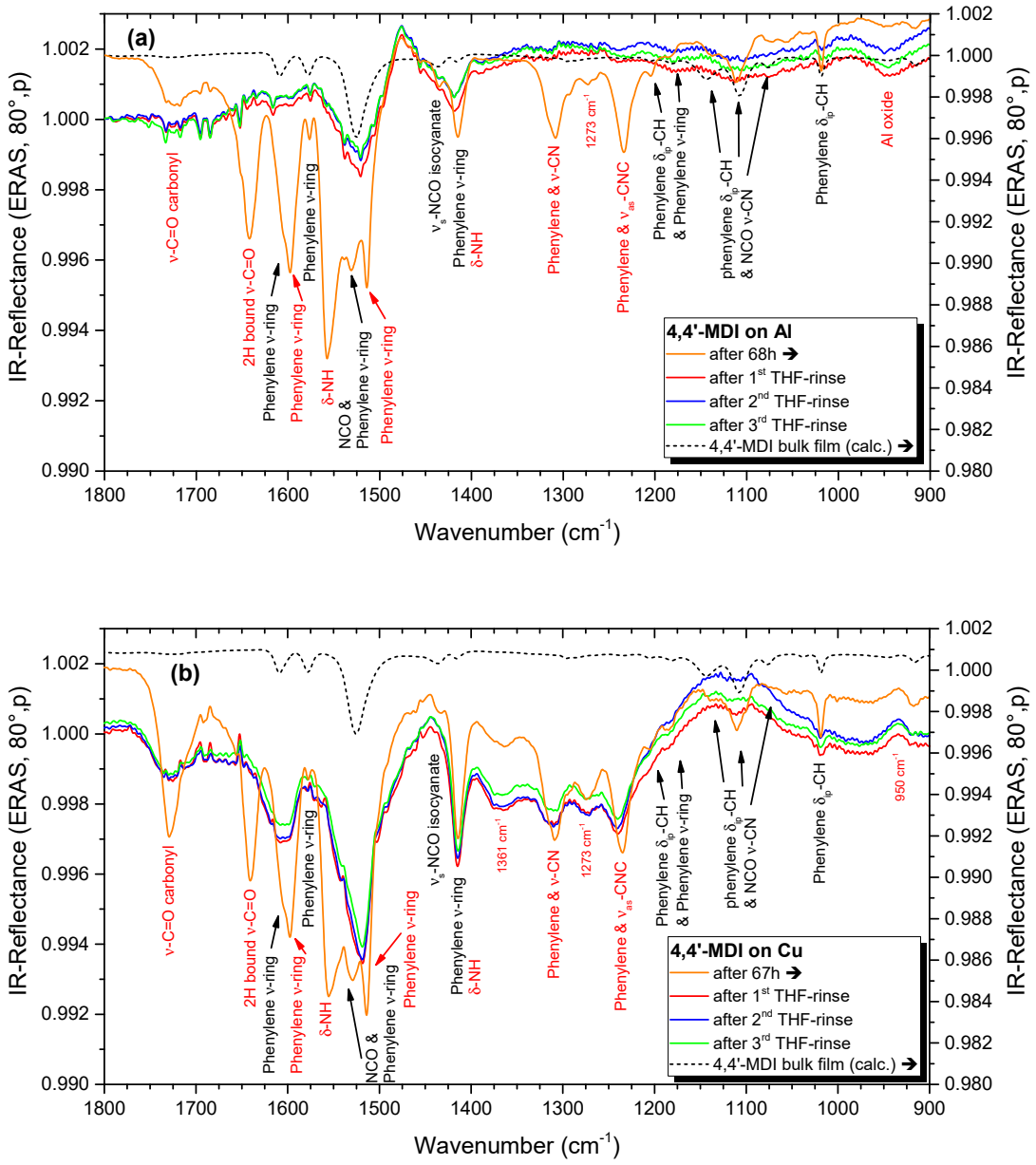

Fig. 6-40 Effect of THF rinse on the 4,4'-MDI layer. (a) On Al after 68 h in dried air, (b) on Cu after 67 h in dried air. Dashed line represents a bulk-like spectrum for qualitative comparison. Band assignment for 4,4'-MDI (black) and new species (red) refers to the layer prior THF rinses.

On both substrates all bands lost intensity after the 1st rinse. Thus, a big part of the deposited MDI is washed off the surfaces and hence is not attached to the native metal oxides. Also an intensity drop is observed for the newly formed bands. Hence part of the corresponding chemical entities is removed from the metal surface as well as they are interacting only weakly with the metal substrates. According to [9, 10] the observed removal of the newly formed species is attributed to molecules that contain urea groups due to the reaction of isocyanates with adsorbed water. They do not attach to the metal substrate.

Several bands remain however. They are located at the ν_a-NCO (2280 cm^{-1}) and in the 1800-1200 cm^{-1} region.

After the 1st rinse all remaining bands are more intense on Cu than on Al. On Al, the isocyanate asymmetric stretch is very weak but stable over the subsequent THF rinses. On Cu the intensity of that band drops after each rinse. Through the solvent rinse the adsorbed molecules momentarily gain some further mobility and hence few NCO groups can again react with adsorbed water. As the intensity of all other bands in the spectrum does not change no further removal of molecules take place during ongoing rinses.

A new stable band emerges at 2190 cm^{-1}. It is only visible on Cu for layers that are stored longer than 24 h in dried air. Most likely some sort of interaction forms between an isocyanate group and another NCO or with the species formed during storage. A particular band assignment was not possible.

Between 1800 and 1600 cm^{-1} (Fig. 6-40b) a large buckle appears on both metals revealing that the remaining carbonyl groups undergo a variety of different interactions with the substrate and with the other remaining molecules. Bands in the 1800-1200 cm^{-1} region show metal-specific features as they exhibit particular shapes and intensity ratios. This specificity was already observed on thin 4,4'-MDI adsorbates from diluted solutions [10, 33]. Hence, MDI layers prepared from gas phase behave very similar to deposits from solution. On Cu, some bands (1730, 1600, 1361, 1308, 1273 and 1233 cm^{-1}) remain where urea bands were located before the rinses. Since urea containing molecules were washed off, these remaining bands are attributed to isocyanate groups that formed a urethane-like bond with the native Cu – Fig. 6-41. On Al, the same features are present but much weaker in intensity and with broader bands.

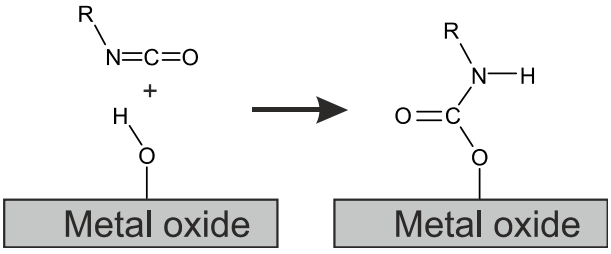

Fig. 6-41 Formation of urethane-like bonds from reaction of isocyanate with hydroxyl groups from the metal oxide.

The band at 1361 cm^{-1} is specific for Cu as it is not present on Al. That proves the specific role of the metal oxide surface state for that adhesive interaction. The presence of an Al oxide band below 1000 cm^{-1} and a negative band at 950 cm^{-1} on Cu further indicate some modification of the amorphous aluminium and copper oxide layers as well.

Further THF rinsing does not change the spectrum significantly. Hence the remaining species are strongly linked to the metal oxide. Thus, it is concluded that before solvent rinse, weakly adsorbed MDI molecules and urea-containing species co-exist with durably adsorbed 4,4'-MDI molecules that establish an adhesive interaction via one of their isocyanate groups on Al and Cu. Moreover, the MDI molecules are at least capable to displace adsorbed carbonaceous contaminations from the oxide surface as they establish these adhesive interactions. Most likely the displaced contaminations mix within the MDI adsorbate during layer deposition in the MLD. Specific removal or desorption of contaminations is not identified due to the very weak band intensity of the contaminations. Modifying the initial amount of deposited MDI has an impact on the amount of remaining species after the solvent rinses. On Al oxide, this type of interaction is independent of deposited MDI quantity. On Cu oxide, more interaction links form when thicker MDI layers are prepared.

The topography of the samples after the THF rinses is identical to virgin metal oxides and hence SFM is not capable to identify the few remaining molecules. It can be assumed that the strongly adsorbed MDI covers the whole substrate surface while weakly adsorbed molecules on top form the actual topography of cones and flat surroundings observed before the solvent rinses.

The achieved deposit of strongly attached MDI to the metal oxides is defined as '*stable MDI deposit*'.

Finally and essential for a subsequent grafting polymerisation, the deposited MDI layers contain intact isocyanate groups on both metals even after 68 h of storage in dried air. Thus, free NCO groups are still present in the adsorbed MDI layers for further reaction with alcohol groups of some co-monomer to form urethane linkages. Especially on Al this band is extremely weak, therefore it is necessary to check if a polyol layer on top of the MDI is capable to react with the strongly attached MDI.

6.5.3 Impact of substrate temperature

As shown in section 6.5.1 the substrate temperature greatly affects the deposition of 4,4'-MDI. Hence substrate temperature during deposition and/or during layer storage may as well have an impact on the layer chemistry and more particularly on the adhesive interactions with the metal. In this section the temperature influence during storage (6.5.3.1) and deposition (6.5.3.2) is studied in more detail. The outcome may be particularly interesting for the subsequent polymerisation reaction as higher temperature enhances molecular mobility and thus reactivity. All experiments in this section are prepared by the same experimental procedure: 4,4'-MDI is evaporated at 180 °C into 5 l/min of N_2 carrier gas at 500 mbar. Deposition on aluminium substrates is stopped at 0.9 nm for the experiments with T_{sample} = 10 °C and at 1.5 nm for the deposition at T_{sample} = 50 °C. N_2-purge is carried out for one hour after deposition. Corresponding layer growth was shown in Fig. 6-27. The layers are then transferred and stored inside the IR spectrometer for 24 h either at RT or at 50 °C. After storage the samples are subject to THF rinses.

6.5.3.1 Effect of temperature during storage after deposition

In this part the impact of temperature during storage of the layers is studied. Layers are deposited at T_{sample} = 10 °C and stored either at RT (ca. 25 °C) or T_{store} = 50 °C for up to 24 h. The 50 °C are achieved by a preheated heating plate attached to the sample holder (cf. Fig. 3-15).

◊ *Deposition at 10 °C on Al and storage at RT*

For RT storage, deposition and behaviour of MDI at 10 °C do not differ from deposits at 30 °C as already discussed in Sect. 6.5.2. The same spectral features and layer stability upon THF rinses are obtained (cf. spectra in Appendix 11.5.4, Fig. 11-14 and Fig. 11-15). Briefly, urea species form during the first 10 h of storage. Upon THF rinses, weakly adsorbed MDI and the urea species are washed off as they are not attached to the metal. Strongly attached MDI, defined as 'stable MDI deposit', undergoing urethane-like adhesive interactions with the metal oxide remain.

◊ *Deposition at 10 °C on Al and storage at 50 °C*

Over the first 30 min. at T_{store} = 50 °C important spectral changes are observed (Fig. 6-42a). Intensities of MDI specific bands (1608, 1578, 1525, 1143, 1108, 1075 and 1018 cm^{-1} as well as the isocyanate stretch at 2287 - Fig. 6-43) drop rapidly and strongly. Meanwhile bands for urea species and urethane-like adhesive interactions (1732, 1595, 1552, 1505, 1312 and 1232 cm^{-1}) start to grow.

Over the next hours of storage (Fig. 6-42b) only minor and weak changes occur in band intensity. The growth of the Al oxide band at 950 cm^{-1} is observed.

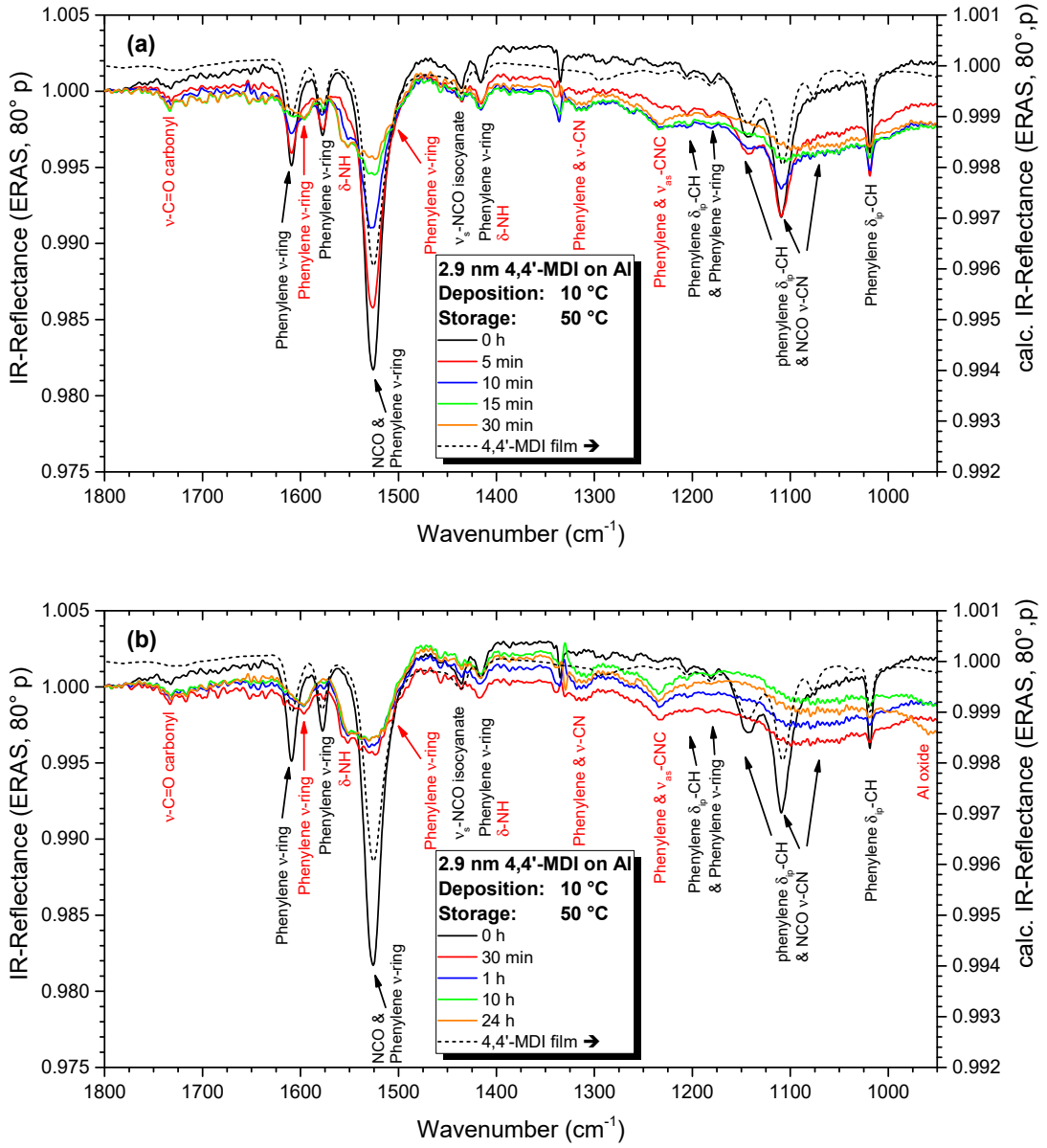

Fig. 6-42 IR-ERA spectra of a 4,4'-MDI layer (initial thickness 2.9 nm) on native Al oxide. Deposition at 10 °C and evolution during 24 h of storage in dried air at 50 °C. Deposition parameters: 500 mbar, 5 l/min. Band assignment for 4,4'-MDI (black) and newly emerging species (red). Dashed line: calculated bulk-like ERA spectrum for qualitative comparison. (a) 0 – 30 min, (b) 0 – 24 h.

For the isocyanate stretch at 2287 cm^{-1} (Fig. 6-43) a massive intensity drop during the first 15 min. at 50 °C is followed by a weak gradual diminution until 24 h of storage.

At first glance most MDI is rapidly consumed at higher storage temperatures. Due to higher mobility of the adsorbed molecules (MDI as well as water and carbonaceous contaminations) can more easily react together and occupy energetically favourable surface sites. However, the amount of formed urea species and urethane-like metal interactions remains low. Increased temperature also implies that it can facilitate desorption of MDI but also different orientations of the molecules with respect to RT. Thus, the behaviour does not correspond to just an increased reaction speed.

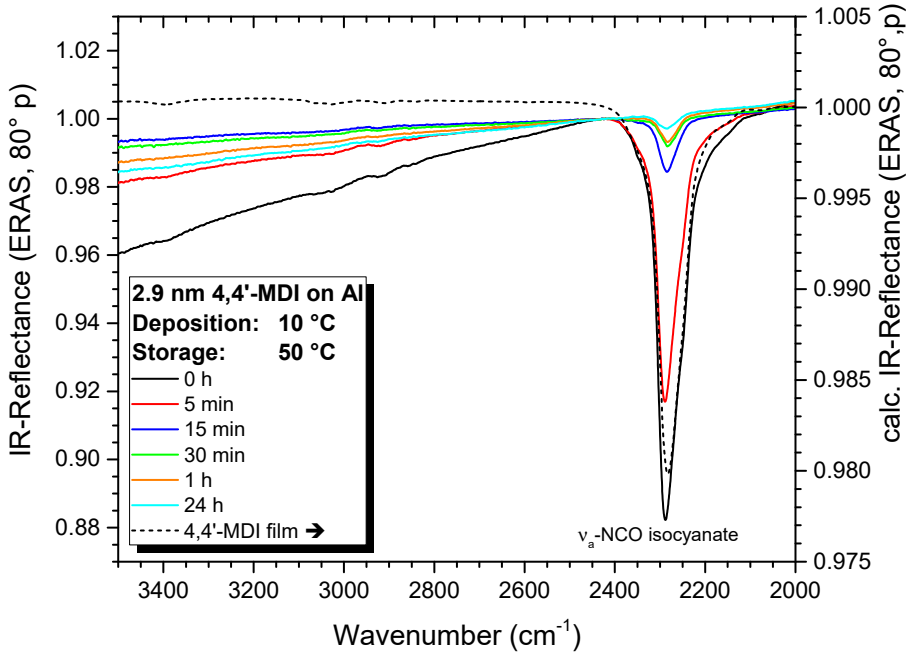

Fig. 6-43 IR-ERA spectra of a 4,4'-MDI layer (2.9 nm initial thickness) on native Al oxide. Deposition at 10 °C and evolution during 24 h of storage in dried air at 50 °C. Deposition parameters: 500 mbar, 5 l/min. Dashed line: Calculated bulk-like ERA spectrum for qualitative comparison.

The stability of the layers upon THF rinses provides further evidence for the observed inconsistency. The layer obtained by storage at 50 °C is nearly immune against subsequent THF rinses (Fig. 6-44).

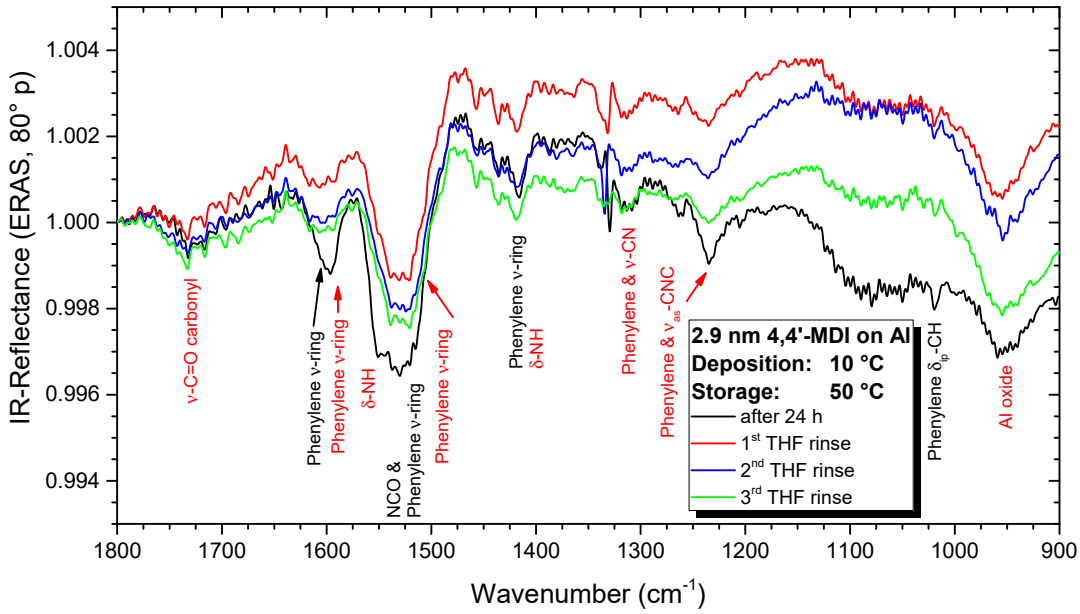

Fig. 6-44 Effect of THF rinse on a 4,4'-MDI layer (2.9 nm initial thickness) on native Al oxide. Deposition at 10 °C and 24 h of storage in dried air at 50 °C. The black line represents the layer before the THF rinses. Band assignment for 4,4'-MDI (black) and newly formed species (red) refers to the layer prior THF rinses.

Most bands do only weakly drop in intensity. The ν_a-NCO band (cf. Appendix 11.5.4, Fig. 11-16) also dropped in intensity and is almost invisible now. Hence, THF removes only few molecules (urea and MDI) from the substrate. The remaining species are strongly attached to the surface as they withstand further rinses. The spectra before and after the solvent rinses do not significantly differ either. They resemble the stable MDI deposit obtained after the rinses for RT stored layers (cf. Fig. 11-15).

The weakly attached MDI is missing in this layer after 24 h storage. Hence, beside ongoing reaction, increased storage temperature also induces desorption of weakly attached MDI which explains the very fast intensity drop over the first 30 min. of storage. As less free isocyanates are available fewer urea species are formed too. Desorption of urea species is not excluded but less likely as molecular weight is almost doubled. The strongly attached MDI dominates the spectrum. At first glance the adhesion of the isocyanates seems not to be affected by the higher storage temperature.

◊ *Comparison between the storage temperatures*

Comparison of two layers stored at 25 and 50 °C, respectively, illustrates the different behaviour.

After deposition (Fig. 11-17) both layers do only show slight band intensity differences due to marginal thickness fluctuation during deposition[41] and slightly different times between end of deposition and start of spectra recording. Up to this point both samples experienced the same temperature regime.

After 24 h of storage (Fig. 6-45) the temperature impact is important. At T_{store} = 50 °C, all bands of the MDI and the formed species are much weaker than for storage at RT. Thus, more MDI disappeared at 50 °C.

Second, urea formation is much faster at T_{store} = 50 °C but does yield much less species as the specific bands are much weaker than for RT storage. This confirms that the intensity drop of the isocyanate specific bands does not mainly come from increased urea formation.

Third, it results from this observation that some part of the unreacted and weakly adsorbed MDI desorbed during the first 30 min. of storage. To its major part, the intensity difference of the isocyanate bands corresponds to the amount of desorbed MDI.

Fourth, as the weakly attached MDI desorbs less urea is formed too, which is in agreement with the observations made for thinner layers[42]. Hence the intensity difference corresponds to all MDI molecules that were only weakly attached to the substrate and were unable to form urea during the initial period of storage.

Fifth, higher T_{store} induces a greater modification of the aluminium oxide as the corresponding band at 950 cm^{-1} is stronger than after storage at RT. This can affect the strong adhesion of the MDI too.

[41] 2.9 nm for the layer stored at RT and 3.2 nm for the layer stored at 50 °C.
[42] Samples of 1 nm MDI were prepared similarly as in Sect. 6.5.2 and compared with the 5 nm deposits.

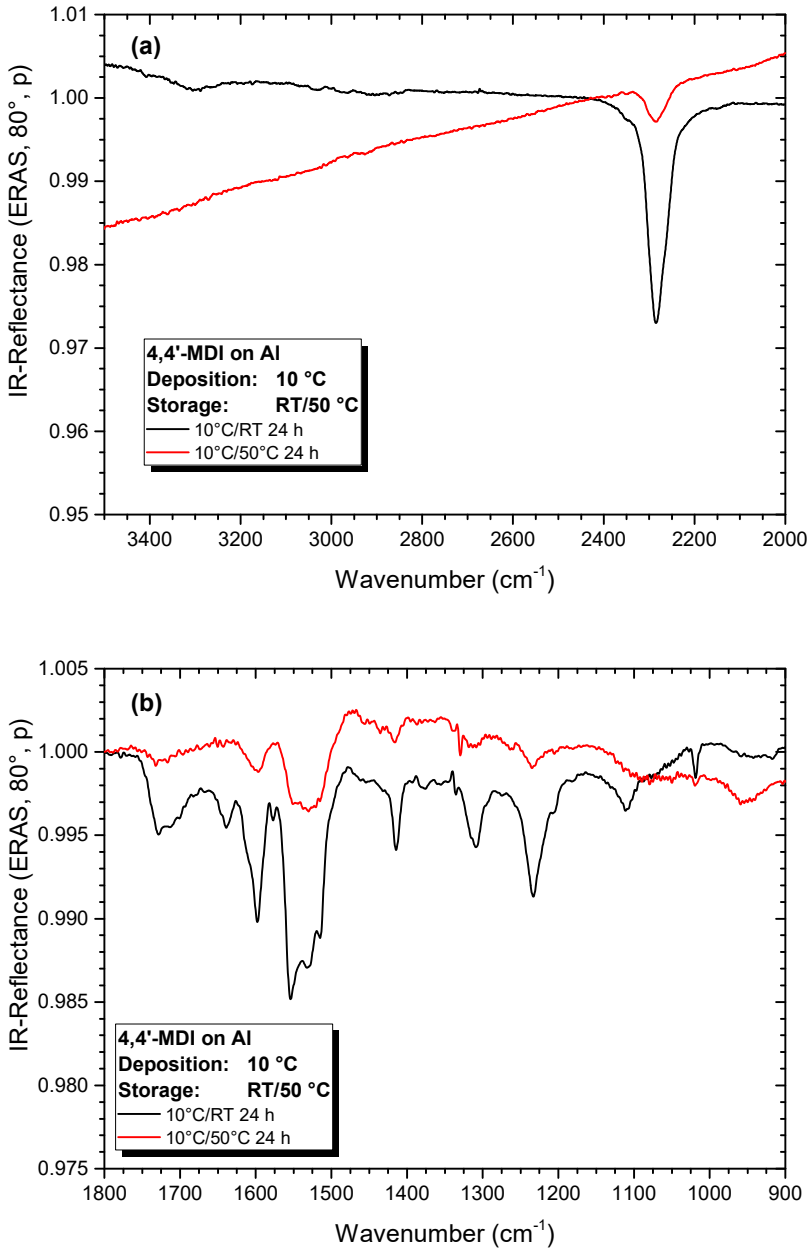

Fig. 6-45 Comparison of two 4,4'-MDI layers deposited on native Al oxide at 10 °C and stored at RT (black) or 50 °C (red). IR-ERA spectra after 24 h of storage. Deposition parameters: 500 mbar, 5 l/min. (a) 3500 – 2000 cm^{-1}, (b) 1800 – 900 cm^{-1}.

Comparison of the layers after three THF rinses (Fig. 6-46) reveals another important point. Both spectra do match much better now as they show similar band shape and position. Slightly more molecules remain in the layer stored at 50 °C as bands are somewhat stronger but the intensity difference does not exceed reproducibility (1 ‰). A few notable differences are present, however. First, the band shapes between 1800 and 1550 cm^{-1} are different. While the RT stored layers exhibit a wide band (~1760 - 1580 cm^{-1}) the layer at T_{store} = 50 °C shows two separate broad bands at 1750 and 1600 cm^{-1}.

Second, the Al oxide band is much larger when stored at 50 °C in dried air. The increased modification of the substrate may well change the surface sites, thus allowing slightly more MDI molecules to attach and develop slightly different interactions leading to the observed differences.

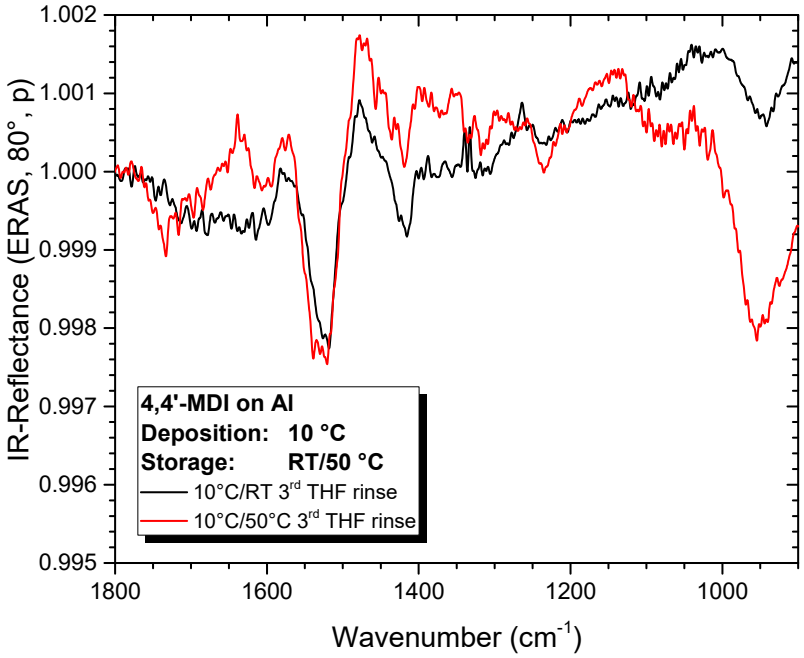

Fig. 6-46 Comparison of two 4,4'-MDI layers on native Al deposited at 10 °C and stored at RT (black) and 50 °C (red). IR-ERA spectra after the 3rd THF rinse. Deposition parameters: 500 mbar, 5 l/min.

Third for T_{store} = 50 °C, the NCO asymmetric stretch (Fig. 6-47) is very weak compared to the RT stored layer. Repetition of these experiments proved that the intensity of this band varies slightly but is always weak. Increased T_{store} does not only improve the rate of the urea formation but also the reactivity of the NCO group in general. Hence, more NCO groups may strongly interact with the substrate leading to an increase of the corresponding fingerprint bands and thus reducing the intensity of the NCO band. At this point it is not possible to state whether the stable MDI deposit is still able to react with a subsequent alcohol layer. This is elucidated in chapter 7.

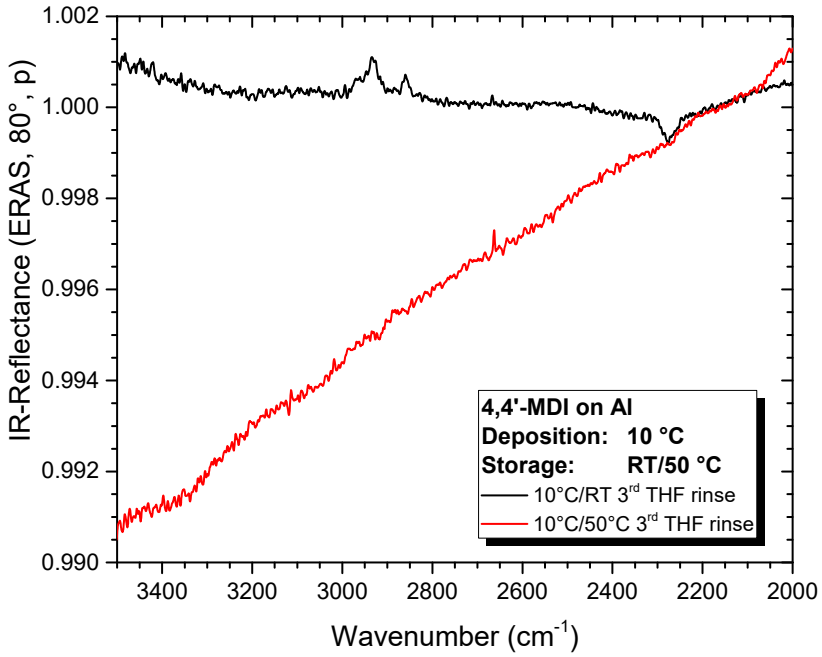

Fig. 6-47 Comparison of two 4,4'-MDI layers deposited on native Al oxide at 10 °C and stored at RT (black) or 50 °C (red). IR-ERA spectra after the 3rd THF rinse. Deposition parameters: 500 mbar, 5 l/min.

Summing up, an increase in storage temperature leads to a layer that nearly complies with the stable MDI deposit obtained by a solvent rinse - except for a few urea molecules that do not desorb without solvent rinse. Although the Al oxide is more modified at higher T_{store}, the strong adhesive interactions of the MDI are not hampered but even somewhat enhanced.

Now instead of changing the storage temperature, T_{sample} in the MLD can be modified too. Hence, in the next section T_{sample} is increased to 50 °C and the behaviour of the layer is studied as before. This can answer the question if a stable MDI deposit could be prepared directly by MLD deposition process.

6.5.3.2 Influence of the substrate temperature during deposition

◊ *Deposition at 50 °C on Al and storage at RT*

While deposition at 10 °C and 30 °C does not show much difference in deposition behaviour and chemistry, a further increase to T_{sample} = 50 °C does change deposition behaviour completely (cf. Fig. 6-27). After switching to non-deposition mode, deposition rapidly reaches a plateau. According to the experiments for T_{store} = 50 °C, desorption of MDI is possible at this temperature and so it will shift the adsorption-desorption balance in the MLD. Some MDI molecules are still present in the carrier gas after closing the deposition valves, of course, but they cannot raise the adsorbed amount anymore and the thickness remains constant due to the new adsorption-desorption equilibrium.

Contrary to the previously discussed layers where the temperature is increased after the deposition, chemical transformation of MDI molecules now massively occurs during deposition. The IR spectrum after deposition (black line in Fig. 6-48) represents the state of the layer at RT after ca. 80 min. at 50 °C. Accordingly, bands of urea species and MDI molecules are present and thus urea formation also accelerated during MDI deposition. During storage at RT, the chemical structure of the layer is very stable and only weak band changes are observed like a slight growth of the wide band in the carbonyl region and a growth of the Al oxide band. The NCO band (2283 cm^{-1}) does not change during storage. Hence, as for the layer at T_{store} = 50 °C, 80 min. at T_{sample} = 50 °C is sufficient to complete urea formation.

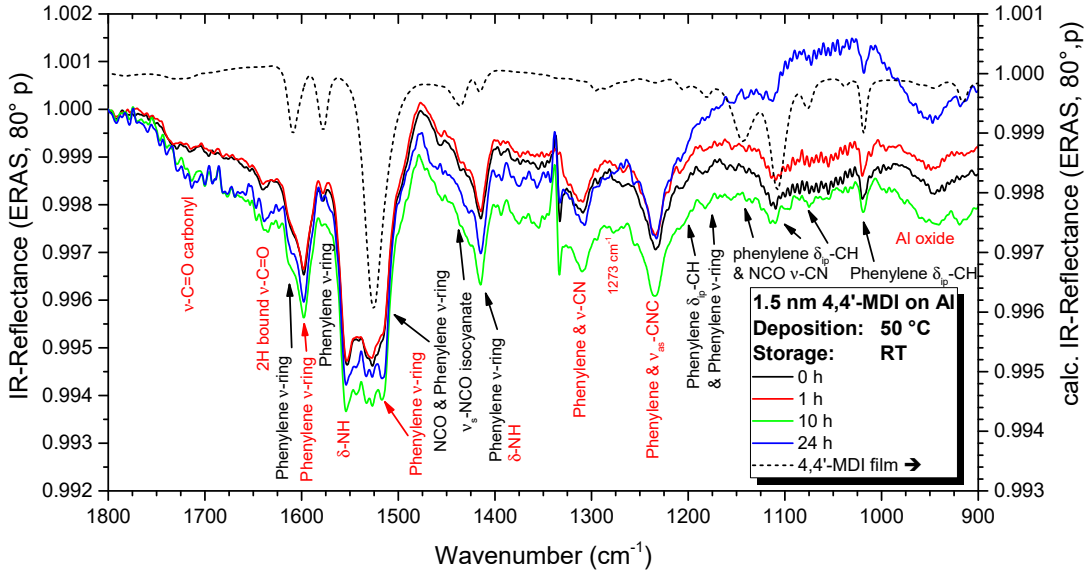

Fig. 6-48 IR-ERA spectra of a 1.5 nm 4,4'-MDI layer on native Al. Deposition at 50 °C and 24 h of storage in dried air at RT. Deposition parameters: 500 mbar, 5 l/min,. Band assignment for 4,4'-MDI (black) and new species (red). The dashed line represents a calculated bulk-like ERA spectrum for qualitative comparison. 1800 – 900 cm^{-1}.

The behaviour of the layer upon THF rinses is shown in Fig. 6-49. After the first solvent rinse urea species and most weakly adsorbed MDI are removed. The intensity drops by about 2 ‰ and spectra before and after THF rinse show slight differences as band intensity ratios change (mainly between 1750 and 1400 cm^{-1}).

The remaining strong adsorbate of MDI withstands all further solvent rinses. Hence a similar behaviour as for the layer stored at 50 °C is observed. The comparison of the three discussed layers hereafter allows for a more detailed conclusion.

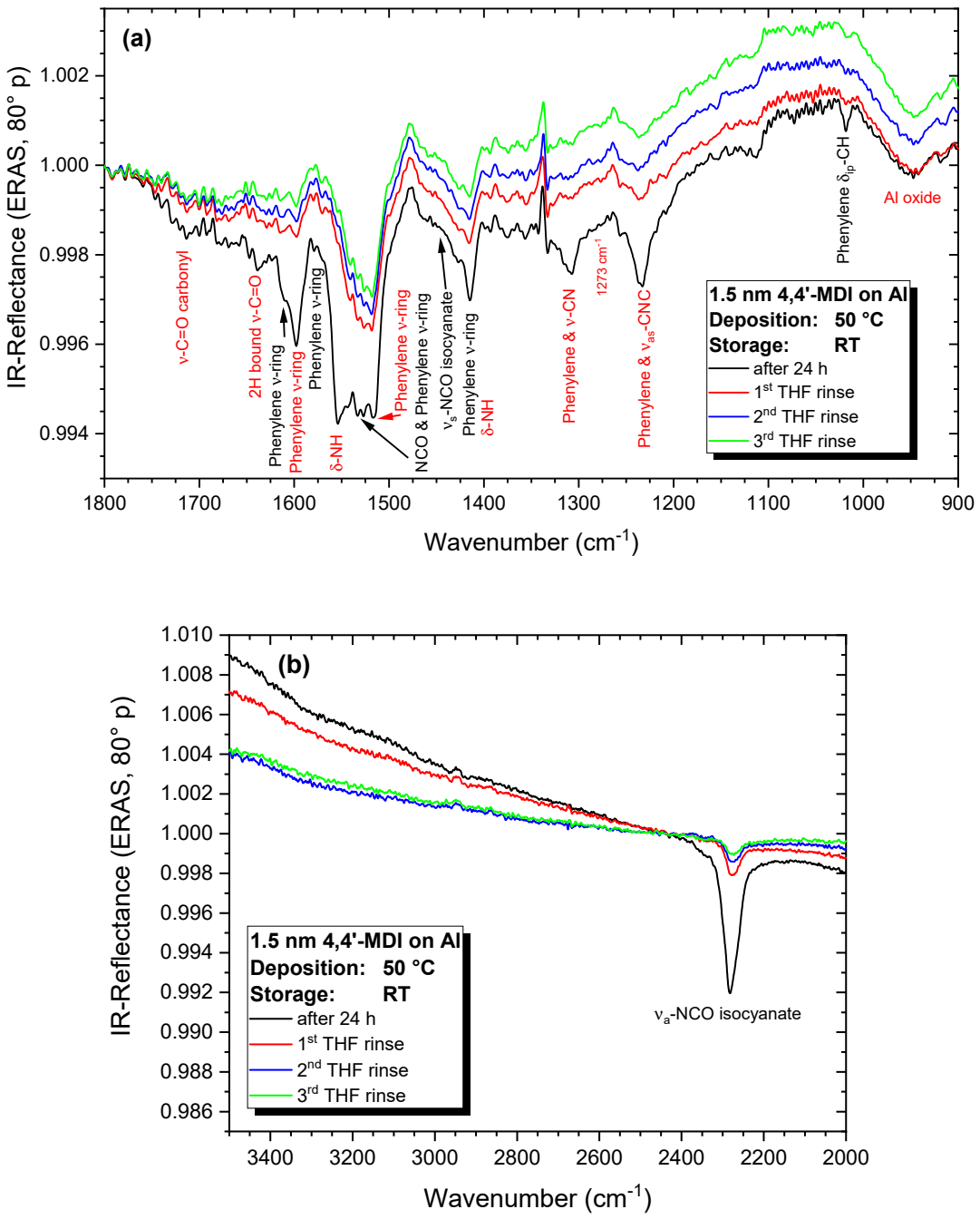

Fig. 6-49 Effect of THF rinse on a 4,4'-MDI layer (1.5 nm initial thickness) on native Al oxide. Deposition at 50 °C and 24 h of storage in dried air at RT. Black line: layer before the THF rinses. Band assignment for 4,4'-MDI (black) and newly formed species (red) refers to the state prior THF rinses. (a) 3500 – 2000 cm^{-1}, (b)1800 – 900 cm^{-1}.

◊ *Comparison between the layers*

After deposition the spectra are obviously different as the layer chemistry is already completed for T_{sample} = 50 °C and is only starting for the T_{sample} = 10 °C layer. Spectra are compared in Fig. 11-18. Moreover less MDI is deposited at higher temperatures (1.5 nm versus ca. 3 nm at 10 °C).

Comparison after 24 h of storage is more interesting because most of the chemical conversion has completed on all three layers (Fig. 6-50). As fewer MDI was deposited the isocyanate band (Fig. 6-50a) is also weaker on the blue spectrum (T_{sample} = 50 °C) compared to the 10 °C deposition (black) but slightly more MDI is present compared to the layer stored at 50 °C (red). Although a deposition plateau is reached some MDI is still offered to the layer during the 50 °C deposition which explains the slightly higher isocyanate band. The remaining region shows that both layers, either prepared or stored at higher temperatures (red and blue line) are very similar in terms of band shape and intensity for all present species. The Al oxide is also similarly modified underneath both layers. Hence up to 24 h no significant difference is seen between deposition at 50 °C or storage at 50 °C in terms of chemical constitution of layer and substrate. Most chemistry is completed within 1 h at 50 °C. Preparation and storage at lower temperature (black spectrum) does show significant differences as discussed in the previous section. Thus, the weakly adsorbed MDI species are only present for layers prepared at lower temperatures and desorbed at higher temperatures. This is helpful if a stable MDI deposit should be prepared without solvent rinse. It can be obtained by sufficiently high T_{sample} in the MLD process itself.

As next step the spectra after the THF stability test are compared (Fig. 6-51). Both layers stored at RT possess nearly identical spectral features with slightly stronger bands for the layer prepared at 50 °C. Band shapes are comparable.

The layer prepared at 10 °C and stored at 50 °C (red) presents slight different bands between 1800 and 1550 cm^{-1}, a weaker NCO band, and a more pronounced Al oxide band. Exposure to oxygen in the IR chamber at 50 °C for 24 h may facilitate additional strong interactions with the substrate.

This part showed a few important aspects of layer behaviour. Temperature increase either during preparation or storage does not significantly improve or alter the chemical interactions of MDI with native Al on a qualitative and quantitative basis. A few differences are observed however. Layer chemistry is accelerated and desorption of weakly attached MDI favoured.

The impact of temperature on the layer morphology as well as a similar study on Cu, which is much more reactive, would be of great interest but such study was not feasible due to lack of time.

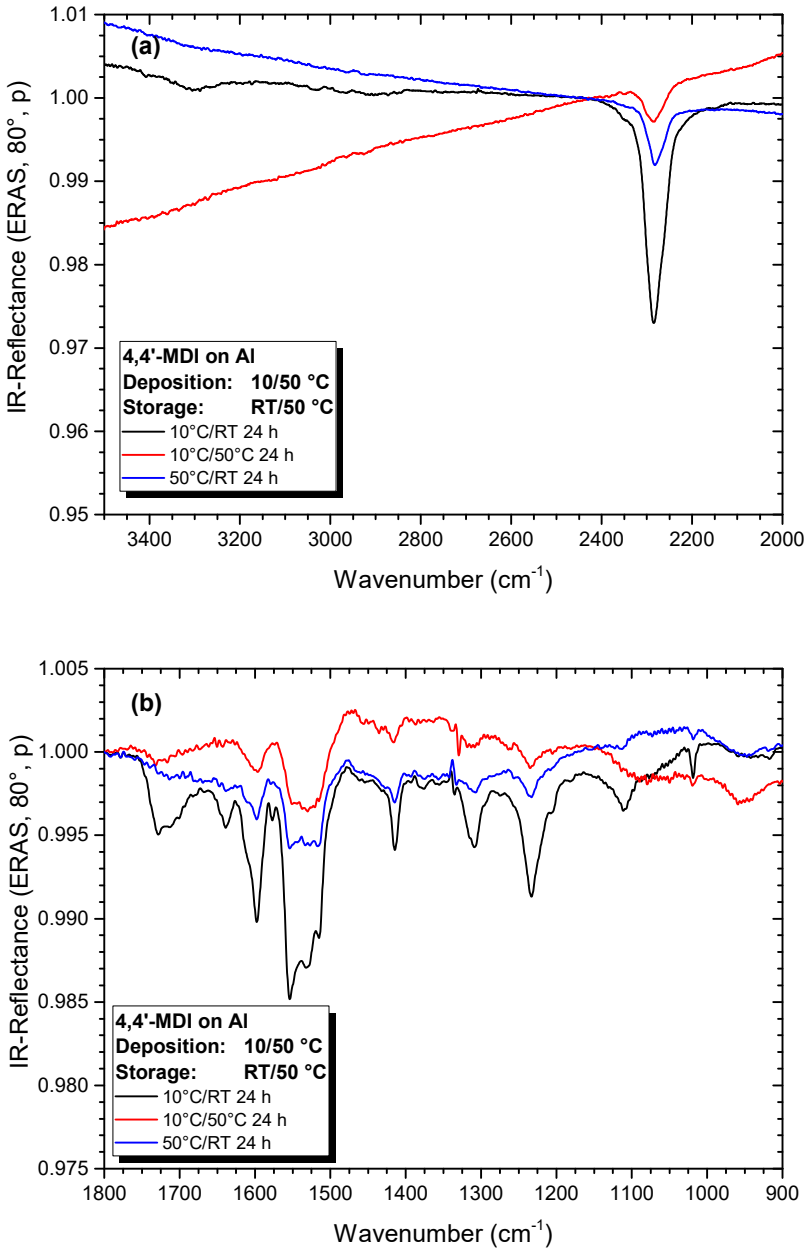

Fig. 6-50 Comparison of three 4,4'-MDI layers on native Al oxide deposited and stored at different temperatures after 24h. Deposition parameters: 500 mbar, 5 l/min. (a) 3500 – 2000 cm^{-1}, (b) 1800 – 900 cm^{-1}. Black line – deposited at 10 °C and stored at RT; red line – deposited at 10 °C and stored at 50 °C; blue line – deposited at 50 °C and stored at RT.

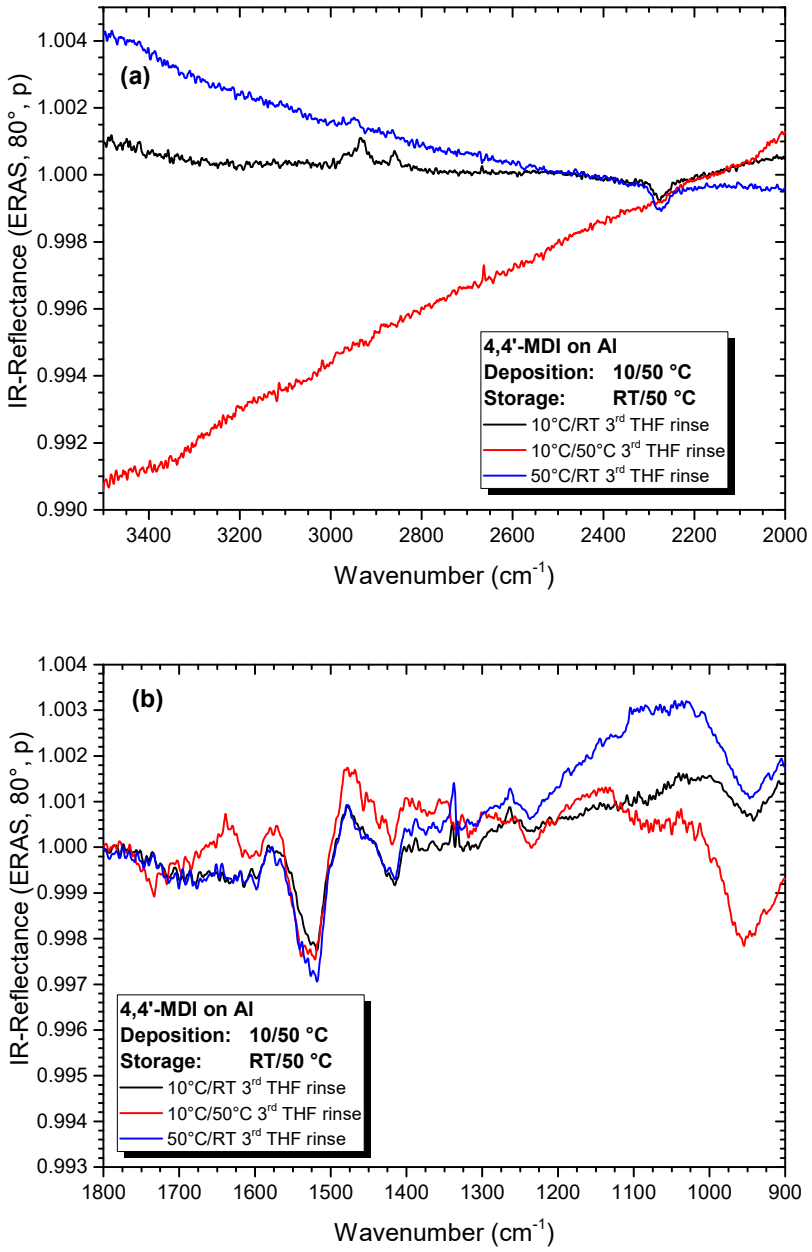

Fig. 6-51 Comparison of three 4,4'-MDI layers on native Al deposited and stored at different temperatures. Black line – deposition at 10 °C, stored at RT; red line – deposition at 10 °C, stored at 50 °C and blue line – deposition at 50 °C, stored at RT.RT. IR-ERA spectra after the 3rd THF rinse. (a) 3500 – 2000 cm^{-1}, (b) 1800 – 900 cm^{-1}.

6.5.4 Intermediate conclusion

From the study of thin 4,4'-MDI layers on native Al and Cu oxide some conclusions can be drawn. The behaviour of this monomer is schematically illustrated in Fig. 6-52 and Fig. 6-53. First, the isocyanate easily adsorbs on both native oxides. Using low deposition temperatures (T_{Sample} < 50 °C) no MDI monolayers are achieved as adsorption is not self-limited. Significant desorption is not verified after deposition and thus intermolecular forces are stronger than for the polyols. Furthermore, MDI present in the pipes continues to adsorb over time leading to ongoing layer growth.

Subsequent storage at RT does not indicate any significant desorption of MDI. Moreover decomposition of the isocyanate molecule is not observed.

Second, during storage MDI undergoes two reactions on both metals in a similar way. In the IR spectra, the reaction products result in metal specific features. Reaction with adsorbed water leads to the formation of urea dimers (Fig. 6-52b – cyan molecules). This reaction is fast in the first 10 h but then continues slowly up to 40 h. The amount of formed urea species depends on the quantity of deposited MDI. Hence, urea formation stops although not all adsorbed water molecules have reacted. It is recalled that water molecules also undergo interactions with the substrate and they need to be overcome in order to react with NCO. Water present in the air does not play a significant role here. This finding confirms previous studies [7]. MDI also undergoes strong interactions with the amorphous metal oxide/hydroxide layers resulting in urethane-like linkages (Fig. 6-52b – green molecules). On Al oxide, this type of interaction is independent of deposited MDI quantity. On Cu oxide, more interaction links form when thicker MDI layers are prepared. The cause of that was not identified. Hence, from this complex interplay the substrate itself including its adsorbed species should be considered as an active reaction partner.

Third, non-uniform deposits are obtained on both metals. Morphology is metal specific. The surface is first covered completely with organic material. MDI that continues to adsorb forms a patchy island-like deposit on top.

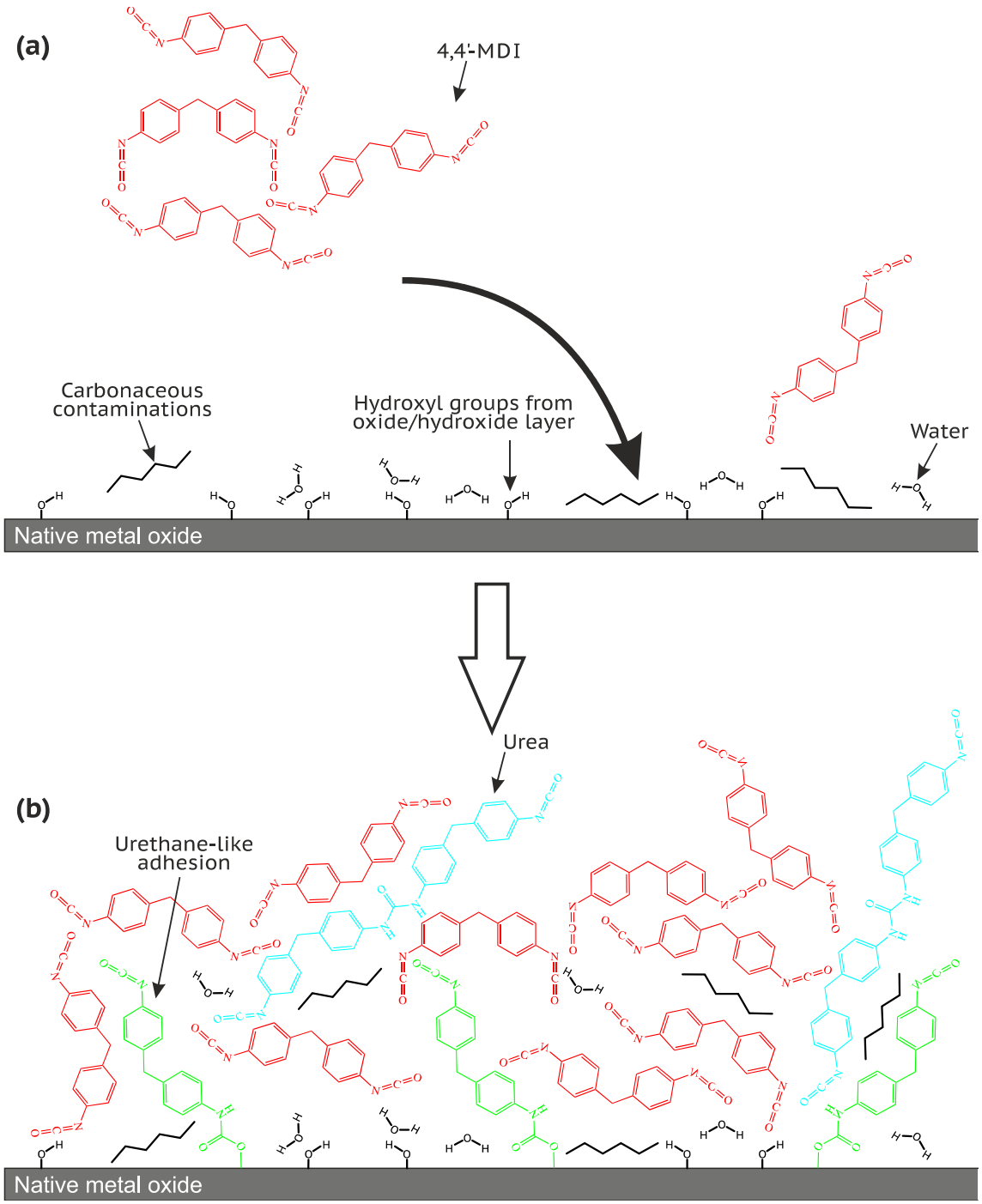

Fig. 6-52 Schematic representation of the behaviour of 4,4'-MDI deposits. (a) Deposition step of the monomer inside the MLD on native metal substrate. (b) Achieved MDI layer after deposition has stopped. Formation of urea (cyan) and urethane-like adhesive interactions (green). MDI tends to replace the carbonaceous contamination.

Fourth, THF rinses remove all weakly adsorbed MDI molecules (Fig. 6-53a – red molecules) as well as the urea dimers (cyan molecules). Hence, urea mainly forms in the physisorbed MDI layer and does not attach to the metal surface. The strongly attached MDI (green molecules) are not removed by the THF and form a stable MDI deposit (Fig. 6-53b).

The remaining deposit show metal specific features in the IR spectra (different intensity ratios and new metal specific bands) as different intermolecular interactions occur and specific molecular orientation patterns form. The same behaviour was found for solvent-based MDI layers (cf. [9, 10, 33] and section 6.1.2).

In forming the strong linkages to the native metal oxide surface MDI is capable to displace the adsorbed carbonaceous contaminations by desorption and subsequent dissolution in the MDI layer or by segregation on top of it. Modification of the amorphous oxide/hydroxide layers by the chemisorption but also by contact with oxygen during storage at dried air is observed too.

Increasing the substrate temperature to 50 °C during deposition or during storage does induce a different behaviour of the MDI deposits. First, physically adsorbed MDI (red molecules) rapidly desorbs and does not require a THF rinse. Second, urea species formation is accelerated and completed within 1 h. Due to parallel desorption of MDI, less urea is formed at 50 °C. A comparable stable MDI deposit can be obtained by deposition at 10 °C followed by storage at 50 °C. The MDI attached to the surface (green molecules) is only slightly modified by the higher temperature - the band shape of only some bands is different.

Higher temperature and contact to oxygen lead to a much larger modification of the Al oxide compared to layers stored at RT but does not hamper the adhesion of MDI. It is even slightly improved.

The isocyanate band is quite weak in the remaining stable MDI deposit especially on Al. In some experiments the corresponding band is nearly invisible. Hence, the ability to react with alcohol remains unproven at this stage but is of crucial interest for the polymerisation.

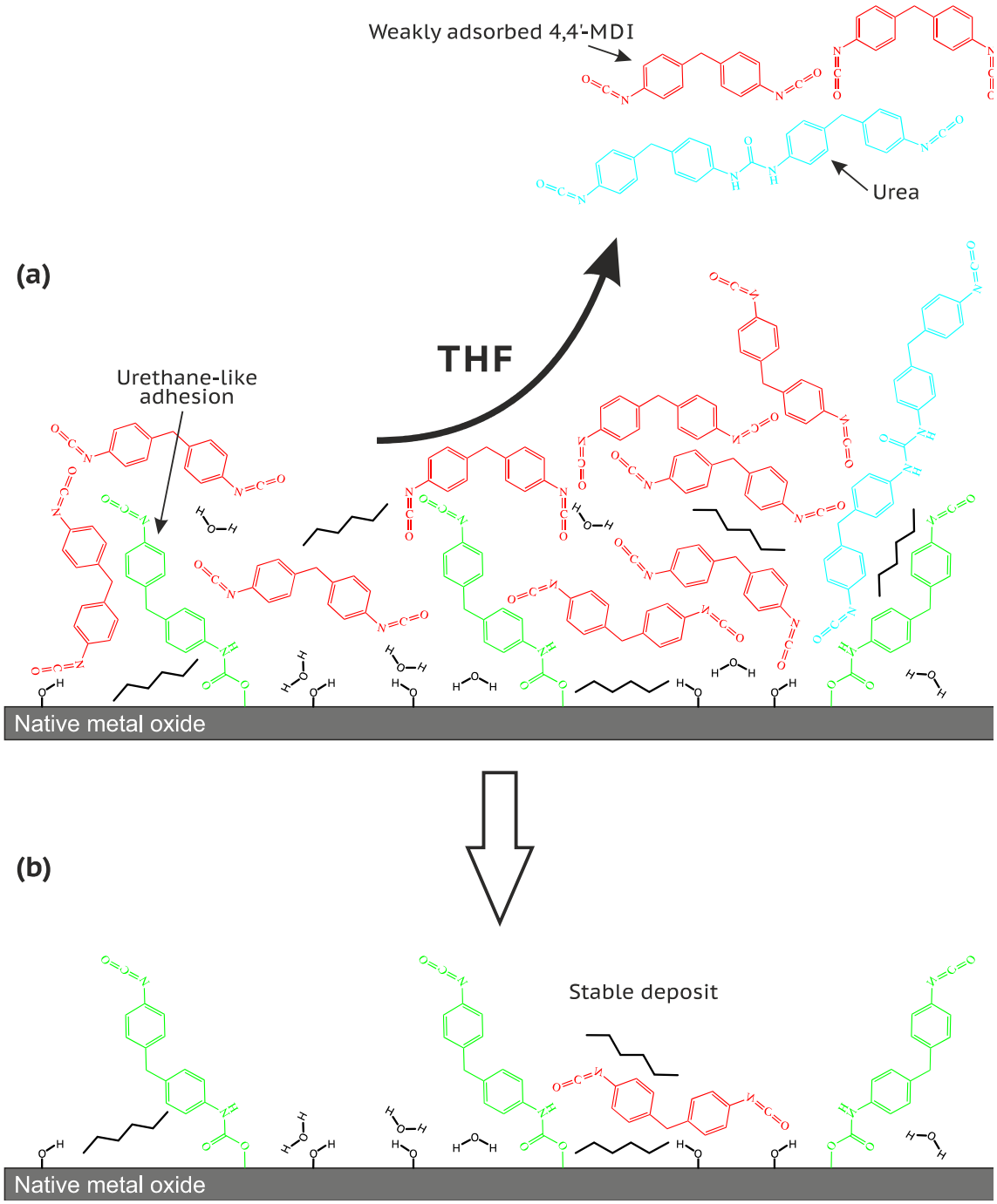

Fig. 6-53 Schematic representation of the behaviour of 4,4'-MDI deposits. (a) Effect of THF rinses. Removal of weakly adsorbed MDI and urea. (b) Stable MDI deposit as result of THF rinse.

6.6 Conclusions

The characterisation of thin monomer deposits from the gas phase onto native metal substrates provided valuable information required for the subsequent thin layer polymer preparation. Intermediate conclusions were made throughout this chapter. This conclusion summarises the most important statements.

The MLD deposition cycle combined with storage of samples in dried air (IR chamber) revealed a fluctuation of carbonaceous contaminations. During each step (MLD deposition and storage, THF rinses), some contamination re-adsorbs onto the samples. Deposited monomers have to displace some of that contamination (competitive adsorption) before they can adhere at the native oxide/hydroxide layer of the substrate.

The deposition and behaviour of the alcohols and the isocyanate are much more complex than the simplified MLD concept discussed in literature. First, none of the monomers forms a monolayer on their own under the studied conditions. Thus, self-limiting adsorption does not take place because omnipresent intermolecular interactions are not negligible. At this point the literature model is oversimplified as intermolecular forces are just considered too weak.

Once the layer formed alcohols and isocyanate behave much different. alcohols do only weakly physically interact with the native Al and Cu oxide surfaces and they desorb nearly completely from the surface either inside the MLD or during storage at RT. Strong chemical links with the metals are not detected. Isocyanates on the other hand do not desorb at RT. Their intermolecular interactions are much stronger than for the alcohols and require elevated temperatures (> 50 °C) for desorption. Contrary to the alcohols one part of the MDI is capable to undergo strong adhesive interactions in the form of urethane-like bonds with the metals. These interactions withstand THF rinses and higher deposition or storage temperatures. They form a *stable MDI deposit*. The other part of the MDI is only physically attached to the first layer and is easily removed by THF or higher temperatures.

Part of the physically adsorbed isocyanate is capable to react with the adsorbed water molecules and forms urea species which do not attach to the native metal surfaces too. Hence MDI displaces adsorbed water from the surface. The complex behaviour demonstrates that the substrate should not be considered as an inert support for the layer but as a chemically active reaction partner for layer formation. This is verified by the appearance of substrate specific bands in the IR spectra.

Scanning force microscopy revealed that the MDI deposits are compact but non-uniform. This produces a further challenge for the subsequent polymer formation. Analysis of the strong deposit using SFM was unable to identify a difference compared to virgin substrates.

Preparation of all these deposits also showed that monomers present inside the MLD apparatus continue to adsorb on the substrates in non-deposition mode as they desorb from the pipes. This has to be considered for the sequential monomer deposition. Further work should aim to introduce appropriate technical modifications on the MLD system in order to avoid or reduce this undesirable effect. For example gate valves placed at the entrance of the reactor chamber could isolate the reactor chamber from the evaporation cells.

In the next chapter alcohols and isocyanates are deposited sequentially in order to form polyurethane layers.

7 Thin polymer deposits

Now that the behaviour of each monomer deposit has been studied in detail, alcohol and isocyanate are brought together in order to form urethane linkages. Due to the complex and different deposition behaviour of both monomers it is first necessary to discuss the consequences and possible limitations that this can bring for the polymer formation with regard to the original MLD model in literature. From here, different paths are followed in order to understand the behaviour of thin polymer layer formation. Layer performance is discussed with regard of urethane conversion, topography, and stability against THF rinses. Finally, as for the monomers, a deposition model can be proposed. Student experimental work [69, 118, 161] made under my supervision provided substantial contributions to this chapter.

7.1 Implications from the monomer behaviour

Through the complex behaviour of each monomer, several points have to be considered before preparing thin polymer layers by sequential monomer deposition.

First, as only isocyanates undergo strong interactions with both metals while polyols experience only weak physical interactions, the layer growth should start with an isocyanate deposit. This allows for strong interactions with the metal from the start. If isocyanate would be deposited on top of the alcohol, it would have to penetrate the alcohol for adhesive bonding at the metal surface, and it is not necessarily evident that this will happen.

Second, the isocyanate deposits showed two types of interactions. A weak physically adsorbed bulk-like layer on top of a ‘stable MDI deposit’ consisting of isocyanate strongly attached to the metal oxides. In order to form a sustainable layer the alcohol must be capable to form urethane linkages with the strongly attached MDI molecules. If polymerisation would take place only in the bulk-like layer, the formed polyurethane would not bind chemically to the substrate. Hence, reaction of alcohol deposits with the stable MDI deposit has to be checked first. Furthermore, as the NCO band is very weak in this case, this point is crucial in order to validate if polyurethanes are feasible via MLD.

The quite rapid desorption of the alcohols is a further obstacle as chemical reactions are not instantaneous and, due to increased confinement in a thin layer, both monomers require some extra time to meet each other for reaction - as shown by the slow urea formation. Even at 50 °C, the reaction requires one hour to be mostly accomplished. Hence, a bigger amount of alcohol has to be deposited in order to enable a sufficient part of it to react with isocyanate groups while the rest of the alcohol desorbs. On top of the MDI, alcohol establishes interactions with isocyanate that are different from the interactions of alcohol to the metal. Hence, desorption behaviour will be modified as well.

Favourable interactions between alcohol and isocyanate monomers would result in slower desorption of alcohol and hence allow for more conversion into urethane. However, if alcohol interacts weaker with isocyanate than with the metal oxides or if the NCO-metal interactions become weakened too, molecules would desorb easier.

Characterisation of monomer deposits also showed that monolayers are not prepared under the applied conditions. Hence, after the verification of the reactivity of the stable 4,4'-MDI deposit with alcohols, experiments should be extended to thicker MDI deposits. This creates two further obstacles. First, monomers from each layer must possess enough mobility to mix in order to form a polymer layer. In particular, the alcohol molecules must be able to reach strongly adsorbed MDI species at the metal interface. Second, the amounts of monomers and thus their mixing ratio will have major impact on the formed molecules. If for example more isocyanate is deposited than alcohol, all OH groups will react with an NCO group and form trimers. At that stage, reaction stops and neither a polymer nor a network is formed. This step allows for a different MLD approach taking into account the observations made for the monomer deposits. Instead of depositing a monolayer of each monomer, thicker layers are deposited which ideally react to a thick polymer layer.

Another important aspect cannot be neglected - the observed non-homogeneity of the deposits. How does this affect the further monomer deposits and reaction? Is the topography preserved or completely changed? These questions have to be answered to understand the layer behaviour and performance.

Last but not least, as shown with the 4,4'-MDI layers, elevated temperatures during deposition and/or storage induce faster reactions. The temperature influence on the polymerisation and hence on the stability of the obtained layer is relevant too.

Finally, stable polyurethane layers must form from the two-layer monomer deposition before further monomer layers can be deposited on top in order to produce thicker layers that progressively polymerise.

7.2 Polyol deposit on top of a stable MDI deposit

In this section polyols are deposited onto the stable MDI deposit[43] in order to verify if the MDI molecules are capable to react with alcohol functionalities. This reaction is crucial in order to form polyurethane tethered to the surface. It is only demonstrated on Al. The stable MDI deposit can be prepared in different ways: by THF rinses of a thick MDI layer (cf. section 6.5.2), or by elevated temperature during deposition or storage (cf. section 6.5.3). In previous work (cf. section 6.1.2 and [8, 10, 33, 36]), stable MDI deposits were obtained by adsorption from a diluted solution of MDI in THF. In order to reduce preparation time of these samples it was decided to prepare them from solution in this section.

In section 7.2.1, preparation of the stable MDI deposits and comparison with MLD deposits are discussed in detail. Then, the stable MDI deposits are exposed to highly diluted triol vapour in the MLD setup in order to adsorb only a few molecules (in part 7.2.2). Reaction of the isocyanates is monitored with IR. Subsequently, stability against THF is checked. Finally, thicker triol layers are deposited on the stable MDI deposits (part 7.2.3). Higher triol contents allow further reaction with isocyanates as triol is longer in contact with the MDI. Furthermore it can be checked if triol can provoke desorption of the strongly attached MDI.

7.2.1 Stable MDI deposits as prepared from solution

Solution deposits are prepared as detailed in section 3.2.2.1. Steps 1 to 3 remain unchanged. In step 4, the diluted 4,4'-MDI - THF solution is applied onto the Al substrate at RT. In order to reduce the amount of the physisorbed MDI, its concentration is reduced to $1.17 \cdot 10^{-2}$ mol/l (0.1752 g 4,4'-MDI per 60 ml THF). Contact time of the MDI solution is 3 minutes.

Then this deposit is rinsed once with pure THF (blue line in Fig. 7-1). All characteristic MDI bands are present as well as specific weak urea and urethane-like bands. This result is in agreement with previous work and with the MDI layers prepared by MLD.

A stable MDI deposit is obtained by another THF rinse (cf. step 5 in section 3.2.2.1). It is performed right after the IR measurement. The resulting IR spectrum is shown as black line in Fig. 7-1. As discussed in section 6.5.2, bulk physisorbed MDI and urea compounds are removed by the solvent and the remaining strongly adsorbed MDI species establish urethane-like interactions with the native metal surface (bands marked in red).

[43] Reminder : The stable MDI deposit is defined as the layer of MDI molecules that are strongly attached to the native metal surfaces and withstand further THF rinses.

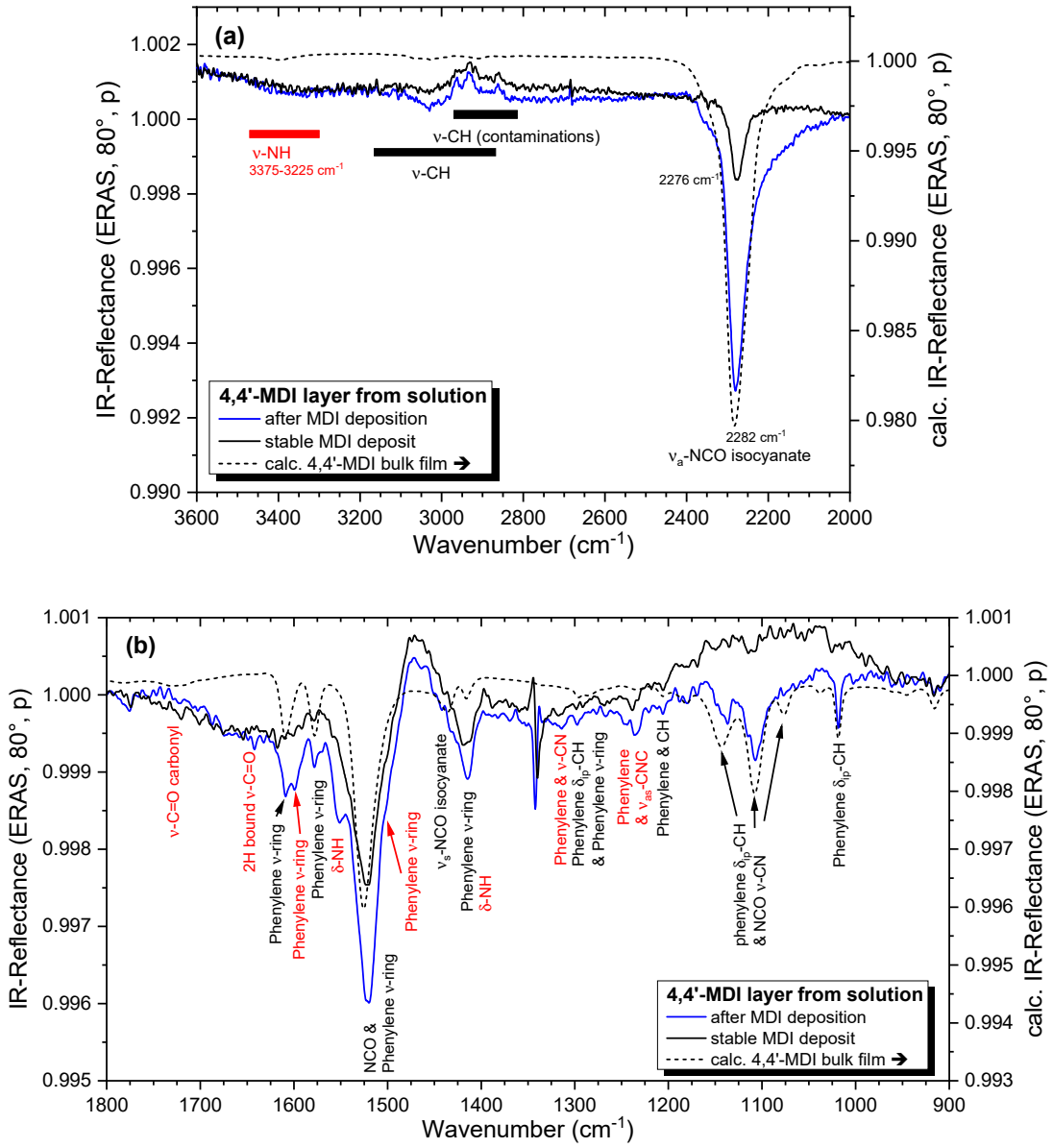

Fig. 7-1 IR-ERA spectra of a 4,4'-MDI layer after solvent deposition (blue) and of a stable 4,4'-MDI deposit (black, after one THF rinse). (a) 3600 – 2000 cm^{-1}, (b) 1800 – 900 cm^{-1}.

Fig. 7-2 compares the spectra of the stable deposit prepared from MLD and from solution deposition. All characteristic bands are present and show identical position and shape. Band intensity is almost the same for all bands except of two. The isocyanate band (2277 cm^{-1}) is by about 1.5 ‰weaker in the layer prepared by MLD. That difference is reproducible. This may originate from the different history of both layers. The MLD layer was prepared at 10 °C and stored at RT for 24 h before being rinsed three times with THF. The layer prepared from solution was not stored for 24 h. During storage, some MDI can react with adsorbed water and form minute amounts of

urea species that are removed by THF. According to [8, 10], the isocyanate band loses some intensity with each THF rinse when layers are prepared from solution.

That loss is either due to removal of a few MDI molecules by the strong solvent or to urea formation. In addition, fluctuations are observed for the intensity of the isocyanate band on MLD layers while band intensities are equal in the fingerprint region. Hence, the small intensity difference can be neglected.

The Al-oxide band at 950 cm^{-1} is second one showing a difference: it is larger for the MLD layer as the substrate continued to oxidise during the longer sample storage in dried air.

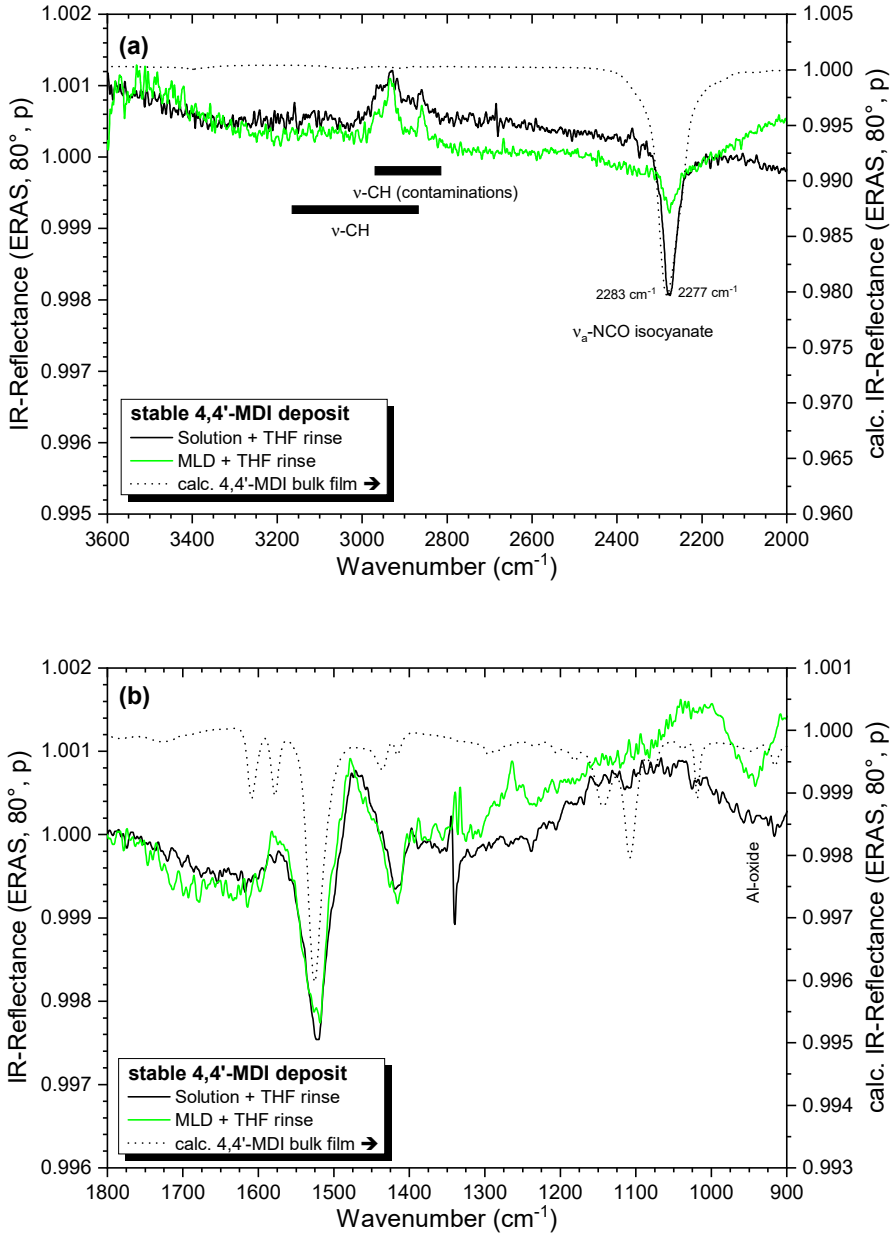

Fig. 7-2 Comparison of two stable 4,4'-MDI deposits as prepared by solvent deposition (black) at RT or by MLD at 10 °C (green). (a) 3600 – 2000 cm^{-1}, (b) 1800 – 900 cm^{-1}.

Despite these little differences, both deposits can be considered as equal and hence the deposit prepared from solution is as well suitable for the polymerisation study with triol.

7.2.2 Deposition of few triol molecules on the stable MDI deposit

As next step, triol is offered to the stable MDI deposit. In a first stage, only few triol molecules are deposited because displacement of the MDI adsorbate due to excessive amounts of alcohol cannot be excluded *a priori*. Furthermore, the weak spectrum of few triol molecules will not mask the weak MDI bands. Triol is chosen because it desorbs much slower than DPG. Therefore, the MLD deposition is slightly modified as well. During the cleaning stage of the MLD system (section 4.4 – step 2), all gate valves of the evaporation cell for the triol are closed without cleaning. Hence, from a previous deposition, little triol remains trapped in the cell. The isocyanate cell is properly cleaned by purging. Now, the substrate with the stable MDI deposit is transferred into the reaction chamber and tempered at 10 °C during the stabilisation step. For triol deposition (section 4.4 – step 4), the gate valves of the almost empty triol evaporation cell are opened and thus the remaining few triol molecules flow to the sample for adsorption at T_{sample} = 10 °C. The MLD process is stopped after 1 h. After transfer into the IR chamber, the sample is monitored at T_{store} = RT for 24 h. Fig. 7-3 and Fig. 7-4 show the IR spectra before (black) and after (red) triol exposure as well as after 24 h of storage (green).

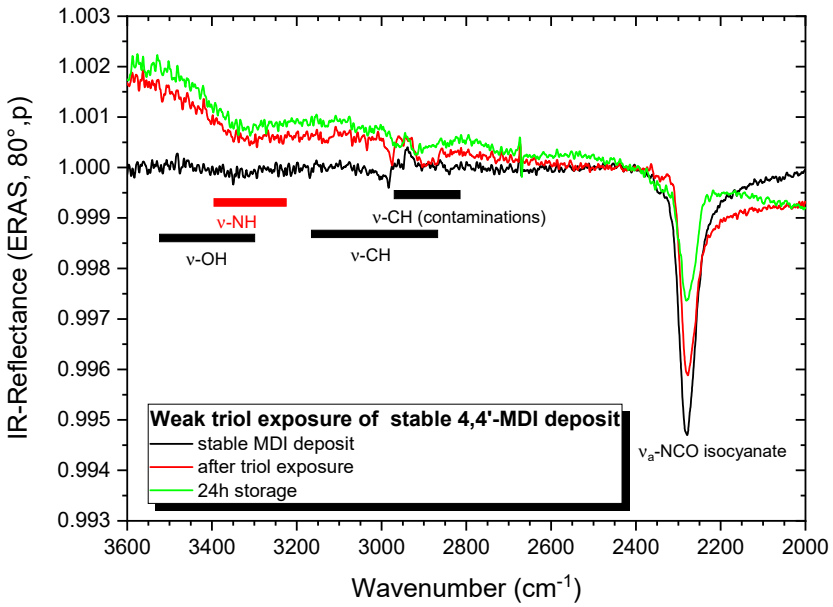

Fig. 7-3 IR-ERA spectra of a stable 4,4'-MDI deposit prepared from solvent deposition before (black line) and after (red line) weak triol exposure in the MLD (500 mbar, T_{sample} = 10 °C, 5 l/min N_2). The obtained layer is stored in dried air at RT for 24 h (green line). 3600 – 2000 cm^{-1}. New bands are assigned in red.

For the initial stable MDI deposit as a reference, the upper spectral range only shows some CH stretches from carbonaceous contaminations and the isocyanate band (2277 cm^{-1}) (Fig. 7-3, black spectrum). After exposure of the sample to triol (red spectrum), the isocyanate band slightly dropped in intensity and a wide band appears between 3400 and 3200 cm^{-1}. In this region, not only the ν-OH of the triol are located but the ν-NH of urethane and urea species as well.

The fingerprint region (Fig. 7-4) is much different. New bands (marked in red) appear after exposure to triol. They include carbonyl stretches (1750 – 1640 cm^{-1}), phenylene ring stretches (1600, 1415 cm^{-1}), N-H deformations (1550, 1415 cm^{-1}) and various carbon-nitrogen vibrations (1300, 1215 cm^{-1}). Another weak new band appears at 1378 cm^{-1}. This band, which not present in the stable MDI deposit or in layers with urea groups, corresponds to the symmetric CH_3 deformation also known as umbrella mode. As CH_3 groups only exist in the triol, this band proves adsorption of some triol. The wide band at 1100 cm^{-1} is coined by bands from the MDI, but it may contain ether stretches from the triol as well. Hence, part of the wide band at 3300 cm^{-1} may also result from the triol OH stretch.

In conclusion, triol adsorbed onto the MDI deposit. The new bands correspond either to urea groups as the isocyanates are still able to form urea species during the storage and/or to urethane species. Previous studies (cf. section 6.1.2) showed however, that urethane species possess very similar bands to urea species. Hence, urethane formation is neither proven nor refuted yet. It is recalled that, due to the confinement in the thin layer, functional groups require additional time to meet each other in order to react. So maybe urethane could be discriminated after additional 24 h of reaction.

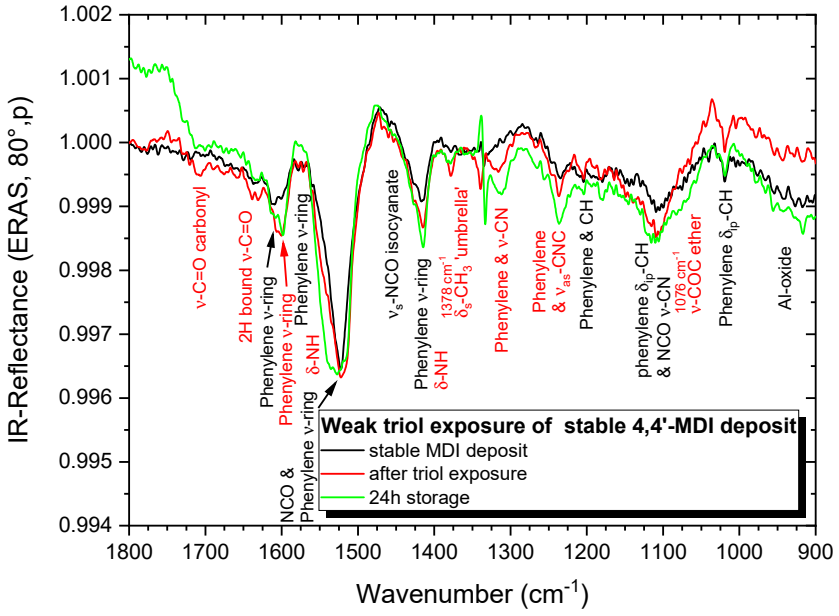

Fig. 7-4 IR-ERA spectra of a stable 4,4'-MDI deposit prepared from solvent deposition before (black line) and after (red line) weak triol exposure in the MLD apparatus (500 mbar, T_{sample} = 10 °C, 5 l/min N_2). The resulting layer is stored in dried air (green line) at RT for 24 h. 1800 – 900 cm^{-1}. New bands are assigned in red.

As seen in Fig. 7-3 and Fig. 7-4, a few things happen during 24 h of storage. The wide band at 3300 cm^{-1} does not change. The isocyanate band continued losing some intensity, i.e. further NCO groups are consumed. In the fingerprint region, all new bands continue to grow. In particular, a wide band forms in the carbonyl region, and the band at 1525 cm^{-1} widens towards higher wavenumbers. Moreover, the CH_3 umbrella deformation (1378 cm^{-1}) slightly loses intensity. This is explained by desorption of a few triol molecules. However, the band remains in the spectrum, and so most triol stays in the layer. All other bands grow as further species are formed. A wide band forms at 1078 cm^{-1}. It may originate from ether groups in vicinity of urethane entity because ether vibrations change upon reaction of the OH into a urethane group [7, 11]. That is a first indication that the strongly adsorbed MDI reacts with alcohol and forms urethane links.

The layer is then rinsed three times with THF. Fig. 7-5 provides the corresponding spectra. Both the band at 3300 cm^{-1} and the isocyanate band lose intensity during the 1st rinse (red line). That holds for the fingerprint region as well, including the newly formed bands. Hence, few molecules are removed by the THF but many are left in the layer. The carbonyl region is somewhat modified, but, from 1625 cm^{-1} downwards, band shape is not significantly changed. The CH_3 umbrella deformation (1378 cm^{-1}) is still strong after the 1st rinse. So THF did not remove all triol. Thus, it is concluded that triol formed urethane links with isocyanate groups. The presence of ether groups is more difficult to see as the region undergoes significant base line changes. The 2nd and 3rd THF rinses do not bring new significant changes to the layer.

The decrease of the 3300 cm^{-1} band and the isocyanate band indicate that another few unreacted triols and some isocyanate species were removed.

In summary, at RT the final adsorbate is composed of the strongly adsorbed MDI, on which part of the isocyanates reacted with the triol and formed urethane groups. Probably urethane *dimers* dominate because a triol molecule loses a lot of mobility after first reaction with an MDI. Hence, as the primary requirement, a successful preparation of PU layers by MLD is achieved. Formation of a few urea species is not excluded as they exhibit the same bands, except the CH_3 umbrella band of course.[44] Furthermore, these experiments show that the isocyanates prefer to react with the alcohol even though adsorbed water is present in the layer. This allows deposition on technically relevant substrate surfaces without expensive and complex preparation steps in ultra-high vacuum.

[44] Urea formation could be detected by a similar experiment without any deposition of triol in a perfectly cleaned MLD apparatus.

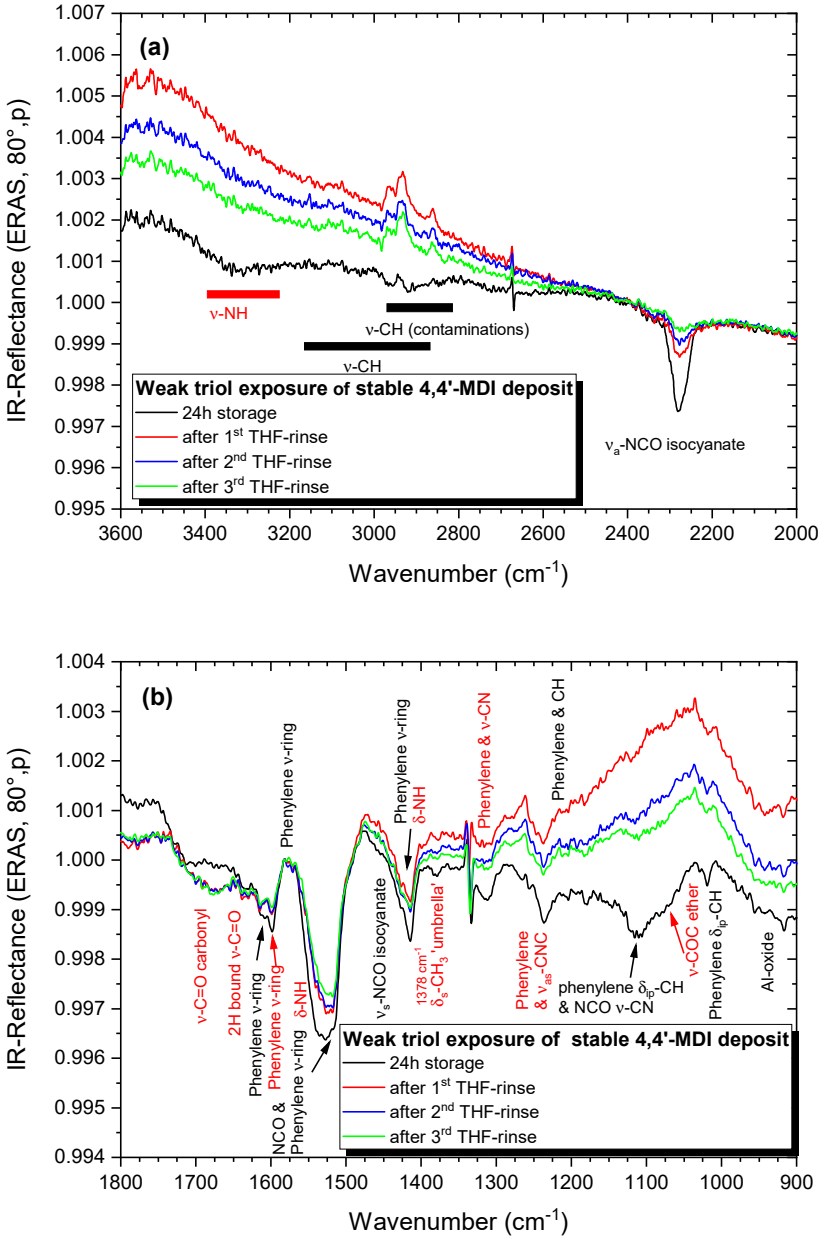

Fig. 7-5 Effect of three THF rinses (coloured lines) on the previously prepared layer after 24 h of storage (black line). Band assignment refers to the layer prior rinsing. (a) 3600 – 2000 cm^{-1}, (b) 1800 – 900 cm^{-1}.

7.2.3 Higher amounts of triol onto the MDI deposit

Weak triol exposure showed that some isocyanates remain, and what spectral regions depict urethane formation. Now, much more triol is offered. This should help to verify if attached isocyanates can be displaced from the surface, and to check if a better conversion of the isocyanate groups can be achieved. As in the previous section, stable MDI deposits are prepared, but then 12 nm of triol is deposited slowly in the MLD during 1 h. The same deposition parameters are used. After deposition, samples are stored inside the IR spectrometer at RT for 24 h. Fig. 7-6 and Fig. 7-7 present the evolution of the spectra.

At 0 h (red spectrum), intense bands of triol (OH stretches, CH stretches and deformations, and very strong ether bands) dominate the spectrum. The ν-OH (3419 cm^{-1}) as well as the ether bands (1150 – 1050 cm^{-1}) are shifted to lower wavenumbers, as it was observed for sheer triol layers (cf. section 6.4.3). Band shape is the same as for bulk triol.

MDI bands from the stable MDI deposit (cf. black spectrum) have changed upon triol deposition. The isocyanate band (2277 cm^{-1}) almost vanished because NCO groups reacted with the triol OH groups during deposition. The most characteristic band for the phenylene-isocyanate entities (1525 cm^{-1}) transformed into two bands (1543 cm^{-1} & 1512 cm^{-1}). As discussed above, additional new bands emerge: carbonyl stretches (1750 – 1650 cm^{-1}) and various phenylene ring stretches (1600, 1543, 1512, and 1414 cm^{-1}).

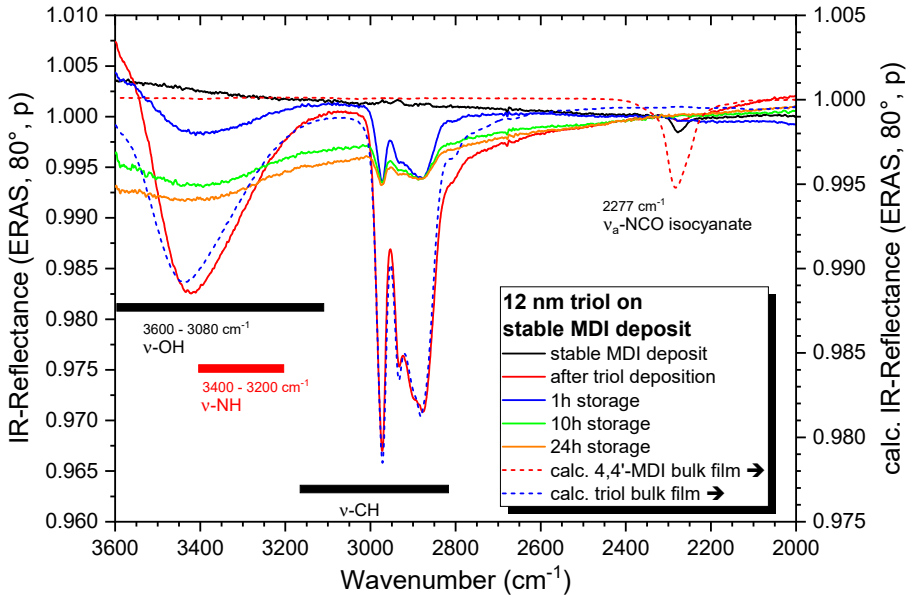

Fig. 7-6 IR-ERA spectra for 12 nm triol on top of a stable MDI layer on native Al during 24 h in dried air at RT. 3600 – 2000 cm^{-1}. Bands are assigned for the monomers (black) and for the new species (red). For qualitative comparison, the dashed lines represent calculated bulk spectra of the monomers.

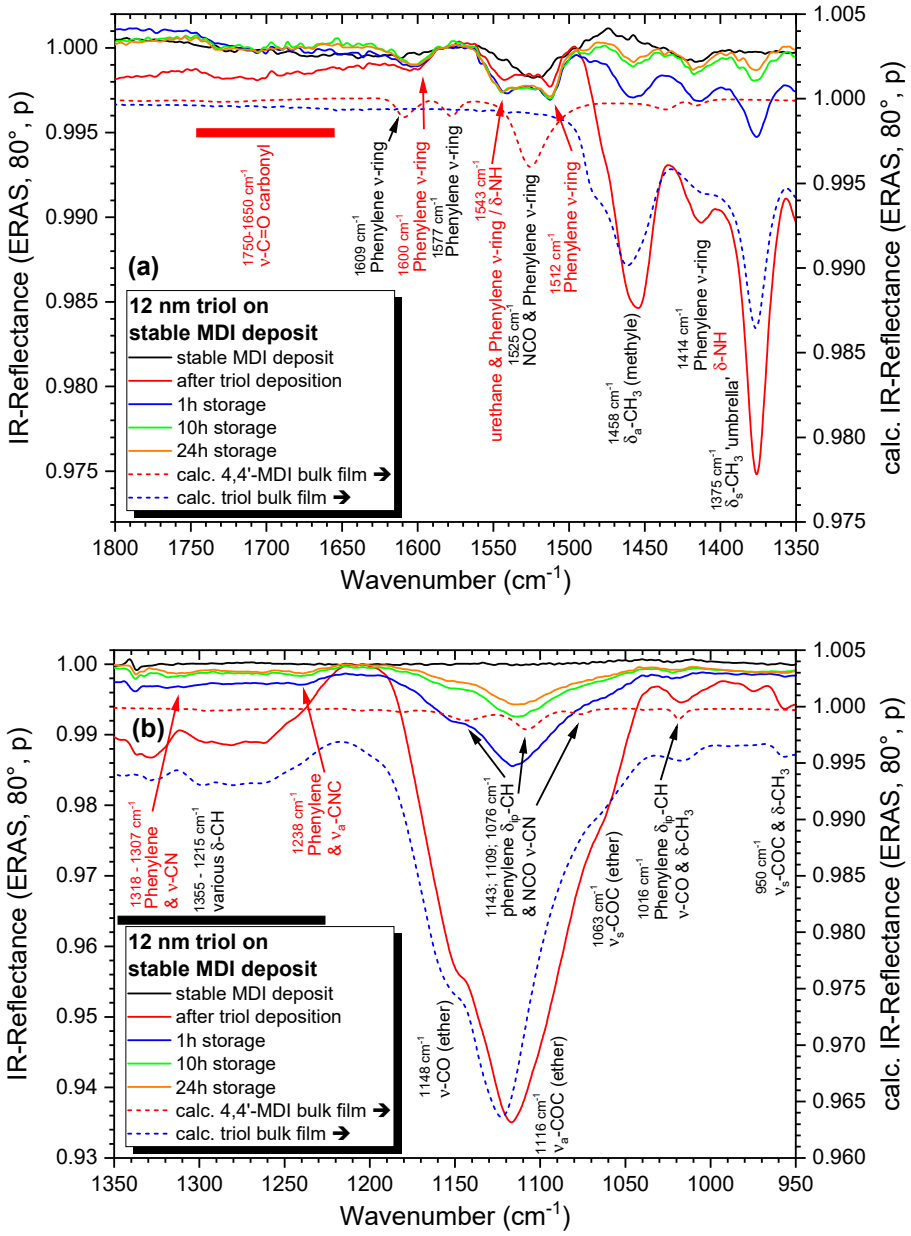

Fig. 7-7 IR-ERA spectra for 12 nm triol on top of a stable MDI layer on native Al during 24 h in dried air at RT. Bands are assigned for the monomers (black) and for the new species (red). For qualitative comparison, the dashed lines represent calculated bulk spectra of the monomers. (a) 1800 – 1350 cm^{-1}, (b) 1350 - 950 cm^{-1}.

The carbon-nitrogen stretches (1315 and 1238 cm^{-1}) are not visible now as they are superimposed by various CH deformations from the triol. Nevertheless, all these bands are attributed to urethane formation.

During storage at RT, intensity loss continues up to 10 h. Sheer 12 nm triol layers desorb within 5 h. Thus, triol molecules interact stronger with the stable MDI deposit than with the bare native Al substrate. The isocyanate band disappears between 1 and 10 h of storage while, simultaneously, the urethane bands grow. Hence, triol bands strongly lose intensity as reaction and desorption take place simultaneously.

After 10 h, no further evolution is observed in the spectra. The large band between 3600 and 3080 cm^{-1} which comprises OH stretches and NH stretches, as well as the other characteristic triol bands (3000 – 2800, 1458, 1375 and 1150 – 1050 cm^{-1}) indicate that triol molecules have been integrated into the layer, but the OH-groups were not fully consumed. The OH residue is quite natural: the OH groups sit at the ends of the three short branches of the triol molecule, and both the stiffness of that molecule and the random spatial distribution of NCO groups in the immobilised MDI will hamper full reaction to urethane.[45] In conclusion, as it was deduced for the layers formed by weak triol exposure, some triol molecules formed urethane groups with the MDI.

After 24 h, triol desorption is complete. For comparison, Fig. 7-8 and Fig. 7-9 depict the spectra for this stage (red), for the stable MDI deposit before triol deposition (black), and for the layer prepared by weak triol exposure and stored for 24 h (green spectrum).

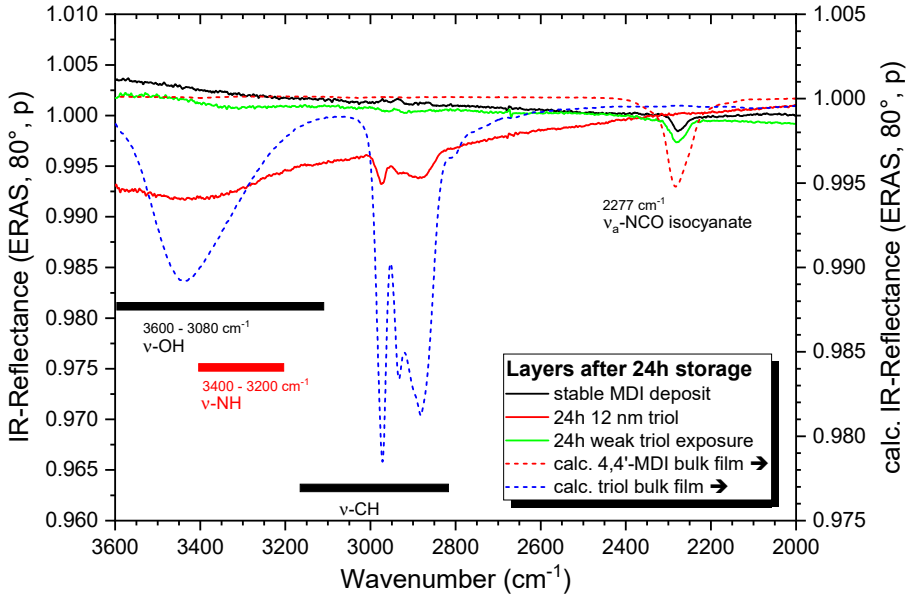

Fig. 7-8 Comparison of IR-ERA spectra of the stable MDI deposit (black) with 24 h stored layers obtained after 12 nm triol deposition (red) or after weak triol exposure (green). The dashed lines represent calculated bulk spectra of the monomers for qualitative comparison. 3600 – 2000 cm^{-1}.

[45] The MDI layer absorbs triol because it mixes with MDI. That solubility is caused by a favourable chemical potential compared to the state the triol molecules experience in the surrounding gas phase during MLD. In fact, chemical affinity to the NCO groups provides part of that driving force but physical interactions between triol and MDI will play their additional role. As described below, THF rinsing tests suggest that more triol could be absorbed than necessary for reaction with the NCO groups.

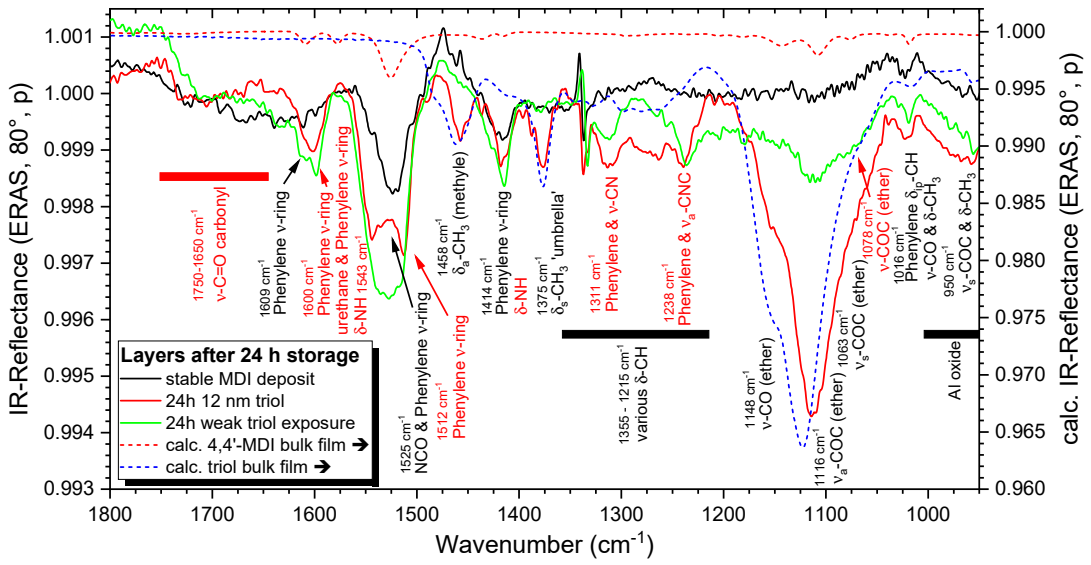

Fig. 7-9 Comparison of IR-ERA spectra of the stable MDI deposit (black) with 24 h stored layers obtained after 12 nm triol deposition (red) or weak triol exposure (green). The dashed lines represent calculated bulk spectra of the monomers for qualitative comparison. 1800 – 950 cm^{-1}.

Comparison of the layers with thick (red) or weak triol deposits (green), with the original stable MDI deposit as a reference, shows that characteristic triol bands (ν-OH/ν-NH, ν-CH, δ-CH and ν-COC) are easily identified, and they are much stronger in the thick layer. However, the wide ν-OH/ν-NH band (between 3600 and 3100 cm^{-1}) is found at different positions. In the layer with initially 12 nm triol, it is located at higher wavenumbers and thus exhibits a pronounced ν-OH character. In the layer with weak triol exposure, it appears at lower wavenumbers indicating a dominating ν-NH character. The NCO band (3100 cm^{-1}) is missing in the red spectrum while some isocyanate remains in the green one. This indicates that all NCO groups have reacted when exposed to enough triol[46].

The fingerprint region shows similarities and differences as well.
In both spectra (red & green), all the characteristic urethane bands are present. The shape of the carbonyl region looks a bit different, but measurements on a set of such layers revealed that this region is hard to reproduce as shape fluctuates for this wide band. A significant difference is found in the region from 1575 to 1475 cm^{-1} where three bands are expected: phenylene ν-ring & urethane and δ-NH – 1543 cm^{-1}, phenylene ν-ring & NCO – 1525 cm^{-1}, and phenylene ν-ring – 1512 cm^{-1}. The triol-rich layer (red spectrum) displays a doublet with peaks at 1544 and 1512 cm^{-1}. Obviously, the doublet is specific for the neighbourhood of a urethane group. Any small amount of residual isocyanate (1525 cm^{-1}) would be hidden between the two peaks.

[46] This means a 100 % *spectroscopic* conversion of the NCO groups. Due to the detection limit of the spectrometer, very few groups could be still present.

In the layer with little triol content (green spectrum), the doublet degenerates into a single wide band with the maximum at 1526 cm^{-1} because of the superposition of the two urethane-related peaks with a contribution from the peak at 1525 cm^{-1}, for the significant amount of isocyanate groups left in that layer.[47] Also, formation of urethane is proven by the two bands (1311 and 1238 cm^{-1}) visible in both layers. In the triol-rich layer (red spectrum), the remarkable intensity between these peaks is caused by CH deformation bands that appear here. In general, intensities of all urethane bands are comparable in both layers.
The ether region, as an unambiguous feature of the triol units, is significantly different for the two layers. In the red spectrum, intensity is high and shape is close to the corresponding band in physisorbed triol because more ether groups are present in the triol-rich layer. In the green spectrum, the ether band is weak as expected for a layer with little triol. Moreover, the band is shifted to lower wavenumbers for both layers, and this effect reveals that the ether groups are sensitive to the specific environment in the ultra-thin layers.

Now, the triol-rich layer is subjected to three THF rinses. This experiment checks for soluble triol species, and it tests the adsorption strength of the formed urethane molecules. The corresponding spectra are shown in Fig. 7-10 and Fig. 7-11.

As a result of the 1st THF rinse, intensity dropped in the CH stretch region and for the band at 3400 cm^{-1}, Fig. 7-10. A weak band at 3300 cm^{-1} remains and represents NH vibrations in urethane groups. Hence, urethane-containing molecules in the layer are, at least in part, able to resist the THF attack. Furthermore, drop of intensity and frequency shift prove that some OH groups are removed, and this is possible only if soluble, triol-containing molecules were present in the layer as well.

[47] It is recalled that this particular band is also characteristic for the MDI in the stable deposit – cf. black spectrum in Fig. 7-9.

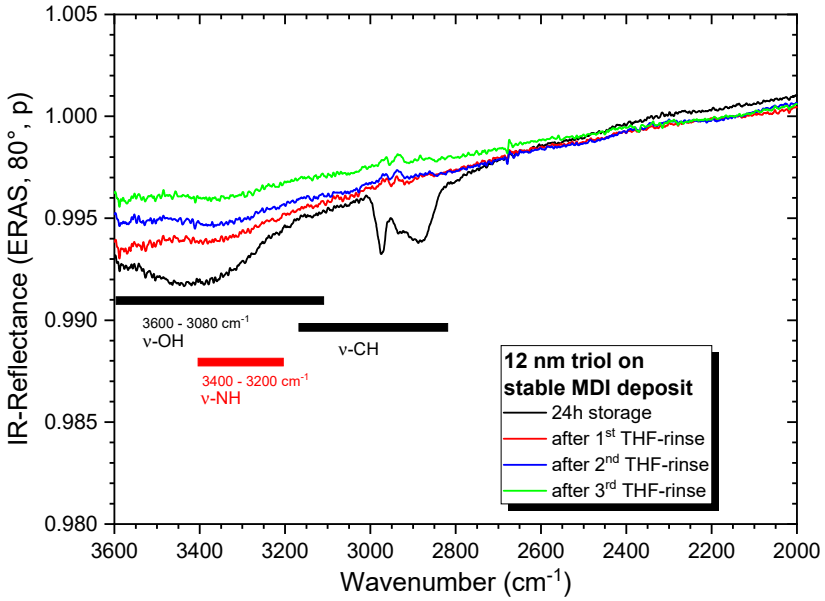

Fig. 7-10 Effect of three THF rinses (coloured spectra) on the prepared layer (deposition of 12 nm triol plus 24 h at RT, black line). Band assignment refers to the state prior to the THF rinses. 3600 – 2000 cm^{-1}.

The THF rinse also affected the fingerprint region in different ways, Fig. 7-11. First, the *carbonyl* region changes shape, but intensity stays almost constant. This finding attests the cross-linked polymeric state of a significant part of the layer and its good adhesive bonding to the native Al substrate. Moreover, the change of shape indicates that the THF introduces a temporary mobility that the layer molecules use for reconfiguration in space. Second, the *urethane* bands at 1603, 1512, 1414 (phenylene ring stretches), 1543 (phenylene ring stretch and δ-NH), 1311, and 1238 cm^{-1} (C-N stretches) as well as the bands attributed to *triol* at 1468, 1375, 1355-1215 (δ-CH), and 1150-1050 cm^{-1} (ether) drop in intensity. That simultaneous drop of intensities implicates interesting conclusions. THF does not just remove residual monomer triol but some of the urethane molecules are soluble as well. As a reminder, the stable MDI deposit was prepared by rinsing with THF and thus the remaining MDI molecules are adhesively bonded to the native Al substrate. That bond involves one of the isocyanate groups of the MDI molecule.

Now, after formation of urethane groups, which definitely prove the reaction of that bonded MDI with triol monomers, THF rinsing removes a part of these urethane species. That is possible only if some of the MDI molecules open their adhesive bond in favour of a reaction with an OH group of a triol molecule. Once that NCO group reacted, the resulting urethane species cannot re-establish adhesion to the surface and is removed by the solvent.

The weak umbrella deformation (1375 cm^{-1}) is not clearly seen as notable background noise is present in its region. The bands at 1603, 1525, 1414, 1311, 1238 cm^{-1} are common for strongly attached MDI, urea, and urethane as well. So they do not prove that formed urethane remain attached onto the surface.

That proof is given by the ν-NH stretch (3300 cm^{-1}) and the wide ether band at 1078 cm^{-1} that are specific for attached urethane.

No spectral change is observed for the 2nd and 3rd THF rinses. Therefore, the remaining molecules adhere well.

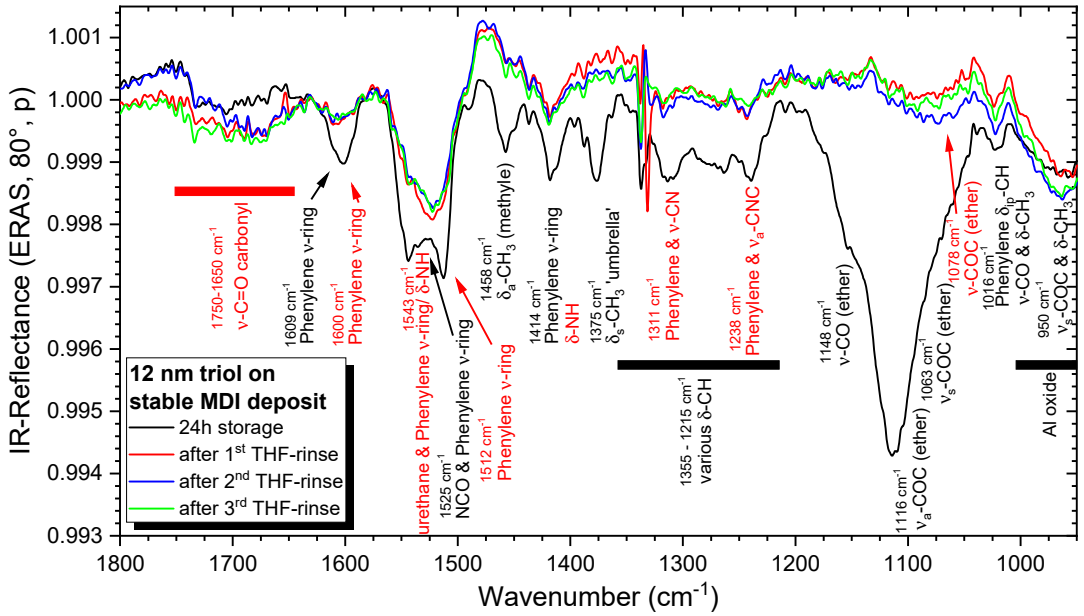

Fig. 7-11 Effect of three THF rinses (coloured lines) on the previously prepared layer (with 12 nm triol) after 24 h of storage (black line). Band assignment refers to the layer prior the THF rinses. 1800 – 950 cm^{-1}.

Fig. 7-12 shows the spectral differences of the adsorbates depending on the amount of deposited triol. The layer which was prepared with a thick triol deposit (Fig. 7-12a, green spectrum), shows a weak NH stretch which is not visible for the layer prepared by weak triol exposure (black spectrum). Opposite is the case for the isocyanate band. The fingerprint region (Fig. 7-12b) exhibits the same bands for both layers. Band shape is similar except for the carbonyl region. Band intensities differ between 1750 and 1150 cm^{-1} for the adsorbates, but these differences do not exceed the noise level. The umbrella deformation (1378 cm^{-1}) is too weak to be distinguished in the green spectrum. Hence, only the wide ether band proves the presence of urethane.

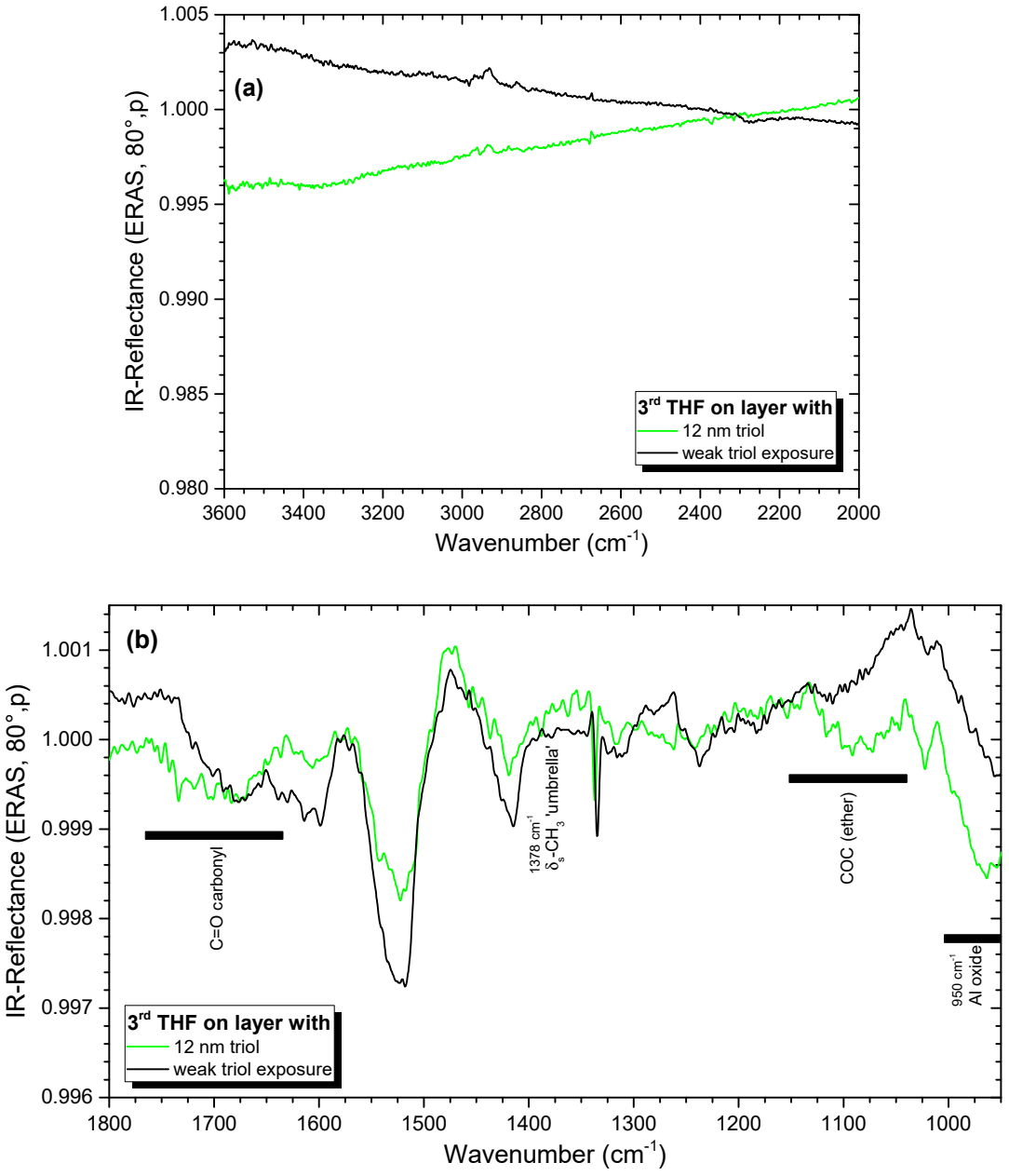

Fig. 7-12 Comparison of the IR-ERA spectra after the 3rd THF rinse of layers formed by thick (green) and weak (black) triol exposure onto a stable MDI deposit. (a) 3600 – 2000 cm^{-1}, (b) 1800 – 950 cm^{-1}.

7.2.4 Intermediate conclusion

In this section the ability of a stable 4,4'-MDI deposit to react with triol was verified. Preparing the strongly attached MDI deposit either by gas phase deposition or by adsorption from a diluted solution leads to comparable stable deposits after removal of weakly adsorbed MDI. This result confirms that in both cases MDI molecules adhere strongly to the metal surface in the same way. Hence, MDI is capable to displace carbonaceous contaminations from the surface.

Compared to triol adsorbates on native Al, desorption of triol slows down on the stable MDI deposit.

The reactivity of MDI in the stable deposit is tested by providing different amounts of triol and observing the chemical reactions that take place. In both cases (weak triol exposure – cf. section 7.2.2 and 12 nm triol layer – cf. section 7.2.3), the MDI adsorbate reacts with alcohols and forms urethane groups. Characteristic urethane bands appear in the IR spectra and isocyanate bands decrease in intensity. If more triol is offered, most isocyanate groups are consumed. Hence, even the strongly attached MDI is capable to react with alcohols. This requirement is fundamental for viable MLD layers that adhere to the substrate.

Stability of the prepared layers is tested by a sequence of THF rinses. They show that part of molecules are removed from the surface. Hence, reaction with alcohol destabilises adhesion of MDI to the surface this points to the complicated form of that adhesion mechanism.

After rinsing, remaining molecules contain urethane groups. Although urethane bands are very similar to urea bands but also to the bands emerging from the strong MDI-surface interactions the spectra provide various proof that urethane groups are formed and that some reacted species remain attached to the surface.

In the next part the impact of the deposition sequence and the type of polyol utilised on the urethane formation is analysed.

7.3 Impact of polyol and deposition sequence

As the previous section showed that alcohols are capable to react with a stable MDI deposit, the requirement for layers to be strongly attached to the substrate is given. As the next step, a second isocyanate monolayer should be precipitated on top of the reacted alcohol. Preparation of such a monolayer is not directly feasible with the MLD, but THF rinses could allow preparing it. However, this route will not necessarily provide results for a couple of reasons.
First, MLD of MDI with the currently used deposition parameters (cf. chapter 6) results in more than one monolayer. IR bands of such layer will superpose with the bands of the strongly adsorbed urethane molecules and hide their spectral features.
Second, application of THF rinses will remove non-attached MDI but will also affect the molecules below: molecular mobility and interdiffusion will increase or even desorption could be induced by the solvent. Interpretation of the IR features may then be difficult.
Third, as only few unreacted alcohol molecules are present in the strongly adsorbed layer, only few of the newly deposited isocyanates will remain attached. Their contribution to the IR spectrum is hard to discriminate. Weak changes in the bands could not only be due to newly formed urethanes, but also to changes in spatial arrangement of the already adsorbed molecules due to increased mobility during THF rinses. Further formation of urea would complicate interpretation as well.

Hence, it was decided to prepare *thicker* deposits of MDI and polyol one by one and to follow their reaction by IR spectroscopy.

As introduced in section 7.1, that preparation route poses its own challenges. Most important, molecular mobility must be good enough in both deposits to get them mixed on the substrate. Furthermore, for a stable layer, alcohol molecules must diffuse to and react with the adhesively bonded MDI molecules at the substrate.

The adsorption study of both monomers, but of the isocyanate in particular, showed that after stopping the deposition mode, molecules in the pipes and the reaction chamber continue to adsorb onto the substrate. Hence, during a sequential deposition some of the first monomer continues to deposit while the second monomer is evaporated. As a consequence, the thickness indicated by the QCM refers to a deposit of some monomer mix. This behaviour is illustrated in Fig. 7-13.
The red curve refers to a deposition of 4,4'-MDI. The evaporation cell is closed at 0.9 nm but deposit steadily grows and thickness arrives at 1.5 nm after 25 min. because MDI molecules continue to flow through the reactor chamber. At 25 min., the deposition protocol is manually modified as if triol deposition would be the next step: QCM thickness is reset to zero and deposit density is switched to triol[48]. Then, the MDI evaporation cell is opened again and MDI deposition proceeds for the next 40 min.

[48] The density change is helpful here to obtain the apparent thickness increase by the MDI only.

For the blue curve, the first deposition step is carried out as before until the QCM measures 1.5 nm MDI after 28 min. Then after zeroing the QCM, the triol evaporation cell is opened for deposition of triol as the second layer. Thickness rises much stronger than for MDI. After another 32 min., deposition is stopped at 9.4 nm. Now for a given moment of deposition, the effective thickness of triol is estimated by the difference between the blue and red line because MDI and triol deposit simultaneously. As an example, 8.4 nm are estimated in Fig. 7-13 as the triol thickness at 32 min. triol deposition time. However, these thickness data are even less reliable than expected from that experimental protocol because of the fluctuations of layer growth observed in the reproducibility tests (cf. section 6.3). Hence, that protocol is not obeyed in the following and all thickness data for the second deposit include the triol plus the few MDI molecules.[49]

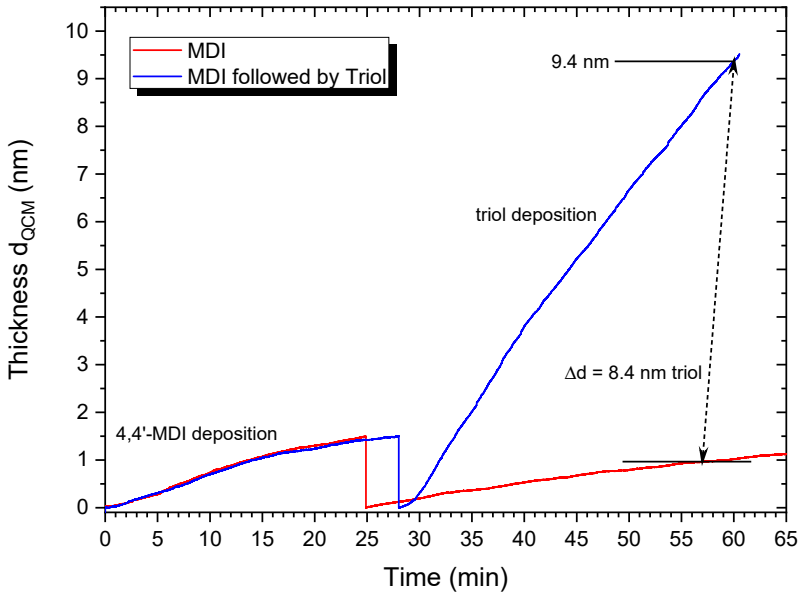

Fig. 7-13 Evolution of the QCM thickness during deposition of 4,4'-MDI alone (red) and subsequent deposition of MDI and triol (blue). In both cases, MDI deposition is stopped after reaching 0.9 nm. At 1.5 nm, thickness is zeroed and, for the blue curve, triol is deposited instead of MDI. Deposition parameters are the same: 5 l/min N_2, 500 mbar, 10 °C substrate temperature, and 180 °C evaporation temperature.

[49] In Fig. 7-13 for example, after 32 min triol deposition, the triol thickness will be 9.4 nm instead of 8.4 nm.

7.3.1 DPG deposited on top of 4,4'-MDI

The first bilayer system is prepared by deposition of DPG onto a 'full' 4,4'-MDI layer without rinsing it down to the stable MDI deposit. The presence of more monomers on the substrate will result in more intense IR spectra and thus allows for a better study of the IR band evolution. The diol will lead to linear urethane chains only. Molecular mobility is also higher than for the triol. Thus, the diol is expected to reach the MDI and form urethane chains rapidly. The bilayer is prepared as described above (cf. Fig. 7-13, 500 mbar, 5 l/min N_2, and 10 °C sample temperature). On top of the 1.5 nm MDI layer, ca. 15 nm[50] of DPG is deposited slowly and steadily[51]. The slow supply balances diol desorption[52] and gives the molecules more time for diffusion into the MDI layer. As another advantage, the facile diol desorption removes non-reacted molecules easily from the sample and thus bands of reacted diol are not covered by physisorbed diol. The polymerisation chemistry, sample topography, and stability against THF exposure are characterised in the following sections.

7.3.1.1 Layer chemistry

Right after deposition, the sample is transferred into the IR spectrometer, and evolution of the chemistry is monitored at room temperature in dried air for at least 24 h. The spectra are first discussed in detail for native Al substrates and then compared to layers prepared on native Cu.

◊ *Behaviour on Aluminium*

The different spectral regions are shown in Fig. 7-14 - Fig. 7-16. Discussion starts with the situation right after sample transfer (i.e. t = 0 h, black spectrum). In the range of high wavenumbers (Fig. 7-14), bands of diol (OH and CH stretches) and the isocyanate asymmetric stretch dominate.[53] Being so strong, the OH and NCO bands attest a lot of unreacted MDI and diol in the layer right after deposition. We conclude that 1 hour of diol deposition is not sufficient for a conversion of all isocyanate groups.

[50] It is recalled that some MDI also adsorbs during DPG deposition. The 15 nm include both monomers in the 2nd layer.

[51] Here, evaporation temperature of the DPG is reduced to 80 °C and deposition time is increased to 1 h.

[52] An increased evaporation temperature leads to a faster diol deposition and thus shorter deposition time. As shown in section 6.4.1 and 6.4.2, diol desorbs very rapidly from the surface under such condition and hence, diol molecules would only have a short contact time with the MDI. As a consequence, fewer urethane linkages are formed [69].

[53] With respect to the bulk spectrum (dashed blue), the broad OH band is slightly shifted to lower wavenumbers, as described in section 6.4 for deposits of pure triol and DPG.

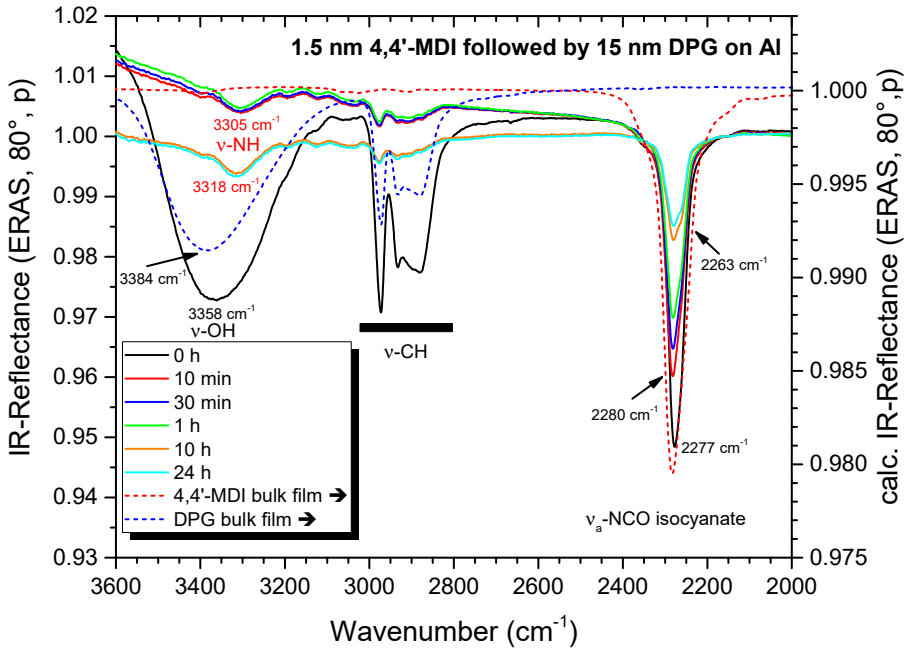

Fig. 7-14 IR-ERA spectra from a bilayer of 15 nm DPG and 1.5 nm MDI on native Al. Storage over 24 h in dried air at RT. 3600 – 2000 cm^{-1}. Bands assigned for the monomer (black) and for new species (red). For qualitative comparison, the dashed lines represent calculated spectra of the bulk monomers.

In the 1800 – 1350 cm^{-1} region (Fig. 7-15), the carbonyl band around 1730 cm^{-1} and the combined phenylene bands between 1650 and 1500 cm^{-1} are of particular interest as they contain information about formation and state of urethane units. These bands are strong right from the start (t = 0 h, black spectrum). That verifies urethane formation during deposition.

Interestingly the carbonyl band is composed of two different stretches at least. According to [145, 162], they are attributed to free carbonyl groups (1729 cm^{-1}) and to carbonyl groups in a single hydrogen bond (1713 cm^{-1}) while carbonyl groups in two hydrogen bonds would produce a band at about 1690 cm^{-1}. At t = 0 h, more free carbonyl groups are present than hydrogen bonded species. A similar effect was observed for the carbonyl groups for urea species (cf. Fig. 6-29). Although in Fig. 7-15 no band is resolved at 1690 cm^{-1}, the right shoulder of the carbonyl band may well contain such carbonyl states. Another weak band is present at 1640 cm^{-1}. It was attributed to double H-bonded carbonyls *in urea* because spectra of of pure MDI layers showed this band as well. It is recalled that isocyanates do not react exclusively with the deposited diol but also react slowly with water adsorbed on the substrate surface. Thus, urea is also formed in our sample but much less than urethane.

Urethane should give rise to other characteristic bands in the spectrum. The NH stretch is not visible at t = 0 h as it is masked by the strong OH stretch of the diol. The combined phenylene ring stretches between 1630 and 1500 cm^{-1} are of particular interest as they are sensitive to the neighbouring functional group.

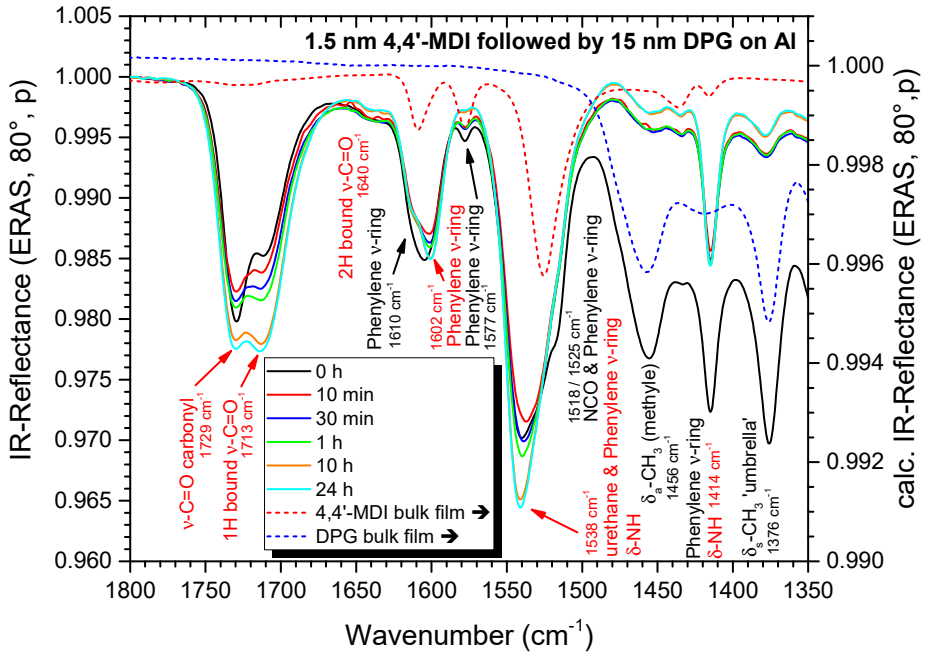

Fig. 7-15 IR-ERA spectra from a bilayer of 15 nm DPG and 1.5 nm MDI on native Al. Storage over 24 h in dried air at RT. 1800 – 1350 cm^{-1}. Bands assigned for the monomer (black) and for new species (red). For qualitative comparison, the dashed lines represent calculated spectra of the bulk monomers.

That is also observed here. Already at t = 0 h, the band at 1605 cm^{-1} is wider, asymmetric, and shifted to lower wavenumbers as compared to the phenylene stretch of 4,4'-MDI (1610 cm^{-1}). Hence, various neighbourhoods contribute to this combined phenylene stretch band: unreacted isocyanates, newly formed urethanes, as well as, to a minor extent, urea, and strongly attached MDI. Superposition of these four vibrations with different intensities results in the observed band.

The phenylene stretch at 1577 cm^{-1} is not sensitive to chemical modification of the neighbourhood. However, the band between 1570 and 1500 cm^{-1} is massively modified compared to bulk 4,4'-MDI. At t = 0 h, maximum is at 1538 cm^{-1} and a shoulder is located at 1518 cm^{-1}. Again, the band contains contributions from phenylene ring vibrations in the neighbourhood to NCO in unreacted free and strongly adhering MDI, to urethane, and to the little urea. Moreover, NH deformations contribute to this band. Most likely, the shoulder at 1518 cm^{-1} corresponds to the contribution from 4,4'-MDI where the combined NCO-phenylene stretch is found at 1525 cm^{-1} in the bulk.

Below 1500 cm^{-1}, various CH deformations of the diol dominate the spectrum. Another phenylene ring stretch at 1414 cm^{-1} is present but its position is not changed in regard of the MDI bulk spectrum but it is stronger because NH deformation vibrations from urethane, strongly attached MDI, and urea contribute to it as well.

In Fig. 7-16, three bands dominate the spectrum below 1350 cm^{-1}. The bands at 1320 and 1230 cm^{-1} correspond to combined stretches of phenylene rings and carbon–nitrogen stretches of the attached functional groups.

These bands are typical for urethane but also for the strongly attached MDI and urea. Both bands are overlapped by various CH deformations of the alcohol.

The most intense band (1190 – 1025 cm^{-1}) is mainly composed of the ether stretch vibrations in the diol. Intensity ratios are slightly different, however: vibrations below 1150 cm^{-1} are stronger than for bulk diol. This is due to two effects: isocyanate vibrations (cf. the dashed red spectrum in Fig. 7-16) and, as seen for the reaction of triol with stable MDI deposits (cf. section 7.2.3, Fig. 7-9), due to a band at approx. 1080 cm^{-1} for triol ether vibrations modified by urethane in the neighbourhood.

To sum up, the strong carbonyl stretches, the two new bands between 1320 and 1230 cm^{-1} as well as the modification of position and shape of many characteristic phenylene bands prove that urethane linkages have formed during the one hour of alcohol deposition. Unreacted monomers are still present to a large extent at this time.

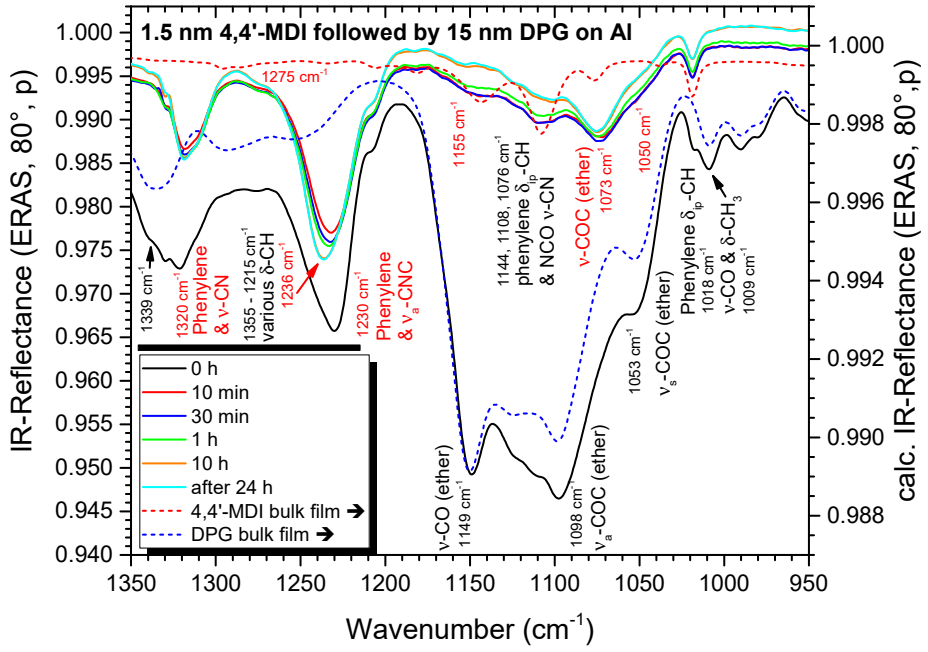

Fig. 7-16 IR-ERA spectra from a bilayer of 15 nm DPG and 1.5 nm MDI on native Al. Storage over 24 h in dried air at RT. 1350 – 950 cm^{-1}. Bands assigned for the monomer (black) and for new species (red). For qualitative comparison, the dashed lines represent calculated spectra of the bulk monomers.

As the next step, the temporal evolution of the spectra in Figs. 8-15 - 8-17 is considered.

During *the first 10 min. of storage* at RT, significant changes occur (black vs. red spectrum).

First, intensity of diol bands (3358, 3000 - 2800, 1500 – 1200 and 1150 – 1025 cm^{-1}) drops massively. This indicates a rapid desorption of much of the monomer diol. As these bands shrink, underlying weaker bands emerge. In particular, the NH-stretch at 3305 cm^{-1} is now visible.

New bands and shoulders at 1155, 1073, and 1050 cm^{-1} emboss the ether region. That is all further proof for urethane formation. Despite the large intensity drop, diol bands remain in the spectrum, in particular the CH stretches and deformations. Now, they mainly correspond to those diols that have reacted with MDI but few monomer diols might still remain in the layer.
Second, the isocyanate band (2280 cm^{-1}) slightly dropped in intensity due to further reaction with alcohol groups[54]. Simultaneously, the ratio switched for carbonyl intensities: free carbonyl decreased in favour of the H-bonded carbonyl. Hence, carbonyl groups rearranged in the layer and formed energetically favourable H-bonds. This intensity change confirms that even in such thin deposit, urethane molecules possess enough mobility to rearrange and take energetically favourable positions. Dimers are more likely than bigger entities with less mobility.
Third, the phenylene ring stretches undergo several changes as well. The band at 1605 cm^{-1} decreased, its former maximum turned into a shoulder at 1610 cm^{-1} and the new maximum is located at 1602 cm^{-1}. Clearly, the band exhibits two underlying vibrations: the phenylene rings of MDI (1610 cm^{-1}) as well as phenylene rings from urethanes (1602 cm^{-1}), latter being more pronounced. The shoulder at 1518 cm^{-1} of the combined phenylene band at 1538 cm^{-1} also vanished. Hence, as more isocyanates reacted with the diol, the specific phenylene vibrations related to the NCO group lost intensity, and thus the band was modified. Simultaneously, urethane specific vibrations continue to grow.
Due to the desorption of unreacted alcohol and thus the reduction of CH deformations, the new bands between 1350 and 1200 cm^{-1} change shape but keep position.

During *further storage up to 10 h*, spectra change much less.
The NH stretch slightly grows and the band gets sharper while slightly shifting upwards to 3318 cm^{-1}. The CH stretch and the deformation bands do not change significantly. Hence, desorption of unreacted species was nearly complete after 1 h. The NCO band (2280 cm^{-1}) continues to drop as more isocyanates are consumed. Furthermore a shoulder at 2263 cm^{-1} appears. The lower frequency indicates an increased interaction energy. It is attributed to the effect of changing chemical environment on some isocyanate groups, including the presence of urethane groups. That driving force and the proven molecular mobility let the isocyanate groups respond by rearranging in space and finding a new balance of interactions that lead to the shoulder in the spectrum. One might speculate that this rearrangement goes with some clustering of NCO groups.
The two carbonyl bands continue to grow during the 10 h storage. Thus, even if the OH stretch is discriminated in the spectrum anymore there are still OH groups present that react with NCO to urethane urethane groups. The reaction implies that molecular mobility is still sufficient. Additionally, band intensity is growing for the H-bonded carbonyls on the cost of the free carbonyls for the full 10 h.

[54] NCO also reacts with the rest of adsorbed water as well.

Knowing that more urethane groups are formed, the changing intensity ratio is attributed to the formation of more H-bonds, which inevitably goes with some spatial rearrangement of urethane groups. Again, this rearrangement requires sufficient mobility for the urethane containing molecules and it might go with some clustering of NCO groups.
Evolution of the phenylene bands corroborates the interpretation. The urethane-related phenylene bands (1602, 1538, and 1414 cm^{-1}) continue to grow. Simultaneously, phenylene vibrations related to MDI continue to shrink with slight changes in band position and shape. Bands at 1320 and 1230 cm^{-1} continue to grow as well. A slight upward shift (1236 cm^{-1}) is observed for the latter band. Likewise, the new ether band at 1073 cm^{-1} grows slightly.

From 10 to 24 h only minor changes occur. Hence, most of the chemistry was terminated during the first 10 h. The weak drop of the NCO stretch band as well as the slight increase observed for carbonyl and phenylene bands verify that just very few isocyanate groups are still capable to form further urethane or urea. Hence, reaction of isocyanates with dipropylene glycol in contact of Al takes approximatively 10 h at RT to reach maximum conversion. Isocyanate groups are still present in the layer. Because of rapid desorption, too little alcohol remains for reaction with all isocyanate groups in the deposit. Further storage up to 48 h (not shown) did not give any further spectral changes compared to 24 h of storage.

◊ *Comparison with deposits on copper*

The chemistry on Cu was studied as for Al. The evolution of the spectra during storage is shown in Appendix 11.6.1 – Fig. 11-19 to Fig. 11-21. Briefly, the monomers behave similar and they react on Cu in the same way. A few notable differences are observed however and are presented in comparative views in Fig. 7-17 to Fig. 7-20.

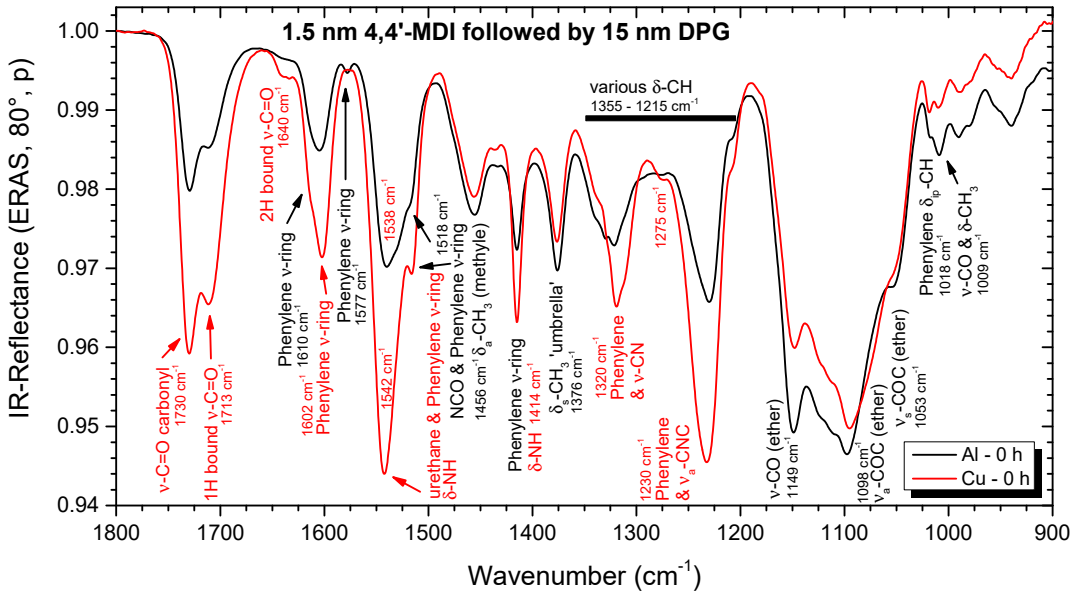

Fig. 7-17 Comparison of a bilayer of 15 nm DPG on top of 1.5 nm 4,4'-MDI on Al (black) or Cu (red), respectively, right after deposition (t = 0 h). 1800 – 900 cm^{-1}. Bands assigned for the monomers (black) and for new species (red).

Right after deposition (t = 0 h, Fig. 7-17), band positions are virtually identical for Al and Cu in the fingerprint region but intensities differ significantly. While the same amounts of monomers have been deposited, all new bands due to MDI adhesion as well as urethane and urea formation are much stronger on Cu than on Al. Hence, the initial rate of formation of urethane as well as of other species is much faster on Cu. This trend was also observed for the 4,4'-MDI layers on Cu (cf. section 7.4.2). Hence, reaction of the isocyanates is accelerated probably due to the catalytic properties of Cu [163-168].

Interestingly, the intensity ratio of the doublet for the two carbonyl states is not modified by the faster reaction. The phenylene bands (1610 – 1500 cm^{-1}) exhibit a more pronounced urethane character on Cu as more isocyanates have reacted and thus the NCO-related phenylene bands contribute less to band intensity and shape. The CH deformations are not affected. Shape and intensity ratio of the ether bands (1150 - 1050 cm^{-1}) are slightly different on both metals as the newly forming but still hidden ether bands (1155, 1073, and 1050 cm^{-1}) provide different contributions on each metal. The slight intensity difference for all alcohol bands originate from either a slightly different amount of DPG deposit or a different transfer time from the MLD to the spectrometer and hence different alcohol desorption.

Parallel to the higher amount of urethanes formed after deposition on Cu, the NCO and OH bands in the upper spectral region are weaker than on Al as more monomer functionalities have been consumed (cf. Fig. 7-18). The shape of the band at 3600 - 3100 cm^{-1} is different due to the increased contribution of the underlying NH stretch that is more obvious by the shoulder at 3200 cm^{-1}. Position and shape of the NCO band is also slightly different on both metals.

On Cu, the band is asymmetric suggesting that isocyanates undergo several different interactions in the formed layer. On Al, these states may be hidden by the large band intensity.

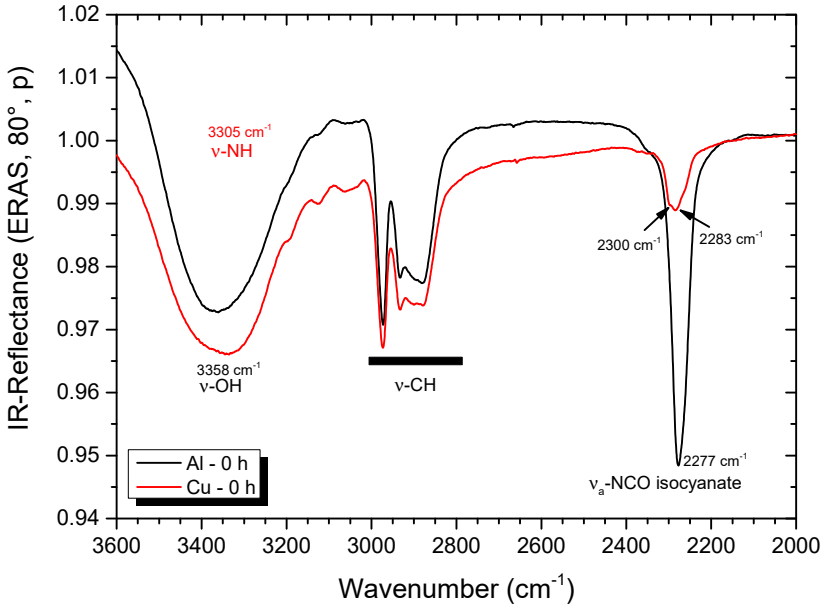

Fig. 7-18 Comparison of a bilayer of 15 nm DPG on top of 1.5 nm 4,4'-MDI on Al (black) or Cu (red), respectively, right after deposition (t = 0 h). 3600 – 2000 cm^{-1}. Bands assigned for the monomers (black) and new species (red).

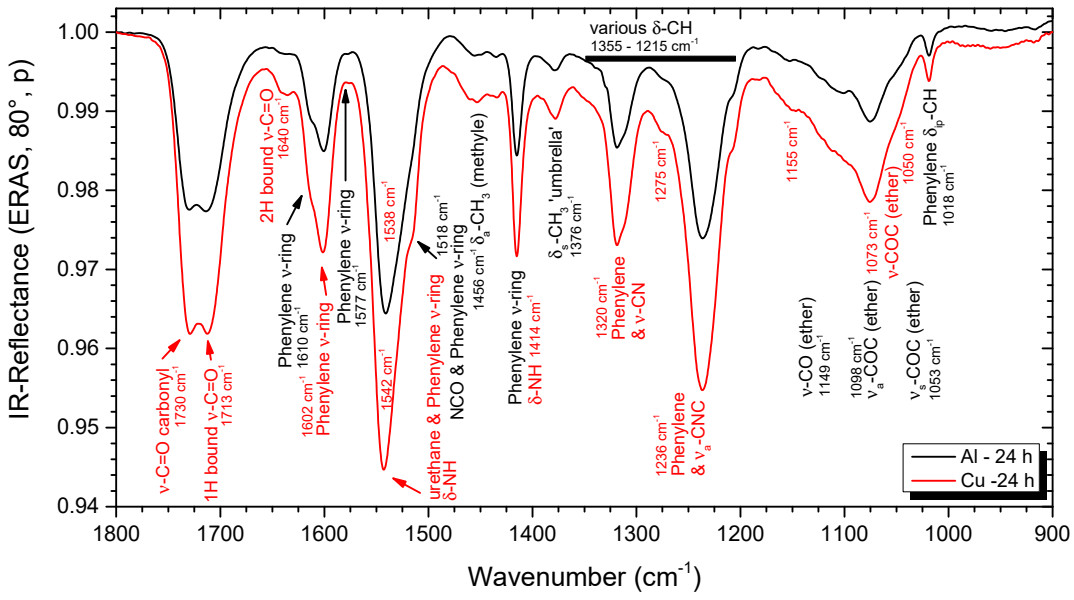

Fig. 7-19 Comparison of a bilayer of 15 nm DPG on top of 1.5 nm 4,4'-MDI on Al (black) or Cu (red), respectively, after 24 h of storage at RT. 1800 – 900 cm^{-1}. Bands assigned for the monomers (black) and new species (red).

After 24 h of storage (Fig. 7-19), the picture has not changed. All new bands on Cu are still stronger than on Al. The evolution of the bands and mainly their corresponding intensity ratios have changed on both metals in the same way. Hence, it is concluded that DPG and MDI react the same way and form the same species on both metals. However, more urethane is formed faster on Cu.

On Cu, the NH band is stronger and well visible now (Fig. 7-20). Remains of unreacted OH groups are indicated by the shoulder around 3400 cm^{-1}. The stronger CH stretches are another indication that on Cu more alcohols have reacted with the isocyanates. The NCO band has changed shape on both metals over time. Peak position tends to be at higher frequency on Cu. There is no shoulder like on Al at 2263 cm^{-1} but the band still has an asymmetry at the low-frequency side on Cu. Hence, on both substrates, some isocyanates establish stronger but metal-specific interactions by rearranging in space while a majority remains in the original chemical environment.

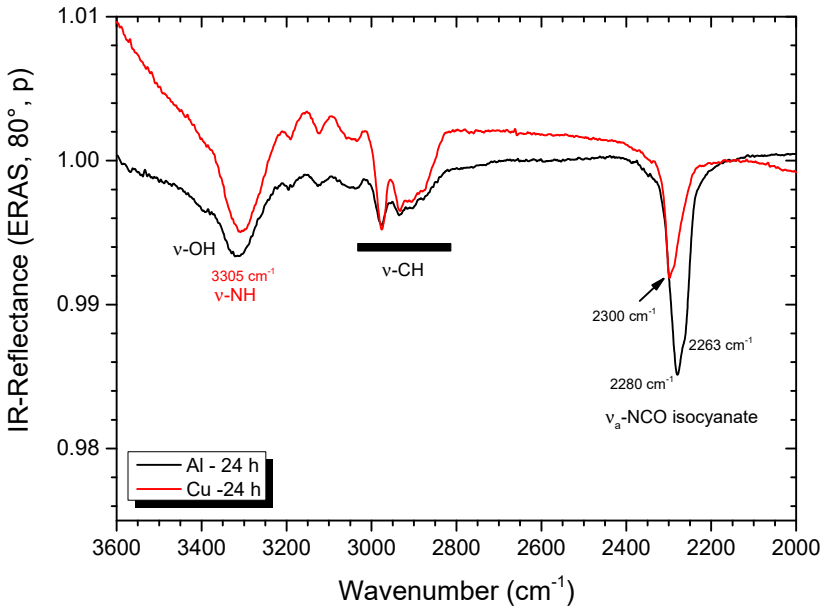

Fig. 7-20 Comparison of a bilayer of 15 nm DPG on top of 1.5 nm 4,4'-MDI on Al (black) or Cu (red), respectively, after 24 h of storage at RT. 3600 – 2000 cm^{-1}. Bands assigned for the monomers (black) and new species (red).

7.3.1.2 Layer Topography

As 4,4'-MDI layers showed rough deposits (cf. Fig. 6-33) it is of great interest to study if and how morphology is changed upon addition of alcohol and reaction with the isocyanate. The morphology of the urethane layers on aluminium and copper is studied with optical microscopy (DIC and DF) and tapping mode Scanning Force Microscopy (SFM) on samples stored ca. 24 h in dried air, i.e. after most of the chemical reactions is over.

DIC and DF images (Fig. 7-21) provide first evidence for a metal-specific structure of the urethane layers. Small 'calottes' disperse evenly on Al. Bigger ones are scattered here and there. On Cu, the surface is completely covered with irregular 'flakes' being much larger than the calottes on Al. Thus, compared to isocyanate layers, the urethane layers possess a completely different morphology. The effect of the metal on the layers is even intensified. Optical microscopy provides only limited access to topographic details, however. As for the MDI layers, DIC can only indicate a change in height but it does not indicate if the 'calottes' are not holes in a homogenous urethane layer.

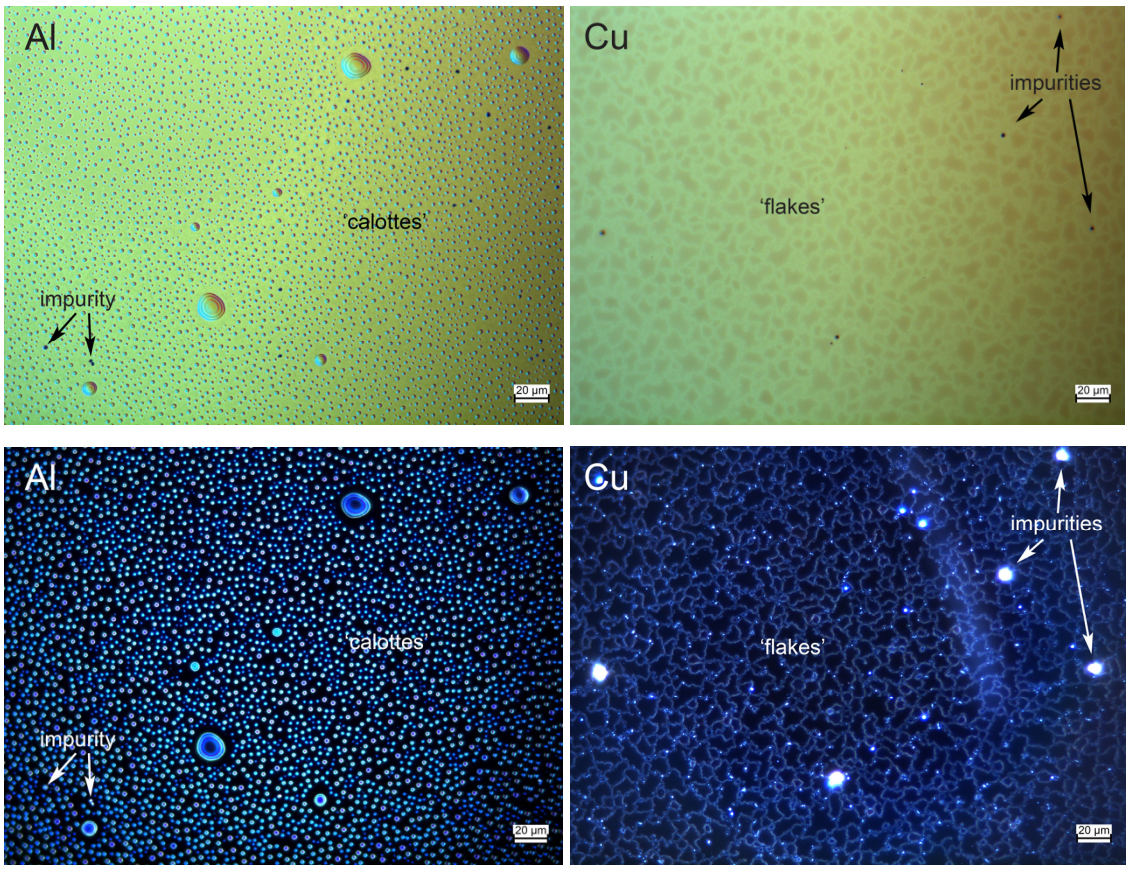

Fig. 7-21 DIC (top) and dark field (DF, bottom) images of PU layers after 24 h at RT in dried air. Left - on Al, right - on Cu. Preparation as given in section 8.3.1.1: deposition (5 l/min N_2, 500 mbar) of ca. 15 nm of DPG on top of 1.5 nm of 4,4'-MDI at 10 °C substrate temperature.

Tapping mode SFM gives deeper insight. Starting with an 80 x 80 µm² scan on Al and Cu (Fig. 7-22), the features seen on the DIC and DF images are verified and identified as topography: the urethane layers are not plain. On Al (Fig. 7-22a), a flat underground (red) is evenly covered by calottes being 60 – 160 nm high. The lateral size of the calottes ranges up to 2 µm. On Cu (Fig. 7-22b), the rather flat surface (green/blue) is grooved by valleys (red). The height difference between valleys and plateaus fluctuates between 12 – 20 nm. The heterogeneous topography again proves that the thickness indicated by the QCM does not mean that the real layer is homogeneous and flat.

The patterns of calottes and groves show similarities with dewetting phenomena and associated crack formation in thin polymer layers (e.g. [169, 170]). It is recalled that MDI layers on both metals already showed some heterogeneity (cf. section 6.5.2 – Fig. 6-35&Fig. 6-37) and this initial topography could also serve as starting point for the discussion of the now observed non-homogeneous deposits. The size of the now observed topographic elements is much larger than the cones of the MDI layers (ca. 300 – 500 nm).[55]

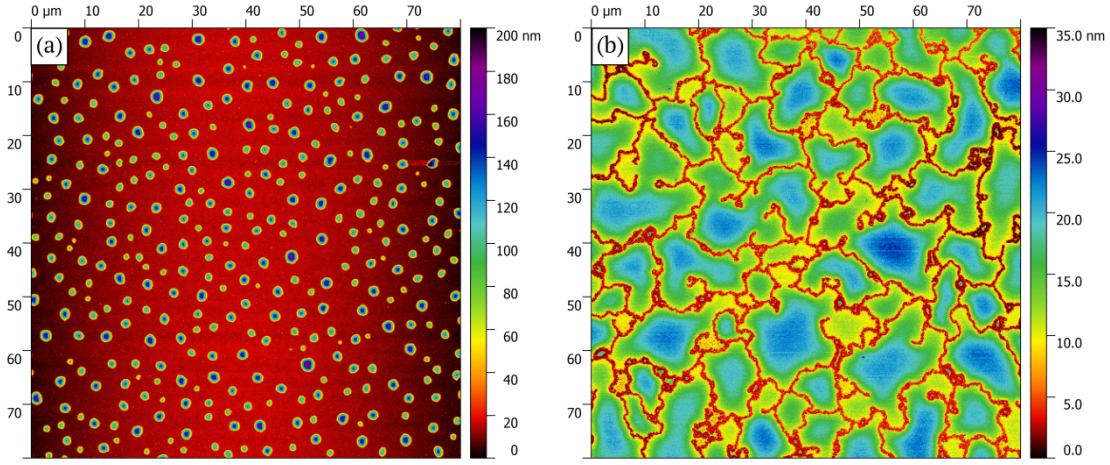

Fig. 7-22 Tapping mode SFM topography images (80 x 80 µm² scan) of the previously prepared urethane layers on native Al (a) and Cu (b) after 24 h of storage in dried air.

According to the height distribution for the whole image (Fig. 7-23a), the most frequent structures are below the 20 nm height level on Al. They correspond to the flat region between the calottes. As the minor features on this sample, the calottes (ca. 60 – 160 nm high) are almost invisible in the height distribution. On Cu, two regions are found in the height distribution (Fig. 7-23b). The first one, with a maximum at ca. 3 nm, corresponds to the valleys while the wide second one (at ca. 8 - 25 nm) corresponds to the plateaus. Now, the height difference, Δh, between the regions ($\Delta h \approx 40 – 140$ nm on Al, $\Delta h \approx 5 – 22$ nm on Cu) shall serve as an estimate for the roughness of the layers.

[55] The new pattern could form during the massive desorption of the alcohol but origin and evolution of the observed topography were not studied as this would exceed the scope of this work.

Both Δh-values are much lower than the wavelengths of light in IR spectroscopy and hence they are too small for a modification of ERA infrared spectroscopic analysis, which presumed deposits as flat and uniform layers. Thus, the topology of the urethane layers on the two metals does not impinge on their spectral features discussed above.

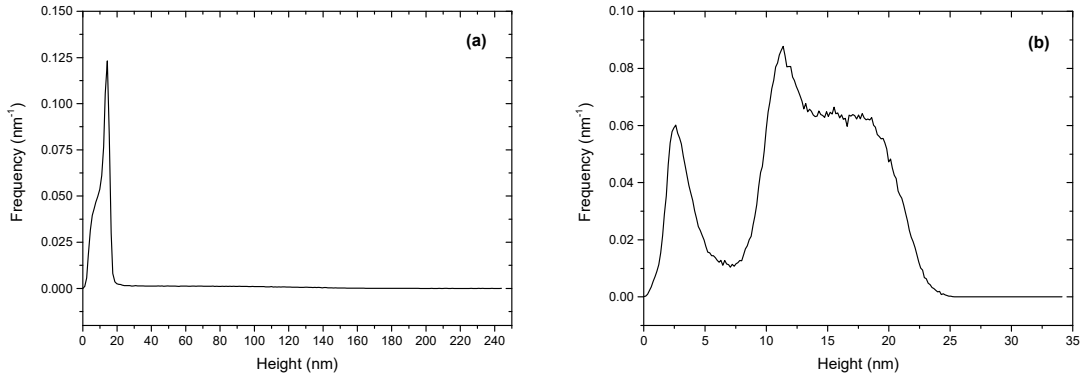

Fig. 7-23 Height histograms of the 80 x 80 µm² scans (Fig. 7-22) of a urethane layer on native Al (a) and Cu (b).

The 5 x 5 µm² scans (Fig. 7-24) reveal the situation in more detail. On aluminium (Fig. 7-24a), the big calottes are surrounded by many small 'bumps' (mainly in yellow) of up to 25 nm height with a diameter of 200 – 300 nm. They are in the size range of the initially deposited 4,4'-MDI cones. The flat region (red) in-between replicates the nodular structure of the polycrystalline aluminium.

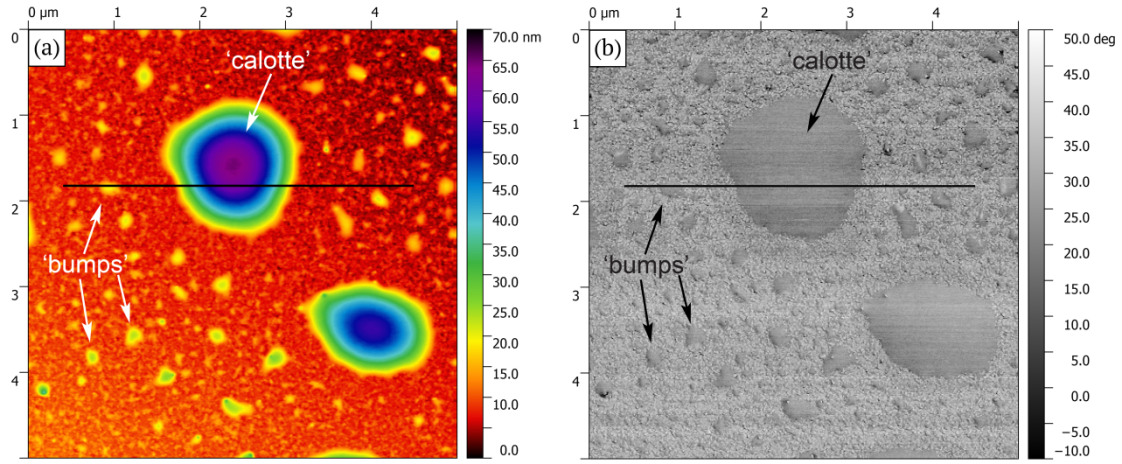

Fig. 7-24 Tapping mode SFM topography (a) and phase contrast (b) image of the urethane layer on native Al. 5 x 5 µm² scan. Black lines indicate the location of height and phase contrast profiles given in Fig. 7-26.

The topography histogram (Fig. 7-25a) of this map shows that the flat regions predominate. Hence, at first glance organic molecules are not directly identified between the calottes and the bumps. However, the phase contrast image (Fig. 7-24b) proves that phase contrast on the flat nodular regions and on the bumps is nearly the same as on top of the calottes, which definitely consist of organic material.

The phase contrast histogram (Fig. 7-25b) supports that interpretation as it shows only one maximum. If regions of uncoated aluminium were present, two distinct maxima would be expected, one for urethane and one for aluminium.

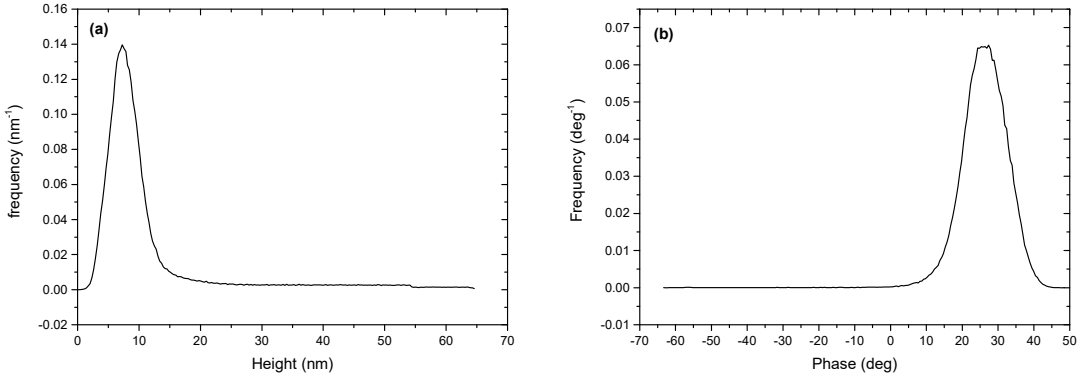

Fig. 7-25 (a) Height distribution of the 5 x 5 µm² scan (cf. Fig. 7-24a) of a urethane layer on native Al. (b) Phase contrast histogram of the 5 x 5 µm² scan (cf. Fig. 7-24b).

This finding is substantiated by the topography and phase contrast profiles in Fig. 7-26. The small decrease (about 6°) in phase contrast on the calotte originates from the big amount of urethane being more compliant than the urethane on the flat regions when tapped with the tip.

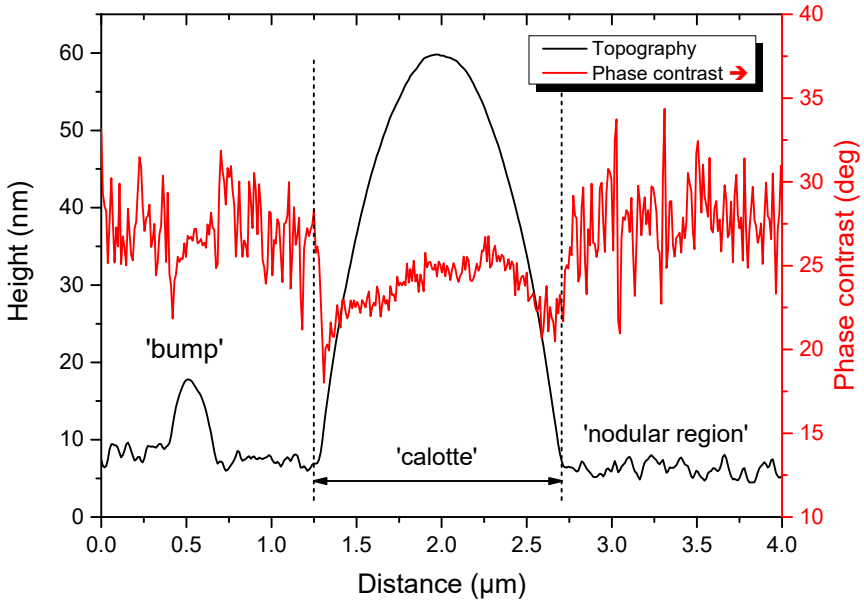

Fig. 7-26 Topography (black) and phase contrast (red) profiles along the lines in Fig. 7-24.

On Cu, the 5 x 5 µm² scan (Fig. 7-27a) zooms into a region with two valleys (red) between three plateaus (green). These structures are very different from the calottes observed on Al and have much larger lateral dimensions. The valleys are about 8 - 10 nm deep and ca. 1 - 2 µm wide. The plateaus extend over several µm.

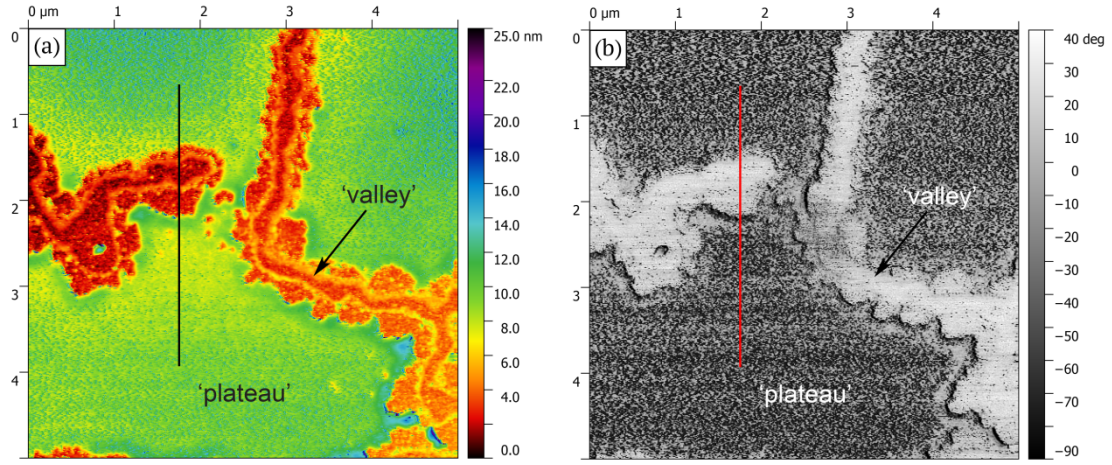

Fig. 7-27 Tapping mode SFM topography (a) and phase contrast (b) image of the urethane layer on native Cu. 5 x 5 µm² scan. Black lines indicate the location of height and phase contrast profiles given in Fig. 7-29.

The topography histogram (Fig. 7-28a) shows two peaks corresponding to valleys and plateaus. The height difference between both peaks is about 8 nm and gives a lower bound for the thickness of the organic layer on copper. The phase contrast map (Fig. 7-27b) indicates a big phase angle difference between plateaus and valleys. This is confirmed by the corresponding phase angle histogram (Fig. 7-28b). The narrow peak around -77° indicates homogeneous material on the plateaus. The valleys possess a much wider phase angle distribution ranging from -20 to 30°. This big difference suggests that no urethane is present in the valleys. However, it is also possible that few urethane molecules are present but are covered by the tip tapping into the substrate. Hence, no unequivocal proof on the presence of urethane inside the valleys is given.

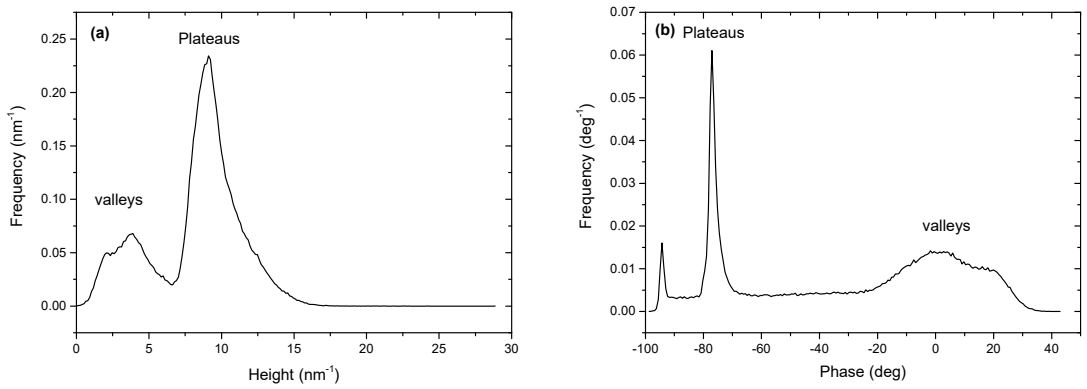

Fig. 7-28 (a) Height distribution of the 5 x 5 µm² scan (cf. Fig. 7-27a) of a urethane layer on native Cu. (b) Phase contrast histogram of the 5 x 5 µm² scan (cf. Fig. 7-27b).

The line profiles in Fig. 7-29 show the sharp transition between the plateaus and the valley.

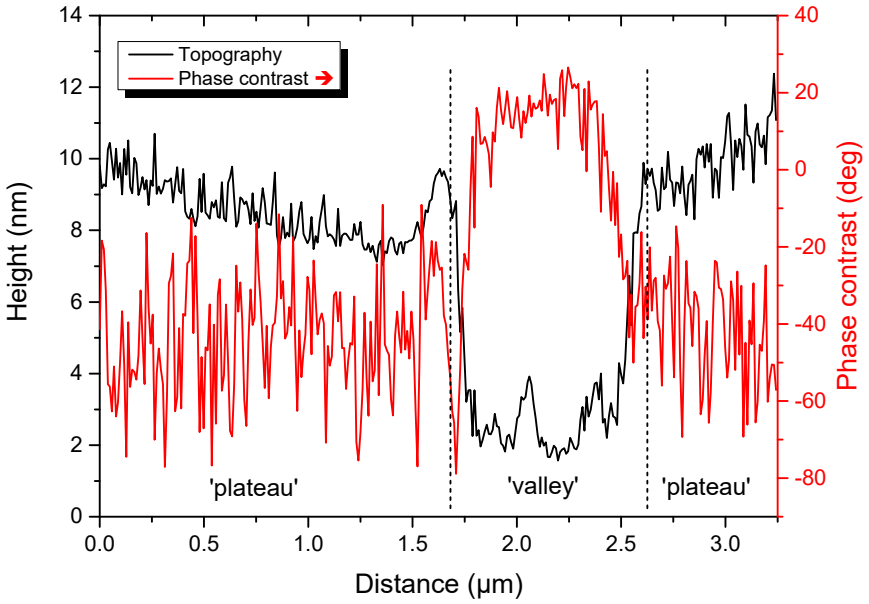

Fig. 7-29 Topography (black) and phase contrast (red) profiles along the lines in Fig. 7-27.

7.3.1.3 Urethane layer stability against THF

◊ *Behaviour on Aluminium and Copper*

The stability of the urethane layers and thus the attachment of the urethane chains to the substrate is probed with subsequent THF rinses. Only if the urethane chains are linked to the substrate a sustainable polymer coating is achieved. Fig. 7-30 to Fig. 7-32 show the spectra after rinsing.

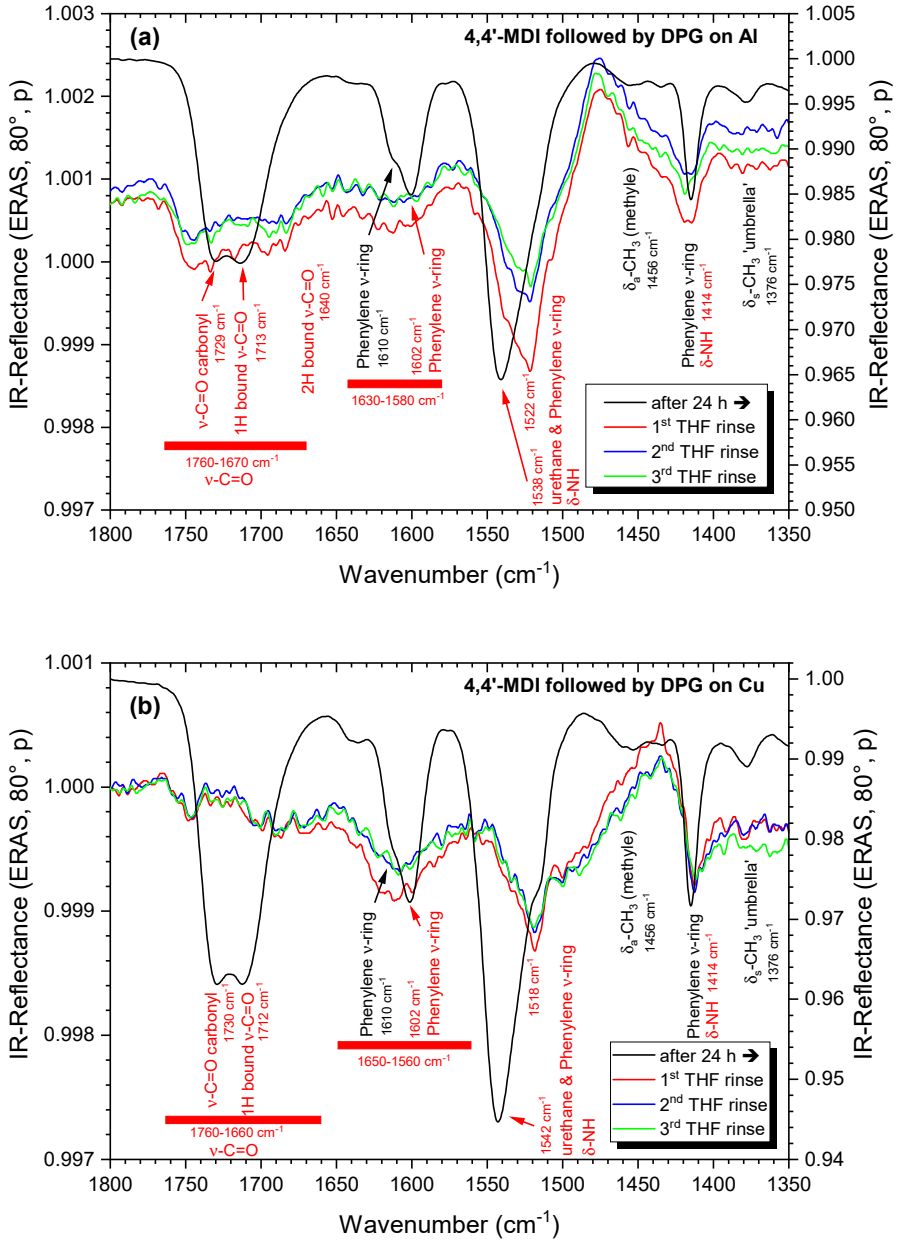

Fig. 7-30 Effect of THF rinse on the urethane layer prepared by deposition of 4,4'-MDI followed by DPG and stored for 24 h in dried air on Al (a) and Cu (b). Band assignment for monomers (black) and new species (red) refers to the situation prior THF rinses.

Starting with the carbonyl - phenylene region (1800 – 1350 cm^{-1}, Fig. 7-30) all bands in the spectrum massively lost intensity on both metals. Obviously, the major part of the layer does not withstand the 1st THF rinse. This implies that most of the urethane molecules do not stick well on the substrate. However, as seen in section 7.2.2 and 7.2.3 the strongly adhering MDI reacts with alcohol and much of the resulting urethane adheres on the substrate. As the consequence of these two results, the simple idea of urethane chains that start at the metal surface and polymerise throughout the whole deposit, is not valid.[56]
Further rinses have no effect. Thus, the molecules remaining after the 1st rinse form a stable residue as for the alcohol deposition on the strongly adhering MDI.

We have seen that urethane formation is possible as soon as isocyanates and alcohols come together. Now, with diffusion of alcohol monomers in the deposit, urethane molecules simultaneously form at many places in the deposit, including the strongly adhering isocyanates at the metal surface. First, dimers emerge but ongoing reaction with other monomers to larger oligomers is getting increasingly difficult because both the number of available monomers and molecular mobility decrease with growing oligomer size.[57] The rinsing tests show that polymer chain growth is very inefficient in the deposits - although urethane reaction works well and some mobility of the entities is given (rearrangement of urethane groups, changes in isocyanate band shape - see above). A few arguments are debated now to understand the situation in more detail.
Once DPG deposition stopped, desorption proceeds very rapidly: most DPG desorbs within the first 10 min. The limited number of remaining alcohol molecules disperses in the MDI deposit. These DPG monomers react with surrounding MDI but then the next DPG is not necessarily available to form polymer chains, and reaction stops at the stage of small oligomers. As a second proof, spectra show a lot of MDI in the deposit after 24 h of storage. Therefore, DPG desorption was so strong that the concentration of remaining OH groups is less than the number of NCO groups. That nonstoichometric ratio provides another argument that DPG molecules mainly react with two MDI molecules thus forming just trimers. Reaction stops as only isocyanate terminated entities remain which do not bond together. In this scenario, most urethane groups originate from these trimers. On the substrate surface, dimers would predominate with one adhesively bonded isocyanate in the MDI unit. At least these species should resist rinsing.

After the rinses spectra show that weak but unusually broad bands remain in the carbonyl (1770 – 1650 cm^{-1}) and phenylene regions (1650 – 1560 cm^{-1}). These bands belong to urethane species that resisted the THF attack. Generally, such band broadening indicates locally varying intermolecular interactions. On Al, the carbonyl region is embossed by a large buckle while two bands (1750 and 1720 – 1660 cm^{-1}) are present on Cu.

[56] See the discussion below for more detail.
[57] Reminder: only linar chains can arise from the addition of DPG and MDI.

Analysis of a set of rinsed samples shows that the carbonyl region as well as the phenylene band between 1650 and 1560 cm^{-1} are prone to slight variations. Hence, intermolecular interaction and orientation vary in the deposits due to rinsing.
The predominant band with the peak at initially approx. 1540 cm^{-1} is broadened and located at 1520 cm^{-1} now, i.e. at the position of the former shoulder. The band is another proof of existence for urethane molecules. For the discussed carbonyl and phenylene bands, band shape and intensity ratio are metal specific.
Between 1430 and 1350 cm^{-1} the band at 1414 cm^{-1} is still strong. It proves the presence of MDI units. The CH deformations from the alcohol units are hard to distinguish. The band at 1456 cm^{-1} is hidden by the baseline underground. The CH_3 umbrella deformation (1376 cm^{-1}), another indicator for urethane molecules, is extremely weak from the start and can only be guessed among the background noise.

Below 1350 cm^{-1} (Fig. 7-31), all bands of the deposit lost intensity as well. After the 1st THF rinse, the phenylene bands (1320 and 1236 cm^{-1}) remain on both metals. Again, they indicate the presence of urethane molecules. A weak trace of the ether band at 1073 cm^{-1} remains on Al but is not distinguished on Cu. Bands at 1155 and 1050 cm^{-1} have disappeared. Hence, the presence of dimers formed by reaction of isocyanate with one DPG is proven again but some of the specific bands are extremely weak and in the range of background noise.

As a side effect, the oxide band below 950 cm^{-1} is visible on Al after rinsing. It reveals that the oxide layer grew underneath the deposit in the course of sample preparation and treatment.

The spectral region between 3600 and 2000 cm^{-1} - Fig. 7-32 provides a last source of information. All bands present after 24 h of storage (NH, CH, and NCO) have vanished. Only on Al, a very weak NCO band remains after the 1st rinse and disappears with subsequent rinses because, most likely, the residual NCO groups took the chance to react with water. Thus, this spectral region does not provide additional evidence for the chemical state of the organic deposit after THF rising.

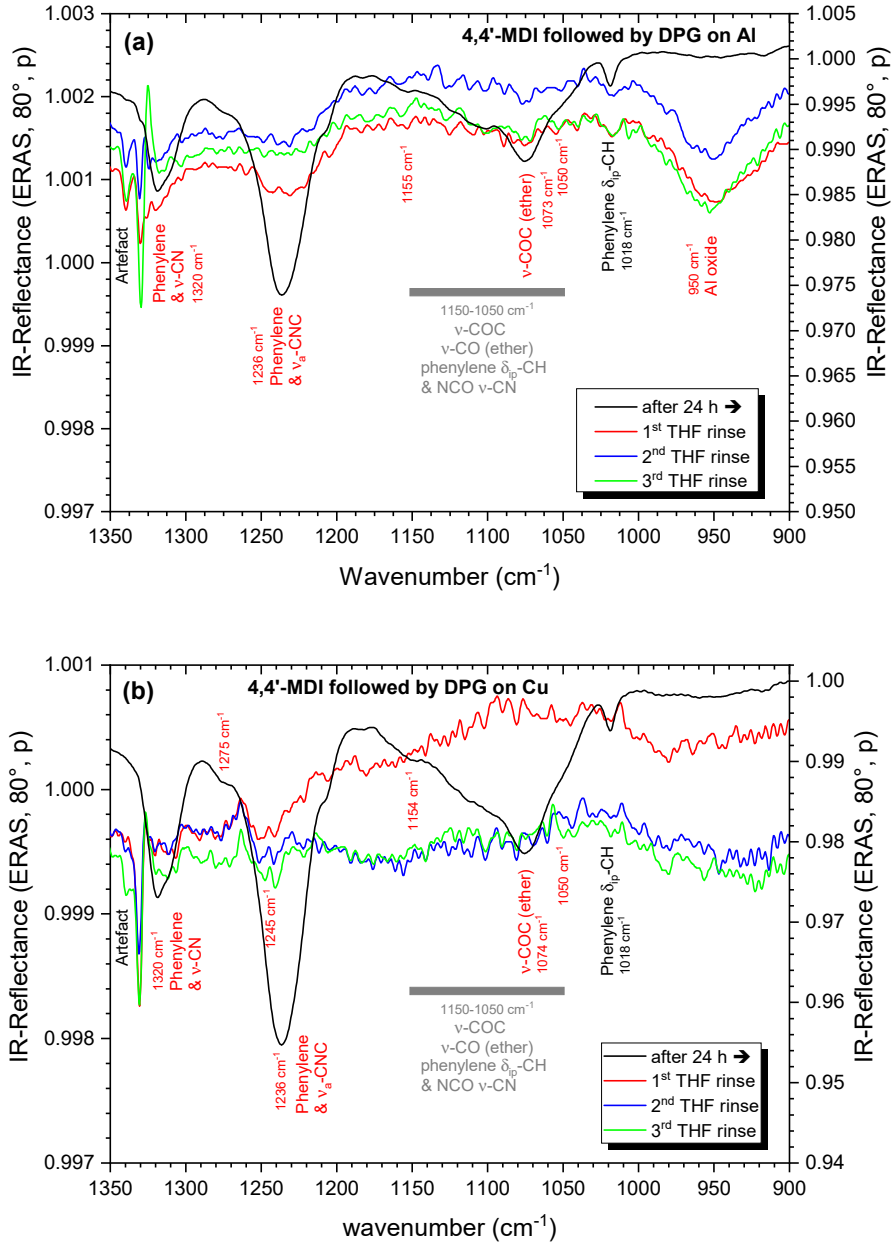

Fig. 7-31 Effect of THF rinse on the urethane layer prepared by deposition of 4,4'-MDI followed by DPG and stored for 24 h in dried air on Al (a) and Cu (b). Band assignment for monomers (black) and new species (red) refers to the deposit prior THF rinses.

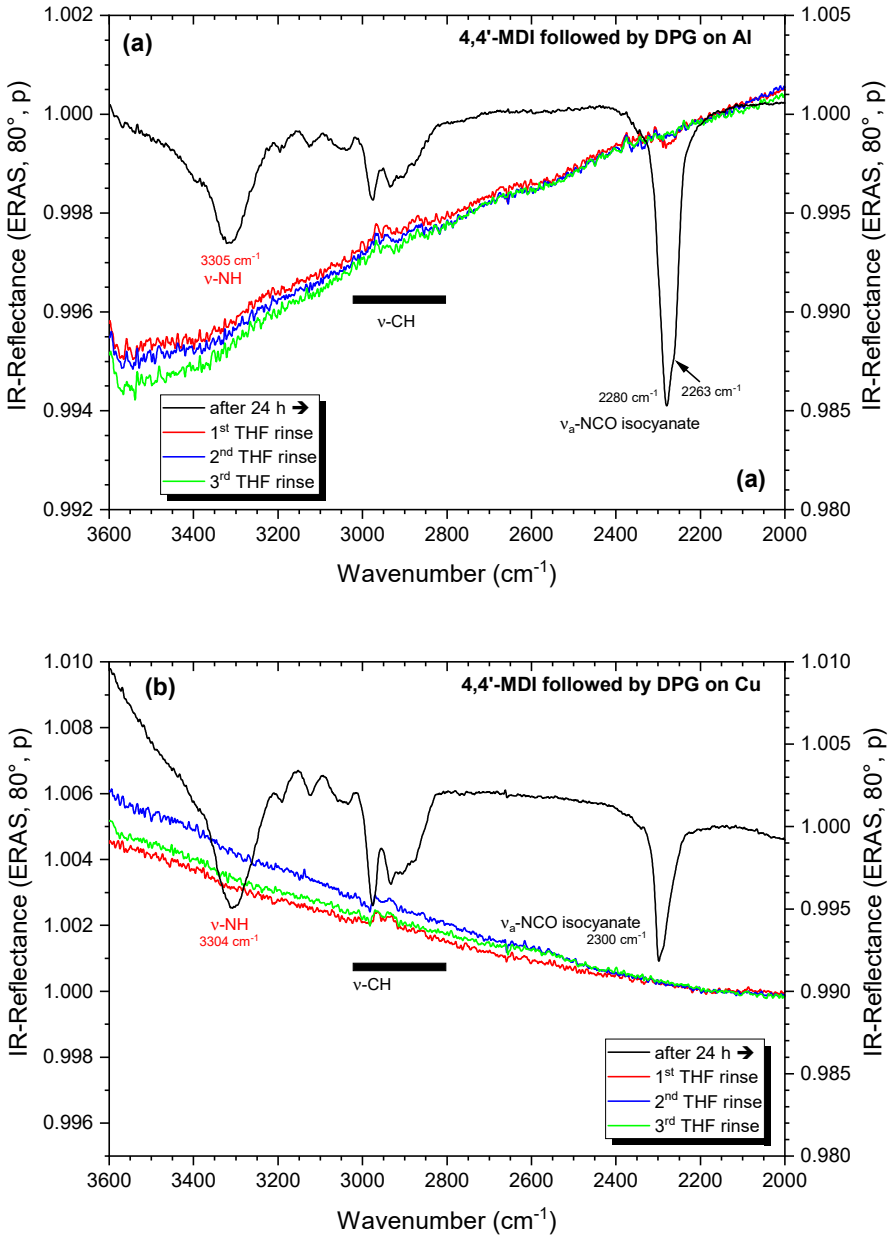

Fig. 7-32 Effect of THF rinse on the urethane layer prepared by deposition of 4,4'-MDI followed by DPG and stored for 24 h in dried air on Al (a) and Cu (b). Band assignment for monomers (black) and new species (red) refers to the deposit prior THF rinses.

◊ *Comparison with stable 4,4'-MDI deposits*

Comparison of the molecules remaining in the DPG-MDI deposit after three THF rinses with a stable 4,4'-MDI deposit[58] (Fig. 7-33) does reveal further important aspects. On the Al substrate (Fig. 7-33a), the green and the red spectrum are very weak but similar in terms of band shape and intensity. Hence, it is concluded that the strong adhesion of NCO groups with the substrate prevails in both deposits. That interaction has not been hampered by the DPG. This conclusion is additionally supported by the findings for the alcohol reaction with the stable MDI deposit (cf. section 7.2).

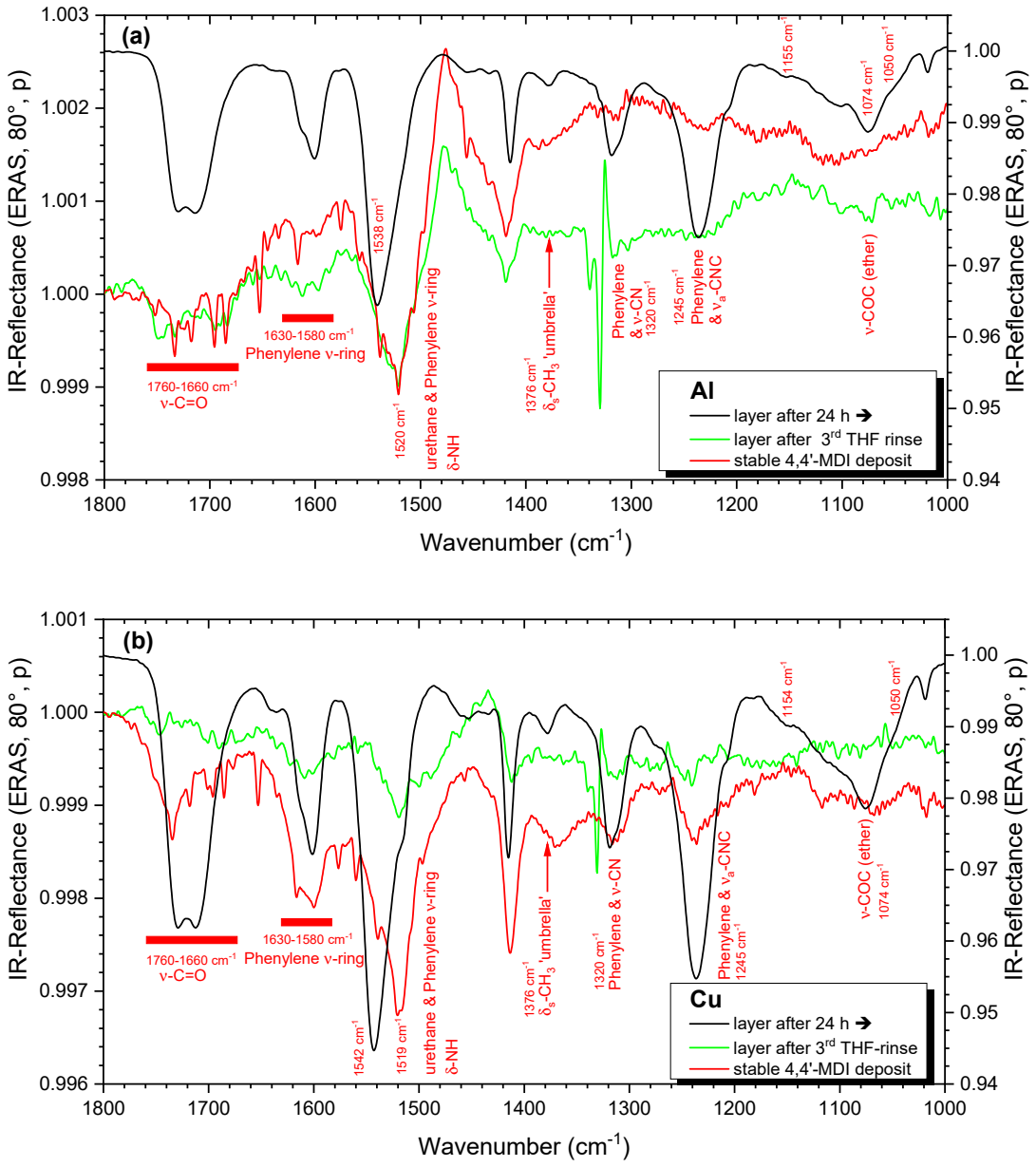

Fig. 7-33 Comparison of layers formed by sequential deposition of MDI followed by DPG after 24 h of storage (black) and three THF rinses (green) with a stable 4,4'-MDI layer (red) on Al (a) and Cu (b).

[58] Note: The stable MDI deposit is prepared by three THF rinses as well – cf. Section 7.2.1.

Particular bands for urethane but also for the reacted alcohol units (mainly CH and ether vibrations) are extremely weak and can only be guessed.

On Cu, the same observations are made in general but with one major difference. The intensity of all bands is now much weaker than on the stable MDI deposit but also weaker than on Al. Hence, much less adhering species remain on Cu after urethane formation and THF rinses. In conclusion, some of the adhesively bonded NCO seems to give up this interaction with the native Cu surface in favour of the addition with the alcohol. This can also explain why during 24 h on Cu more urethane molecules are formed than on Al.

In conclusion, urethane does not form with the physisorbed MDI only but also affects the strong adhesion of NCO with the substrate, at least on Cu. Furthermore, mobility of all species in the thin deposit is still high after THF rinse.

7.3.1.4 Intermediate conclusion

Deposition experiments with dipropylene glycol on top of ca. 1.5 nm 4,4'-MDI result in several conclusions and help to update our layer model.

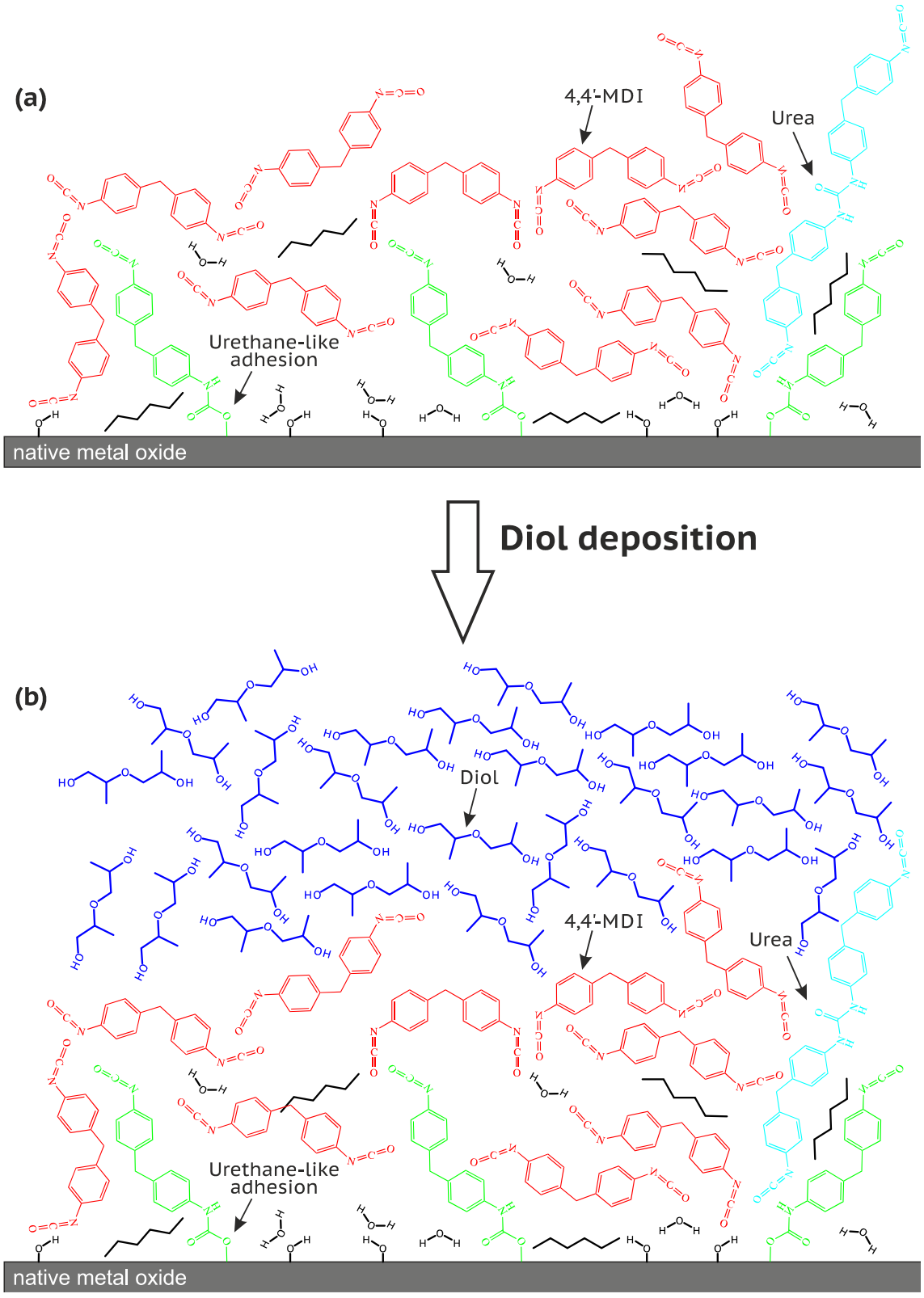

Fig. 7-34 Schematic representation of the behaviour of DPG deposited on top of 4,4'-MDI. (a) Original thick 4,4'-MDI layer. (b) As-prepared state of DPG deposit on top of the MDI.

A first model update is illustrated in Fig. 7-34. Unlike the common idea in literature, no monolayers but thick multi-layers of both monomers are sequentially deposited. Fig. 7-34b represents the idealised initial state where DPG has just been deposited without any diffusion or chemical reaction.

Most of the DPG desorbs from top of 4,4'-MDI within 10 min. On the other hand, the urethane reaction requires up to 10 h. Over this period of time, the intensity ratios of the carbonyl and phenylene bands indicate that the formed urethane molecules possess enough mobility in the thin deposit to rearrange for energetically favourable hydrogen bonds. As many urethane molecules are formed, the monomers are also mobile enough to mix together. These aspects are illustrated in Fig. 7-35. The omnipresent contaminations are also capable to mix with the complete layer.

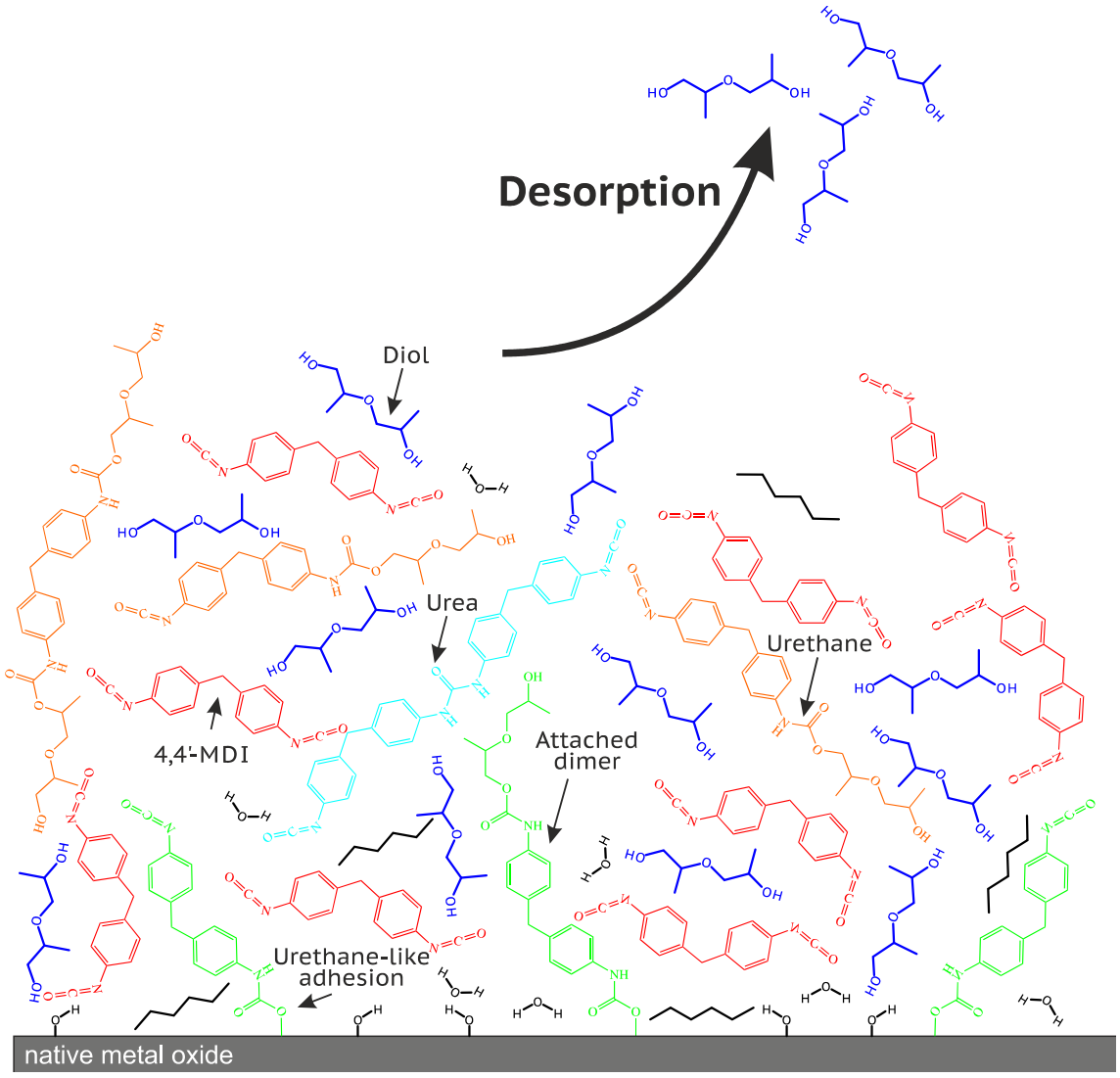

Fig. 7-35 Schematic representation of the behaviour of DPG deposited on top of 4,4'-MDI. Fast desorption of unreacted DPG and mixing of monomers and formed urethanes.

Over storage time, the polymerisation reaction slows down and comes to a stop after ca. 10 h. On one hand, this happens because unreacted alcohols rapidly desorbed and hence are not available anymore. Unreacted isocyanate groups are still available after 24 h. On the other hand, as urethane oligomers continue to grow with ongoing reaction, mobility of the species fades, and at some point functional groups cannot reach each other anymore. So some alcohol groups could be present even if the OH stretch is not explicitly visible in the IR spectrum. Metal specificity is observed for the urethane reaction as more urethanes are formed faster on Cu compared to Al.

Now, our deposit is composed of linear urethane oligomers and residual monomers. Some unreacted monomer functionalities are present at these monomers or as termination of the formed chains. Few urea has formed as well. Last but not least, species strongly adhering to the surface are also present. The layer after 24 h of storage is illustrated in Fig. 7-36. They all contribute to the particular band shape of the carbonyl and phenylene bands.

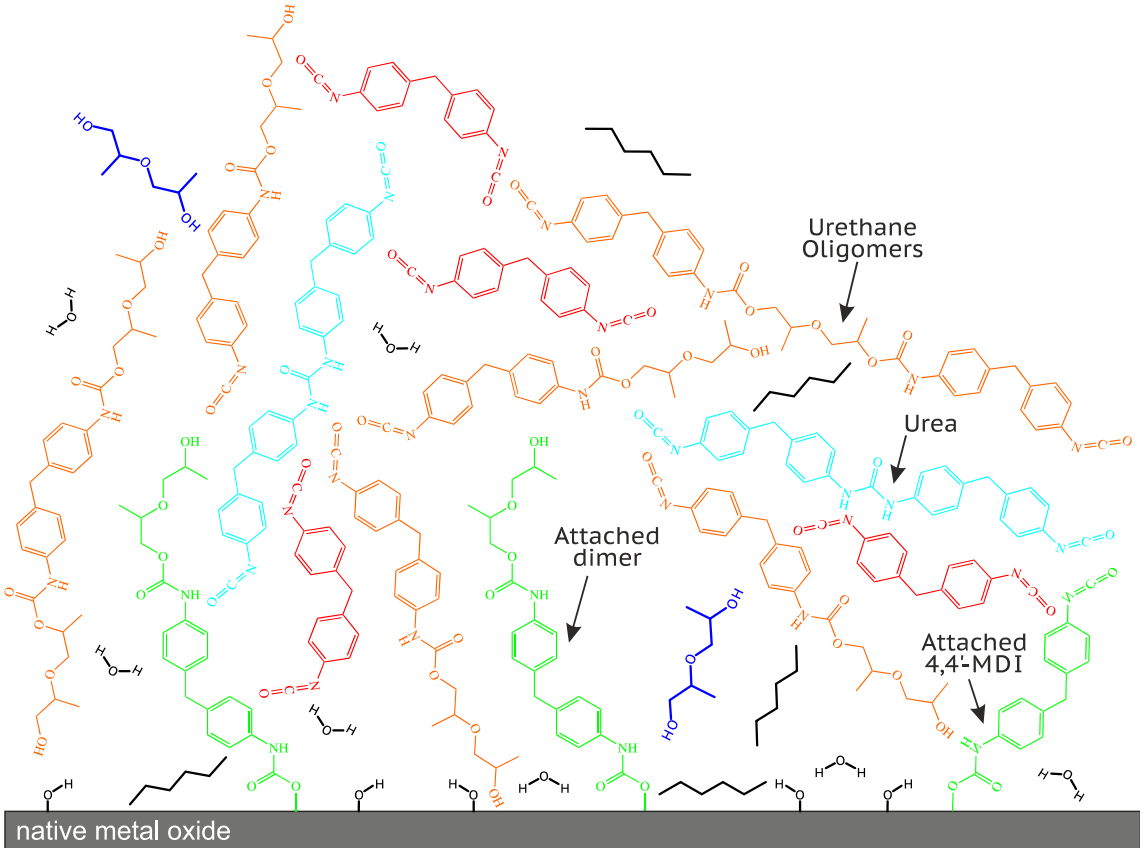

Fig. 7-36 Schematic representation of the layer formed by DPG deposited on top of 4,4'-MDI after 24 h of storage.

Topography of the layer reveals a rough and metal specific deposit. Obviously, the addition of alcohol on top of the already non-homogeneous MDI deposit has not allowed for a homogenisation of the layer. Besides diol desorption, dewetting could happen.

Finally, the stability of the deposit is poor on both metals as most of the molecules are removed by THF rinsing. Fig. 7-37 provides an attempt to illustrate this. Most of the urethane oligomers are washed away, as they are not linked to the surface. Urea and residual monomers are removed as well. Interestingly, much more material is removed on Cu than on Al. Compared to stable 4,4'-MDI deposits, stability on Cu is extremely poor. Even more, some of the strongly attached molecules have also been removed. Thus, some of the adhesive bonds open in order to react with diol. Identification of the remaining species has proven to be difficult as band intensity is very weak. Fortunately, remains of phenylene and carbonyl bands indicate the presence of MDI units, but bands for the alcohol units (CH and ether vibrations) that have reacted with the MDI can only be guessed. Due to the high monomer mobility and to the findings that stable MDI deposits are capable to react with alcohol (cf. section 7.2.3) they should be present.

Hence, the urethane layers prepared by MLD perform poorly. This is not in agreement with previous studies of thin layers prepared from diluted solutions. They behave very well (cf. 6.1.2 & [11, 157]) and show excellent stability against THF. The reason for that difference is seen in the finding that the forming urethane oligomers are not capable to bind to the stable MDI deposit from MLD. One reason could be the fast desorption of the diol. Depletion of that monomer brings the reaction to a stop. Furthermore, as more NCO than OH groups are present after diol desorption, virtually all DPG monomers react with two isocyanates and form a MDI-DPG-MDI trimer. These trimers are NCO-terminated and thus not able to form true chains or to react with the adhering MDI.

In conclusion, properties of the MLD deposit could be improved by reducing the alcohol desorption rate significantly and by offering a triol for crosslinking instead of chain polymerisation. The behaviour of such layers is discussed in the next section.

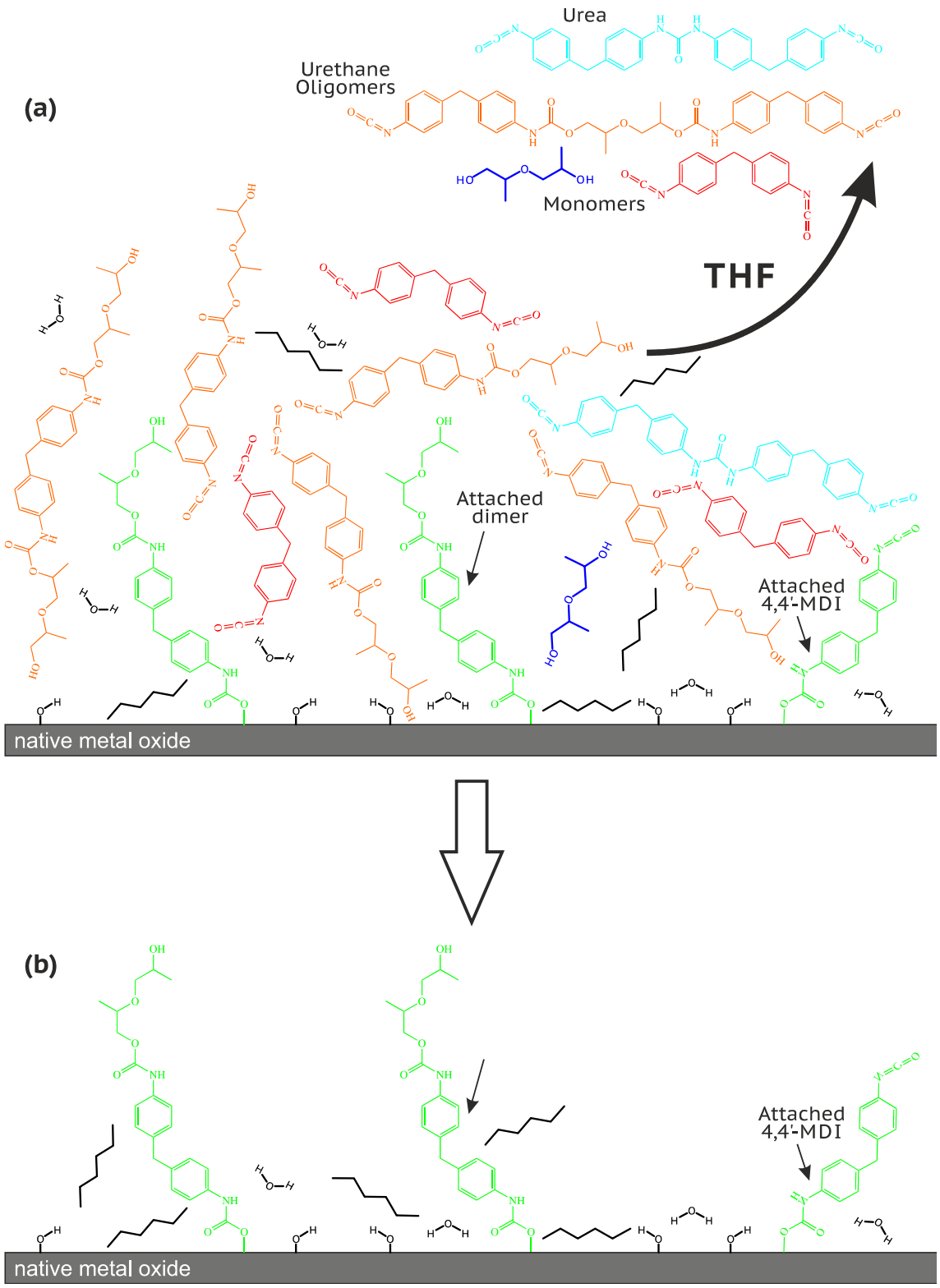

Fig. 7-37 Schematic representation of the effect of THF on the layer formed by DPG deposited on top of 4,4'-MDI. (a) Removal of species by the THF. (b) Final layer after the rinses.

7.3.2 Deposition of triol instead of diol

Sequential deposition of isocyanate followed by triol is carried out the same way as for the previously discussed layers. Experimental parameters are kept unchanged (except for the evaporation temperature of the triol). The deposited thicknesses are maintained. Moreover, the deposition sequence is switched in one series of depositions. On top of the alcohol, MDI should mix stronger with the alcohol because the option of strong adhesive interactions will force the MDI to move to the substrate. Hence, this experiment helps to confirm the mobility of the confined molecules.

7.3.2.1 Differences during storage time

Detailed evolution of the layers on Al and Cu over 24 h of storage at RT is provided in appendix 11.6.2 - 11.6.5. This section mainly aims to highlight the differences observed when the diol is replaced by the triol. The reaction of MDI with alcohol is identical in all cases and the same characteristic urethane bands are obtained as with the diol. In particular, the carbonyl group forms hydrogen bonds, and the progressive change of intensity ratio between free carbonyl and hydrogen bonded carbonyl groups is always observed.

Specific features and differences between the metals are discussed hereafter.

◊ *Triol deposited on top of 4,4'-MDI layers*

Triol desorbs slower than diol (cf. sections 11.6.2 and 11.6.3). Desorption take place over 10 h as CH vibrations continuously lose intensity. Hence, unreacted triol is available throughout the complete reaction time, and some OH groups remain even after 24 h as seen by the weak shoulder around 3430 cm^{-1}.

As for the diol deposit, urethane forms faster on Cu but the reaction comes to a stop after 10 h of storage on both metals.

Fig. 7-38 compares the layers on Al and Cu after 24 h.
The spectra on both metals are very similar except of a few bands. First, the shape of the carbonyl bands (1730 and 1711cm^{-1}) is different. On Cu, less carbonyl groups are involved in H-bonds than on Al. As triol is larger than diol and can react with three isocyanates, the resulting urethane species are less mobile. This mobility difference on each native metal is visible in the spectra. At higher wavenumbers, more unreacted hydroxyl groups are present on Cu. The shape of the CH stretches is also metal specific. It is noted that on Cu no NCO band is left. Hence, all isocyanates have reacted with hydroxyl groups. That also explains why more unreacted hydroxyl groups are present.
The ether band exhibits a particular shape as it is now formed by the superposition of the ether vibrations of the unreacted hydroxyl groups and of ether near urethane groups (1154, 1075 and 1050 cm^{-1}). The newly formed ether vibrations are identical to those found with the diol.
The remaining parts of the fingerprint region are comparable.

In conclusion, except for a few minor features no major differences are found compared to urethane layers prepared with diol.

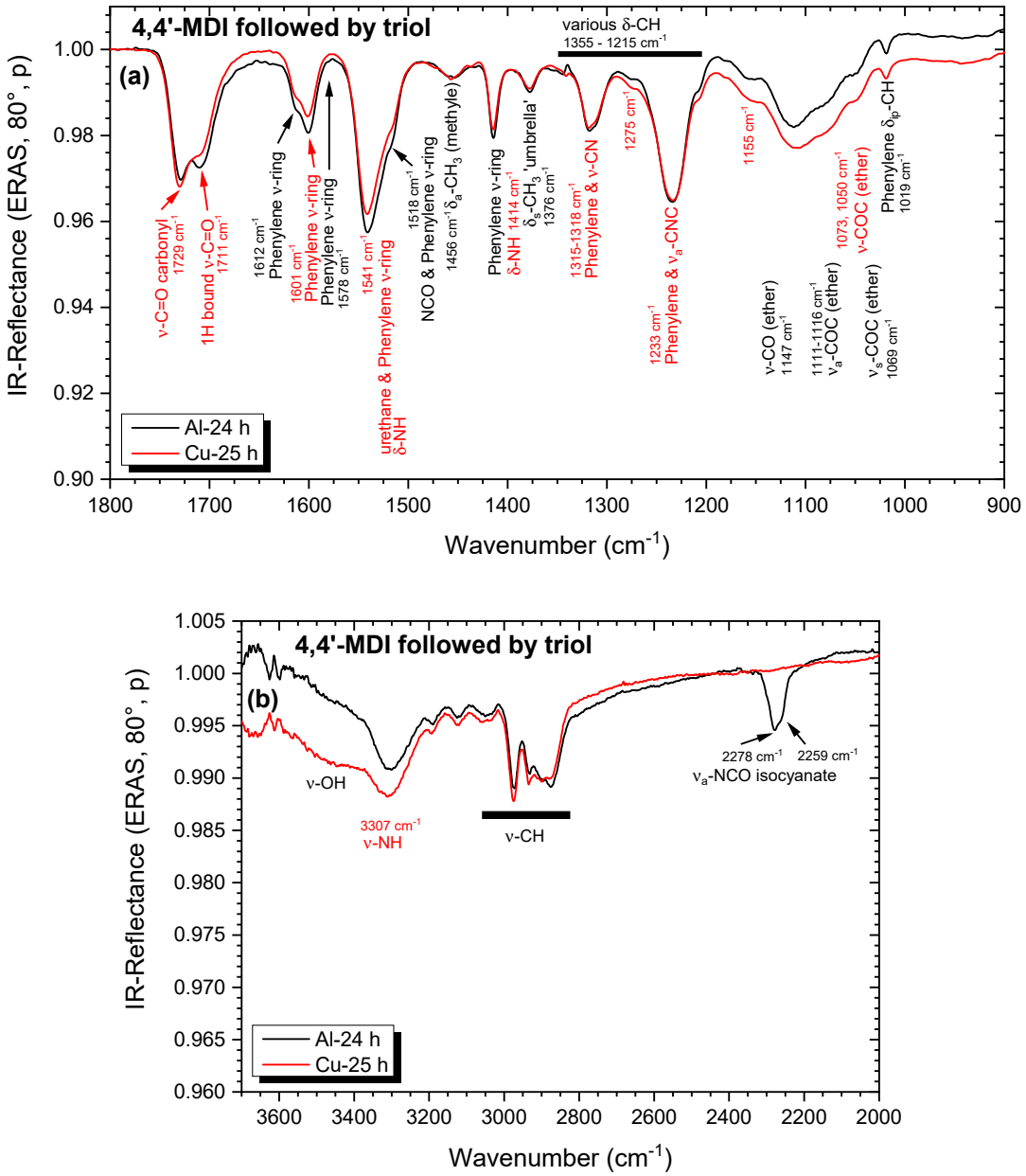

Fig. 7-38 Spectra of deposits of 15 nm triol on top of 1.5 nm 4,4'-MDI on Al (black) or Cu (red) after 24 h of storage. Bands assigned for the monomers (black) and new species (red). (a) 1800 – 900 cm^{-1}, (b) 3700 – 2000 cm^{-1}.

◊ *4,4'-MDI deposited on top of triol layers*

Now triol is deposited first on the metal substrates. Triol thickness is only 10 nm now and desorption is going on while MDI is deposited. Hence, the alcohol bands are weaker than for the case of triol deposition on top of MDI (cf. Fig. 7-40 and sections 11.6.4 and 11.6.5). Urethane bands are stronger and NCO bands weaker on Cu than on Al. Hence, urethane formation is faster on Cu. After 24 h storage, some unreacted OH groups are still present on Cu, similar to the layers where triol is deposited on top of MDI. The deposition sequence of the monomers does not produce any evidence for a difference at this point.

Fig. 7-39 and Fig. 7-40 reveal that for both deposition sequences and similar to the layers with DPG more urethane groups are formed on Cu. Furthermore, no isocyanate band remains on Cu and thus more unreacted OH groups are present. The intensity ratio of the carbonyl groups is metal specific again. The shape of the ether band is different because more unreacted triol remains on Cu. The other spectral features are identical on both metals.

The spectral region above 2000 cm^{-1} show that no NCO groups are left with triol on Cu while free NCO groups remain on Al. Due to the depletion of NCO, more OH groups remain on Cu.

Beside the few minor differences in the spectra between Al and Cu behaviour of the layers during storage time is equivalent to those prepared before.

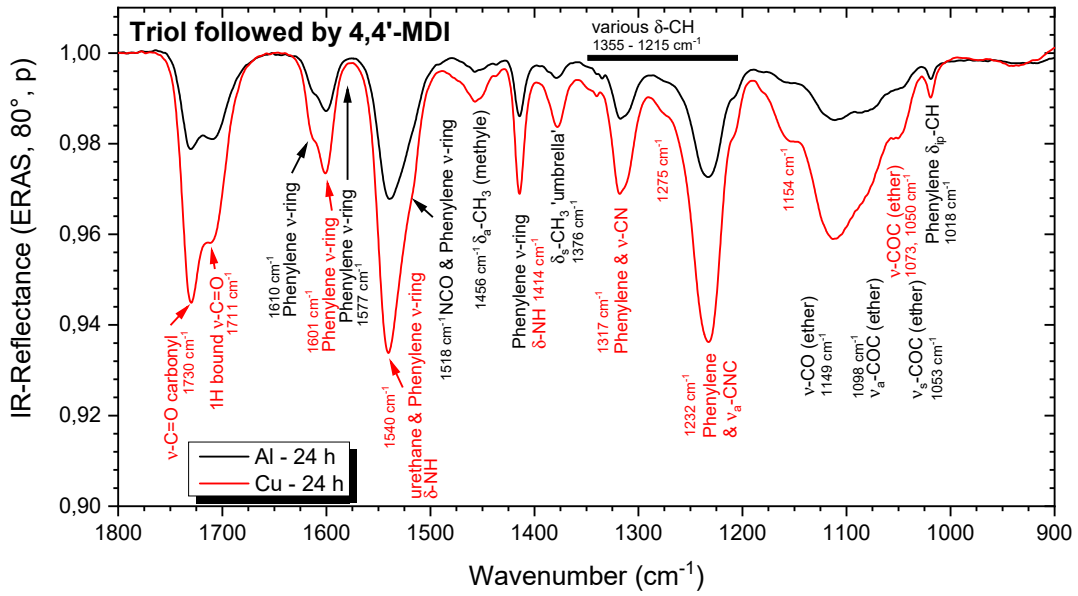

Fig. 7-39 Spectra of deposits of 1.5 nm 4,4'-MDI deposited on top of 10 nm triol on Al (black) or Cu (red) after 24 h of storage. 1800 – 900 cm^{-1}. Bands assigned for the monomers (black) and new species (red).

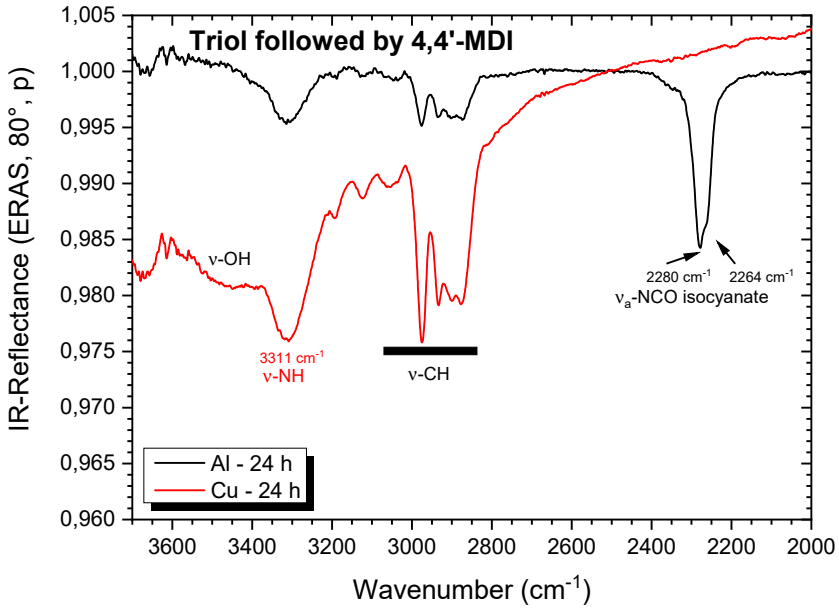

Fig. 7-40 Spectra of deposits of initially 1.5 nm 4,4'-MDI on top of 10 nm triol on Al (black) or Cu (red) after 24 h of storage. 3700 – 2000 cm^{-1}. Bands assigned for the monomers (black) and new species (red).

7.3.2.2 Comparison of the deposits after 24 h of storage

For each metal separately, the layers are compared now with respect to the chosen alcohol monomer and to the deposition sequence of triol and MDI.

◊ *Behaviour on Aluminium*

Starting with aluminium, the spectra of the three layers show that generally the same bands are present after storage (Fig. 7-41). Unreacted NCO groups are present on all layers. Band intensity and intensity ratios between bands are different though.

First, the intensity ratio of the carbonyl vibrations is related to the type of polyol used. For DPG (red spectrum, Fig. 7-41a) free carbonyl groups and hydrogen bound carbonyl groups are equally present. For both triol containing deposits (green - MDI on triol, blue – triol on MDI) free carbonyl groups dominate. While free carbonyl groups are formed with the urethane molecule itself, H-bonds require the urethane groups to assemble in a specific orientation. This becomes more difficult for larger molecules. Hence, as the diol is smaller than the triol, which in addition can bond up to three isocyanates, mobility is lower and less H-bonding takes place in the triol-based deposits. However, mobility is still good enough in the triol layers to allow reorientation of the urethane groups over storage time. This is seen by a progressing intensity ratio change of the involved carbonyl bands (cf. Fig. 11-23 & Fig. 11-32).

Second, the ether region (1175 – 1000 cm^{-1}) is significantly modified when the diol is replaced by triol. Several reasons cause this difference.

All three layers have in common that upon urethane formation the ether vibrations are modified as seen by the appearance of bands at 1154, 1073, and 1050 cm^{-1}. These bands are superimposed by the original bands if unreacted alcohol remains in the layer. This is in particular the case for the layers with triol. Furthermore, MDI bands are also present in that region. The superposition of all these bands with different intensities results in the particular shape of the ether region.

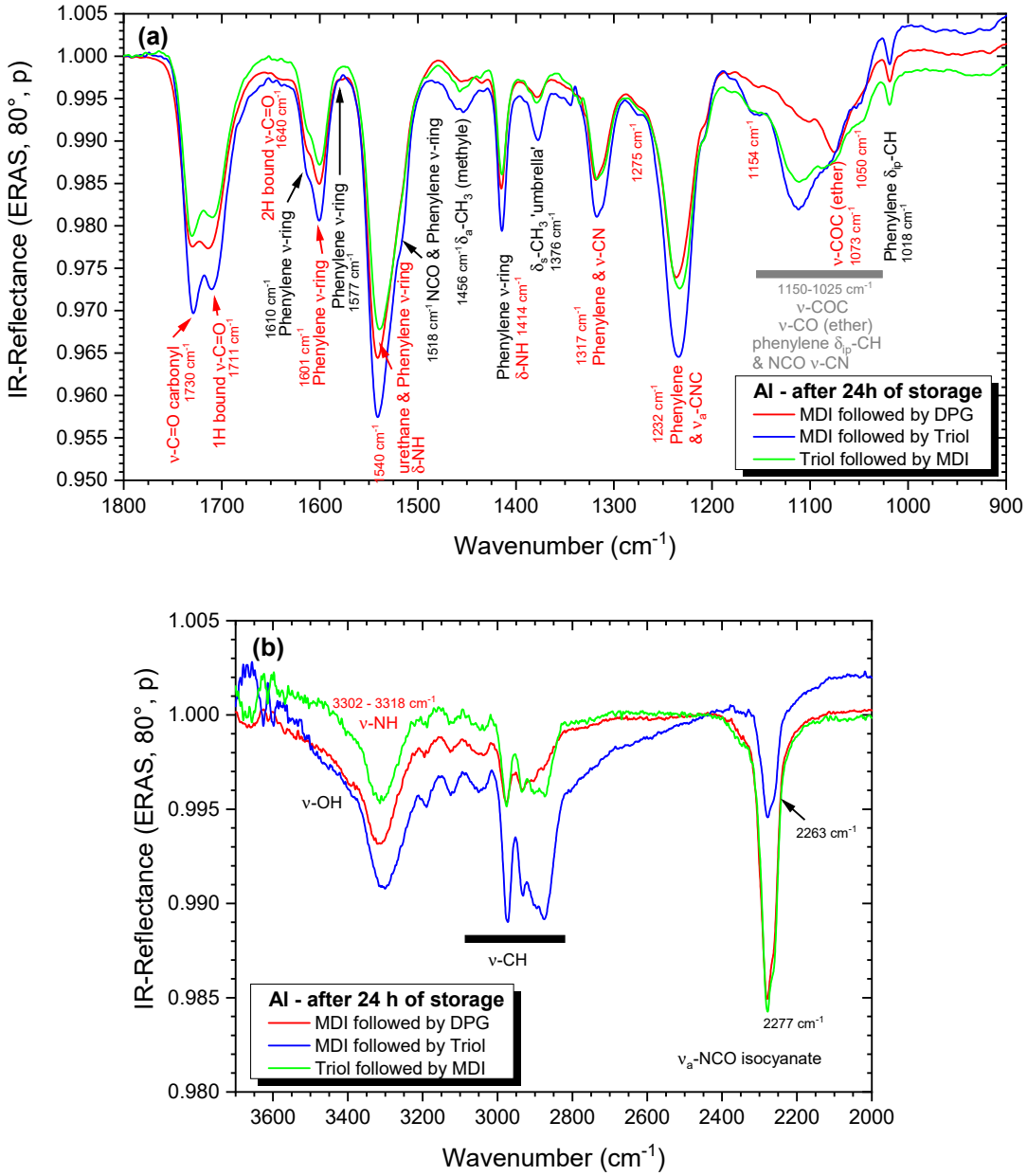

Fig. 7-41 Spectra of urethane layers on Al after 24 h of storage. Bands assigned for the monomers (black, grey) and new species (red). (a) 1800 – 900 cm^{-1}, (b) 3700 - 2000 cm^{-1}.

Third, above 3300 cm^{-1} (Fig. 7-41b), a shoulder indicates remaining OH groups in the triol layers which corroborate the findings for the ether region.

Finally, it is noted that the overall intensity differences between the layers are small (they do not exceed 1 % of reflectance - cf. Fig. 7-41). Most urethane forms in the layer with triol on top of MDI (blue spectrum). The other two layers have comparable band intensities.

In conclusion, the monomer deposition sequence does not matter very much on native Al in terms of layer thickness.

◊ *Behaviour on Copper*

On Cu (Fig. 7-42 and Fig. 7-43), similar observations are made as for the Al substrate. A few differences are present, however.

The overall spectral intensity of all three layers is larger on Cu. Moreover, the intensity difference is of about 2-3 % between the layers on Cu. That is significantly more than on Al.

Deposition of MDI on top of triol (green spectrum, Fig. 7-42) yields most urethane, followed by the layer with diol on MDI. Least urethane is obtained when triol is deposited on top of MDI. Hence, on Cu, urethane formation depends not only on the chosen monomers but on their deposition sequence as well.

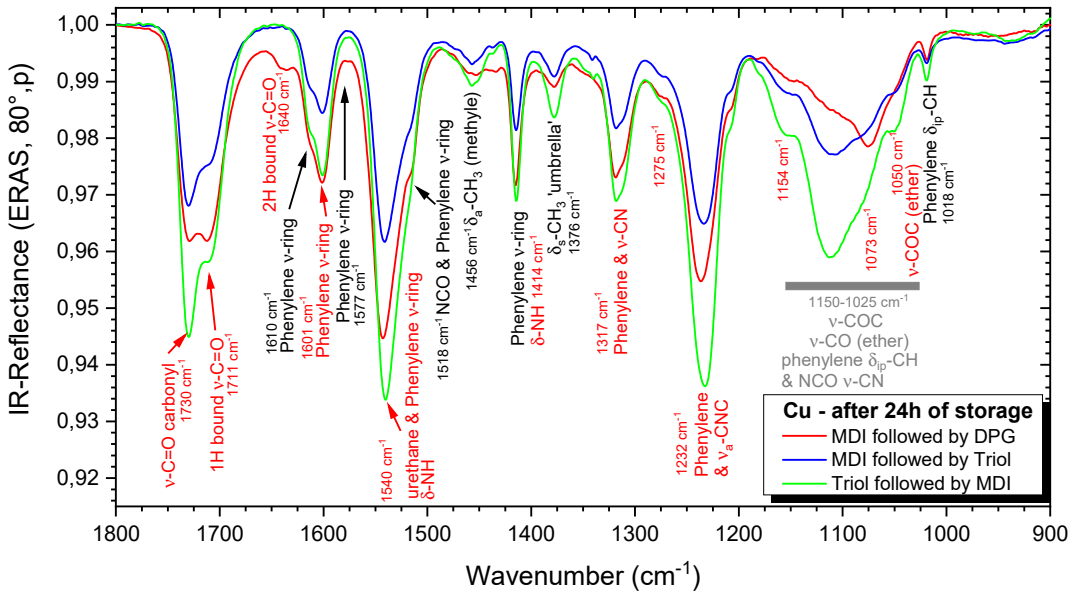

Fig. 7-42 Spectra of urethane layers on Cu after 24 h of storage. 1800 – 900 cm^{-1}. Bands assigned for the monomers (black, grey) and new species (red).

The upper spectral region (Fig. 7-43) illustrates the presence of residual OH groups in the layers made with triol. A wide band is present at the OH vibrational region (green and blue spectra). This is in accordance with the presence of ether vibrations from the triol (1175 – 1000 cm^{-1}) that modify the shape of the ether band.

In parallel, the layers with triol do not exhibit a NCO band. NCO is only observed for the layer with diol (red). This observation implies a complete conversion of isocyanates as supported by the unreacted OH groups in the triol-containing layers. However, specific phenylene bands (e.g. 1610, 1577, 1518 cm^{-1}) attributed to unreacted MDI are still present. This finding represents an apparent contradiction as it may indicate the presence of particular orientations of the isocyanate molecules on the surface[59].

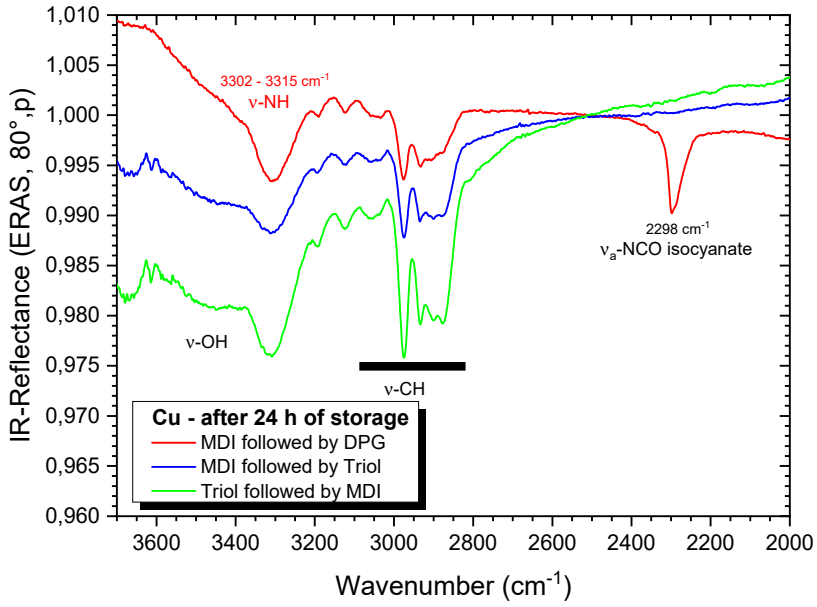

Fig. 7-43 Spectra of urethane layers on Cu after 24 h of storage. 3700 – 2000 cm^{-1}. Bands assigned for the monomers (black) and new species (red).

◊ *Consequences of the alcohol exchange*

Substitution of diol by triol does not fundamentally change chemistry in the deposits during storage time. Urethane formation works very well with both alcohols. Switching the monomer deposition sequence does not affect the reactivity at all.

However, mobility of the bulky triol molecules is less and they can operate as crosslinks in the forming urethane oligomers. The obtained spectral features, as for example the intensity ratios of the carbonyl or ether bands, are specific for the used alcohol, but the evolution of these bands is similar over storage time.

[59] Reminder: particular orientations of the transition dipole moment of a given vibration with regard of the p-polarised IR beam are responsible for a loss or an increase of band intensity in the ERA spectrum.

In addition, it will be interesting to look at the topography of the layers - if and how the triol-containing deposits would modify morphology. Furthermore, the stability of the layers is another key issue. Would crosslinking capability of the triol monomer result in a urethane network?

7.3.2.3 Layer topography after storage

20 x 20 µm^2 scans of the triol-containing layers prepared on Al and Cu are shown in Fig. 7-44 to Fig. 7-46. Topographies of the layers prepared with diol (cf. section 7.3.1.2) are shown for comparison.

Starting with the urethane layers on aluminium, calottes and bumps are present as topographic features on all three layers. The frequency and coverage of these features is different however. On the layer prepared by deposition of MDI followed by triol (Fig. 7-44, left) a multitude of small bumps (ca. 30 nm high) are dispersed between round calottes of up to 80 to 90 nm high. Switching the deposition order (Fig. 7-45, left) nearly all bumps grown into small calottes. Most calottes are up to 45 nm high with a few reaching up to 60 nm. As a consequence, the increase of calottes leads to a reduction of their height.
Compared to the layer prepared by deposition of diol on MDI (Fig. 7-46, left), much more calottes and bumps are present on the layers with triol. Their lateral size is also smaller. These differences may be triggered by the different rate of desorption of the alcohols. The fast desorption of DPG does not allow to form a multitude of smaller calottes. As triol desorbs much slower the molecules have enough time to move on the layer surface and agglomerate at energetically favourable positions. It is also noted, that even if the MDI forms a rough deposit when deposited first (cf. Fig. 6-33), the topography is not significantly modified when the deposition order is changed.

On Cu, the topography differences are much more pronounced (Fig. 7-44 to Fig. 7-46, right). The layers prepared with triol exhibit widespread calottes while bumps are rare. Furthermore, the calottes are much larger and less high (ca. 45 – 50 nm) than on Al. The layer with triol deposited first (Fig. 7-45, right) shows an intermediate between the calottes of the ‘triol-on-MDI’ layer (Fig. 7-44, right) and the plateau and valley structure seen on the ‘diol-on-MDI’ layer (Fig. 7-46, right). The calottes are much larger again and their distance is reduced or occupied by shallow plateaus, respectively. Hence, the deposition order and the type of alcohol do affect the topography.

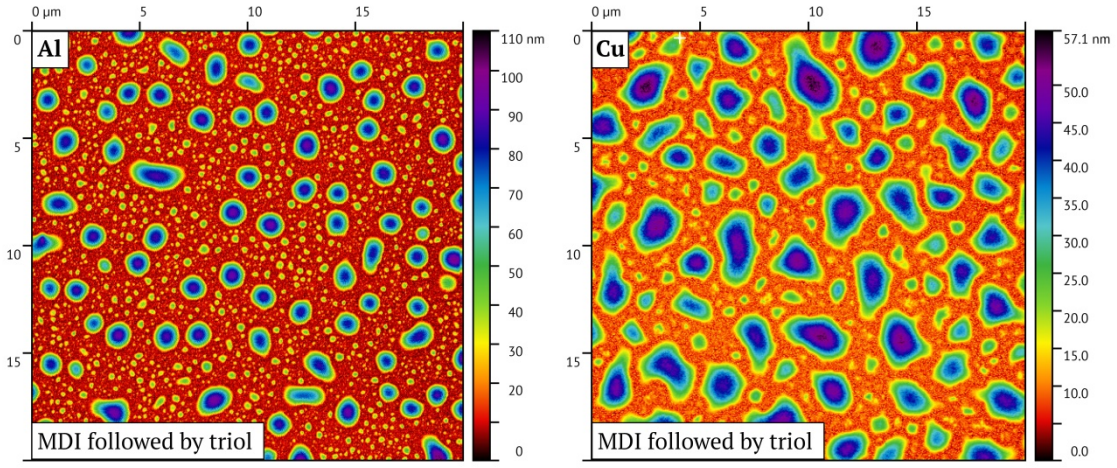

Fig. 7-44 Tapping mode SFM topographic views of 24 h stored layers prepared on Al (left) and Cu (right) by deposition of triol on 4,4'-MDI. 20 x 20 µm² scan.

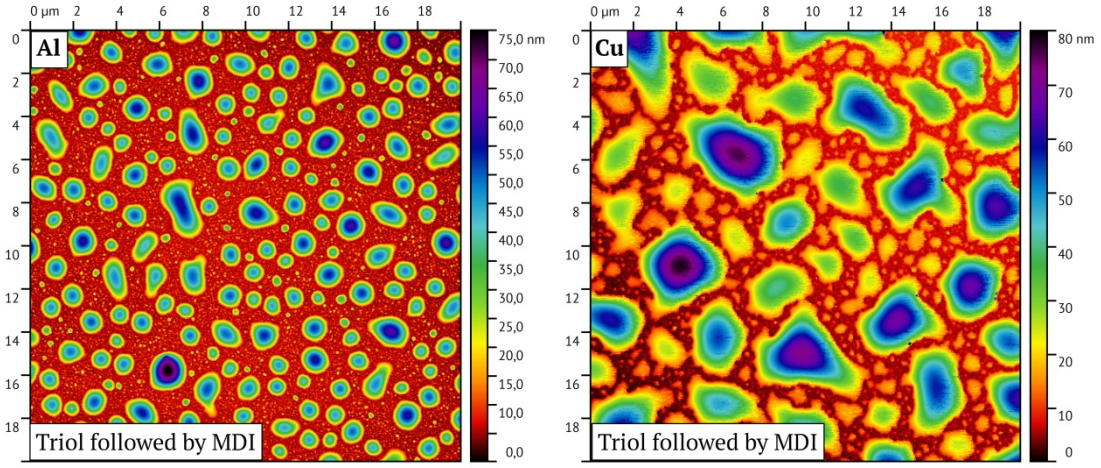

Fig. 7-45 Tapping mode SFM topographic views of 24 h stored layers prepared on Al (left) or Cu (right) by deposition of 4,4'-MDI on triol . 20 x 20 µm² scan.

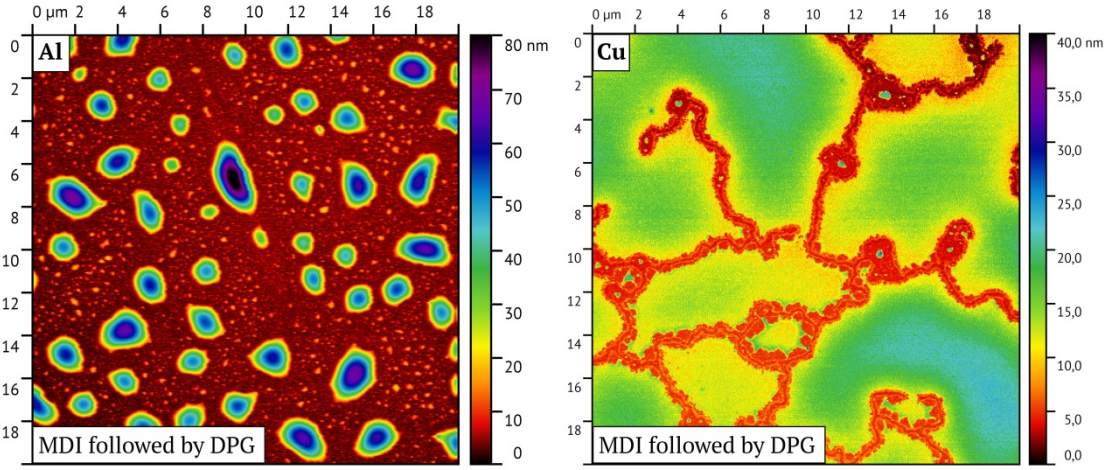

Fig. 7-46 Tapping mode SFM topographic views of 24 h stored layers prepared on Al (left) or Cu (right) by deposition of diol on 4,4'-MDI . 20 x 20 µm² scan.

The 5 x 5 µm² scans reveal more detail of the layer topography - Fig. 7-47. On Al, the 'triol-on-MDI' layer exhibits few round calottes that are 1.25 µm wide and up to 80 nm high (Fig. 7-47a). They are surrounded by many smaller bumps (0.4 µm wide and 35 nm high). The flat region in between (red) replicates the nodular polycrystalline structure of the aluminium.

The 'MDI-on-triol' layer (Fig. 7-47c) features more calottes than the previous layer. Their width ranges from 0.9 µm up to 2 µm and their height from 30 to 50 nm. Hence, they are larger and less round but flatter. Very small bumps (0.2 µm wide and ca. 15 nm high) are hardly distinguished from the nodular aluminium underground.
Fig. 7-47b, d, show that the phase contrast on the flat nodular regions is nearly the same as on top of the calottes and bumps. Hence, similarly to the urethane layers prepared with diol, the substrate is fully covered with organic material. The phase contrast profile lines (Fig. 7-48) support this conclusion.

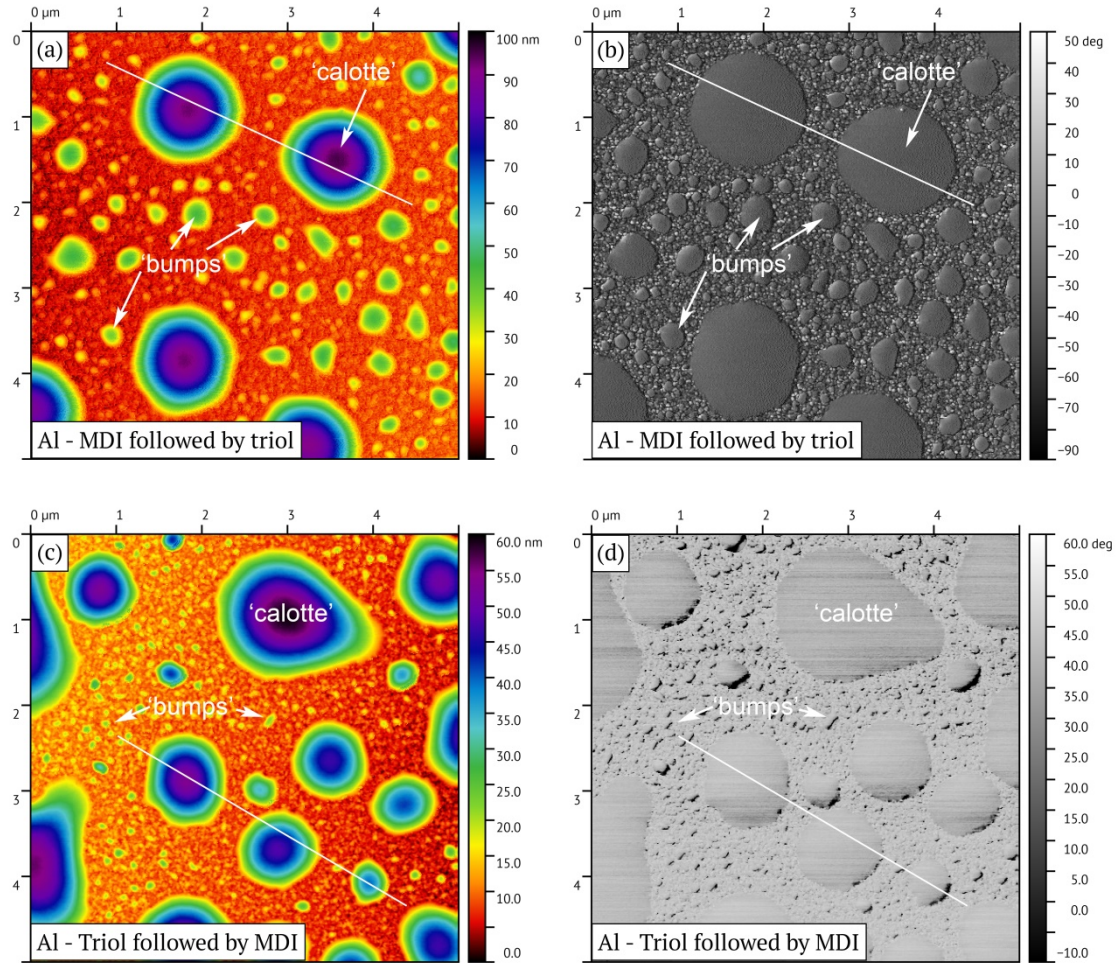

Fig. 7-47 Tapping mode SFM topography (a, c) and phase contrast (b, d) images of the urethane layers prepared on Al by deposition of triol on MDI (a, b) or by deposition of MDI on triol (c, d). 5 x 5 µm² scan. White lines indicate the location of height and phase contrast profiles given in Fig. 7-48.

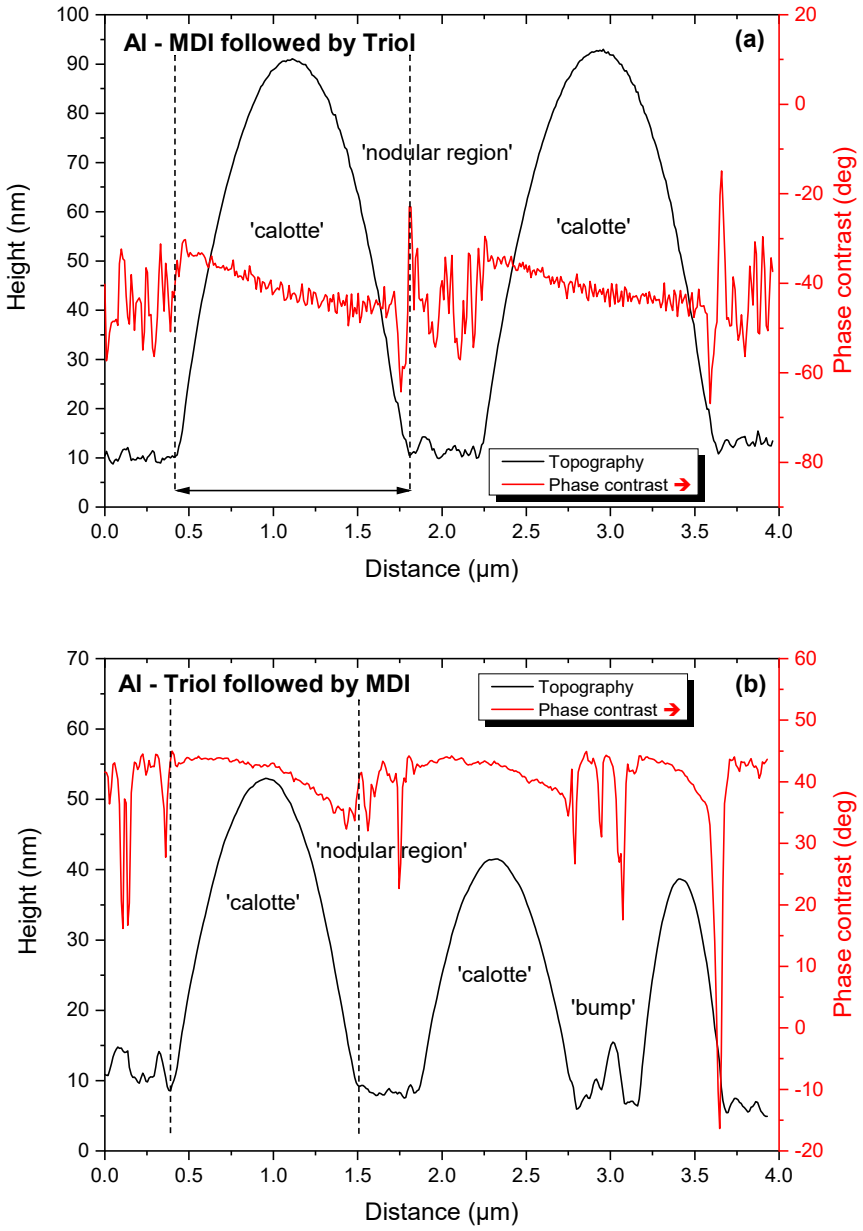

Fig. 7-48 Topography (black) and phase contrast (red) profiles along the lines shown in Fig. 7-47 for the 'triol-on-MDI' layer (a) and the 'MDI-on-triol' layer (b) on Al.

Along the profile line passing calottes and their surroundings, the phase contrast on both layers fluctuates around – 40° or 40°, respectively.[60] Phase contrast jumps are registered at the nodule boundaries in the flat region. The calottes show a much smoother phase contrast that does not significantly differ from their surroundings.

[60] Note: Scanning parameters need to be adjusted individually for each sample. As a consequence, the absolute values of phase contrast are so much different on both urethane layers and must not be discussed or compared with data from other layers like virgin Al substrates, for example.

On Cu, starting with the 'triol-on-MDI' layer (Fig. 7-49a) topography is shaped by large irregular calottes of up to 3 µm wide and 50 to 60 nm high as well as few shallow bumps ranging from 0.5 to 1 µm width and up to 30 nm height. The area in between (red region) replicates the nodular polycrystalline structure. Compared to the layers on Al the calottes and bumps are much larger on Cu.

The 'MDI-on-triol' deposition (Fig. 7-49c) drives this trend further. Irregularity of shape and size of the calottes rose. In between, the flat regions are less than 0.5 µm wide and can be considered as valleys now. At some places, calottes and bumps are interconnected.

Both phase contrast images (Fig. 7-49b, d) show a significant difference between the flat surroundings and the calottes or bumps. This feature was observed for the layer prepared with diol too.

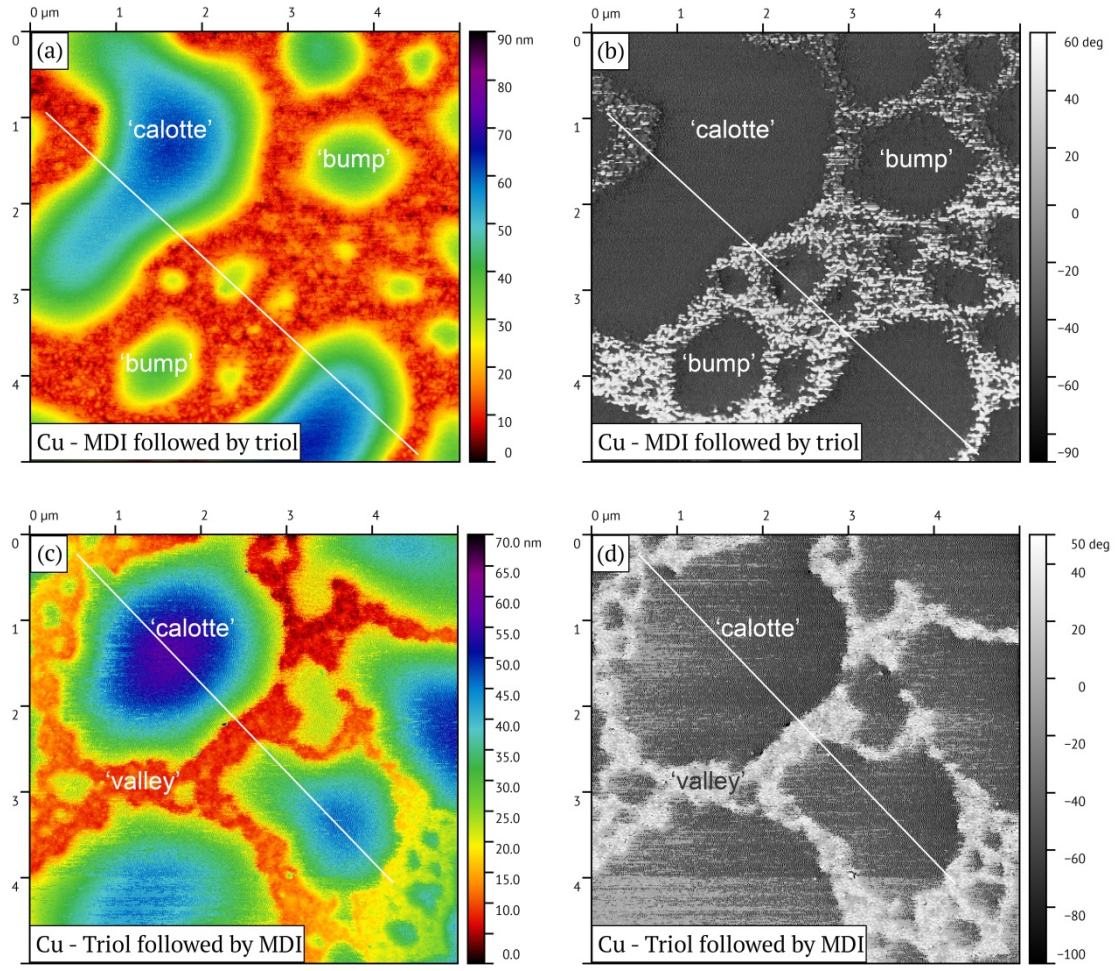

Fig. 7-49 Tapping mode SFM topography (a, c) and phase contrast (b, d) images of 'triol-on-MDI' urethane layers (a, b) and 'MDI-on-triol' layers (c, d) on Cu. 5 x 5 µm² scan. White lines indicate the location of height and phase contrast profiles given in Fig. 7-50.

The phase contrast is very smooth inside the calottes (-40 to -50°) and experiences a large phase angle difference when passing into the valleys. As this behaviour is observed on all layers prepared on Cu, the suggestion that urethane is only present in the calottes and bumps is substantiated.

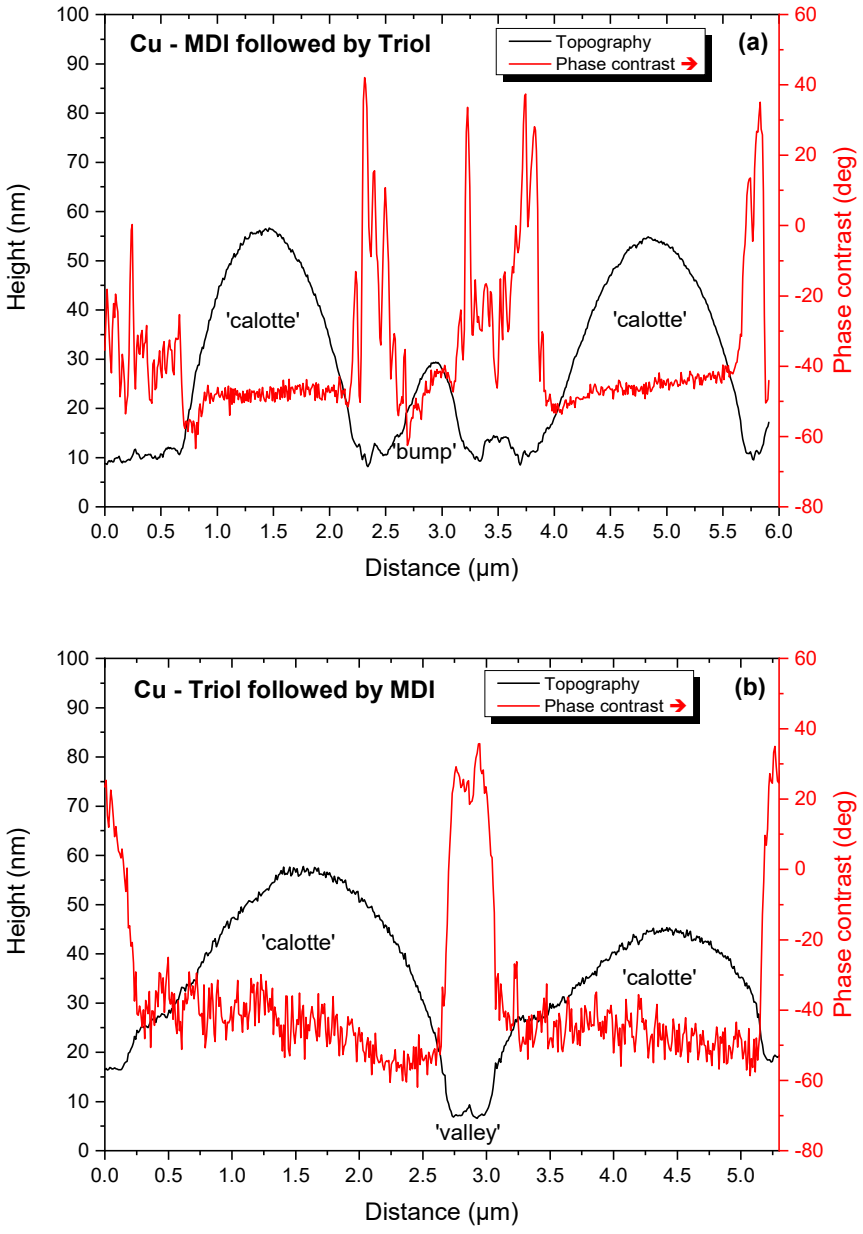

Fig. 7-50 Topography (black) and phase contrast (red) profiles along the lines in Fig. 7-49 for the ‘triol-on-MDI’ layers (a) and the ‘MDI-on-triol’ layers (b) on Cu.

Comparison of the topography of the prepared layers yields a further conclusion. Provided that the topography results from dewetting of the deposited monomers, the layers on Cu show the different stages of dewetting. Starting with the diol-containing layer, large plateaus are separated by small valleys. For enhanced dewetting, the valleys grow and irregular calottes and bumbs are formed (‘MDI-on-triol’ layer). For strongest dewetting, these structural elements separate further and grow in height.
Furthermore, on Al only the calottes and bumps are observed. Hence, dewetting would be more effective than on Cu. However, wetting is incomplete in all cases as the whole surface is still covered with organic material.
Topography measurements at different storage times would be necessary to obtain further proof for this hypothesis.

7.3.2.4 Layer stability towards THF

Unfortunately, all four layers prepared with triol do perform poorly in the THF rinsing test. Examples are given for the layer prepared by deposition of triol on 4,4'-MDI. For the other three layers, results are given in Appendix 11.6.3 to 11.6.5.

As observed for the layers made with DPG, the 1st THF rinse removes most of the formed urethane and unreacted monomers as in the spectrum all bands massively lose intensity (cf. Fig. 7-51 to Fig. 7-53). Hence, the crosslinking anticipated for the triol does not work for the preparation at room temperature. Further THF rinses do only remove few molecules.

Starting at 1800 cm^{-1} (Fig. 7-51), the carbonyl region is embossed by a wide buckle at the limit of resolution. Diverse phenylene bands (1630-1580, 1550-1500 and 1414 cm^{-1}) are seen well, including the phenylene at urethane. Their band shapes correspond to those in previous layers. Interestingly, some CH_3 deformations, in particular the umbrella deformation (1376 cm^{-1}) are still visible after the 3rd THF rinse. This confirms that triol reacted with the adhesively bonded MDI and formed dimers at least.

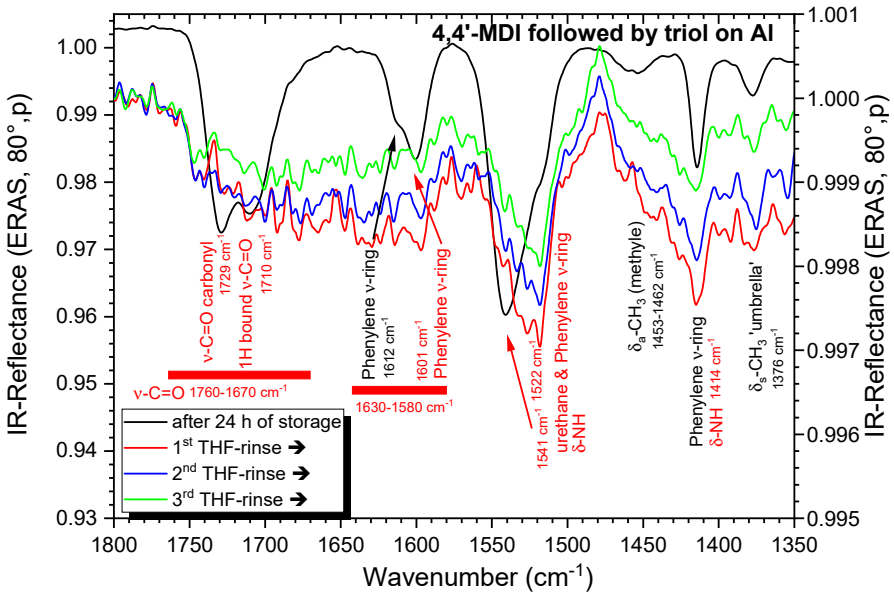

Fig. 7-51 Effect of THF rinses on a layer prepared by deposition of 4,4'-MDI followed by triol on Al after 24 h of storage in dried air at RT. 1800 – 1350 cm^{-1}. The black spectrum represents the layer prior to rinsing. Band assignment for the monomers (black) and the new species (red) refers to the black spectrum.

Below 1350 cm^{-1} (Fig. 7-52), remains of the combined phenylene vibrations are present. The ether region with its three specific bands for urethane species (1155, 1073, and 1050 cm^{-1}) is difficult to analyse due to the large baseline buckle. A weak band around 1155 cm^{-1} can only be guessed. Hence, they do not provide additional evidence for urethanes in the remaining layer. Below 1000 cm^{-1}, the spectrum is dominated by the large Al oxide band. It is not excluded that the buckle in the ether region is also due to the modification of the oxide over time.

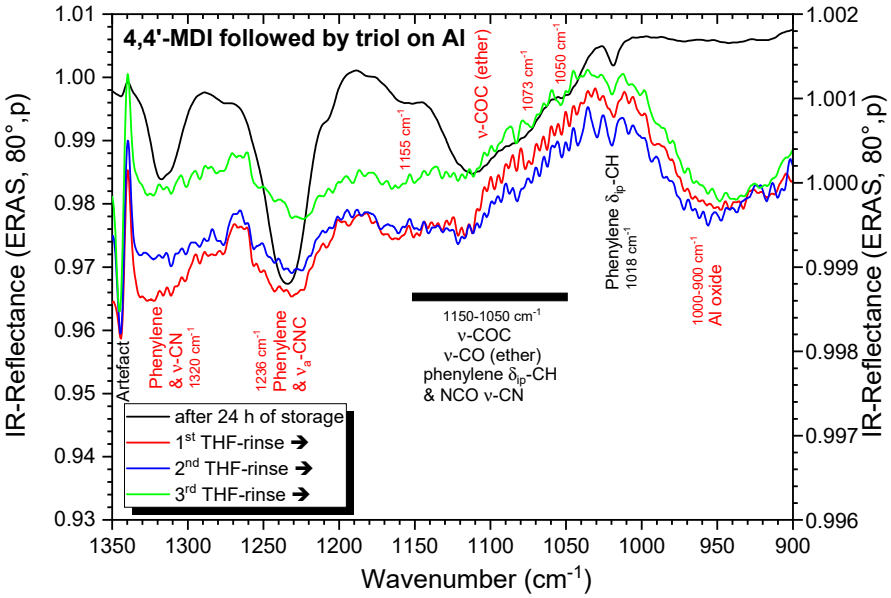

Fig. 7-52 Effect of THF rinses on a layer prepared by deposition of 4,4'-MDI followed by triol on Al after 24 h of storage in dried air at RT. 1350 – 900 cm^{-1}. The black spectrum represents the layer prior to the THF rinses. Band assignment for the monomers (black) and new species (red) refers to the black spectrum.

The spectral region over 2000 cm^{-1} (Fig. 7-53) does not provide any additional information as all bands (remains of OH stretches, NH, CH and NCO) have vanished.

In conclusion, the layer after the 3rd THF rinse strongly resembles the layers prepared by deposition of triol on the stable MDI deposit (cf. Fig. 7-12).

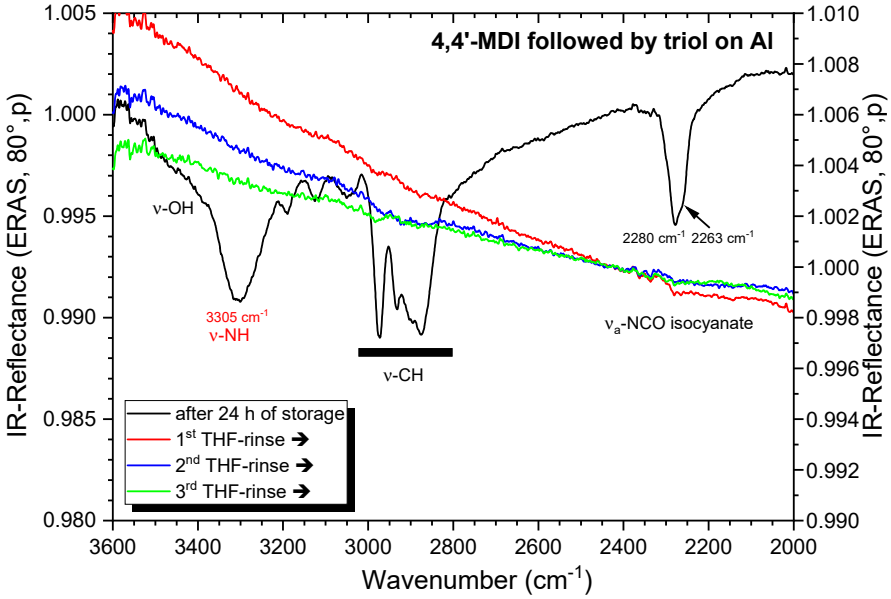

Fig. 7-53 Effect of THF rinses on a layer prepared by deposition of 4,4'-MDI followed by triol on Al after 24 h of storage in dried air at RT. 3600 – 2000 cm^{-1}. The black spectrum represents the layer prior to the THF rinses. Band assignment for the monomers (black) and new species (red) refers to the black spectrum.

The other three layers behave similarly. The few differences between the layers are shown in the comparative spectra (Fig. 7-54) for each metal.

On aluminium, the spectra are very similar for the three layers. Band shape differences in the 1760 – 1550 cm^{-1} region are assessed as random fluctuations because such differences are observed with a set of similar layers too. The combined phenylene stretch (1580 – 1476 cm^{-1}) is the most intense band in the spectra. Its shape and position are the same for the three urethane layers, and they compare to the band for a MDI layer (black dashed spectrum). This band is slightly stronger for the 'MDI-on-triol' layer (green) than for the other two layers having comparable intensities.

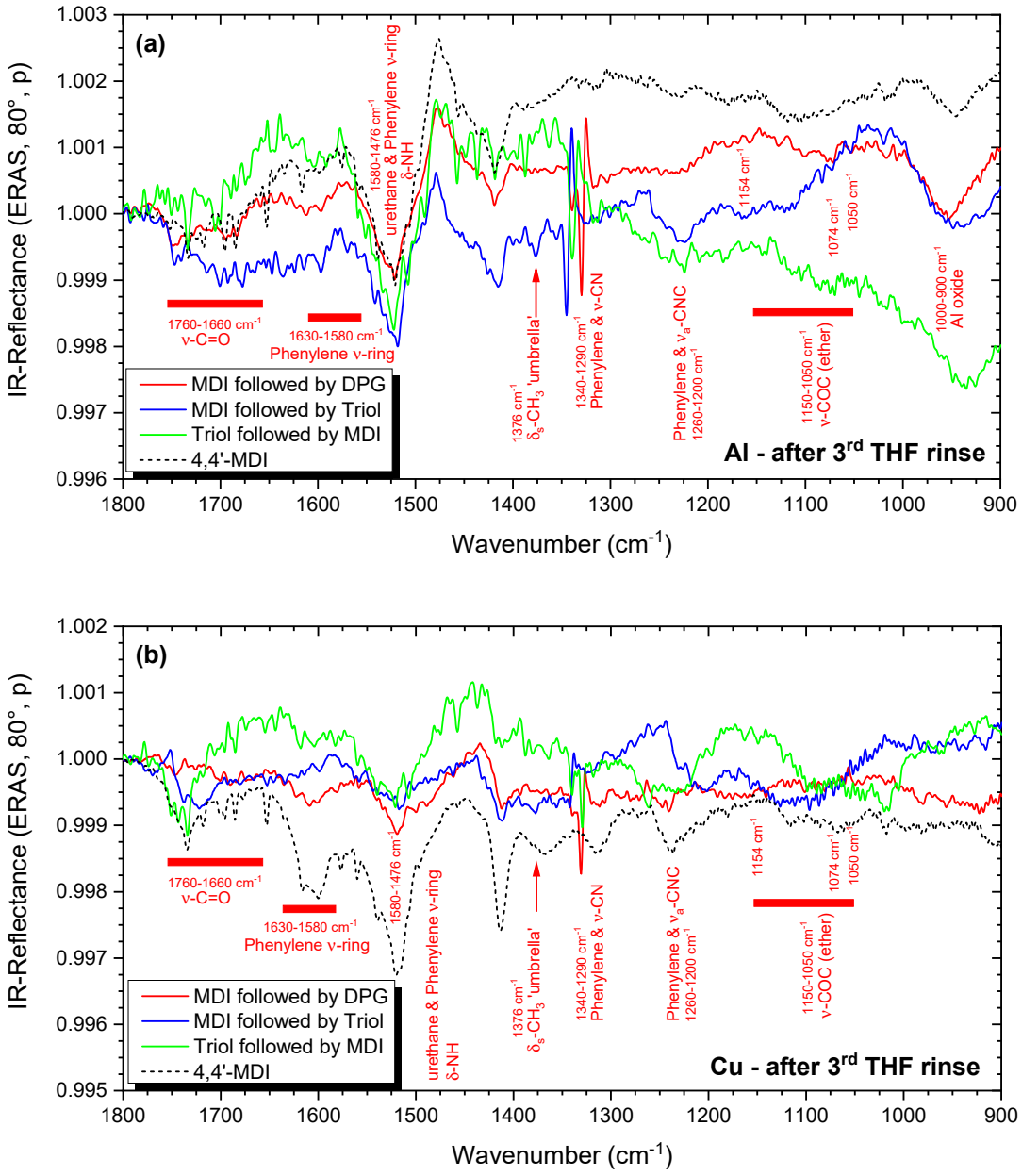

Fig. 7-54 Comparison of urethane layers deposited on Al (a) and Cu (b) after the 3rd THF rinse. The dashed spectrum represents a 4,4'-MDI layer after the 3rd THF rinse. 1800 – 900 cm^{-1}. Assignment is given for typical urethane bands.

Both the MDI layer and the urethane layers possess the strong urethane-like adhesion interactions. Now as the urethane layers possess a further urethane linkage between the adhering isocyanates and an alcohol, these specific bands are increased. It is also observed that the Al oxide band below 1000 cm^{-1} is broader and more intense than on the MDI layer.

On Cu, similar observations are made with some differences though. First, the carbonyl region shows copper specific features for all layers, in particular a sharper band between 1760 and 1700 cm^{-1}. The 'MDI-on-triol' layer (green spectrum) also exhibits slightly stronger bands than the other two layers. Although the differences are small, stability of this layer is hence marginally improved on both metals.

After the 3rd THF rinse, all band intensities are significantly weaker on the urethane layers than on an 4,4'-MDI layer. It is very likely that some isocyanates give up adhesion to the Cu substrate for the reaction with the alcohol. This behaviour, as seen with the DPG layers before, is confirmed by the other two layers now. This indicates that the MDI adhesion seems to be less stable on Cu than on Al.

In conclusion, during the storage time switching from diol to triol resulted in promising layer features after 24 h storage at RT, i.e. slower alcohol desorption and remaining OH groups (IR spectra), but also a significant modification of the topography is found. Unfortunately, as seen by the rinsing test, the triol does not provide improved chemical bonding in the layer. Neither crosslinking of the urethane oligomers nor their chemical bonding to the adhering dimers is significant.

7.3.3 Intermediate conclusion

Urethane formation was studied on native Al or Cu in dried air at RT by varying the alcohol and the deposition sequence on MDI layers much thicker than the stable MDI deposit (cf. section 7.2).

On all layers, alcohol desorbs during and after deposition. Desorption is faster for DPG (within 10 min.) than for the triol (more than 10 h). In either case of preparation, urethane is forming over 10 h and then stops. As many urethane oligomers are formed, monomers possess sufficient mobility and they are able to mix in the confined deposit. Mobility of the formed urethanes is confirmed by the change in intensity ratio of the carbonyl bands. Thus, the stop of reaction is not caused by insufficient diffusion but by depletion of one monomer or because the functional groups at the formed oligomers cannot collide properly for reaction. The latter conclusion is additionally validated by the finding that unreacted OH groups and free NCO groups are identified in the triol-containing layers even after 24 h. Hence, over reaction time molecular mobility drops so much that reactive functional groups do not met anymore.
Deposition of monomer in reverse order proved that miscibility of both monomers inside the confined layer is good. The MDI is capable to reach the surface and the same strong adhesive interactions are formed.
On Cu, urethane formation is faster than on Al. More urethanes are also formed.

SFM showed that all deposits possess a rough surface. The topography depends specifically on the native metal underneath. Variation of the alcohol and the deposition sequence does not bring any improvement of smoothness.

Stability tests using several THF rinses show that none of the layers resists the attack. Although more urethanes were formed on Cu, the stability of the layers is very poor. For all urethane layers, even less molecules remain as compared to a stable MDI deposit. Some of the strongly attached MDI give up this interaction to react with alcohol. THF dissolves most urethane, and only little organic material remains on the substrates.[61] This proves that *poly*urethane is not formed, neither as linear chains with diol nor as a network with triol. Instead, trimers of the type MDI-alcohol-MDI or alcohol-MDI-alcohol[62] are formed for at least two reasons: the NCO:OH ratio is not stoichiometric in the deposits, and alcohol desorption competes against diffusion which is an requirement for the chemical reaction with MDI. Polyaddition at the adhering MDI is impeded for similar reasons.

[61] Stability of the ‘MDI-on-triol’ layers is slightly better. This could also be related to the different monomer ratio initially deposited.
[62] For deposition of alcohol on top of a thick MDI layer, diffusing diol or triol molecules saturate in the first place with two or three MDI, respectively. Following alcohol monomers bind most likely to other MDI monomers instead of linking to the bulky, less mobile trimers. According to the rinsing tests, the final step, connection of the trimers with alcohol monomers, is lacking. Inversely, for deposition of MDI on top of a triol layer, diffusing MDI molecules most likely saturate with two triols. Hence, it is unlikely that both types of trimer form in the same deposit.

Furthermore, the spectra after the stability tests showed remaining bands of CH_3 and ether bands. This confirms that both alcohols are capable to react with the adhering MDI molecules. First indications shown in section 7.2 are thus verified.

In conclusion, gas phase MLD of alcohols and MDI in dried air at RT triggers a complex interplay of transport (desorption, diffusion) processes and chemical reactions, changing molecular mobility and intermolecular physical interactions. As the result, urethane molecules do form but they do not combine to a polymer structure. Further adjustment of the layer preparation parameters is necessary.

7.4 Temperature influence

The poor attachment of the formed urethane oligomers may be due to various reasons. First, as with ongoing reaction the oligomers become larger, their mobility is reduced. Furthermore, the formation of H-bonds of the carbonyl groups also reduces the mobility. At that stage, the oligomers are just unable to react with the MDI adhering to the substrate.
Second, the adhering molecules on the substrate do not tend to grow either. After reaction of a first triol with an adhering MDI, further MDI does not react with alcohol.

An increase of the sample temperature, T_{sample}, will boost molecular mobility during urethane formation. This could improve the attachment of the oligomers to the substrate. An increased T_{sample} has additional impact on the layer, however. As seen for 4,4'-MDI deposits, T_{sample} = 50 °C results in forced desorption of MDI from the metal surface (cf. section 6.5.3.2). Alcohol should desorb much faster as well. Thus, the deposition-desorption ratios of both monomers are different now while urethane formation is running. As the result, the isocyanate-alcohol ratio is changing continuously while urethane is forming, and the layer should be much thinner. This can either improve or degrade urethane quality on the substrate.

As a consequence, two scenarios will be considered in the next section.
First, T_{sample} is increased above RT during monomer deposition while the temperature, T_{store}, during storage is kept at RT. Hence, less molecules adsorb on the substrate over deposition time but chemical reaction rate is quite the same during storage.
Second, T_{sample} is decreased below RT while T_{store} is increased above RT. Now, monomer deposition is intensified, and urethane formation slows down during deposition while during storage, the urethane formation rate is higher and more monomers desorb than at RT.

Both scenarios are studied on Al. MDI is deposited first and triol follows. Beside chemistry and stability of the layers, the impact of temperature on the layer topography is analysed.

7.4.1 Increased deposition temperature

Increasing T_{sample} during deposition from 10 °C to 50 °C significantly decreases the adsorption-desorption ratios of both monomers. Hence, properties of the layer are mainly defined during the deposition step. For example, the deposit is much thinner at T_{sample} = 50 °C than 10 °C. The evolution of the IR spectra over the 24 h of storage at RT is shown in Fig. 7-55 and Fig. 7-56.

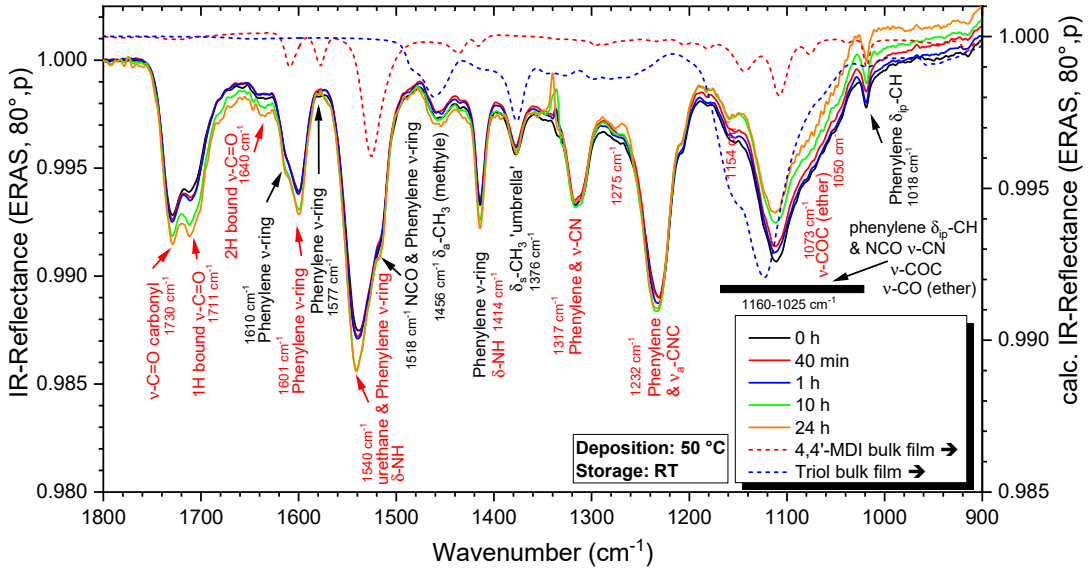

Fig. 7-55 IR-ERA spectra of an initially 1.5 nm MDI layer on native Al followed by ca. 1.3 nm triol (1 h deposition time). T_{sample} = 50 °C. Storage in dried air at T_{store} = RT for 24 h. 1800 – 900 cm^{-1}. Bands assigned for the monomers (black) and new species (red). The dashed lines represent calculated bulk spectra of the monomers for qualitative comparison.

Starting with the fingerprint region (Fig. 7-55) all typical urethane bands (1730, 1711, 1601, 1540, 1414, 1317, 1275, 1232, 1154, 1073, and 1050 cm^{-1} – marked in red) are well developed right after monomer deposition. Through the increased substrate temperature, monomer mobility and reactivity are increased and hence urethane formation is much faster. The band at 1640 cm^{-1} indicates an enhanced formation of double H-bonded carbonyls[63]. The shoulders at the phenylene bands at 1610 and 1518 cm^{-1} confirm that unreacted MDI is still present after storage at RT.

During storage, evolution of the bands is weak and does not exceed 2 ‰. The carbonyl bands (1730 and 1711 cm^{-1}) and the phenylene bands (1601, 1540 cm^{-1}) grow slightly. Hence, only few urethane groups form at RT. The intensity ratio of both ν-C=O bands changes a bit thus verifying that urethane groups also rearrange and form hydrogen bonds during RT storage. The other bands do not change significantly.

[63] Again, some MDI could form few urea groups with adsorbed water but this cannot be discriminated in the spectra.

The NCO asymmetric stretch decreases over the first 10 h of storage (Fig. 7-56). Interestingly, the large tail at the NH stretch (~3440 cm^{-1}) indicates some remaining OH groups.

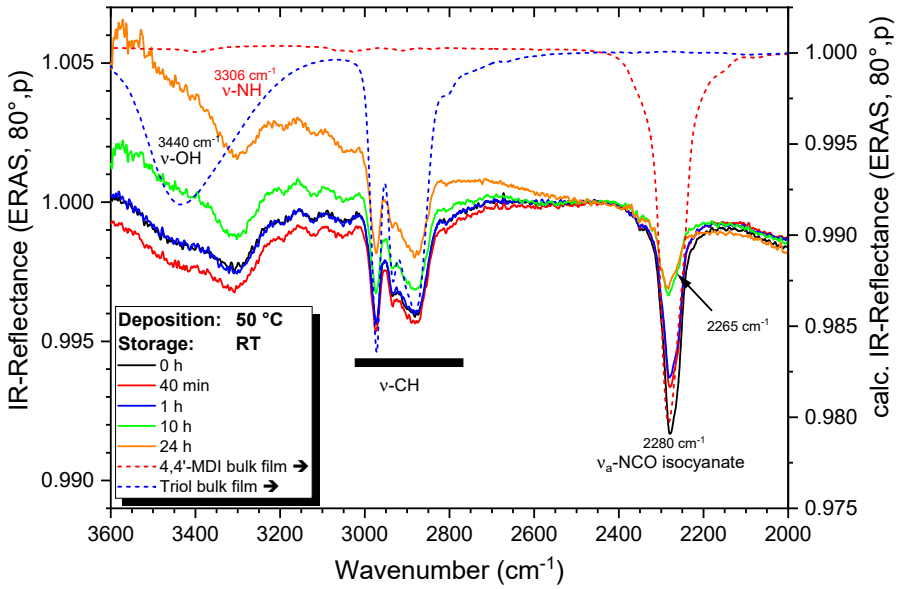

Fig. 7-56 IR-ERA spectra of an initially 1.5 nm MDI layer on native Al followed by ca. 1.3 nm triol (1 h deposition time). T_{sample} = 50 °C. Storage in dried air at T_{store} = RT for 24 h. 3600 – 2000 cm^{-1}. Bands assigned for the monomers (black) and new species (red). The dashed lines represent calculated bulk spectra of the monomers for qualitative comparison.

Summing up, the IR spectra are not much different from layers deposited at T_{sample} = 10 °C, except that urethane formation mainly took place during deposition at 50 °C.

Now the stability against THF is probed in order to evaluate if performance of the layer is improved by higher deposition temperature. The fingerprint region (Fig. 7-57a) reveals a significant removal of urethane upon the 1st THF rinse at RT. Further rinses do not affect the remaining molecules. It is noted however, that the remaining bands are much sharper than for similar layers prepared at 10 °C. All urethane specific bands and, in particular, the umbrella deformations (1376 cm^{-1}) and ether vibrations (1150 – 1050 cm^{-1}) are well visible in the spectra after the rinses. NH and CH stretches are clearly present at higher wavenumbers (cf. Fig. 7-57b). All bands are much sharper and noise is much less than after THF rinsing for T_{sample} = 10 °C / T_{store} = RT (cf. section 7.3.2.4).

Hence, despite THF still removes many urethane molecules, these spectra unequivocally confirm that more of these species attach well to the surface now. In view of the findings in section 7.3.2, it is concluded that for the preparation regime T_{sample} = 50 °C / T_{store} = RT, some degree of crosslinking is established in the urethane deposit.

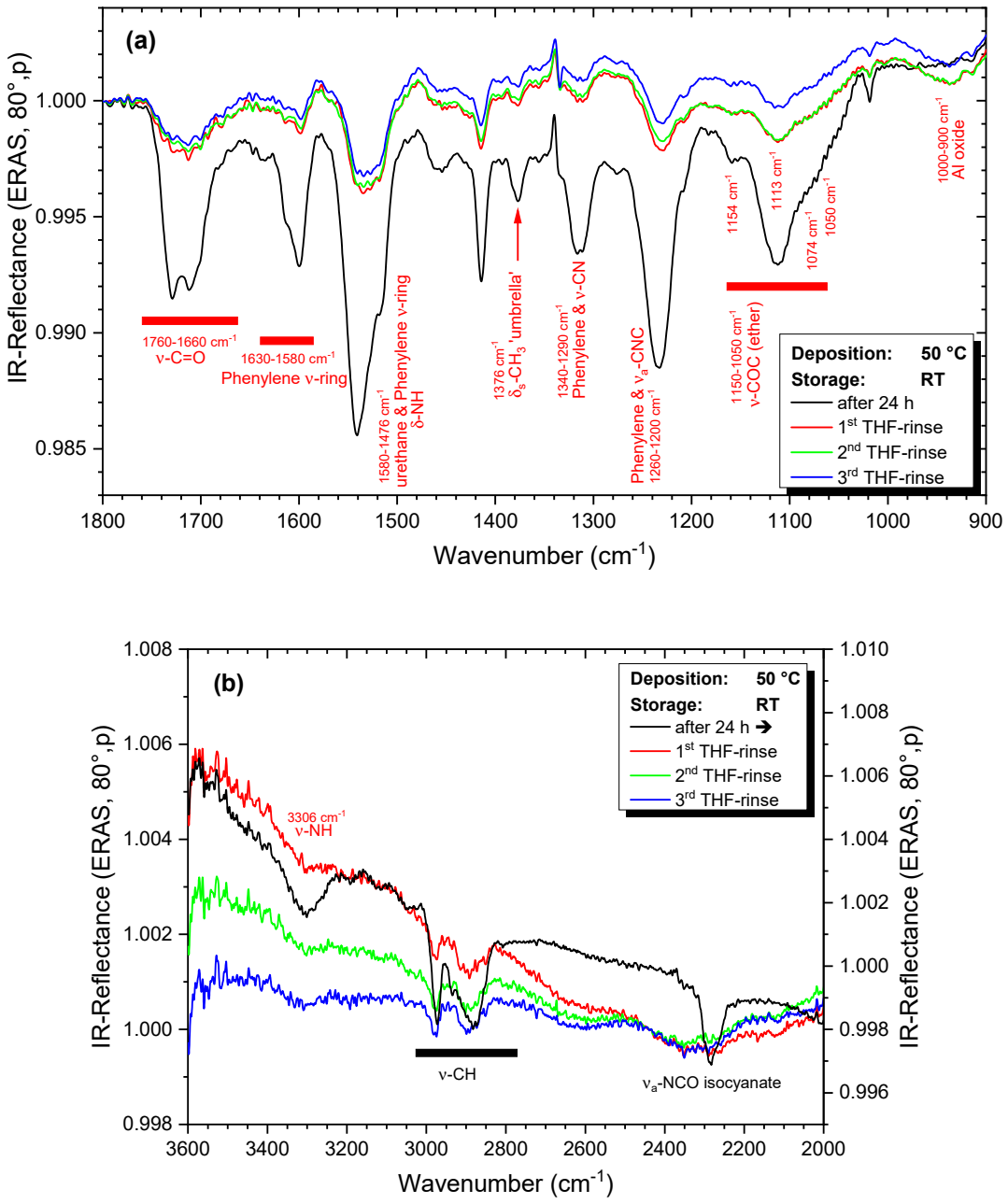

Fig. 7-57 Effect of THF rinses on a layer prepared by deposition of 4,4'-MDI followed by triol on Al. Deposition at 50 °C and 24 h of storage in dried air at RT. (a) 1800 – 900 cm^{-1}, (b) 3600 – 2000 cm^{-1}. The black spectrum represents the layer prior to the THF rinses. Urethane bands are assigned in red.

7.4.2 Effect of increased storage temperature

In the second scenario, T_{sample} is kept at 10 °C. Hence, during deposition the same layer is prepared as in section 7.3.2. Only during storage, the temperature is increased to 50 °C.

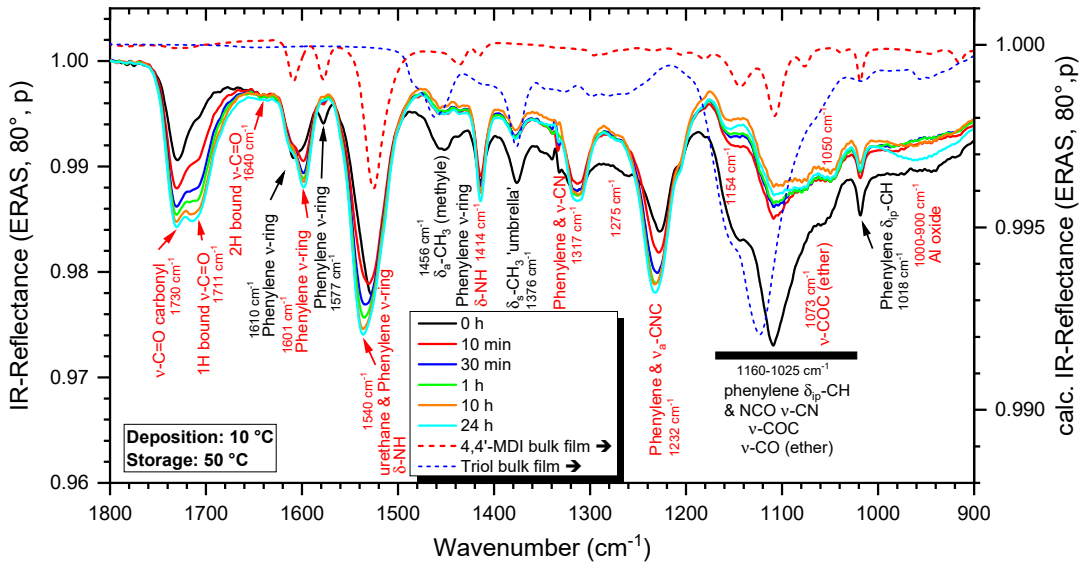

Fig. 7-58 IR-ERA spectra of an initially 1.5 nm MDI layer on native Al followed by 1 h of triol deposited on top. Deposition temperature: 10 °C. Storage in dried air at 50 °C over 24 h. 1800 – 900 cm^{-1}. Bands assigned for the monomers (black) and new species (red). The dashed lines represent calculated bulk spectra of the monomers for qualitative comparison.

Starting with the fingerprint region (Fig. 7-58), urethane bands (1730, 1711, 1601, 1540, 1414, 1317, 1232 cm^{-1}) rapidly grow over the first hour at T_{store} = 50 °C. The carbonyl bands rise quickly and the intensity ratio changes as more urethane groups form H-bonds. The combined phenyl band at 1540 cm^{-1} progressively changes position from 1525 to 1540 cm^{-1} due to the formation of urethanes as well as to depletion and desorption of MDI. CH deformations (1456-1340 cm^{-1}) decrease rapidly during the first 10 min. as triol desorbs from the sample. In parallel, the ether band massively looses intensity. Band shape changes as new ether bands (1154, 1073, and 1050 cm^{-1}) emerge during urethane formation. After one hour, urethane formation rapidly slows down and urethane bands grow marginally only.

In the upper wavenumber region (Fig. 7-59), the OH stretch present after deposition rapidly decreases during the first 10 minutes as most polyol desorbs. This is confirmed by the decrease of the CH stretches as well as of the CH deformations and ether vibrations. The massive intensity drop of the isocyanate during the first 30 min. is also mainly caused by desorption of MDI while some isocyanates are consumed by the urethane formation. This is in agreement with results for MDI layers stored at 50 °C (see section 6.5.3.1).

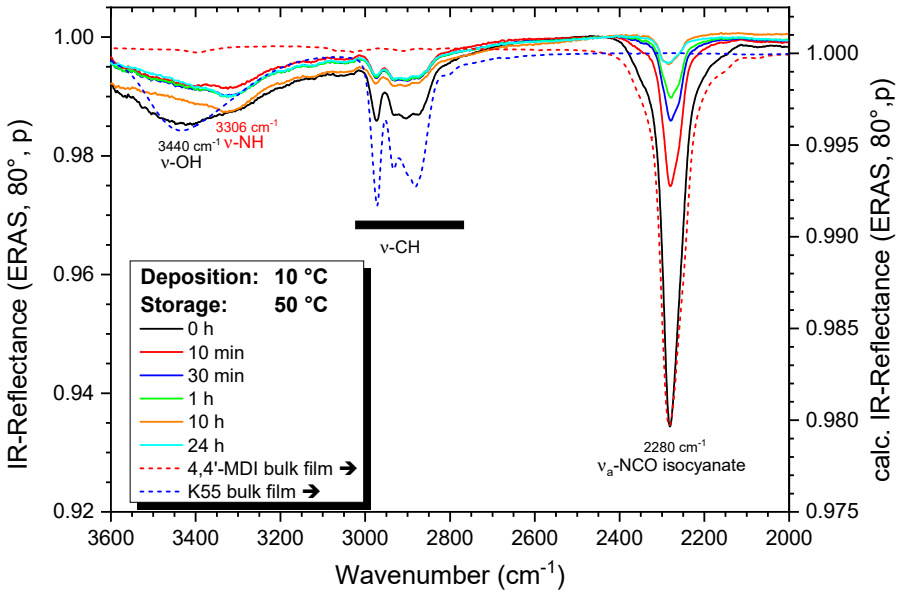

Fig. 7-59 IR-ERA spectra of an initially 1.5 nm MDI layer on native Al followed by 1 h of triol deposited on top. Deposition temperature: 10 °C. Storage over 24 h in dried air at 50 °C. 3600 – 2000 cm^{-1}. Bands assigned for the monomers (black) and new species (red). The dashed lines represent calculated bulk spectra of the monomers for qualitative comparison.

Summing up, the increased storage temperature induces a rapid desorption of both monomers while mobility and hence reactivity of urethane formation is increased. At first glance, the spectral features of the achieved layer in terms of band shape and position are not affected by T_{store}.

After storage, heating is switched off and the sample is allowed to cool down to RT before the THF rinses are performed.

Upon the 1st THF rinse (Fig. 7-60), intensity of all bands has only slightly dropped by ca. 5 ‰. Shape and intensity ratios of the bands have not changed at all. Particularly, the band intensity ratio of carbonyl or of phenylene at urethane and isocyanate groups (1630-1580 cm^{-1}) remains unchanged. Hence, only few urethane oligomers have been removed from the sample. The remaining material resists further THF rinses. This is also confirmed by very well developed NH and CH stretches at higher wavenumbers (Fig. 7-60b). Furthermore, unreacted NCO groups are present which is in agreement with the shoulder of the phenylene ring stretch at 1610 cm^{-1}. Interestingly, 2nd and 3rd rinse do not change the NCO band intensity. Such stability was not found for the storage at RT and hence these remaining free NCO groups are chemically bonded to the urethane network.

In conclusion, the increased storage temperature has significantly improved layer stability. Many urethane units are now capable to crosslink and this network adheres well to the substrate. Layer performance is now similar as for layers prepared from diluted solution and stored at RT (see 6.1.2 and [11]).

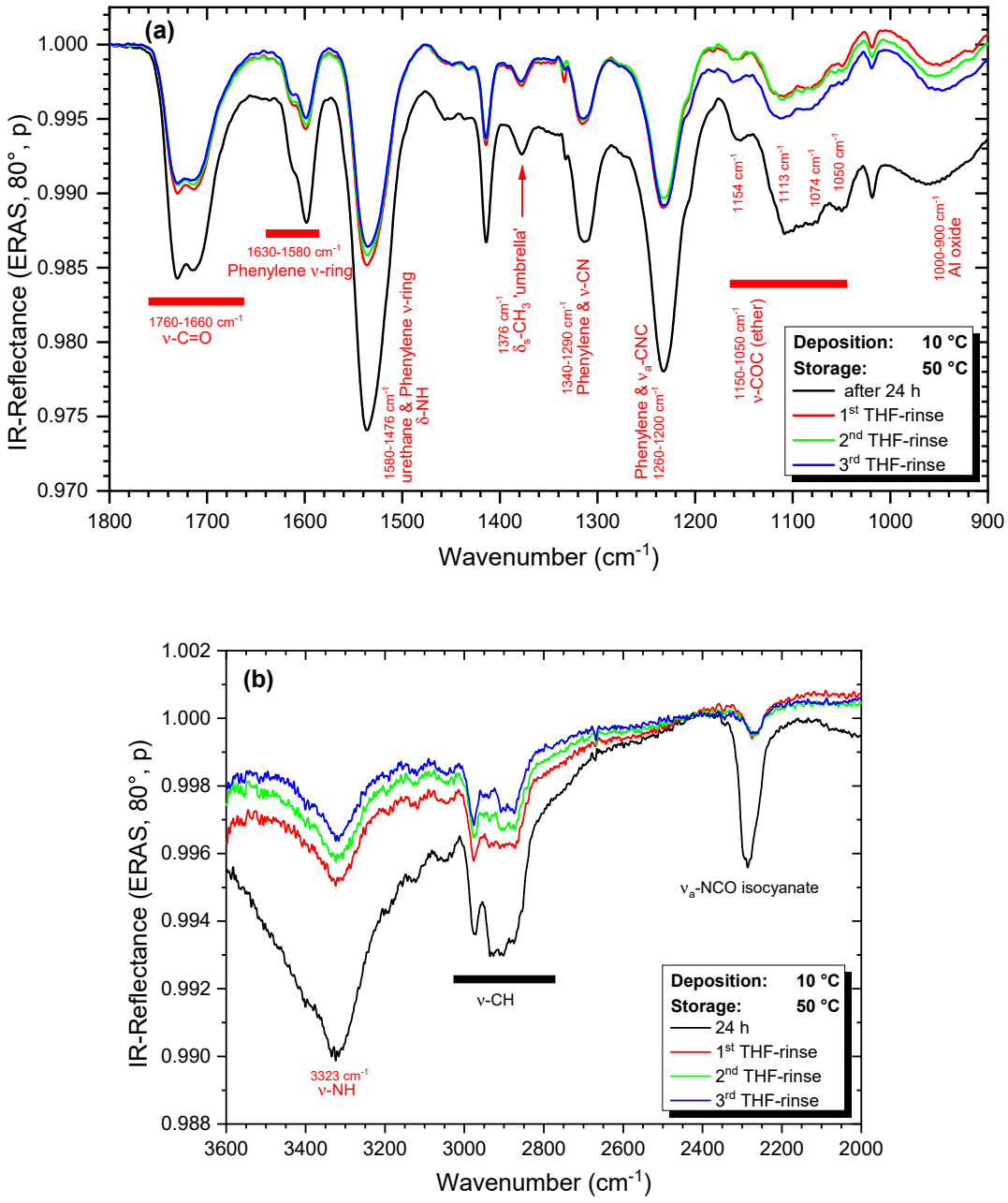

Fig. 7-60 Effect of THF rinses on a layer prepared by deposition of 4,4'-MDI followed by triol on Al. Deposition at 10 °C and 24 h of storage in dried air at 50 °C. (a) 1800 – 900 cm^{-1}, (b) 3600 – 2000 cm^{-1}. The black spectrum represents the layer prior to the THF rinses. Urethane bands are assigned in red.

7.4.3 Comparison of layer behaviour

Comparison of the two previously prepared layers with a layer deposited at 10 °C and stored at RT allows highlighting some further differences.

The spectra after 24 h of storage (Fig. 7-61) reveal that the quantities of urethane and residual monomers depend strongly on the deposition and storage conditions. Layers deposited at 10 °C and stored at RT (black spectrum) exhibit most urethane and unreacted isocyanate (NCO band, phenylene bands at 1610 and 1518 cm^{-1}). That makes sense as desorption of MDI is extremely low during desorption and storage at low temperature. For the same deposition temperature, storage at 50 °C (green spectrum) yields less urethane because MDI desorbs in part during storage. Alcohol desorption is accelerated as well. Eventually, the layer deposited at high temperature (red spectrum) exhibits the least amount of urethane as much less monomers stick on the surface.

Concerning the structure of the spectra, all characteristic urethane bands are present on all three layers. The carbonyl band ratio is the same for the layers either prepared or stored at higher temperatures while slightly more free carbonyl groups are present for the layer handled at low temperatures (black spectrum). Hence, increased temperature allows for higher mobility of the species in the layer, and that results in more hydrogen bonding. The shape of the ether band is specific for each layer. This band is composed of the ether vibrations of unreacted triol, ether vibrations close to urethane groups and also of some MDI-specific vibrations. The band shape changes as the content of these species varies for the three layers.

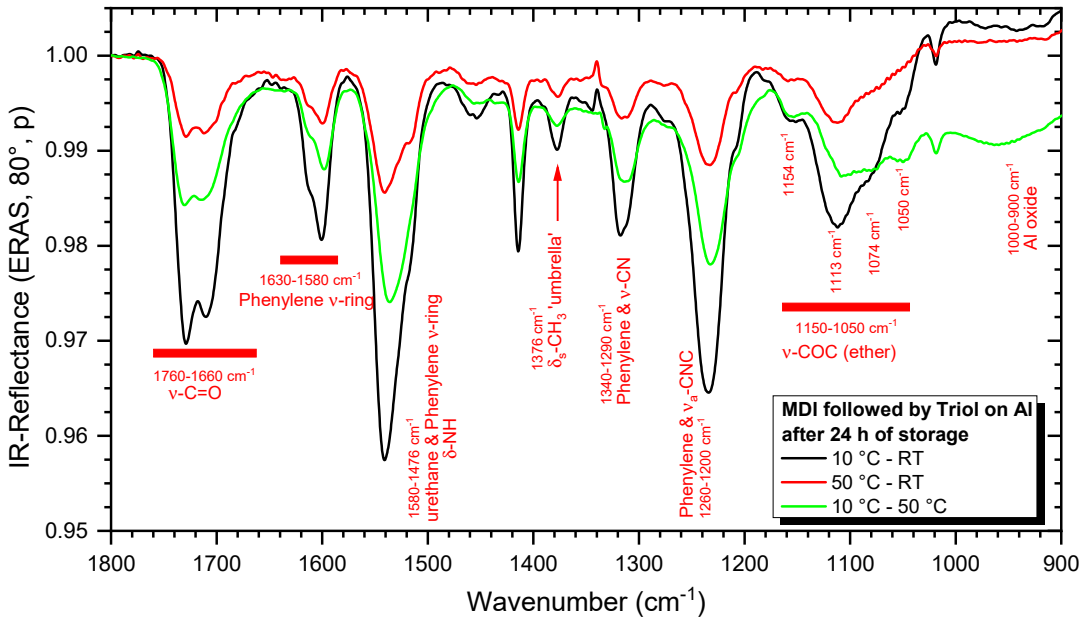

Fig. 7-61 Comparison of urethane layers on Al after 24 h of storage. The layers are prepared at different deposition and storage temperatures. 1800 – 900 cm^{-1}. Characteristic urethane bands are assigned in red.

Upon THF rinse, the significantly different behaviour of each layer is emphasised - Fig. 7-62. The layer prepared at 10 °C and stored at RT shows only few weak bands and rather large noisy buckles (black spectrum). Elevated deposition temperature (red spectrum) increased band intensity to 2 ‰ at most. That slightly increased amount of attached urethanes is sufficient to identify all specific urethane bands in the spectrum. Increased storage temperature (green spectrum), on the other hand, massively increases the amount of urethanes attached to the surface. This layer is significantly different from the previous two.

It is noted in passing that the aluminium oxide rises with the time the sample was exposed to 50 °C. The sample stored 24 h at 50 °C exhibits increased Al oxide vibrations (1000 – 500 cm^{-1}) and hence stronger oxide growth than samples subjected to 50 °C during deposition for a short time and stored at RT. The Al-oxide modification does not significantly change the adhesion interactions, however, as seen previously for the MDI layers stored at elevated temperatures – cf. section 6.5.3.1. Hence, elevated storage temperature boosts processes in the deposit that result in the formation of a urethane network attached to the metal substrate.

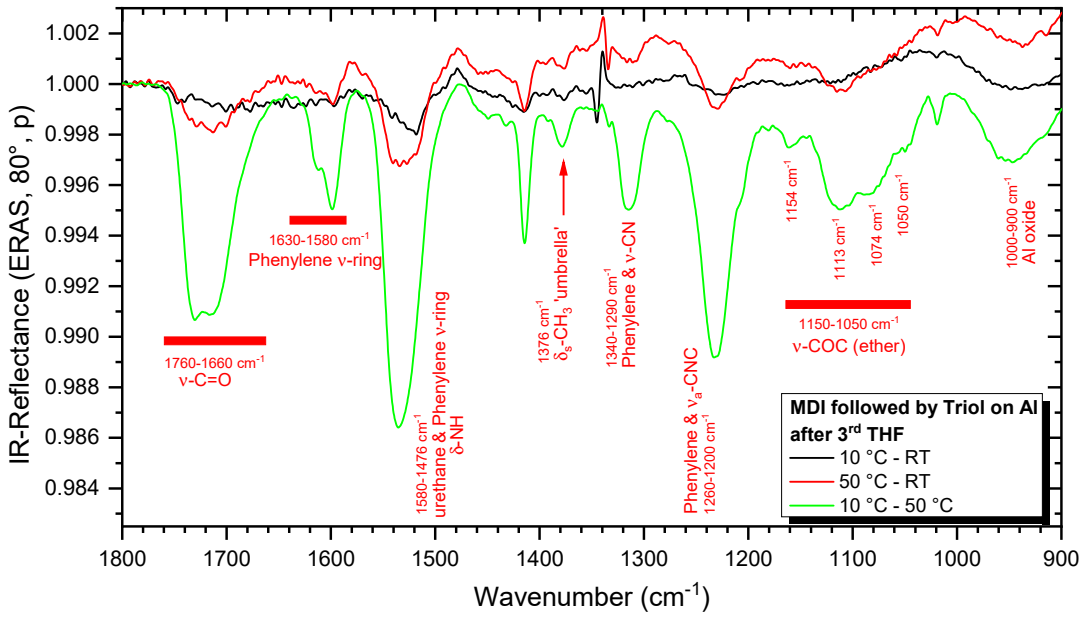

Fig. 7-62 Comparison of urethane layers on Al after the 3rd THF rinse. The layers were prepared at different deposition and storage temperatures. 1800 – 900 cm^{-1}. Characteristic urethane bands are assigned in red.

7.4.4 Impact on topography

◊ *Topography after 24 h of storage*

Fig. 7-63 compares the topography of urethane layers prepared either at elevated T_{sample} or T_{store} to the previously prepared urethane layer with T_{sample} = 10 °C and T_{store} = RT.

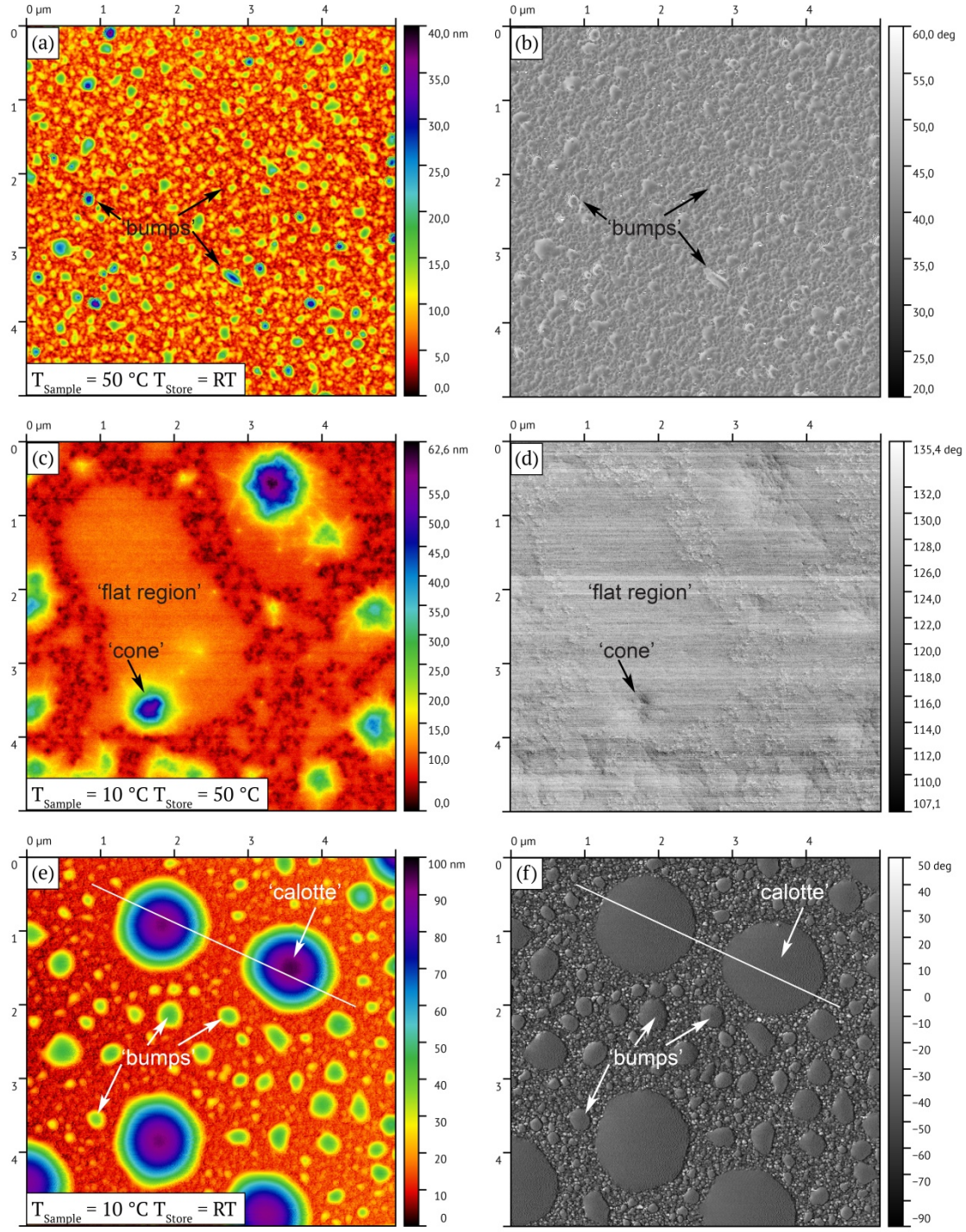

Fig. 7-63 Tapping mode SFM topography (a, c, e) and corresponding phase contrast (b, d, f) images of urethane layers prepared by deposition of MDI followed by triol on Al at various T_{Sample} and T_{Store}. 5 x 5 µm² scan.

Starting with the layer prepared at T_{sample} = 50 °C during deposition and T_{store} = RT (Fig. 7-63a, b) topography is much smoother than layers prepared at T_{sample} = 10 °C. No calottes are there but a multitude of tiny bumps (0.2 – 0.3 µm diameter and 10 – 25 nm high) are evenly spread over the substrate. They are significantly smaller than the bumps found on reference layers prepared at T_{sample} = 10 °C and stored at RT (bumps of 0.4 µm diameter and up to 35 nm high, plus calottes of 1.3 µm in diameter and up to 80 nm high). Smaller topographic structures also go with deposition of less molecules. Hence, increased T_{sample} changes the adsorption-desorption behaviour of the molecules during deposition and, as a consequence, topography is improved. The phase contrast fluctuation of ca. 7° is small and hence the whole surface is covered with organic material.

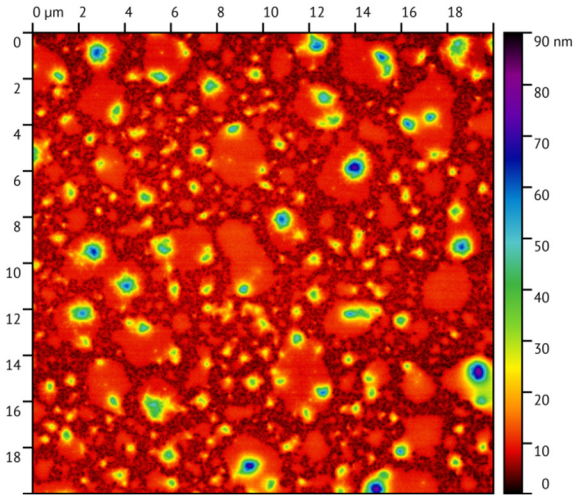

Fig. 7-64 20 x 20 µm² tapping mode topography image of a urethane layer prepared by deposition of MDI followed by triol on Al at T_{sample} = 10 °C and T_{store} = 50 °C.

The layer prepared at T_{sample} = 10 °C and stored at T_{store} = 50 °C (Fig. 7-63c, d and Fig. 7-64) possesses its own topography. Large flat regions (up to 3.6 µm wide and only 5 nm high) dominate. They are separated by rougher nodular regions, as on the reference layers (Fig. 7-63e). On the flat regions, cones of 1 – 1.3 µm width and 40 – 50 nm height are present. Much fewer bumps and cones are present than for the reference layer. The phase contrast is homogeneous over the whole sample and fluctuates only by ca. 5 degrees. Hence, the whole sample is covered with organic material too.

The elevated storage temperature also significantly modified the topography. For monomer deposition at T_{sample} = 10 °C, sample topography is characterised by calottes and bumps (Fig. 7-63e). If T_{store} is increased, MDI and triol start to desorb while urethane formation accelerates. Thus, since more molecules desorb as compared to storage at RT, calottes and bumps shrink.

In conclusion, increased temperature during deposition or storage does significantly modify the layer topography and improves smoothness.

◊ *Topography after THF rinses*

The layer prepared at T_{sample} = 10 °C and stored at T_{store} = 50 °C showed the most promising results in terms of layer stability. SFM measurements after the stability test are feasible, as more urethane remains attached.

The cones and flat regions have disappeared - Fig. 7-65. Instead, a smooth topography prevails. The surface is scattered with many small dots of 100 nm width and up to 15 nm high. Here and there, larger plateaus of up to 0.8 µm width and 10 nm height variation are present. The nodular structure of the aluminium oxide is visible in between. The phase contrast variation is ca. 5 degrees and that confirms the complete coverage of the sample with organic material.

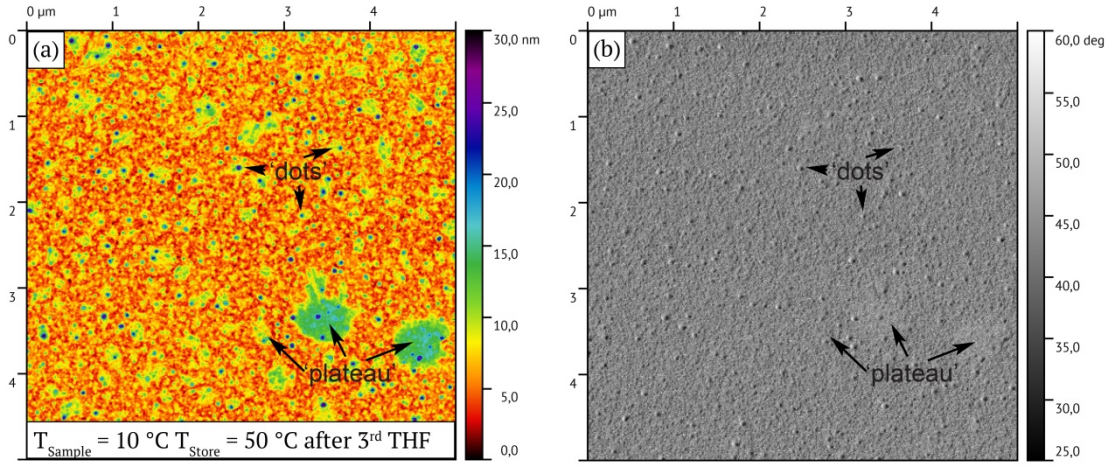

Fig. 7-65 Tapping mode SFM topography (a) and corresponding phase contrast (b) images after the 3rd THF rinse of a urethane layer prepared by deposition of MDI followed by triol on Al with T_{sample} = 10 °C and T_{store} = 50 °C. 5 x 5 µm² scan.

Hence, THF rinse is changing topography by removing the cones and reshaping the flat regions observed before. It is likely that the solvent-enhanced molecular mobility promoted reorganisation of the attached urethane. This idea is substanciated by the formation of the multitude of small dots.

In conclusion, this kind of preparation in a dried air stream, i.e. sequential monomer deposition (triol on MDI) at T_{sample} = 10 °C, urethane formation at T_{store} = 50 °C /24 h, and threefold rinsing with THF at RT, produces the favoured result: a crosslinked, amorphous, uniform urethane layer sticking well on the native Al substrate. However, the structure of that layer is far from the idea of an alternating layer-by layer sequence of monomers as it is anticipated in literature on MLD. Such an idealised conception fails because it ignores the significant effect of physical intermolecular interactions and mobility on chemical reactions and structure formation. Obviously, these effects are not specific for urethane layers but they are ubiquituous for the deposition of polymerising organic layers.

7.4.5 Conclusion on temperature influence

The increase of temperature during layer preparation or storage does significantly change the resulting urethane layers.

First, urethane formation is accelerated at 50 °C. Maximum conversion requires ca. 1 h while 10 h are necessary at RT. From the IR spectra, urethane chemistry is however comparable to layers prepared and stored at lower temperatures. 50 °C are mild enough to maintain the chemical reactions and to avoid undesired additional reactions.

Second, an increased temperature changes the adsorption-desorption ratio of the monomers, both for deposition and storage. Desorption is facilitated and hence monomers are required to go to energetically more favourable sites for stable adhesion to the surface. Hence less urethane is formed, which better resists THF rinses, however.

Third, increased storage temperature induces a fast desorption of deposited MDI and alcohol. Again, less urethane is formed but the overall stability is much improved. The remaining deposit performs as well as solvent-based layers (cf. 6.1.2 & [11]).

Fourth, the NCO : OH ratio is modified compared to deposition / storage at lower temperatures[64] The combination of deposition at T_{sample} = 10 °C and storage at T_{store} = 50 °C still ends with a significant number of residual functional groups but it facilitates the formation of a urethane network. Further experiments showed, however, that a modification of the NCO : OH ratio by depositing more or less alcohol dramatically changes the stability of resulting urethane layer.

Fifth, topography of the deposits is also greatly modified by the combination of deposition and storage temperatures. In general, a temperature rise results in homogenised deposits as a desired result.

An increase of temperature above 50 °C could provide further improved layers.[65] Several factors have to be considered however. On one hand, molecular mobility and reactivity would increase thus possibly leading to faster urethane formation and less heterogeneous deposits. On the other hand, faster desorption of alcohol and MDI, as well as possibile parasitic reactions of the isocyanate could impinge layer stability. Hence, a balanced compromise has to be found in future research.

[64] At any stage of preparation, available experimental techniques do not provide data for the NCO : OH ratio.

[65] Such a step would need strong modification of the actual MLD setup. That was beyond the schedule of this project.

7.5 Outcomes for thin urethane layers prepared by MLD

The characterisation of thin urethane deposits from the gas phase onto native Al or Cu metal substrates revealed the highly complex interplay between monomer adsorption and desorption behaviour, intermolecular interactions, molecular mobility, and substrate influence. Intermediate conclusions were given throughout this chapter. This conclusion associates the most important statements.

First, only isocyanate undergoes strong adhesive interactions with the substrates[66] That fundamental requirement for achieving any sustainable layer defines the sequence of monomer deposition: alcohol on top of MDI. Deposition of alcohols onto stable MDI deposits verified that adhesively bonded MDI is capable to react with the alcohol. However, affinity of the alcohol – MDI reaction is strong enough to break some of the isocyanate-metal interactions[67]. These findings consolidate the conclusion given in previous work [8, 10, 11] that the strong adhesion between the NCO group and the native metal oxide surface exhibit a donor-acceptor character.

Neither MDI nor alcohol monolayers have been obtained directly from the MLD. This may result from our specific deposition conditions, but, generally, the interplay of physical interactions, molecular mobility, and chemical reactivity exert strong and evolving influence on structure formation at any stage of layer preparation.

Hence, thicker monomer deposits have been prepared. DPG and triol are used and the deposition sequence with MDI was switched as well. All layers showed that urethane forms very well although most part of the alcohol desorbs. Molecular mobility is high even in these confined thin layers. The formed urethanes possess enough mobility to rearrange and form energetically favourable hydrogen bonds[68]. At RT, urethane reaction requires at least 10 h to complete. This slow reaction rate will be an obstacle if multiple monomer deposition steps should be applied in order to form thicker layers.

Switching from diol to triol in order to allow crosslinking does not improve this behaviour. Furthermore inverting the deposition order of the monomers confirmed the high mobility of the molecules on the surface and the good mixability of the MDI with the polyols.

Stability is poor for all layers (T_{sample} = 10 °C; T_{store} = RT), however[69]. The remaining molecules are composed of the strongly attached MDI and reacted alcohol[70]. Hence, instead of forming a polymer network only short-chained oligomers are formed[71].

[66] Even after THF rinses, weak urethane bands remain in the IR-ERA spectra.
[67] As subsequent THF rinses showed.
[68] This is shown by the change of intensity ratio of the carbonyl bands.
[69] Much monomer desorbs and most of the urethane is removed by THF.
[70] Urethane specific bands are present.
[71] This behaviour is only observed on MLD layers. Layers prepared from solution deposition are much more stable.

This is the result of the fast desorption of the alcohol, as depletion of one monomer brings the urethane reaction to a stop. Furthermore, our MLD deposition conditions do not allow for a stoichiometric ratio of isocyanate and alcohol functionalities. As the result, the degree of polymerisation is weak and oligomers of the type MDI-alcohol-MDI or alcohol-MDI-alcohol can predominantly be formed. They are unable to react with each other or link to the strongly attached species on the surface.

Layers on Al and Cu behave similarly but a few differences are found. On Cu, urethane formation is faster and more urethanes also formed than on Al. Moreover, MDI adhesion is weaker on Cu[72]. Hence, more adhesively bonded MDI is capable to detach from the native Cu surface and to react with alcohol. This further confirms the donor-acceptor character of the NCO-metal oxide interactions.

An increase of sample temperature during deposition or storage accelerates urethane formation and significantly improves layer stability. Best performance is achieved by low temperature deposition at 10 °C followed by 50 °C storage. It compares to stability of solution deposited layers. An increase of temperature intensifies molecular mobility. Moreover, MDI starts to desorb at 50 °C. Simultaneous desorption of MDI and OH leads to a varying MDI : OH ratio, which turns out to facilitate formation of a urethane network. Of course, a variation of the deposition ratio of monomers will affect amount and structure of the resulting network as well[73].

Topography of all layers turns out to be specific for the deposition sequence, the temperature during deposition and formation, and for the native metal underneath[74]. Increased temperature goes with smoothing of topography as more uniform deposits are achieved.

In conclusion, our layer formation model is by far more complex than the conceptions in MLD literature.

[72] Less urethane molecules remain compared to a stable MDI deposit.
[73] Such experiments would be subject of future research.
[74] Hence, deposition of alcohol on top of a rough MDI layer does not improve topography.

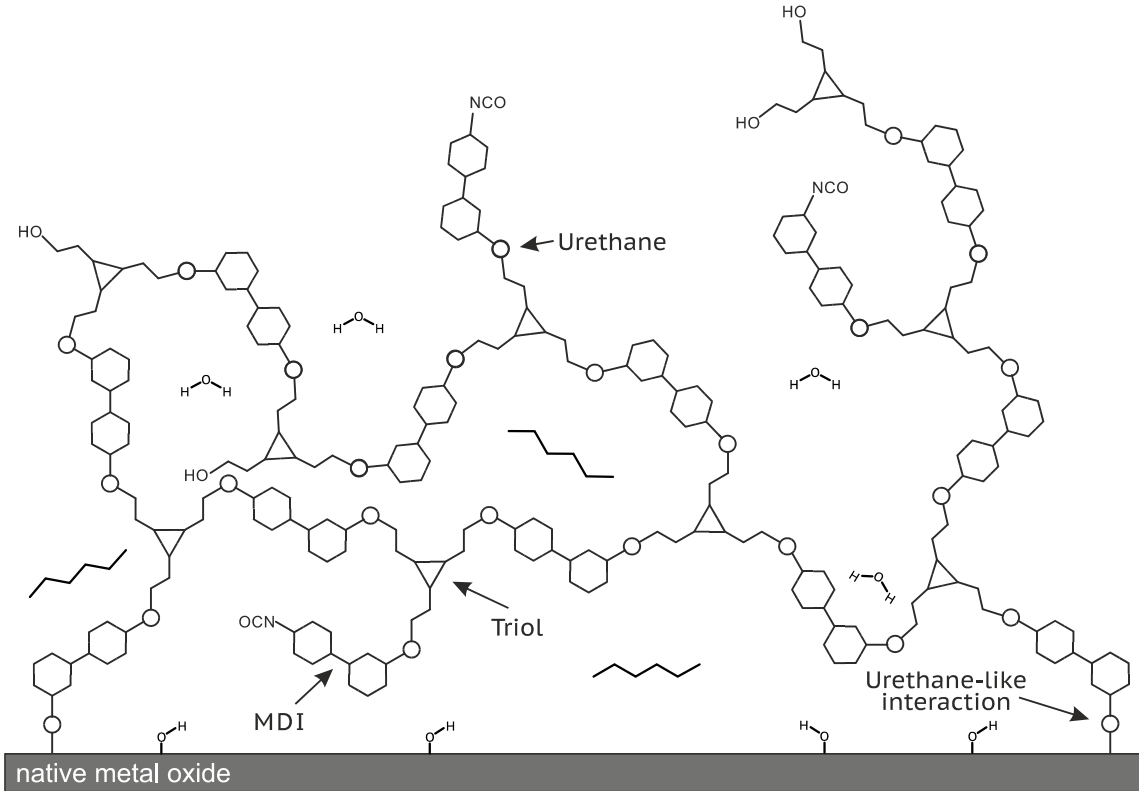

Fig. 7-66 Schematic representation of the attached polymer network after THF rinses. The layer is prepared by low temperature deposition at 10 °C followed by 50 °C storage.

For the most stable layer, the model for the crosslinked urethane after THF treatment is represented in Fig. 7-66. The solvent removed all residual monomers and the free urethane oligomers. An imperfect network remains because it is attached by strong urethane-like adhesive interactions to the metal oxide[75]. Free alcohol and isocyanate functionalities remain and thus, in principle, allow for further layer growth.

Summing up, thin crosslinked urethane layers can be prepared by molecular layer deposition. However, some questions remain open. First, how important is the MDI : OH ratio for layer stability? Second, how would additional monomer deposits behave in terms of chemistry and topography? Could a thick PU layer be prepared in a step-by-step like manner?

So far, storage of the prepared layers was performed in the IR chamber. Further improvements of the deposition process could allow for *in situ* storage inside the MLD. This would also allow for supplemental monomer deposits on top.

[75] Using triol allows for the formation of crosslinks.

8 Conclusion

The main question settled at the beginning of this work was if it is possible to prepare thin polyurethane layers on native Al and Cu from gas phase deposition.

In order to answer this question three challenges had to be overcome. First, a suitable Molecular Layer Deposition apparatus has to be setup and the deposition process controlled. Second, throughout the preparation of single monomer deposits, deposition parameters can be optimised and the behaviour of each polyurethane component studied in terms of chemistry, chemical interaction and topography. Finally, polyols and isocyanates are deposited sequentially in order to allow formation of polyurethane on the substrate.

The setup of the MLD apparatus that allows for a controlled deposition of thin monomer layers was highly complex and required refinement steps. During the stability test runs it was found out that the measurement of the deposited amount of monomers could not be obtained quantitatively. Too many approximations are necessary in order to use the frequency change of the quartz crystal microbalance (QCM) as quantitative measure of the deposited mass or thickness of the layer. Furthermore, the QCM showed to be highly sensitive upon temperature and pressure changes inside the MLD. This required the implementation of room temperature control, isolation and heating of electronic compenents and stable thermostatic baths. Condensation of monomers in the piping had also to be reduced and heated pipes were implemented.

Several conclusions can be drawn from the characterisation of single monomer deposits. Using TGA-IR and MLD deposits it was possible to conclude that the chosen monomers only undergo evaporation without any thermal degradation. This is an important requirement for gas phase deposits.

Atmospheric contaminents were identified on the substrates. MLD deposition regimes, THF rinses and storage in the IR spectrometer modifies the amount of these contaminants. Hence, they should be considered as a further component in the layer. Deposited monomers thus need to interact with these contaminents by either displacing them from the substrate surface, allow mixing inside the monomer deposit or even by partial desorption of the contaminants.

Alcohols and isocyanates deposited on native surfaces of Al and Cu show a significant different behaviour. Alcohols do only undergo weak physical interactions with the metals. Rapid and nearly quantitative desorption takes place. Isocyanates on the other hand do not desorb at RT but form thicker layers. Contrary to literature models no monolayers are directly achieved as intermolecular interactions are not negligible in our case. Some isocyanates react with adsorbed water from the surface and form urea species. THF rinses remove part of the MDI that is only weakly attached to the surface as well as the formed urea species.

Another part of the MDI withstands the solvent as it undergoes a strong attachment to the substrate. This part is defined as *stable MDI deposit* as single molecules are attached to the surface. Complete or homogeneous coverage is not expected. New metal specific IR bands indicate an adhesion mechanism that involves the formation of urethane-like functionalities between the isocyanate groups and hydroxide/oxide from the metal surface. Further experiments confirm this hypothesis. Moreover this strong interaction has a pronounced donor-acceptor interaction character as in certain cases some of the attached MDI can give up this interaction.

The weakly attached MDI can either be removed by THF or by increased temperature. The strongly attached part is not sensitive to temperature increase of up to 50 °C. SFM reveals that rough deposits are achieved through the MLD process. On one hand this can be the consequence of local variations of chemical composition and reactivity of the surface sites of the native oxide films on the two metals. Hence, through the gas phase deposition monomers have the choice to select specific surface sites. On the other hand the obtained topographies could also indicate partial dewetting of the surface. Increased temperature during layer deposition or over storage improves the homogeneity of the layers probably caused by increased molecular mobility.

Sequential deposition of isocyanate and alcohol revealed further singular properties. First it could be shown that stable MDI deposits of strongly attached MDI are capable to react with deposited alcohols on top. This constitutes a major requirement in order to form PU layers attached to the substrate. Deposition of thicker alcohol layers leads to reduced stability as some MDI give up their strong interaction. Hence, the hypothesis of the donor-acceptor character of the adhesive interaction is further consolidated.

Sequential deposition of normal MDI and alcohol layers show that urethane reaction requires up to 10 h at RT before stopping. Progressive change of the intensity ratio of the carbonyl bands indicates a good molecular mobility of the formed urethanes in the confined space of the thin layer and their ability to form energetically favourable hydrogen bonds on both metals.

The topography of the layers is metal specific and dependant on the deposited alcohol and the deposition sequence. In each case rough deposits are achieved. It is likely that the preferential isocyanate adsorption induces this behaviour as similarities with MDI layers are present.

Stability of all prepared layers against THF is very poor. Most formed urethane is removed. No crosslinked polymer network is formed but rather short-chained oligomers that are not capable to react with the strongly attached MDI. Only few urethanes remain attached to the substrate. On Cu stability is worst as although more urethanes are formed faster than on Al, much more species are removed. Even part of the strong attached MDI is removed too.

Significant improvement is achieved through increased storage temperature. Beside faster urethane formation over 1 h, topography is much more homogeneous and stability is significantly better. It is now comparable to layers previously prepared by solvent deposition. Increased temperature is coupled with other factors that are also responsible for this improvement. Higher temperatures lead to the parallel desorption of alcohol and isocyanate. Hence, in this case the ratio NCO:OH is rectified and probably approaches a near stoichiometric ratio. In this case much longer crosslinked urethane chains are obtained. Furthermore, the mobility of all species is increased and more functional groups can reach each other in the confined space of the layer.

All these results have for consequence that the behaviour during layer formation is much more complex compared to the simplified layer model proposed in literature.

Finally this work confirms that it is possible to prepare stable PU layers from gas phase deposits.

9 Outlook

From this study several questions have emerged and remain unanswered. The increase of temperature has shown to be the best way to optimise the stability of the layers. The ratio NCO:OH can possibly play a major role and greatly influence the chemical structure and morphology of the achieved polyurethane. Further experiments where this ratio is deliberately changed and the resulting stability measured would make sense.

Layers prepared in this work consist only of one sequential deposition of MDI and alcohol. The major advantage of the MLD process and thus its flexibility consists in repeating this deposition sequence several times and allow for a step by step growth of the layer. Due to the difficulty to achieve stable layers further deposits were not tested in this work. The results show that unreacted functionalities are present in the layers and hence further reaction is possible. The evolution of the layer properties in terms of topography and stability after each further deposit remain open at this point.

Further development of this deposition technique offers a great potential for the preparation of innovative coatings. The deposition of different monomers during layer growth can lead to the formation of different polymers or a modification of the network and hence a progressive change in properties.

Conditions necessary for both monomers to react could also be provided locally, for example elevated temperature achieved by laser irradiation. Hence, the monomer would only react at certain locations on the substrate while the monomer gases remains inactive on others. This would allow patterning of substrates or even additive manufacturing from the gas phase.

The lack of solvents can also contribute to environmental friendlier fabrication of coatings.

10 References

[1] P. M. Martin,
Handbook of Deposition Technologies for Films and Coatings: Science, Applications and Technology,
3rd Edition, William Andrew, Oxford, UK, **2010**, ISBN 978-0-8155-2031-3.

[2] W. Knoll, R. C. Advincula,
Functional Polymer Films - Volume 1,
Wiley-VCH, Weinheim, **2011**, ISBN 978-3-527-32190-2.

[3] M. Ohring,
The Materials Science of Thin Films,
2nd, Academic Press, San Diego, **2002**, ISBN 0-12-524975-6.

[4] W. Knoll, R. C. Advincula,
Functional Polymer Films - Volume 2,
Wiley-VCH, Weinheim, **2011**, ISBN 978-3-527-32190-2.

[5] J.O.Akindoyo, M.D.H.Beg, S.Ghazali, M.R.Islam, N.Jeyaratnam, A.R.Yuvaraj,
Polyurethane types, synthesis and applications - a review,
RSC Advances **2016**, *6*, p. 114453-114482.

[6] C. Wehlack, W. Possart, J. K. Krüger, U. Müller,
Epoxy and Polyurethane Networks in Thin Films On Metals - Formation, Structure, Properties,
Soft Materials **2007**, *5* (2&3), p. 87-134.

[7] C. Wehlack,
Chemische Struktur und ihre Entstehung in dünnen Epoxid- und Polyurethanschichten auf Metallen,
Dissertation, Universität des Saarlandes, Saarbrücken, **2008**.

[8] C.Nies, C.Wehlack, H.Ehbing, D.J.Dijkstra, W.Possart,
Adhesive Interactions of Polyurethane Monomers with Native Metal Surfaces,
Journal of Adhesion **2012**, *88* (8), p. 665-683.

[9] C.Nies, F.Fug, C.Otto, W.Possart,
Adhesion of polyurethanes on native metal surfaces - stability and the role of urea-like species,
International Journal of Adhesion and Adhesives **2014**, *52* (0), p. 19-25.

[10] F.Fug, C.Nies, W.Possart,
In situ FTIR study of adhesive interactions of 4,4'-methylene diphenyl diisocyanate and native metals,
International Journal of Adhesion and Adhesives **2014**, *52* (0), p. 66-76.

[11] M. Reznik,
Adsorption eines reaktiven Polyurethansystems auf nativen Metallen,
Masterarbeit, Universität des Saarlandes, Saarbrücken, **2015**.

[12] Stephen J.Martin, Victoria Edwards Granstaff, Gregory C.Frye,
Characterization of a Quartz Crystal Microbalance with Simultaneous Mass and Liquid Loading,
American Chemical Society **1991**, *63* (20).

[13] V.M.Mece,
Is quartz crystal microbalance really a mass sensor?,
science direct **2006**.

[14] Quartz Crystal Theory,
Technical Information Sheet,
Jauch Quartz GmbH, **2007**.

[15] H.Tiersten,
Linear Piezoelectric Plate Vibrations,
Plenum Press, New York, **1969**, ISBN 978-1-4899-6453-3.

[16] Rock type Quartz, https://commons.wikimedia.org/w/index.php?curid=9065051">Link. Didier Descouens. (2010 Jan 23).

[17] G.Sauerbrey, .,
Verwendung von Schwingquarzen zur Wägung dünner Schichten und zur Mikrowägung,
Z. Physik **1959**, *155*, p. 206-222.

[18] Günter Sauerbrey,
Experimentelle Untersuchung der Dickenscherungs-Schwingung piezoelektrisch angeregter Quarzplatten,
Doktor-Ingenieur Dissertation, Fakultät für Allgemein Ingenieurwissenschaften der technischen Universität Berlin, Berlin, **1963**.

[19] T.Pauporé & D.Lincot. Microbalance à cristal de quartz. *Techniques de l´ingénieur* INPL. (2013).

[20] O.Kurtz, J.Barthelmes, R.Rüther, M.Wünsche, C.Donner,
Quartz Crystal Microbalance used to Characterize Electrochemical Metal Deposition,
Electrochemistry and Plating Technology **2010**.

[21] V.Tsionsky, E.Gileadi,
Use of the Quartz Crystal Microbalance for the study of Adsorption from the Gas Phase,
Langmuir **1994**, *10*, p. 2830-2835.

[22] Milad Navaei,
Quartz Crystal Microbalance Adsoption Apparatus For High Pressure Gas Adsorption Measurements in Nanomaterials,
Thesis, Institute of Technology, Georgia, **2011**.

[23] A.A.Vives,
Piezoelectric Transducers and Applications,
2, **2008**, ISBN 978-3-540-77507-2.

[24] Oszillator-KnowHow, http://www.auris-gmbh.de/3xios/index1.php?sbsh=cms&ber=katalog&pos_top=7&pos_left=3&hk=5&uk=14&klick=3&tiefe=0. Auris. (2016 Dec 08).

[25] C.Lu and A.W.Czanderna,
Applications of piezoelectric quarz crystal microbalance,
Elsevier Science Publishers, Amsterdam, **1984**, ISBN 0-444-42277-3.

[26] J.Hlavay, G.G.Guilbault,
Applications of the Piezoelectric Crystal Detector in Analytical Chemistry,
New Orleans, **1977**, ISBN 0-444-42277-3.

[27] RQCM - Research Quartz Crystal Microbalance,
Technical Datasheet,
Inficon, **2007**.

[28] N. J. Harrick,
Internal Refection Spectroscopy,
Harrick Scientific Corporation, Ossining, New York, **1979**.

[29] M.Milosevic,
Internal reflection and ATR spectroscopy,
1, John Wiley & Sons, Hoboken, **2012**, ISBN 978-0-470-27832-1.

[30] F. M. Mirabella,
Attenuated Total Reflection Spectroscopy,
F. M. Mirabella (Ed.),
Modern Techniques in Applied Molecular Spectroscopy (Techniques in Analytical Chemistry Series), Chapter 4,
John Wiley & Sons, New York, 1998, ISBN 0-471-12359-5, p. 127-184.

[31] V. P. Tolstoy, I. V. Chernyshova, V. A. Skryshevsky,
Handbook of Infrared Spectroscopy of Ultrathin Films,
Wiley Interscience, New Jersey, **2003**, ISBN 0-471-35404-X.

[32] S. Ekgasit,
ATR Spectral Intensity: What is the Upper Limit of Weak Absorption?,
Applied Spectroscopy **2000**, *54* (5), p. 756-758.

[33] F.Fug,
Chemische Adhäsionswechselwirkungen zwischen Isocyanaten und Metallsubstraten,
Diploma Thesis, Saarland University, Saarbrücken, **2011**.

[34] A.Ghorbal, R.Ben Arfi, S.Bistac, M.Brogly,
Polystyrene chains orientation: A rubbed and non-rubbed polymer comparative study,
Chemical Physics Letters **2007**, *443* (4-6), p. 352-355.

[35] B.Bengu, F.J.Boerio,
Interaction of Epoxy/Dicyandiamide Adhesives with Metal Substrates,
Journal of Adhesion **2006**, *82* (12), p. 1133-1155.

[36] C.Nies,
Chemische Adhäsionswechselwirkungen zwischen Polyurethan-Monomeren und Metallsubstraten,
Diploma Thesis, Saarland University, Saarbrücken, **2010**.

[37] C.Nies, C.Wehlack, H.Ehbling, D.J.Dijkstra, W.Possart,
Formation, structure and morphology of polyurethane-metal interphases,
Proc. , 4th World Congress on Adhesion and Related Phenomena (WCARP IV) **2010**,
p. 23ff.

[38] D.J.Ondrus, F.J.Boerio, K.J.Grannen,
Molecular Structure of Polymer/Metal Interphases,
Journal of Adhesion **1989**, *29* (1-4), p. 27-42.

[39] F.J.Boerio, S.L.Chen,
Reflection-Absorption Infrared Spectroscopy and Ellipsometry of Epoxy Films on Metals,
Applied Spectroscopy **1979**, *33* (2), p. 121-126.

[40] M.Brogly, S.Bistac, J.Schultz,
Persistence of Molecular Orientation in Adsorbed Ethylene-Vinyl Acetate Copolymer Nanofilm Studied by Fourier Transform Infrared Reflectance Spectroscopy,
Macromolecules **1998**, *31* (12), p. 3967-3973.

[41] M.Brogly, S.Bistac, J.Schultz,
A new theoretical approach for the determination of molecular orientation persistence length of adsorbed nanofilms by FTIR reflectance spectroscopy,
Macromolecular Theory and Simulations **1998**, *7* (1), p. 65-68.

[42] P.I Rosales, F.J.Boerio,
Molecular Structure of the Interphase Formed by Plasma-Polymerized Acetylene Films and Steel Substrates,
Journal of Adhesion **2007**, *83* (3), p. 267-287.

[43] S.G.Hong, F.J.Boerio,
Effect of silanes on the interfacial compositions of epoxy/metal adhesive bonds: XPS and RAIR analyses,
Surface and Interface Analysis **1994**, *21* (9), p. 650-658.

[44] T.Elzein, M.Brogly, J.Schultz,
Crystallinity measurements of polyamides adsorbed as thin films,
Polymer **2002**, *43* (17), p. 4811-4822.

[45] T.Elzein, M.Brogly, J.Schultz,
Quantitative calculation of the orientation angles of adsorbed polyamides nanofilms,
Polymer **2003**, *44* (13), p. 3649-3660.

[46] T.Elzein, M.Brogly, J.Schultz,
Adhesion - Current Research and Application,
1. Auflage, Wiley-VCH, Weinheim, **2005**, ISBN 3-527-31263-3.

[47] T.Elzein, A.Fahs, M.Brogly,
Adsorption of Alkanethiols on Gold Surfaces: PM-IRRAS Study of the Influence of Terminal Functionality on Alkyl Chain Orientation,
Journal of Adhesion **2013**, *89* (5), p. 416-432.

[48] C. Wehlack, W. Possart,
Formation, structure and morphology of polyurethane-metal interphases,
IOP Conference Series: Materials Science and Engineering **2009**, *5*, p. 012003ff.

[49] O. Stenzel,
Das Dünnschichtspektrum,
1. Auflage, Akademie Verlag, Berlin, **1996**, ISBN 3-05-501728-5.

[50] S. Berg,
Versuchsführung und Informationsumfang der Brewsterwinkel-Spektroskopie im Vergleich zur Externen Reflexions-Absorptions-Spektroskopie,
Diplomarbeit, Universität des Saarlandes, Saarbrücken, **1998**.

[51] *TGA-IR Modul*,
Benutzerhandbuch, Bruker Optik GmbH, Ettlingen, **2005**.

[52] C. W. Peterson, B. W. Knight,
Causality calculations in the time domain: An efficient alternative to the Kramers-Kronig method,
Journal of the Optical Society of America **1973**, *63* (10), p. 1238-1242.

[53] C. Wehlack, W. Possart,
Characterization of the epoxy-metal interphase: FTIR-ERAS and spectra calculation for ultra-thin films,
Macromolecular. Symposia. **2004**, *205* (1), p. 251-262.

[54] D. Lin-Vien, N. B. Colthup, W. G. Fateley, J. G. Grasselli,
The Handbook of Infrared and Raman Characteristic Frequencies of Organic Molecules,
Academic Press, Boston, **1991**, ISBN 0-12-451160-0.

[55] N. P. G. Roeges,
A Guide to the Complete Interpretation of Infrared Spectra of Organic Structures,
John Wiley & Sons, Chichester, **1994**, ISBN 0-471-93998-6.

[56] B. Smith,
Infrared Spectral Interpretation - A Systematic Approach,
CRC Press, Boca Raton, **1999**, ISBN 0-8493-2463-7.

[57] G. Socrates,
Infrared Characteristic Group Frequencies - Tables and Charts,
2nd Edition, John Wiley & Sons, Chichester, **1994**, ISBN 0-471-94230-8.

[58] *IR Mentor Pro®*,
Software-Datenbank V2.0, Bio Rad Laboratories, Sadtler Division,
Philadelphia, PA, USA, **1996**.

[59] H. Günzler, A. Williams,
Handbook of Analytical Techniques,
Wiley-VCH Verlag, Weinheim, **2001**, ISBN 3-527-30165-8.

[60] Frank Fug, Kevin Rohe, Jorge Vargas, Christophe Nies, Michael Springborg, Wulff Possart,
4,4'-methylene diphenyl diisocyanate - Conformational space, normal vibrations and infrared spectra,
Polymer **2016**, *99* (0), p. 671-683.

[61] G. Ehrenstein, W., G. Riedel, P. Trawiel,
Praxis der Thermischen Analyse von Kunststoffen,
2., völlig überarb. Aufl., Hanser, München, **2003**, ISBN 3-446-22340-1.

[62] D.B.Murphy, M.W.Davidson,
Fundamentals of Light Microscopy and Electronic Imaging,
2. Edition., John Wiley & Sons, Hoboken, **2013**, ISBN 978-0-471-69214-0.

[63] M.Mulisch, U.Welsch,
Romeis Mikroskopische Technik,
18. Aufl., Spektrum Akademischer Verlag, Heidelberg, **2010**, ISBN 978-3-8274-1676-6.

[64] H. Schumann,
Metallographie, Kapitel 1.2: Lichtmikroskopie,
13. Auflage, Deutscher Verlag für Grundstoffindustrie, Leipzig, 1991, ISBN 3-342-00431-2, p. 46-49.

[65] K. S. Birdi, Birdi,
Scanning Probe Microscopes: Applications in Science and Technology,
CRC Press, Boca Raton, **2003**, ISBN 0-8493-0930-1.

[66] E.Meyer, H.J.Hug, R.Bennewitz,
Scanning Probe Microscopy,
Springer-Verlag, Berlin Heidelberg, **2004**, ISBN 978-3-642-07737-1.

[67] K. C. Khulbe, C. Y. Feng, T. Matsuura,
Synthetic Polymeric Membranes: Characterization by Atomic Force Microscopy,
Springer Verlag, Berlin, **2008**, ISBN 978-3-540-73994-4.

[68] N. Yao, Z. L. Wang,
Handbook of Microscopy for Nanotechnology,
Kluwer Academic Publishers, New York, **2005**, ISBN 1-4020-8006-9.

[69] H. Jost,
Molekulare Schichten von Polyurethan und seinen Monomeren auf Metallen – Gasphasenabscheidung und Charakterisierung,
Masterarbeit, Universität des Saarlandes, Saarbrücken, **2015**.

[70] C. Otto,
Auslegung eines Geräts zur Abscheidung von monomolekularen Monomerschichten auf natürlichen Metalloberflächen,
Studienarbeit, Universität des Saarlandes, Saarbrücken, **2011**.

[71] C. Otto,
Vollständige Darstellung des Rechenweges mit Beispielrechnung für Dipropylenglycol,
Addendum zur Studienarbeit, Universität des Saarlandes, Saarbrücken, **2011**.

[72] C. Otto,
Abscheidung organischer Monomere auf nativen Metalloberflächen,
Diplomarbeit, Universität des Saarlandes, Saarbrücken, **2012**.

[73] A. Petry,
Einfluss der experimentellen Parameter auf die Stabilität der Quarzkristallmikrowaage,
Studienarbeit, Universität des Saarlandes, Saarbrücken, **2014**.

[74] A. Petry,
Abscheidung von PU-Monomeren aus der Gasphase auf nativen Metallen,
Masterarbeit, Universität des Saarlandes, Saarbrücken, **2014**.

[75] H. Jost,
Optimierung der Gasphasenabscheidung von Dipropylenglykol,
Universität des Saarlandes, Saarbrücken, **2012**.

[76] D. M. Mattox,
Handbook of Physical Vapor Deposition (PVD) Processing,
Noyes Publications, Westwood, New Jersey, USA, **1998**, ISBN 0-8155-1422-0.

[77] K.L.Choy,
Chemical vapour deposition of coatings,
Prog. Mater. Sci. **2003**, *48*, p. 57-170.

[78] S.M.Geoge,
Atomic Layer Deposition: An Overview,
Chem. Rev. **2010**, *110*, p. 111-131.

[79] A.Kubono, N.Okui,
Polymer thin films prepared by vapour deposition,
Prog. Polym. Sci. **1994**, *19*, p. 389-438.

[80] M.E.Alf, A.Asatekin, M.C.Barr, S.H.Baxamusa, H.Chelawat, G.Ozaydin-Ince,
Chemical Vapor Deposition of Conformal, Functional, and Responsive Polymer Films,
Adv. Mater. **2010**, *22*, p. 1993-2027.

[81] G.Ozaydin-Ince, A.M.Coclite, K.K.Gleason,
CVD of polymeric thin films: applications in sensors, biotechnology, microelectronics/organic electronics, microfluidics, MEMS, composites and membranes,
Rep. Prog. Phys. **2012**, *75*, p. 016501ff.

[82] S.M.Geoge, B.Yoon, A.A.Dameron,
Surface Chemistry for Molecular Layer Deposition of Organic and Hybrid Organic-Inorganic Polymers,
Accounts Chem. Res. **2009**, *42* (4), p. 498-508.

[83] P.Sundberg, M.Karppinnen,
Organic and inorganic–organic thin film structures by molecular layer deposition: A review,
Beilstein J. Nanotechnol. **2009**, *5*, p. 1104-1136.

[84] Y.Du, S.M.Geoge,
Molecular Layer Deposition of Nylon 66 Films Examined Using in Situ FTIR Spectroscopy,
J. Phys. Chem. C **2007**, *111* (24), p. 8509-8517.

[85] X.Du, Y.Du, S.M.Geoge,
In situ examination of tin oxide atomic layer deposition using Quartz microbalance and fourier transform infrared spectroscopy,
J. Vac. Sci. Technol. A **2005**, *23* (4), p. 581ff.

[86] Y.Du, X.Du, S.M.Geoge,
SiO2 film growth at low temperatures by catalyzed atomic layer deposition in a viscous flow reactor,
Thin Solid Films **2005**, *491*, p. 43-53.

[87] G. Wedler, H.-J. Freund,
Lehrbuch der Physikalischen Chemie, 6. Auflage,
Wiley-VHC Verlag, Weinheim, **2012**, ISBN 978-3-527-32909-0.

[88] P. W. Atkins, J. De Paula,
Physikalische Chemie, 5. Auflage,
Wiley-VHC Verlag, Weinheim, **2013**, ISBN 978-3-527-33247-2.

[89] EL-Flow Select broschüre, https://www.bronkhorst-nord.de/files/downloads/brochures_duits/folder_elflow_ger.pdf. Bronkhorst Deutschland Nord GmbH. (2018 Jun 15).

[90] M.-C. Desjonquères, D. Spanjaard,
Concepts in Surface Physics,
2nd Edition, Springer-Verlag, Berlin, **1998**, ISBN 3-540-58622-9.

[91] A. Groß,
Theoretical Surface Science. A Microscopic Perspective,
Springer, Berlin, Heidelberg, **2003**, ISBN 3-540-43903-X.

[92] C. Bockenheimer,
Epoxid und Aluminium im Klebverbund nach mechanischer Vorbehandlung und nach Alterung,
Dissertation, Universität des Saarlandes, Saarbrücken, **2003**.

[93] J. C. Bolger,
Acid Base Interactions Between Oxide Surfaces and Polar Organic Compounds,
K. L. Mittal (Ed.),
Adhesion Aspects of Polymeric Coatings,
Plenum Press, New York, 1983, ISBN 0-306-41250-0, p. 3-18.

[94] S. Dieckhoff, W. Brockmann, F. Faupel, W. Possart, J. K. Krüger,
Adhäsions- und Alterungsmechanismen in Polymer-Metall-Übergängen,
Abschlußbericht, BMBF-Projekt 03D0074, TIB Hannover, **2004**.

[95] T. Morimoto, M. Nagao, F. Tokuda,
The Relation between the Amounts of Chemisorbed and Physisorbed Water on Metal Oxides,
The Journal of Physical Chemistry **1969**, *73* (1), p. 243-248.

[96] F.Sugimoto, S.Okamura,
Adsorption Behavior of Organic Contaminants on a Silicon Wafer Surface,
Journal of the Electrochemical Society **1999**, *146* (7), p. 2725-2729.

[97] W. Possart,
Auswertung der XPS der Al-PVD Schicht auf Si(100),
Report, LAIP, Universität des Saarlandes, Saarbrücken, **2017**.

[98] C. Hepburn,
Polyurethane Elastomers,
2nd Edition, Elsevier Applied Science, London, New York, **1992**, ISBN 1-85166-589-7.

[99] G. Oertel, G. W. Becker, D. Braun,
Polyurethane (Kunststoff-Handbuch 7),
3. Auflage, Carl Hanser Verlag, München, **1993**, ISBN 3-446-16263-1.

[100] M. Szycher,
Szycher's Handbook of Polyurethanes,
CRC Press, London, **1999**, ISBN 0-8493-0602-7.

[101] P. Thomas, C. Varron, P. Ardaud, J.-M. Bernard, M. Cowley, T. Jeanette, J. Maxted, G. Rayner, B. Storer, A. Shields, N. Wheat,
Waterborne & Solvent Based Surface Coating Resins and their Applications: Volume III - Polyurethanes,
John Wiley & Sons, Chichester, New York, **1998**, ISBN 0-471-97886-8.

[102] M. Szycher,
Szycher's Handbook of Polyurethanes,
CRC Press, London, **1999**, ISBN 0-8493-0602-7.

[103] G. Oertel, G. W. Becker, D. Braun,
Polyurethane (Kunststoff-Handbuch 7),
3. Auflage, Carl Hanser Verlag, München, **1993**, ISBN 3-446-16263-1.

[104] B. Tieke,
Makromolekulare Chemie - Eine Einführung,
Zweite, vollständig überarbeitete und erweiterte Auflage, VCH Verlagsgesellschaft, Weinheim, **2005**, ISBN 978-3-527-31379-2.

[105] H. Ulrich,
Chemistry and Technology of Isocyanates,
John WIley and Sons, **1997**, ISBN 0-471-96371-2.

[106] A.D.McNaught, A.Wilkinson,
IUPAC. Compendium of Chemical Terminology ("the Gold Book"),
2nd Edition, Blackwell Scientific Publications, Oxford, **1997**, ISBN 0865426848.

[107] A. Farkas, G. A. Mills,
Catalytic Effects in Isocyanate Reactions,
Advances in Catalysis **1962**, *13*, p. 393-446.

[108] G.Borkent,
Advances in Urethane: Science and Technology,
Technomic Publishing Co, Westport, Conn., **1974**.

[109] N. Luo, D.-N. Wang, S.-K. Ying,
Effect of Urea Groups on Reaction Kinetics of Polyurethane Formation,
Journal of Applied Polymer Science **1996**, *61* (2), p. 367-370.

[110] K. Uhlig,
Polyurethan Taschenbuch,
3. Auflage, Carl Hanser Verlag, München, **2006**, ISBN 3-446-40307-8.

[111] K. Wagner, K. Findeisen, W. Schäfer, W. Dietrich,
α,ω-Diisocyanato-carbodiimide und -polycarbodiimide sowie ihre Derivate,
Angewandte Chemie **1981**, *93* (10), p. 855-866.

[112] E.Z.Zhuravlev, P.V.Mulyanov, N.M.Moncharzh,
Dielectric constants and dipole moments of some organic isocyanates,
Zhurnal Obshchei Khimii **1975**, *45*, p. 1605-1610.

[113] K. Oberbach,
Saechtling Kunststoff Taschenbuch,
26. Ausgabe, Carl Hanser Verlag, München, **1995**, ISBN 3-446-17855-4.

[114] *Desmophen® 1380 BT*,
Produktinformation, Bayer AG, Leverkusen, **2003**.

[115] *Dipropylenglykol LO+*,
Sicherheitsdatenblatt, Dow Chemical, **2011**.

[116] A. S. Ahmed,
Dünne Schichten aus trifunktionellem Alkohol auf nativen Metalloberflächen,
Bachelorarbeit, Universität des Saarlandes, Saarbrücken, **2017**.

[117] B. Gilbert,
Contaminations on native metal surfaces,
Projektbericht, Universität des Saarlandes, Saarbrücken, **2015**.

[118] E. Ziegler,
Einfluss der Temperatur auf die Polyaddition von dünnen PU MLD-Schichten,
Bachelorarbeit, Universität des Saarlandes, Saarbrücken, **2019**.

[119] C.Pirro,
Einfluss von Temperatur und Zusammensetzung auf die Eigenschaften dünner Urethan MLD-Schichten,
Masterarbeit, Universität des Saarlandes, Saarbrücken, **2020**.

[120] A.Ahmed,
Molecular Layer Deposition - Erzeugung ultradünner PU-Netzwerke in der Anlage,
Masterarbeit, Universität des Saarlandes, Saarbrücken, **2019**.

[121] S.M.George, B.Yoon, A.A.Dameron,
Surface Chemistry for Molecular Layer Deposition of Organic and Hybrid Organic-Inorganic Polymers,
Accounts Chem. Res. **2009**, *42* (4), p. 498-508.

[122] A.Kubono, N.Yuasa, H.Shao, S.Umemoto, N.Okui,
In-situ study on alternating vapor deposition polymerization of alkyl polyamide with normal molecular orientation,
Thin Solid Films **1996**, *289*, p. 107-111.

[123] A.Nagai, H.Shao, S.Umemoto, T.Kikutani, N.Okui,
Quadruple aliphatic polyamide systems prepared by a layer-by-layer alternating vapour deposition method,
High Perform. Polym. **2001**, *13*, p. S169-S179ff.

[124] H.Shao, S.Umemoto, T.Kikutani, N.Okui,
Layer-by-layer polycondensation of nylon 66 by alternating vapour deposition polymerization,
Polymer **1997**, *38* (2), p. 459-462.

[125] Q.Peng, K.Efimenko, J.Genzer, G.Parsons,
Oligomer Orientation in Vapor-Molecular-Layer-Deposited Alkyl Aromatic Polyamide Films,
Langmuir **2012**, *28*, p. 10464-10470.

[126] N.M.Adamczyk, A.A.Dameron, S.M.George,
Molecular Layer Deposition of Poly(p-phenylene terephtalamide) Films Using Terephthalayl Chloride and p-Phenylenediamine,
Langmuir **2008**, *24*, p. 2081-2089.

[127] M.Putkonen, J.Harjuoja, T.Sajavaara, L.Niinistö,
Atomic layer deposition of polyimide thin films,
J. Mater. Chem. **2007**, *17*, p. 664-669.

[128] L.D.Salmi, E.Puukilainen, M.Vehkamäki, M.Heikkilä, M.Ritala,
Atomic Layer Deposition of Ta_2O_5/Polyimide Nanolaminates,
Chem. Vap. Deposition **2009**, *15*, p. 221-226.

[129] S.Yoshida, T.Ono, M.Esashi,
Local electrical modification of a conductivity-switching polyimide film formed by molecular layer deposition,
Nanotechnology **2011**, *22*, p. 335302ff.

[130] S.Haq, N.V.Richardson,
Organic Beam Epitaxy Using Controlled PMDA-ODA Coupling Reactions on Cu{110},
J. Phys. Chem. B **1999**, *103*, p. 5256-5265.

[131] T.Miyamae, K.Tsukagoshi, O.Matsuoka, S.Yamamoto, H.Nozoye,
Preparation of Polyimide-Polyamide Random Copolymer Thin Film by Sequential Vapor Deposition Polymerization,
Jpn. J. Appl. Phys. **2002**, *41*, p. 746-748.

[132] A.Kim, M.A.Filler, S.Kim, S.F.Bent,
Layer-by-Layer Growth on Ge(100) via Spontaneous Urea Coupling Reactions,
Journal of the American Chemical Society **2005**, *127*, p. 6123-6132.

[133] P.W.Loscutoff, H.Zhou, S.B.Clendenning, S.F.Bent,
Formation of Organic Nanoscale Laminates and Blends by Molecular Layer Deposition,
American Chemical Society **2010**, *4* (1), p. 331-341.

[134] C.Prasittichai, H.Zhou, S.F.Bent,
Area Selective Molecular Layer Deposition of Polyurea Films,
Appl. Mater. Interfaces **2013**, *5*, p. 13391-13396.

[135] H.Zhou, S.F.Bent,
Molecular Layer Deposition of Functional Thin Films for Advanced Lithographic Patterning,
Appl. Mater. Interfaces **2011**, *3*, p. 505-511.

[136] H.Zhou, M.F.Toney, S.F.Bent,
Cross-Linked Ultrathin Polyurea Films via Molecular Layer Deposition,
Macromolecules **2013**, *46*, p. 5638-5643.

[137] Y.Chen, B.Zhang, Z.Gao, C.Chen, S.Zhao, Y.Qin,
Functionalization of multiwalled carbon nanotubes with uniform polyurea coatings by molecular layer deposition,
Carbon **2015**, *82*, p. 470-478.

[138] J.S.Lee, Y.-J.Lee, E.L.Tae, Y.S.Park, K.B.Yoon,
Synthesis of Zeolite As Ordered Multicrystal Arrays,
Science **2003**, *301*, p. 818-821.

[139] P.W.Loscutoff, H.Lee, S.F.Bent,
Deposition of Ultrathin Polythiourea Films by Molecular Layer Deposition,
Chem. Mater. **2010**, *22*, p. 5563-5569.

[140] T.V.Ivanova, P.S.Maydannik, D.C.Cameron,
Molecular layer deposition of polyethylene terephtalate thin films,
J. Vac. Sci. Technol. A **2012**, *30*, p. 01A121ff.

[141] T.Yoshimura, S.Tatsuura, W.Sotoyama, A.Matsuura, T.Hayano,
Quantum wire and dot formation by chemical vapor deposition and molecular layer deposition of one-dimensional conjugated polymer,
Appl. Phys. Lett. **1992**, *60*, p. 268-470.

[142] T.Yoshimura, Y.Kudo,
Monomolecular-Step Polymer Wire Growth from Seed Core Molecules by Carrier-Gas-Type Molecular Layer Deposition,
Appl. Phys. Express **2009**, *2*, p. 015502ff.

[143] T.Yoshimura, S.Ito, T.Nakayama, K.Matsumoto,
Orientation-controlled molecule-by-molecule polymer wire growth by the carrier-gas-type organic chemical vapor deposition and the molecular layer deposition,
Appl. Phys. Lett. **2007**, *91*, p. 033103ff.

[144] C.Mui, J.H.Han, G.T.Wang, C.B.Musgrave, S.F.Bent,
Proton Transfer Reactions on Semiconductor Surfaces,
Journal of the American Chemical Society **2002**, *124*, p. 4027-4038.

[145] M.M.Coleman, K.H.Lee, D.J.Skrovanek, P.C.Painter,
Hydrogen Bonding in Polymers. 4. Infrared Temperature Studies of a Simple Polyurethane,
Macromolecules **1986**, *19*, p. 2149-2157.

[146] R. G. Dillingham, C. J. Moriarty,
The Adhesion of Isocyanate-Based Polymers to Steel,
Journal of Adhesion **2003**, *79* (3), p. 269-285.

[147] M. M. Chehimi, J. F. Watts,
An XPS study of the steel-aromatic moisture-cured urethane interface,
Journal of Adhesion Science and Technology **1992**, *6* (3), p. 377-393.

[148] J. Kim, J. Cho, Y.-S. Lim,
Bonding of urethane reactants to aluminum surface,
Journal of Material Science **2005**, *40*, p. 2789-2794.

[149] D. Tang, Y. Guo, X. Zhang, J. Liu, .,
Interfacial reactions in an interpenetrating polymer network thin film on an aluminium sustrate,
Surface and Interface Analysis **2009**, *41*, p. 974-980.

[150] K. Shimizu, C. Phanopoulos, R. Loenders, M.-L. Abel, J. F. Watts,
The characterization of the interfacial interaction between polymeric methylene diphenyl diisocianate and aluminum: A ToF-SIMS and XPS study,
Surface and Interface Analysis **2010**, *42*, p. 1432-1444.

[151] D. D. Eley, G. M. Kiwanuka, C. H. Rochester,
Infra-red Study of the Reactictions between Ethyl Isocyanate and the surface of magnesium oxide,
Journal of the Chemical Society, Faraday Transactions 1: Physical Chemistry in Condensed Phases **1974**, *70* (6), p. 1099-1108.

[152] P. G. Harrison, E. W. Thornton,
Tin oxide surfaces. 3. Infra-red Study of the adsorption of small organic molecules on tin(IV) oxide,
Journal of the Chemical Society, Faraday Transactions 1: Physical Chemistry in Condensed Phases **1975**, *71* (12), p. 2468-2477.

[153] A. Pizzi, K. L. Mittal,
Handbook of Adhesive Technology - 2nd Edition, Revised and Expanded,
2nd Edition, CRC Press, New York, **2003**, ISBN 0-8247-0986-1.

[154] P. G. Belelli, M. M. Branda, G. R. Garda, R. M. Ferullo, N. J. Castellani,
Chemisorption of isocyanate (NCO) on the Pd(100) surface at different coverages,
Surface Science **2010**, *604*, p. 442-450.

[155] G. R. Garda, R. M. Ferullo, N. J. Castellani,
Chemisorption of NCO on the Cu(100): A density functional theory study,
Surface Science **2005**, *598*, p. 57-67.

[156] R. M. Ferullo, M. M. Branda, G. R. Garda, N. J. Castellani,
Ab initio study of the isocyanate surface complex over silica and alumina,
Journal of Molecular Catalysis A: Chemical **2001**, *167*, p. 115-119.

[157] J. Summa,
Co-Adsorption von Polyurethanmonomeren auf nativem Aluminium,
Masterarbeit, Universität des Saarlandes, Saarbrücken, **2014**.

[158] F.Sugimoto, S.Okamura,
Adsorption Behavior of Organic Contaminants on a Silicon Wafer Surface,
Journal of the Electrochemical Society **1999**, *146* (7), p. 2725-2729.

[159] Nathalie Hayeck,
Contamination des wafers et de l'atmosphère des salles blanches de la microélectronique: développement analytique et étude in-situ,
Dissertation, Aix-Marseille Université, Marseille, **2015**.

[160] N.Hayeck, S.Gligorovsky, I.Poulet, H.Wortham,
Validation of thermodesorption method for analysis of semi-volatile organic compounds adsorbed on wafer surface,
Talanta **2014**, *122*, p. 63-69.

[161] M. Andres,
Dünne PU-Schichten aus der MLD - Kontaminationen und Stabilität,
Projektbericht, Universität des Saarlandes, Saarbrücken, **2018**.

[162] M.M.Coleman, D.J.Skrovanek, J.Hu, P.C.Painter,
Hydrogen Bonding in Polymer Blends. 1. FTIR Studies of Urethane-Ether Blends,
Macromolecules **1988**, *21*, p. 59-65.

[163] S. D. Evans, R. P. Houghton,
On the mechanism of the copper(II) catalysis of the formation of urethanes from alcohols and isocyanates,
Journal of Molecular Catalysis A: Chemical **2000**, *164* (1-2), p. 157-164.

[164] R. A. Ligabue, A. L. Monteiro, R. F. de Souza, M. O. de Souza,
Catalytic properties of $Fe(acac)_3$ and $Cu(acac)_2$ in the formation of urethane from a diisocyanate derivative and EtOH,
Journal of Molecular Catalysis A: Chemical **1998**, *130* (1-2), p. 101-105.

[165] T. E. Lipatova, Y. N. Nizel'skii,
Mechanism of Urethane Formation Through Catalyst Complex with Rfactants,
Doklady Akademii Nauk Sssr **1970**, *190* (4), p. 880-883.

[166] T. E. Lipatova, Y. N. Nizel'skii,
Mechanism of Catalysis by Copper Chelates of Urethane Formation,
Zhurnal Fizicheskoi Khimii **1972**, *46* (9), p. 2294-2297.

[167] T. E. Lipatova, Y. N. Nizel'skii,
Coordination Catalysis in Reactions of Polyaddition,
Advances in Urethane Science and Technology **1981**, *8*, p. 217-243.

[168] Y. N. Nizelsky, S. S. Ishchenko, T. E. Lipatova,
Study of Catalytic Activity of Cu(II) Coordination Compounds in Reaction of Urethane Formation,
Dopovidi Akademii Nauk Ukrainskoi Rsr, Seriya B **1973**, *35*, p. 431-435.

[169] L.Weh,
Surface Structures in Thin Polymer Layers Caused by Coupling of Diffusion-Controlled Marangoni Instability and Local horizontal Temperature Gradient,
Macromol. Mater. Eng. **2005**, *290*, p. 976-986.

[170] L.Weh, A.Venthur,
Crack Pattern in Thin Polymer Layers,
Macromol. Mater. Eng. **2004**, *289*, p. 227-237.

[171] Colnatec RC Quartz,
Technical Datasheet,
Colnatec, **2014**.

[172] https://www.brukerafmprobes.com/p-3726-scanasyst-air.aspx. (2020 Jun 23).

[173] *4,4'-methylene diphenylene diisocyanate*,
Safety Data Sheet, Acros Organics, Geel, **2013**.

[174] *Dipropylenglykol LO+*,
Safety Data Sheet, The Dow Chemical Company, **2014**.

[175] *Baygal® K55*,
Safety Data Sheet, Bayer MaterialsScience AG, Leverkusen, **2005**.

[176] *Baygal® K55*,
Product Information sheet, Bayer MaterialsScience AG, Leverkusen, **2006**.

[177] *Tetrahydrofuran*,
Safety Data Sheet, Sigma-Aldrich GmbH, Steinheim, **2013**.

11 Appendix

11.1 Technical data on characterisation methods

11.1.1 Quartz crystal microbalance

Table 11-1 Characteristics of the utilised Quartz crystals [27, 171].

Manufacturer/Description	Colnatec RC™ Quartz
Cut	AT-cut
Typical resonance frequency f_0	5,975 – 5,993 MHz
Quartz diameter	14 mm
Thickness	0.2 mm
Quartz Holder hole diameter	8.1 mm
Accessible surface for deposition monitoring $A = A_{geo}$	0.52 cm^2
Electrode material	Gold
Roughness R_{RMS}	7 µm

11.1.2 Infrared spectroscopy

Table 11-2 Technical data of the IR spectrometer and typical parameters for reflection measurements (ATR & ERAS).

Manufacturer/Description	Biorad/Digilab FTS 3000 Excalibur
Source	MIR-Glowbar
Beam splitter	KBr
Polarisation filter	Grid on KRS-5
Mirror speed	20 kHz
Phase correction	Mertz
Apodisation	Norton-Beer medium
Wavenumber range	4000 – 400 cm^{-1}
Resolution	4 cm^{-1}
Zero filling factor	8
IR-ATR measurements (internal reflection)	
Detector	MCT
Reflection unit	Harrick Seagull®
ATR crystal	ZnSe hemisphere
Angle of incidence	60 °
Polarisation	p-polarisation
Aperture	5.6 mm
Co-added scans	500
IR-ERAS measurements (external reflection)	
Detector	MCT
Reflection unit	Harrick Seagull®
Angle of incidence	80 °
Polarisation	p-polarisation
Aperture	5.6 mm
Co-added scans	200-500

11.1.3 Thermogravimetric Analysis (TGA)

Table 11-3 Technical data of the TGA and typical parameters for measurements with coupled FTIR.

Manufacturer/Description	TA Instruments/Q5000-IR
Gas selection	Nitrogen
Gas flow balance	10 ml/min
Gas flow furnace	240 ml/min
Total gas flow	250 ml/min
Evolved gas selector temperature	ca. 120 °C
Transfer pipe temperature	200 °C

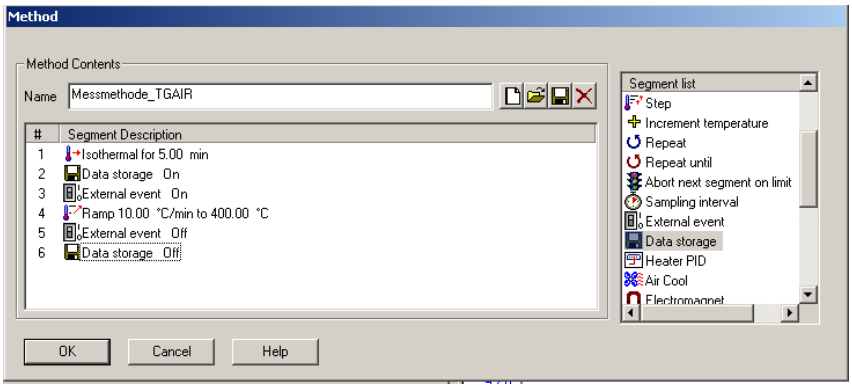

Fig. 11-1 TGA measurement method for coupling with IR transmission

Table 11-4 Technical data of the IR spectrometer and typical parameters for transmission measurements in continuous mode.

Manufacturer/Description	Bruker/Tensor 27
Source	MIR-Glowbar
Beam splitter	KBr
Mirror speed	20 kHz
Phase correction	Mertz
Apodisation	Norton-Beer strong
Wavenumber range	4000 – 400 cm^{-1}
Resolution	4 cm^{-1}
Zero filling factor	2
Aperture	2.5 mm
Co-added scans	32
Detector	MCT
Transmission cell temperature	200 °C

11.1.4 Scanning force microscopy (SFM)

Table 11-5 Technical data and properties of the cantilever [172].

Manufacturer/Description	Bruker Dimension Icon®
Form	triangular
Resonance frequency range	45 – 95 kHz
Normal resonance frequency	70 kHz
E modulus range	0.2 – 0.8 N/m
Normal E modulus	0.4 N/m
Normal length	115 µm
Normal width	25 µm

Table 11-6 Properties of the Tip [172].

Manufacturer/Description	Bruker Scanasyst-Air
Height	2.5 – 8 µm
Tip angle	15 ± 8.0 °
Normal tip radius	2 nm
Maximum tip radius	12 nm

Table 11-7 SFM Tapping mode scan parameters.

Scan rate	0.996 Hz (1x1 μm^2 and 5x5 μm^2) 0.498 Hz (10x10 μm^2) 0.33 Hz (20x20 μm^2)
Samples per line	512
Lines	512
Amplitude Setpoint	65 – 160 mV
Drive Amplitude	275 – 7080 mV
Integral gain	0.5 – 1
Proportional gain	1 – 1.5

11.2 Technical data on substrate preparation

Table 11-8 Parameters for the Al-, Cu- and Au-PVD sample preparation on polished silicon wafers.

Manufacturer/Description	Emitech / K975 Turbo Evaporator		
Evaporating Metal	Al	Cu	Au
Mass of evaporation metal (mg)	26	200	390
Diameter of tungsten wire (mm)	0.5		
Dimension of wire basket cone (cm)	Height: 0.9; base diameter: 0.9		
Distance basket – substrate (cm)	15		
Electric current for glowing (A)	10		
Electric current for evaporation (A)	16	20	25
Voltage (V)	15		
Initial pressure (mbar)	$5 \cdot 10^{-5}$		
Deposition time (Glowing /Evaporation) (min)	20 / 60		
Argon Purging time (before and after deposition) (min)	0.5 / max. 4		

11.3 Physical properties of the monomers

11.3.1 4,4'-methylene diphenyl diisocyanate (4,4'-MDI)

Table 11-9 Physical properties of 4,4'-MDI [173].

Product	4,4'-methylene diphenylene diisocyanate
Manufacturer	Acros Organics
Product type	Aromatic isocyanate
Molecular weight (g/mol)	250.26
NCO functionality	2
Density (g/cm^3) at T = 20 °C	1.190
Viscosity (mPa·s) at T = 42 °C	3-6
Melting temperature (°C)	40
Boiling temperature (°C)	392
Vapour pressure (hPa) at T = 20 °C	< 10^{-5}

11.3.2 Dipropylene glycol (DPG)

Table 11-10 Physical properties of DPG - Diol [174].

Product	DPG LO+
Manufacturer	The Dow Chemical Company
Product type	Dipropylene glycol
Molecular weight (g/mol)	134.2
OH functionality	2
Density (g/cm^3) at T = 25 °C	1.022
Viscosity (mPa·s) at T = 25 °C	75
Boiling temperature (°C)	228-236
Vapour pressure (hPa) at T = 20 °C	< 10^{-5}

11.3.3 Baygal®K55

Table 11-11 Physical properties of Baygal®K55 – Triol [175, 176].

Product	Baygal®K55
Manufacturer	Bayer MaterialScience AG
Product type	Trifunctional polypropylene ether polyol
Molecular weight (g/mol)	444
OH functionality	3
Density (g/cm^3) at T = 25 °C	1.0252
Viscosity (mPa·s) at T = 25 °C	550-750
Boiling temperature (°C)	290
Vapour pressure (hPa) at T = 20 °C	2

11.3.4 Tetrahydrofuran (THF)

Table 11-12 Physical properties of THF [177].

Product	Tetrahydrofuran
Manufacturer	Sigma-Aldrich Chemie GmbH
Product type	Aliphatic cyclic ether
Molecular weight (g/mol)	72.11
Density (g/cm^3) at T = 20 °C	0.8892
Boiling temperature (°C)	65.5
Vapour pressure (hPa) at T = 20 °C	200

11.4 Technical Data of the MLD apparatus

11.4.1 Pipes and tubing

Table 11-13 Diameter of the pipes and tubes built in the evaporation stage, reactor chamber and vacuum stage.

Description	Diameter [mm]
Main pipe entrance from gas stage	40
Main pipe and intersections	70
Flexible metal tubes to evaporation cells and to cryo trap	16
Evaporation cells	40
Flexible tubes to vacuum pump	32

11.4.2 Evaporation unit

Fig. 11-2 Front view of the Thermoknud controller for the evaporation unit heating.

For each cell the set point temperature is choosen using the round dial. The values for the set point are listed in Table 11-14.

Table 11-14 Set point values for the Thermoknud temperature controller.

Evaporation cell temperature	Initial set point	Final set point at temperature
80 °C	4.3	4.8 at 65 °C
90 °C	4.7	5.2 at 75 °C
180 °C	10	9.3 at 175 °C

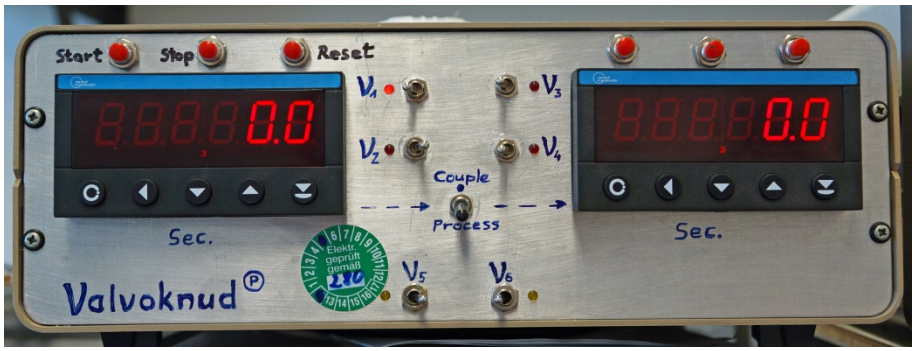

Fig. 11-3 Front view of the Valvoknud controller for the electro pneumatic valves.

The correspondence of Valves V1 to V6 is given in Table 11-15. The displays enable to set the switching time of the gate valves. The couple process switch permits to initiate the switching of the valves of cell 2 after they have switched over in cell 1.

Table 11-15 Valve correspondence of the Valvoknud controller.

Valve description on Valvoknud	Corresponding valve
V1 (Cell1) / V3 (Cell 2)	Cleaning/non deposition mode gate valve (evaporation cells)
V2 (Cell1) / V4 (Cell 2)	Deposition mode gate valves (evaporation cells)
V5	Cleaning mode vacuum valve (vacuum stage)
V6	Deposition/ non-deposition mode vacuum valve (vacuum stage)

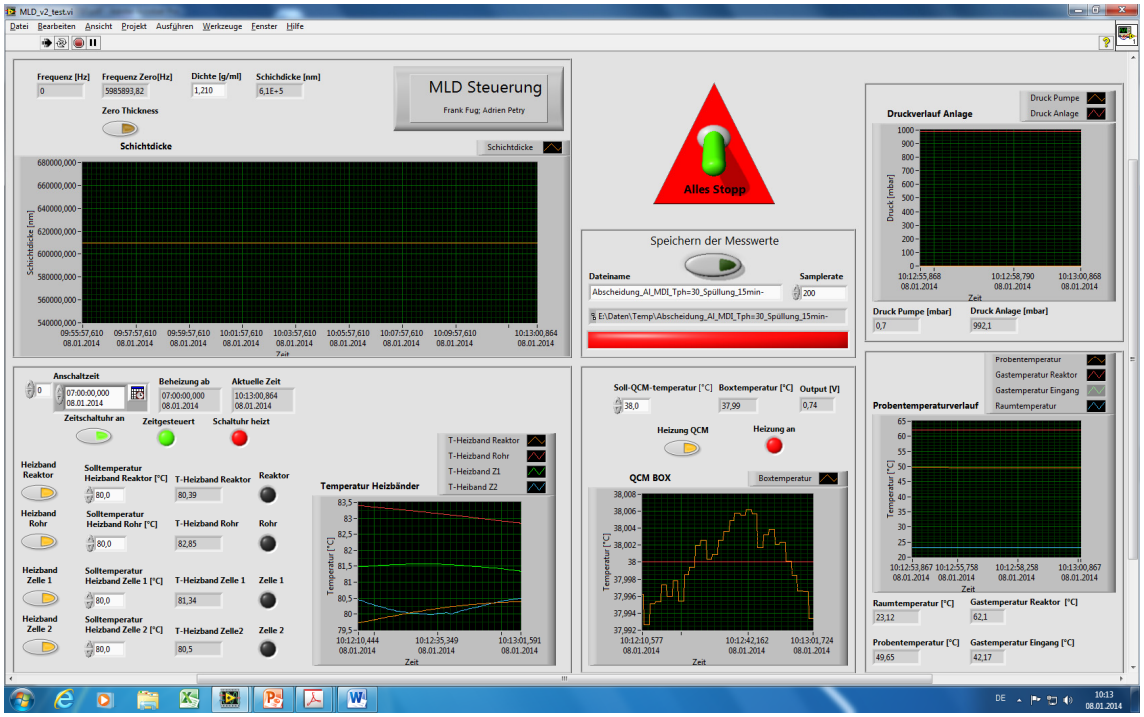

Fig. 11-4 Screenshot of the LABVIEW interface for MLD control.

11.4.3 Reactor chamber

Fig. 11-5 Front view of the SubstratTherm controller for the substrate temperature. T_2 = gas temperature inside the reactor; T_3 = gas temperature at the evaporation stage entrance.

Table 11-16 Set point values for the thermostatic bath for the temperature control of substrate and QCM quartz.

Sample temperature	Set point temperature of thermostatic bath
10 °C	8.12 °C
30 °C	29 °C
50 °C	50 °C

11.5 Thin monomer deposits

11.5.1 DPG layers on native Cu

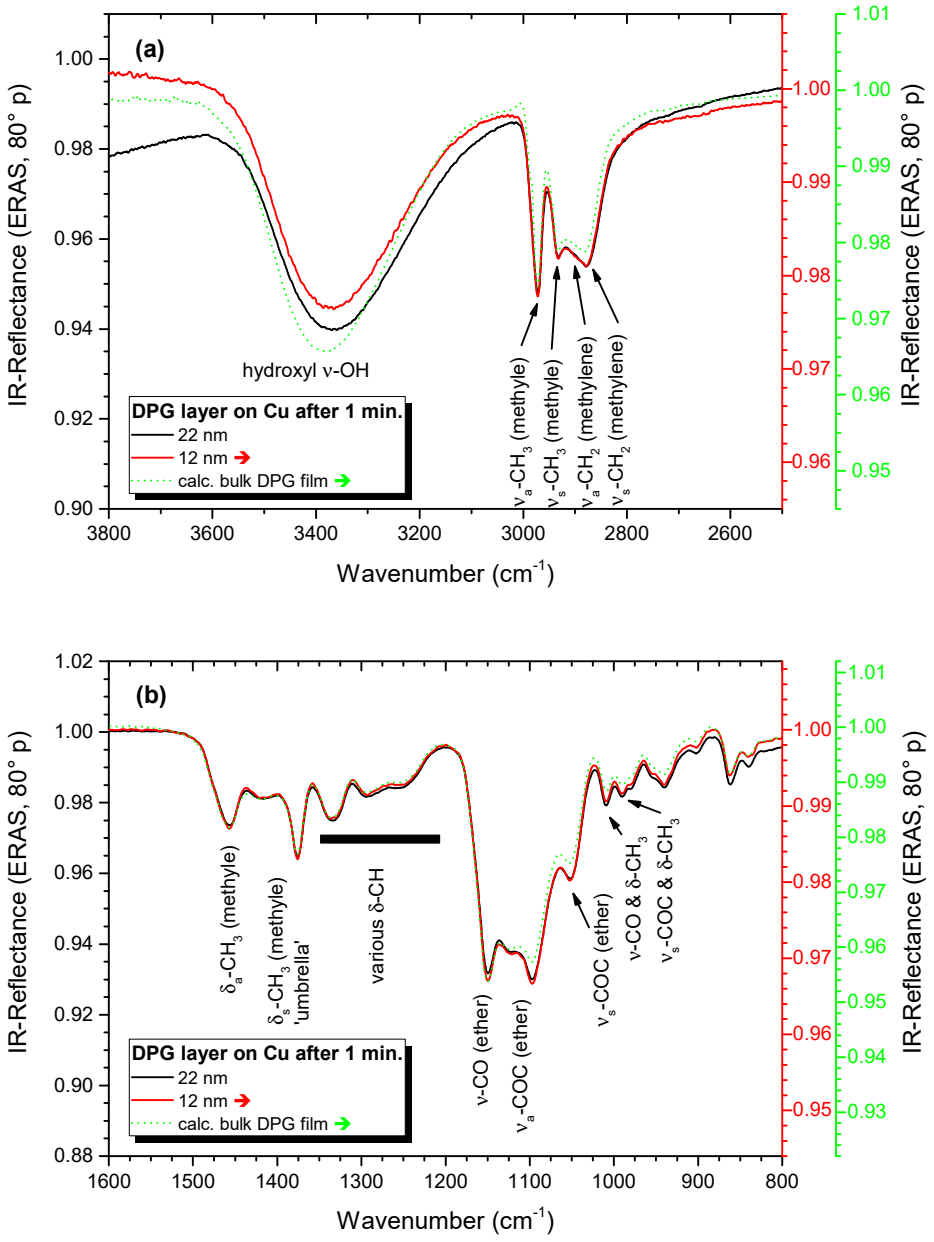

Fig. 11-6 Comparison of IR-ERA spectra of 22 nm (black) and 12 nm (red) DPG layers on Cu after deposition. The spectrum of each layer is scaled differently. The dashed spectrum represents a calculated bulk-like ERA spectrum of DPG for comparison. (a) 3800 – 2500 cm^{-1}, (b) 1600 – 800 cm^{-1}.

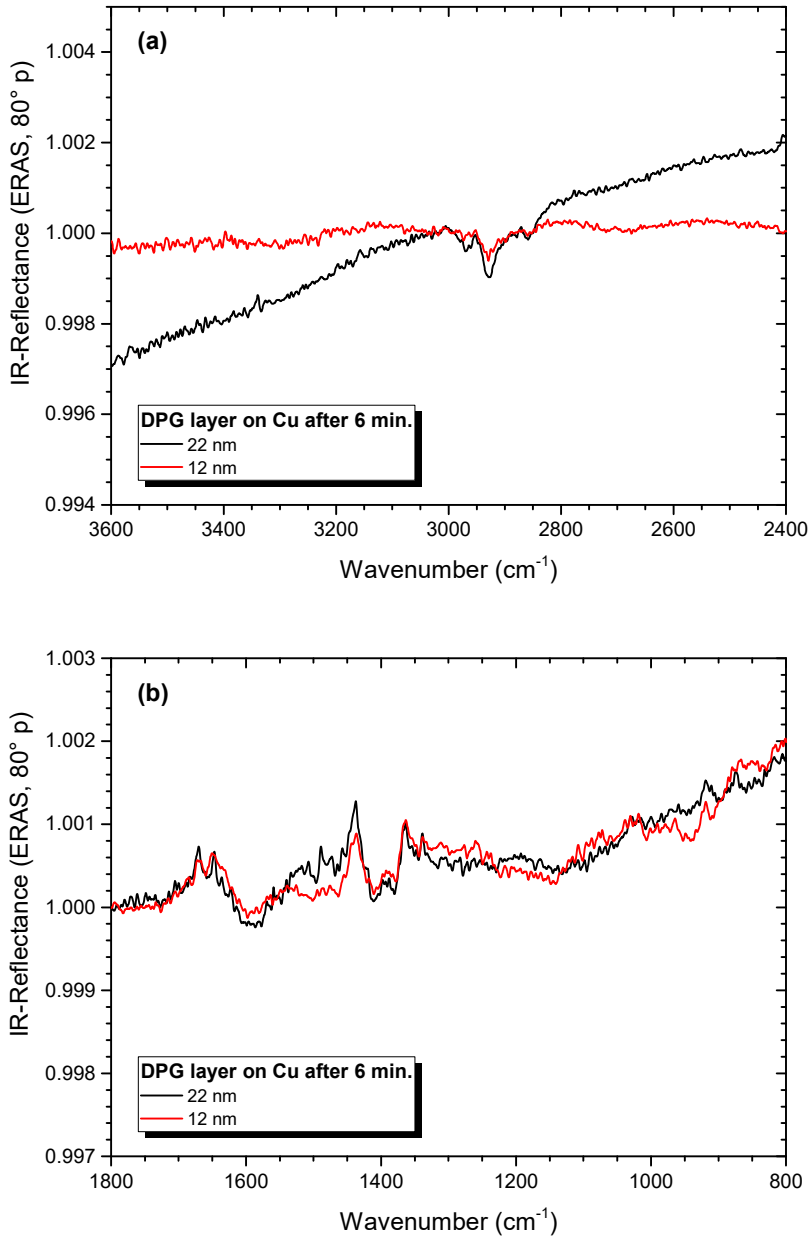

Fig. 11-7 Comparison of IR-ERA spectra of 22 nm (black) and 12 nm (red) DPG layers on Cu after complete desorption. (a) 3600 – 2400 cm^{-1}, (b) 1800 – 800 cm^{-1}.

11.5.2 Triol layers on native Cu

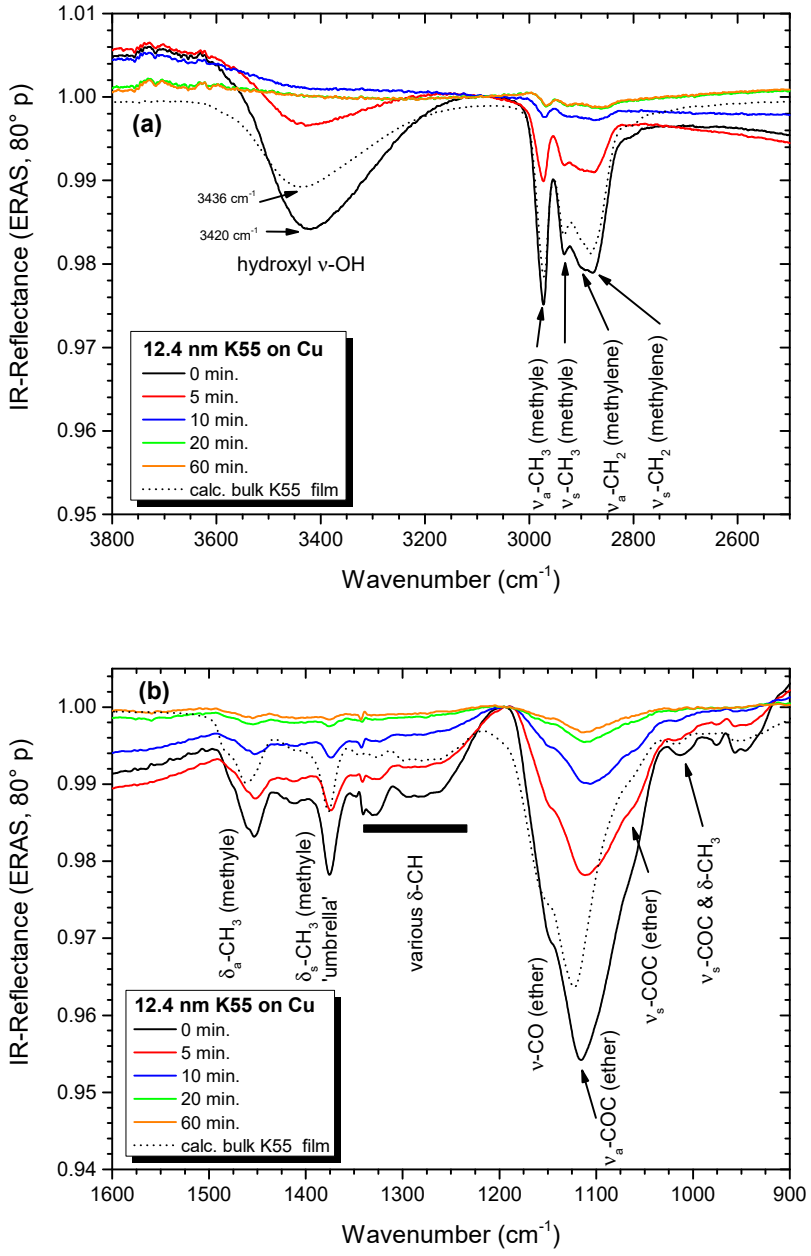

Fig. 11-8 IR-ERA spectra evolution of a 12.4 nm thin triol layer on Cu during the first hour of storage in dried air at RT. (a) 3800 – 2500 cm^{-1}, (b) 1600 – 900 cm^{-1}. The dashed spectrum presents a calculated bulk-like ERA spectrum for qualitative comparison. Deposition parameters: 500 mbar, 2 l/min, 10 °C substrate temperature.

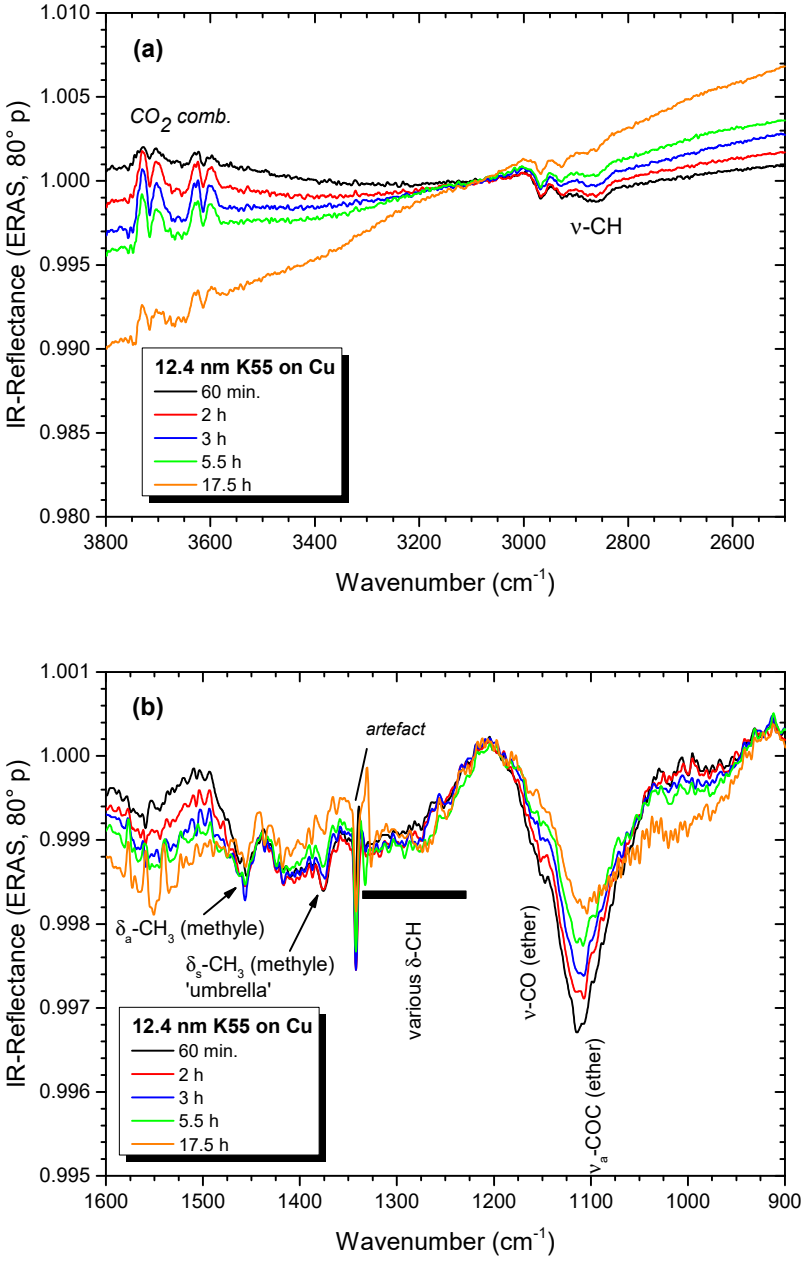

Fig. 11-9 IR-ERA spectra of a triol layer (12.4 nm initial thickness) on Cu during 18 h of storage in dried air at RT. (a) 3800 – 2500 cm^{-1}, (b) 1600 – 900 cm^{-1}. Deposition parameters: 500 mbar, 2 l/min, 10 °C substrate temperature.

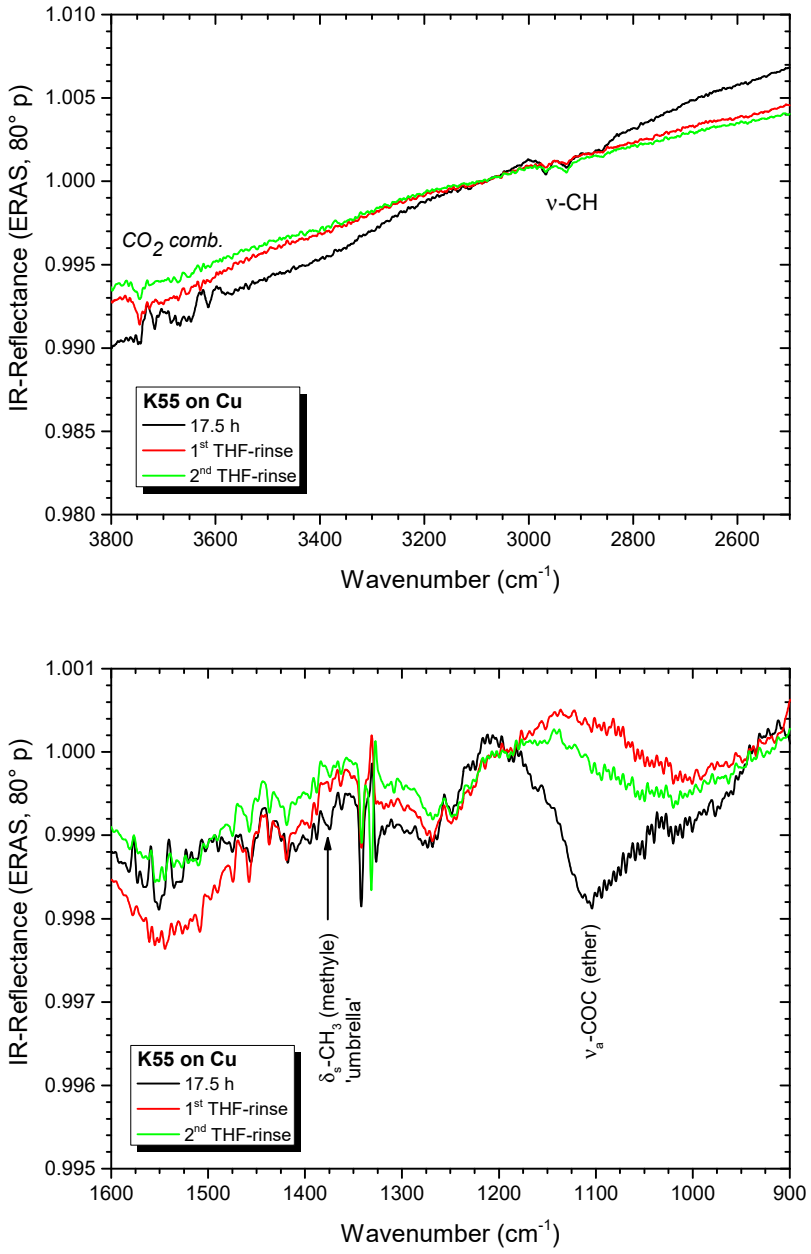

Fig. 11-10 IR-ERA spectra of a 12 nm thin triol layer on Cu after 18 h of storage in dried air at RT (black line) and after two subsequent THF rinses (red, green)). (a) 3800 – 2500 cm-1, (b) 1600 – 900 cm-1.

11.5.3 4,4'-MDI layers on native Cu

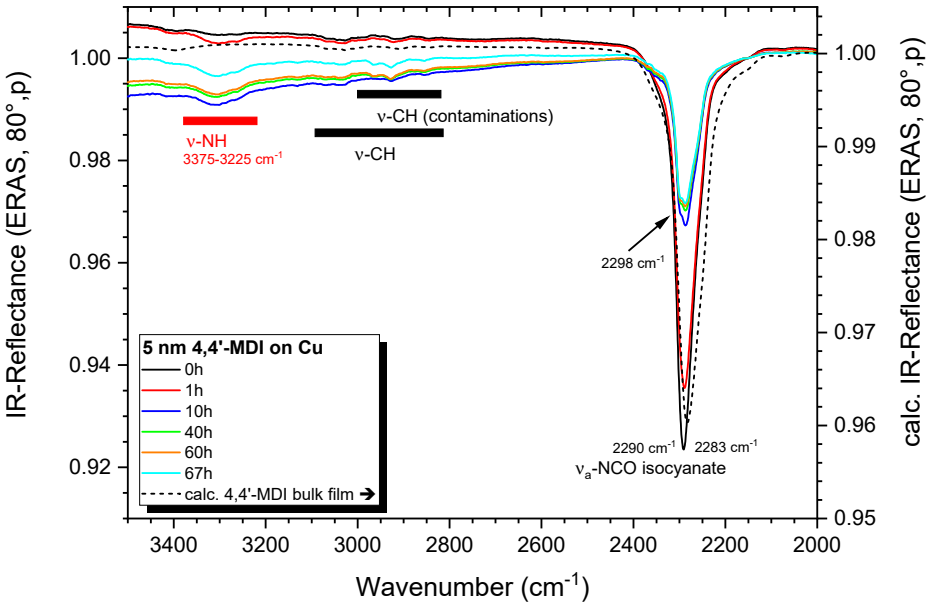

Fig. 11-11 IR-ERA spectra of a 5 nm 4,4'-MDI layer on native Cu oxide during 67 h of storage in dried air at RT. 3500 – 2000 cm^{-1}. Deposition parameters: 500 mbar, 2 l/min, 30 °C substrate temperature. Band assignment for 4,4'-MDI (black) and new species (red). The dashed line represents a calculated bulk-like ERA spectrum for qualitative comparison.

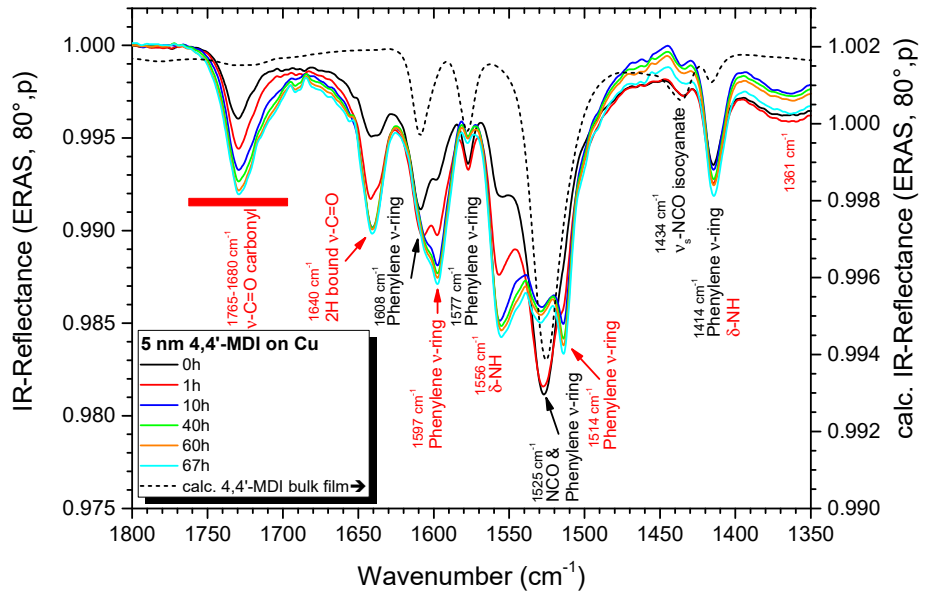

Fig. 11-12 IR-ERA spectra of a 5 nm 4,4'-MDI layer on native Cu oxide during 67 h of storage in dried air at RT. 1800 – 1350 cm^{-1}. Deposition parameters: 500 mbar, 2 l/min, 30 °C substrate temperature. Band assignment for 4,4'-MDI (black) and new species (red). The dashed line represents a calculated bulk-like ERA spectrum for qualitative comparison.

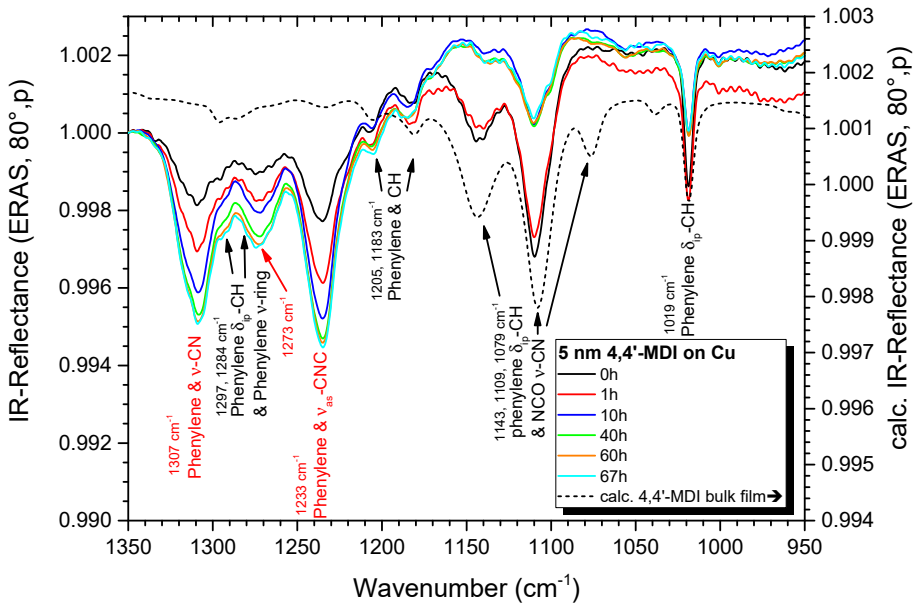

Fig. 11-13 IR-ERA spectra of a 5 nm 4,4'-MDI layer on native Cu oxide during 67 h of storage in dried air at RT. 1350 – 950 cm^{-1}. Deposition parameters: 500 mbar, 2 l/min, 30 °C substrate temperature. Band assignment for 4,4'-MDI (black) and new species (red). The dashed line represents a calculated bulk-like ERA spectrum for qualitative comparison.

11.5.4 Temperature influence on 4,4'-MDI layers

◊ *Deposition at 10 °C on Al and storage at RT*

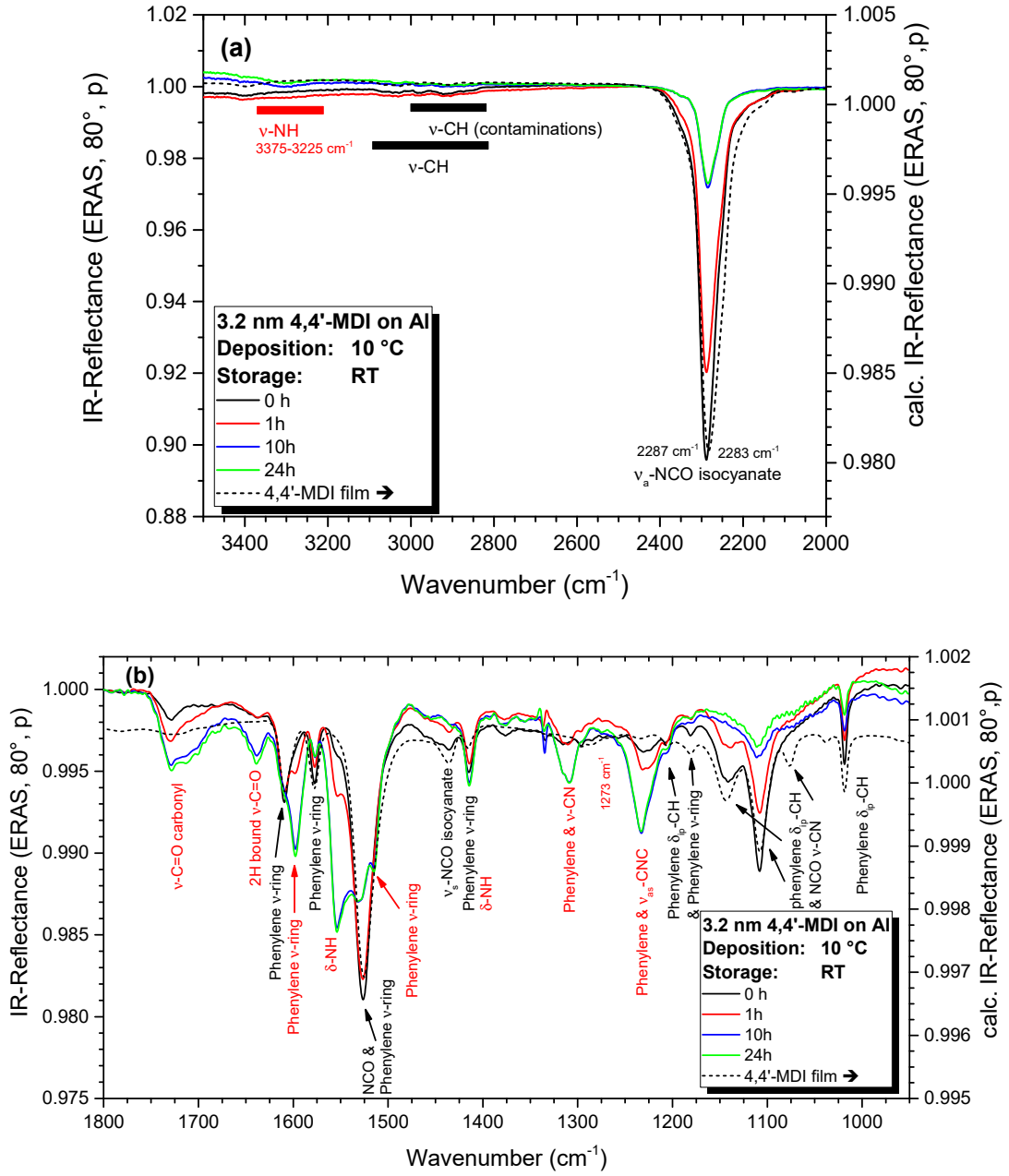

Fig. 11-14 IR-ERA spectra of a 4,4'-MDI layer (initial thickness 3.2 nm) on native Al oxide. Deposition at 10 °C and evolution during 24 h of storage in dried air at RT. Deposition parameters: 500 mbar, 5 l/min,. Band assignment for 4,4'-MDI (black) and newly emerging species (red). Dashed line: calculated bulk-like ERA spectrum for qualitative comparison. (a) 3500 – 2000 cm^{-1}, (b) 1800 – 950 cm^{-1}.

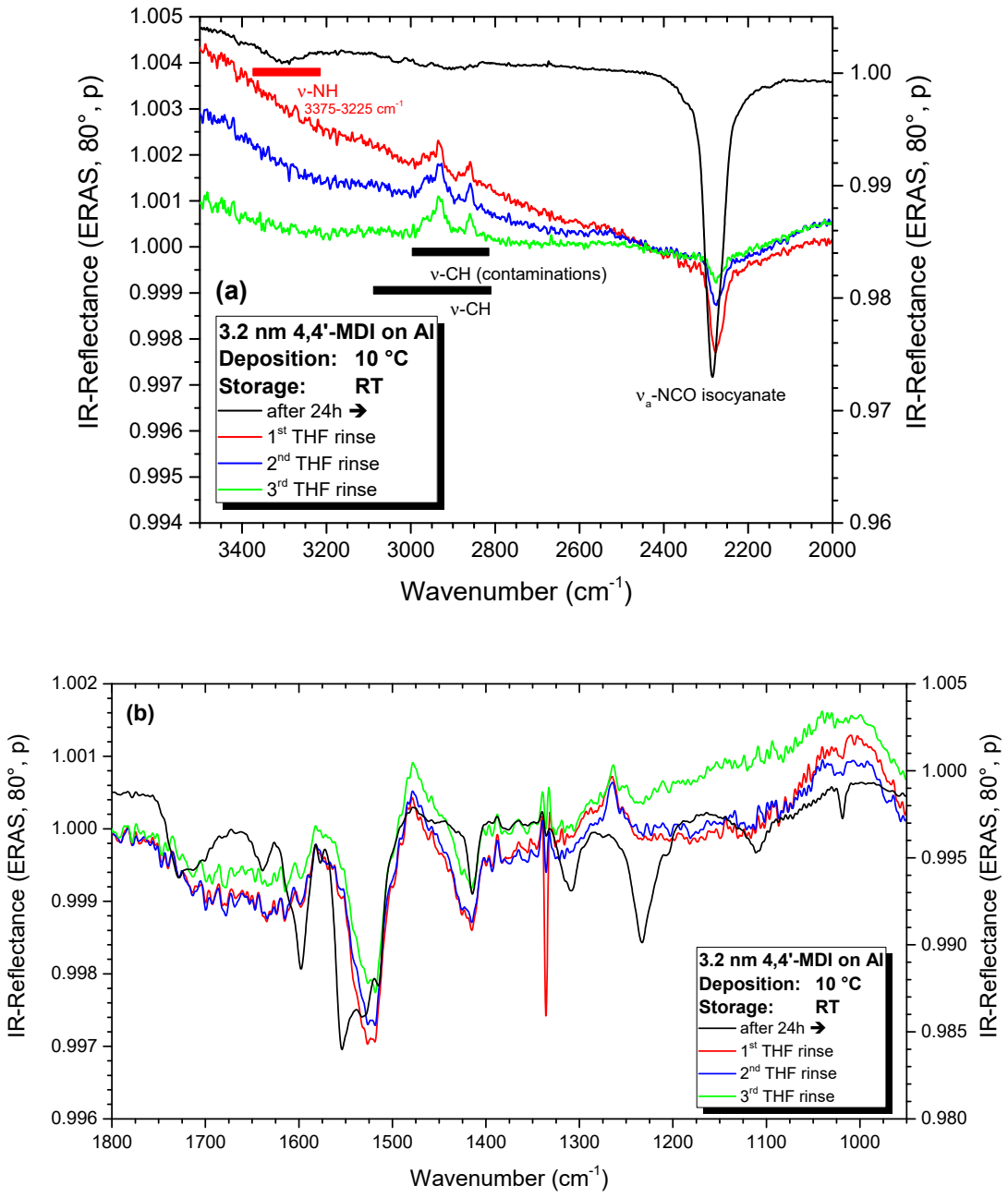

Fig. 11-15 Effect of THF rinse on a 4,4'-MDI layer (initial thickness 3.2 nm) on native Al oxide. Deposition at 10 °C and 24 h of storage in dried air at RT. The black line represents the layer before the THF rinses. (a) 3500 – 2000 cm^{-1}, (b) 1800 – 950 cm^{-1}.

◊ *Deposition at 10 °C on Al and storage at 50 °C*

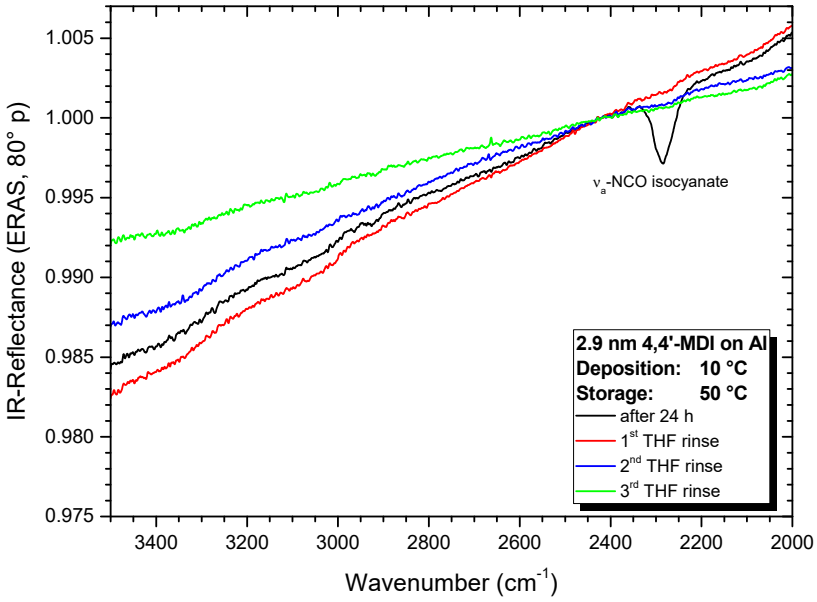

Fig. 11-16 Effect of THF rinse on a 4,4'-MDI layer (initial thickness 2.9 nm) on native Al oxide. Deposition at 10 °C and 24 h of storage in dried air at 50 °C. The black line represents the layer before the THF rinses. 3500 – 2000 cm^{-1}.

◊ *Comparison of layers deposited at 10 °C on Al and stored at RT or 50 °C*

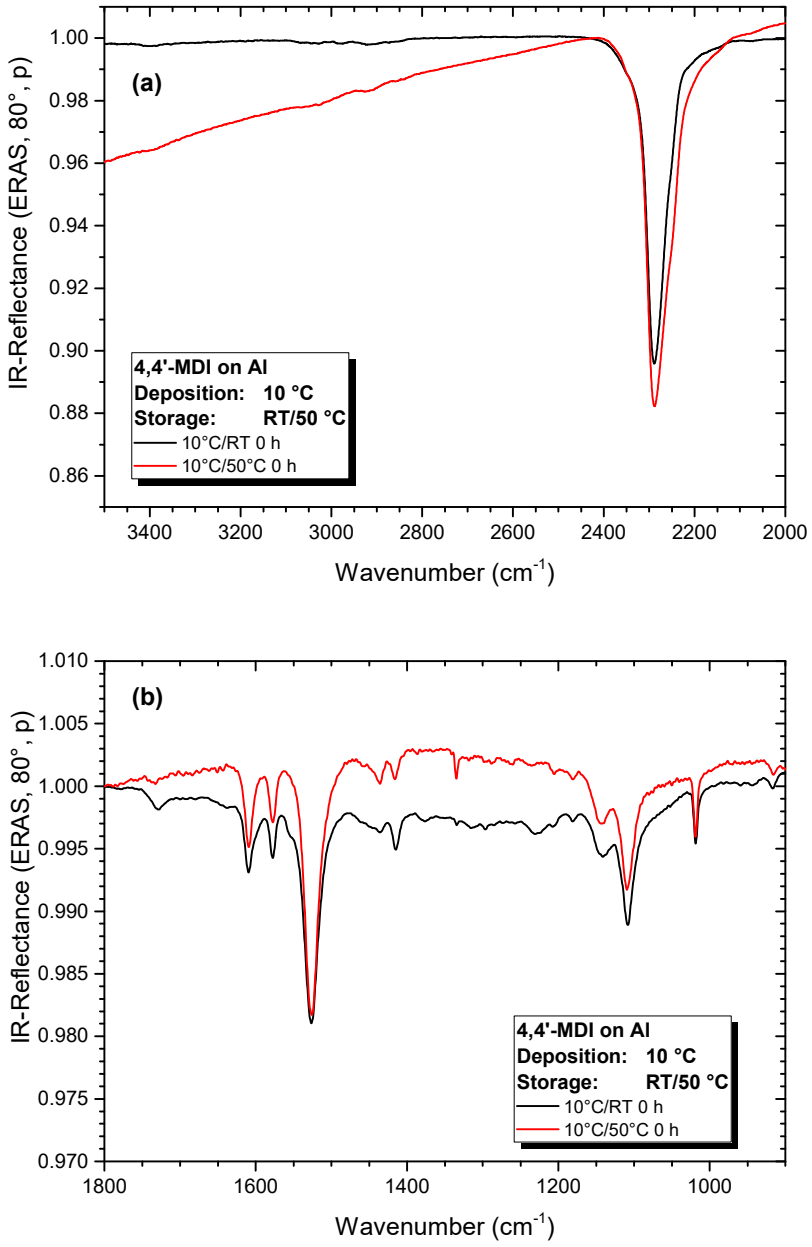

Fig. 11-17 Comparison of two 4,4'-MDI layers deposited on native Al oxide at 10 °C and stored at RT (black) or 50 °C (red). IR-ERA spectra right after deposition and thermal equilibration (Storage time = 0 h). Deposition parameters: 500 mbar, 5 l/min. (a) 3500 – 2000 cm^{-1}, (b) 1800 – 900 cm^{-1}.

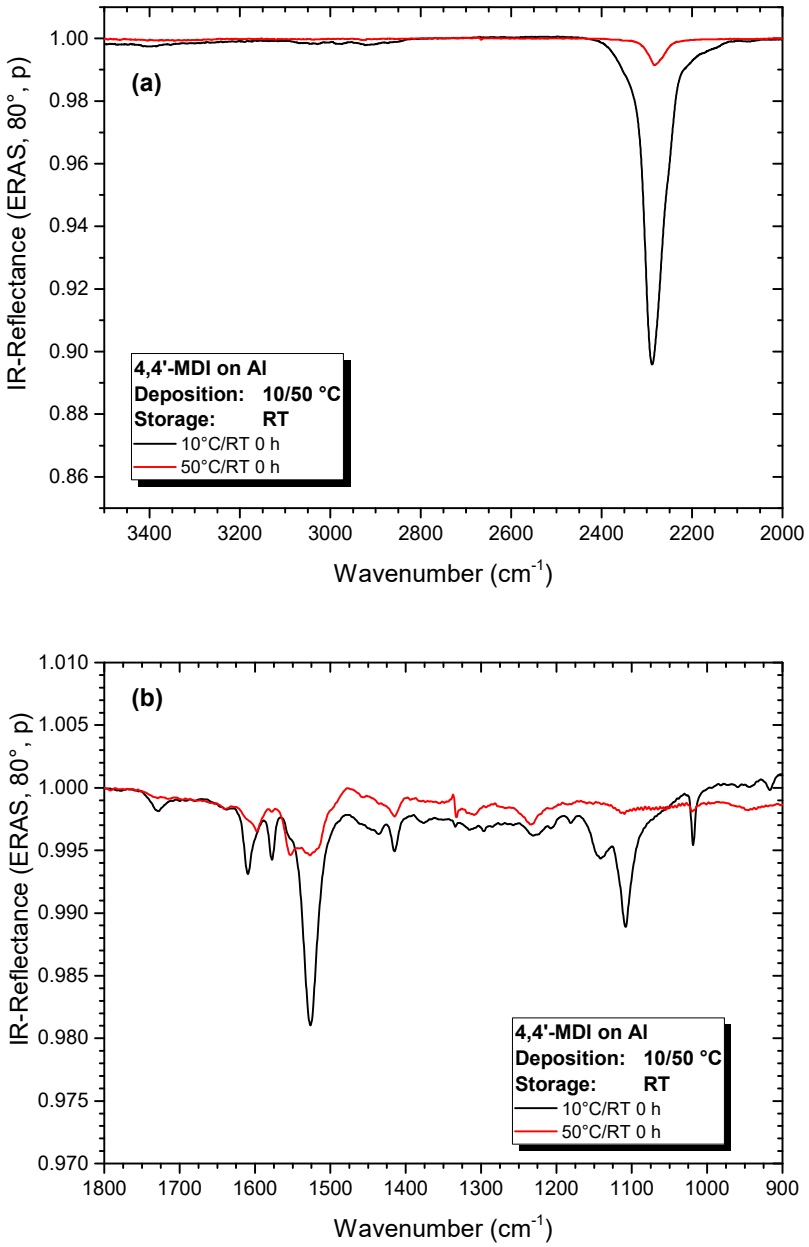

Fig. 11-18 Comparison of two 4,4'-MDI layers on native Al oxide deposited at 10 °C (black) and 50 °C (red) and then stored at RT. IR-ERA spectra right after deposition (Storage time = 0 h). Deposition parameters: 500 mbar, 5 l/min. (a) 3500 – 2000 cm^{-1}, (b) 1800 – 900 cm^{-1}.

11.6 Thin polymer deposits

11.6.1 DPG deposited on top of 4,4'-MDI on Cu

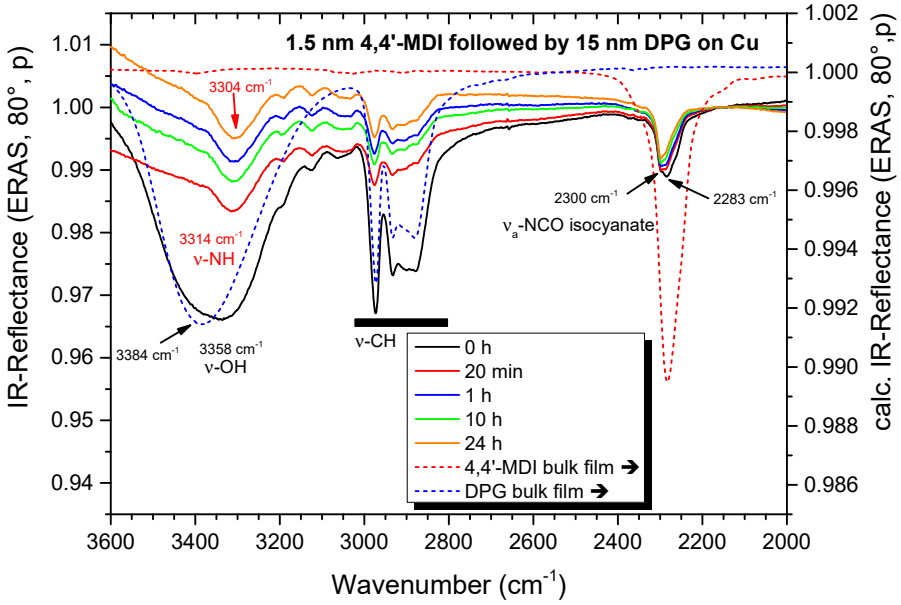

Fig. 11-19 IR-ERA spectra from a bilayer of 1.5 nm MDI and 15 nm DPG on native Cu. Storage time over 24 h in dried air at RT. 3600 – 2000 cm^{-1}. Band assignment for the monomers (black) and for new species (red). For qualitative comparison, the dashed lines represent calculated spectra of the bulk monomers.

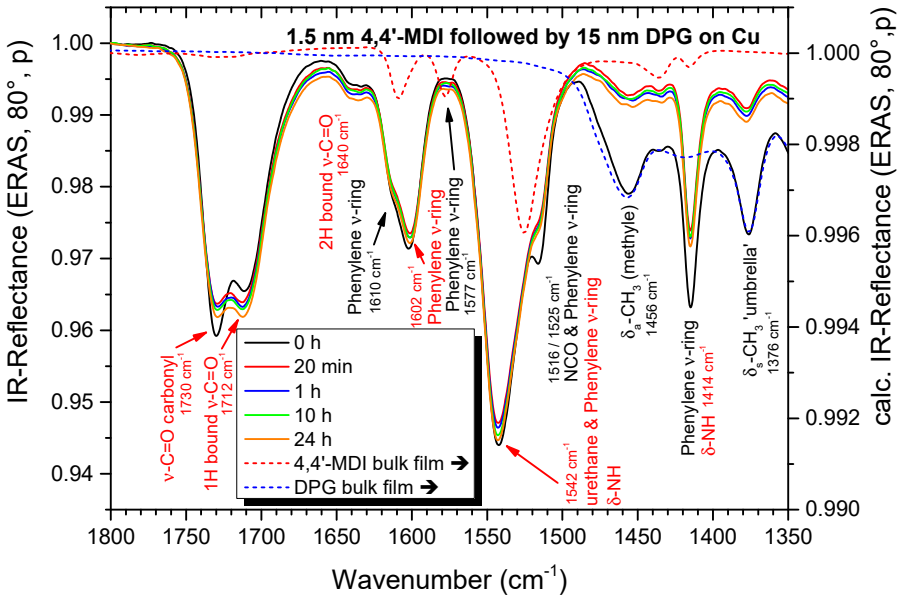

Fig. 11-20 IR-ERA spectra from a bilayer of 1.5 nm MDI and 15 nm DPG on native Cu. Storage time over 24 h in dried air at RT. 1800 – 1350 cm^{-1}. Band assignment for the monomers (black) and new species (red). For qualitative comparison, the dashed lines represent calculated spectra of the bulk monomers.

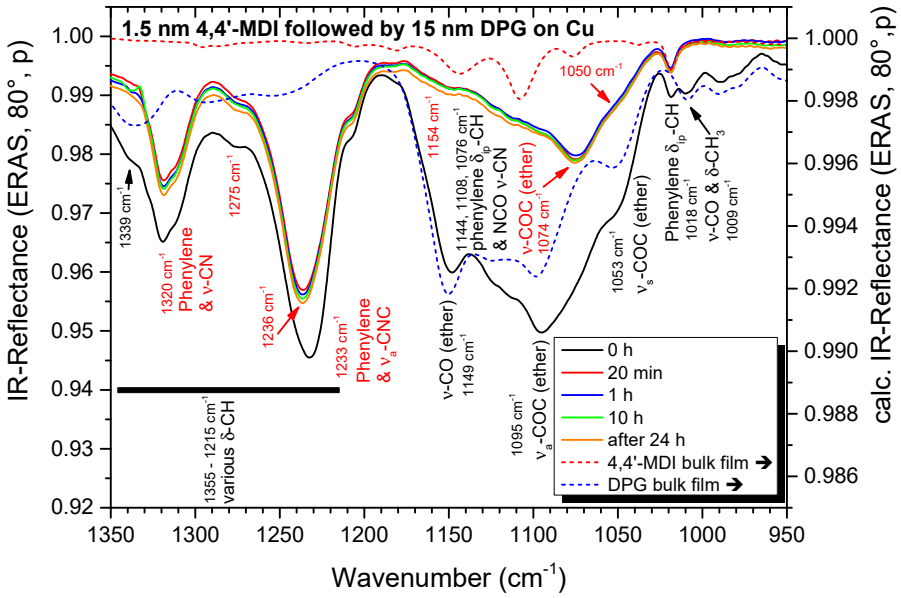

Fig. 11-21 IR-ERA spectra from a bilayer of 1.5 nm MDI and 15 nm DPG on native Cu. Storage time over 24 h in dried air at RT. 1350 – 950 cm^{-1}. Band assignment for the monomers (black) and new species (red). For qualitative comparison, the dashed lines represent calculated spectra of the bulk monomers.

11.6.2 Triol deposited on top of 4,4'-MDI on Al

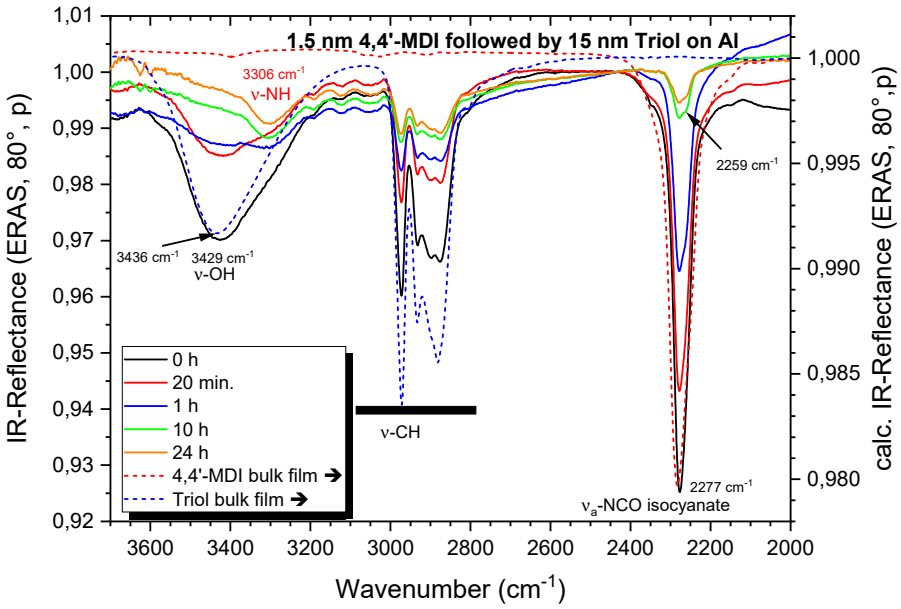

Fig. 11-22 IR-ERA spectra from a bilayer of a 1.5 nm MDI and 15 nm triol on native Al Storage time over 24 h in dried air at RT. 3600 – 2000 cm^{-1}. Band assignment for the monomers (black) and new species (red). For qualitative comparison, the dashed lines represent calculated spectra of the bulk monomers.

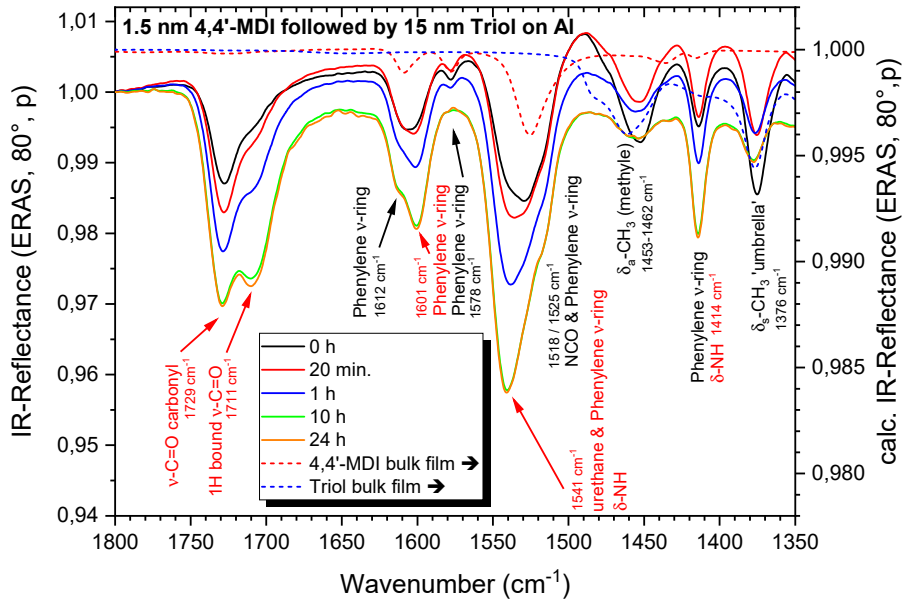

Fig. 11-23 IR-ERA spectra from a bilayer of a 1.5 nm MDI and 15 nm triol on native Al Storage time over 24 h in dried air at RT. 1800 – 1350 cm^{-1}. Band assignment for the monomers (black) and new species (red). For qualitative comparison, the dashed lines represent calculated spectra of the bulk monomers.

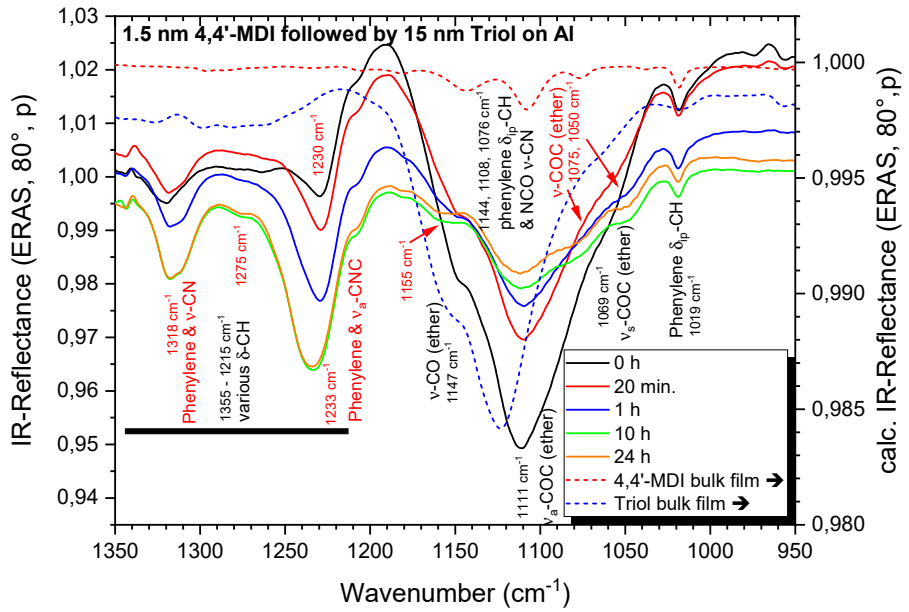

Fig. 11-24 IR-ERA spectra from a bilayer of a 1.5 nm MDI and 15 nm triol on native Al Storage time over 24 h in dried air at RT. 1350 – 950 cm^{-1}. Band assignment for the monomers (black) and new species (red). For qualitative comparison, the dashed lines represent calculated spectra of the bulk monomers.

11.6.3 Triol deposited on top of 4,4'-MDI on Cu

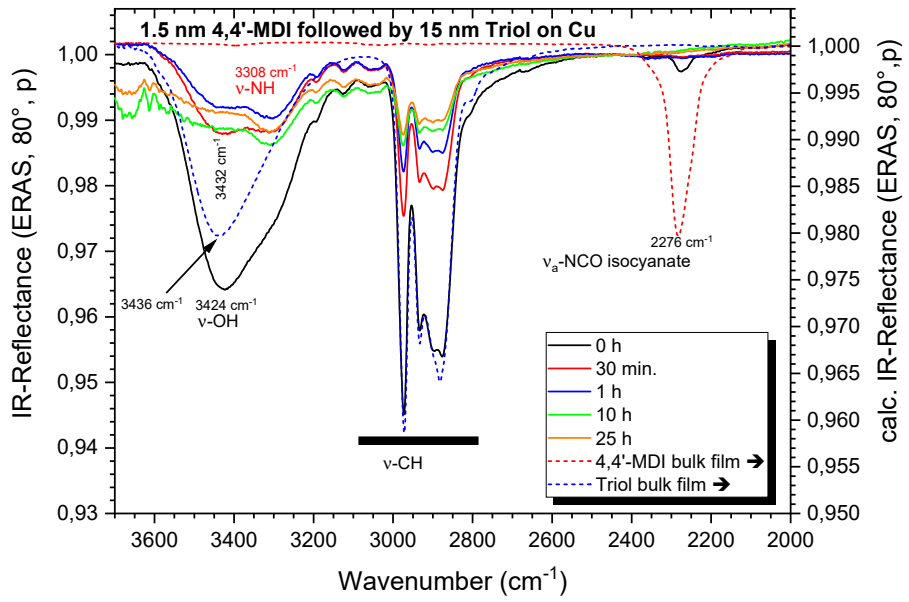

Fig. 11-25 IR-ERA spectra from a bilayer of 1.5 nm MDI and 15 nm triol on native Cu. Storage time over 24 h in dried air at RT. 3600 – 2000 cm^{-1}. Band assignment for the monomers (black) and new species (red). For qualitative comparison, the dashed lines represent calculated spectra of the bulk monomers.

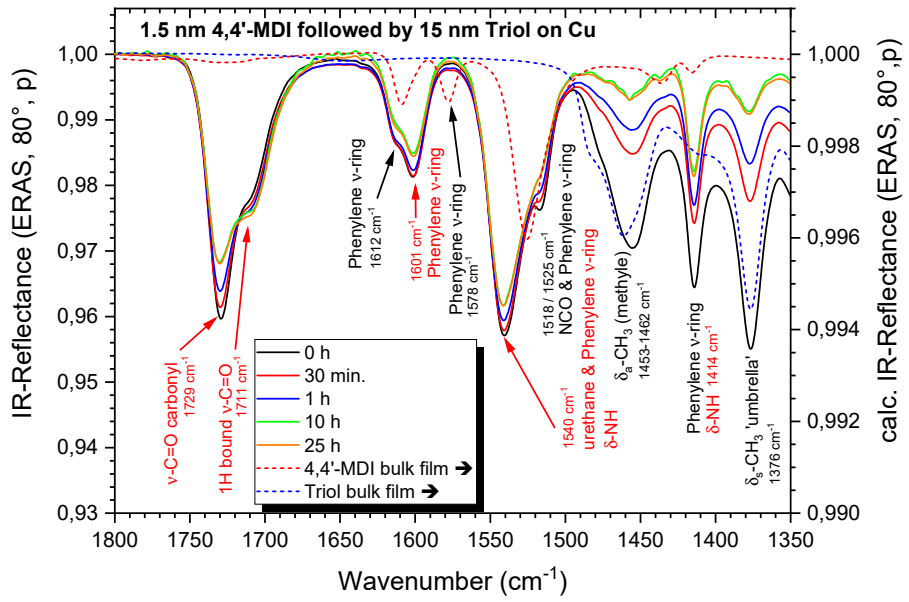

Fig. 11-26 IR-ERA spectra from a bilayer of 1.5 nm MDI and 15 nm triol on native Cu. Storage time over 24 h in dried air at RT. 1800 – 1350 cm^{-1}. Band assignment for the monomers (black) and new species (red). For qualitative comparison, the dashed lines represent calculated spectra of the bulk monomers.

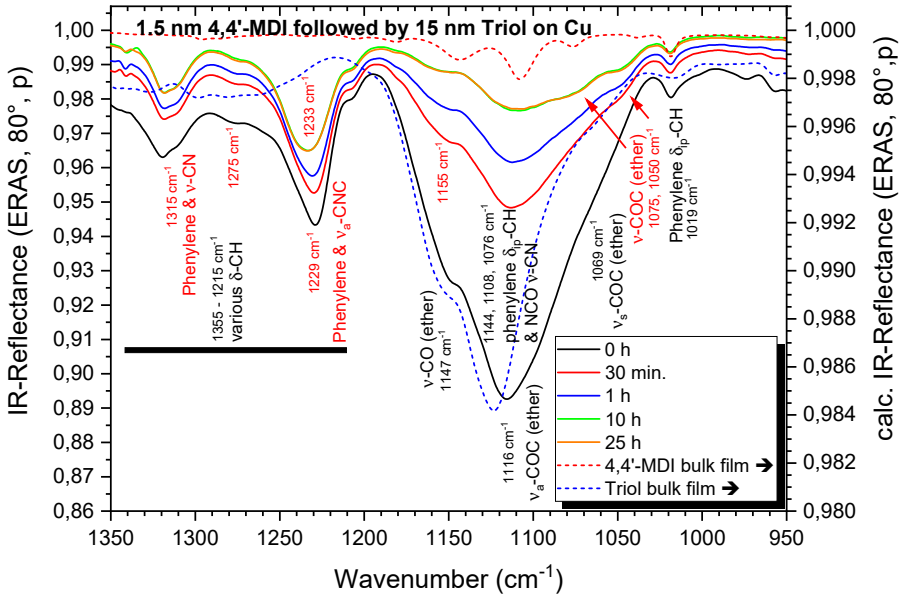

Fig. 11-27 IR-ERA spectra from a bilayer of 1.5 nm MDI and 15 nm triol on native Cu. Storage time over 24 h in dried air at RT. 1350 – 950 cm^{-1}. Band assignment for the monomers (black) and new species (red). For qualitative comparison, the dashed lines represent calculated spectra of the bulk monomers.

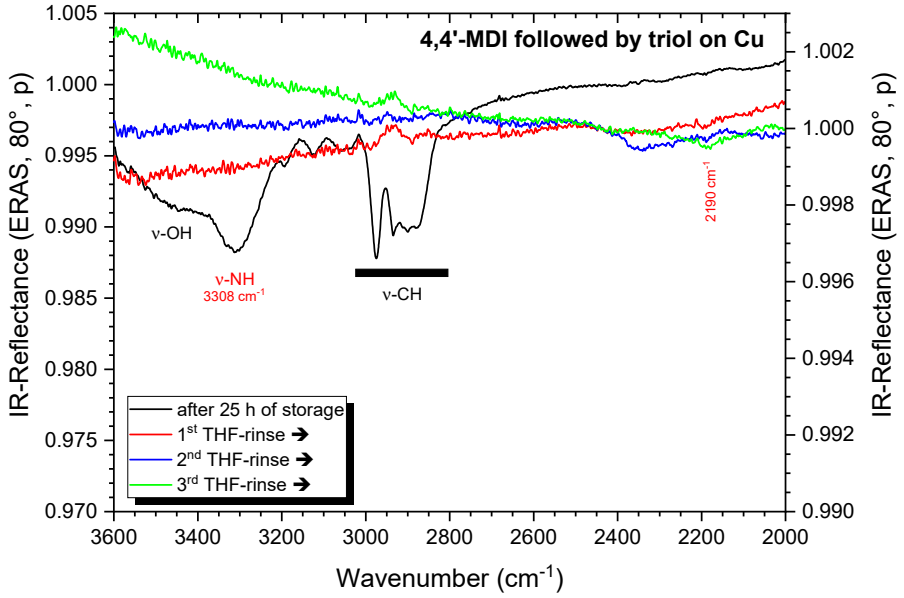

Fig. 11-28 Effect of THF rinses on a layer prepared by deposition of 4,4'-MDI followed by triol on Cu after 25 h of storage in dried air at RT. 3600 – 2000 cm^{-1}. The black spectrum represents the layer prior to the THF rinses. Band assignment for the monomers (black) and new species (red) refer to the black spectrum.

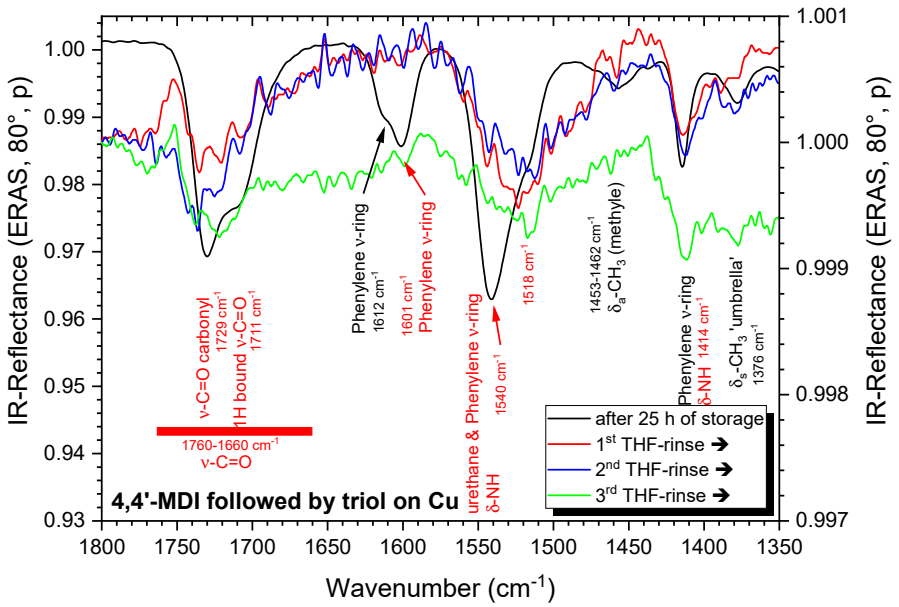

Fig. 11-29 Effect of THF rinses on a layer prepared by deposition of 4,4'-MDI followed by triol on Cu after 25 h of storage in dried air at RT. 1800 – 1350 cm^{-1}. The black spectrum represents the layer prior to the THF rinses. Band assignment for the monomers (black) and new species (red) refer to the black spectrum.

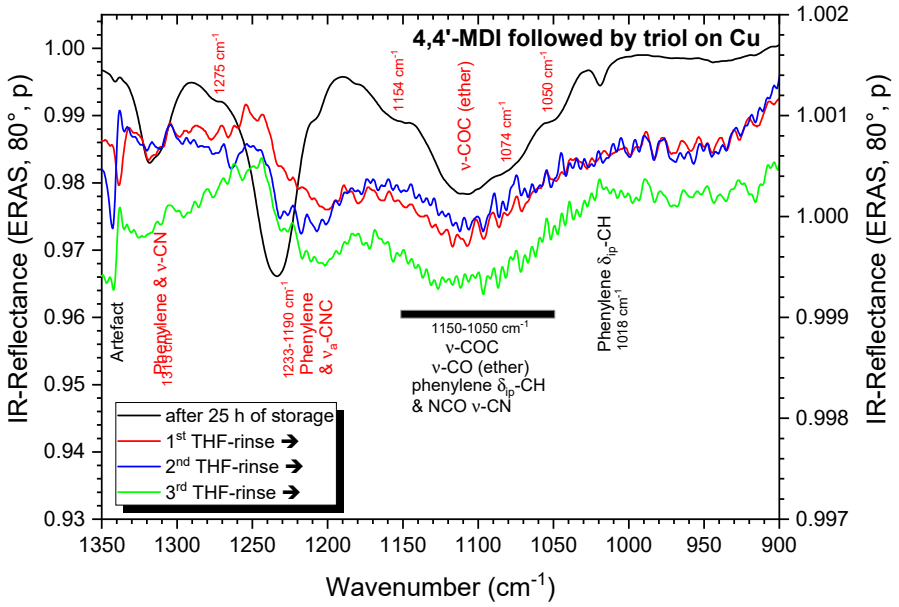

Fig. 11-30 Effect of THF rinses on a layer prepared by deposition of 4,4'-MDI followed by triol on Cu after 25 h of storage in dried air at RT. 1350 – 900 cm^{-1}. The black spectrum represents the layer prior to the THF rinses. Band assignment for the monomers (black) and new species (red) refer to the black spectrum.

11.6.4 4,4'-MDI deposited on top of triol on Al

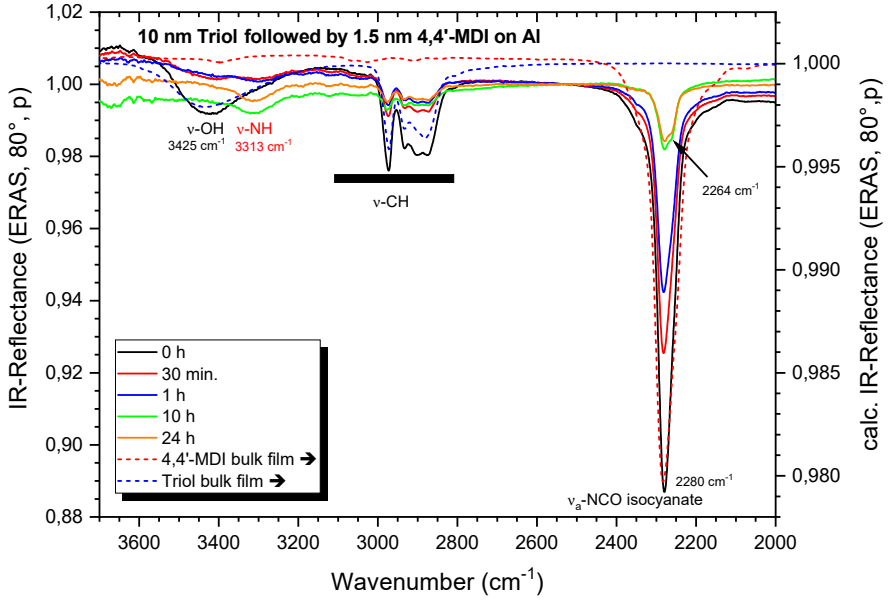

Fig. 11-31 IR-ERA spectra from a bilayer of 10 nm triol and 1.5 nm MDI on native Al. Storage time over 24 h in dried air at RT. 3600 – 2000 cm^{-1}. Band assignment for the monomers (black) and new species (red). For qualitative comparison, the dashed lines represent calculated spectra of the bulk monomers.

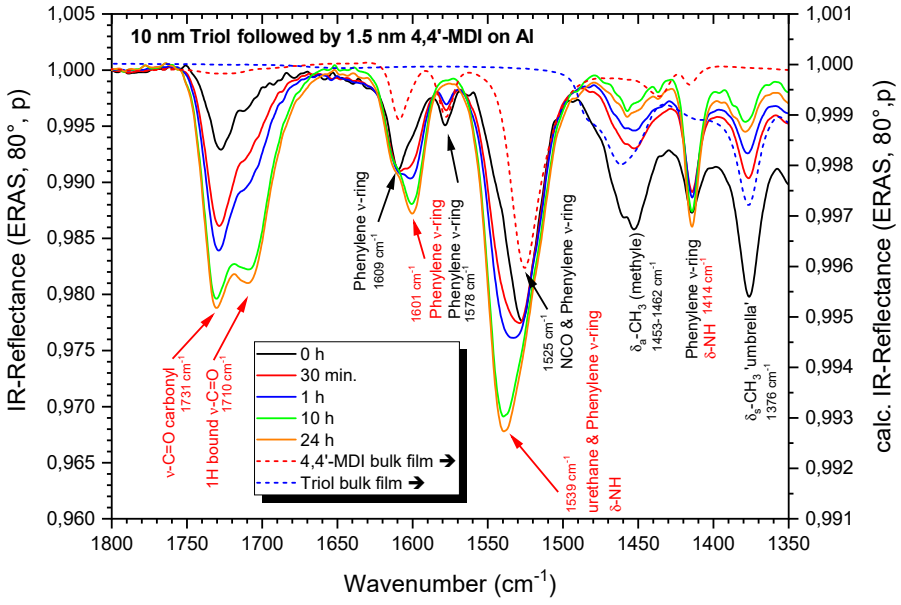

Fig. 11-32 IR-ERA spectra from a bilayer of 10 nm triol and 1.5 nm MDI on native Al. Storage time over 24 h in dried air at RT. 1800 – 1350 cm^{-1}. Band assignment for the monomers (black) and new species (red). For qualitative comparison, the dashed lines represent calculated spectra of the bulk monomers.

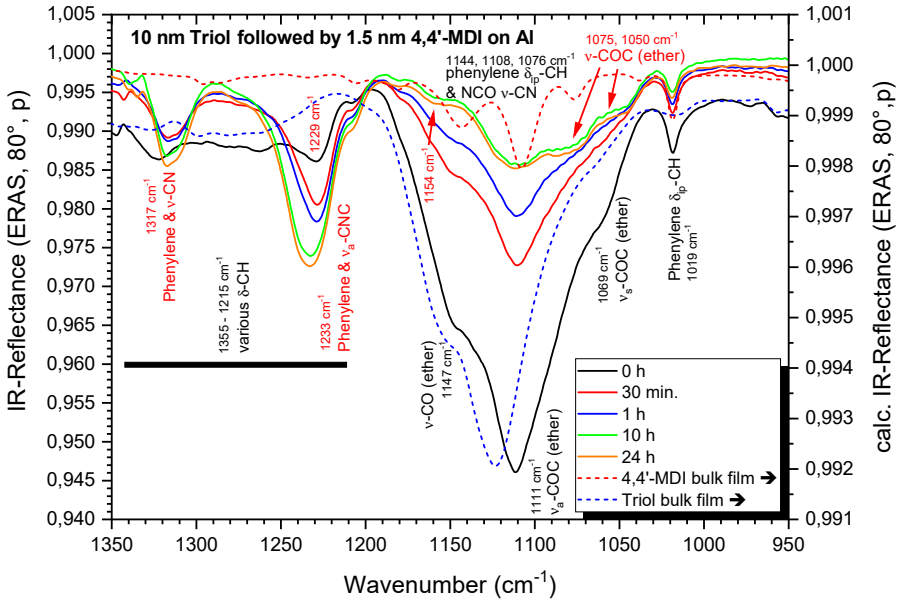

Fig. 11-33 IR-ERA spectra from a bilayer of 10 nm triol and 1.5 nm MDI on native Al. Storage time over 24 h in dried air at RT. 1350 – 950 cm^{-1}. Band assignment for the monomers (black) and new species (red). For qualitative comparison, the dashed lines represent calculated spectra of the bulk monomers.

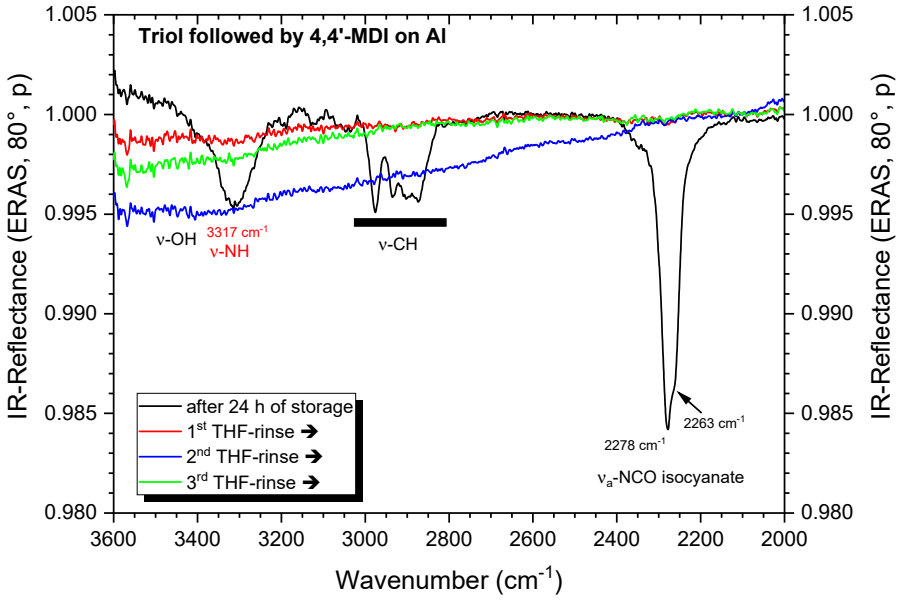

Fig. 11-34 Effect of THF rinses on a layer prepared by deposition of triol followed by 4,4'-MDI on Al after 24 h of storage in dried air at RT. 3600 – 2000 cm^{-1}. The black spectrum represents the layer prior to the THF rinses. Band assignment for the monomers (black) and new species (red) refer to the black spectrum.

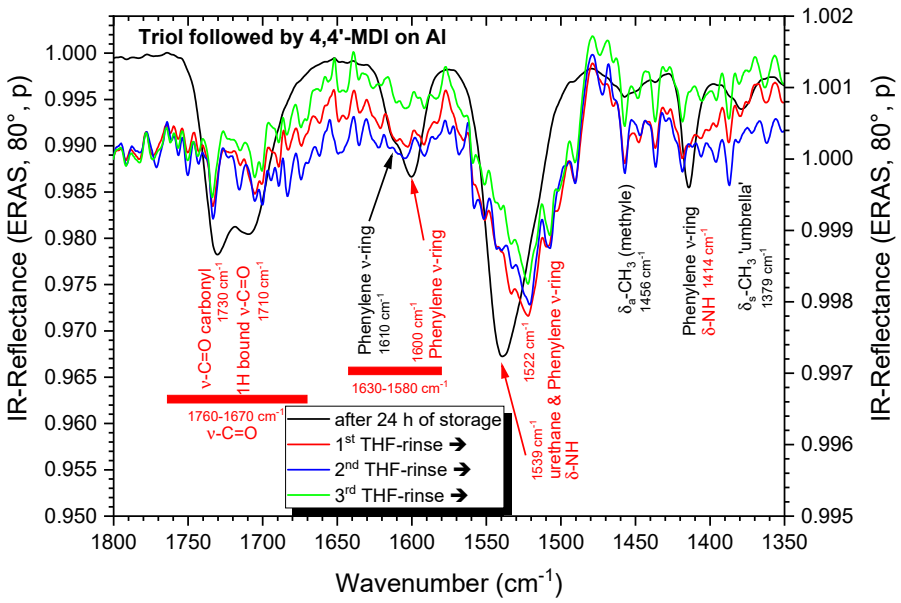

Fig. 11-35 Effect of THF rinses on a layer prepared by deposition of triol followed by 4,4'-MDI on Al after 24 h of storage in dried air at RT. 1800 – 1350 cm^{-1}. The black spectrum represents the layer prior to the THF rinses. Band assignment for the monomers (black) and new species (red) refer to the black spectrum.

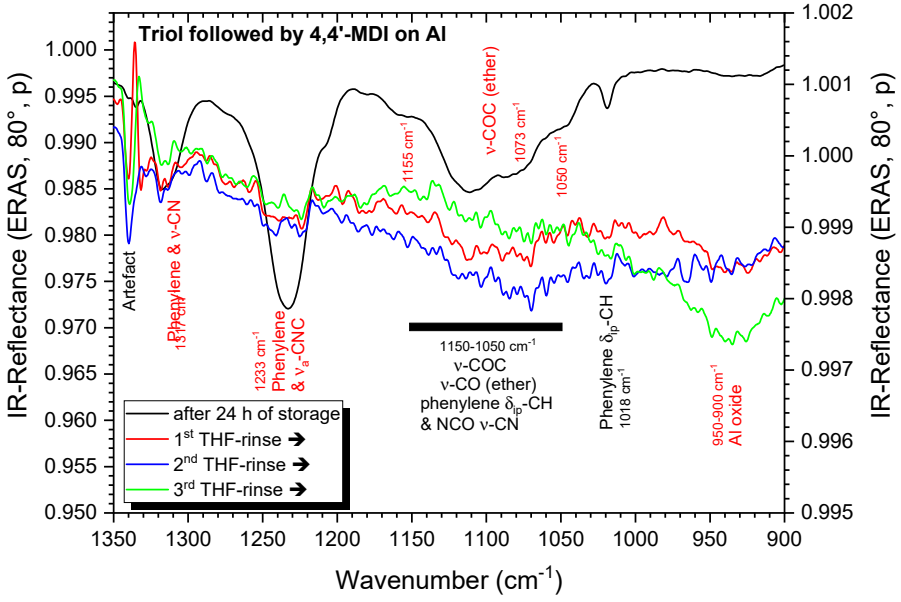

Fig. 11-36 Effect of THF rinses on a layer prepared by deposition of triol followed by 4,4'-MDI on Al after 24 h of storage in dried air at RT. 1350 – 900 cm^{-1}. The black spectrum represents the layer prior to the THF rinses. Band assignment for the monomers (black) and new species (red) refer to the black spectrum.

11.6.5 4,4'-MDI deposited on top of triol on Cu

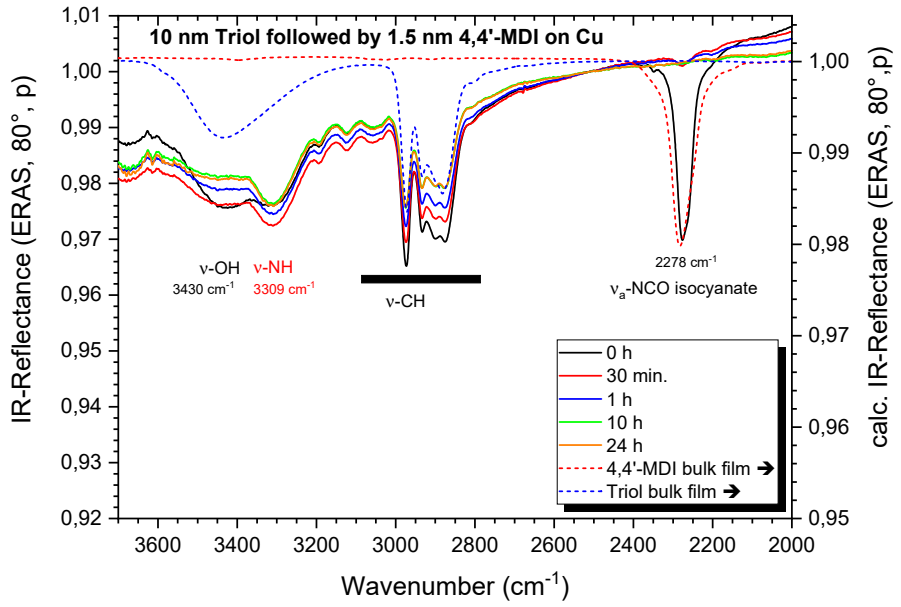

Fig. 11-37 IR-ERA spectra from a bilayer of 10 nm triol and 1.5 nm MDI on native Cu Storage time over 24 h in dried air at RT. 3600 – 2000 cm^{-1}. Band assignment for the monomers (black) and new species (red). For qualitative comparison, the dashed lines represent calculated spectra of the bulk monomers.

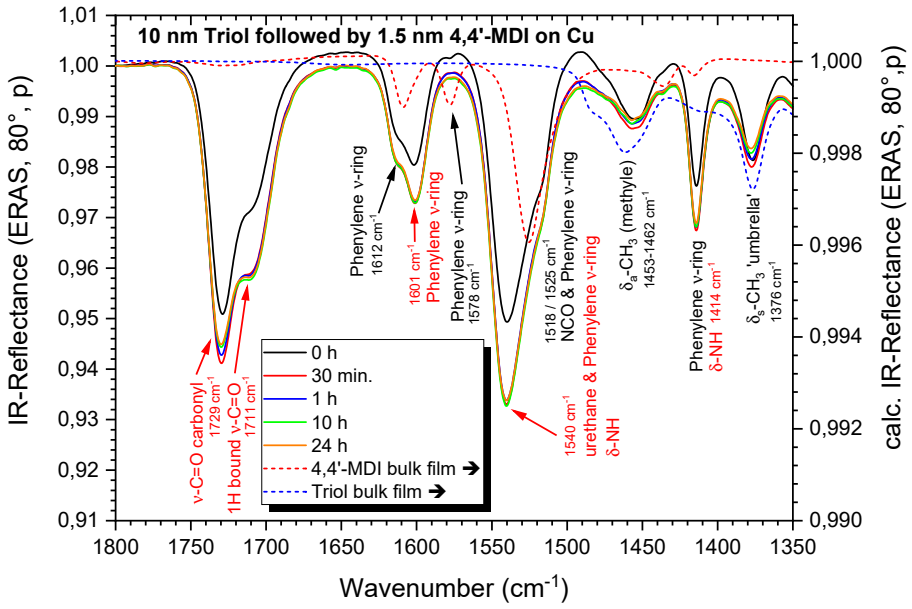

Fig. 11-38 IR-ERA spectra from a bilayer of 10 nm triol and 1.5 nm MDI on native Cu Storage time over 24 h in dried air at RT. 1800 – 1350 cm^{-1}. Band assignment for the monomers (black) and new species (red). For qualitative comparison, the dashed lines represent calculated spectra of the bulk monomers.

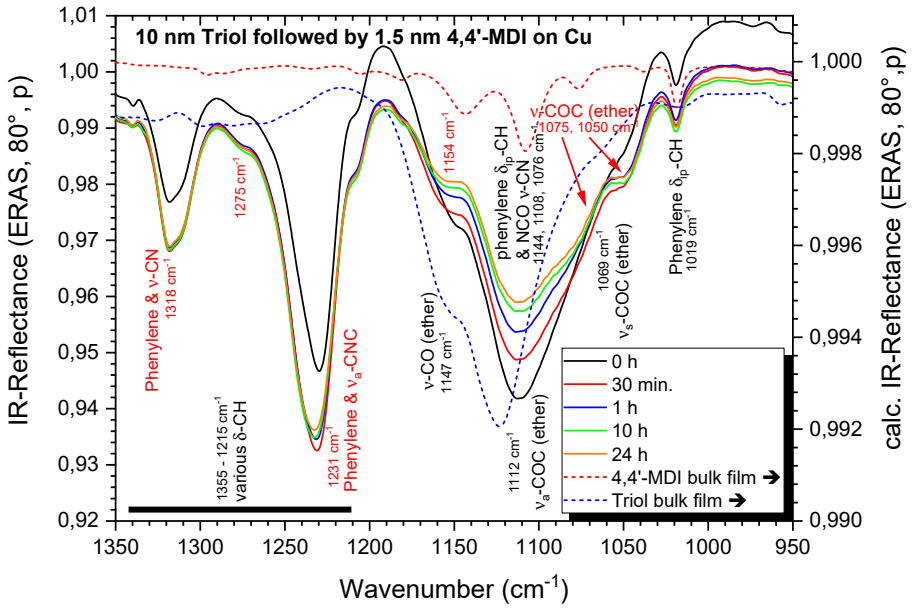

Fig. 11-39 IR-ERA spectra from a bilayer of 10 nm triol and 1.5 nm MDI on native Cu Storage time over 24 h in dried air at RT. 1350 – 950 cm^{-1}. Band assignment for the monomers (black) and new species (red). For qualitative comparison, the dashed lines represent calculated spectra of the bulk monomers.

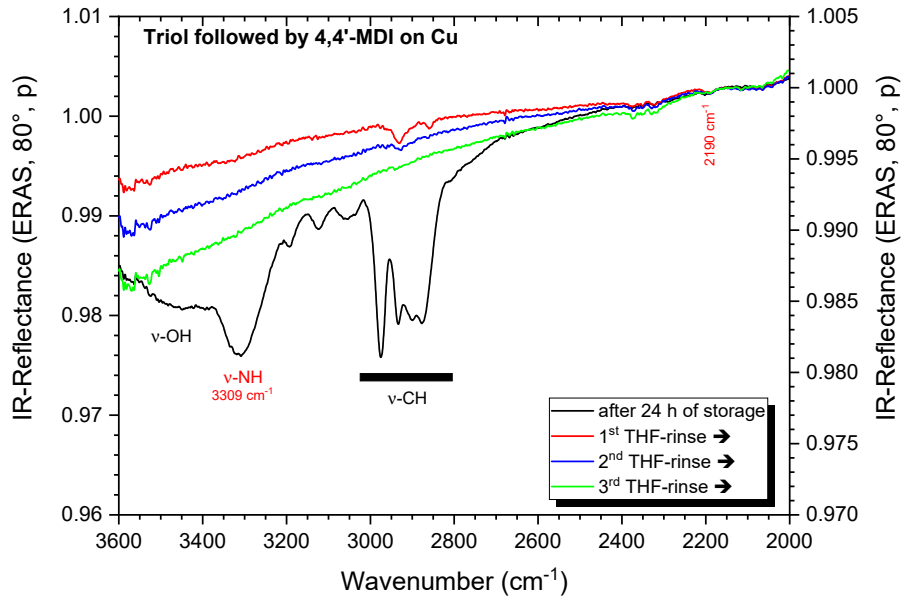

Fig. 11-40 Effect of THF rinses on a layer prepared by deposition of triol followed by 4,4'-MDI on Cu after 24 h of storage in dried air at RT. 3600 – 2000 cm^{-1}. The black spectrum represents the layer prior to the THF rinses. Band assignment for the monomers (black) and new species (red) refer to the black spectrum.

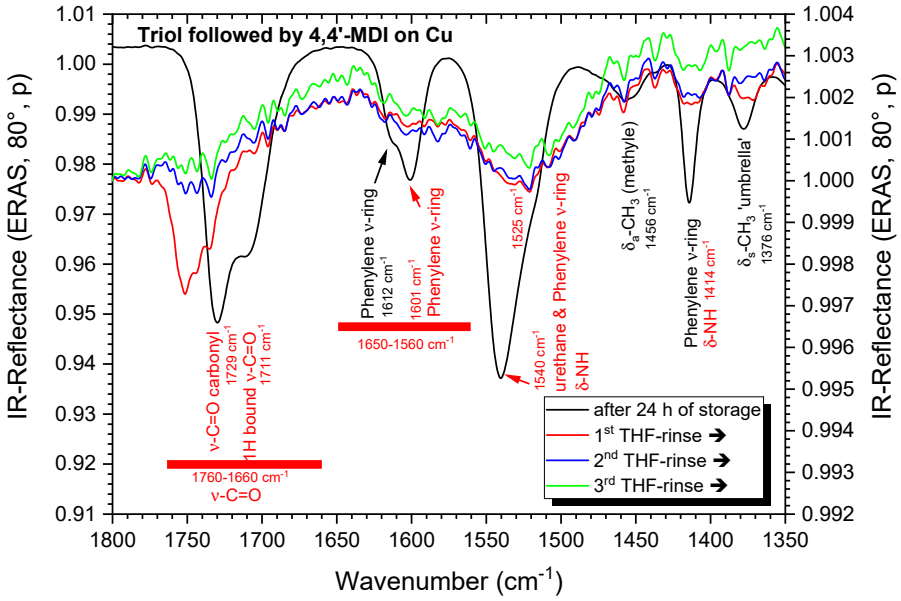

Fig. 11-41 Effect of THF rinses on a layer prepared by deposition of triol followed by 4,4'-MDI on Cu after 24 h of storage in dried air at RT. 1800 – 1350 cm^{-1}. The black spectrum represents the layer prior to the THF rinses. Band assignment for the monomers (black) and new species (red) refer to the black spectrum.

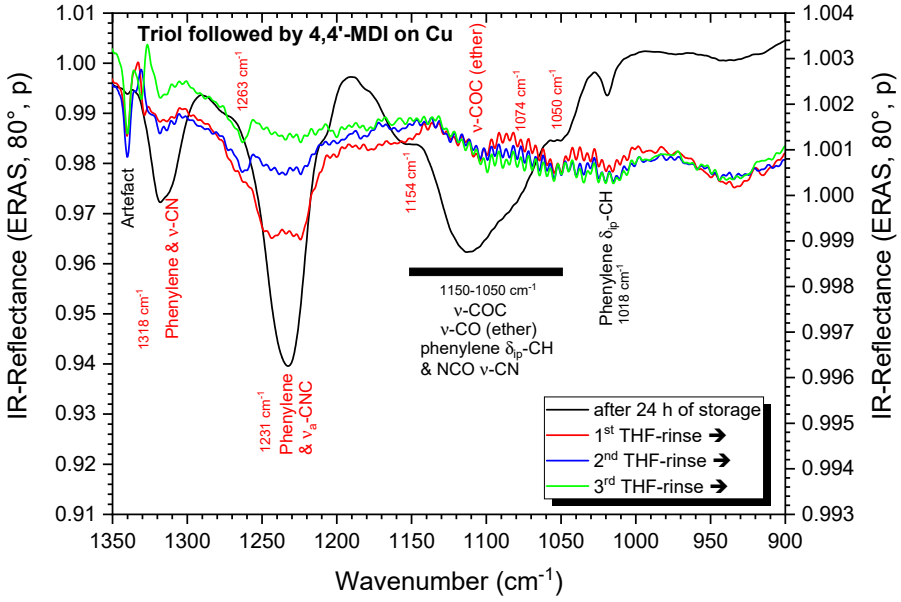

Fig. 11-42 Effect of THF rinses on a layer prepared by deposition of triol followed by 4,4'-MDI on Cu after 24 h of storage in dried air at RT. 1350 – 900 cm^{-1}. The black spectrum represents the layer prior to the THF rinses. Band assignment for the monomers (black) and new species (red) refer to the black spectrum.